Imperial College London

An Investigation into H_2 Production by Sorbent Enhanced Steam Reforming of Biomass

Peter Thomas Clough

Supervised by Professor Paul Fennell

Department of Chemical Engineering

Imperial College London of Science, Technology and Medicine

Thesis submitted for the degree of Doctor of Philosophy (PhD) to

Imperial College London of Science, Technology and Medicine

June 2017

Abstract

This thesis is based around the production of H_2 via a process called Sorbent Enhanced Steam Reforming (SESR), which has the potential to drastically reduce CO_2 emissions from H_2 production therefore abating climate change. SESR is a combination of traditional Steam Methane Reforming (SMR) and Calcium Looping (CaL, a form of Carbon Capture and Storage, CCS), whereby the CaL sorbent removes CO_2 from the gas stream and drives the reactions equilibrium to produce more H_2. With the application of biomass as the fuel feedstock this process has the potential to produce H_2 with net-negative CO_2 emissions.

Two main areas of work were conducted within this thesis, namely: examining the performance of CaL sorbents and novel sorbents under industrial conditions, and the development of combined multifunctional sorbent and catalyst particles for SESR with biomass. These particles were tested within a reactor that was specifically constructed for this set of work.

A detailed investigation into the effects of various parameters on the rate of limestone calcination was conducted within an atmospheric fluidised bed reactor utilising high-temperatures and CO_2 partial pressures. These conditions would typically be present within a CaL/SESR calciner and thus kinetic data with this environment was determined. Further to this, a single particle model was developed to shed light on the variances observed when calcining limestone in the presence of CO_2 and steam or CO_2 and N_2. The application of a novel synthetic sorbent was also investigated under similar calcination conditions showing the impacts on the sorbents carrying capacity caused by high-temperature CO_2 sintering.

A mild-pressure, high-temperature spout-fluidised bed reactor was constructed for the purpose of continuous biomass feeding for SESR. Combined particles of catalyst, sorbent and a dicalcium silicate support were tested. These combined particles were manufactured utilising a simple and inexpensive method. An enhanced H_2 yield of 120 $g_{H_2}/kg_{biomass}$ was produced at ~75 % purity at a stoichiometric steam to carbon ratio.

Declaration of Originality

I declare that the work presented in this is thesis is primarily my own and otherwise appropriately referenced. I declare that I am the primary person responsible for the design, construction and preparation of this manuscript including the analysis of all the experimental data presented. Any work carried out as part of a collaborative work have been explicitly stated in the text and the acknowledgements.

Peter Thomas Clough, June 2017

Copyright Declaration

Acknowledgements

Firstly, I would like to thank Professor Paul Fennell for his assistance, support and guidance throughout my PhD. I have learnt a great deal during my PhD which would not have been possible without the freedom to explore the wider research area, for this I am truly grateful. My PhD has been a challenge and a very valuable experience which will serve me in good stead for my future. I would also like to thank Paul for giving me the opportunity to work with so many masters and undergraduate students throughout my time, as this has been an invaluable experience to me.

I would like to thank Dr Joseph Yao in particular for his consistent friendship, patience in explaining core concepts and the help that he has provided me throughout my PhD. I would also like to thank Monica Retrosi for conducting the calcination experiments with N_2, and Dr Matt Boot-Handford and Dr Zili Zhang for their assistance throughout my PhD and for sharing their expertise in reactor design. To Dr Liya "work wife" Zheng, you were a great friend and I am very thankful for your assistance in running some of the XRD and XRF analyses and for the many material science discussions we had.

My PhD was heavily dependent upon the construction of the reactor and I am therefore very thankful for the assistance provided by Richard Wallington, Tony Meredith and the other workshop team members. I would also like to express my thanks to Patricia Carry and Andrew Macey for their help in the analytical lab, Chin Lang from electronics, Keith Walker and Ben Kistnah from Chemical Engineering Stores; and to Sarah Payne, Louise Le-Cornu, Sara McCallum and Susi Underwood for administrative support.

I would also like to say thank you to all the past and present members of the Fennell group and wider department community, I wish you nothing but success in everything you do.

Finally to my wife, Isobel. Thank you for putting up with me complaining about my commute and my work. Thank you for being there when I needed you and having the patience to listen to me and put up with me, my hobbies and this PhD.

"There is no such thing as a 'self-made' man. We are made up of thousands of others. Everyone who has ever done a kind deed for us, or spoken one word of encouragement to us, has entered into the make-up of our character and of our thoughts, as well as our success."

- George Matthew Adams

Acronyms

BECCS	Bio-Energy Carbon Capture and Storage
BET	Brunauer–Emmett–Teller
BFB	Bubbling Fluidised Bed Reactor
BJH	Barrett-Joyner-Halenda analysis
CaL	Calcium Looping
CCS	Carbon Capture and Storage
CCU	Carbon Capture and Utilisation
CFB	Circulating Fluidised Bed Reactor
CSTR	Continuously Stirred Tank Reactor
EFR	Entrained Flow Reactor
FBR	Fluidised Bed Reactor
GHG	Green House Gas
Htlc	Hydrotalcite
IPCC	Intergovernmental Panel on Climate Change
MIP	Mercury Intrusion Porosimetry
PFD	Process Flow Diagram
PFR	Plug Flow Reactor
SEM	Scanning Electron Microscope
SESR	Sorbent Enhanced Steam Reforming
SE-SMR	Sorption Enhanced – Steam Methane Reforming
SMR	Steam Methane Reforming
SSE	Sum of the Square Errors
TEM	Transmission Electron Microscope
TGA	Thermogravimetric Analyser
XRD	X-ray Diffraction
XRF	X-ray Florescence
WGS	Water-Gas Shift

Table of Contents

List of Figures

List of Tables

Chapter 1 – Introduction

The continued global increase in energy demand and socio-economic development of the world's population since the 1700s (when the western industrial revolution began) has led to an increase in Greenhouse Gas (GHG) emissions and atmospheric pollution, predominantly by CO_2. In the latest report by the Intergovernmental Panel on Climate Change (IPCC) (IPCC, 2013) it was concluded that the measured rise in global temperatures can be directly attributed to the anthropogenic release of GHG's. This increase in global (ocean, atmospheric and surface) temperatures has been correlated with climatic changes such as sea level rise, ice-shelf and glacier melting, precipitation distribution changes, an increased number of extreme weather events and season weather pattern shifts. The impact of these changes is difficult to predict on a local level precisely, nevertheless even with conservative estimates the changes could accumulate into a very different world compared to the one in which we are used to (IPCC, 2014).

It is for these potential impacts that, along with changes to other sectors, we must alter the ways in which we generate energy such that the impact on the environment is minimised. Many believe that renewable energy systems (wind, solar tidal, wave and hydro-power) are the final end goal of a decarbonised energy sector. However many industries cannot be entirely electrified and as such still require the combustion of fossil energy sources. Furthermore the intermittency of some renewables limits their deployment at scale (Heuberger et al., 2017a). An alternative is to utilise fossil energy sources but in a more sustainable way by preventing the release of CO_2, which can be achieved through Carbon Capture and Storage (CCS) (Boot-Handford et al., 2014). CCS can be divided into three general subheadings each of which are described below.

- Post-combustion capture:

Where by the CO_2 is separated from the other gases after the combustion reaction has taken place. Currently, the most developed technology in this field is amine scrubbing due to the technology being utilised for decades in the natural gas refining industry (Rochelle, 2009). Post combustion capture systems have the potential to be retrofitted to existing facilities.

- Pre-combustion capture:

This process involves the gasification/reforming of a fuel primarily into a mixture of CO, CH_4, CO_2 and H_2. This gas is then further processed via the water-gas-shift reaction, the removal of sulphur and other impurities and pressure swing adsorption. CO_2 is then selectively removed from the gas stream thereby forming a separated streams of CO_2 and H_2. The hydrogen can then be combusted as a CO_2 free fuel source or utilised as a process feedstock (Global CCS Institute, 2012).

- Oxy-fuel:

Fuel is combusted in the presence of oxygen and CO_2 only which means the generated products are predominately CO_2 and H_2O, which can be separated relatively easily via condensation (Eon, 2009). This process negates the need to separate CO_2 and N_2 which is relatively difficult to do compared to the separation of CO_2 and H_2O. The process does require an air separation unit which can increase the capital cost significantly, although prices are falling.

Through the utilisation of biomass energy crops and CCS together it is possible that energy can be generated with negative CO_2 emissions, which is commonly referred to as Biomass energy and carbon capture and storage (BECCS). This is because through the lifetime of the plant CO_2 will be absorbed via photosynthesis which if then captured during energy generation and stored then CO_2 is actually being removed from the atmosphere. Biomass is however a difficult fuel to work with as its properties are quite different to coal and requires much more stringent safety precautions in its handling (Basu, 2010).

The full market deployment of CCS has been predicted on many occasions however this has not come to fruition as predicted because new CCS plants are very costly to design (and cancel, thanks George (House of Commons Committee of Public Accounts, 2017) (BBC, 2015)) and require large amounts of state funding. CCS plants do require a significant initial investment as the risks are high for a new technology at this scale. It was explained within the Oxburgh report (Oxburgh, 2016) that the main areas of risk for CCS deployment are with regards to the transport and storage of the CO_2 but the UK is well placed to take advantage of its natural CO_2 storage capacity in the North Sea. The levelised cost

of avoiding the CO_2 emissions has been modelled and estimated to lie in the range of €100-150/MWh but is highly dependent on fuel costs and furthermore as the USA and others begin to bring CCS plants online for enhanced oil recovery, costs will come down (Porter et al., 2017).

An somewhat newly established form of CCS, which is adaptable to both pre-combustion and post-combustion applications, is Calcium Looping (CaL) (Dean et al., 2011a). CaL utilises CaO based materials to cyclically react with and release CO_2, by doing so a stream of CO_2 can be produced which requires minimal purification before transportation and storage. The energy efficiency penalty of a CCS plant is also an important factor to consider, CaL is one of the lowest impacting technologies with this regard of only 4-5 percentage points (Fennell, 2015a). CaL can be further combined with the knowledge and experience of the Steam Methane Reforming (SMR) industry to increase the efficiency of hydrogen production; the amalgamation of these two technologies is referred to Sorbent Enhanced Steam Reforming (SESR). The aim of both SMR and SESR is to produce hydrogen, however SESR produces hydrogen via a pre-combustion process that facilitates the separation and capture of CO_2 thereby preventing its release into the environment. The general reaction equation for SESR is shown below as equation 1.1.

Equation 1.1 - Overall SESR of methane:

$$CH_4 + 2H_2O + CaO \rightarrow 4H_2 + CaCO_3 \qquad \Delta H^\circ_{298K} \approx -13\ \mathrm{kJ/mol}$$

As can be seen, under ideal conditions all the methane and steam are shifted to H_2 and all the CO_2 is captured by the CaO and as is done in CaL the formed $CaCO_3$ is cycled into a calciner where the material is converted back into CaO for reuse. However the reversibility of the sorbent to undergo these reactions is limited by issues such as attrition, sintering, sulphation and CaO entrapment (Fennell et al., 2007). Furthermore a catalyst (commonly nickel) is required to increase the rate of these reactions, which itself has issues of sintering, coking and sulphur poisoning (Sehested, 2006).

A recent advance in optimising the combination of the sorbent and catalyst materials for SESR is the incorporation of both materials into a single particle. This has the benefit of reducing the distance that the gas molecules need to travel in order to reach the relevant active sites (Lugo and Wilhite, 2016).

By substituting the fuel source from methane/natural gas to biomass it is possible to create H_2 with net-negative CO_2 emissions. In making this change a separate pyrolysis/gasification reactor may be required in order to prevent coking damage to the particles and to ensure that each process operates at the optimal conditions for the reactions taking place (Florin and Harris, 2008b).

At present H_2 is predominantly utilised by oil refineries, fertiliser/chemical production industries and the food industry (Balat, 2008). Further to these current uses, H_2 is also being considered as a replacement for natural gas for domestic heating purposes (Bockris, 2002) (Sadler, 2016), the benefit of this being that the polluting element of the fuel (CO_2) can be removed at scale at a point source ready for transportation and storage. In replacing natural gas for H_2 for domestic heating it would also decarbonise one of the largest energy demands within the UK, currently ~ 29 % of total energy demands (BEIS, 2016). Furthermore, the produced hydrogen could be combusted at source for large scale electricity generation thus demonstrating the flexibility of hydrogen whose production can be ramped to meet demands and distributed to multiple commercial partners as markets dictate.

1.1. Project Aims

The general aim of this research will endeavour to investigate the potential of utilising biomass as the feedstock material and conduct the gasification and SESR reactions within a single stage reactor for the production of high purity H_2. A significant benefit of SESR is that the main reactions can occur within one reactor, which therefore eliminates the need for multiple costly reactors each doing a specific task. This process simplification does however lead to a higher degree of system complexity and it is therefore paramount to ensure the operating conditions are suitably controlled and monitored. Concluding from this introduction and the information gathered within the literature review presented in Chapter 2 to conduct this research the following items had to be addressed:

- The design and construction of a spout-fluidised bed reactor suitable for conducting gasification and SESR reactions
- The feedability and general operation with biomass as feedstock for SESR
- The development of high-temperature CaO-based sorbents that minimise the decay in carrying capacity
- The development and testing of a combined sorbent and catalyst particle effective for SESR

1.2. Thesis Outline

Chapter 2 – This chapter looked into the available literature and reviewed the current knowledge and experience of previous researchers. The information gathered here influenced the direction of the future research plan based on the identified gaps in the research.

Chapter 3 – This chapter presents the details of the reactor design, biomass feeding system, steam system and gas analysis system. This chapter also presents some initial combustion, steam gasification and SESR reactions which assess the positives and drawbacks of this reactor.

Chapter 4 – This chapter presents a set of limestone calcination experiments to determine the influence of many parameters on the rate of calcination. This work was conducted within a small atmospheric fluidised bed reactor and the kinetic experiments were conducted under realistic commercially applicable conditions. A comparison between steam and N_2 was made and following this a single particle model was developed, validated and compared to the experimental data.

Chapter 5 – This chapter details a published investigation into the use of a novel, synthetic and polymorphic CaO-based sorbent utilising a dicalcium silicate support structure. Again this sorbent was tested under realistic conditions and highlighted the errors that can be produced if a material is not tested under appropriate conditions.

Chapter 6 – This chapter presents the main experiments conducted within the reactor constructed within chapter 3. The work utilised a low steam to carbon ratio with oak biomass as the feedstock for SESR, generating a separable stream of H_2 and CO_2. This chapter also presents the development and use of cheap and simple multifunctional materials suitable for fluidised bed operation composed of a Ni based catalyst and CaO based sorbent. A discussion of coke formation and its impacts on operation with combined particles is presented here. This chapter also investigates the observed and intrinsic rate kinetics of these combined particles within a mild pressure fluidised bed reactor.

Chapter 2 – Literature Review

2.1. An Introduction to Calcium Looping

Calcium looping (CaL) for CO_2 capture, was first suggested by Shimizu in 1999 (Shimizu et al., 1999), since then the technology has been widely researched and has multiple large scale reactors in operation – see section 2.12. A typical, simplified post combustion CaL process flow diagram is displayed in Figure 2.1, showing the main features, which are a carbonator and a calciner (Blamey et al., 2010).

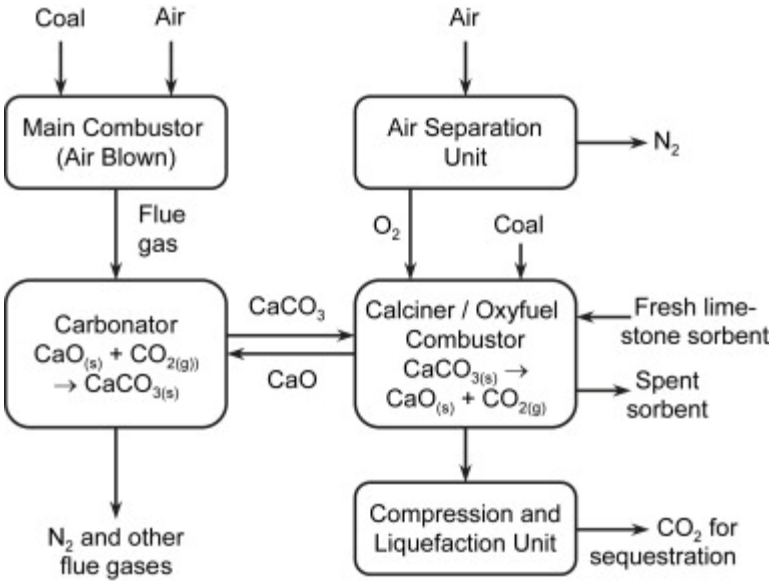

Figure 2.1 – A process flow diagram of a typical post-combustion calcium looping system (Blamey et al., 2010).

The general description of a CaL process is a Ca-based CO_2 sorbent, typically CaO, is cycled between two reactors; a carbonator where CO_2 is absorbed into the CaO matrix to form $CaCO_3$ and a calciner where the CO_2 is released thereby generating a high purity CO_2 stream that can be cleaned, compressed, transported and stored. The process relies on the reversibility of the sorbent to undergo multiple carbonations (forwards direction of Equation 2.1) and calcinations (reverse direction of Equation 2.1). One of the main issues with CaL is the reversibility of the sorbent via this reaction; the issues regarding sorbent reversibility will be discussed in section 2.9.

Equation 2.1 - Calcium looping – Carbonation forwards and calcination reverse:

$$CaO + CO_2 \rightleftharpoons CaCO_3 \qquad \Delta H°_{298K} = -178\ \text{kJ/mol}$$

The benefits of CaL are that the high operating temperatures of the system permits a steam cycle to be run off the excess heat generated by the exothermic carbonation reaction, thereby offsetting some of the other energy losses associated with the capture system. Furthermore due the oxy-combustion of fuel in the calciner, which is required to raise the reactors temperature, a near pure stream of CO_2 and steam is generated. The steam can then be easily separated from the CO_2 before the CO_2 is sent for compression and storage. In a post-combustion setting the CO_2 to be captured will be present with N_2 and other gases such as SOx and NOx. Within the operating conditions of a CaL process, the reaction between SOx and CaO can be assumed to be irreversible, which may thought of as a positive, in that a power station will no longer be required to install a flue gas desulphurisation unit. The sulphation of CaL sorbents does however mean that the carrying capacity for CO_2 is diminished and therefore the sorbents require a higher rate of replenishment (Coppola et al., 2012). The replenishment of spent sorbent for fresh limestone occurs in the calciner, this spent sorbent can then be utilised within the cement industry as a raw feedstock material (Dean et al., 2011a).

2.2. An Introduction to Steam Methane Reforming

Steam Methane Reforming (SMR) is currently the most common method of producing H_2, with approximately 50 % of the market share (IEA, 2015). The benefits of a H_2 economy have been debated for decades since Bockris first realised its potential (Bockris and Appleby, 1972). H_2 is utilised mostly within the oil and gas, chemical synthesis and food industries with some other smaller niche applications (Balat, 2008). Further to these current uses, H_2 has been suggested as a fuel supply for the generation of electricity and as an alternative to natural gas for domestic heating purposes (Bockris, 2002) (Sadler, 2016).

Advantages of utilising H_2 as an energy carrier as opposed to fossil fuels, are that it has a high calorific value (per unit mass) and upon combustion only water is produced. This being said it, by utilising SMR CO_2 is still generated and released into the environment but at the point of generation instead of at the point of combustion. If H_2 is to be utilised as a fuel then the CO_2 must be captured and safely stored as it is in CCS and not released into the atmosphere. The main disadvantage of H_2 is its low bulk gas density and infamous flammability, the H_2 therefore requires large, pressurised, safe and monitored storage vessels. H_2 storage systems are currently being developed and the main options currently include storing the H_2 as a cryogenic liquid, binding the H_2 to a metal hydrate, carbon nanostructured formations or simply as a compressed gas (Dutta, 2014). A general process flow diagram of SMR is displayed as Figure 2.2.

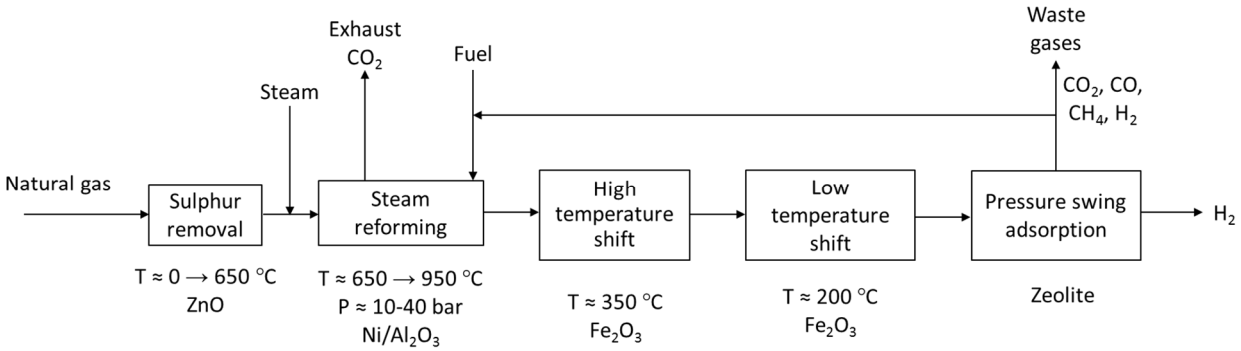

Figure 2.2 – A typical process flow diagram of steam methane reforming, adapted from (Gupta, 2008).

This process operates across multiple fixed bed reactors each serving their own purpose to enhance the yield and purity of H_2 generated. Firstly the natural gas is desulphurised, typically over a bed of ZnO, it is then steam reformed following Equation 2.2 over a bed of reduced Ni. The reforming reaction is endothermic and is therefore carried out at high-temperatures, the methane is typically introduced into the reactor between ~550 and 650 °C and then heated externally up to ~850 - 950 °C. The gas leaving the reactor is typically only 50 % pure H_2, therefore the gas is passed over beds of iron oxide at lower temperatures in excess steam to undergo the water-gas-shift reaction (Equation 2.3). Finally, remaining methane, CO and CO_2 is scrubbed out of the system or a pressure swing adsorption unit is utilised resulting in very high purity hydrogen (99.9 % pure) (Gupta, 2008).

Equation 2.2 - Steam methane reforming:

$$CH_4 + H_2O \rightleftharpoons CO + 3H_2 \qquad \Delta H°_{298K} = +206.2\ \text{kJ/mol}$$

Equation 2.3 - Water-gas shift reaction:

$$CO + H_2O \rightleftharpoons CO_2 + H_2 \qquad \Delta H°_{298K} = -41.2\ \text{kJ/mol}$$

A major issue for SMR operation is the poisoning of the expensive Ni based catalyst by coke formation or by sulphation. Typically the catalyst is supported on an alumina support which is required to minimise sintering and to reduce the cost of the reactor bed material. By pressurising the system the generated H_2 is at a pressure suitable for the H_2 users, which typically require high-pressure (2 MPa) H_2 for operation anyway, and furthermore the pressurisation reduces the amount of catalyst required and therefore the size of the required plant. With careful operation and a suitable desulphurisation unit the catalyst beds have a lifetime of about 3 years before requiring complete replacement (Malhotra, 2012).

2.3. Sorbent Enhanced Steam Reforming

2.3.1. An overview

Sorbent Enhanced Steam Reforming (SESR) is the amalgamation of CaL and SMR. It utilises the knowledge and experience of both industries and combines the technologies into one simplified process with the aim of producing H_2 without releasing CO_2 to the atmosphere. Figure 2.3 shows a simplified process flow diagram of SESR.

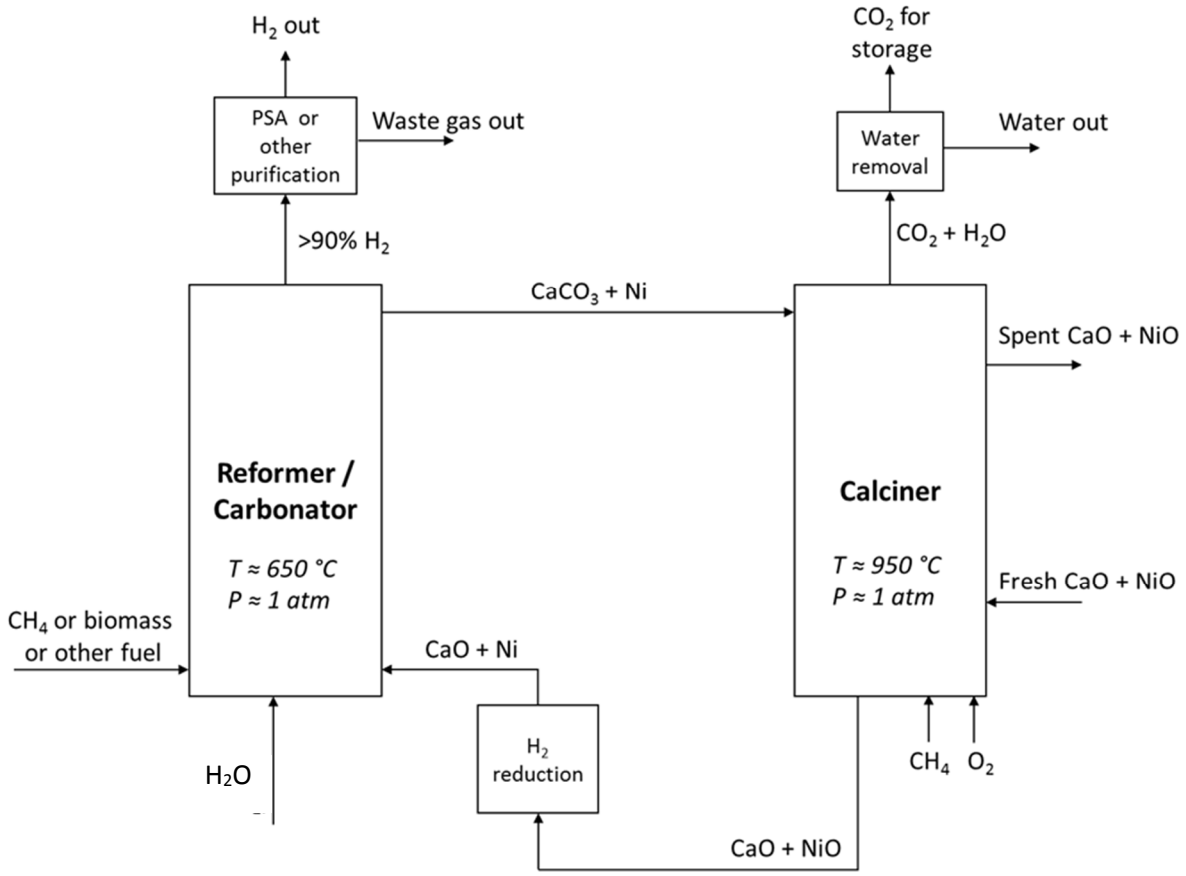

Figure 2.3 – A simplified process flow diagram of SESR.

SESR is based around using two reactors, a carbonator where CO_2 is absorbed into a sorbent and a calciner where CO_2 is released from the sorbent, as it is in CaL. However within the carbonator there are a multitude of other reactions taking place simultaneously, which include the steam reforming and water-gas-shift reactions of the SMR process (Equation 2.2 and Equation 2.3). By the addition of a CO_2 sorbent to the carbonator/reformer reactor, the CO_2 is removed from the system thereby lowering the

CO_2 partial pressure, and by Le Chatelier's Principle, driving the reforming reactions to produce more CO_2 and consequentially more H_2. Based on this SESR is a process by which two product gas streams are generated, the first is rich in H_2 (from the carbonator/reformer) and the second is rich in CO_2 (from the calciner) (Harrison, 2008).

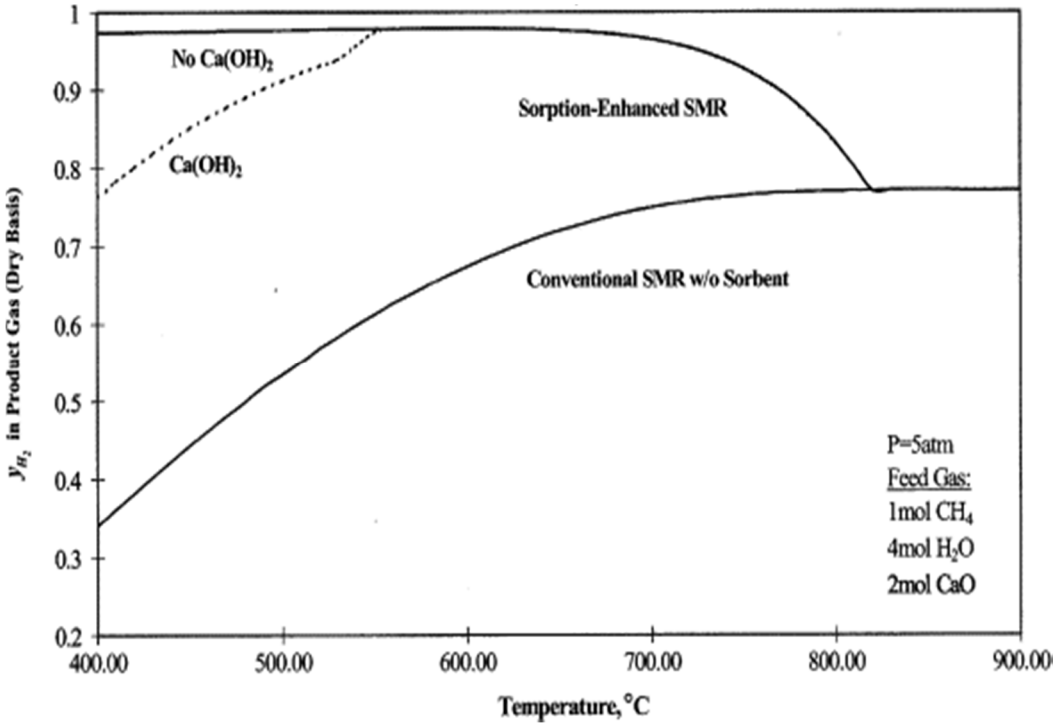

Figure 2.4 – Thermodynamic equilibrium position of SESR systems compared to SMR systems (Barelli et al., 2008).

The operating conditions of the SESR reactors are similar to that of a CaL system whereby the carbonator/reformer operates at ~650 °C and the calciner operates at ~950 °C (García-Lario et al., 2015a). The reforming reactions within the carbonator/reformer do take place at the lower carbonator temperatures with a similar effectiveness to the overall SMR process because the CO_2 sorbent that is present is driving the reactions and altering the thermodynamic equilibrium position as can be observed in Figure 2.4. The SESR process is generally considered to favour lower pressures due to the greater number of moles produced than fed in as shown by Equation 2.4 (the overall SESR of methane), however kinetics and the final use of the H_2 may dictate that an elevated operating pressure would be required (Barelli et al., 2008).

Equation 2.4 - Overall SESR of methane:

$$CH_4 + 2H_2O + CaO \rightarrow 4H_2 + CaCO_3$$

The bed material is cycled between the two reactors as it is in CaL, this does however introduce a slight difficulty in that the Ni catalyst will likely oxidise in the oxy-fired calciner, Equation 2.9 (Antzara et al., 2016). Therefore a H_2 pre-reduction step may be required before the bed material renters the carbonator/reformer, however it may also be possible that the reforming reactions which generate reducing agents (CO, CH_4 and H_2) could be utilised to reduce the catalyst within the main carbonator/reformer reactor as shown by Equation 2.5, Equation 2.6, Equation 2.7 and Equation 2.8 (Antzara et al., 2016) (Xiao et al., 2017). The requirement of a reduction step is currently unclear from the available literature as most research has only be conducted at lab scale and under laboratory conditions.

Equation 2.5 - Nickel oxide partial reduction by methane:

$$CH_4 + NiO \rightarrow CO + H_2 + Ni \qquad \Delta H°_{298K} = +203 \text{ kJ/mol}$$

Equation 2.6 - Nickel oxide total reduction by methane:

$$\frac{1}{4}CH_4 + NiO \rightarrow \frac{1}{4}CO_2 + \frac{1}{2}H_2O + Ni \qquad \Delta H°_{298K} = +31 \text{ kJ/mol}$$

Equation 2.7 - Nickel oxide reduction by CO:

$$CO + NiO \rightleftharpoons CO_2 + Ni \qquad \Delta H°_{298K} = -43 \text{ kJ/mol}$$

Equation 2.8 - Nickel oxide reduction by H_2:

$$H_2 + NiO \rightleftharpoons H_2O + Ni \qquad \Delta H°_{298K} = -2 \text{ kJ/mol}$$

Equation 2.9 - Nickel oxidation by O_2:

$$Ni + \frac{1}{2}O_2 \rightarrow NiO \qquad \Delta H°_{298K} = -240 \text{ kJ/mol}$$

The production of coke from the reforming reactions is also a problem for the sorbent and catalyst, as it leads to pore blockages of the sorbent and it has the potential to poison the catalyst. The coke formation on the bed material, if controlled, may be beneficial in that a lower fuel duty will be required within the calciner as the coke will be burned off thus generating heat and raising the temperature of the reactor (Wang et al., 2004). Along these ideas there is potential that with careful reactor design and operation the carbonator/reformer may be able to operate as an autothermal reactor, meaning that little extra energy will be required to heat the system as the reaction heats balance out (Iordanidis et al., 2006).

2.4. The potential of biomass

The application of biomass within a SESR system in replacement of natural gas has the benefit of providing the possibilities of negative emissions due to the fact that biomass absorbed CO_2 during its growing period. However sourcing this biomass must be done responsibly and sustainably.

The properties of biomass are inherently different compared to coal and because of this it behaves differently upon combustion and other safety factors must be taken into account during handling. Biomass is constructed of 3 main components, they are (McKendry, 2002): Lignin (~15-25 wt.%), Cellulose (~35-45 wt.%) and Hemicellulose (~20-30 wt.%). Lignin has been shown to be a highly aromatic structure with various branches leading to a prolonged degradation. Hemicellulose is a random and highly branched structure meaning many smaller molecules are easily removed. Conversely, Cellulose and are constructed of long, strong polymers with few branches producing a high thermal stability (Yang et al., 2007).

Comparatively, coal varies with rank (an intrinsic property, dependent upon the temperature and pressure of its formation) such that, lower ranking coals (most recently formed) have high hydrogen to carbon and oxygen to carbon ratios and vice versa for high ranking coals (Neavel Richard, 1981). It has also been shown that as the rank of coal increases the aromaticity increases, while in comparison volatility and reactivity of the functional groups produced decreases (Tillman, 2000). This implies that

with the knowledge of rank, any coal's properties can be generalised for use; however, biomass is less simple as there can be great variation between biomass species due to the diverse proportion of Lignin, Cellulose and Hemicellulose, each of which can directly affect the rate of thermal decomposition (Gottipati and Mishra, 2011). It has also been shown that biomasses that contain higher hemicellulose and cellulose contents produce larger quantities of gaseous products; this is especially useful information for the selection of the most appropriate biomass for conversion into gaseous products. (Burhenne et al., 2013).

Another major influencing factor with regards to the use of biomass as a fuel is the moisture content. Where coals intrinsic moisture content is ~3-45 wt.% (high to low rank coals), biomass's moisture content is far higher, averaging at ~55 wt.% (10-65 wt.% for differing biomasses) for fresh green biomass (Biomass Energy Centre and Forestry Commission, 2011) (Speight, 2005). Due to the higher moisture content within biomass it typically has a significantly lower calorific value than even low rank coals and therefore the biomass is often dried prior to use and moreover larger quantities of biomass are needed to produce an equivalent amount of energy (Demirbas, 2004) (Basu, 2010). However by air-drying the biomass its calorific value can increase by ~50 %, which brings biomass more in line with low rank coals (Van Loo and Koppejan, 2008).

The lignocellulosic makeup has been shown to be an influencing factor with regards to the heating value, in that the greater the percentage of lignin present the higher the heating value is. Cellulose and hemicellulose have a slightly lower heating value in comparison to lignin due to the higher percentage of oxygen present within the structures (Demirbaş, 2005). The heating values of biomass are also affected further by chemical constituents within the fuel. Multiple models have been produced to estimate the heating value based upon the Carbon, Oxygen, Hydrogen and other elements, however most models suffered inaccuracies due to a small sample sizes and assumptions which are not valid for all types of biomass (Sheng and Azevedo, 2005) (Demirbaş, 2001).

The mineral composition of biomass is an import factor to consider if it is to be utilised fully. This is because the high inorganic mineral content of biomass leads to slagging and fouling, inevitably raising the cost of operation and maintenance due to equipment corrosion leading to shortened equipment

lifetime, increased number of cleaning cycles and inefficient heat transfer (Teixeira et al., 2012). Comparing coal and biomass in terms of mineralogy, biomass tends to contain higher concentrations of silicon, chlorine and potassium yet lower concentrations of aluminium, iron and sulphur (Khan et al., 2009). Potassium, chlorine and silicon contents within biomass are the leading causes for slagging (ash collecting and forming slag in the sections exposed to radiated heat) and fouling (formations in the convective heat areas) due to these components forming low-temperature eutectic melts (potassium-silicates). Calcium within the mixtures helps to raise the fusion temperature of these slags due to the formation of potassium-calcium-silicates (Teixeira et al., 2012). Sulphur and chlorine are responsible for much of the fouling within the systems due to the formation of sulphates and chlorides, which become elutriated with fine particles and end up in heat exchangers and on the walls of the combustion chamber (Nutalapati et al., 2007).

Fluidised bed technology is currently favoured for biomass combustion due to its fuel flexibility and ability to operate at low-temperatures (Koppejan and van Loo, 2012). The fouling of bed fluidisation material can lead to bed agglomeration, reduced heat transfer, incomplete combustion and the possibility of complete bed defluidisation (Öhman et al., 2000) (Llorente and García, 2005) (Lundholm et al., 2005). It is therefore paramount that the selection of biomass fuels is done with attention to the mineral content to minimise this propensity of biomass to slag and foul during thermal degradation.

A further downside to biomass is that it lacks the high energy and bulk densities of coal; typically coal has an energy density ~5 times greater than biomass and a bulk density ~2-3 times higher too (Carbon Trust, 2012). This means larger storage areas are required to store the same timescales energy supply relative to coal (Basu, 2013).

A further factor that should be considered when prospecting biomass as a fuel source is the flexible nature of the feedstock and its available quantities and qualities. Not all biomass may be clean and new, some maybe construction or agricultural wastes. The UK government commissioned a report into the market of waste wood in the UK and evaluated that the majority of the waste wood that is currently available is contaminated; this means that the management of contaminated feedstock must be developed (Department for Environment Food and Rural Affairs, 2008).

2.5. Biomass conversion technologies

To utilise biomass within an SESR process for H_2 production it is important to understand the thermochemical conversion processes that are undertaken during biomass pyrolysis/gasification. The use of biomass with a CO_2 sorbent enhanced process is not new (Mahishi et al., 2007), but many researchers utilise a separated gasification reactor compared to the carbonator/reformer such that the conditions of each reactor can be optimised (Florin and Harris, 2008a) (Li et al., 2017).

The gasification of biomass requires an oxidation gas to be present, this can be air/O_2/CO_2 or steam. By utilising air the product gas is diluted by nitrogen thereby requiring further processing. Oxygen can positively increase the thermodynamic efficiency due to the partial oxidation of the fuel being exothermic. Nonetheless, using steam as the gasification agent is favoured due to the production of additional H_2 from the reduction of the water (Kalinci et al., 2009). A recent review paper has extensively verified that steam is the best gasification agent for H_2 production (Udomsirichakorn and Salam, 2014).

The main reaction pathways of biomass gasification is shown below as Figure 2.5and can be represented overall as Equation 2.10 (Florin and Harris, 2008a).

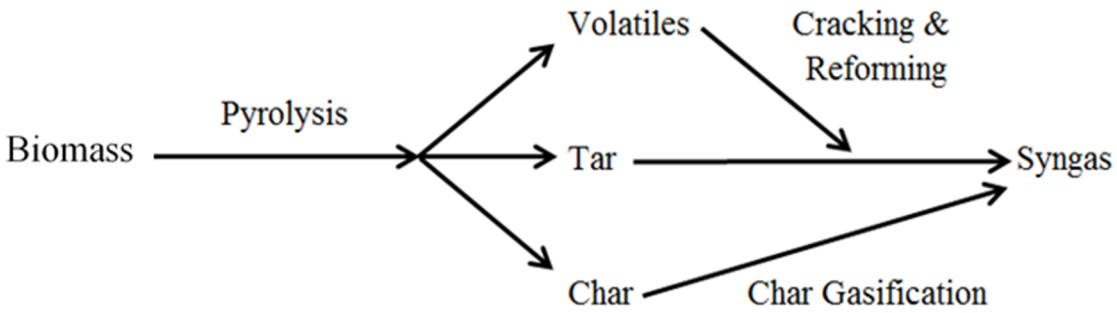

Figure 2.5 – Gasification mechanism. Adapted from Florin and Harris (Florin and Harris, 2008a).

The initial pyrolysis reaction occurs within the particle as the temperature rises to ~500°C, whilst the tar and volatile cracking occurs beyond 600 °C and char gasification above 800 °C (Florin and Harris, 2008a). It is in the initial pyrolysis where the devolatilisation occurs and the three main products are

separated; namely gas, tar and char. Biomass, in comparison to coal, produces a far greater quantity of volatiles at lower temperatures due to its molecular makeup (McKendry, 2002). Additionally, biomass can undergo complete gasification at much lower temperatures than coal, due to its branched structure with lower aromaticity making it more reactive (Tanksale et al., 2010).

Equation 2.10:

$$Biomass + Heat + Steam \rightarrow H_2 + CO + CO_2 + CH_4 + H_2O + Tar + Char$$

Dissecting the overall steam gasification Equation 2.10 the following reactions can be said to occur during the process (Widyawati et al., 2011) (Florin and Harris, 2007). The overall gasification process and the individual equations themselves are of course controlled by the ratio of steam to fuel and by the optimisation of the reaction temperature, heating rate, pressure and particle size (Sikarwar et al., 2016).

Equation 2.11 - Water-gas shift reaction:

$$CO + H_2O \rightleftharpoons CO_2 + H_2 \qquad \Delta H°_{298K} = -41.2 \text{ kJ/mol}$$

Equation 2.12 - Steam methane reforming:

$$CH_4 + H_2O \rightarrow CO + 3H_2 \qquad \Delta H°_{298K} = +206.2 \text{ kJ/mol}$$

Equation 2.13 - Steam reforming of tars:

$$C_nH_mO_p + (2n - p)H_2O \rightarrow nCO_2 + \left(\frac{m}{2} + 2n - p\right)H_2 \quad \Delta H°_{298K} > 0 \text{ kJ/mol}$$

Equation 2.14 - Water-gas reaction 1:

$$C + H_2O \rightarrow CO + H_2 \qquad \Delta H°_{298K} = +131.3 \text{ kJ/mol}$$

Equation 2.15 - Water-gas reaction 2:

$$C + 2H_2O \rightarrow CO_2 + 2H_2 \qquad \Delta H°_{298K} = +90.1 \text{ kJ/mol}$$

Equation 2.16 - Boudouard reaction:

$$C + CO_2 \rightarrow 2CO \qquad \Delta H°_{298K} = +172.5 \text{ kJ/mol}$$

Equation 2.17 - Methanation reaction:

$$C + 2H_2 \rightarrow CH_4 \qquad \Delta H°_{298K} = -74.9 \text{ kJ/mol}$$

Equation 2.18 - Thermal cracking of chars/tars:

$$C_nH_m \rightarrow C_{n-x}H_{m-y} + H_2 + CH_4 + C \qquad \Delta H°_{298K} > 0 \text{ kJ/mol}$$

$$Where\ C_{n-x}H_{m-y}\ represents\ any\ compound\ lighter\ than\ C_nH_m$$

It can be seen that a large number of complex and interlinked reactions have to occur to produce H_2 from the gasification of biomass. It is therefore necessary to optimise the reaction conditions so that the yield and purity of H_2 can be maximised. By simply optimising the operating conditions of steam gasification of biomass, the yields of H_2 generally peak around 40 – 50 vol.% (Florin and Harris, 2007) (Ni et al., 2006). This purity is simply not high enough for the commercial use of H_2, thus shift reactors and pressure swing absorbers can be applied to increase the purity as they are in SMR but at a cost of additional reactors (Florin and Harris, 2008a). It is for these reasons that SESR comes into its own, whereby the multiple reactions take place within only one reactor and there is the further possibility that the biomass steam gasification process could also be conducted within this one reactor as well, simplifying the process further.

2.6. Reactor Design and Operation

There are many different types of reactors that could be utilised for biomass steam gasification and SESR and this section will explain their differences, advantages and disadvantages, and how possible they are for operation within a SESR process.

2.6.1. Fixed beds

Fixed bed gasification units predominantly utilise either a down-draft (fuel and gas enters from the top) or an up-draft (fuel enters from the top and gas enters counter-currently from the bottom) operating set-up, although down-draft gasifiers are limited to low moisture content biomasses. Down-draft operation provides volatiles a greater reaction time with the oxidation gas; the volatiles are also released at a higher temperature and therefore have a smaller molecular weight compared to the up-draft released molecules that typically contain a higher unfavourable tar content (Paisley, 2000) (Sikarwar et al., 2016). A scrubbing bed is often required after gasification to enhance the qualities of the syngas, mostly to decrease the tar content (Corella et al., 1999).

For the application of SESR, fixed beds are generally limited to sorbent enhanced steam methane reforming (SE-SMR) where methane instead of biomass is utilised as the feedstock (Florin et al., 2015). Although the use of liquids such as waste cooking oil as a fuel feedstock for SESR has also been investigated (Pimenidou et al., 2010). Cycling of the bed material (sorbent and catalyst) could be performed within the one bed, by altering the operating conditions to switch between carbonation and calcination although the biggest issue with this is stable production and the operation of high-temperature valves, typically the operation is limited to small scale batch production (Harrison, 2008). Therefore two parallel fixed bed reactors are typically suggested (S G Adiya et al., 2017). Due to the bed material remaining within the same bed the attrition rates are lower (Corella et al., 1999).

2.6.2. Fluidised beds

Fluidised beds can be separated into two main types: bubbling fluidised beds (BFB) and circulating fluidised beds (CFB). The bed material within a BFB remains within one reactor vessel and has a support/gas distribution plate beneath the material to prevent the material from dropping below the gas injection points. CFBs operate at a faster fluidisation rate compared to BFBs and as such the particles gradually become entrained and flow out of one reactor and into another. The use of two interconnected CFBs is generally proposed for large scale CaL systems (Blamey et al., 2010).

As a bed formed of particles resting on the gas distributer plate is subjected to an increasing gas velocity from below, the bed material begins to experience an upward force. As this gas velocity is increased further the bed material begins to surpasses a critical point called the 'minimum fluidisation velocity' (U_{mf}) thereby forming a BFB. Increasing the flow rate further forms a CFB and further again forming an entrained flow reactor. Often an inert bed material such as sand is added to the bed to increase the gas mixing and even out the heat distribution (Paisley, 2000) (Higman and van der Burgt, 2008) (Johnsen et al., 2006b).

BFBs have been well utilised for steam gasification and even sorption enhanced steam gasification of biomass previously as they are simple and cost effective to operate (Han et al., 2011). The produced gases also have a long residence time within the bed such that the tar and unreacted carbon contents are low (Alauddin et al., 2010) (Rapagnà et al., 2000). CFBs have also been utilised for steam gasification of biomass, but are a relatively newer technology for the application (Li et al., 2004) (Ahrenfeldt et al., 2013).

The use of two BFBs operating in parallel but in anti-phase with each other's cycle has been modelled for SESR but not yet tested (Kinoshita and Turn, 2003). This system would work like so: biomass is added to one reactor to undergo SESR whilst the other reactor undergoes calcination and burn-off. After the reactions have completed, fuel and gas lines along with the operating conditions of the beds are switched and thus continuous operation is achieved. Due to the sorbent and catalyst particles remaining

within one bed only, there is a reduced attrition rate on the CaO and thus a lower replenishment rate (Florin and Harris, 2008a).

In terms of SESR the use of interconnected CFBs has the advantage that it can deliver the hot bed material from the calciner to the carbonator/reformer thereby minimising heat demand, however a balance between the cycling delivery of hot CaO and the CO_2 capture efficiency must be made to ensure continual and effective operation.

2.6.3. Spouting beds

Spouting beds differ from fluidised beds by one main factor, the lack of a gas distribution plate. This means the full weight of the bed material must be supported or semi-entrained by the movement of the gas. Because of this, they are typically restricted to small bench-scale systems with the laboratory that require continuous solids feeding.

Spouting beds often have a conical shaped base with a cylindrical section above this; however it is possible to produce spouting beds that are only cylindrical or only conical. The angle of the gas inlet to wall radius determines the amount of un-fluidised particles otherwise referred to as dead spaces. It is ideal to minimise dead spaces and maximise the dispersed flow into the annular region surrounding the central spout. The central spouting fluid allows particles to be picked up and entrained into the fluid from the bottom, carried up to the top of the bed and produce a fountain of particles falling back onto the top of the bed where they progress back down to the bottom of the bed through the dense phase annular region (Epstein and Grace, 2011).

A recommended cone angle of the conical section is between 28° and 60°, as <28° leads to instability of the bed and >60° can prevent solids from circulating efficiently. There are some common characteristic relationships of spouted beds to ensure stable operation; such as the ratio of inlet diameter to particle diameter which should be less than 25 ($D_i/d_p \leq 25$) and that the ratio of inlet diameter to cylinder diameter should be less than the minimum fluidisation voidage to the power of the Richardson-Zaki index n divided by 2($D_i/D \leq \varepsilon_{mf}^{n/2}$) (Epstein and Grace, 2011).

Whilst spouting beds as of yet haven't been utilised for SESR they have been operating as pyrolysis units for woody biomass owing to their ability of being able to continually process irregular, fine particles with a wide size distribution (Amutio et al., 2012) (Olazar et al., 2000).

2.6.4. Entrained flow reactors

Entrained flow reactors (EFR) are effectively very fast fluidising CFBs which utilise a small particle size such that attrition of particles is no longer a problem. EFRs come in two main types top-fed and side-fed. Top-fed EFRs feed the biomass in from the top whilst the burner sits at the bottom meaning the produced gas can exit from the side and the ash can fall to the bottom. Side-fed EFRs, as the name suggests, feed the biomass and gasification agents in at the sides and then gas flows up and ash falls down. The use of entrained flow reactors can be difficult to operate with the irregularity of a typical biomass particle morphology (Sikarwar et al., 2016).

One company has recently developed several new EFR designs including, the '*Calix Flash Calciner*' and the '*ENDEX'* reactor which they are aiming to apply to the cement industry in a way that utilises the basic principles of CaL (Sceats, 2017) (Sceats and Horley, 2014) (Vincent et al., 2016).

There are other advanced processes for the gasification of biomass such as, plasma gasification, supercritical water gasification, gasification for co/poly-generation and integration with pyrolysis plants however they have not been discussed here as a lengthy review paper was published detailing the advantages, disadvantages and developments in these areas (Sikarwar et al., 2016).

All of these reactors require careful, consistent and safe operation to achieve a high H_2 purity and yield, but whichever design/reactor type is utilised, the operating conditions probably affect the end product more.

2.7. Operating Conditions

2.7.1. Effect of temperature and pressure

SESR requires CO_2 to be removed from the system as it is produced, which in turn requires the balancing of Equation 2.1 with all the other chemical reactions (Equation 2.10 to Equation 2.18) that are taking place within the gasifier/reformer/carbonator, each of which, are dependent upon and favour different temperatures and pressures.

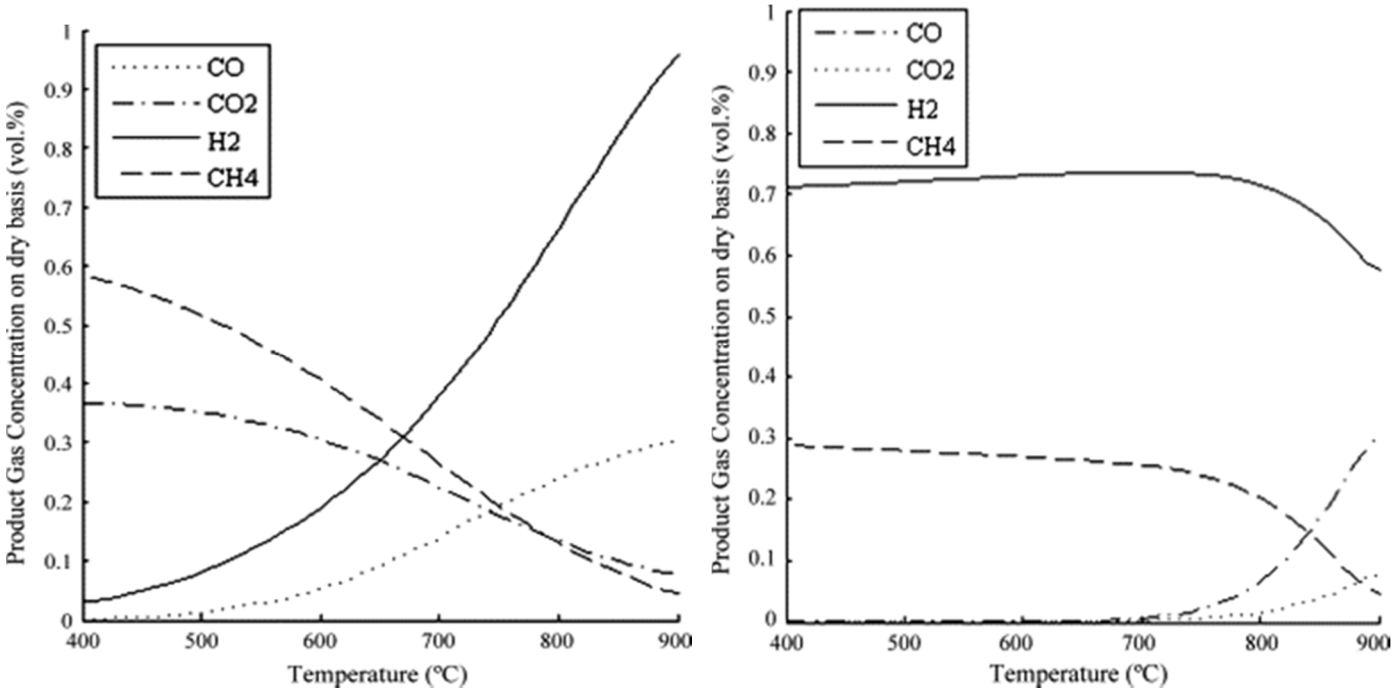

Figure 2.6a and b – Product gas composition of SMR and SE-SMR with respect to temperature at 15 bar. Input (a - left): 1 mole CH_4, 1 mole CO, and 2 moles H_2O. Input (b - right): 1 mole CaO, 1 mole CH_4, 1 mole CO, and 2 moles H_2O (McBride et al., 2004) (Dean et al., 2011a).

By observing Figure 2.6a and b it is possible to see benefit of CaO addition on the product gas composition of SMR at thermodynamic equilibrium conditions across a range of potential operating conditions. It can also be seen that the addition of CaO (Figure 2.6b) dramatically increases the H_2 purity at all temperatures below 700 °C, thereby demonstrating that it is possible to operate at lower temperatures than traditional SMR (Mahishi and Goswami, 2007) (Comas et al., 2004).

Figure 2.6a shows that above ~650 °C, the endothermic reactions are favoured, thereby allowing the reforming reactions to dominate. This can be confirmed by the rising H_2 and CO concentrations, yet falling CO_2 and CH4 concentrations. Whilst at the lower temperature range (<650 °C) the exothermic reactions are favoured, meaning the water-gas shift reaction dominates as revealed by the high CO_2 and CH_4 concentrations.

Figure 2.6b shows that the carbonation of the CaO is driving the reactions reforming and water-gas shift reactions and consequently the yield of H_2 was significantly higher in the lower temperature range. Beyond 700 °C, the $CaCO_3$ began to calcine and release CO_2. This resulted in a much lower driving force for the reforming and water-gas shift reactions hence the drop off in H_2 production.

It should be noted that whilst the steam reforming reactions (Equation 2.12 and Equation 2.13) are endothermic, the incorporation of the exothermic gas-solid carbonation reaction (Equation 2.1) and the mildly exothermic water –gas shift reaction (Equation 2.11), can provide a significant proportion of the heat required for the reforming. Any excess heat could also be utilised to drive a steam cycle (Martínez et al., 2013b).

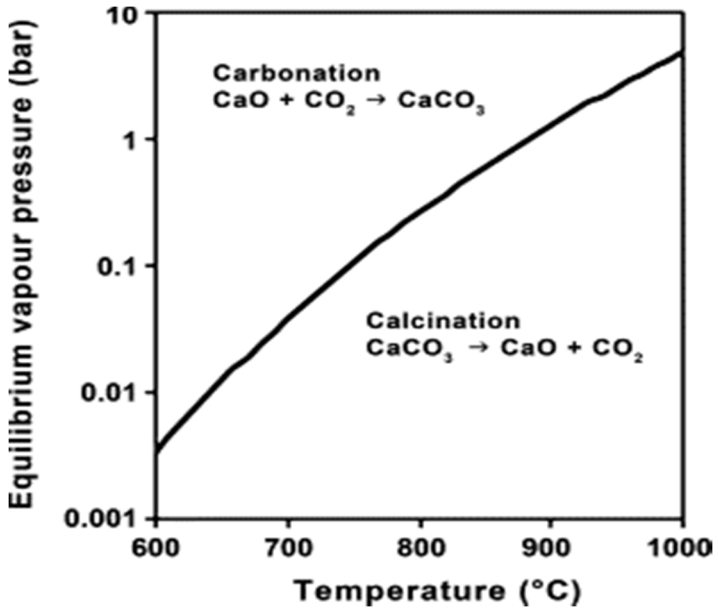

Figure 2.7 – Equilibrium vapour pressure of CO2 reacting with CaO across a range of operating temperature (McBride et al., 2004) (Dean et al., 2011a).

Utilising Figure 2.7 it is possible to set out a range of possible operating scenarios such that carbonation is favoured over calcination which in turn drives the other SESR reactions. This figure also highlights the increase in temperature required to begin calcination of the carbonated sorbent when under the high partial pressures of CO_2 expected (at 80 - 100 vol.% CO_2, more than ~900 °C is required) (Florin and Harris, 2008a).

A range of views have been expressed with regards to whether a higher pressure aids the production of H_2 or not. Hanaoka et al and Lopez Ortiz et al, showed that operating the carbonator/reformer at a raised pressure (between ~6 - 15 bar) improved the concentration of H_2 produced, however many other researchers – Martinez et al, Mahishi and Goswami, Comas et al, Wang et al and Florin and Harris – have showed that counter to this argument, an optimal H_2 production is achieved at atmospheric pressure (Lopez Ortiz and Harrison, 2001) (Hanaoka et al., 2005) (Martínez et al., 2013a) (Mahishi and Goswami, 2007) (Comas et al., 2004) (Wang et al., 2011) (Florin and Harris, 2007). Some of the differences in results may be due to the use of different fuel feedstocks, i.e. methane, representative model biomass compounds or biomass itself. But it is more likely that the differences are due to the modelled assumptions, reactor type/design, operational accuracy and the whether or not a catalyst was applied. Due to the quantity of recent research that has suggested atmospheric operation is optimal it is likely to be correct, but this will be assessed as pressure may influence the kinetics more than the thermodynamics.

2.7.2. Effect of steam to biomass ratio

It has been shown that as the value of the steam to biomass ratio (S:B) rises, the conversion of the fuel increases (Equation 2.12 and Equation 2.13) and the amount of deposited carbon decreases (Equation 2.14 and Equation 2.15). The increase in conversion is because of an increased rate of steam reforming and there being minimal limitation on the rate by steam quantity and the decrease in the coke formation is because of an increased rate of char steam gasification otherwise known as the water-gas reactions. An increase in S:B ratio is generally considered positive for the majority of gasification and reforming

reactions which take place however excessive S:B ratios could lead to an increased energy penalty and if high enough could lower the partial pressure of CO_2 such that the driving force for carbonation is diminished (Martínez et al., 2013a) (García-Lario et al., 2015b). There is also a possible side effect of having an excess quantity of H_2O in the reactor as it will inevitably exit with the H_2 thus diluting the purity and adding a potential extra purification step (Udomsirichakorn and Salam, 2014).

Equation 2.19 shows the formula for calculating the S:B ratio (in terms of mass flow rate) when it is necessary to take account of the inherent moisture within the biomass (Kalinci et al., 2009).

Equation 2.19 - Steam to biomass ratio formula:

$$S/B = \frac{\dot{m}_{steam} + (\dot{m}_{wet\ biomass} \times water_{wt.\%\ in\ biomass})}{\dot{m}_{wet\ biomass}(1 - water_{wt.\%\ in\ biomass})}$$

The use of biomass is often swapped for model compounds of biomass/tars (Gil et al., 2015) (Gil et al., 2016) (Esteban-Díez et al., 2016) (Gil et al., 2015) (Zamboni et al., 2014) (Fu et al., 2013) (D'Orazio et al., 2013), glycerol (a side product of bio-diesel production) (Garcia et al., 2000) (Dou et al., 2009) (Dou et al., 2013) (Wang et al., 2015) (Dang et al., 2016) or methane (Reijers et al., 2006) (Broda et al., 2013) (Radfarnia and Iliuta, 2014) (Dou et al., 2016) within the available literature Due to this, not all literature uses steam to biomass ratios and instead utilises steam to carbon ratios or steam to methane ratios.

It has been shown that the optimal S:B ratio depends upon the proportional content of cellulose, lignin and hemicellulose of the biomass and the individual elemental (C/H/O) breakdown (Widyawati et al., 2011). This leads to the prospect of possibly predicting the optimal S:B ratio simply by investigating the proportions of cellulose, lignin and hemicellulose within the biomass. Nevertheless, the effect of steam addition is clear; it dramatically improves H_2 purity, H_2 yield, CH_4 conversion, CO_2 capture rates (which can be observed in Figure 2.8) and decreases coke formation by favouring the forwards reactions of Equation 2.11 to Equation 2.17 (Yang et al., 2011) (Antzara et al., 2015) (Yan et al., 2010) (Rapagnà et al., 2000).

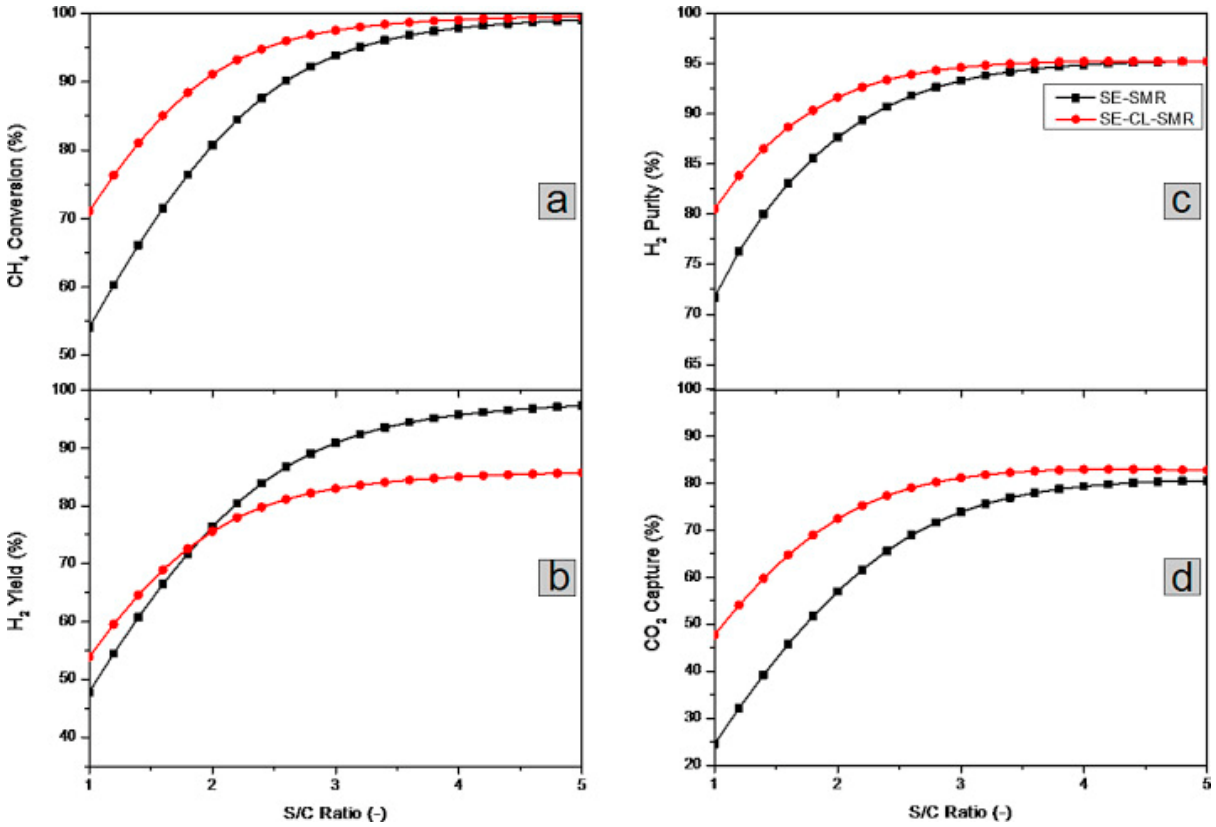

Figure 2.8 – CH_4 conversion (a), H_2 yield (b), H_2 purity (c) and CO_2 capture efficiency (d) as a function of S:C ratio for SE-SMR and SE-CL-SMR (Temperature = 650 °C, Pressure = 1 atm, CaO:C ratio = 1, NiO:CaO ratio = 0.5) (Antzara et al., 2015).

2.7.3. Effect of sorbent to biomass and sorbent to catalyst ratios

Some work has been undertaken with respect to assessing the impact of altering the sorbent to biomass ratio, often denoted as calcium to carbon ratio Ca:C. Hanaoka et al did show that a maximum H_2 yield was obtained at a CaO:C ratio of 2 (Hanaoka et al., 2005). It has been (Wang et al., 2014b)shown that the addition of CaO sorbent beyond a ratio of 1 (for when coal was utilised as the fuel feedstock) shows little improvement in terms of gas yield, evidenced by Figure 2.9Figure 2.9 – Effect of CaO:C on product gas composition (Experimental conditions: 750 °C, 4 bar, H_2O:C = 2 and a coal feeding rate: 9 g/min) (Wang et al., 2014b)..

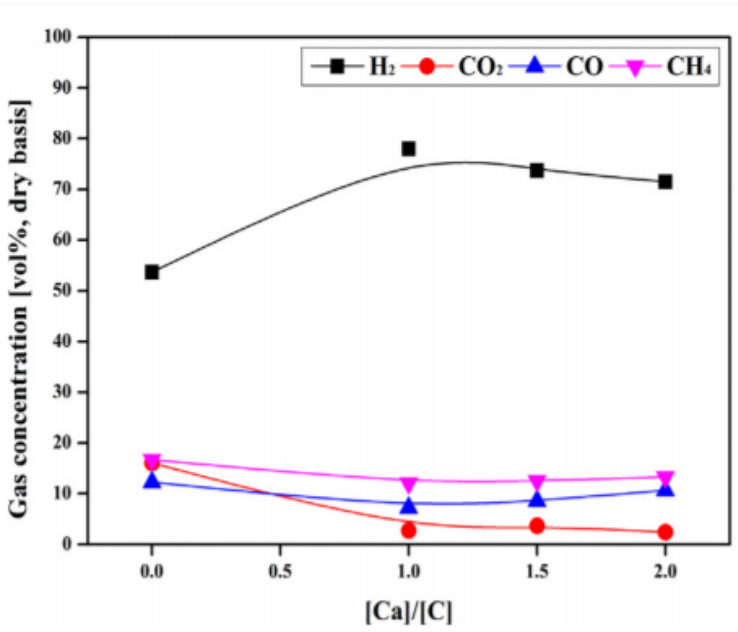

Figure 2.9 – Effect of CaO:C on product gas composition (Experimental conditions: 750 °C, 4 bar, H_2O:C = 2 and a coal feeding rate: 9 g/min) (Wang et al., 2014b).

It has been further shown that by further increasing the ratio of sorbent to biomass the gas conversion was increased due to an increased amount of contact between the tars and the CaO (Li and Suzuki, 2009) (Hanaoka et al., 2005). Biomass in particular produces high levels of tars when thermally processed due to its high reactivity at lower temperatures and its higher hydrogen to carbon ratio compared to coal. Tars can cause operational problems and increase the required maintenance and down time of the system. High tar content in the hydrogen rich product gas stream can reduce the usability of that gas. Tars are regarded as condensable organic fractions consisting mostly of aromatic molecules, although it should be noted that not all the tars formed are condensable (Milne et al., 1998).

There is a tar class grading system, running from 1-5 (Li and Suzuki, 2009): 1 being the very large hydrocarbons that are actually undetectable by Gas Chromatography (GC), 2 being heterocyclic aromatics such as pyridine and phenol, 3-5 are all aromatic molecules but have an increasing number of rings with 3 having just 1 ring and 5 having 4-7 rings. This system can be essentially reduced to light and heavy tars, where lighter tars have lower aromaticity and more aliphatic and heavy tars are the opposite. Heavier tars are more difficult to breakdown and tend to form coke when they do, especially

in low steam to carbon ratio environments. Heavy tars will typically have a lower volatility, higher viscosity, higher boiling points and more phenolic groups. Varying the operating conditions (heating rate, temperature, oxidising gas content, particle surface area, degree of mixing and residence time) alters the characteristic tar class achieved (Narváez et al., 1996). It is of course favourable to encourage the formation of lighter tars over heavier tars due to their ease of being decomposed during steam reforming.

This shows that CaO has some ability to catalytically crack the tars, which was investigated further by Udomsirichakorn et al (Udomsirichakorn et al., 2013); they showed that the tar content decreased with temperature and the tars that are present after the gasification with CaO were less aromatic.

It has been discussed that the reason for CaO possessing catalytic ability to crack/degrade tar species is because of O^{2-} ions which form active sites on the CaO; these ions have very diffusive electron clouds and can interact with nearby tar molecules by interrupting the stability of the π-electron clouds, which weakens the aromatic rings and leads to ring splitting (Udomsirichakorn et al., 2013) (Tingyu et al., 2000) (Yongbin et al., 2004).

Some thermodynamic modelling by Florin and Harris, conducted into the variance of sorbent to biomass ratios; it was found that a peak of CO_2 removal and subsequent H_2 production purity was observed at a ratio of 0.9 (S:B). It was predicted that any further increase to the ratio would not lead to an decreased CO_2 concentration, nor would it aid the production of H_2 (Florin and Harris, 2007). In saying this, it seems only high-temperatures and only a small range of sorbent to biomass ratios were actually considered and wider trends may exist, especially with the addition of a catalyst. Sorbents with a proportion content of Mg within their structure have also been shown to be effective at tar elimination that those without Mg content, indicating that the addition or use of dolomites may be beneficial for biomass gasification (Di Felice et al., 2010) (Myrén et al., 2002) (Delgado et al., 1997).

Sorbent to catalyst ratios were suggested to be independent of one and other and produce negligible effect upon the H_2 purity or methane conversion (Xie et al., 2012b). However contrary to this, Arstad et al displayed a better analysis of the effect of changing the sorbent to catalyst ratios and showed that

a lower percentage of catalyst in comparison to sorbent (20:80 was used) produced inferior results when compared to an equal ratio (50:50). Under the equal ratio scenario the results showed methane conversion close to equilibrium, a very high (97-98%) H_2 yield and a stable gas production during the 8 hours of cycling between the dual fluidised beds (Arstad et al., 2012). It was however noted that no attempt was made to maintain the amount of sorbent present, which implies that an excess quantity of sorbent may be necessary to ensure the CO_2 is sufficiently captured and the CO_2 impurity to the H_2 stream is minimised.

2.7.4. Effect of particle size

Particle size will directly impact on the minimum fluidisation velocity and the gas-solid contact efficiency; it is therefore an import parameter to study when considering the rate and extent of reactions. Xie et al (Xie et al., 2012b) investigated the sorption-enhancement of SMR with a Ni based catalyst and CaO within a Ca-based support structure and found that larger particles lowered the conversion of Methane in comparison to smaller particles, which is not surprising as smaller particles generally possess a higher effectiveness factor and lower the internal diffusion limitations within the particle (Fogler, 2006).

Based on the information described within this section and an extensive thermodynamic model the optimal conditions for SESR can be found to lie in the range of values displayed in Table 2.1 (Antzara et al., 2015).

Table 2.1 - Optimal operation condition ranges for SESR of biomass based on the evidence in this section and the thermodynamic modelling by Antzara et al. (Antzara et al., 2015).

Reforming cycle **Carbonation/reforming reactor**	**Regeneration cycle** **Calcination/oxidation reactor**
Temperature: 550 – 650 °C	Temperature: 850 – 900 °C
Pressure: 1 – 4 atm	Pressure near atmospheric
Steam/carbon ratio: 2 - 3	Type of oxidant: Oxygen
CaO/carbon ratio: 0.8 – 1	
NiO/CaO ratio: 0.2 – 0.7	

2.8. Reaction Profile

The SESR reaction between CaO and methane (methane is utilised as an example here for simplicity, but the same pathway is followed for all hydrocarbon based fuels) can be broken down into four predominant sections, as can be observed in Figure 2.10:

1. *Start-up* – Characterised by a sharp rise in H_2 and a sharp fall in the CH_4 as the reforming reactions begin to take place. CO and CO_2 do decrease, but from lower levels so the change is less noticeable.

2. *Pre-breakthrough* – The SESR equilibrium is reached, displaying the peak yields of H_2 and total gas production and very low levels of CO and CO_2. Some CH_4 does remain at the equilibrium position due to incomplete reactions or gas bypass.

3. *Breakthrough* – Once all readily available (external surface area) CaO has been converted to $CaCO_3$, the H_2 concentration begins to decrease and all other gas components begin to increase. It is a gradual change as some internal CaO still reacts with CO_2 but at a slower rate due to product layer diffusion.

4. *Post-breakthrough* – This is the final equilibrium stage and represents the equilibrium achieved by conventional SMR as if no sorbent were present. This is due to the sorbents carrying capacity being fully utilised.

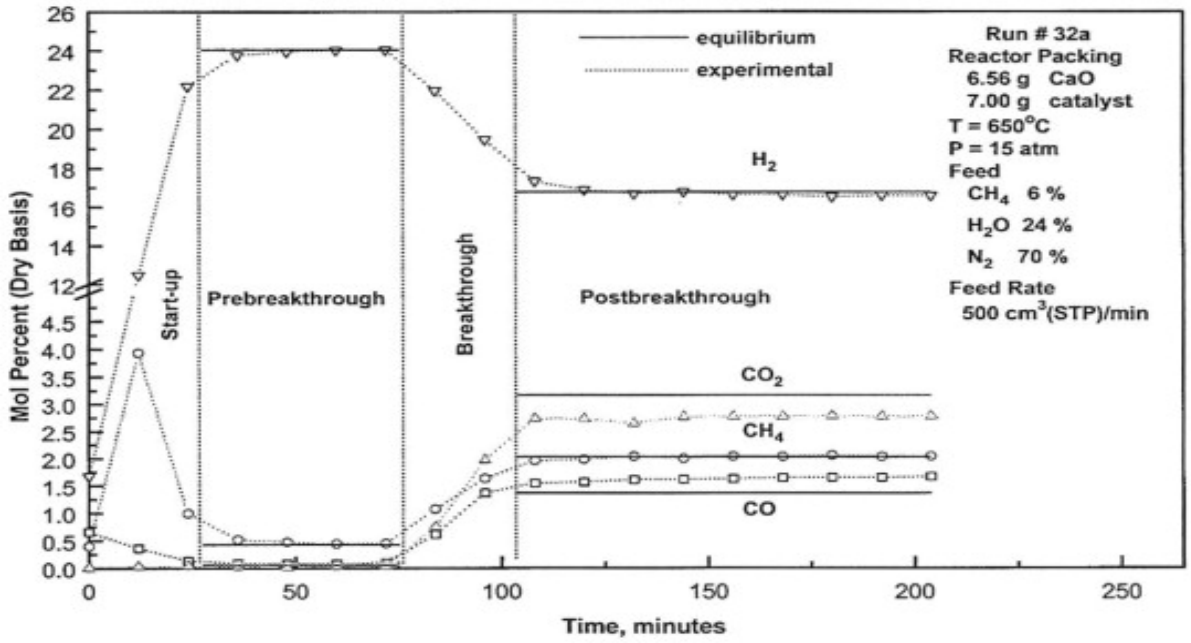

Figure 2.10 – Typical reaction profile of SESR of methane (Barelli et al., 2008).

The reason for the H_2 mole percent reaching its equilibrium at ~24 mol.% was because the feed gas was diluted with N_2. It can be noted that these differing periods are caused by the varying carbonation rates caused by the structure of the sorbent. As the sorbent becomes more saturated with CO_2, the total available reactive surface area goes down. It can be seen from Figure 2.10 that the initial increase in H_2 production during the start-up phase was much more rapid than the following decline in the breakthrough period. Thus showing that initially, there is a fast reaction rate where CO_2 is readily adsorbed onto the surface of the sorbent, after this the sorbent relies upon the slow diffusion of CO_2 into the pores through the carbonate product layer (Barelli et al., 2008).

The initial chemisorption reaction onto the outer surface of the CaO sorbent forms a thick and compact layer of $CaCO_3$. This thick layer impinges upon the diffusion rate limiting reaction through this product layer, which is the cause for the slower rate of carbonation. The carbonation reaction ceases to occur when the pores are blocked sufficiently so that the CO_2 cannot overcome the strong intra-particle limitation of the $CaCO_3$ (Abanades and Alvarez, 2003).

The shrinking core model is commonly utilised to describe the rate of carbonation of CaO through the product layer and it is simple and assumes a thin reaction wave that gradually progresses to within the particle, acting evenly from all sides (Li et al., 2016b) (Barelli et al., 2008) (Živković et al., 2016). An alternative model suggested is the unreacted core model which is similar to the shrinking core model but an unreacted core gradually increases with time. This model displays particular likeness to experimental observations as shown by Lysikov et al (Lysikov et al., 2007). They demonstrated that with consecutive CaO ↔ $CaCO_3$ cycling, unreacted CaO eventually ends up trapped within a matrix of $CaCO_3$, a graphic of the process by Lysikov et al is displayed in Figure 2.11. Calcium carbonate has a higher molecular weight and is therefore has a large molecular diameter, additionally to this, $CaCO_3$ is actually less dense than CaO meaning it has the ability to expand and block the pore entrances to the unreacted CaO (Blamey et al., 2015b). This process is accelerated by a process called sintering, which is discussed later.

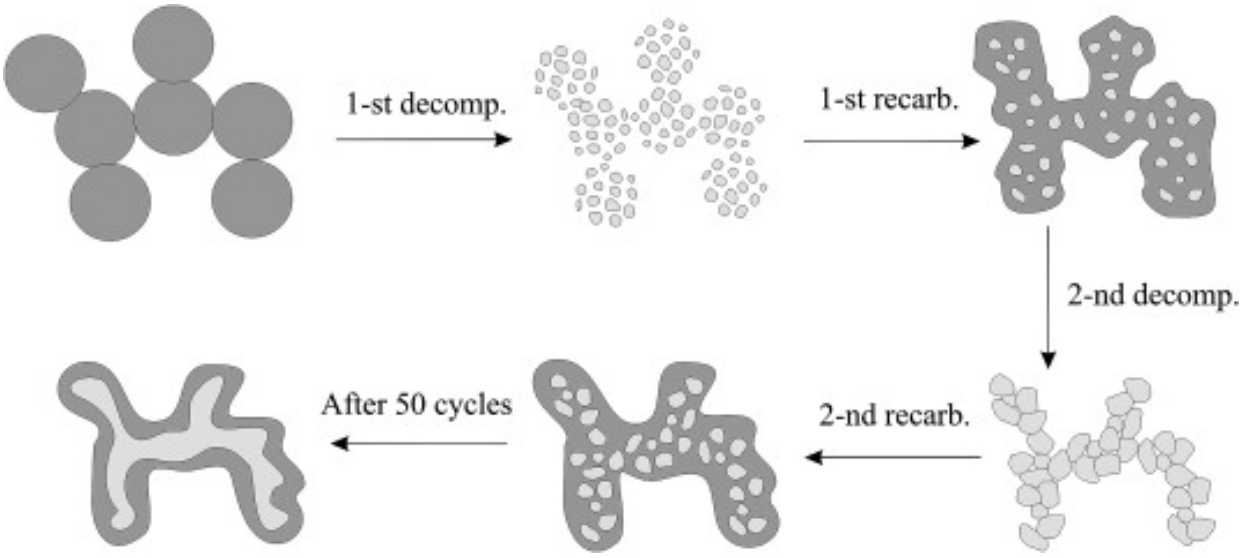

Figure 2.11 – A graphical representation of repeated CaO ↔ $CaCO_3$ cycling showing likeness to the unreacted core model for particle reaction kinetics (Lysikov et al., 2007).

2.9. Sorbent Selection

The sorbent within the SESR process is an essential part of the equation as it provides the main driving force for the production of high purity hydrogen. The appropriate method of selecting a sorbent was discussed by (Dou et al., 2013); they argued that a sorbent should have the following properties:

- A high long-term reactivity and sufficiently sized CO_2 carrying capacity for steam reforming – it is preferable for the reactivity to be at its greatest at lower temperatures
- The decomposition/calcination should occur in temperature range higher than that of the carbonation temperature range
- The particles should be resistant to attritional degradation and sintering
- The rate of CO_2 chemisorption should be sufficiently fast
- The sorbent shouldn't lose a large percentage of its initial carrying capacity during the cycling process
- The sorbent shouldn't have an unreasonable expense
- The spent sorbent should have properties that allow it to be useful in another market application

The sorbent predominantly utilised within the literature is CaO or CaO based sorbents, however it should be noted that other novel synthetic sorbents are also being investigated for CaL which may also have applications within SESR; these include low-temperature sorbents such as: Na_2ZrO_3, Li_2ZrO_3 and Li_4SiO_4 (Li_2ZrO_3 has received most of the literature attention) (Collins-Martinez et al., 2013) (Nair et al., 2004) (Ida and Lin, 2003) (Xiao et al., 2011) (Iwan et al., 2009) (Halabi et al., 2012) (Fauth et al., 2005), medium temperature sorbents such as: Hydrotalcites (additionally K-promoted variants) (Halabi et al., 2012) (Broda et al., 2013) (Wu et al., 2012) and natural or synthetic blends of Ca and Mg carbonates (Dolomite / Huntite) (Fermoso et al., 2012) (Lopez Ortiz and Harrison, 2001).

The reasoning for focusing upon CaO based sorbents is that they meet most of the above requirements (Dean et al., 2011a) (Florin and Harris, 2008a) (Dean et al., 2013). They can be obtained from readily available, cheap and environmentally benign sources such as limestone. The spent sorbent can be

potentially utilised within the cement industry as a precursor material (possibly not if it has been used for SESR due to contamination with Ni). It has a suitable calcination-carbonation temperature range and is sufficiently active with regards to the reaction rates. Most importantly though, CaO has an initially large carrying capacity (orders of magnitude higher than other synthetic or hydrotalcite sorbents) which if were maintained during cycling would bring the technology to market rapidly (Manovic and Anthony, 2009a).

Synthetic CaO based sorbents do possess some of the properties above, such as low regeneration temperature and long lasting carrying capacity over multiple cycles. However the initial carrying capacity is much lower than natural limestones and the shear cost of the manufacturing the sorbents is likely to be their biggest downfall. Abanades et al (Abanades et al., 2004) stated that for Li based sorbents to be economically competitive they must be capable of undergoing tens of thousands of cycles without degradation, which seems unlikely.

2.9.1. Carrying capacity and deactivation

CaO based sorbents are widely known for use in the calcium looping process and it may be possible to take the experience gained from that process and apply it to SESR. One of the biggest problems associated with the calcium looping process is the sorbents loss of carrying capacity during cycling (Fennell et al., 2007) (Sun et al., 2008c). In a purely theoretical context, 1 mole of CO_2 would react with 1 mole of CaO to form 1 mole of $CaCO_3$; however this is difficult to achieve due to a number of reasons such as some parts of the particle being inaccessible to gas absorption through the carbonate product layer and the materials reactivity loss by the following mechanisms. The decline in the sorbents carrying capacity from its initially high level can be observed in Figure 2.12. What should be additionally noted from Figure 2.12 is that there is a fast and slow stage to the carbonation of the sorbent. This is because initially the CO_2 reacts with the outer surface region of the particles and is controlled by the kinetics of the reaction, after this a slower solid state diffusion reaction occurs through the outer carbonate product surface structure (Abanades and Alvarez, 2003).

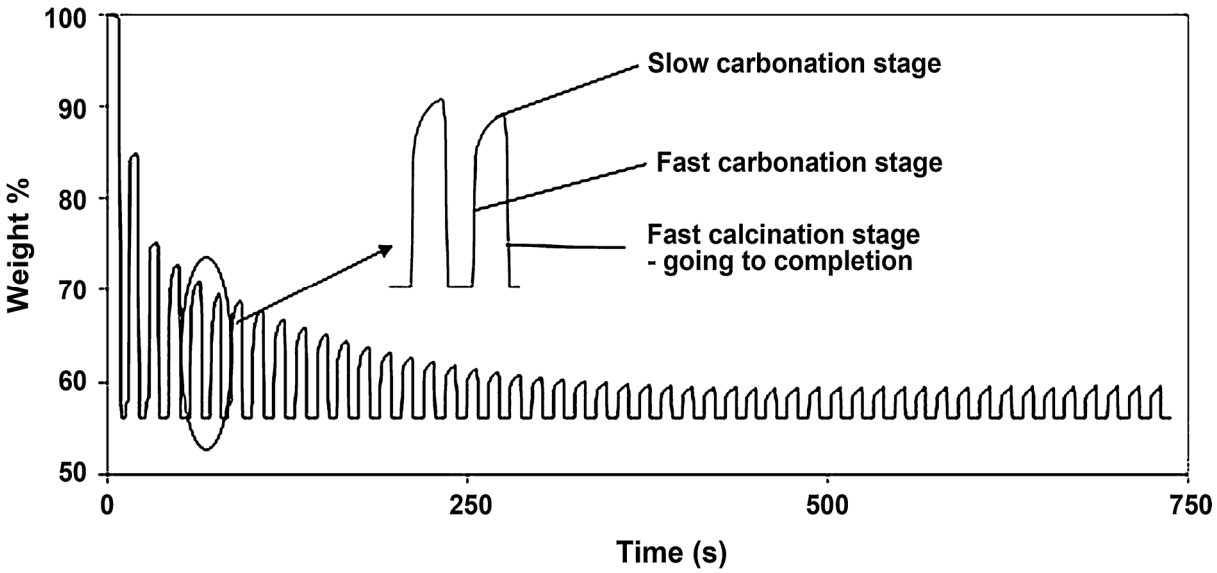

Figure 2.12 – A visulasation of the decrease in carrying capacity with increasing number of cycles of a CaO sorbent, additionally showing the fast and slow carbonation phases (Dean et al., 2011a). The x-axis on this figure is believed to actually be minutes, not seconds.

The loss of carrying capacity is caused by sintering, sulphation and ash fouling of the particles. A popular equation to describe the loss in reactivity with cycling is the Grasa equation, Equation 2.20 (Grasa and Abanades, 2006).

Equation 2.20 – Grasa equation (Grasa and Abanades, 2006):

$$a_N = \left(\frac{1}{1/(1-a_\infty)} + kN\right) + a_\infty$$

Where a_N is the maximum carbonation conversion of the sorbent in cycle N, a_∞ is the residual conversion of the sorbent after a large number of cycles, and k is a decay rate constant. This model was developed to characterise the initially fast drop off in carrying capacity followed by a levelling off of the carrying capacity after many multiple cycles.

The attrition of the sorbent particles is can be a leading cause for drop off from the initial activity and occurs by particles 'bumping into each other' within the fluidised bed and knocking off smaller fragments of the particles. This is because fines are broken off from the main particle and eluted with the exiting gases thus loosing available capturing material. It has been proven that most of the attritional

loss occurs during the first calcination; after this however the proportion of the particle that does remain has the strongest structure and thus the attritional degradation of the particles tapers off (Jia et al., 2007) (González et al., 2010). Further cycling inevitably leads to sintering and a progression of the sulphating reactions which further strengthens the bonding of the remaining particles (Chu and Hwang, 2002). The study by Chu et al. also showed that a smaller particle size of a calcium sorbent had a higher attrition rate which can be explained by considering the total exposed surface area of the particle, which is higher for smaller particles. When natural limestone sorbent precursors are utilised the scale of the attritional loss is largely dependent upon the type of limestone (Arias et al., 2013). Chen et al. (Chen et al., 2013) showed that the degree of the attrition can be decreased by cementing the sorbent into an alumina support, they added starch to act as a pore forming agent so that the high CO_2 capture capacity wasn't adversely affected by any pore blocking. Chen et al. have further developed this method by isolating an optimal ratio of alumina to limestone and proposed that the addition of the alumina increased the sintering temperature due to its inherently higher melting point (Chen et al., 2012b). Additionally they remark that the a high-temperature of calcination followed by high gas velocity and longer length of calcination time are the main influencing factors for attrition, which is in accordance with other researchers (Harrison, 2008) (Grasa et al., 2008) (Montagnaro et al., 2010). It has been shown that a mild attrition can remove the unreactive blocking outer product layer of $CaCO_3$, thereby exposing fresh surface area ready for carbonation (Chen et al., 2012b). This implies a weigh off between loosing sorbent mass (which potentially could be calcined making it useful for further cycles) and reducing the carrying capacity drop off during that specific cycle. An alternative is to operate a entrained flow reactor with very small, dust like particles such that attrition can be disregarded (Sceats and Horley, 2014).

Sintering of sorbents is the main cause for the drop off in long-term carrying capacity. It is understood that main mechanism of sorbent sintering is the solid state ionic movement of Ca^{2+} and CO_3^{2-} ions within the lattice caused by lattice defects (H. Borgwardt, 1989). This sintering leads to changes in the pores shape and structure through grain growth and pore collapse and occurs at elevated temperatures, above the Tammann temperature (half the melting point, the temperature above which atoms have sufficient energy for bulk movement within the lattice structure) (Baerns, 2013) (H. Borgwardt, 1989). This

eventually leads to a drop off in reactive surface area and therefore a drop-off in reactivity, which is only made worse by increasing the partial pressure of CO_2 and/or steam during the calcination process (Borgwardt, 1989b). This was also shown to applicable for synthetic sorbents as well as natural sorbents (Clough et al., 2016). The sintering process leads to a reduction in average pore diameter such that it becomes rate limiting and is caused by the intrinsically larger molar volume of $CaCO_3$ than CaO (Barker, 1973b) (Green and Perry, 2007) (Grasa and Abanades, 2006).

A side effect of utilising limestone based sorbents is that they also react with SO_2 to form calcium sulphate which can be present in the gases produced by the reforming and gasification of biomass (Manovic et al., 2010). The formation of $CaSO_4$ can be detrimental to the CO_2 carrying capacity of CaO due to the active sites being utilised and due to the fact that under normal CaL operating conditions the $CaSO_4$ will not be decomposed (due to a temperature of >1300 °C being required) (Coppola et al., 2012) (Luo et al., 2014). Within the carbonator/reformer reactor of the SESR process (where the majority of the sulphur containing products will be formed due to the fuel being gasified) the reducing conditions will likely favour the production of CaS rather than $CaSO_4$ but it will likely be converted within the calciner to $CaSO_4$ (Hansen et al., 1993). Sulphation is certainly bad in terms of CO_2 carrying capacity, but it is possible that the sulphation process is useful as it strips the sulphur from the gas stream thereby purifying the H_2 slightly more and reducing further processing steps; and if the sorbent has a high purge/make up rate then sulphation maybe considered beneficial.

2.9.2. Pre-activation and reactivation

To counter the sorbents carrying capacity degradation some researchers have developed methods to overcome or prevent it from occurring. One method of reactivating calcium based sorbents that has been proved to enhance the sorbents long term carrying capacity is by steam hydration during the CaL cycling (Manovic and Anthony, 2007) (Blamey et al., 2011). Hydration is where the calcined sorbent is cooled to ~250-450 °C and subjected to high partial pressures of steam or liquid water, in doing so the CaO converts to $Ca(OH)_2$ which is more reactive towards CO_2 and leads to a higher conversion.

The benefit of steam hydration can be observed with reference to Figure 2.13, showing the addition of steam after 13 cycles (Blamey et al., 2015a). The subsequent carbonation can be undertaken via two methods, direct carbonation where the hydrated sorbent is sent directly to the carbonator, and indirect carbonation where the sorbent is first calcined before being moved to the carbonator; direct carbonation was found to be better due to the a higher resultant carrying capacity (Blamey et al., 2015a).

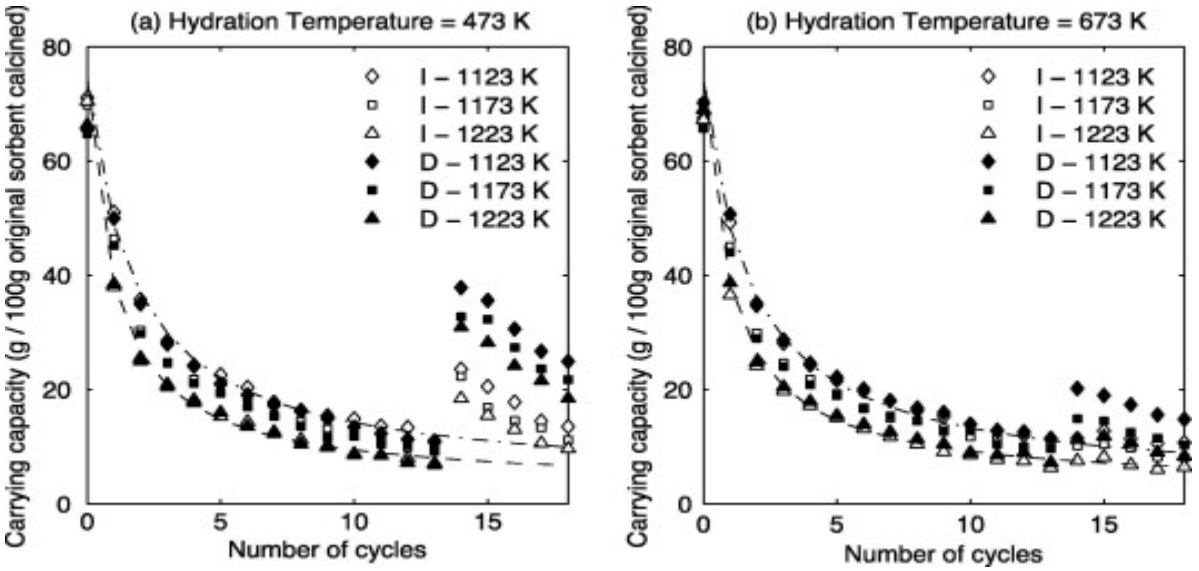

Figure 2.13 – Carrying capacity as a function of cycle number for hydration temperatures of (a) 473 K and (b) 673 K with calcination temperature varied before hydration (1123, 1173 and 1223 K) using indirect (I) and direct (D) carbonation as reactivation strategies – also shown are fits of Eq. (1) to data obtained for calcination temperatures of 1123 and 1222 K before hydration (Blamey et al., 2015a).

The length of time that hydration takes place for should be minimised as much as reasonably possible as it has been discovered that long hydration periods can lead to ‘cramming’ which is a consequence of chemical sintering (Coppola et al., 2014a). However this research was conducted using liquid phase water as opposed to vapour phase water and therefore there may be other factors at play. It would be more suitable to utilise vapour phase steam for hydration as it would remove the need to cool and reheat the particles between carbonation and calcination reactors. Liquid phase and vapour phase hydration was examined and found that vapour phase hydration was most effective at maintaining the carrying capacity (Kuramoto et al., 2003).

In other work by Donat et al (Donat et al., 2011) has concluded that it is beneficial to have steam present during the calcination and carbonation cycles. Steam within the calcination reaction intentionally sinters the particles in a controlled manner to alter the surface characteristics and increase larger pore volumes, seemingly making a stronger structure. They state that the addition of steam within the carbonation reaction leads to a reduction in the diffusion resistance through the product carbonate layer.

A relatively simple method which is being investigated pre-activate the sorbent is a method called thermal activation, which works by subjecting the sorbent to high-temperatures for a prolonged period of time prior to use. This high-temperature process influences the pore skeleton structure such that the sorbent is positively sintered to provide an attrition resistance sorbent that has a particle morphology suitable for capturing CO_2 (Manovic et al., 2008) (Jia et al., 2007) (Manovic and Anthony, 2008b). It has been shown that the beneficial pore structure can develop during high-temperature cycling, which is called self-activation (Stendardo et al., 2013). However the final carrying capacity of either method of thermal treatment has been shown to result is a carrying capacity little better than non-thermally treated sorbents (Blamey et al., 2015b).

Another simple method of increasing the long term carrying capacity of natural sorbents is by the addition of minor constituents, often salts, within the sorbent's matrix. This is commonly referred to as doping. A reason for this technique being investigated is that is a relatively cheap route to increasing the longevity of the sorbents carrying capacity. Work by Gonzalez et al (González et al., 2011) compared KCl and K_2CO_3 doped sorbents within a TGA and a fluidised bed reactor and noticed that KCl doped sorbents had a lower initial carrying capacity, however this carrying capacity was prolonged and less degraded with cycling. Other dopants have also been tested, to varying degrees of success: Na_2CO_3 and NaCl (Salvador et al., 2003) (Abanades and Alvarez, 2003), Cs (Reddy and Smirniotis, 2004), Al_2O_3 (Sun et al., 2008b), Li_2CO_3 (Florin and Harris, 2008c), $MgCl_2$, $CaCl_2$, $Mg(NO_3)_2$, and the Grignard reagent isopropyl-magnesium chloride (Al-Jeboori et al., 2012), $CaBr_2$ (Manovic et al., 2013). An explanation of how the dopants work and therefore can be optimised was given by Al-Jeboori et al (Al-Jeboori et al., 2012). It was stated that addition of dopants increases the volume of 100nm diameter pores and significantly alters the pore size distribution in order to favour the diffusion of CO_2 into pores.

Their work also showed there is a maximum limit to the benefit gained; thereby showing a further increase in dopant quantity does not necessarily lead to a higher concentration of dopant ions within the structure or carrying capacity. The application of steam and doping has been shown to be synergetic in the enhancement of long term cycling carrying capacity (Manovic et al., 2013). A key piece of research investigated the use of a variety of mineral acids (HCl, HBr, HI, HNO_3) and demonstrated that HBr doped limestones have a significantly higher carrying capacity, which they suggest is due to the molecular size of the HBr and the pore size required for CO_2 capture (Al-Jeboori et al., 2013). XRF analysis showed that the majority of the dopant ions remained within the sorbent matrix during cycling. It has been further shown to the work of Manovic et al. and Al-Jeborri et al., that application of steam and HBr doping produced a carrying capacity that was approximately 3 times higher (after 15 cycles) than the an undoped no steam system (González et al., 2016). HBr is often utilised as a bromine source in many organic reactions however the sustainability of HBr production has received little attention, it is noted that HBr is sometimes produced as a waste material from other industrial processes (Eissen, 2012).

2.10. Catalyst Selection

The catalysts' role within the SESR process is to accelerate the rate of reforming and gasification as well as aid the cracking of the hydrocarbon fuel and its associated tars. The catalysts increase the rate of reaction by encouraging alterative reaction pathways; however they do not revise the position of thermodynamic equilibrium (Fogler, 2006).

Nickel based catalysts are currently industrially favoured for steam reforming as they present a relatively lower overall cost (compared to rare earth metals like Pt and Pd which are also active for these reactions) and have a high catalytic performance (Nieva et al., 2014). Nickel catalysts however are prone to coking. This is where carbon is deposited onto the surface leading to blocking of the active sites and has the potential to fracture the catalyst in to finer particles if deposited in sufficient amounts within the pores. Coking occurs mainly due to the products of decomposition of the fuel source,

however it can also be caused by the disproportionation of CO (Li et al., 2012). When deposited within the structure of the catalyst the carbon formations are referred to as 'whiskers' (Sehested, 2006). The surface structure of a catalyst can be broken down into two main sections, 'Steps' and 'Terraces'; steps being edges to the flat terraces. It was observed and calculated that steps were generally favoured for carbon deposition because the Ni's atoms are more loosely packed and therefore make them suitable easy to access nucleation points (Helveg et al., 2004). As was stated earlier, a higher steam to carbon ratio minimises the deposition of carbon. Coked catalysts have traditionally been combusted in air to remove the carbon; however this leads to sintering of the particles and metal agglomeration and can lead to residual ash deposition on the catalyst (Moulijn et al., 2001).

Another cause of deactivation of the catalyst is particle sintering, which occurs due to the high-temperatures at which the particles can be subjected to. The high-temperatures required for sintering are mostly likely to occur within the particles on a localised basis during the exothermic regeneration of the catalyst and within the calciner. The main mechanisms of sintering are as follows: (Sehested et al., 2004)

- *Particle migration* – Catalyst crystallites move towards each other and coalesce
- *Ostwald ripening* – Individual atoms of the catalyst are transported from one crystallite to another
- *Vapour transport* – This only occurs at very high-temperatures where atomised catalyst ions are transported in the vapour phase to other crystallites

It has been shown that the most influential factors involved with particle sintering are the temperature and the composition of gas in which the catalyst is present. Further to this point, a higher steam concentration over the catalyst leads to an acceleration of the sintering process (Bartholomew, 1993). However, this may minimising steam use may not be possible due to the requirement of a high steam partial pressures to reduce coking and increase H_2 purity and yield. Because the mechanisms of sintering are dependent upon the support structure on which the catalyst lies, it is imperative to make sure the support material does not increase the probability of sintering by sintering itself. A higher surface area

of the support structure has been shown to increase the stability of the catalyst with regards to sintering, likely because an increased distance between catalyst particles reduces their ability to migrate and coalesce (Richardson and Crump, 1979) (Sehested et al., 2001) (Richardson and Propp, 1986) (Ruckenstein and Pulvermacher, 1975). A summary of the available knowledge on the effect of step and particle sizes on the activity of Ni steam reforming catalysts was performed by Sehested (Sehested, 2006); evidence was displayed that showed an increase in crystallite particle size decreased the activity of the catalyst, hence showing a strong link between particle growth via sintering and activity.

Sulphur poisoning can be completely debilitating for Ni based catalysts below 700 °C. The process by which sulphur can poison the catalyst is as follows. Sulphur containing compounds in the fuel are converted into H_2S (reduced form because of the reducing environment of the carbonator/reformer of SESR) (Sehested, 2006). The sulphur atom is then strongly adsorbed onto the surface of the Ni leading to an inactive site; this process is displayed by Equation 2.21.

Equation 2.21 – Sulphur deposition on Ni catalysts:

$$H_2S + Ni^*_{Surface} \rightleftharpoons Ni_{surface} \cdot S + H_2$$

In general the detrimental effect of sulphur on the catalyst is dependent upon the percentage of sulphur within the fuel and the catalysts surface area available for attack and hence this is dependent upon the shape and pore structure of the particle (Sehested, 2006).

It is well known that it is highly favourable to achieve close contact between the catalyst and the fuel source, thereby permitting enhanced catalytic fuel conversion efficiencies (Richardson et al., 2012). This can be difficult to achieve with solid fuels such as biomass as they are homogeneous in phase. There are two ways to overcome this dilemma; it is possible to wet impregnate the solid fuel prior to gasification thereby achieving an in-situ catalyst. The main drawback to this technique is the cost of drying the fuel after impregnation and recovery of the catalyst (Moulijn et al., 2001). The second and somewhat simpler method of achieving good contact is by grinding the fuel to reduce particle size

thereby increasing the surface area and then physically mix the ground fuel and catalyst particles (Thangalazhy-Gopakumar et al., 2011).

To utilise the Ni based catalysts, the nickel must be in the zero valent metallic form, which is its active form. In this active form the Ni particles show a more even distribution through the main support, which aids the prevention of carbon whiskers forming (Tomishige et al., 1999). After the production of the catalysts, they are usually in the NiO (Ni^{2+}) form which has been shown to be ineffective at catalysing the reformation reactions (Swaan et al., 1994). Li et al (Li et al., 2012) has described the method in which the catalyst is activated by flowing H_2 over the Ni; the reaction for this is displayed below as Equation 2.22.

Equation 2.22 – Ni reduction:

$$Ni^{2+} + H_2 \rightleftharpoons Ni^0 + 2H^+$$

The activation process varies between different research papers due to the experiment being conducted under idealised laboratory conditions rather than experimentally accurate conditions. The biggest discrepancy is regarding the activation/reduction time, some researchers (Li et al., 2007) (Fermoso et al., 2012) (Wu et al., 2013) have utilised 5-24 hours, some (D'Orazio et al., 2013) (Dou et al., 2013) (Martavaltzi and Lemonidou, 2010) (Phromprasit et al., 2013) 1-4 hours, some (Xie et al., 2012b) as little as 30 minutes and others (Couttenye et al., 2005) suggest there is no requirement for an activation period at all as the H_2 produced from the gasification and reforming reactions is sufficient to activate the catalyst in situ (Cheng and Dupont, 2017) (Antzara et al., 2016) (Xiao et al., 2017). Over time due to coking, sintering and sulphation the catalyst can require reactivation with H_2 although, Li showed that the doping of the catalyst with Rh could produce a self-regenerative property (Li et al., 2007).

Iron is another metal that has been suggested for use as a gasification and tar destruction catalyst (Fukase and Suzuka, 1993). The benefit of utilising Fe as a catalyst as opposed to Ni is that when the particles are spent they are likely to be sold to the cement industry which add Fe to cement to increase its strength (Taylor, 1997), so by the use of Fe based catalysts the product would not be limited in its

reusability. Additionally, Fe is a cheaper, more prominent in the earth's crust and is less toxic than Ni (Di Felice et al., 2010). Fe impregnated onto an alumina support has been shown to be an effective catalyst, increasing the hydrogen produced during steam reforming (Matsuoka et al., 2006) (Urasaki et al., 2005). Di Felice et al, found in their study of biomass tar degradation that the oxidation state of Fe that occurs is strongly dependent upon the other materials within the bed; for example, when MgO is present, Fe^{2+} exists as the most stable form but when CaO is present Fe^{3+} is the most favoured form (Fe^{3+} is stabilised by the formation of $Ca_2Fe_2O_5$ despite it actually being thermodynamically unstable state of Fe when oxidisation agents are present) (Di Felice et al., 2010). This is an important fact to consider because if side reactions are occurring between the CaO and the Fe then this could potentially lead to fewer CO_2 sorption sites being available, it was also shown in this study that $Ca_2Fe_2O_5$ is not active as a catalyst and resists reduction to Fe^0. Nordgreen et al, has shown that Fe^0 is the most active form of iron for catalytically cracking tars and thus iron should be reduced prior to use so as to activate it (Nordgreen et al., 2006a) (Nordgreen et al., 2006b). They have also shown that Iron oxides did not demonstrate any catalytic ability to crack tars. Fe stabilised onto an alumina support when MgO was present was found to be an ineffective catalyst due to an inactive $Mg_x{-}Fe_{1-x}{-}Al_2O_3$ spinel mixture being formed (Polychronopoulou et al., 2006).

Coking is a major problem for Ni based catalysts, however is less of a problem for Fe based catalysts (Azhar Uddin et al., 2008). When coking does occur, it has been shown that the pathway of coke formation is via thin filamentous carbon whiskers forming first with iron carbide (Fe_3C) particles along their length which then spurred further thick coke formation around these areas of iron carbide (Zhang et al., 2003). It has further been shown that iron can migrate into the coke itself, which when the coke is removed via oxidation the migrated iron crystals are lost with the carbon, leading to catalysts mass loss (Xie et al., 2009).

Sintering is still a problem for iron catalysts, as it is for nickel ones. The main reason for iron particles sintering occurring is due to the agglomeration of FeO (wustite) due to the redox reactions occurring during cycling at temperatures greater than 800 °C (Fukase and Suzuka, 1993) (Tamhankar et al., 1985) (Otsuka et al., 2003a). Otsuka et al. indicated that sintering could not be minimised by the doping of

certain rare earth metals (Otsuka et al., 2003b). With repetitive cycling the surface area of the Fe catalyst has been shown to nearly halved from its initial value thereby displaying evidence of sintering, small quantities of palladium was however revealed to decrease the rate of sintering (Urasaki et al., 2005). The suggested method of why palladium reduces sintering was that most of the sintering occurs during the reduction of the catalyst to regenerate it, so by adding palladium the reduction rate of the iron oxide was increased and thus the length of the reduction stage was decreased meaning the particles are reduced for a shorted length of time.

Uddin et al, (Azhar Uddin et al., 2008) demonstrated that Fe_2O_3 supported on Al_2O_3 provided the correct conditions for the production of Fe_3O_4, which despite previous knowledge that iron oxides were inactive catalysts for SESR reactions, the transitional state of Fe_3O_4 was active for the gasification and water-gas shift reactions. The catalyst was able to decompose >90 % of the tars into light volatiles and was a stable tar decomposer throughout cycling; however their definition of cycling involved no regeneration, so in reality it was more like continual use of the same catalyst.

In comparison of Fe and Ni based catalysts for SESR, Polychronopoulou et al have shown that Fe based catalysts can perform as adequately as commercial Ni catalyst's (Polychronopoulou et al., 2006). Xie et al, showed that Ni was a more effective catalyst in improving the quality of the product gas but Fe was more effective at promoting the water gas shift and reforming reactions, when utilising biomass as the feed (Xie et al., 2009).

The careful use of the reforming catalysts is necessary to improve the resistance to sulphation, carbon deposition and activity loss, whilst simultaneously achieving effective inter-particle contact for complete fuel conversion and not impinging upon the CO_2 capture by the sorbent. Combined multifunctional catalysts and sorbents have been shown to be the most effective particle system for SESR but more work is needed to ensure the properties of the particles are retained over the long term operation and their method of production is not too expensive, this is discussed further within chapter 6.

2.11. Support Selection

The mechanical stability of the catalyst and sorbent is not always assured and therefore supports have been developed to increase the long term stability of the particles. A suitable support material would provide an even distribution of catalyst and sorbent crystallites and possess the ability to resist the sintering mechanisms previously discussed. It has also been shown that the sorbent on a support structure maintains more of its initial carrying capacity for longer, which gives good precedent for further work into this area (Broda et al., 2013). Li et al. (Li et al., 2012) has recently collated a substantial collection of other individuals' work that utilised biomass tars as the fuel feedstock and based their catalysts upon nickel. They have also showed that the addition of CeO_2 and MnO to a Ni catalyst in an Al_2O_3 support particle exhibits: increased activity, suppression of coke formation, less of a drop off in catalytic performance with time and MgO leads to an increased gas yield. In other work by Nishikawa et al. it was successfully shown that the addition of noble metals such as Pt negates the need for the reduction in H_2 and it additionally produces self-regeneration properties (to counter sintering and coke formation) for the supported catalysts (Nishikawa et al., 2008). Recently in a review by Angeli et al. the assertion has been made that there is currently no systematic understanding of the effect of adding a promoting element or compound to the matrix (Angeli et al., 2014). They did however note that the Ni crystal size is the key element for coke suppression and boosting the activity of the catalyst. Additionally it was suggested that CeO_2 and ZrO_2 are key promoters for an increase in activity and a decrease in coking (Angeli et al., 2014). Further to this point, doping of trace metals (K, Co and Fe) with the wet impregnation of the Ni catalyst into a CaO support/sorbent has shown to beneficial with regards to the tar cracking ability and doping with potassium actually increased the hydrogen yield.

By observing the available literature, Al_2O_3 seems to be a conventionally utilised support; Al_2O_3 is present in two main forms α-Al_2O_3 and γ-Al_2O_3 which symbolise the crystal structure of the compound, α- being the predominantly utilised form due to its greater mechanical strength. The activity of the catalyst upon its support is measured using H_2 adsorption. Utilising this method Miyazawa et al.

(Miyazawa et al., 2006) demonstrated that the order of steam reforming activity for various supports was in descending order: $Ni/ZrO_2 > Ni/TiO_2 > Ni/Al_2O_3 > Ni/CeO_2 > Ni/MgO$, the first three presented very similar levels in activity that were significantly greater that the last two supports. When consideration had been made to the coking suppression and tar reformation Ni/CeO_2 turned out to be the most effective, yet Ni/Al_2O_3 was the most stable; therefore CeO_2 was used as an additive to the matrix and produced a particle that had a high activity and good resistance to coke deposition. Pt and MgO were further added to promote the catalysts' reducibility and Ni particle redistribution (negative effects of distribution of Ni are caused by sintering) respectively (Li et al., 2012). Limestone derived CaO supported on a commercial aluminate cement has been shown to enable the CaO to retain a much greater quantity of its carrying capacity (28%) over 1000 cycles due to a change in the morphology that favours nano-pores. Within this work it was also shown that smaller particles tend to present a high strength and durability to multiple cycles than larger particles (Manovic and Anthony, 2009b).

Another type of support material that has received seldom attention is based on Silica. The reason these supports are being considered is the fact that when bonded, the calcium the silica ions form structures like Ca_2SiO_4, which is known within the cement industry by its crystal name, Belite (Zhao et al., 2012) (Taylor, 1997). This is important as it has been shown previously that dicalcium silicate is a polymorphic material, which means its molar volume varies with temperature due to crystal structure phase changes that occur. The benefit of this is that as the volume of the polymorphic material changes, it has been shown to have the ability to reopen the previously sintered structure of the $CaCO_3$, thus increasing the porosity and permeability of the particle meaning that in during the following carbonation cycle the sorbent should be able access more of the CO_2 that it would otherwise be able to (Zhao et al., 2012). The benefits of utilising this sorbent support are discussed further within chapters 5 and 6. Three important phases of Ca_2SiO_4 exist, they are γ-, a'- and β- Ca_2SiO_4. As the temperature increases beyond ~780-860°C γ-Ca_2SiO_4 converts to a'-Ca_2SiO_4, a subsequent decrease in temperature (~630-680°C) converts the Ca_2SiO_4 into β-Ca_2SiO_4 which can be regenerated into a'-Ca_2SiO_4 by raising the temperature (~690°C), further cooling (<500°C) of β-Ca_2SiO_4 forms γ-Ca_2SiO_4 again. From the cement industry, knowledge of Belites crystalline transitions is known and specifies that the volume expansion

that occurs between β-Ca_2SiO_4 and γ-Ca_2SiO_4 produces approximately a 10% volume increase whereas between a'-Ca_2SiO_4 and β-Ca_2SiO_4 only ~2% volume expansion occurs (Remy et al., 1995) (Taylor, 1997) (Remy et al., 1997). The advantage of Ca_2SiO_4 is that the temperatures for support structural cycling are fairly similar to that of the CaL/SESR cycling temperatures. Additionally, possessing silica within the structure of the particle may actually make it more beneficial to the cement industry when the particles are purged from the system as silica is a main constituent within cement. It should be noted though that a 10% increase in volume is likely to fray the particles and lead to bed material loss by elutation, therefore allowing the temperature of operation to drop close to 500 °C or less should be avoided. It has currently not been proved in the available literature that a 2% increase in support volume would negatively fracture the particles but careful consideration as to the ratios of support to other constituents within the particle and their possible interactions will have to be considered if this support is utilised. One paper has utilised SiO_2 supported CaO sorbent to produce a multifunctional particle in which it was assured that the addition of SiO_2 as a support does stabilise the particles and increases the coking resistance (Zhao et al., 2012). SiO_2 and Al_2O_3 supported metals have also been utilised in the chemical looping research sector in comparison to each other but both performed equally well at stabilising the particles (Song et al., 2014) (Peterson et al., 2013).

It has been noted that the combination of catalyst and sorbent into a combined matrix produces a joint catalyst/sorbent/support particle that has a greater resistance to carbon deposition and additionally possess a higher particle stability, whilst still achieving a high feedstock conversion (D'Orazio et al., 2013). Xie et al (Xie et al., 2012b) utilised a combined particle supported by $Ca_9Al_6O_{18}$ which joined with the conventional nickel catalyst and CaO sorbent produced exceptional long term carrying capacity and increased the methane conversion during the pre-breakthrough period. These multifunctional combined catalyst, sorbent and support particles have been also tested on the glycerol, ethanol, toluene, methane and biomass sorbent enhanced steam reforming; again they outperformed their separate original components (Dou et al., 2013) (Wu et al., 2012) (Di Felice et al., 2009) (Rout and Jakobsen, 2012) (Wu et al., 2013). This idea along with the most recent literature is discussed in chapter 6.

2.12. Progress towards commercialisation

Currently there are no full scale commercial scale SESR projects active, however there are numerous CaL investigations in fluidised bed systems and some SESR demonstration projects, as outlined in Table 2.2.

Table 2.2 – Large scale demonstration projects of CaL and SESR (Letcher et al., 2012) (Blamey et al., 2010).

Project	Size	End use	Reference
Commercially active SESR – None			
SESR (no catalyst) in dual fluidised bed, Guessing, Austria	8 MW_{th}	Combined heat and power	(Koppatz et al., 2009)
CaL, bubbling fluidised bed carbonator and an oxy-fired rotary kiln calciner at the Industrial Technology Research Institute (ITRI) of Taiwan	1.9 MW_{th} pilot plant (30 MW_{th} demonstration plant to be constructed)	N/A	(Chang et al., 2014)
CaL, pilot plant with dual CFBCs, CaOling project, La Pereda, Spain	1.7 MW_{th}	N/A	(Arias et al., 2013)
CaL, dual fluidised bed pilot plant at University of Darmstadt, Germany	1 MW_{th}	N/A	(Ströhle et al., 2014)
Indirectly heated, CaL, dual fluidised bed pilot plant at University of Darmstadt, Germany	300 kW_{th}	N/A	(Reitz et al., 2016)
CaL, dual fluidised bed pilot plant at The University of Stuttgart	200 kW_{th}	N/A	(Hawthorne et al., 2011) (Dieter et al., 2014)

CaL, dual fluidised bed pilot plant at CanmetEnergy, Canada	75 kW_{th}	N/A	(Lu et al., 2008)
CaL, dual fluidised bed pilot plant at Instituto Nacional del Carbón (INCAR-CSIC)	30 kW_{th}	N/A	(Charitos et al., 2011)

2.13. Conclusions from the Literature Review

Concluding on the information gathered within this review it has been realised that there are several key areas of ongoing research and some areas that are yet to be fully understood. It has also been recognised that SESR does have the potential to provide a low carbon source of H_2 if the CO_2 stream generated is sequestered. Furthermore, coupling SESR with sustainable biomass resources has also been shown to provide a greater benefit in that CO_2 is effectively removed from the atmosphere, although the literature has demonstrated that utilising biomass can cause additional problems during operation due to slagging, fouling, taring, and storage and handling issues.

There are several reactor types that have been utilised for CaL and SESR previously and were discussed in detail within this review, notably these include fixed, fluidised, spouted beds and entrained flow reactors. Of these, fluidised bed reactors are the most commonly utilised at commercial scale for CaL. The operating conditions of any reactor are a key influencing factor of the process efficiency and overall H_2 production. SESR has been shown to be mainly dependant on the operating temperature, pressure, steam to biomass ratio and particle size.

The main issues with regards to this process are in the use of the sorbent and catalyst themselves. This is because the sorbent is prone to sintering at high partial pressures of CO_2 and temperatures, attrition, and sulphation and as such the CO_2 sorption carrying capacity decreases with increased use. Several methods have been tested for regenerating and improving the longevity of the sorbent over multiple cycles, with the best found to be HBr doping with steam addition.

Catalysts for SESR (typically nickel) suffer from coking, sulphur poisoning and sintering. Whilst it has been shown that there are some ways of reducing the impact of these effects most measures are based

on preventing a situation occurring whereby the catalyst could be coked or sulphated by operating with a large excess of steam or by pre-removing the sulphur compounds. The H_2 reduction period of Ni catalysts was found, within this review, to vary greatly between different authors and was not always based on the optimal time for the catalyst.

The interconnection and closeness of the sorbent and catalyst grains was also discussed as this has been shown to be highly beneficial for minimising the diffusion distance of the produced gas molecules during SESR. Because of this combined multifunctional particles were found to produce a higher H_2 yield. Further to this the addition of a support to these particle was also reviewed as it was deemed likely to be required in order to minimise sintering and grain agglomeration.

Chapter 3 – Reactor Design, Construction and Commissioning

3.1. Introduction

This chapter describes the design, construction and commissioning of a mildly pressurised (1-5 barg), high-temperature (up to ~1000 °C) spouted bed reactor for Sorbent Enhanced Steam Reforming (SESR) of biomass for the production of "CO_2 negative" H_2. This reactor was constructed to study the impacts of biomass char production and coking on the long term operational efficiency of combined multifunctional (sorbent and catalyst) SESR particles. An image of the final reactor is displayed as Figure 3.17 and an accompanying PFD of the reactor is shown in Figure 3.16.

3.2. Design specification

This reactor was constructed based on the aims of the research and with the aid of information gathered by the literature review presented in chapter 2. The following fundamental design requirements and desired operating conditions were selected and in turn were utilised to aid the design of the reactor.

- A well-mixed and evenly heated reaction zone that can operate stably at a set value in the range of 600 – 700 °C
- The ability to safely operate at temperatures > 900 °C for the calcination of $CaCO_3$
- A sealed reactor to prevent the release of flammable or harmful gases being released into the environment
- Reactor capacity large enough to contain 20-60 g of bed material expanded with bed porosity of 85 %
- Safely operate under mild pressurisation, 1 – 5 bar(a)
- Typically operate as continuous system but with the option to easily transfer to a batch system
- Continuous solid fuel feeding system with the option to utilised methane alternatively
- Feeding rates of solid fuel approximately ~0.5-3 g per minute (equivalent molar rate of carbon from methane flow)

- The ability to generate stable steam flow rates with a molar steam to carbon ratio of up to 5 (however only 50% excess to the stoichiometry is required)
- An gas outlet which can maintain operability even with the production of significant quantities of tars, chars and fines
- A flare stack to fully combust the flammable and harmful off-gases

Based on these design specifications and desired operating conditions a decision was made to construct a high-temperature, mild pressure, spout-fluidised bed reactor as this would facilitate the majority of the design criteria. In addition a flare stack, gas cooling system, steam generator, fuel feeding and delivery system and data collection system were also constructed, which are discussed in this chapter.

3.3. Sizing and Heating of the Reactor

The outer reactor body consisted of a 650 mm length of incoloy 800-HT pipe, NPS 1 ½" schedule 80 with an outer diameter of 48.3 mm and a wall thickness of 5.1 mm (supplied by Philip Cornes & Co Ltd). The wall thickness was reduced to 2.5 mm at either end, observable in Figure 3.1, to allow for two stainless steel half-moon positioning rings to be installed at each end; which in turn positioned the bolted stainless steel flanges in place. The bottom flange had a 5/16" Swagelok fitting welded centrally in place enabling the inlet tube to be fixed in position. The inlet tube had an outer diameter of 5/16" and was utilised to direct the gas flow and solid fuel feeding into the bottom of the quartz reaction liner to form the spouted bed system. The spouted bed system was selected over a traditional fluidised bed system due to the requirement to feed solid fuels directly into the bed material. The reaction vessel, which was positioned inside the incoloy reactor tube, was a manufactured quartz liner (supplied by Soham Scientific) and had an outer diameter of 36 mm, a wall thickness of 1.5 mm and a total length of 405 mm. The quartz liner sat on a support disc which itself was connected to the gas inlet tube, the liner was pressed down and fixed in position by the use of a counter weight sitting on top of the liner. The minimal gap between the top of the counter weight and the base of the top flange was occupied by a 2.5 mm thick disc of Kaowool. The flange at the top of the reactor had a 5/8" Swagelok fitting welded

into it which in turn was reduced to a ½" outer diameter fitting via a Swagelok reducer. A larger exit diameter was selected to minimise the resistance to the gas flow after the reactor and to enable a sand feeding tube to be inserted into the top of the reactor. A copper O-ring was placed between the flanges and the reactor pipe at both ends, this expanded during heating thus creating a seal. The reactor was sized so as to accommodate the volume of a 40g bed of sand when fluidised such that the bed expanded to form a bed voidage of 85%; this value is the estimated maximum value of bed voidage within a fluidised bed (Basu, 2006).

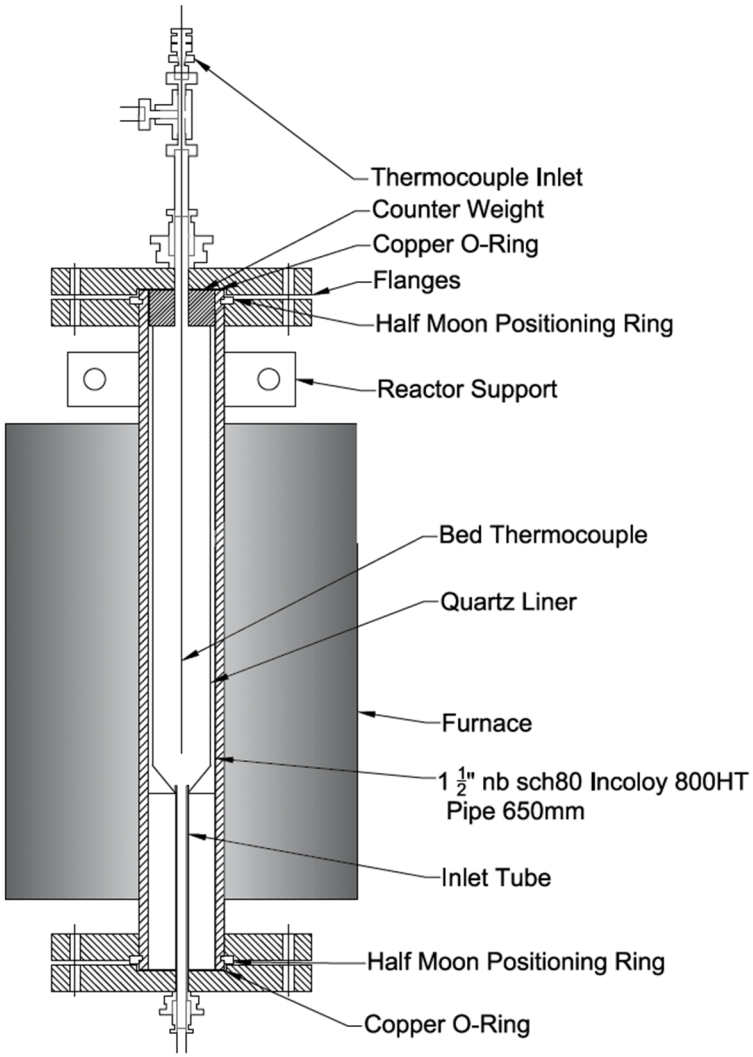

Figure 3.1 – CAD drawing of the reactor body design and details of the major components.

Utilising the information enclosed within section 3.5.1.2 of the British Standards Institutes' Published Document PD 5500:2012+A2:2013 (BSI, 2012) and Equation 3.1, the pressure that this pipe can therefore safely operate up to is ~15.9 bar(a).

Equation 3.1:

$$P = \frac{2fw}{D_o - w}$$

Where P is the Pressure, f is the design rupture strength of the vessel material at the chosen temperature and lifespan (13 MPa at 925 °C and 10,000 hours) (SpecialMetalsCorporation, 2004), w is the wall thickness at the thinnest part (2.5 mm) and D_o is the outer diameter at the thinnest part (43.26 mm).

A vertical split tube furnace (supplied by Lenton Furnaces) was utilised for heating this reactor as the furnace could produce a stable temperature up to a maximum of 1150 °C with a heated length of 300 mm and a power output of 1.5 kW. Figure 3.2 shows the temperature profile of the empty reactor when heated to 650 °C. Wall and bed temperature was measured with 3 mm outer diameter type K thermocouple (supplied by TC direct). The bed thermocouple was secured in place using a Spectite fitting (1/4" M-NPT) which applied a Viton sealant around the thermocouple, which itself was resistant to oils, solvents, fuels and temperatures up to 225 °C.

The data from the thermocouples was recorded via a thermocouple data acquisition card (DAQ, supplied by Meilhaus Computing) and then relayed to a computer running a bespoke control program in Agilent VEE Pro which displayed and saved the data for future analysis. The user interface panel of this control program is displayed in Figure 3.4.

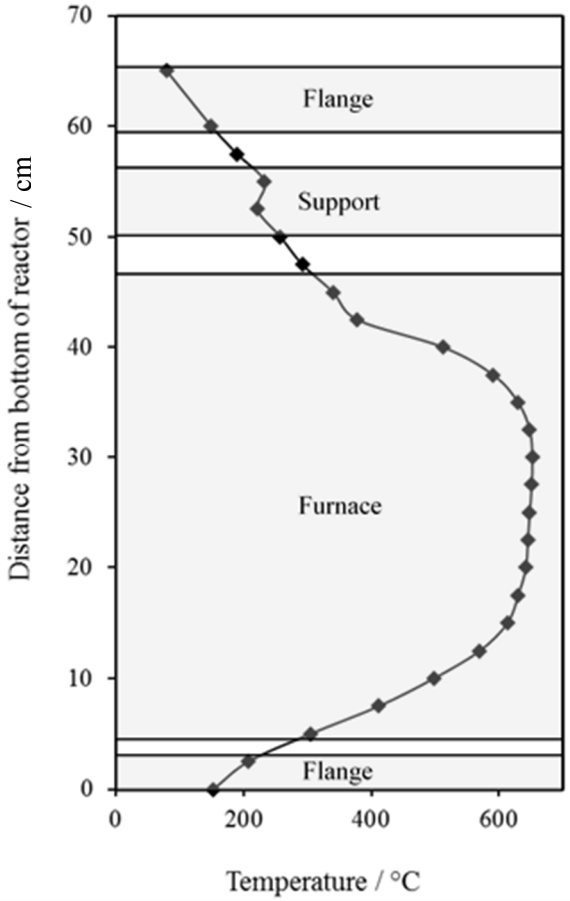

Figure 3.2 – Temperature profile of the reactor with an empty bed heated to 650 °C with the approximate locations of important components superimposed as shaded areas.

The reactor pipe was held in position by 4 pieces of stainless steel with cut semi-circles designed to fit around the pipe, these were clamped around the pipe by the use of two aluminium angle bars. The angle bars were fixed onto a frame constructed from aluminium profile (supplied by KJN Aluminium Profiles Ltd). This system can be observed in Figure 3.3. Superwool (supplied by RS Components Ltd), a thermal insulating blanket, was subsequently wrapped in multiple layers around all exposed parts to minimise any heat loss.

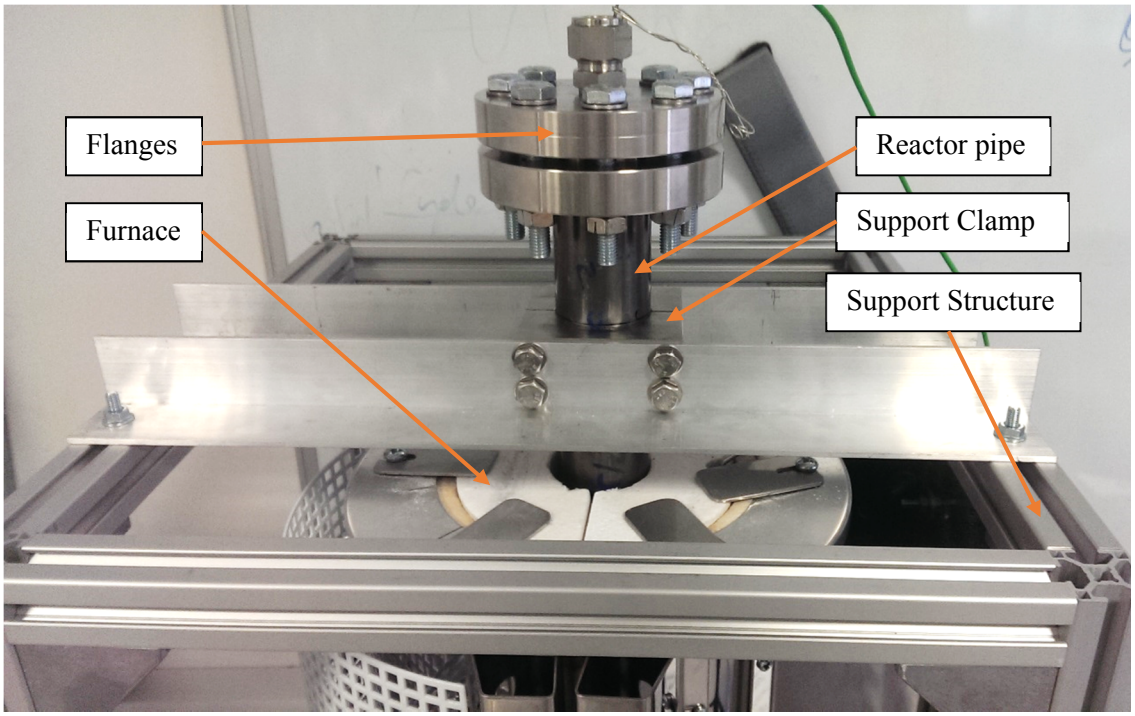

Figure 3.3 – Top of reactor, showing the support structure and flanges.

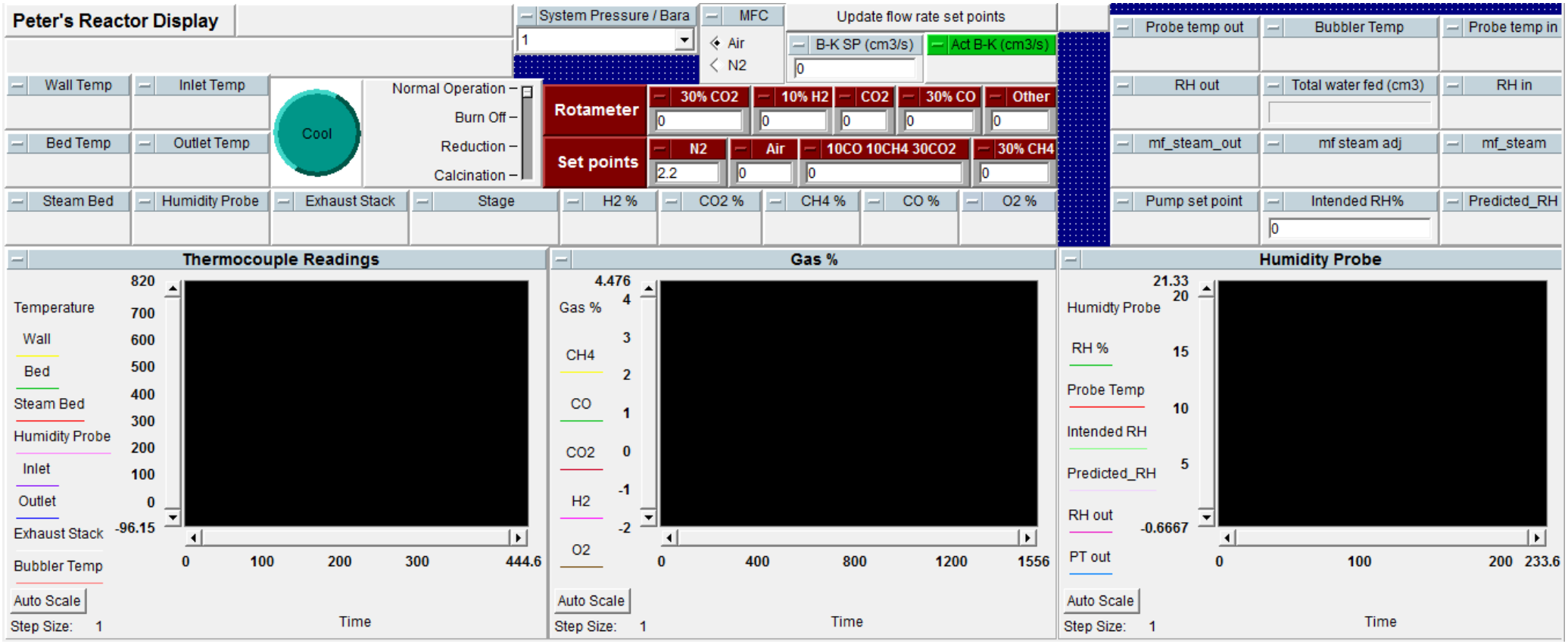

Figure 3.4 – Agilent VEE control program, graphical user interface panel.

3.4. Fluidisation Velocity

The minimum fluidisation velocity was calculated using the Wen & Yu correlation (Wen and Yu, 1966) which is described by Equation 3.2, Equation 3.3 and Equation 3.4.

Equation 3.2:

$$Ar = \frac{{d_p}^3 \rho(\rho_p - \rho) g}{\mu^2}$$

Equation 3.3:

$$Re_{mf} = \sqrt{(33.7^2 + 0.0408 Ar)} - 33.7$$

Equation 3.4:

$$u_{mf} = \frac{\mu \, Re_{mf}}{\rho \, d_p}$$

Where: Ar is the Archimedes number, Re_{mf} is Reynolds number at the minimum fluidisation, u_{mf} is the minimum fluidisation velocity, d_p is the particle diameter, ρ is the fluidising gas density, ρ_p is the particle density, g is the gravitational constant (9.81 m/s^2) and μ is the dynamic viscosity.

Table 3.1 displays an example calculation of the minimum fluidisation velocity and therefore the required volumetric flow rate at Normal Temperature and Pressure (NTP) to achieve a specific U/U_{mf} value. A U/U_{mf} value of 3 was chosen for this example however specific U/U_{mf} were calculated and are specified for each set of experiments.

Table 3.1 - Parameters and calculation of the minimum fluidisation velocity and required volumetric flow rate at Normal Temperature and Pressure (NTP) to achieve a U/U_{mf} of 3.

Parameter		**Value**	**Unit**
Quartz liner inner diameter	d_i	0.034	m
N_2 density (650 °C & 1 atm)	ρ_g	0.346	kg/m^3
Envelope particle density	ρ_p	2600	kg/m^3
Temperature	T	650	°C
Particle diameter (geometric mean)	d_p	461	μm
Gravitational acceleration	g	9.81	m/s^2
Dynamic viscosity (650 °C & 1 atm)	μ	4.09×10^{-5}	Pa·s
Archimedes number	Ar	517.73	
Reynolds number at minimum fluidisation	Re_{mf}	0.312	
Minimum fluidisation velocity @ T	u_{mf}	0.080	m/s
Volumetric flow rate at minimum fluidisation @ T	V_{mf}	7.04×10^{-5}	m^3/s
Volumetric flow rate at minimum fluidisation @ T	V_{mf}	70.4	cm^3/s
Volumetric flow rate at minimum fluidisation @ NTP	V_{mf}	22.7	cm^3/s
Ratio of flow rate to minimum fluidisation	U/U_{mf}	3	
Volumetric flow rate @ NTP	V_{mf}	68.2	cm^3/s

3.5. Solid Fuel Feeding

3.5.1. Design and operation

The ability to feed solid fuels continuously and reproducibly proved to be one of the most challenging aspects of the reactor construction and required many design iterations. A continuous solid fuel feeding system that had been previously utilised to continuously feed coal was chosen as a starting point for the design; this design consisted of ¼" Swagelok plug valve which was adapted so as to allow for continuous rotation, like an industrial rotary valve feeder (Dai et al., 2012). The channel within the plug valve was blocked with blue-tac leaving only small cup-like indents where the channel previously was. A plug valve was utilised as it is constructed of one solid piece of metal and limits the number of moving parts, this maintains operability when using finely ground material which can easily clog up moving parts. The feeder was rotated with a DC motor, the voltage could be altered to adjust the speed of rotation. The main issue with this system was that a ¼" valve was too small to produce a steady flow of material from the hopper. Solid fuel was known (from initial biomass feeding experiments) to bridge at the valve entrance and stick to the blue-tac minimising the cup volume available for feeding. Additionally, the fuel was reported to block after the feeding system if it encountered a step change in tubing size – i.e. a reducer from one size to another.

Based on these issues the design was adjusted. A solid piece of stainless steel was lathed down to fit into a ½" plug valve fitting and one 5 mm wide by 4 mm deep cup was drilled into the feeder. The feeder also had grooves machined in to match the locations of the original O-rings and retaining ring, such that when inserted into the valve body the feeding cups lined up with the centre of valve entrance and exit. An image of this feeder and valve body can be observed in Figure 3.5.

Figure 3.5 – ½” Stainless steel feeder with drilled cup and valve body.

At the base of the feeder a ½” tee was installed which allowed the main gas flow to be connected in. Another alteration that was made, was to construct a ½” to 5/16” reducer, the ½” side connects to the bottom of the ½” tee piece and the 5/16” side connects to the U-bend and thus to the inlet of the reactor; Figure 3.6 illustrates this. The aim of this custom made reducer was to remove the lips formed at the transition between the two dimensions, thus minimising the risk of solid fuel bridging and getting stuck at that point.

This system utilised entrained flow to feed the solid fuel into the reactor, therefore it was ensured that the gas velocity in the U-bend was greater than the terminal velocity of the solid fuel. As an example, Table 3.2 shows the calculations for the terminal velocity of a particle of biomass (212-300 µm in a N_2 gas stream at 110 °C) using Equation 3.5, Equation 3.6 and Equation 3.7.

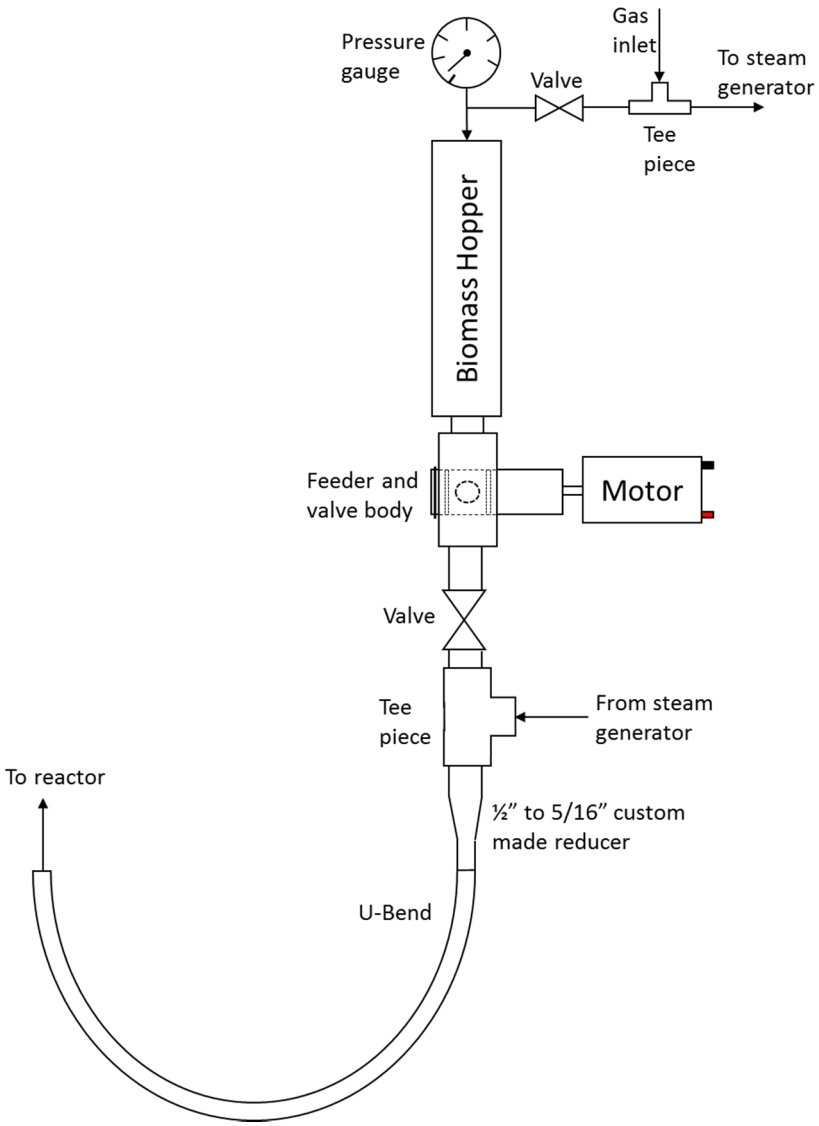

Figure 3.6 – Reactor inlet and feeding design.

Equation 3.5:

$$u_t = u_t^* \left[\frac{\rho_g^2}{\mu(\rho_p - \rho_g)g} \right]^{-\frac{1}{3}}$$

Equation 3.6:

$$u_t^* = \left[\frac{18}{(d_p^*)^2} + \frac{(2.335 - 1.744\psi_p)}{(d_p^*)^{0.5}} \right]^{-1}$$

Equation 3.7:

$$d_p^* = Ar^{\frac{1}{3}}$$

Table 3.2 – Example calculation for the terminal velocity of biomass.

Parameter		Value	Unit
N_2 density (110 °C & 1 atm)	ρ_g	0.891	kg/m^3
Envelope particle density	ρ_p	600	kg/m^3
Temperature	T	110	°C
Particle diameter (geometric mean)	d_p	252	μm
Gravitational acceleration	g	9.81	m/s^2
Dynamic viscosity (110 °C & 1 atm)	μ	2.153	$\times 10^{-5}$ Pa·s
Sphericity	ψ	0.8	
Archimedes number	Ar	181.24	
	dp^*	5.66	
	ut^*	1.04	
Terminal velocity of particle	ut	0.92	m/s

Utilising the volumetric flow rate calculated in the example calculation of Table 3.2, it can be calculated that the flow rate 68.2 cm^3/s @ NTP would equate to a gas velocity of 2.4 m/s in a 5/16" tube at 110 °C thus demonstrating the theoretical entrainment of the biomass. 110 °C was utilised for these examples as the inlet gas stream was preheated. This same flow rate within a ½" tube has a gas velocity of 0.87 m/s indicating that the biomass was unlikely to be entrained in the tee piece or joining section and therefore the particles should proceed to entrained flow in the 5/16" tube. Understandably there was likely to be a considerable amount of mixing/gas swirling within the ½" joining section which could have inhibited transport of the solid fuel.

3.5.2. Testing the feeding system

Utilising the feeding system described above a range of biomass particle size fractions and motor voltage levels were tested, which lead to a biomass size fraction 212-300 µm and a motor voltage level of 6 V being found to be optimal at minimising bridging of biomass particles and preventing overheating of the motor and feeding system. A small motor with a custom made knocker was installed to vibrate and knock the biomass within the hopper such that the biomass remained un-bridged and ready to be collected by the rotating cups. Four different biomass types were also assessed for their feedability, as shown in Figure 3.7 oak was the most successful and reliable feeding material, which was most likely to be due to the shape of the biomass particles. Miscanthus (a straw) and spruce (a softwood), are known to break down into irregular needle-like particles which easily form an interlocking mesh which prevents the biomass moving through the feeding system (Dai et al., 2008) (Guo et al., 2012). Due to its feedability oak was selected for all subsequent experiments, with the intention of using a more sustainable biomass in later research.

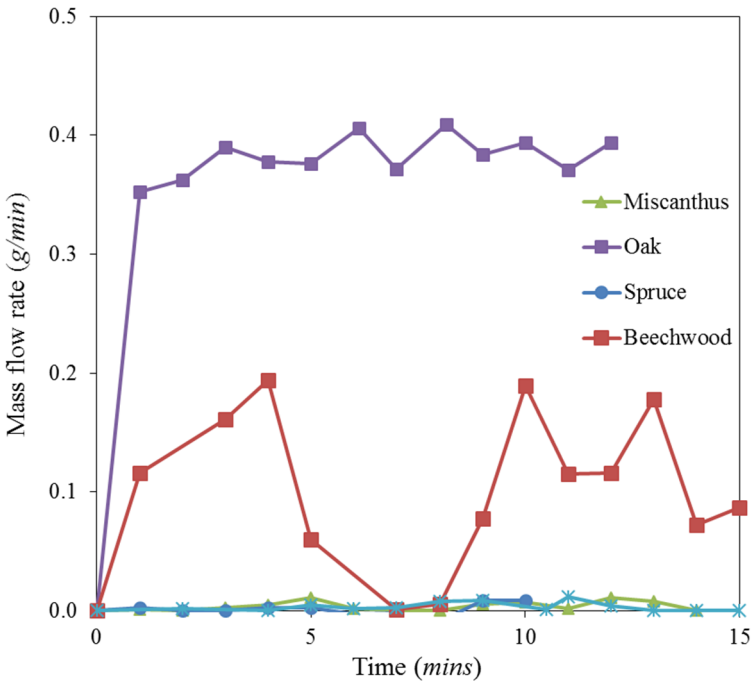

Figure 3.7 – Feeding tests of miscanthus, oak, spruce and beech wood biomasses utilising the stainless steel feeder (one 5 mm wide by 4 mm deep cup) rotating with an applied voltage of 6 V.

3.5.3. Modification to the feeding system

After undertaking some initial biomass combustion experiments it became apparent that the feeding rate of the biomass was too low to make a big enough observable difference to the gas concentrations compared to the measured baseline. It was also noted that the stainless steel feeder was suffering some pitting damage due to biomass getting stuck between the rotating feeder and the valve body. Because of these reasons a set of plastic (Delrin, Polyoxymethylene supplied by DuPont) feeders were manufactured, identical to the stainless steel feeder but initially without any cups drilled. Delrin was chosen for its relatively high stiffness, low friction and temperature resistance, it also had the ability to deform preferentially over the stainless steel valve body instead of causing a jam in the feeding system. Building a set of these feeders at once enabled the quick prototyping of different cup designs; a range of cup designs were tested and the results of the feeding tests are observable in Figure 3.8.

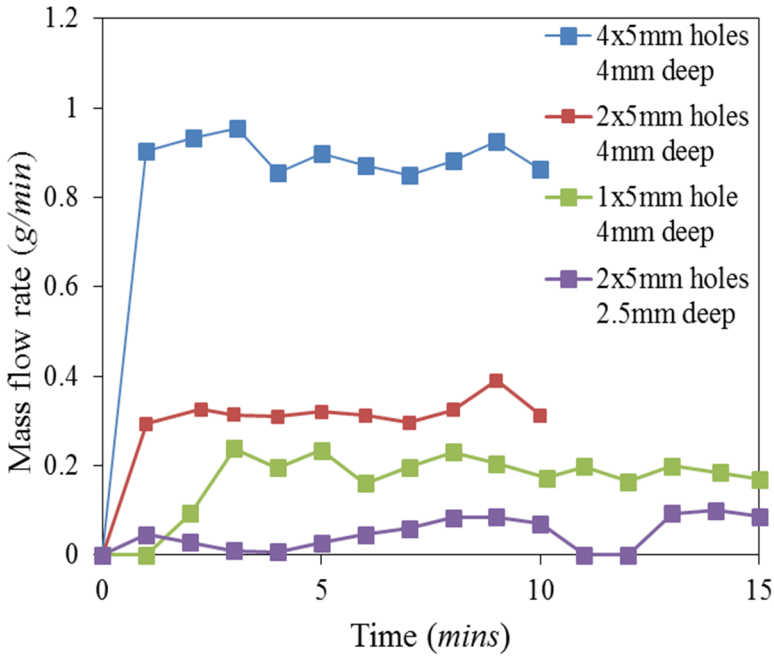

Figure 3.8 – Feeding stability tests of different rotary cup designs using the Delrin plastic feeders at an applied voltage of 6 V.

A maximum cup width of 5 mm was utilised as this was limited by the valve body dimensions. The results obtained and displayed in Figure 3.8 led to the selection of four 5 mm holes each 4 mm deep as the preferred feeding cup design. The initial testing of this system with steam present indicated that steam was condensing at the base of the feeder and making the biomass particles 'sticky' such that they weren't falling into the gas stream and were instead being continually rotated. Based on this evidence, a 1/8" tube was bent, inserted and silver-soldered into a ½" tube, which replaced the small section of tubing between the valve body and tee piece. This part was coined the 'Bio-knocker' and an illustration of this piece and its installation location is shown in Figure 3.9. This 1/8" tube was connected to a mass flow controller which supplied a small stream of air/N_2 to the bottom of the valve body, where the biomass should exit. The aim of this was to lower the humidity in that crucial section of the feeder, knock/aid the biomass out of the rotating cups and aid the flow of the biomass down into the main gas stream.

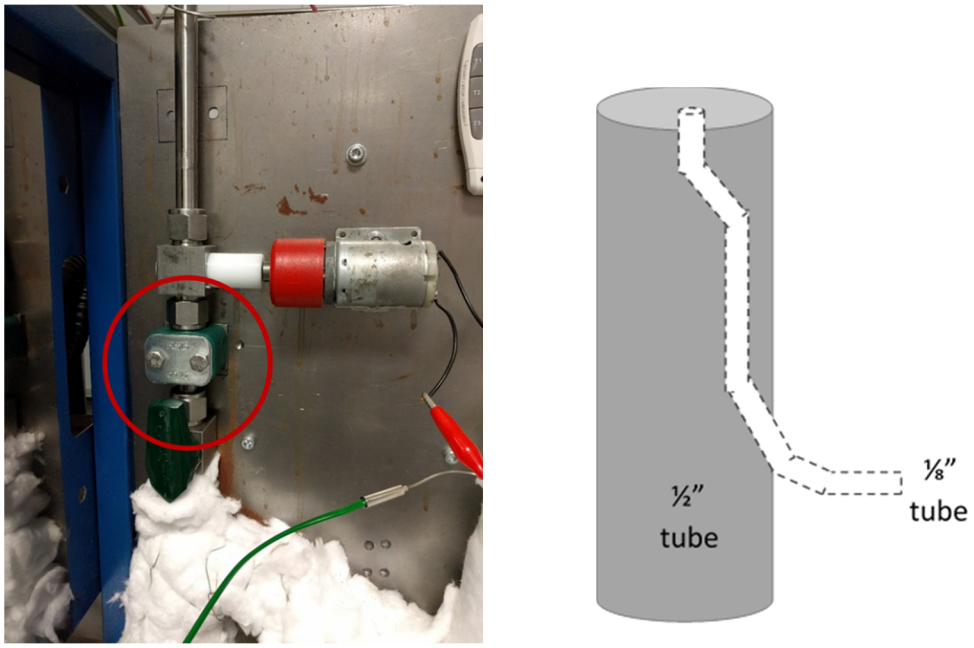

Figure 3.9 – Left: The red circle indicates the installation location of the bio-knocker. Right: Diagram of the 'Bio-knocker', used to reduce the humidity beneath the feeder exit and knock the biomass out of the cups.

3.6. Steam Generation

3.6.1. Design and operation

A stable steam concentration was another vital requirement for SESR as the reactions are highly dependent upon the steam to carbon ratio, thus considerable time was spent on achieving a stable steam generation system. The first design (shown in Figure 3.10) consisted of a HPLC pump pushing deionised (DI) water through a 1/16" tube into the top of a 30 cm long ¾" tube packed with 5 mm diameter SS balls. A HPLC pump was known to produce pulses at the outlet due to its mechanical operation, so any design had to reduce the size of these spikes such that the produced steam concentration was smooth. The packed column was heated using a heating tape (supplied by omega) which was powered using a heating control box (custom built using among other components, a transformer, solid state relay and PID controller, all components supplied by RS) and controlled with a type K thermocouple attached to the outside wall of the tube. Gas was passed over the SS balls to act as a carrier gas and 'collect' the steam as it was vaporised. A secondary gas stream was teed in after the packed bed to dilute the steam concentration to the desired level. This system resulted in a very irregular, spiky steam concentration due to the water flashing off as soon as it hit the hot SS balls.

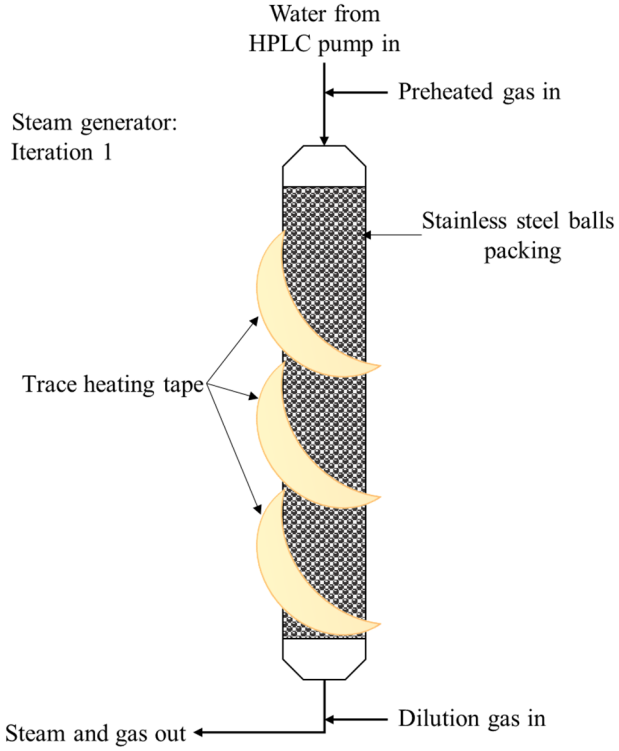

Figure 3.10 – Steam generator: iteration 1.

The following design iteration (shown in Figure 3.11) included a 3 m coil of ¼" tubing heated to ~120 °C after the packed bed to try and distribute the steam concentration spikes out. Two operation modes were tested, the first was to superheat the packed column to ~300 °C such that the water flashed off and then passed through the coil to distribute out – this operation regime just exacerbated the HPLC spikes. The second operating mode used a much lower temperature of about ~75 °C in the packed bed, such that the water didn't evaporate instantly but instead gradually vaporised as it was pushed through the column by the carrier gas. This system was significantly improved at low concentrations but at higher steam concentrations, ~15%, the water was not being evaporated fast enough and as such made it all the way through the packed bed and into the coil thus producing spikes.

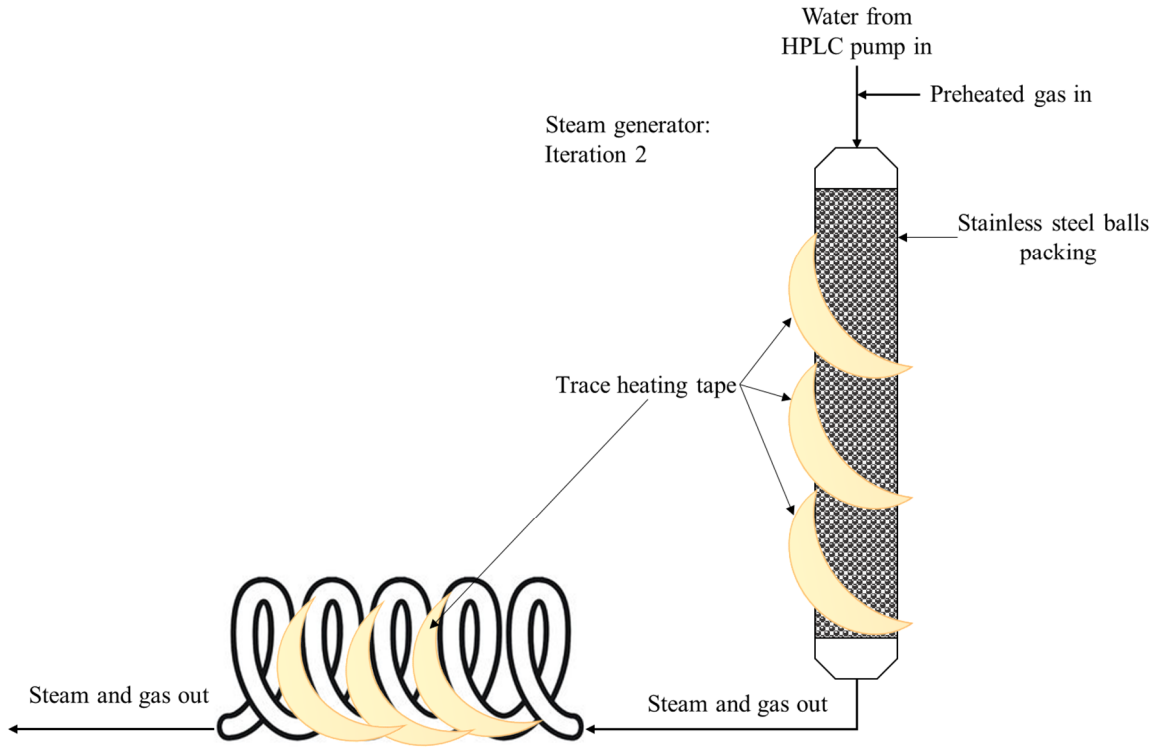

Figure 3.11 – Steam generator: iteration 2.

The next and final iteration (shown in Figure 3.12) utilised a 30 cm long 1” tube, half filled with DI water, wrapped in heating tape to produce a bubbler. At the top of the bubbler there was ¼” cross allowing a type K thermocouple and 1/16” HPLC line to be fully inserted into the column of water. At the bottom of the bubbler there was a 1/8” tube inserted approximately 7 cm into the column of water. This 1/8” tube had its end squeezed shut and had twelve 1 mm diameter, evenly distributed, holes drilled into the sides of the tube to force the gas to flow outwards into the water column, creating multiple streams of bubbles thus maximising the water vapour collection.

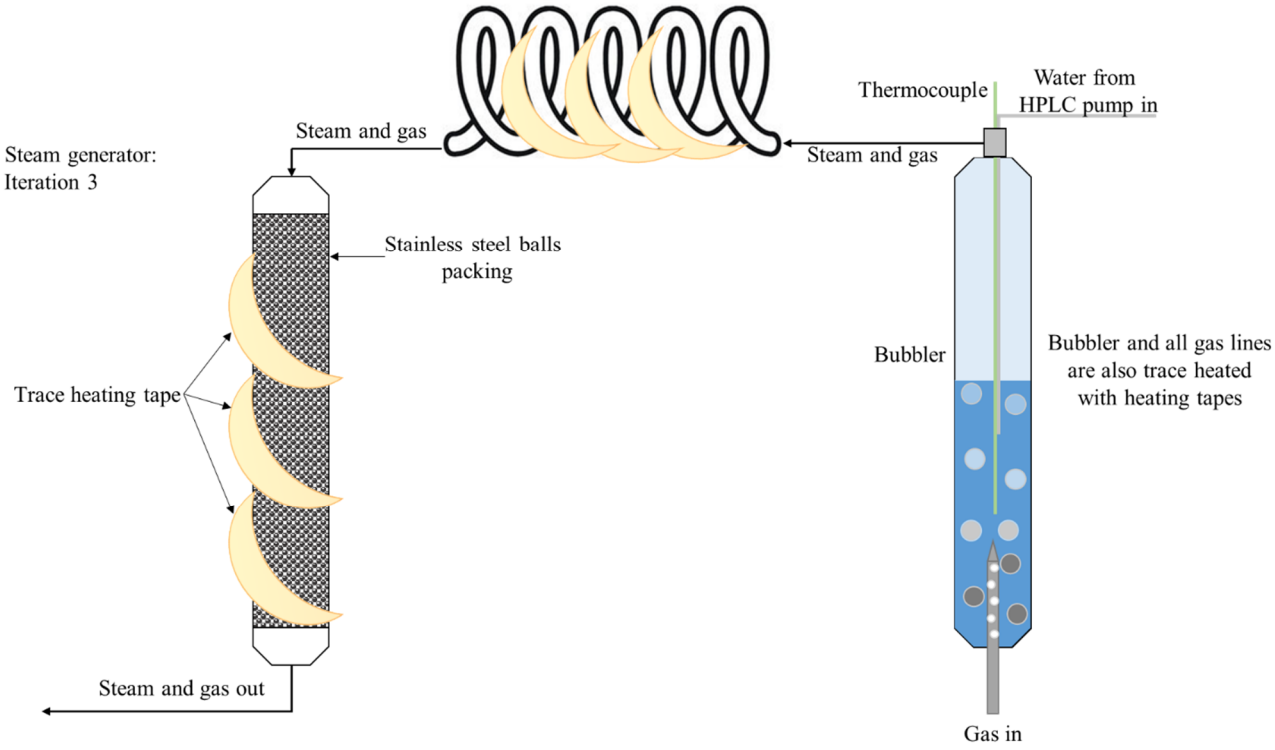

Figure 3.12 – Steam generator: iteration 3.

3.6.2. Testing the steam generation system

The temperature of the bubbler was controlled with the bubbler-bed temperature thermocouple and the relative humidity production was calibrated to produce Figure 3.13. The water flow rate from the HPLC was also calibrated and was set to a value that matched the rate at which water was converting to steam and being carried away thus maintaining a stable water inventory inside the bubbler.

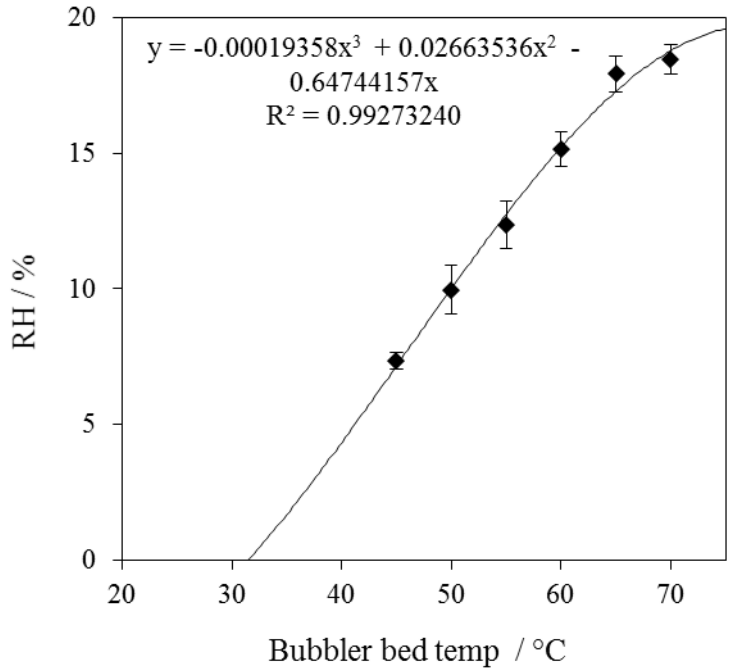

Figure 3.13 – Calibration curve for produced relative humidity (RH %) against bubbler bed temperature at 1 atm and with a 60 cm^3/s N_2 carrier gas flow rate.

The mole fraction of steam produced by the bubbler system was measured using a relative humidity (RH) probe (HMT334 supplied by Vaisala), the humidity probe was calibrated by utilising a Controlled Evaporation and Mixing (CEM) system (supplied by Bronkhorst) which is known for its high levels of steam stability. The first humidity probe was positioned directly after the steam generation and before the tee piece that connected to the base of the feeding system. A second humidity probe was placed at the outlet of the reactor, however due to tar production and the potential to contaminate the instrument this probe was not always used, it will be stated if it was used during a particular experiment. All gas lines after and 50 cm prior to the steam generation system were trace heated (to a suitable temperature

to stop the steam condensing and to preheat the gas before entering the system) with heating tapes controlled by their own wall temperature type K thermocouples and corresponding heating control box. Figure 3.14 displays an example of the steam system starting up, operating and turning off. This figure also shows the stability of the steam system when aiming to achieve 15 % relative humidity indicating an acceptable deviation of about ± 1 $_{abs.}$% from the set point.

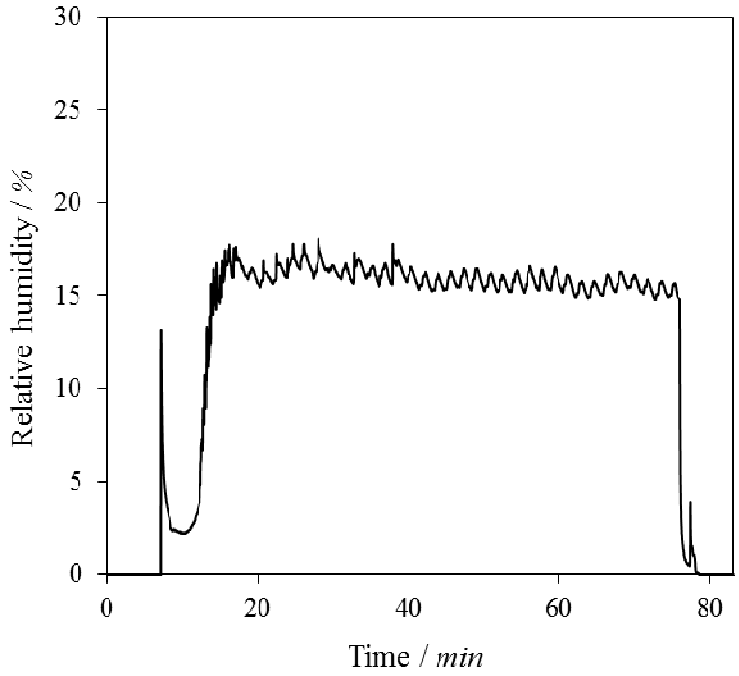

Figure 3.14 – Steam generation system operation and stability when aiming for 15% relative humidity at 1 atm with a 60 cm^3/s N_2 carrier gas flow rate.

3.7. Heat Exchanger – Tar and Water Trap

At the outlet of the reactor, the gases were passed through a trace heated, Superwool wrapped, ½" tube packed with glass wool to trap any fines which have elutriated from the reactor. After this the gas continued through another ½" tube packed with glass wool, except this tube was enclosed within a separate 1" tube where ice cooled water was pumped counter currently, thus cooling the gas stream down. This setup effectively forms a single tube in shell heat exchanger to condense majority of the water and tars. The cooled section was approximately 60 cm long and was sized based on standard heat

exchanger calculations, whilst making sensible assumptions of the temperatures, flow rates and properties of each stream (Sinnott, 2005).

Condensed water gradually moved down the tar and water trap and into a 30 cm long 1" tube at a slight angle which collected the water; this water collection tube could be periodically emptied through a plug valve. Once the gas had moved through this system it was finally passed through a 20 cm 1" tube filled with $CaCl_2$ to chemically remove any left over water before going on to the gas analysers.

3.8. Product Gas Analysis

The main gases that were expected to be generated were CO_2, CO, CH_4 and H_2, based on this two analysers were selected and utilised in series. A regulated quantity of gas was sent to the analysers throughout each experiment, this was controlled by a rotameter and the remaining gas was diverted directly to the flare stack. The first analyser (supplied by ADC Gas Analysis Ltd) was capable of measuring CO_2, CO, CH_4 and O_2 by use of non-dispersive infrared absorption (except O_2 which was measured by a chemical oxygen sensor). The second analyser (supplied by ABB) measured H_2 via thermal conductivity. The data from these analysers was outputted to a data acquisition card (Redlab 1208FS DAQ card, supplied by Meilhaus Computing) via analog differential signal in a twisted pair, from which the data was digitised and transferred to the Agilent VEE control program on the control computer.

Post gas analysis the gases were vented to a local exhaust ventilation chimney fitted with a Bunsen burner (referred to as a 'flare stack' and combusted propane which was supplied by BOC) to combust any remaining flammable or harmful gases. Due to some of the produced gases being flammable, several flashback arrestors were positioned in key locations across the reactor; they included: after the gas analysers but before the flare stack, at the position where any air lines joined the main gas lines and on all pressure relief lines.

The ABB H_2 analyser utilised a Wheatstone bridge and a calibrated hot wire to measure the relative proportion of H_2 in N_2, however the product gases from the analyser also included gases other than N_2 which affected the reported thermal conductivity. Whilst there are models such as the Chapman-Enskog model (Chapman and Cowling, 1970) and the Wilke gas mixing model (Cheung et al., 1962) (Wilke, 1950) to predict the combined thermal conductivity of a gas mixture of known concentrations, they cannot be rearranged to determine an unknown mole fraction of H_2 (and thus an unknown mole fraction of N_2) – which was the purpose of the analyser. Therefore to overcome these difficulties initially the H_2 analyser was calibrated using several known H_2 concentrations (10% H_2 in N_2 calibration gas supplied by BOC). Following this other calibration gases (30% CO_2 in N_2 and 10% CO, 10% CH_4, 30% CO_2 in N_2 both supplied by BOC) were utilised to record the reported H_2 concentration (a function of gas thermal conductivity) from the analyser. Based on the relative effect that other gases have on the reported H_2 concentration, caused by their own inherent thermal conductivities, a correction was formulated using the weighted sum of individual thermal conductivities relative to the measured H_2 gas. This equation is displayed as Equation 3.8, where *i* represents the gases for which the H_2 analyser has been corrected for: CO_2, CO and CH_4, $x_{H_2\,mix}$ is the reported H_2 mole fraction outputted from the H_2 analyser and x_i is the calibrated mole fraction of gas *i*. To utilise this equation the thermal conductivity of the individual gas species (λ_i) must be multiplied by -1 if $\lambda_i > \lambda_{N_2}$.

Equation 3.8:

$$x_{H_2} = \sum \left(\frac{\lambda_i}{\lambda_{H_2}} x_i \right) + x_{H_2\,mix}$$

Utilising Equation 3.8 comparisons of the reported H_2 vol.% and corrected H_2 vol.% are displayed in Equation 3.12a and Equation 3.12b against addition of other gases. A representative equation is provided below as Equation 3.9. All thermal conductivities applied were assumed to be at standard temperature and pressure (STP, 20 °C and 1 atm).

Equation 3.9:

$$x_{H_2} = \left(\frac{\lambda_{CO_2}}{\lambda_{H_2}} x_{CO_2} + \frac{\lambda_{CO}}{\lambda_{H_2}} x_{CO} - \frac{\lambda_{CH_4}}{\lambda_{H_2}} x_{CH_4} - \frac{\lambda_{O_2}}{\lambda_{H_2}} x_{O_2} \right) + x_{H_2\,mix}$$

It can be seen from Figure 2.12a and Figure 2.12b that the corrected H_2 concentration was significantly improved from the value reported from the analyser with no correction applied. The aim of these corrections was to achieve a response of 0 vol.% H_2 when there was no H_2 was present, yet respond accurately when there is H_2 present, irrelevant of any other gases being present.

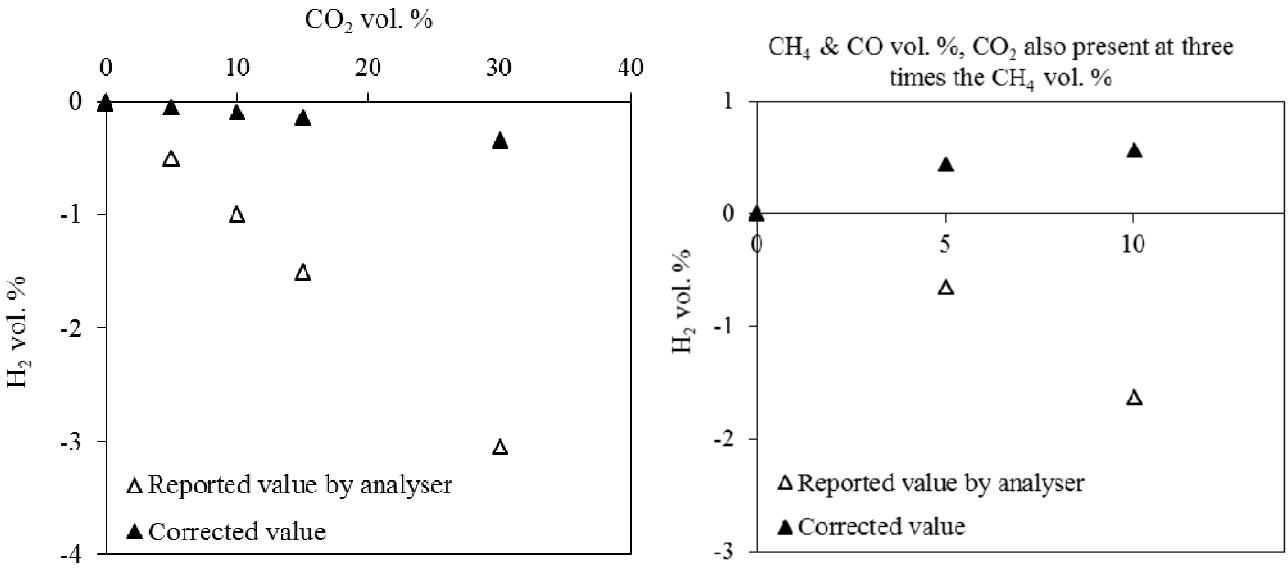

Figure 3.15a – (left) and 3.12b (right) display the reported H_2 concentration from the analyser and the H_2 concentration after the correction via Equation 3.8 has been applied.

3.9. Schematic and Photograph

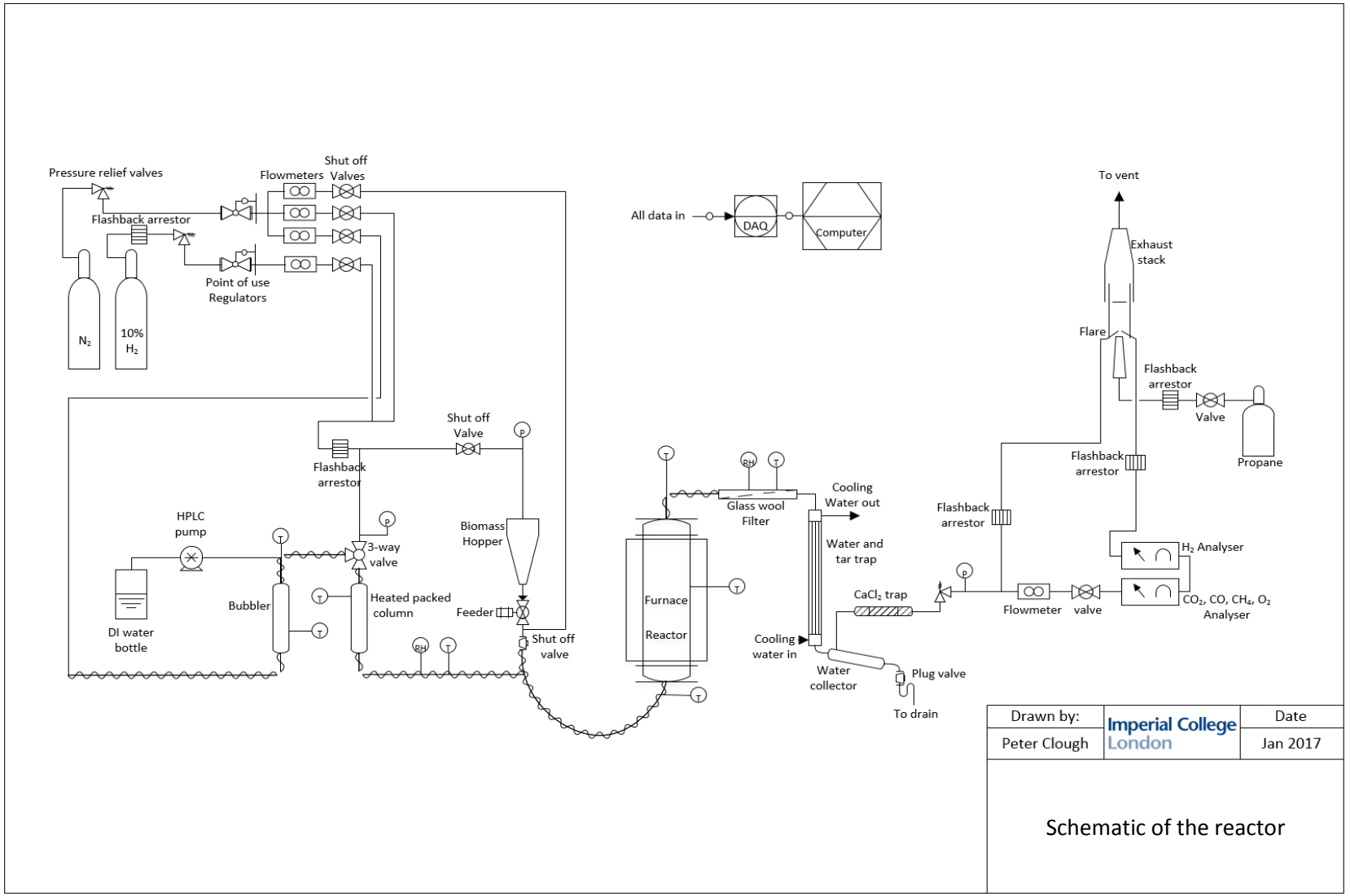

Figure 3.16 – Schematic of the reactor when set up for SESR.

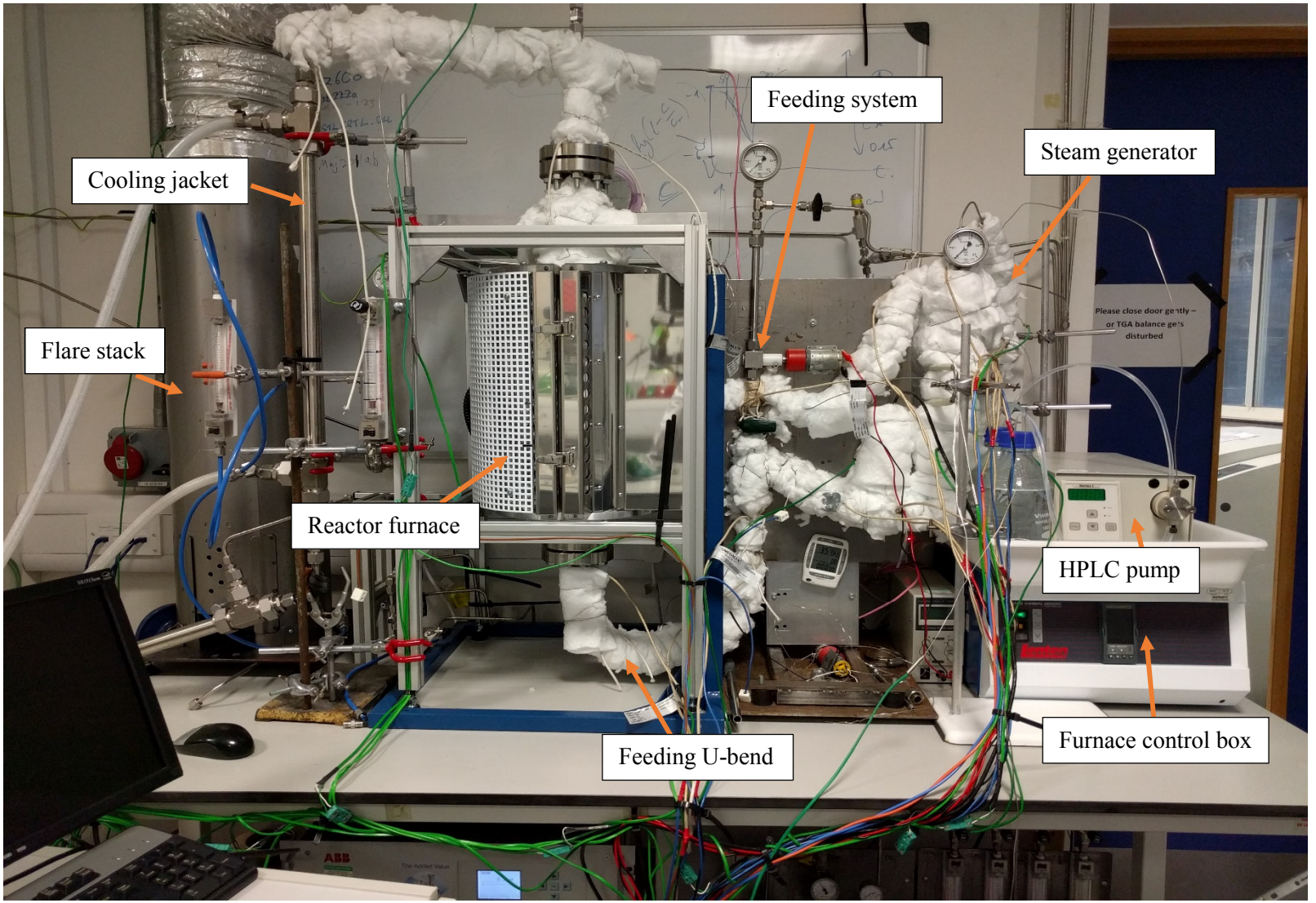

Figure 3.17 – Photograph of the reactor when set up for SESR.

3.10. Reactor Limitations

This reactor was designed to be operated manually, meaning gas flows were controlled with rotameters (supplied by Roxspur Measurement & Control Ltd) and the reactor pressure was controlled with a bonnet needle valve (supplied by Swagelok) after the $CaCl_2$ residual moisture trap. This meant that some manual experimental error could be introduced into the results due to observational inaccuracies when setting the desired values on the rotameters and pressure gauges.

The temperature of the furnace and heating control boxes were also controlled with manually inputted set points, although the furnace and control boxes did have their own PID software to reach and control at these set points.

The ADC mulit-gas analyser had an intrinsic manufacturer defined accuracy of 1 % of the reading and a noise stability error of 0.5 % FS (full scale). The ABB thermal conductivity gas analyser (H_2 in N_2 Caldos27) had an accuracy of ≤ 2 % of span and a repeatability of 1 %. The Vaisala humidity probes had a manufacturer defined accuracy of ± (1.5 + 0.015 × RH% reading).

This reactor in its current set up would be unsuitable for conducting kinetic measurements utilising the current gas analyses as they both utilised small gas cells which limits the allowable flow rate into the analysers. This was also evident from calculating the response time constant, τ_m, of CO_2 to be 6.6 s, following the method described by Fennell et al (Fennell et al., 2009).

3.11. Reactor Operation

A detailed description of the standard operating procedure can be found in Appendix I.

3.12. Initial Commissioning Experiments

3.12.1. Combustion of coal and biomass

An initial set of coal and biomass combustion experiments were conducted to confirm feeding stability and to assess the integration of the whole system during simple experimental operation. The experimental conditions utilised for these combustion reactions were: 650 °C, 1 atm, an air to fuel ratio (λ) of 2 and a total flow rate of 73 cm^3/s (@ 293 K – $U/U_{mf} \approx 3$). The coal utilised was Longannet blended coal (supplied by Scottish Power Ltd), it was crushed and sieved to a size fraction 212-300 µm and had the following ultimate analysis: 83 wt.% C, 5 wt.% H, 10 wt.% O and 2 wt.% other (oxygen calculated by difference, S and N were not defined on data sheet). Proximate analysis of the coal led to the following results: moisture 0 wt.%, volatile matter 0.6 wt.%, fixed carbon 90.3 wt.% and ash 9.1 wt.%. The biomass utilised was oak wood, it was also milled and sieved to a size fraction 212-300 µm and had the following ultimate analysis: 45.7 wt.% C, 6.1 wt.% H, 48.3 wt.% O (oxygen calculated by difference, S and N tested for but were below the level of detection). Proximate analysis of the biomass lead to the following results: moisture 1.3 wt.%, volatile matter 80.0 wt.%, fixed carbon 14.2 wt.% and ash 4.5 wt.%. The inherent oxygen content of the materials was not taken account of during the air to fuel ratio calculation. The results presented were averaged across three separate four minute long experiments utilising the stainless steel feeder at a coal feeding rate of ~0.52 g/min and biomass feeding rate of ~0.18 g/min. Figure 3.18 presents the percentage of gaseous and solid products of oxidation of coal (left bar) and biomass (right bar).

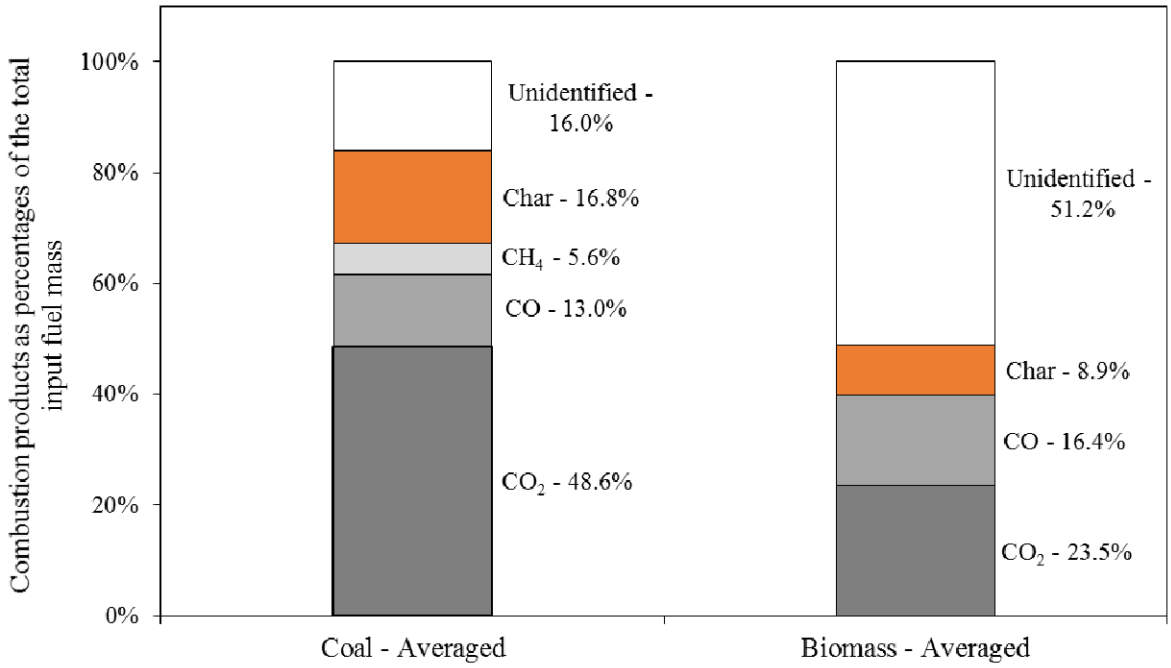

Figure 3.18 – Oxidation products as percentages from coal and biomass oxidation experiments, 650 °C, $\lambda = 2$.

The segments of the two stacked bars corresponding to 'Unidentified' are functions of steam, ash, tars and inaccuracies in experimental measurements. Steam concentration was not measured after the reactor due to the potential contamination that tar deposition could cause to the humidity probe. Tars were also not collected or analysed as they were distributed across a large collection area and so were almost impossible to collect. Elutriated fine chars from the top of the reactor where the gas exits and passes through a glass wool filter were collected and weighed. Overall molar carbon balances for the two sets of experiments were 74 vol.% and 86 vol.% for coal and biomass respectively.

Oddly, the quantity of CH_4 produced in the biomass oxidation experiments was below the level of detection, this could possibly be due to the devolatilisation process of the biomass. The low CH_4 content of the gas stream and the large proportion of 'Unidentified' indicates that significant tar production occurred. It is possible that any light hydrocarbons, like CH_4, that could have partially oxidised with any unreacted O_2 the CH_4 to CO, at the lower temperatures as the gas was exiting the reactors' oxidation zone. The oxidation of biomass is controlled by the devolatilisation of the volatile matter which

subsequently reacts with O_2 within the gas film surrounding the particle, this leads to a greater chance for tars to exit the reactor without reacting if there was a limitation on the diffusion of oxygen to the surface of the particles (Nussbaumer, 2003). Conversely, the coal had relatively little volatile matter and is generally considered a less reactive fuel than biomass. The coal was thought to combust mostly as char meaning the oxidation of the coal was limited by the diffusion of O_2 to the reaction front and by the transfer of heat to the particles. As the temperature of the reactor was ~ 650 °C it is expected that the particles in both systems would have been limited mostly by heat transfer, but if the temperature were higher (800 °C and above) then O_2 diffusion would have played a greater role in limiting the reactions. Additionally, the coal was denser and thus the particles spend longer within the reactor bed before becoming fine enough to be elutriated by the gas flow and as such the gases were favourably converted to CO_2 (Basu, 2006).

3.12.2. Steam gasification of biomass

Further commissioning required a set of experiments to highlight the potential of SESR compared to conventional steam gasification and demonstrate that the reactor produces results comparable to those from the literature. Figure 3.19 displays the products of the SESR reactions broken down as a mass percentage of the initial biomass input. The bed material was varied to demonstrate the effect of each type of bed material on the product gases and most importantly purity and yield of H_2, as these are the main aims of SESR.

These experiments were all conducted at 650 ± 7 °C, 1 atm, ~12 ± 1 vol.% steam and a total flow rate of 73 cm^3/s (@ 293 K – $U/U_{mf} \approx 3$). The biomass utilised in each of these experiments was the same oak biomass previously utilised. These experiments were all conducted with a 0.9 g/min biomass feeding rate using the plastic feeder. Biomass feeding was conducted for multiple one minute periods to provide an estimation of the error, calculated by the standard deviation of the mean. One minute batch feeding was utilised so as to demonstrate the idealised response of the system, i.e. before the surface of the catalyst/sorbent becomes coked, carbonated or poisoned. All steam gasification runs were

followed by an oxidation period after to burn off any coke or remaining char – the released CO and CO_2 during this period was recorded as Char (burned off) in Figure 3.19. The experiments with a catalyst present involved a 10 minute 5 vol.% hydrogen reduction period to re-reduce the catalyst. For the experiments with a sorbent present, it was expected that the absorbed CO_2 was released during the burn off period as the temperature in the reactor reached ~750 °C. The bar segments of Figure 3.19 displayed as 'Unidentified' represent all components not recorded during these experiments, which include tars, ash, steam from the biomass and inaccuracies in experimental measurements. 'Collected chars' displayed in Figure 3.19 were the chars collected in the glass wool trap at the outlet of the reactor. The glass wool was weighed before and after to calculate the quantity of tars collected. The unidentified section of the mass fraction was calculated by difference from 100 % and not by measurement.

The catalyst utilised for these experiments was a commercially available Ni based steam reforming catalyst (HiFUEL R110, 15.9-20 wt.% Ni, supported on an alumina and silica structure, supplied by Alfa Aesar), and was crushed and sieved to a particle size 300-425 μm. A commercial catalyst was utilised for these experiments to ensure the catalytic activity was unimpeded. The sorbent utilised was Longcliffe limestone calcined in-situ prior to the SESR experiment at 850 °C for 30 minutes; the raw limestone was crushed and sieved to particle size 355-425 μm. 5 g of the catalyst and 20 g of the sorbent (CaO) was utilised for experiments involving each respective component, however the total bed mass was always 40 g and was balanced to this mass by adding sand (425-500 μm). The molar ratio of calcium (from the sorbent) to carbon (from the biomass), [Ca]/[C], was ~33.1 over a one minute period of feeding, thereby ensuring the quantity of sorbent was not a limiting factor during the reactions. The molar ratio of the nickel (from the catalyst) to carbon, [Ni]/[C], was ~1.7 over a one minute period of feeding.

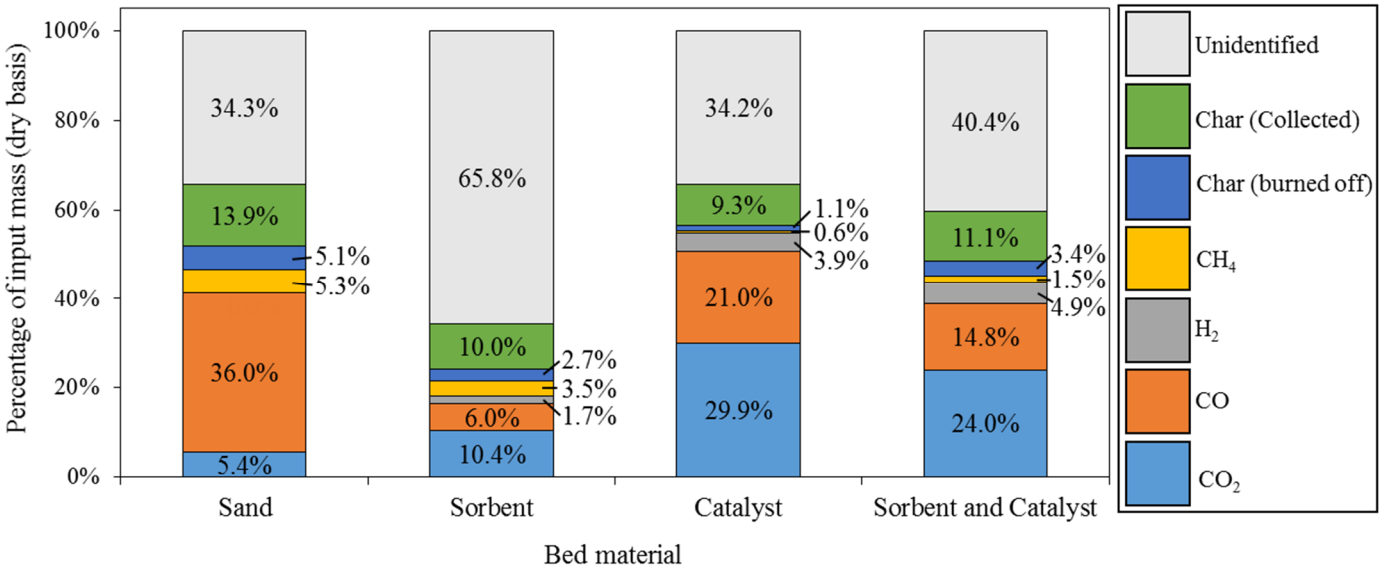

Figure 3.19 – Percentage breakdown (in terms of mass) of outlet components on a dry basis during steam gasification when varying the bed material, 650 °C, 12 vol.% steam, 0.9 g/min oak biomass feeding rate, 1 min of feeding per run, 40 g total bed mass, 5 g HiFUEL R110 catalyst and/or 20 g CaO sorbent (where used).

The significant unidentified proportion within the 'Sorbent' stacked bar shown in Figure 3.19 could be explained by a larger proportion of light tars (C2-C4) being produced due to larger hydrocarbon tars being cracked into smaller hydrocarbons on the surface of the CaO, as reported by many researchers (Devi et al., 2003) (Yu et al., 2009). These smaller hydrocarbons/light tars would not be trapped in the tar and water trap as the trap operates at temperatures >0 °C which is above the boiling points of the smaller hydrocarbons. Wei et al reasoned that during steam gasification of biomass with CaO present, the observed decrease in CH_4 concentration was attributed to steam reforming and dry reforming of the CH_4 catalysed by CaO (Wei et al., 2008). The observed increase in H_2 when the sorbent was present was likely due to the enhanced water gas shift reaction, where CO_2 is removed from the system by the sorbent thereby driving the reaction pathway to the right and thus generating more H_2 simultaneously.

Qualitatively, it can be stated that the tars produced during the reactions with a sorbent present appeared to be a light straw-yellow colour whereas without the sorbent present the tars were a darker brown colour. Furthermore to this point, the addition of the sorbent and catalyst together significantly reduced

the quantity of tars trapped/observed/produced. This result was also noted by Mahishi et Goswami (Mahishi and Goswami, 2007) who suggested the CaO sorbent was acting as a tar cracking catalyst and a CO_2 sorbent. A full tar analysis was not conducted on these samples as this was outside of the primary research scope.

Table 3.3 displays the molar carbon balance for each bed material steam gasification reactions. For the purpose of this carbon balance all char collected at the outlet of the reactor was assumed to be carbon. Utilising the rules of propagated errors the uncertainty of the carbon balances is provided in Table 3.3 as well. The equation for the carbon balance is provided as Equation 3.10.

Table 3.3 – Molar carbon balances for the steam gasification reactions when varying the bed material, 650 °C, 12 vol.% steam, 0.9 g oak biomass, 40 g total bed mass, 5 g HiFUEL R110 catalyst and/or 20 g CaO sorbent (where used).

SESR system	**Moles of carbon - In**	**Moles of carbon - Out**	**Molar carbon balance**	**Uncertainty**
Sand	0.034	0.030	86.4%	4.3%
Sorbent	0.034	0.015	44.6%	3.7%
Catalyst	0.034	0.021	61.2%	5.3%
Sorbent & Catalyst	0.034	0.021	62.0%	3.7%

Equation 3.10 - Carbon balance:

$$C_{balance} = \frac{n_{C\ out}}{n_{C\ in}} \times 100\%$$

Where $n_{C\ in}$ is the moles of carbon from the biomass (from a C, H, N analysis) and $n_{C\ out}$ is the moles of carbon from the char and gas (CH_4, CO and CO_2). Because of high tarring potential of these reactions and the desire to minimise contamination, a humidity probe was only placed at the exit of the reactor for one of the experimental runs to gauge the relative drop in steam concentration. This relative drop

was then applied to all other runs of that experiment type to produce the mole fraction of steam out; this has meant that only a carbon balance can be accurately calculated. The equations utilised to determine the produced moles of each of the gas components are detailed and explained below.

The outlet gas concentration of gas component, *i* (where *i* represents H_2, H_2O, CH_4, CO and CO_2), was adjusted by removing the baseline/inlet concentration of that gas component by applying a one dimensional sloped fit as follows.

Equation 3.11:

$$[i]_{released} = [i]_{out} - [i]_{in}$$

Equation 3.12 - The inlet molar flow rate, F_{in}, was calculated by:

$$F_{in} = \frac{P\,\dot{V}}{R\,T}$$

During the steam gasification experiments only N_2 and H_2O were used to fluidise the particles meaning the inlet N_2 mole fraction can be calculated by the following equation. During the oxidation phase the mole fraction of H_2O was replaced by a constant value equal to the mole fraction of O_2 at steady state after oxidation was complete.

Equation 3.13:

$$x_{N_2\,in} = 1 - x_{H_2O\,in}$$

The outlet mole fraction of N_2 can be calculated by subtracting the mole fractions of all other gas components, *i*:

Equation 3.14:

$$x_{N_2\,out} = 1 - \sum x_{i\,out}$$

Equation 3.15 - The total outlet molar flow rate, F_{out}, was calculated by:

$$F_{out} = \frac{F_{in}\,x_{N_2\,in}}{x_{N_2\,out}}$$

Equation 3.16 - The outlet moles of gas component, *i*, was calculated by:

$$n_{i\ released} = \int_{t=0}^{t=end} F_{out}\ x_{i\ out}$$

Equation 3.17 - The purity (which is essentially the volumetric gas percentage) of gas component *i* was calculated by:

$$i_{purity\ vol.\ \%} = \frac{n_i}{n_{total}} * 100\%$$

Equation 3.18 - The closure of the carbon balance was performed on a mass basis and calculated across both the whole experiment and across each individual reaction phase by:

$$\xi_C = \frac{n_C\ M_C}{F_{biomass}\ x_{C\ biomass}} * 100\%$$

Where:

ξ Closure of the carbon balance as a percentage, %

$[i]$ Concentration of gas component *i*, vol.%

F_{in} Molar flow rate into the reactor, mol/s

F_{out} Molar flow rate out of the reactor, mol/s

$F_{biomass}$ Mass flow rate of biomas into the reactor, g/s

i Gas component *i* can represent N_2, H_2O, CO_2, CO, CH_4, O_2 or H_2

i_{Purity} Volumetric gas % of component *i*, vol.%

$n_{i\ released}$ Moles of component *i* released during the reaction, moles

$n_{C,H,O}$ Total moles of C, H and O measured during a phase of the experiment, mole

n_{total} Total moles of gas components CO_2, CO, CH_4, O_2 and H_2 (depending on experiment phase)

$M_{C,H,O}$ Relative molecular masses of C, H and O, g/moles

P Pressure, assuming 1 atm = 101,325 Pa, Pa

R Universal gas constant, 8.314 J/mol K

t Time, s

T Temperature, 298 K

V Volumetric flow rate, m^3/s

$x_{i\ in}$ Mole fraction of component *i* in

$x_{i\ out}$ Mole fraction of component *i* out

Figure 3.20 shows the moles produced for each of the measured gas components from the steam gasification reactions when varying the bed material. It can be noted from this figure that the moles of hydrogen produced during steam gasification where the reactor bed contains both a sorbent and a catalyst was increased by ~23.8 % (relative to a bed of catalyst and sand) and 186.8 % (relative to a bed of sorbent and sand). It can further be noted that the combined bed of sorbent and catalyst resulted in a 19.6 % readuction in the quantity of CO_2 released. Furthermore, the combined sorbent and catalyst reactor bed produced a hydrogen purity of 67.6 vol.% (N_2 and steam free), although it should be stated that for most commerical applications hydrogen purities should be >99.95 % (Ball and Wietschel, 2009). It was calculated with the use of FactSage thermodynamic software that under the conditions utilised here, the thermodynamic limit for H_2 production would be ≈73.9 vol.% thereby showing that the system operated very close the thermodynamic limit.

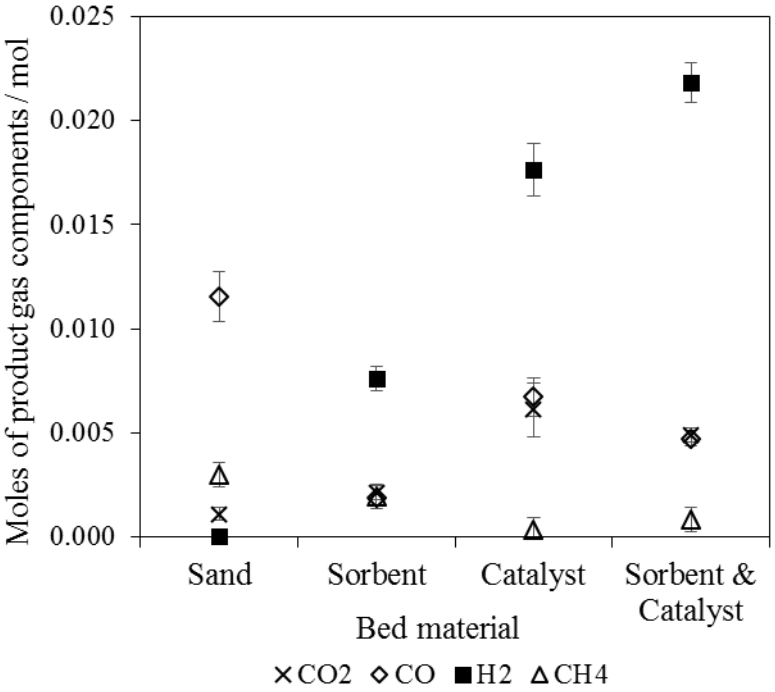

Figure 3.20 – Moles of the produced gases from steam gasification when varying the bed material, 650 °C, 12 vol.% steam, 0.9 g oak biomass, 40 g total bed mass, 5 g HiFUEL R110 catalyst and/or 20 g CaO sorbent (where used).

Sisinni et al (Sisinni et al., 2013), have previously conducted biomass SESR experiments utilising a fixed bed of HiFUEL R110 catalyst and calcined dolomite which was reacted with a small quantity of the product gas from a fluidised bed biomass gasifier (operating at 850 °C) where a bed material consisting of olivine sand. The SESR reactor had a steam to biomass ratio of 0.8 and a bed temperature of 650 °C, from this dual reactor setup they were able to establish a H_2 purity of ~90 vol.% over multiple SESR cycles. The benefit of their system was that the gasification and SESR reactions occurred in separate reactors meaning the impact of coking on the sorbent and catalyst was minimal and the operating conditions of each reactor could be optimised. H_2 production from the use of toluene (D'Orazio et al., 2013) and methane (Batini et al., 2017) have also been investigated with the use of a HiFUEL R110 catalyst however these were performed under very idealised SESR conditions.

3.13. Conclusions

A spout-fluidised bed reactor has been designed, constructed and commissioned to investigate the production of H_2 via Sorbent Enhanced Steam Reforming (SESR) with biomass as the input feedstock. A custom made feeding system was constructed, tested and modified; multiple different types of biomass were tested for their feed-ability, however only hardwoods were successfully fed continuously. A steam generation system was also iteratively constructed and achieved stable steam production of up to 20 vol.%.

Initially the reactor was commissioned by conducting a series of biomass and coal oxidation experiments. These reactions demonstrated the reactor was suitably equipped to monitor the progress of the oxidation experiments; overall molar carbon balances for the coal and biomass oxidation experiments were 73.8 vol.% and 85.9 vol.% respectively. The reactor was subsequently operated as a steam gasifier whilst testing the impact of different bed materials for their impact on hydrogen production. The bed materials investigated were calcined longcliffe limestone as a CO_2 sorbent and a commercial Ni-based catalyst (HiFUEL R110) for the reforming reactions. During the biomass SESR experiments the reactor produced a H_2 purity of 67.6 vol.% (N_2 and steam free) and had a carbon balance of 62 vol.%. Further improvements to H_2 yeild and purity could of course be made by optimising all of the dependant parameters, however the aim of the work presented here was only to demonstrate the feasibilty of this reactor and undertake intitial commissioning experiements.

Chapter 4 – An Investigation into Calcium Carbonate Decomposition: Fluidised Bed Kinetics and Particle Scale Modelling

4.1. Introduction

An integral part of the calcium looping (CaL) process is the ability to regenerate the CO_2 sorbent such that it can absorb CO_2 again in the subsequent carbonation stage. The process of decomposing calcium carbonate into calcium oxide is referred to as calcination, the end result of this process is to produce a highly porous sorbent , which lowers the diffusion resistance of CO_2 through the particles structure and thus enable a sustained fast carbonation reaction to proceed (Manovic and Anthony, 2010c). Carbonation is known to occur first with a rapid reaction of CO_2 at the exterior particle surface and at the interior pore walls, followed by a slower diffusion controlled reaction through the newly formed product layer. In comparison, calcination is thought to occur at a progressive steady rate across the radius of a particle throughout the whole reaction (Grasa and Abanades, 2006).

In a post-combustion CaL setting, the calciner subjects the carbonated particles to high-temperatures (>900 °C) and high CO_2 concentrations (80-100 % CO_2), due to the oxy-combustion of a fuel to raise the bed temperature high enough to overcome the thermodynamic equilibrium and thus release the CO_2 from the sorbent (Vorrias et al., 2013) (Martínez et al., 2012). These two factors drive the sintering process (Borgwardt, 1989) and greatly influence the carrying capacity of the sorbent (as demonstrated in chapter 5). Over multiple cycles this sintering will lead to a sorbent that has a lower available carrying capacity and a smaller surface area (Grasa et al., 2008).

Furthermore, due to the high equilibrium partial pressure of CO_2 at these operating temperatures there is often only minimal driving force for the reaction, which impedes its rate, unless of course the temperature of the calciner is increased further (Manovic et al., 2009). Figure 4.1 shows the CO_2 equilibrium partial pressure at a range of system pressures for the reaction between CaO and CO_2 forming $CaCO_3$ (Equation 2.1). Though increasing the temperature of the calcination reactor would lead to a faster rate of reaction there would also be a greater chance of debilitating the sorbent further due to

an increased extent of sintering (Blamey et al., 2010). Moreover a higher temperature would require more fuel to be burnt, more steam to be generated, and a larger reactor to be built, in all leading to more cost and operational complexity. Thus a balance must be made when designing these reactors based upon the desired CO_2 capture rate, temperature of operation and CAPEX and OPEX.

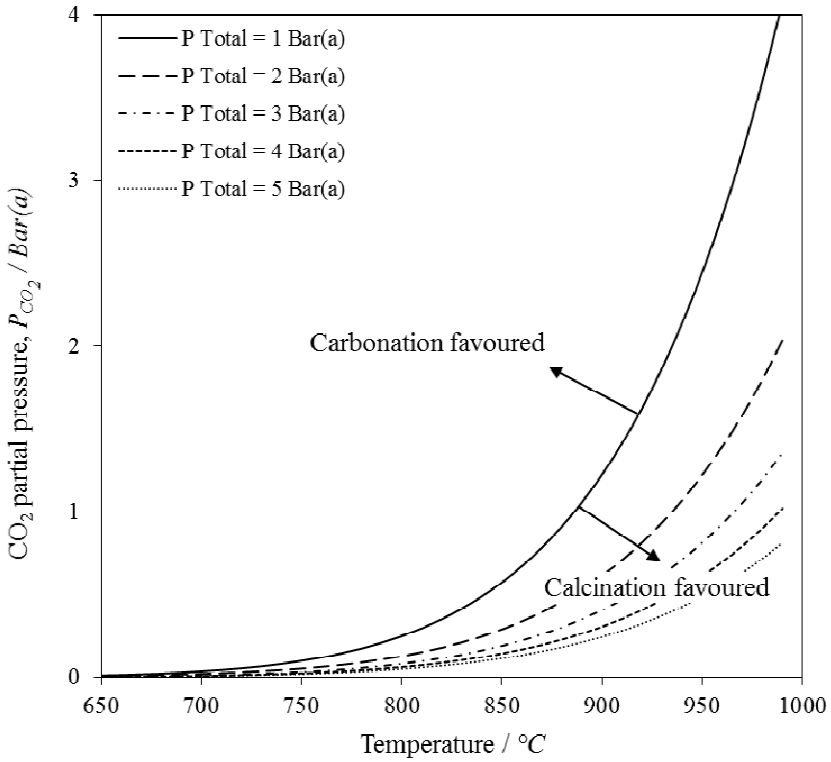

Figure 4.1 – Thermodynamic equilibrium of CaO and CO_2 (Equation 2.1), produced for total pressures 1-5 bar(a) using ThermoVader (McBride et al., 2004).

The kinetics of limestone calcination has been studied previously by Dennis and Hayhurst (Dennis and Hayhurst, 1987) who utilised a fluidised bed reactor with an atmosphere of air/N_2 and up to 20 vol.% CO_2. They showed that the calcination rate was slower when higher CO_2 concentrations, higher total pressures and larger particle diameters were used. Wang et al., (Wang et al., 2007) have also studied the pseudo-kinetics of limestone calcination within a 1 m high continuously operated fluidised bed reactor with a 20 vol.% CO_2 atmosphere, this work examined the hydration and carbonation extent of the calcined material to determine the degree of calcination. The results obtained by this work found a

calcination conversion of 95 % at 1293 K after a 70 min average residence time indicating significant mass transfer limitations within the reactor set up, furthermore the method of analysing the extent of conversion opened itself up to multiple sources of error. This work was later followed up by the same researchers (Wang et al., 2008) utilising the same reactor but with a 20 % steam or N_2 dilution, both of which increased the extent of conversion, steam slightly more so. Martinez et al., (Martínez et al., 2012) have previously conducted a thorough kinetic investigation into limestone calcination kinetics within a thermogravimetric analyser (TGA) with a range of CO_2 partial pressures (0 - 101 kPa), and temperatures (820 - 910 °C) and particle sizes (75 - 125 μm). Their work resulted in calculated activation energies of ~100 kJ/mol, they then applied a simplified reaction controlled shrinking core model with good agreement to their experimental data. Another study of calcination kinetics was conducted in TGA by Garcia-Labiano et al (García-Labiano et al., 2002) who investigated the effects of calcination temperature (1048 - 1173 K), particle size (0.4 – 2.0 mm), CO_2 concentration (0 – 80 %) and total pressure (0.1 – 1.5 MPa). Their research applied a Langmuir-Hinshelwood-type kinetic model which was very successful in predicting the calcination conversion extent in a range of CO_2 partial pressures and total system pressures.

In a commercial setting, the main gaseous component, other than CO_2, present within the calciner will be steam due to the combustion of fuel; other minor constituent gases may include O_2, N_2, SO_x and NO_x (Blamey et al., 2010) (Diego et al., 2014) (Diego et al., 2015). Steam has been shown to positively influence on the long term carrying capacity of CaO-based CO_2 sorbents when it is present during both the carbonation and calcination phases (Champagne et al., 2013) (Donat et al., 2012). Steam helps maintain some of the sorbents CO_2 carrying by lowering the diffusion resistance during the carbonation phase and steam sinters the sorbents in a way that preserves the larger pores, beneficial for CO_2 transport, during the calcination phase (Donat et al., 2012) (Wang et al., 2008) (Manovic and Anthony, 2010a). The effect of steam and CO_2 on the decomposition of calcite was studied by Wang and Thomson (Wang and Thomson, 1995) using dynamic X-ray diffraction (DXRD) at relatively low calcination temperatures 440 – 560 °C. Their research illustrated that the kinetic enhancement observed when steam is present was due to steam having a faster adsorptive properties than CO_2, which was modelled

following a Langmuir-Hinshelwood derivation assuming a weakly bonded intermediately of steam on a $CaCO_3$ active site. Recently this work by Wang and Thomson was refitted to derive the kinetic parameters for a single particle model, which was used to study the influence of steam on the rate of calcination (Yin et al., 2014). It was found that the catalytic effect of steam had a far greater influence than any physical property of the steam and helium mixture. These kinetic parameters were extrapolated from the narrow temperature range utilised by Wang and Thomson and as such their findings may not be representative of the kinetics at higher operating temperatures. A fluidised bed reactor was utilised to calcine limestone and note effect of steam on the extent of limestone calcination, however the calcination extent was measured with the use of a TGA which could have introduced a systematic error to their results (Wang et al., 2008). Recently, Li et al., (Li et al., 2016a) have also utilised a TGA to study the effect of steam *vs*. N_2 on rate of limestone decomposition, they observed a faster reaction time when an equivalent quantity of steam was used in place of N_2.

Some researchers (Furnas, 1931) (Dennis and Hayhurst, 1987) have suggested that calcination proceeds through a particle from the surface at a constant rate, resulting in a sharp reaction boundary between calcined and uncalcined material, thus a large number of researchers in the literature have applied the shrinking core model to their work. Stanmore and Gilot (Stanmore and Gilot, 2005) provided a review in 2005 of calcination and carbonation kinetic studies, which described the range of sintering and reaction models that have been previously applied. From work conducted in a drop tube furnace by Angew et al (Agnew et al., 2000), it was shown that the rate of calcination is comparable or less than the rate of sintering, both of which are highly dependent on temperature, heating rate and the presence of CO_2 and H_2O, confirming the work by Borgwart (Borgwardt, 1985). A recent in depth study (Li et al., 2016b) into $CaCO_3$ pore structure accurately describes the effect on pore distribution as sintering worsens, they have also provided a kinetic model that describes the pore shifting effect due to sintering.

Industrially, the calcination process is likely to be performed in a circulating fluidised bed or entrained flow reactor and thus kinetic data should be gathered within similar apparatus whilst operating at conditions that are most representative of the commercial system (Wojciechowski and Rice, 2003). Moreover $CaCO_3$ calcination is endothermic (see Equation 2.1) and at a CO_2 partial pressures of ~80

kPa (at a system pressure of 1 atm) the reaction is only thermodynamically possible at temperatures above ~873 °C (see Figure 4.1).

Equation 2.1:

$$CaCO_3 \rightleftharpoons CaO + CO_2 \qquad \Delta H_r^0 \approx -178 \text{ kJ/mol}$$

Based on the available literature it is evident that there have been many calcination kinetic studies but none have investigated these kinetics at high partial pressures of CO_2 with steam in an industrially representative fluidised bed reactor. Therefore the focus of this work was to study which parameters affect the rate of calcination at realistic industrial conditions. The range of parameters studied were: CO_2 partial pressure (10 – 80 vol.% CO_2), influence of secondary gas (steam or N_2), bed temperature (900 – 970 °C), particle size (212 – 850 μm), limestone type and sample mass. Following this a particle scale model was developed to describe the calcination reaction at these conditions. The experimental data gathered with N_2 present suffered from a low signal to noise ratio and as such produced physically unrepresentative values when utilising it to determine kinetic parameters. The experimental data as a whole should be thought of as an experimental validation of the single particle model.

As a declaration of originality, it must be stated that the calcination experiments with N_2 present were conducted by Masters student Monica Retrosi.

4.2. Materials and Experimental Methods

The fundamental experimental method applied in this study consisted of adding a small mass of limestone into a hot fluidised bed of sand, the limestone samples' temperature then rises and thus the sample begins to calcine. This investigation utilised an atmospheric fluidised bed reactor that has been described previously (Donat et al., 2012), a pictorial overview of the reactor and in particular the steam generation system is presented as Figure 4.2. The fluidised bed, which was contained within a quartz liner, consisted of 12 ± 0.05 g of sand of particle size fraction of 425 - 500 μm and had a skeletal density of 2600 kg/m^3.

During the investigations with steam, the change in CO_2 concentration was measured indirectly by analysing the change in relative humidity and hence steam concentration. This method of measuring secondary kinetics was implemented as the concentration of CO_2 was above the measurable range of any suitable analyser. For the experiments with N_2 in replacement of steam it was necessary to measure variation of CO_2 concentration with time, but there are inherent difficulties in measuring very high CO_2 concentrations as they were out of the range of any standard analyser. An FTIR analyser with a gas cell could have measured the high CO_2 concentrations but the response times are too slow for determining kinetic data and the accuracy would have been limited due to the background noise of the system. A thermal conductivity analyser could have been utilised but the resolution would have been insufficient to observe the small changes from the baseline. It was therefore decided that the gas stream from the reactor should be diluted with a known, fixed flow rate of N_2 to bring the concentration of CO_2 down to a level that was measurable by an IR multigas analyser (ADC MGA-3000).

The experiments were conducted with a calibrated mix of CO_2 (BOC) and steam or CO_2 and N_2 (BOC). The total flow rate of all gases was fixed to 50 cm^3/s at 298 K and 1 bar(g). This flow rate was chosen based on the minimum fluidisation calculations to achieve a $U/U_{mf} \approx 5.5$ at 950 °C with sand of particle size fraction of 425 - 500 μm and skeletal density of 2600 kg/m^3. The high U/U_{mf} ensured effective mixing and minimised the bulk diffusion resistance and maximised the heat transfer within the bed. The flow rate was not adjusted for temperature in order to maintain the U/U_{mf} ratio because the range of

temperatures investigated was small and was calculated to make no more than ~8 % relative difference to the U/U_{mf}. Some preliminary experiments and calculations of the amount of CO_2 released compared to the amount of gas passing through the system confirmed that the reactor was operating as a differential reactor; meaning that the particles of limestone can be assumed to always be reacting within the gaseous environment of the inlet of the reactor. The CO_2 and N_2 flow rates were controlled with rotameters, however the steam was generated using a specifically constructed bubbler system which is represented in Figure 4.2. The steam generator was immersed within a large heated bath of water with a temperature controlled heating system; the large dimensions of the water bath effectively maintained a constant thermal mass within the bubbler, which was crucial for generating a stable steam concentration. The CO_2 gas was utilised as the carrier gas for the bubbler but was first preheated in a coil (also immersed within the water bath) before bubbling up through the column of water within the bubbler thus picking up the water vapour. The amount of water vapour collected depended primarily on the water temperature within the bubbler and the gas flow rate. The flow rate of CO_2 was adjusted based on the relative humidity produced, so as to maintain a constant 50 cm^3/s total flow rate entering the reactor. The gas lines leading to the reactor were trace heated to ~200 °C for all experiments.

At the outlet of the reactor a sample probe was embedded about 10 cm into the top of quartz liner, a constant flow rate of gas was withdrawn from the reactor and controlled by a separate pump and rotameter. For the reactions with steam the gas was passed over a relative humidity probe (Vaisala) and post-measurement the gases were cooled and the water vapour was condensed using an ice trap before the gas was vented to the local exhaust ventilation. The response time of the relative humidity probe and the total system was measured by employing the method described by Fennell et al. (Fennell et al., 2009). The final response time constant to reach 95% of the final value was calculated to be ~1.4 s. When measuring kinetic data, a response time constant less than 6 seconds means the data gathered is suitable for deconvoluting by assuming a CSTR model, this method is described later.

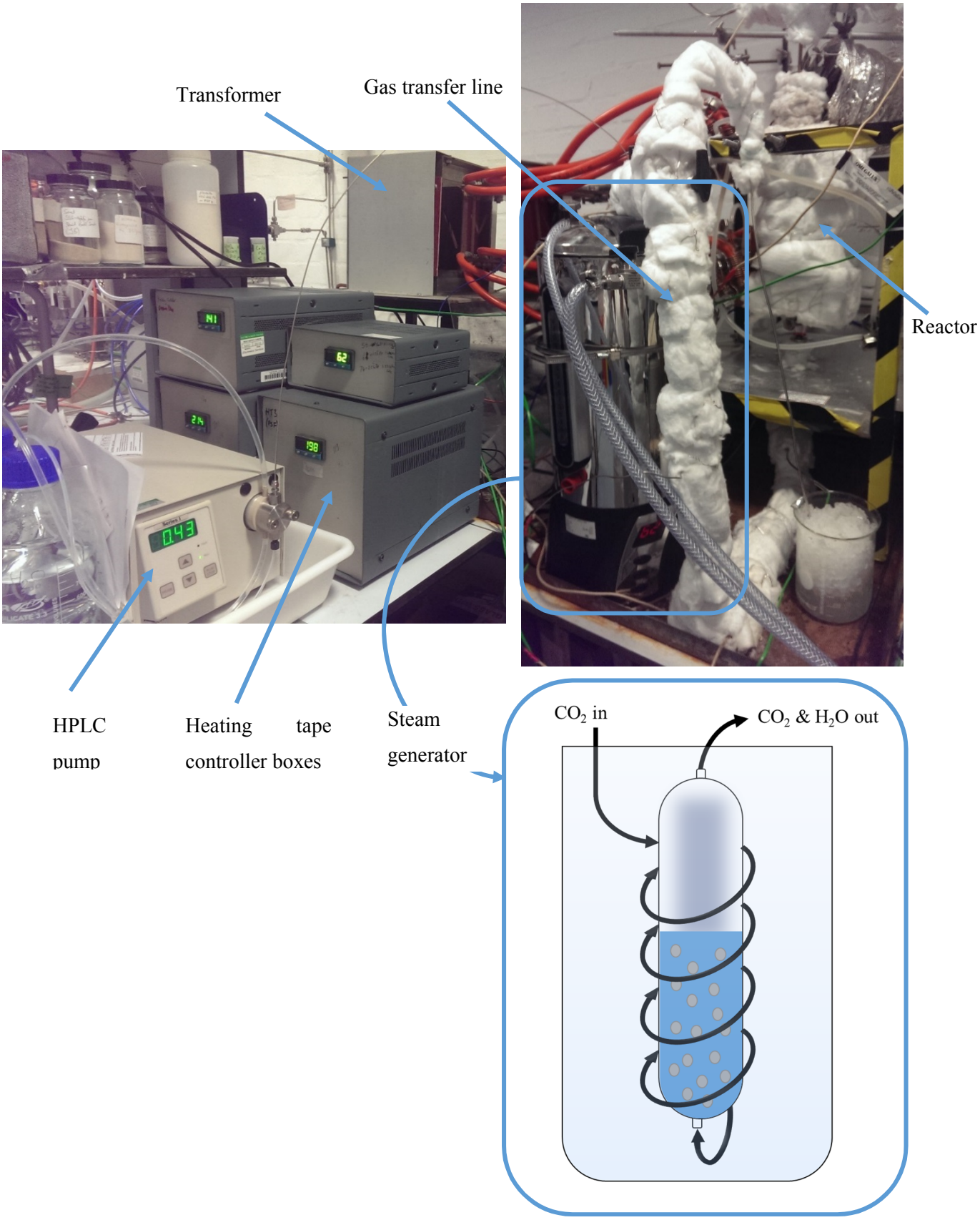

Figure 4.2 – Pictorial representation of the reactor and steam generation system.

For the reactions with N_2 in replacement of steam the humidity probe and ice trap were removed and replaced with a small calcium chloride trap to collect any water vapour produced during the limestone calcination. The exit gases were sampled using the same sampling probe as was used in the steam system but the gases were mixed with a calibrated, fixed quantity of N_2 to reduce the CO_2 concentration and then the CO_2 concentration was measured with the gas analyser. The same negative gauge pressure post-analysis pump and rotameter was utilised for these reactions. The response time constant was also measured for this system and was found to be ~3 s.

The limestone that was primarily used in these experiments was Longcliffe limestone (Longcliffe Quarries Ltd, Derbyshire, UK). XRF data for the different types of limestone utilised in this study can be observed in Table 4.1.

A mix of 80 vol.% CO_2 and 20 vol.% steam at 950 °C was utilised as a base case for the comparison against other data, this configuration was considered most likely to match the conditions within a commercial calciner. Unless stated otherwise, it can be assumed that a particle size of 500 – 710 μm and a sample mass of 0.25 g was utilised. Some preliminary experiments were conducted to determine the most suitable mass of sample to use based on the minimising the inter-particle diffusion effects of large sample masses whilst producing a sufficiently large signal to noise ratio. To investigate the effect on the kinetics of limestone calcination the operational parameters were individually altered and are discussed in detail throughout this chapter.

Table 4.1 – XRF data in mol.% of the limestones utilised in this study (Alonso et al., 2014).

	Limestone type			
Species mol.% by XRF	**Longcliffe**	**Havelok**	**Cadomin**	**Imeco**
$CaCO_3$	98.89	96.30	94.34	96.10
SiO_2	0.16	2.38	2.59	1.10
Fe_2O_3	0.01	0.10	0.10	0.20
Al_2O_3	0.10	0.28	0.06	0.10
MgO	0.50	0.56	2.08	1.20
K_2O	0.05	0.05	0.06	0.05
MnO	0.29	0.29	0.21	-
SrO	-	0.03	0.02	-

4.2.1. Method to analyse calcination data with steam and CO_2 present

To analyse the data from the steam and CO_2 experiments a mole balance was performed around the boundary of the reactor, which can be been summarised in the following series of equations.

Equation 4.19 - Total molar flow rate in was composed of CO_2 and steam:

$$\dot{n}_{T\ in} = \dot{n}_{CO_2\ in} + \dot{n}_{H_2O\ in}$$

Equation 4.20 - Assuming no steam reacts:

$$\dot{n}_{H_2O\ out} = \dot{n}_{H_2O\ in}$$

The total amount of CO_2 leaving the reactor was equal to the amount of CO_2 that enters plus the amount generated from the calcination.

Equation 4.21:

$$\dot{n}_{CO_2\ out} = \dot{n}_{CO_2\ in} + r_{CO_2\ gen}$$

The mole fraction of steam entering the reactor was defined as the molar flow rate of steam in divided by the total molar flow rate in.

Equation 4.22:

$$x_{H_2O\ in} = \frac{\dot{n}_{H_2O\ in}}{\dot{n}_{T\ in}} = \frac{\dot{n}_{H_2O\ in}}{\dot{n}_{H_2O\ in} + \dot{n}_{CO_2\ in}}$$

Then by defining the mole fraction of steam at the outlet in the same manner and then substituting in Equation 4.20 and Equation 4.21 into Equation 4.22 it possible to define the outlet mole fraction of steam (a measurable quantity) in terms of the inlet molar flow rates.

Equation 4.23:

$$x_{H_2O\ out} = \frac{\dot{n}_{H_2O\ out}}{\dot{n}_{T\ out}} = \frac{\dot{n}_{H_2O\ out}}{\dot{n}_{H_2O\ out} + \dot{n}_{CO_2\ out}} = \frac{\dot{n}_{H_2O\ in}}{\dot{n}_{H_2O\ in} + \dot{n}_{CO_2\ in} + r_{CO_2\ gen}}$$

Equation 4.24 - By rearranging Equation 4.23:

$$x_{H_2O\ out} \cdot (\dot{n}_{H_2O\ in} + \dot{n}_{CO_2\ in} + r_{CO_2\ gen}) = \dot{n}_{H_2O\ in}$$

Equation 4.25 - Then by re-arranging again and substituting in Equation 4.19:

$$r_{CO_2\ gen} = \frac{\dot{n}_{H_2O\ in}}{x_{H_2O\ out}} - \dot{n}_{T\ in}$$

Equation 4.26 - Finally, substituting in Equation 4.22:

$$r_{CO_2\ gen} = \dot{n}_{T\ in}\left(\frac{x_{H_2O\ in}}{x_{H_2O\ out}} - 1\right)$$

The mole fractions were measured by the relative humidity and converted into partial pressures by use of the saturation vapour pressures determined from the Clausius-Clapeyron equation. The inlet mole fraction of steam was taken as the averaged baseline before and after the reaction.

Equation 4.27:

$$x_{H_2O\ out} = \frac{p_{w\ out}}{p_T} = \frac{\frac{RH\ \%}{100} p_{ws}}{p_T}$$

4.2.2. Method to analyse calcination data with N_2 and CO_2 present

To analyse the data from the N_2 and CO_2 experiments a mole balance was performed around a boundary of the reactor and the dilution system, which have been summarised in the following series of equations and is illustrated in Figure 4.3.

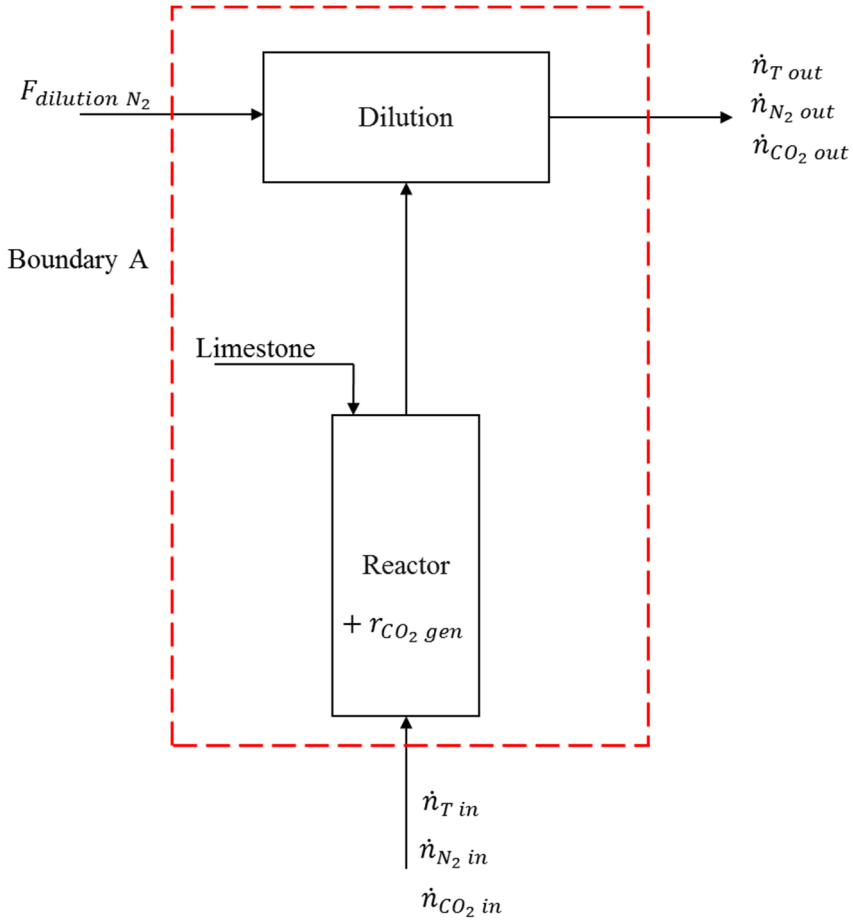

Figure 4.3 – Mole balance around the reactor and dilution system, showing inputs and outputs and the assumed reaction boundary.

Equation 4.28 - N_2 mole balance assuming continuity:

$$\dot{n}_{N_2\ out} = \dot{n}_{N_2\ in} + F_{dilution\ N_2}$$

$F_{dilution}$ is the extra N_2 that was added after the reactor to reduce the CO_2 concentration entering the analyser.

The mole fractions of N_2 in and out were defined as follows.

Equation 4.29:

$$x_{N_2\ in} = \frac{\dot{n}_{N_2\ in}}{\dot{n}_{T\ in}}$$

Equation 4.30:

$$x_{N_2\ out} = \frac{\dot{n}_{N_2\ out}}{\dot{n}_{T\ out}}$$

Equation 4.31 - Substituting The mole fractions of N_2 in and out were defined as follows.

Equation 4.29 and Equation 4.30 into Equation 4.28:

$$\dot{n}_{T\ in}x_{N_2\ in} + F_{dilution\ N_2} = \dot{n}_{T\ out}x_{N_2\ out}$$

Equation 4.32 - Recognising that the system is composed only of CO_2 and N_2:

$$x_{N_2\ in} = 1 - x_{CO_2\ in}$$

Equation 4.33:

$$x_{N_2\ out} = 1 - x_{CO_2\ out}$$

Equation 4.34 - Then substituting Equation 4.32 and Equation 4.33 into Equation 4.31:

$$\dot{n}_{T\ in}(1 - x_{CO_2\ in}) + F_{dilution\ N_2} = \dot{n}_{T\ out}(1 - x_{CO_2\ out})$$

Equation 4.35 - Rearranging to derive an expression for the total molar flow rate out:

$$\dot{n}_{T\ out} = \frac{\dot{n}_{T\ in}\left(1 - x_{CO_2\ in}\right) + F_{dilution\ N_2}}{(1 - x_{CO_2\ out})}$$

Equation 4.36 - CO_2 mole balance assuming continuity:

$$\dot{n}_{CO_2\ out} = \dot{n}_{CO_2\ in} + r_{CO_2\ gen}$$

The mole fractions of CO_2 in and out were defined as follows.

Equation 4.37:

$$x_{CO_2\ in} = \frac{\dot{n}_{CO_2\ in}}{\dot{n}_{T\ in}}$$

Equation 4.38:

$$x_{CO_2\ out} = \frac{\dot{n}_{CO_2\ out}}{\dot{n}_{T\ out}}$$

Equation 4.39 - Substituting Equation 4.37 and Equation 4.38 into Equation 4.36 and rearranging:

$$\dot{n}_{T\ out}x_{CO_2\ out} - \dot{n}_{T\ in}x_{CO_2\ in} = r_{CO_2\ gen}$$

Equation 4.40 - Substituting Equation 4.35 into Equation 4.39:

$$\frac{\dot{n}_{T\ in}(1 - x_{CO_2\ in}) + F_{dilution\ N_2}}{(1 - x_{CO_2\ out})}x_{CO_2\ out} - \dot{n}_{T\ in}x_{CO_2\ in} = r_{CO_2\ gen}$$

Equation 4.41 - Rearranging the left hand side of Equation 4.40:

$$\frac{\dot{n}_{T\ in}(1 - x_{CO_2\ in})x_{CO_2\ out} + F_{dilution\ N_2}x_{CO_2\ out}}{(1 - x_{CO_2\ out})} - \dot{n}_{T\ in}x_{CO_2\ in} = r_{CO_2\ gen}$$

Equation 4.42 – Expanding and rearranging the left hand side of Equation 4.41:

$$\dot{n}_{T\ in}\left[(1 - x_{CO_2\ in})x_{CO_2\ out} - (1 - x_{CO_2\ out})x_{CO_2\ in}\right] + F_{dilution\ N_2}x_{CO_2\ out} = (1 - x_{CO_2\ out})r_{CO_2\ gen}$$

Equation 4.43 - Rearranging the left hand side of Equation 4.42:

$$\dot{n}_{T\ in}\left[x_{CO_2\ out} \cancel{- x_{CO_2\ out}x_{CO_2\ in}} - x_{CO_2\ in} \cancel{+ x_{CO_2\ out}x_{CO_2\ in}}\right] + F_{dilution\ N_2}x_{CO_2\ out}$$
$$= r_{CO_2\ gen}(1 - x_{CO_2\ out})$$

Equation 4.44 - Simplifying Equation 4.43 leads to the final expression:

$$r_{CO_2\ gen} = \frac{\dot{n}_{T\ in}\left(x_{CO_2\ out} - x_{CO_2\ in}\right) + F_{dilution\ N_2}\ x_{CO_2\ out}}{\left(1 - x_{CO_2\ out}\right)}$$

In this equation, the term $F_{dilution\ N2}\, x_{CO_2 out}$ effectively scales the measured CO_2 moles up to the correct value, as if no dilution had taken place.

4.2.3. Rate constant derivation

The rate data was deconvoluted via Equation 4.45 as described by Fennell et al. (Fennell et al., 2009).

Equation 4.45:

$$C_t = C_m + \tau \frac{dC_m}{dt}$$

The peak rates of reaction were taken as the maximum rate observed (after deconvolution) and was assumed to be equal to the initial rate of reaction. It was also assumed that after the peak rate of reaction was observed the rate at all subsequent times was limited by some other factor.

Equation 4.46 - Following an assumed first order derivation the rate constants were calculated using:

$$r_{calc} = k_{calc}\left(C^*_{CO_2} - C_{CO_2}\right)^n$$

Where r_{calc} was the observed peak rate of calcination, k_{calc} was the observed rate constant calculated and described by Equation 4.48, $C^*_{CO_2}$was the equilibrium CO_2 concentration and C_{CO_2} was the CO_2 concentration at the peak rate in units of mol/m^3. n was the order or reaction assumed to be first order in both cases, as demonstrated by (Borgwardt, 1985) (Silcox et al., 1989) (Dennis and Hayhurst, 1987) (Agnew et al., 2000) this is a valid assumption. The equilibrium CO_2 concentration (p_{CO_2}/R_iT) was determined from the thermodynamic data shown in Figure 4.1. The rates were sometimes plotted in units of s^{-1} in this case they were converted from mol/g.s to s^{-1} by multiplying by the molar mass of $CaCO_3$.

Equation 4.47 - Arrhenius equations for calculating k_{calc}:

$$k_{calc} = k_0 e^{-\frac{E_A}{R_i T}} \quad \text{and} \quad \ln(k_{calc}) = \left(\frac{-E_A}{R_i}\right)\left(\frac{1}{T}\right) + \ln(k_0)$$

Where k_0 was the pre-exponential factor representing the frequency of collisions in units of s^{-1}, E_A was the activation energy of the system in J/mol, T was the reaction temperature in kelvin and R_i was the ideal gas constant in units of J/mol.K.

4.3. Results and Discussion

The main difference observed between calcinations that were conducted in the presence of steam compared to N_2 was the rate of reaction. As can be seen from Figure 4.4 where the convoluted CO_2 rate responses for the two systems have been overlaid, the calcination in the presence of steam was approximately 4 times faster than that with N_2 instead. This chapter will investigate the reasons behind this observed difference.

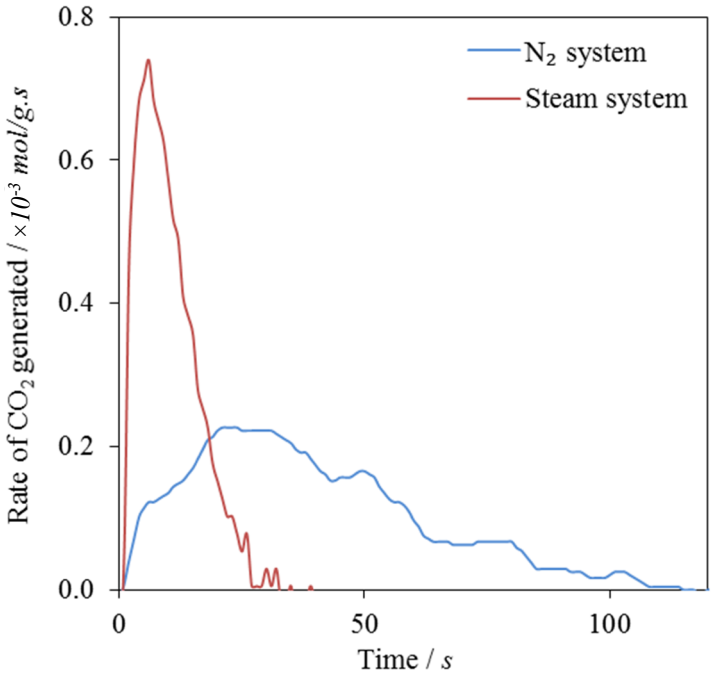

Figure 4.4 – Convoluted CO_2 response from the calcination of 0.25 g of longcliffe limestone (500-710 µm) in 80% CO_2 and 20% steam (red line) and 80% CO_2 and 20% N_2 (blue line).

4.3.1. Effect of varying bed temperature

The bed temperature was set to a calibrated value, 8-15°C above the desired bed temperature such that when the cold aliquot of limestone was added, the sample absorbed some of the bed's heat thus dropping the bed temperature and allowing the sample to react at the desired set point temperature. Figure 4.5 displays the bed temperature and analyser response when 0.25 g of longcliffe limestone (500-710 μm) was added into the reactor. Figure 4.5a shows the system response when the bed was fluidised by 80 vol.% CO_2 and 20 vol.% steam and Figure 4.5b shows the response when the bed was fluidised by 80 vol.% CO_2 and 20 vol.% N_2. To ensure the precision and accuracy of the experimental work, great care was taken to validate that the reactions occurred as close to the set values as possible, because of this each experiment was repeated a minimum of 4 times.

Observing the typical temperature response displayed in Figure 4.5a shows a pseudo-isothermal state throughout the main calcination period; the bed temperature only begins to recover when the reaction is almost finished. Figure 4.5b displays a much more pronounced initial drop in temperature when the sample is added. Furthermore, there was a noticeable difference in the rate of reaction and the rate of bed temperature recovery when the calcination was conducted with N_2 in replacement of steam. The observed bed temperature responses of the endothermic calcination reactions with steam imply that the reaction rate was sufficiently fast to limit the rate at which the bed temperature heated back up. Conversely, the observed temperature response of limestone calcination with N_2 present show that the slow rate of reaction dispersed the samples enthalpy of reaction, thereby enabling the bed temperature to gradually recover whilst the reaction took place. This effect led to the incorporation of a common systematic error with regards to the reaction temperature measurement. To compare the data accurately between these two systems, the temperatures stated will be given with a standard deviation error calculated across the period between 0 and 90 % conversion and across each of the samples.

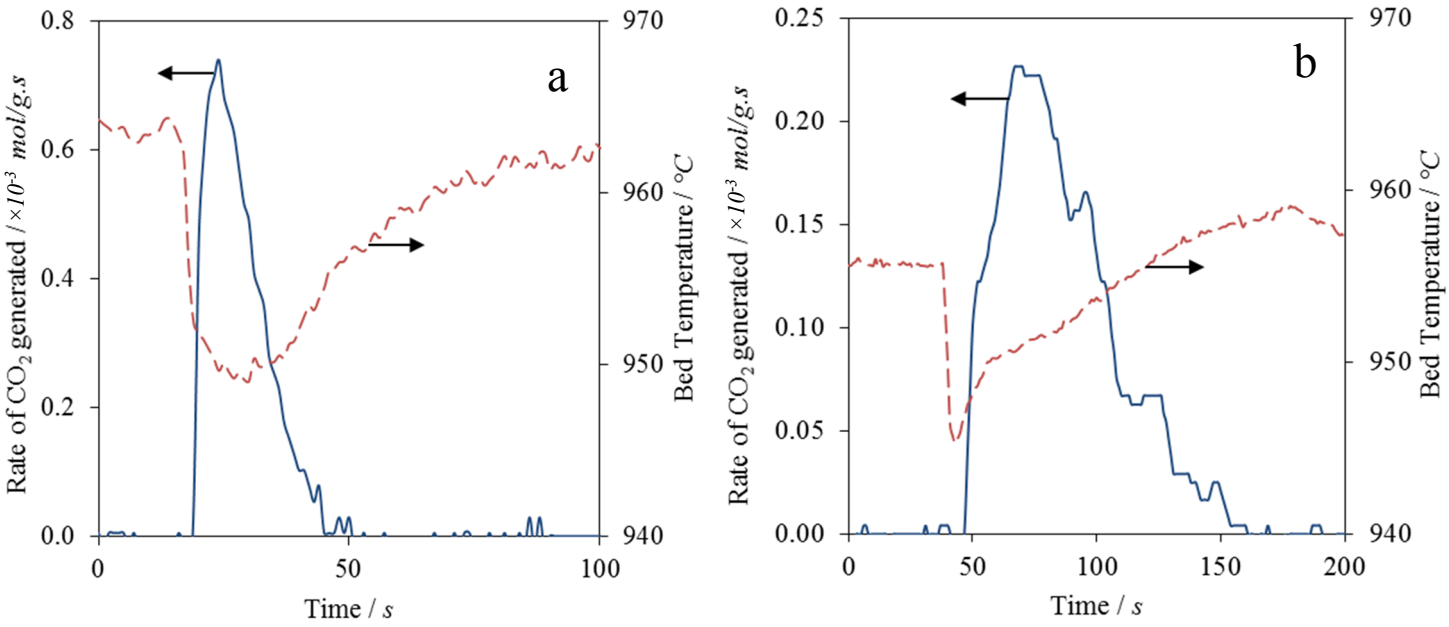

Figure 4.5 – (a) Bed temperature and convoluted CO_2 response from the calcination of 0.25 g of longcliffe limestone (500-710 µm) in 80% CO_2 and 20% steam (b) Bed temperature and convoluted CO_2 response from the calcination of 0.25 g of longcliffe limestone (500-710 µm) in 80% CO_2 and 20% N_2. Vertical dashed lines indicate the point at which the reaction had visibly begun to react.

The response of the bed temperature profile, when compared to the response of CO_2 concentration, showed a discrepancy as to when the reaction actually began. A vertical dashed line has been added to Figure 4.5a and Figure 4.5b to highlight the offset between the two responses. The CO_2 responses have both been shifted by the measured system lag time (measured by calculating the gas velocity in the tubing and multiplying by the length of tubing) yet the N_2 system still presented ~7 s of delay between the temperature responding to the addition of the cold sample and the CO_2 being detected by the analyser. It was thought this could be due to a difference in heating rates of the sample caused by the different gas composition. Because of these two fundamentally different responses it was initially thought that the steam was able to facilitate the transfer of heat to the limestones surface more effectively than N_2. The heat transfer coefficient of the steam system was calculated to be 471 $W/m^2.K$ which is slightly greater than the value calculated for the N_2 system of 414 $W/m^2.K$. It is not thought that a difference of ~55 $W/m^2.K$ would account fully for the difference in heating rates observed but it likely played a part. The second half of this work will aim to explain the difference in reaction rate by developing a particle model for these two systems.

Figure 4.6a and b and Figure 4.7a and b show the reaction and conversion profiles for limestone calcination in 20% steam 80% CO_2 and 20% N_2 80% CO_2 when the bed temperature is altered. Although the temperature range is not significantly large, there is a clear difference in rate of reaction and length of time for the reactions to complete, with the steam calcination taking approximately half the amount of time as the N_2 calcinations. The variation in conversion profiles is due to measurement inaccuracies caused mostly by the signal to noise ratio being low.

The rate of these reactions was limited by the thermodynamic equilibrium position of $CaCO_3$ within the high CO_2 atmosphere, which at 80 vol.% CO_2 the equilibrium temperature was calculated to be ~873 °C. This means that the calcination reactions would not be thermodynamically feasible until temperatures above this value were reached. Experiments were conducted initially at 900 °C but at this temperature the signal to noise ratio was too low to accurately assess when the reaction was happening. The upper limit for the bed temperature was set by the material properties of the reactor and controlled by the rate at which heat could be transferred into the bed from the hot exterior wall. When operating at 950 °C with steam and CO_2 the reactor wall temperature reached ~1200 °C in order to maintain the bed temperature. On the other hand, the N_2 system could reach bed temperatures ~970 °C with the same wall temperature. It was deemed unsafe to take the reactor to above these wall temperatures consequently the experimental results for varying bed temperature were limited to this range. The reason for the N_2 system being able to reach higher temperatures with the same wall temperature was thought to be due to the specific heat capacity of N_2 being approximately half that of steam at the same temperature (Rogers and Mayhew, 1995).

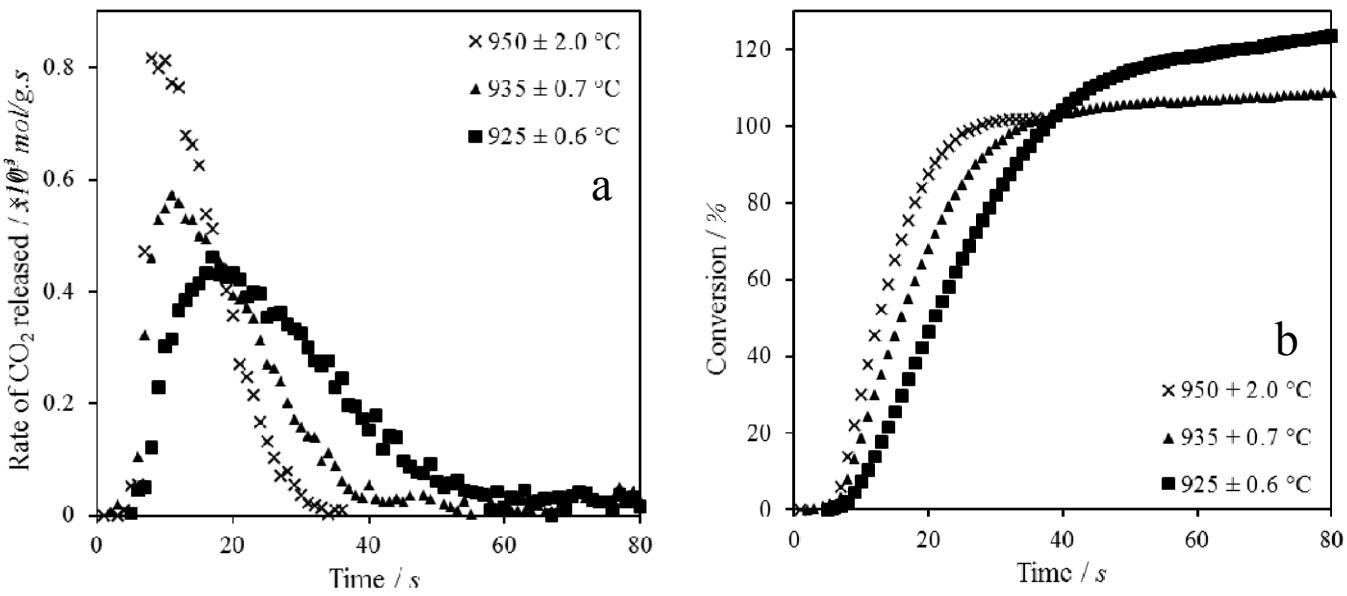

Figure 4.6 – Averaged reaction and conversion profiles for limestone calcination in 20 vol.% steam and 80 vol.% CO_2 when varying the bed temperature.

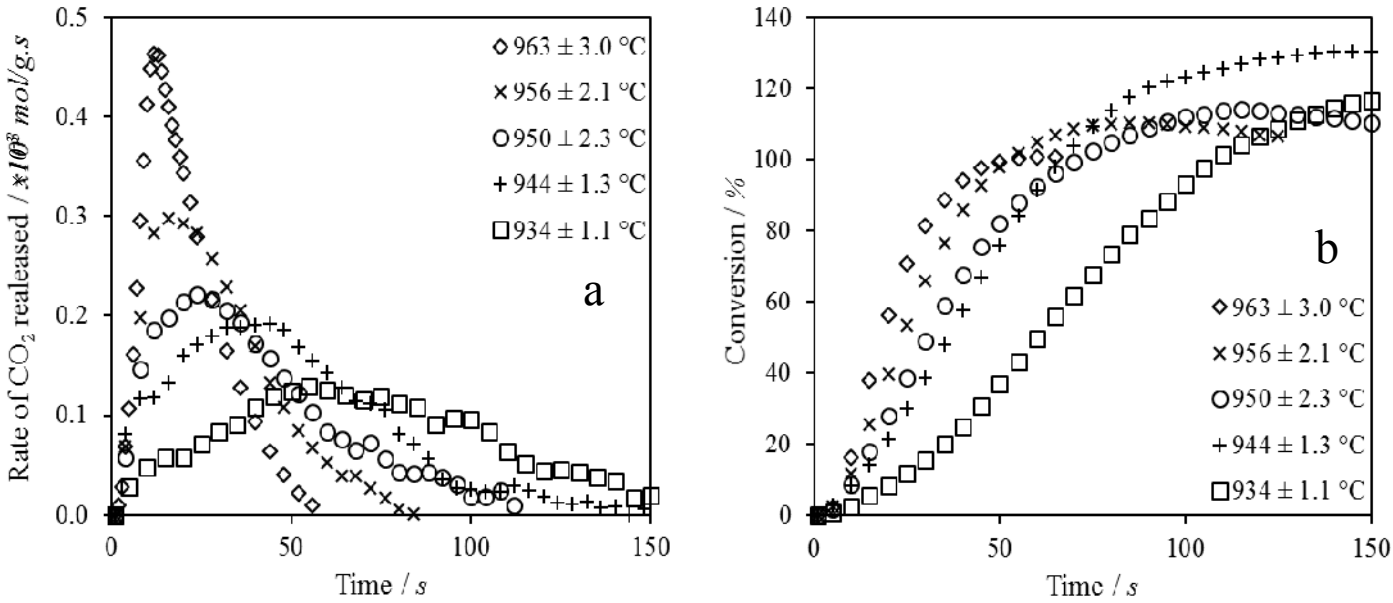

Figure 4.7 – Averaged reaction and conversion profiles for limestone calcination in 20 vol.% N_2 and 80 vol.% CO_2 when varying the bed temperature.

The data presented from all experiments with N_2 present utilised a sampling rate of 1 sample per second, however this data was thinned for clarification when plotting.

The reaction rate constants applied in Figure 4.8 were calculated utilising the method described in section 4.2.3. Activation energies for the two systems were calculated by plotting the reciprocal of the bed temperature against the natural logarithm of the observed first order (with respect to $C_{CO_2eq} - C_{CO_2}$) reaction rate constants in units of s^{-1}, this Arrhenius plot shown in Figure 4.8. The slope and intercept of this graph represent the activation energy divided by the universal gas constant and natural logarithm of the pre-exponential factor respectively. The activation energies and pre-exponential factors were substituted into the Arrhenius equation to calculate the rate constant at a given temperature. The activation energies calculated were 78.8 kJ/mol and 253.7 kJ/mol for the steam and N_2 system respectively as shown in Table 4.2. Other researchers in the literature have provided values for the Arrhenius parameters of limestone calcination under similar conditions; these have been summarised in Table 4.3. The values calculated from this work sit well within the expected range of literature activation energies (García-Labiano et al., 2002). The activation energies also demonstrate that steam lowers the activation energy of limestone calcination.

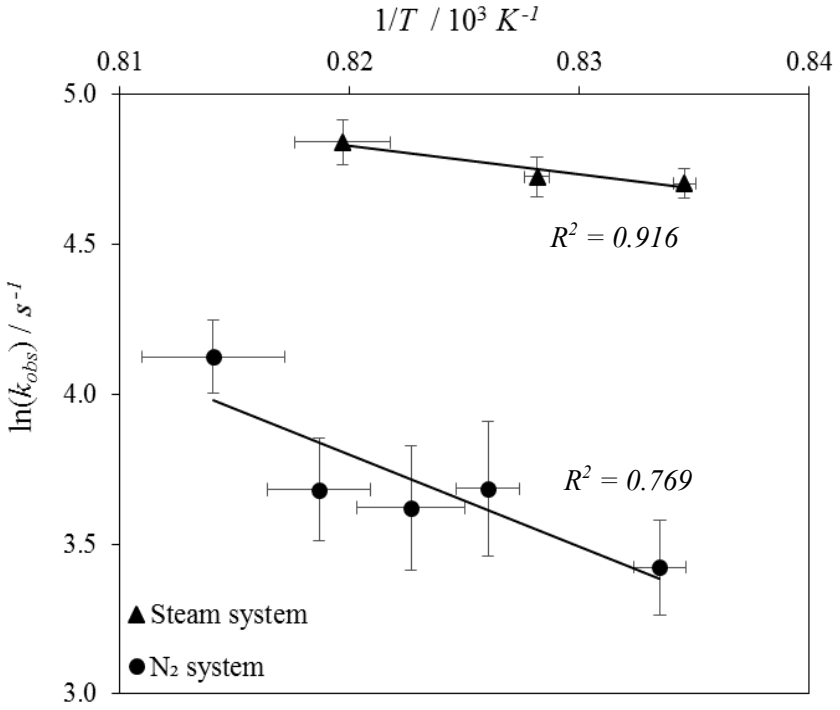

Figure 4.8 – Arrhenius plot for the observed first order kinetics of limestone calcination in 80 vol.% CO_2 and either 20 vol.% steam or N_2.

The error bars shown in Figure 4.8 were calculated from a standard deviation of the repeated experiments which were then adjusted via the laws of error propagation. The deviation from the mean value was greater for temperature because it was difficult to ensure the reactor behaved and responded exactly the same for each experiment.

Table 4.2 – Arrhenius parameters for the observed first order kinetics of limestone calcination in 80 vol.% CO_2 and either 20 vol.% steam or N_2.

	Steam system		**N_2 system**	
	$k_{0\,obs}$ (s^{-1})	E_a (kJ/mol)	$k_{0\,obs}$ (s^{-1})	E_a (kJ/mol)
Observed first order kinetics	2.8×10^5	78.8 ± 23.7	2.8×10^{12}	253.7 ± 80.4

It is understood that the range of temperatures for which these activation energies have been calculated was small, especially so with the steam system. This was due to reactor and gas analysis limitations. Nevertheless these results do provide an indication of the approximate activation energies and pre-exponential factors for the calcination of limestone within a fluidised bed operating under realistic temperatures and concentrations. The activation energies obtained by previous researchers is shown in Table 4.3 and shows that the values determined in this set of work were within a similar range and order of magnitude. Purity, or rather impurities, do seem to affect the rate of calcination and hence the calculated activation energies; this is evident by looking at the activation energies obtained by Garcia-Labiano et al. and Martinez et al. whose studies overlapped in the conditions applied, yet quite diverse values were produced which is likely to be because of the impurities in the starting materials. Most of the previous experimental work looking into the kinetics of calcination utilised a TGA however kinetic data gathered via this apparatus is known to suffer from many external diffusional issues which impede the accuracy of the resulting kinetic data (Liu et al., 2012).

Table 4.3 – A comparison of literature values for the activation energy of limestone calcination.

Limestone sample characteristics	**Measurement technique and conditions**	**Activation energy / kJ/mol**	**Authors**
Two limestones of particle size fractions: 75 − 125, 125 − 300, 300 − 600, and 600 − 800 μm	2 mg of sample analysed in an atmospheric pressure TGA under 100 % N_2 between 820 to 910 °C	102.1 ± 10.4	(Martínez et al., 2012)
Calcite samples of > 98 % purity	10 mg of sample analysed in an atmospheric pressure TGA under 100 % N_2 between 500 to 700 °C	109.0 for 98.2% purity 193.8 for 99.5% purity	(Calvo et al., 1990)
Limestone of particle size fraction 1 − 90 μm	Modelled kinetics based on BET surface area measurements of samples calcined within a differential flow reactor under 100 % N_2 between 516 to 1000 °C	205.0 ± 8.4	(Borgwardt, 1985)
Limestone of particle size fraction 0.4 − 2.0 mm	3.5 g sample batches added to a fluidised bed reactor at varying system and partial pressures of CO_2 (E_a given under 20 % CO_2, 80 % N_2 between 800 to 975 °C)	169.0	(Dennis and Hayhurst, 1987)
Two limestone and one dolomite of particle size fractions 0.8 − 1 mm	10 mg samples analysed in an atmospheric pressure TGA under 100 % N_2 between 775 to 900 °C	166.0, 131.0 and 114.0 for the different limestones	(García-Labiano et al., 2002)
Calcite samples of mean particle diameter 1.8 μm	Least squares fitting to data from *in-situ* dynamic XRD analysis between 440 to 560 °C. Pure He and ~20% H_2O in He respectively	192.0 ± 13 in 100 % He 247.0 ± 17 in 20 % steam, 80 % He	(Wang and Thomson, 1995)

4.3.2. Effect of varying CO_2 partial pressure

The order of reaction and hence influence of the different gases (CO_2, steam and N_2) was determined by varying the concentration of steam (12, 21, 29 and 39 vol.%) and N_2 (10, 20, 30, 40, 50, 60, 70 and 80 vol.%), then fitting the data to a simple differential rate law. The influence of steam and N_2 partial pressure on the rate of calcination was initially found by plotting ln of the rate against ln of the partial pressure, this is presented as Figure 4.9. The experimental data gathered for the calcinations in the presence of 70 and 90 vol.% CO_2 were not included in these calculations as the observed conversions were well above experimental error, as can be seen in Table 4.4.

It can be observed that the order of reaction with respect to steam concentration, given by the slope of the best fit line, was approximately zeroth order, indicating that a steam concentration above ~12% had very little influence on the rate of calcination. The independence of steam concentration on the rate of reaction can be observed by reference to Figure 4.10a and b which display the observed rate of calcination and observed conversion, both against time.

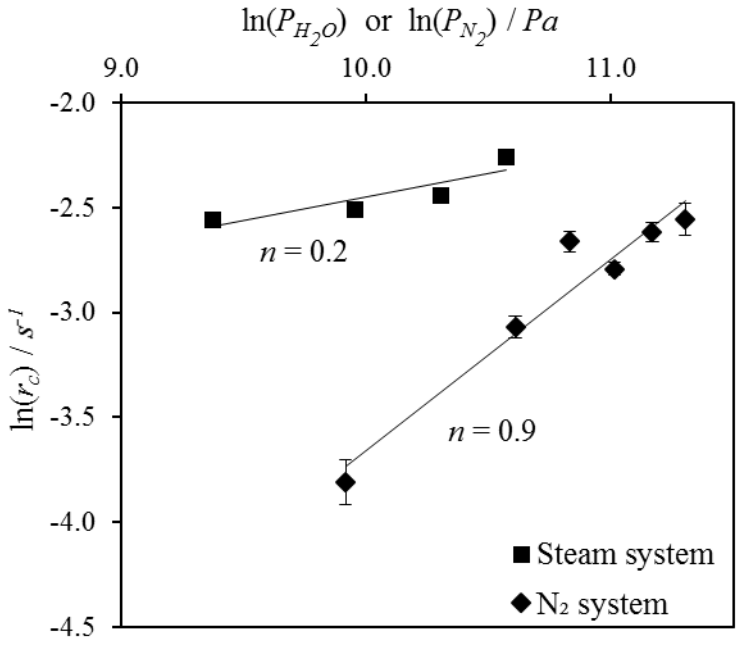

Figure 4.9 – Influence of steam and N_2 concentration on the rate of calcination. *n* represents the apparent order of reaction. Kinetic experiments conducted at 950 °C, 1 bar(a).

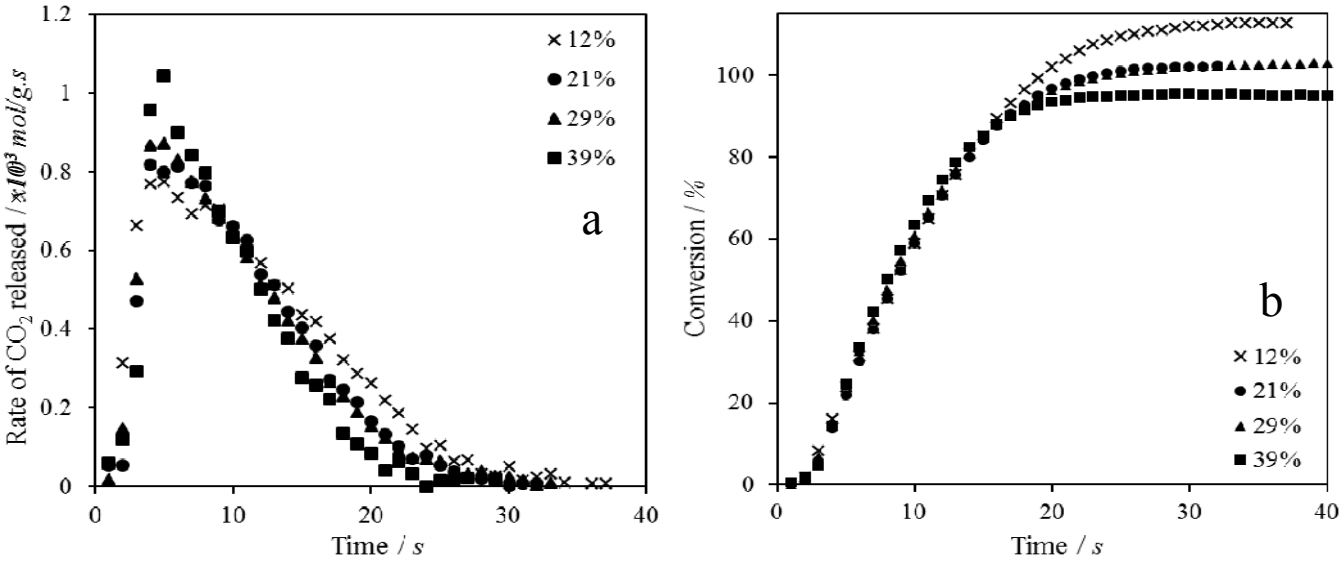

Figure 4.10 – Reaction and conversion profiles for limestone calcination at 950 °C with varying steam and CO_2 concentrations. The percentages specified in the legends are the steam vol.% concentrations.

The reaction order with respect to N_2 was also fitted via the same method as steam was and is again presented in Figure 4.9. An approximate first order relationship was found between the concentration of N_2 and the rate of calcination at all concentrations of N_2. This relationship is shown further in Figure 4.11a and b which display the observed rate of CO_2 released vs time and conversion vs time.

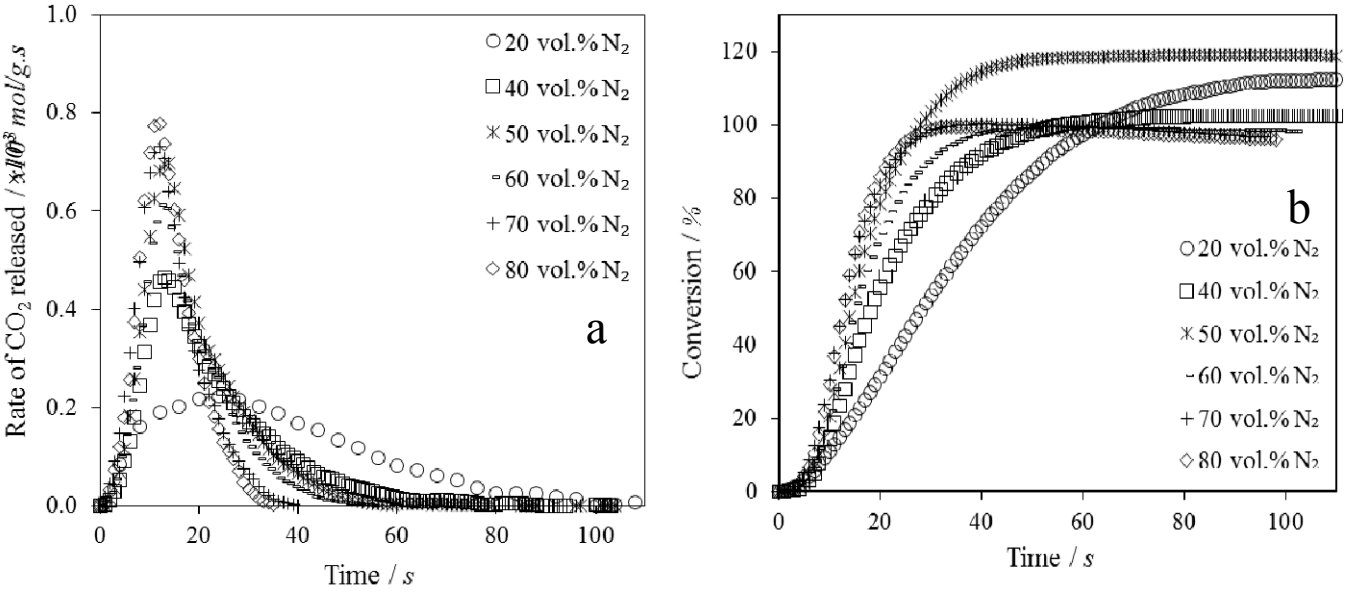

Figure 4.11 – Reaction and conversion profiles for limestone calcination in at 950 °C with varying N_2 and CO_2 concentrations. The percentages specified in the legends are the N_2 vol.% concentrations.

The influence of CO_2 partial pressure on the rate of reaction was determined next. A full description of the work that conducted is presented within appendix II. The final rate equations are shown as Equation 4.48 and Equation 4.49 for the N_2 system and steam system respectively. The N_2 system displayed an approximately first order relationship with respect to the partial pressure of CO_2, whereas the steam system data displayed a good fit to a Langmuir Hinshelwood derived rate equation.

Equation 4.48:

$$r_{calc} = k_T S_A \frac{P_{CO_2}}{R_i T}$$

Equation 4.49:

$$-r_{calc} = \frac{S_A}{R_i T} \cdot \frac{k_{calc} P_{CO_2}}{K_A + K_B P_{H_2O} + K_C P_{CO_2} + K_D P_{H_2O} P_{CO_2} + K_E P_{H_2O}^2 P_{CO_2}}$$

Figure 4.11b and Table 4.4 show the variation of recorded conversions during the N_2 calcination reactions. The amount of measured over calcination was generally greater for the experiments with higher CO_2, lower N_2 concentrations. This was caused by a low signal to noise ratio which itself was limited by the calcining sample only producing a very small change in the bulk gas concentration which was dispersed over a reaction period up to 200 seconds. In addition, the exit gases were subsequently further diluted with N_2 to produce a CO_2 concentration that was measurable by the analyser, this led a greater systematic error in the experiments with a higher CO_2 partial pressure as they required more N_2 dilution. The data for 70 vol.% CO_2 and 90 vol.% CO_2 (balanced with N_2) were excluded from the calculations as the measured conversions were excessively large and outside the expected deviation due to experimental error. Through applying the laws of error propagation (Equation 4.50 and Equation 4.51), an error analysis of the mass balance can be conducted.

Equation 4.50 – Laws of error propagation when calculating the summation or difference:

$$\delta q \approx \delta x + \delta y$$

Equation 4.51 – Laws of error propagation when calculating the product or quotient:

$$\frac{\delta q}{|q|} \approx \frac{\delta x}{|x|} + \frac{\delta y}{|y|}$$

Substituting Equation 4.50 and Equation 4.51 into Equation 4.44 (the general mass balance equation for the N_2 balanced system with dilution) it is possible to calculate the relative uncertainty in the measured values. The ADC (MGA-3000) multi-gas analysers' intrinsic accuracy was stated to be 1 % of the reading, and it was assumed that it was only possible to read a rotameter to within half the smallest division (0.05 L/min, therefore ~6.25% accuracy). Utilising these values within Equation 4.50 and Equation 4.51, it was calculated that for a system of 10 vol.% CO_2 inlet and no dilution, the relative uncertainty in the measurement was up to 18.4 %; whereas for a system of 90 vol.% CO_2 inlet with enough dilution to bring the CO_2 concentration to a measurable 35 vol.%, the relative uncertainty was found to be up to 86.1 %. This difference in error was observed because the relatively small sample mass used, produced only a small difference in the CO_2 concentration (<1 percentage point difference at the 90 vol.% CO_2 inlet condition) and this CO_2 was distributed across a large time scale (~100 s).

Table 4.4 – Recorded conversions for N_2 system calcinations when varying the CO_2 concentration. The theoretical moles of CO_2 released from a 0.25 g sample of limestone ($CaCO_3$ purity = 98.9 mol.%) is ~2.5 $\times 10^{-3}$ moles.

CO_2 / vol.%	**90**	**80**	**70**	**60**	**50**	**40**	**30**	**20**
N_2 / vol.%	10	20	30	40	50	60	70	80
Moles of CO_2 measured / mol	4.2×10^{-3}	2.8×10^{-3}	3.5×10^{-3}	2.5×10^{-3}	2.9×10^{-3}	2.5×10^{-3}	2.4×10^{-3}	2.4×10^{-3}
Conversion / %	171.5	111.2	140.6	102.6	117.5	98.2	95.6	95.1

4.3.3. Effect of varying particle size

The influence of particle size is an important parameter to optimise when conducting kinetic experiments, as generally the larger the particle the more internal mass transfer diffusion there is. This potential internal diffusion can limit the rate of reaction significantly leading to erroneous kinetic data. During the bulk of this work the particle size fraction utilised was 500 - 710 μm and was chosen based on its availability. Subsequently, when analysing the data it was noted that there was difference in rate between the size fraction utilised (500 - 710 μm) and the smallest size fraction (355 - 425 μm). This signifies that intra-particle diffusion did play a role in limiting the rate of calcination. Figure 4.14a shows the difference in rate caused by changing the particle size fraction of limestone for calcination in 20 vol.% steam 80 vol.% CO_2 at 950 °C and Figure 4.15a shows the equivalent data for limestone calcination with varying particle size fraction in 20 vol.% N_2 and 80 vol.% CO_2. The data in Figure 4.14a and Figure 4.15a shows the rate data normalised for the mass of sample. The difference in peak rate between the utilised size fraction and the smallest size fraction was ~38 % greater for the steam system and ~72 % for the N_2 system.

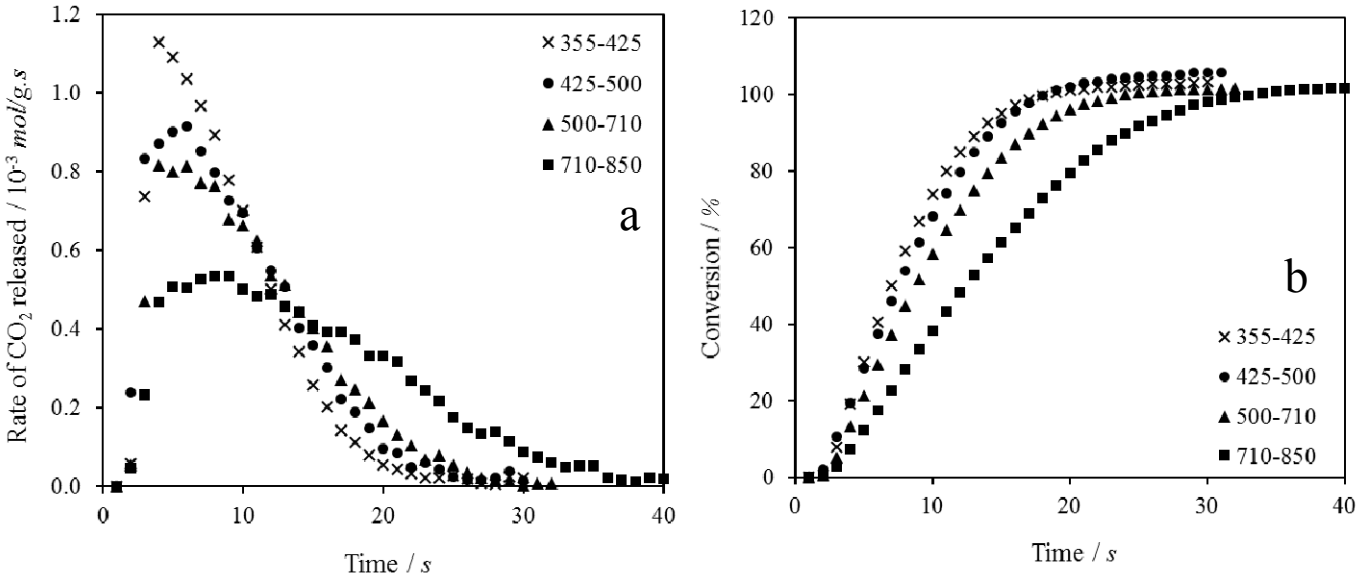

Figure 4.12 – Calcination rate and conversion profile of different limestone particle size fractions at 950 °C in 20 vol.% steam 80 vol.% CO_2.

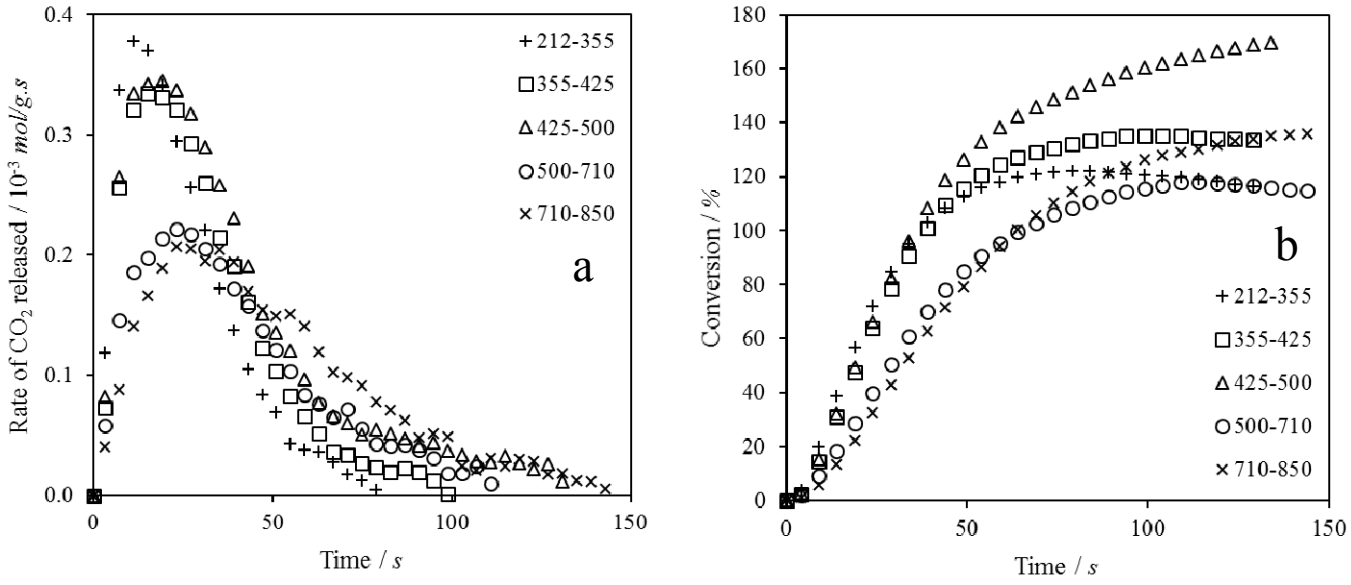

Figure 4.13 – Calcination reaction and conversion profiles of different limestone particle size fractions at 950 °C in 20 vol.% N_2 80 vol.% CO_2.

As can be observed from Figure 4.14 and Figure 4.15 there was a noticeable difference in the rates of calcination between the different particle size fractions. Differences in the structural characteristics of each particle size fraction may have been the cause of the variance in kinetic results obtained. To quantify the limestone particles' characteristics the following analytical techniques were performed.

Mercury intrusion porosimetry (MIP, Micromeritrics – AutoPore IV) was utilised to calculate the pore volume utilising an arbitrary pore diameter cut-off of 30 μm, assuming that all pore volume above this size fraction was inter-particle void space. Helium adsorption measurements (Accupyc, Micromeritics - AccuPyc II 1340 Series Pycnometer) were utilised to calculate the skeletal densities, and powder density measurements (geopyc, Micromeritics, GeoPyc-1365) were utilised to verify the envelope density and porosity obtained. The porosity of the material was initially calculated via the following set of equations utilising the data from the MIP and helium adsorption.

Equation 4.52 - The specific solid volume was defined as the reciprocal of the pore volume:

$$V_S = \frac{1}{\rho_S}$$

Equation 4.53 - Porosity was defined as the volume of the pores relative to the total volume:

$$\varepsilon = \frac{V_P}{V_S + V_P}$$

Equation 4.54 - Envelope density was defined as the reciprocal of the total specific volume:

$$\rho_e = \frac{1}{V_S + V_P} = \rho_s(1 - \varepsilon)$$

These equations were utilised to calculate the values recorded in Table 4.5, this table also presents the data from the powder density measurements.

Table 4.5 – Particle characterisation by helium adsorption density, powder density and mercury porosimetry.

Longcliffe		Helium adsorption (Accupyc)	Powder density (Geopyc)		Hg intrusion porosimetry (< 30 μm)			
Particle size fraction (*μm*)	Geometric mean diameter (*μm*)	Skeletal density (g/cm^3)	Envelope density (g/cm^3)	Geopyc porosity (*%*)	Pore volume (cm^3/g)	Solid volume (cm^3/g)	Calculated porosity (*%*)	Calculated envelope density (g/cm^3)
212 - 355	274.3	2.77 ± 0.002	1.82 ± 0.010	34.2 %	0.024	0.362	6.2 %	2.59
355 - 425	388.4	2.70 ± 0.001	1.94 ± 0.013	28.3 %	0.020	0.370	5.1 %	2.57
425 - 500	461.0	2.71 ± 0.001	2.02 ± 0.011	25.2 %	0.019	0.369	4.9 %	2.58
500 - 710	595.8	2.81 ± 0.001	2.18 ± 0.026	22.5 %	0.016	0.356	4.2 %	2.69
710 - 850	776.9	2.92 ± 0.006	2.34 ± 0.061	20.2 %	0.008	0.343	2.2 %	2.85
Cadomin								
500 - 710	595.8	2.90 ± 0.006	2.19 ± 0.013	24.7 %	0.011	0.345	3.1 %	2.81
Havelok								
500 - 710	595.8	2.92 ± 0.002	2.14 ± 0.011	26.8 %	0.012	0.343	3.4 %	2.82
Imeco								
500 - 710	595.8	2.94 ± 0.007	2.11 ± 0.014	28.3 %	0.008	0.3407	2.4 %	2.86

Comparing the porosities derived from Equation 4.52 to Equation 4.54 and the porosities from the powder density measurements there was a significant difference, which is likely to be because of the selected MIP cut off value and the experimental errors in the powder density measurements. The cut-off value was selected based on a best estimate as there was no precise way to define which pore volume changes were from actual pore space and which were pore volume change due to inter-particle void space. The cut-off point is shown in Figure 4.14 (as a red dashed line on the inserted figure) on the raw MIP data of different limestone particle sizes. The large amount of noise in this data indicates the low permeability and porosity of these limestone particles, furthermore the noise was influenced by the particles having no consistent pore structure. As can be observed there is a continuum between void space and pore space which is the cause for inaccurate porosity measurements.

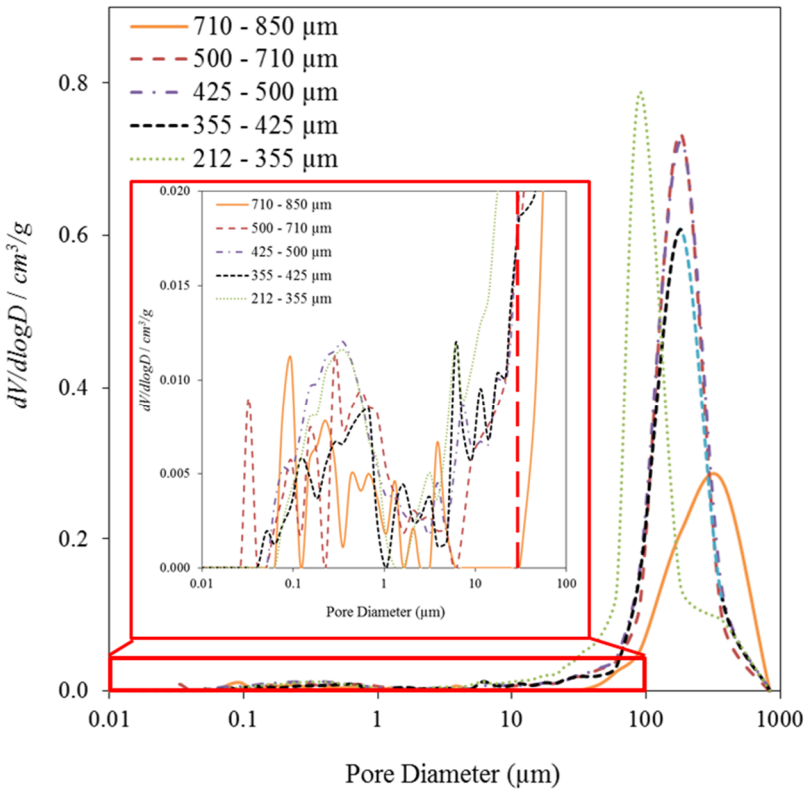

Figure 4.14 – Raw mercury intrusion porosimetry data for different limestone particle sizes, highlighting the difficulty in selecting a suitable pore volume cut off value for non-porous and non-permeable materials.

Based on this evidence a best fit line was plotted for the average of both porosities (calculation from MIP and helium adsorption data and measured Geopyc porosity) and is presented as Figure 4.15. This best fit line provided an equation to describe the porosity with changing particle size of Longcliffe limestone.

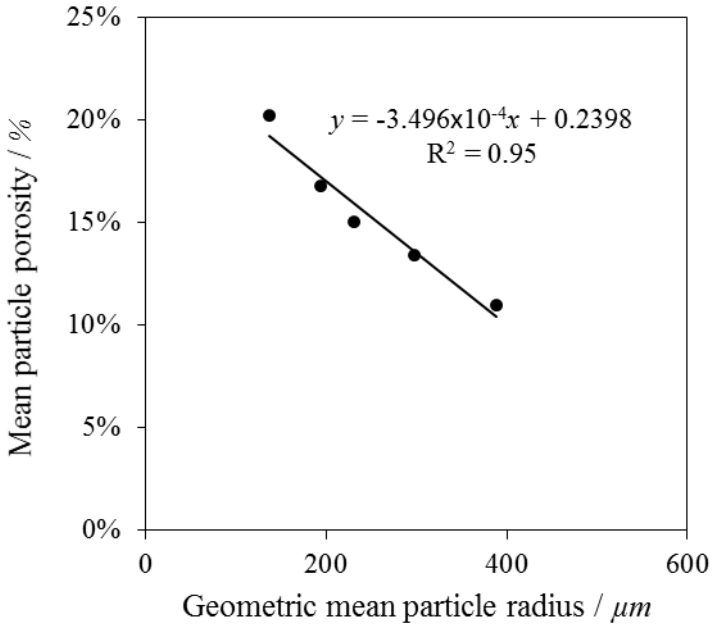

Figure 4.15 – Mean porosity vs geometric mean particle radius.

To investigate the influence of porosity on the observed rate of calcination, the original kinetic data presented in Figure 4.14 and Figure 4.15 was normalised for envelope density (which is a function of porosity) by dividing the mass specific rates by the envelope density (units g/cm^3) therefore generating the rate data in a volume dependant form; this data is presented in Figure 4.16a and b. The envelope density was recalculated using Equation 4.54 and the porosity equation shown in Figure 4.15 to give the values displayed in Table 4.6.

Table 4.6 – Adjusted envelope densities of different Longcliffe limestone particle sizes.

Particle size fraction / *μm*	**Geometric mean particle radius / *μm***	**Calculated porosity / *%***	**Recalculated envelope density / *g/cm^3***
212 - 355	137.2	19.2	2.23
355 - 425	194.2	17.2	2.24
425 - 500	230.5	15.9	2.28
500 - 710	297.9	13.6	2.43
710 - 850	388.4	10.4	2.61

The difference in peak rate between the smallest particle size fraction and 500 – 710 μm was subsequently found to be ~27 % (for the steam system) and ~57 % (for the N_2 system) suggesting that the porosity of the particles did impact on the rate but it wasn't responsible for all the difference. The remaining explanation for the difference in rates must be due to the internal mass transfer diffusion which was itself dependent upon the structural differences and the pore evolution mechanisms. This internal mass transfer diffusion means that the results are comparable but not perfect, it would obviously be better to repeat the experiments with a smaller particle size to generate kinetic data closer to the intrinsic values.

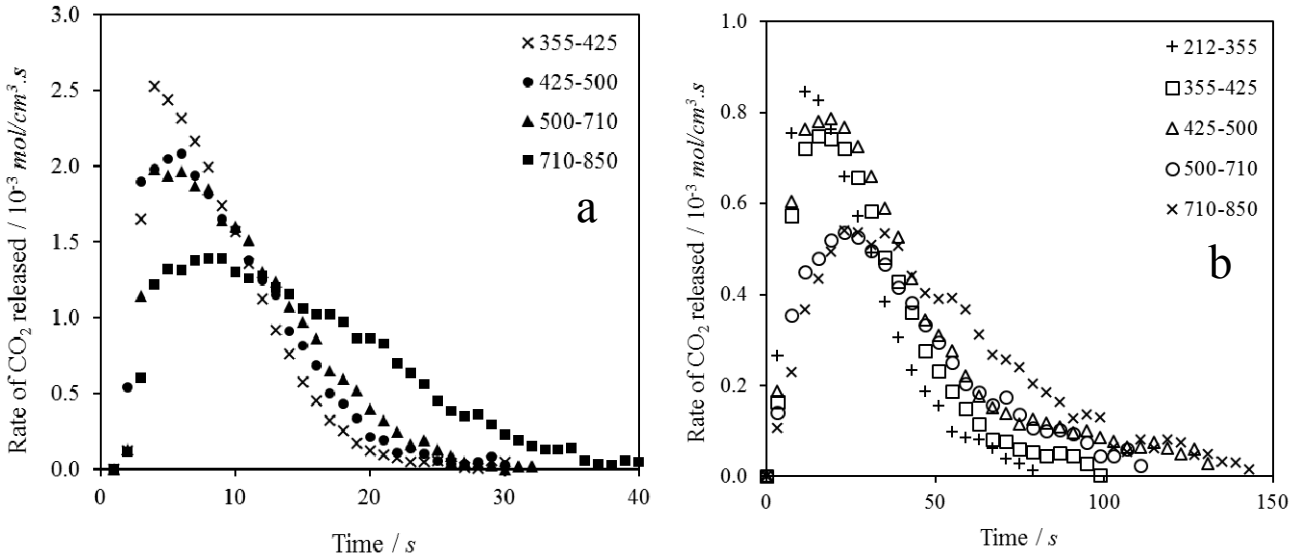

Figure 4.16 – Rate profiles for the calcination of different limestone particle size fractions at 950 °C in (a) 20 vol.% steam and 80 vol.% CO_2, and (b) 20 vol.% N_2 and 80 vol.% CO_2 when normalised for envelope density.

BET (Micromeritics,TriStar II) analysis (data presented in Table 4.7) was also performed on the limestone samples to determine the surface area of the different particle size fractions. There was little observed correlation between the particle size fraction and measured BET surface area, it was not possible to say that smaller particles have an increased surface area and therefore had a faster rate of reaction. The BET data, like the MIP data, was very noisy due to the particles having no consistent pore structure. It was also not possible to correct the observed kinetic data into intrinsic kinetic data via the effectiveness factor model or tortuosity factor, as these particles are inherently non-porous and therefore will have a low Thiele modulus meaning the effectiveness factor model is not appropriate.

Table 4.7 – BET data for different particle size fractions of limestone.

Particle size fraction / *μm*	**BET surface area / m^2/g**
Longcliffe	
212 - 355	0.05 ± 0.01
355 - 425	0.01 ± 0.01
425 - 500	0.05 ± 0.01
500 - 710	0.10 ± 0.01
710 - 850	0.07 ± 0.01
Average	0.06 ± 0.01
Havelok	
500 - 710	0.46 ± 0.01
Cadomin	
500 - 710	1.05 ± 0.01
Imeco	
500 - 710	0.21 ± 0.01

4.3.4. Effect of varying sample mass

The mass of sample added to the reactor was altered to study the impact of external bulk diffusion resistance within the fluidised bed, the results of which can be observed within Figure 4.17 and Figure 4.18 for the steam and N_2 experiments respectively. The data presented was normalised for sample mass so that the influence caused by changing the sample mass can be observed equally. The results of the experiments in the presence of steam indicate that there was minimal external mass transfer resistance within the beds at all sample masses <0.5 g. This was not shown to be analogous to the experiments conducted within the presence of N_2 as the results indicated in Figure 4.18a. This figure shows that there was no sample mass utilised at which external mass transfer resistance became negligible. Despite this a sample mass of 0.25 g was utilised for these kinetic experiments as the difference in observed peak rate between 0.125 g and 0.25 g was ~17 % and when utilising a sample mass of 0.125 g the error from the signal to noise ratio was such that a conversion of ~155 % was recorded indicating significant error in the measurements.

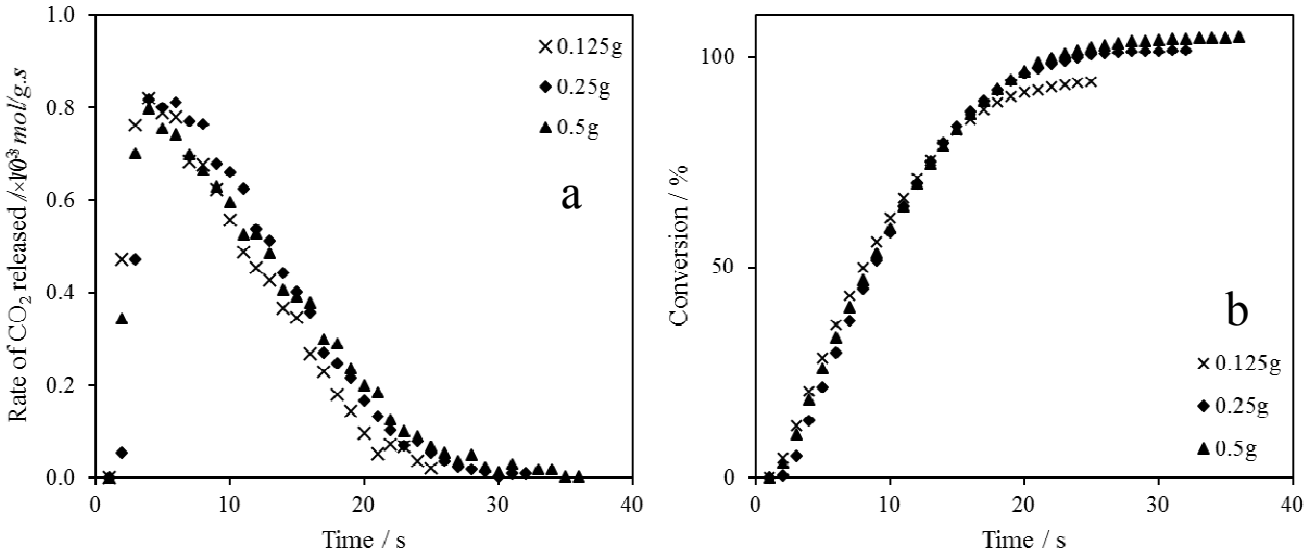

Figure 4.17 – Reaction and conversion profiles for the calcination of different limestone sample masses at 950 °C in 20 vol.% steam and 80 vol.% CO_2.

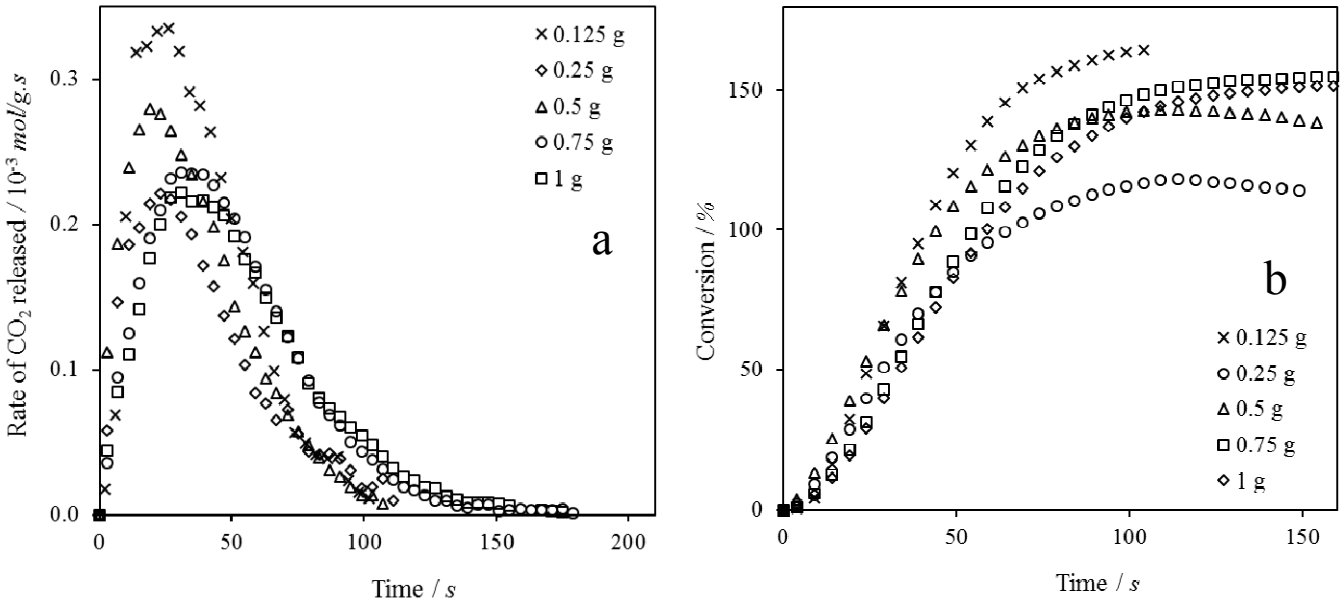

Figure 4.18 – Reaction and conversion profiles for the calcination of different limestone sample masses at 950 °C in 20 vol.% N_2 and 80 vol.% CO_2.

4.3.5. Effect of varying limestone type

The variance in particle characteristics (densities, porosities and surface areas) of the different limestone types was minimal as evidenced in Table 4.5 and Table 4.7. It was therefore expected that the limestones would calcine relatively similarly. The main difference in limestone composition between the four limestones investigated was the silica content (denoted as SiO_2 in Table 4.1) which was ~15 times greater in the other limestones compared to longcliffe. This silica content is known to exist in the form of agglomerated flints rather than an evenly dispersed mixture (Wu et al., 2010). Longcliffe limestone had the highest $CaCO_3$ purity of all the limestones tested in this work, which although may be useful for the CO_2 sorption potential per g of material, there have been many studies indicating that minor chemical impurities were beneficial on the overall extent of carbonation (Manovic and Anthony, 2008a) (Hughes et al., 2004) (Manovic et al., 2008) (H. Borgwardt, 1989).

From the results of the calcination experiments with steam present, displayed in Figure 4.19, it can be reasonably concluded that the change in limestone type (and their inherent impurities) made little difference to the rate of calcination and the results were within expected experimental error, as can be observed from the extent of conversion in Figure 4.19b. However, when considering the experiments with N_2 present the results, displayed in Figure 4.20, show a significant difference due to limestone type; this could plausibly be explained by steam aiding the calcination reaction but it is not enhanced with N_2 present meaning the difference in limestone types becomes apparent.

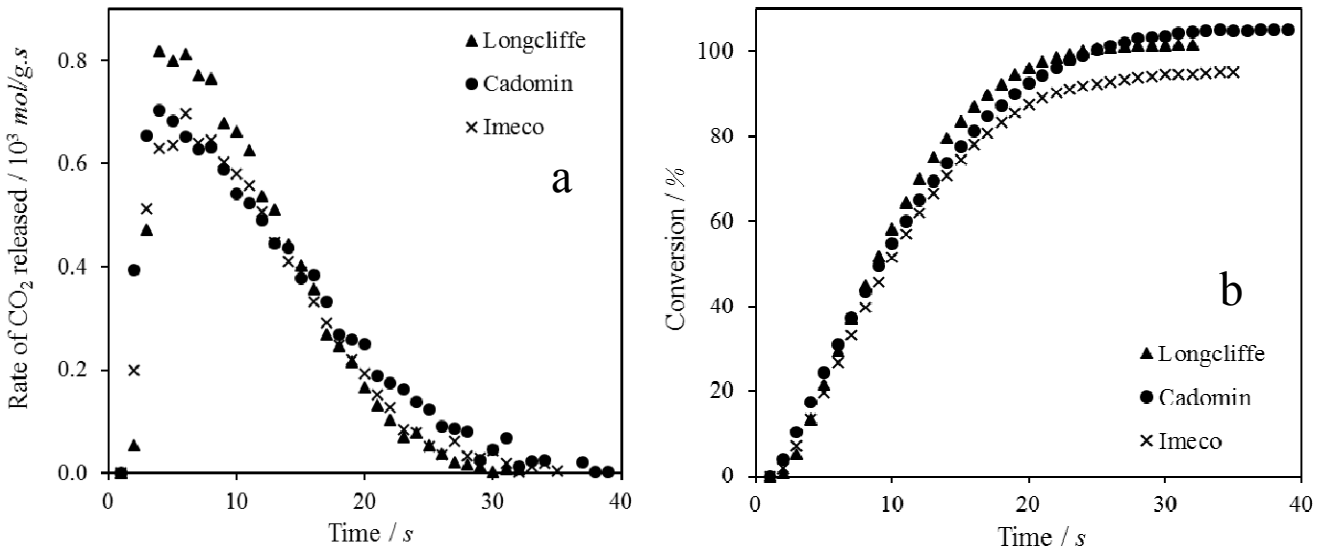

Figure 4.19 – Reaction and conversion profiles for the calcination of different limestones at 950 °C in 20 vol.% steam and 80 vol.% CO_2.

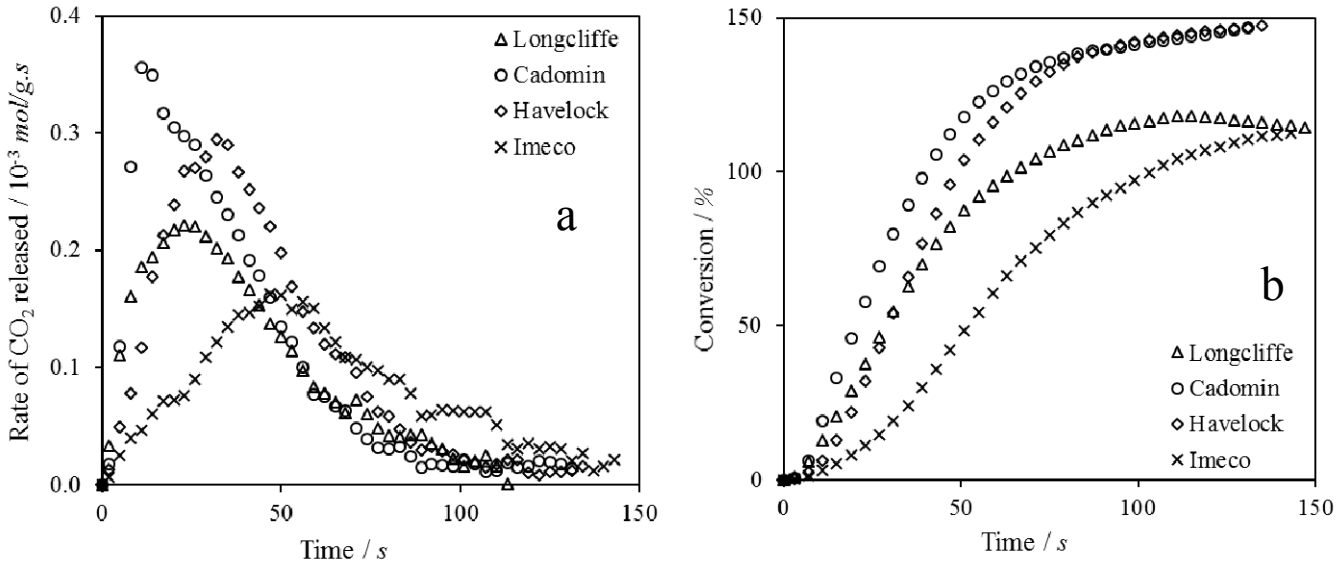

Figure 4.20 – Reaction and conversion profiles for the calcination of different limestones at 950 °C in 20 vol.% N_2 and 80 vol.% CO_2.

4.4. Single Particle Modelling of Limestone Calcination

Calcium carbonate decomposition has been modelled within several studies, each of these based there models on different parameters, methodologies and research aims. The aim of the calcination modelling within this set of work was to break down the calcination reaction into the fundamental governing equations with the aim of solving the following questions produced from the experimental investigation.

1. Could the gas composition be influencing the heating rate of the particle?
2. Is steam influencing the calcination rate in purely a physical way or is there evidence of catalytic activity?
3. How do the other secondary gases (steam and N_2) affect the rate of calcination?

This model was set up as a one dimensional spherical particle model under unsteady state conditions subject to the assumptions listed below.

- The $CaCO_3$ began at standard temperature and pressure in air
- The size and shape of the $CaCO_3$ particle was unchanged during the reaction
- The particle was assumed to be spherical with no lateral variation in temperature, gas concentrations or particle properties
- Radiation to or from the particle was negligible and thus not included in this model
- The bulk composition of the gas was uniform and not subject to local concentration differences
- The bulk gas temperature was constant and the system as a whole was adiabatic
- The ideal gas law was assumed where non-ideal relationships were not available
- The sorbent did not sinter during the reaction
- The particle was composed of $CaCO_3$ and CaO only

The model was numerically solved in Matlab using *ODE15s* using central and forward differences methods, the particle to be solved was divided into 100 ‘shells’ along the length of a particles’ radius.

4.4.1. Nomenclature

Although it is not specified for readability, most parameters were spatially, temperature and time dependant within the particle.

Dimensionless groups

Nu Nusselt number

Sh Sherwood number

Sc Schmidt number

Pr Prandtl number

Re Reynolds number

Z Expansion factor

Greek letters

α_{CO_2} Polarisability of the non-polar molecule CO_2, Ä^3

α_{CO2}* Reduced polarisability of the non-polar molecule, Ä^3

ΔH Enthalpy of reaction for calcination/carbonation, (178) kJ/mol

ε_{eff} Effective porosity, %

ε Lennard-Jones parameter, representing the ('well depth') strength of bonding potential

λ_{α}^{T} Thermal conductivity of primary gas (CO_2) at temperature = T, W/m.K

λ_{β}^{T} Thermal conductivity of secondary gas (H_2O or N_2) at temperature = T, W/m.K

λ_{CaO} Thermal conductivity of CaO, W/m.K

λ_{CaCO_3} Thermal conductivity of $CaCO_3$, W/m.K

λ_{eff} Effective thermal conductivity, W/m.K

λ_{gas} Thermal conductivity of gas, W/m.K

λ_{solid} Thermal conductivity of solid, W/m.K

μ_{α} Viscosity of primary gas (CO_2), Pa.s

μ_{β} Viscosity of secondary gas (H_2O or N_2), Pa.s

μ_{gas} Dynamic viscosity of the gas, Pa.s

μ_{H_2O} Polar dipole moment of H_2O

$\mu^*_{H_2O}$ Reduced polar moment of the H_2O

ρ_α Density of the primary gas (CO_2), kg/m^3

ρ_β Density of the secondary gas (H_2O or N_2), kg/m^3

ρ_{CaO} Skeletal density of CaO, kg/m^3

ρ_{CaCO_3} Skeletal density of $CaCO_3$, kg/m^3

$\rho^m_{CaCO_3}$ Molar skeletal density of $CaCO_3$, mol/m^3

ρ_{gas} Density of the gas, kg/m^3

$\rho_{particle}$ Skeletal density of particle at time = t, kg/m^3

$\sigma_{\alpha\beta}$ Lennard-Jones parameter representing a finite distance where the inter-molecule potential is zero

τ_r Shrinking core model, time to complete till complete reaction, s

υ^T Flow rate at temperature, m^3/s

ξ Correction factor for polarisation of H_2O molecule

$\Phi_{\alpha\alpha}$, $\Phi_{\alpha\beta}$, $\Phi_{\beta\alpha}$, $\Phi_{\beta\beta}$ Multicomponent extension to the Chapman-Enskog theory

Ω_{11} Collision integrals (Klein and Smith, 1968)

Further parameters

A Pre-exponential factor, s^{-1}

A_{bed} Area of bed, m^2

C_{CO_2} Concentration of CO_2, mol/m^3

C_{p_α} Specific heat capacity of the primary gas (CO_2), kg/m^3

C_{p_β} Specific heat capacity of the secondary gas (H_2O or N_2), kg/m^3

$C_{p_{CaO}}$ Specific heat capacity of CaO, J/mol.K

$C_{p_{CaCO_3}}$ Specific heat capacity of $CaCO_3$, J/mol.K

$C_{p\ particle}$ Specific heat capacity of the particle, J/mol.K

D_b Bulk Diffusivity, m^2/s

D_{eff} Effective diffusivity, m^2/s

D_k Knudsen diffusivity, m^2/s

E_a Activation energy of the reaction, kJ/mol

k_g Mass transfer coefficient, m/s

k_T Rate constant at temperature, s^{-1}

h Heat transfer coefficient, $W/m^2.K$

l Characteristic length, diameter of particle, m

M_α Relative molecular mass of primary gas (CO_2), g/mol

M_β Relative molecular mass of secondary gas (H_2O or N_2), g/mol

M_{CaO} Relative molecular mass of CaO, g/mol

M_{CaCO_3} Relative molecular mass of $CaCO_3$, g/mol

n Exponent of P_{CO_2} dependency, a value of 1-2 is typical (Yin et al., 2014) (García-Labiano et al., 2002) (Rao, 1996) (Silcox et al., 1989) (Fuertes et al., 1993) (Hu and Scaroni, 1996). A value of 1 is applied within this work

P Pressure, atm

P_{CO_2} Partial pressure of CO_2, Pa

$P_{CO_2\,0}$ Initial partial pressure within the particle, Pa

$P_{CO_2\,b}$ Partial pressure of CO_2 of the bulk gas, Pa

$P_{CO_2\,eq}$ Equilibrium partial pressure of CO_2, Pa

$P_{CO_2\,surface}$ Partial pressure of CO_2 at the surface of the particle, Pa

r radii to point in shell of particle, m

r_{calc} Rate of calcination reaction, $mol/m^3.s$

R radius of particle, m

R_i Ideal gas constant, J/mol.K

S_A Specific surface area of reactant shell, m^2/m^3

S_{CaO} Specific surface area of CaO, m^2/m^3

S_{CaCO_3} Specific surface area of $CaCO_3$, m^2/m^3

S_i Initial specific surface area of reactant shell, m^2/m^3

t Time at which $X_{(r,t)}$ occurs, s

t_r Shrinking core model, a time point throughout the reaction, s

T Temperature, K

T_0 Initial temperature of the particle, K

T_b Temperature of the bulk gas, K

u_{gas} Superficial gas velocity, m/s

U_{gas} Superficial gas velocity, m/s

x_α Mole fraction of primary gas (CO_2)

x_β Mole fraction of secondary gas (H_2O or N_2)

x_{CO_2} Mole fraction of CO_2 in the gas stream

x_{H_2O} Mole fraction of H_2O in the gas stream

x_{N_2} Mole fraction of N_2 in the gas stream

X_0 Initial conversion

X Conversion, %

$X_{r,\ CaCO_3}$ Conversion at position r in the particle of $CaCO_3$, %

4.4.2. Governing Equations: Heat transfer

The general partial differential equation (PDE) that describes the movement of heat through a spherical object was defined as Equation 4.55 and the required initial and boundary conditions are specified beneath.

Equation 4.55:

$$\frac{\partial T}{\partial t} = \underbrace{\frac{1}{r^2}\frac{\partial}{\partial r}\left(\alpha_{eff} r^2 \frac{\partial T}{\partial r}\right)}_{\substack{Heat\ transfer\ through \\ the\ particle\ body}} + \underbrace{\frac{r_{calc}(-\Delta H)}{(\rho C_P)_{particle}}(1-X)}_{\substack{Rate\ of\ heat\ consumption\ by \\ the\ calcination\ reaction}}$$

Initial Condition 1

$$T = T_b \qquad t = 0$$

Initial Condition 2

$$T = T_0 \qquad \begin{matrix} t = 0 \\ r = 0 \rightarrow R \end{matrix}$$

Boundary Condition 1

$$\frac{\partial T}{\partial r} = 0 \qquad \begin{matrix} t \geq 0 \\ r = 0 \end{matrix}$$

Boundary Condition 2

$$T = T_b \qquad \begin{matrix} t > 0 \\ r > R \end{matrix}$$

Boundary Condition 3

$$\lambda_{eff}\frac{\partial T}{\partial r} = h(T_{bulk} - T_{particle}) \qquad \begin{matrix} t \geq 0 \\ r = R \end{matrix}$$

Equation 4.56 - Where α_{eff} is the thermal diffusivity, m^2/s:

$$\alpha_{eff} = \frac{\lambda_{eff}}{(\rho C_P)_{particle}}$$

The PDE was discretised into an ODE by use of the finite differences method as shown below. Firstly, the product rule was utilised to simplify the first term on the right hand side of Equation 4.55.

Equation 4.57:

$$\frac{\partial}{\partial r}\left(\alpha_{eff} r^2 \frac{\partial T}{\partial r}\right) = \frac{\partial (uv)}{\partial r}$$

Equation 4.58 and Equation 4.59:

$$u = \alpha_{eff} r^2 \qquad\qquad v = \frac{dT}{dr}$$

Equation 4.60 and Equation 4.61:

$$\frac{du}{dr} = 2\alpha_{eff} r \qquad\qquad \frac{dv}{dr} = \frac{d^2T}{dr^2}$$

Equation 4.62:

$$\frac{\partial (uv)}{\partial r} = \alpha_{eff} r^2 \frac{d^2T}{dr^2} + 2\alpha_{eff} r \frac{dT}{dr} = \alpha_{eff} \frac{d^2T}{dr^2} + \frac{2\alpha_{eff}}{r} \frac{dT}{dr}$$

The particle was then divided into 100 points, *i*, along the length of a radius, which is simplistically displayed in Equation 4.38.

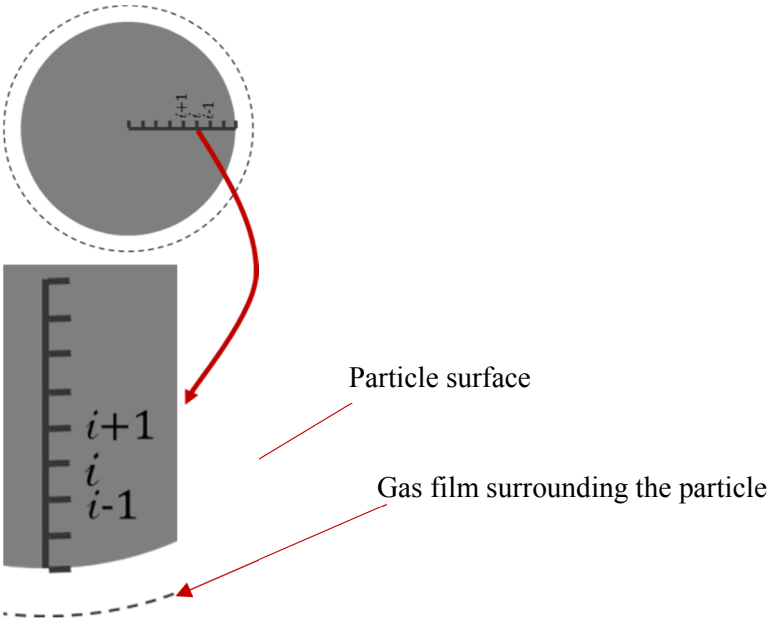

Figure 4.21 – Division of the spherical particle for the models' discretisation.

Equation 4.63 - Discretisation by the central finite differences approach was then conducted on the second order term in Equation 4.55 across $i = 0$ to $i = n$:

$$\frac{d^2T}{dr^2} = \frac{\frac{dT}{dr}\Big|_{i+1} - \frac{dT}{dr}\Big|_{i-1}}{dr} = \frac{T_{i+1} - 2T_i + T_{i-1}}{dr^2}$$

Equation 4.64 - Discretisation by the upwind finite differences approach was then conducted on the first order term in Equation 4.55 across $i = 0$ to $i = n$:

$$\frac{dT}{dr} = \frac{T_{i+1} - T_i}{dr}$$

Equation 4.65 - From this derivation the final discretised heat transfer balance within the particle becomes, where $i = 0$ to $n\text{-}1$:

$$\frac{dT}{dt} = \alpha_{eff}\frac{T_{i+1} - 2T_i + T_{i-1}}{dr^2} + \frac{2\alpha_{eff}}{r}\frac{T_{i+1} - T_i}{dr} + \frac{r_{calc}(-\Delta H)}{(\rho C_P)_{particle}}(1 - X)T_i$$

Equation 4.66 - And the final discretised heat transfer balance at the surface of the particle becomes, where $i = n$:

$$\frac{dT}{dt} = \alpha_{eff}\frac{-2T_n + T_{n-1}}{dr^2} + \frac{2\alpha_{eff}}{r}\frac{-T_n}{dr} + \alpha_{eff}T_b\left[\frac{1}{dr^2} + \frac{2}{rdr}\right]T_n + \frac{h\left(T_b - T_{surface}\right)}{(\rho C_P)_{particle}}\left[\frac{1}{dr^2} + \frac{2}{rdr}\right]T_n + \frac{r_{calc}(-\Delta H)}{(\rho C_P)_{particle}}(1 - X)T_n$$

Equation 4.67 - These ODEs were then implemented in Matlab via the use of sparse matrices to save computational power:

$$\frac{dT}{dt} = \frac{\alpha_{eff}}{dr^2}\begin{bmatrix} -1 & 1 & 0 & \cdots & 0 \\ 1 & -2 & 1 & \ddots & \vdots \\ 0 & \ddots & \ddots & \ddots & \vdots \\ \vdots & \ddots & 1 & -2 & 1 \\ 0 & \cdots & 0 & 1 & -2 \end{bmatrix} + \frac{2\alpha_{eff}}{rdr}\begin{bmatrix} -1 & 1 & 0 & \cdots & 0 \\ 0 & -1 & 1 & \ddots & \vdots \\ \vdots & \ddots & \ddots & \ddots & \vdots \\ \vdots & \ddots & \ddots & -1 & 1 \\ 0 & \cdots & \cdots & 0 & -1 \end{bmatrix} + \alpha_{eff}T_b\left[\frac{1}{dr^2} + \frac{2}{rdr}\right]\begin{bmatrix} 0 \\ \vdots \\ 0 \\ 1 \end{bmatrix} + \frac{h\left(T_b - T_{surface}\right)}{(\rho C_P)_{particle}}\left[\frac{1}{dr} + \frac{2}{r}\right]\begin{bmatrix} 0 \\ \vdots \\ 0 \\ 1 \end{bmatrix} + r_{calc}\frac{-\Delta H}{(\rho C_P)_{particle}}(1 - X)\begin{bmatrix} 1 \\ \vdots \\ n-1 \\ n \end{bmatrix}$$

4.4.3. Governing Equations: Mass transfer

The general PDE that describes the movement of the gas (the example shown here is for CO_2 however the same equations and derivation was utilised for H_2O and N_2 bar the reaction term) through a spherical object was defined as Equation 4.68 and its respective initial and boundary conditions are specified beneath.

Equation 4.68:

$$\frac{\partial P_{CO_2}}{\partial t} = \underbrace{\frac{1}{r^2}\frac{\partial}{\partial r}\left(\mathcal{D}_{eff} r^2 \frac{\partial P_{CO_2}}{\partial r}\right)}_{\substack{Mass\ transfer\ through \\ the\ particle\ body}} + \underbrace{r_{calc} R_i T_{(r,t)}(1-X)}_{\substack{Rate\ of\ CO_2\ generation\ by \\ the\ calcination\ reaction}}$$

Initial Condition 1

$$P_{CO_2} = P_{CO_{2_b}} \qquad t = 0$$

Initial Condition 2

$$P_{CO_2} = P_{CO_{2_0}} \qquad \begin{matrix} t = 0 \\ r = 0 \rightarrow R \end{matrix}$$

Boundary Condition 1

$$\frac{\partial P_{CO_2}}{\partial r} = 0 \qquad \begin{matrix} t \geq 0 \\ r = 0 \end{matrix}$$

Boundary Condition 2

$$P_{CO_2} = P_{CO_{2_b}} \qquad \begin{matrix} t > 0 \\ r > R \end{matrix}$$

Boundary Condition 3

$$\mathcal{D}_{eff}\frac{\partial P_{CO_2}}{\partial r} = k_g(P_{CO_{2\,bulk}} - P_{CO_{2\,particle}}) \qquad \begin{matrix} t \geq 0 \\ r = R \end{matrix}$$

The PDE describing the mass transfer of the gases was solved for the specified boundary conditions and discretised using the same method described for heat transfer.

Equation 4.69 - From which the mass balance within the particle becomes, where $i = 0$ to n-1:

$$\frac{dP_{CO_2}}{dt} = \mathcal{D}_{eff}\frac{P_{CO_{2_{i+1}}} - 2P_{CO_{2_i}} + P_{CO_{2_{i-1}}}}{dr^2} + \frac{2D_{eff}}{r}\frac{P_{CO_{2_{i+1}}} - P_{CO_{2_i}}}{dr} + r_{calc}R_iT_{(i,t)}(1-X)P_{CO_{2_i}}$$

Equation 4.70 - And the final discretised heat transfer balance at the surface of the particle becomes, where $i = n$:

$$\begin{aligned}\frac{dP_{CO_2}}{dt} = \mathcal{D}_{eff}&\frac{-2P_{CO_{2_n}} + P_{CO_{2_{n-1}}}}{dr^2} + \frac{2D_{eff}}{r}\frac{-P_{CO_{2_n}}}{dr} \\ &+ \mathcal{D}_{eff}P_{CO_2 b}\left[\frac{1}{dr^2} + \frac{2}{rdr}\right]P_{CO_{2_n}} + k_g\left(P_{CO_2 b} - P_{CO_2\,surface}\right)\left[\frac{1}{dr} + \frac{2}{r}\right]P_{CO_{2_n}} \\ &+ r_{calc}R_iT_{(n,t)}(1-X)P_{CO_{2_n}}\end{aligned}$$

Equation 4.71 - These ODEs were then implemented in Matlab via the use of sparse matrices to save computational power:

$$\begin{aligned}\frac{dPCO_2}{dt} = &\frac{\mathcal{D}_{eff}}{dr^2}\begin{bmatrix}-1 & 1 & 0 & \cdots & 0\\ 1 & -2 & 1 & \ddots & \vdots\\ 0 & \ddots & \ddots & \ddots & \vdots\\ \vdots & \ddots & 1 & -2 & 1\\ 0 & \cdots & 0 & 1 & -2\end{bmatrix} + \frac{2\mathcal{D}_{eff}}{rdr}\begin{bmatrix}-1 & 1 & 0 & \cdots & 0\\ 0 & -1 & 1 & \ddots & \vdots\\ \vdots & \ddots & \ddots & \ddots & \vdots\\ \vdots & \ddots & \ddots & -1 & 1\\ 0 & \cdots & \cdots & 0 & -1\end{bmatrix} \\ &+ \mathcal{D}_{eff}P_{CO_2 b}\left[\frac{1}{dr^2} + \frac{2}{rdr}\right]\begin{bmatrix}0\\ \vdots\\ 0\\ 1\end{bmatrix} + k_g\left(P_{CO_2 b} - P_{surface}\right)\left[\frac{1}{dr} + \frac{2}{r}\right]\begin{bmatrix}0\\ \vdots\\ 0\\ 1\end{bmatrix} \\ &+ r_{calc}R_iT(1-X)\begin{bmatrix}1\\ \vdots\\ n-1\\ n\end{bmatrix}\end{aligned}$$

4.4.4. Kinetics

The rate of calcination, r_{calc}, in the presence of steam and N_2 by Equation 4.72 and Equation 4.73 respectively, based on the work conducted within section 4.3.2.

Equation 4.72:

$$r_{calc} = \frac{S_A}{R_i T} \cdot \frac{k_T P_{CO_2}}{K_A + K_B P_{H_2O} + K_C P_{CO_2} + K_D P_{H_2O} P_{CO_2} + K_E P_{H_2O}^2 P_{CO_2}} \left(1 - \frac{P_{CO_2}}{P_{CO_2 eq}}\right)^n$$

Equation 4.73:

$$r_{calc} = k_T S_A \frac{P_{CO_2}}{R_i T} \left(1 - \frac{P_{CO_2}}{P_{CO_2 eq}}\right)^n$$

Figure 4.22 shows a vastly extended range of the utilisation of Equation 4.72. It can be seen that below a P_{CO_2} of ~5.5 $\times 10^4$ Pa the predicted rate value tends to infinity, therefore within the implementation of this equation in the model the rate of calcination was set to zero when the partial pressure of CO_2 was below 5.5 $\times 10^4$ Pa. This did not affect the results of the model, as it will be demonstrated later on that the diffusion CO_2 into the particle from the bulk gas was very fast and thus the required conditions of calcination did not occur below this value anyway. An upper limit of applicability for Equation 4.72 was not set as the rate only tended towards zero which was considered quite realistic. A limiting term of $(1-P_{CO_2}/P_{CO_2 eq})$ was also added to the rate equations which effectively reduced the rate of calcination the closer the partial pressure of CO_2 got to the equilibrium partial pressure of CO_2. This limiting term has been applied many times elsewhere in the literature, an exponent of *n* on this term varying between 1 and 2 has previously been suggested and through some initial tests a value of 1 was selected based on the fit to experimental data (García-Labiano et al., 2002) (Silcox et al., 1989) (Yin et al., 2014) (Rao, 1996).

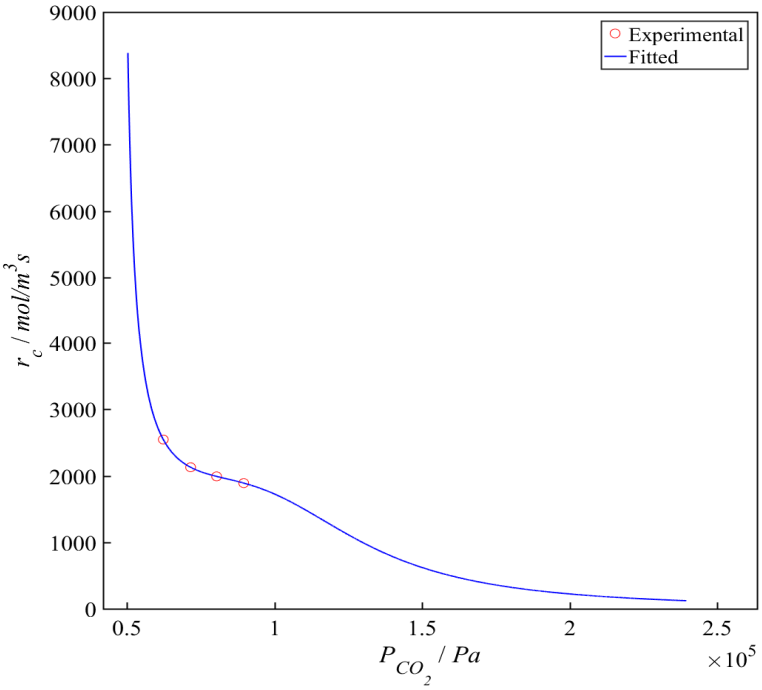

Figure 4.22 – Extended range of the rate value predicted by the use of Equation 4.72 thereby showing the range of applicability.

The rate constant with respect to temperature, k_T, was calculated from the Arrhenius equation parameters presented in Table II.2 (within Appendix II) and was converted into units of *m/s* by dividing by the initial specific surface area.

Equation 4.74:

$$k_T = Ae^{-\frac{E_a}{R_i T}}$$

The conversion, X, at a particular distance from the centre of the particle and time from the start of the model running was calculated by the ODE solver by providing the solver with a vector of the differential conversion with respect to time at each radii, and was calculated using Equation 4.75.

Equation 4.75:

$$\frac{dX(shell, 0 \rightarrow t)}{dt} = \frac{converted\ shell\ moles}{initial\ shell\ moles} = \frac{r_{calc}(1-X)}{\frac{\rho_{CaCO_3}}{M_{CaCO_3}}}$$

4.4.5. Other parameters

The parameters and their respect equations listed within this section were utilised to calculate the required variables for the discretised PDE's and the kinetic expressions listed above.

Equation 4.76 - Equilibrium partial pressure of CO_2, P_{CO_2eq}:

Derived from a 5th order polynomial from ThermoVader modelling for the reaction between CaO and CO_2 forming $CaCO_3$ (McBride et al., 2004). For this equation only: P_{CO_2eq} is in bar and T is in °C.

$$P_{CO_2eq} = 7.35x10^{-13}T^5 - 2.51x10^{-9}T^4 + 3.46x10^{-6}T^3 - 2.42x10^{-3}T^2 + 0.85T - 21.16$$

P_{CO_2eq} was limited to zero at temperatures below 600 °C as this was outside of the fitting range.

Equation 4.77 - Surface area, S_A:

$$S_A = \left[S_{CaO} \cdot X + S_{CaCO_3}(1 - X)\right]\left[\frac{X}{\rho_{CaO}} + \frac{1 - X}{\rho_{CaCO_3}}\right]^{-1}\left(1 - \varepsilon_{eff}\right)$$

Equation 4.78 - Effective porosity, ε_{eff}:

$$\varepsilon_{eff} = \varepsilon_{CaCO_3} - (Z - 1)\left(1 - \varepsilon_{CaCO_3}\right)X$$

Equation 4.79 - Expansion factor, Z:

$$Z = \frac{M_{CaO}}{M_{CaCO_3}} \cdot \frac{\rho_{CaCO_3}}{\rho_{CaO}}$$

Equation 4.80 - Effective thermal conductivity by extended Maxwell model, λ_{eff}:

$$\lambda_{eff} = \lambda_{solid}\left(\frac{\left(\frac{2\lambda_{solid}}{\lambda_{gas}} + 1\right) - 2\varepsilon_{eff}\left(\frac{\lambda_{solid}}{\lambda_{gas}} - 1\right)}{\left(\frac{2\lambda_{solid}}{\lambda_{gas}} + 1\right) + \varepsilon_{eff}\left(\frac{\lambda_{solid}}{\lambda_{gas}} - 1\right)}\right)$$

Equation 4.81 - Thermal conductivity of solid, λ_{solid}:

$$\lambda_{solid} = \frac{1}{\frac{X}{\lambda_{CaO}} + \frac{1 - X}{\lambda_{CaCO_3}}}$$

Equation 4.82 - Thermal conductivity of gas, λ_{gas}:

$$\lambda_{gas} = \left(\frac{x_\alpha \lambda_\alpha^T}{x_\alpha \phi_{\alpha\alpha} + x_\alpha \phi_{\alpha\beta}} + \frac{x_\beta \lambda_\beta^T}{x_\beta \phi_{\beta\beta} + x_\beta \phi_{\beta\alpha}} \right)$$

Equation 4.83 - Multicomponent extension to the Chapman-Enskog theory, $\Phi_{\alpha\beta}$:

$$\phi_{\alpha\beta} = \frac{1}{\sqrt{8}} \left(1 + \frac{M_\alpha}{M_\beta} \right)^{-1/2} \left[1 + \left(\frac{\mu_\alpha}{\mu_\beta} \right)^{1/2} \left(\frac{M_\beta}{M_\alpha} \right)^{1/4} \right]^2$$

Equation 4.84 - Skeletal density of particle, $\rho_{particle}$:

$$\rho_{particle} = \varepsilon_{eff} \rho_{CaO} + (1 - \varepsilon_{eff}) \rho_{CaCO_3}$$

Equation 4.85 - Specific heat capacity of the particle, $Cp_{particle}$:

$$C_{p_{particle}} = \varepsilon_{eff} \, C_{p_{CaO}} + (1 - \varepsilon_{eff}) C_{p_{CaCO_3}}$$

Equation 4.86 - Heat transfer coefficient, h:

$$h = \frac{Nu \, \lambda_{eff}}{2R}$$

Equation 4.87 - Nusselt number, Nu:

$$Nu = \frac{h \, l}{\lambda_{eff}} = 2 + 0.6 \, Re^{\frac{1}{2}} \, Pr^{\frac{1}{3}}$$

Equation 4.88 - Reynolds number, Re:

$$Re = \frac{\rho_{gas} U_{gas} l}{\mu_{gas}}$$

Equation 4.89 - Prandtl number, Pr:

$$Pr = \frac{C_{p\,gas} \, \mu_{gas}}{\lambda_{gas}}$$

Equation 4.90 - Density of gas, ρ_{gas}:

$$\rho_{gas} = \left(\frac{x_\alpha \rho_\alpha^T}{x_\alpha \phi_{\alpha\alpha} + x_\alpha \phi_{\alpha\beta}} + \frac{x_\beta \rho_\beta^T}{x_\beta \phi_{\beta\beta} + x_\beta \phi_{\beta\alpha}} \right)$$

Equation 4.91 - Viscosity of gas, μ_{gas}:

$$\mu_{gas} = \left(\frac{x_\alpha \mu_\alpha^T}{x_\alpha \phi_{\alpha\alpha} + x_\alpha \phi_{\alpha\beta}} + \frac{x_\beta \mu_\beta^T}{x_\beta \phi_{\beta\beta} + x_\beta \phi_{\beta\alpha}} \right)$$

Equation 4.92 - Specific heat capacity of gas, Cp_{gas}:

$$C_{p\,gas} = \left(\frac{x_\alpha C_{p\,\alpha}^{\;T}}{x_\alpha \phi_{\alpha\alpha} + x_\alpha \phi_{\alpha\beta}} + \frac{x_\beta C_{p\,\beta}^{\;T}}{x_\beta \phi_{\beta\beta} + x_\beta \phi_{\beta\alpha}} \right)$$

Equation 4.93 - Superficial gas velocity, u_{gas}:

$$u_{gas} = \frac{v^T}{A_{bed}}$$

Equation 4.94 - Mass transfer coefficient, k_g:

$$k_g = \frac{Sh\, D_b}{2R}$$

Equation 4.95 - Effective diffusivity, $\mathcal{D}_{eff}$ (Satterfield, 1970):

$$\mathcal{D}_{eff} = \frac{\varepsilon}{\tau} \cdot \frac{1}{\frac{1}{\mathcal{D}_b} + \frac{1}{\mathcal{D}_k}} = \varepsilon^2 \cdot \frac{1}{\frac{1}{\mathcal{D}_b} + \frac{1}{\mathcal{D}_k}}$$

Where the tortuosity, τ, is assumed to be $1/\varepsilon$.

Equation 4.96 - Bulk diffusivity, $\mathcal{D}_b$:

$$\mathcal{D}_b = 1.858 \times 10^{-7} T^{\frac{3}{2}} \frac{\sqrt{\left(\frac{1}{M_\alpha} + \frac{1}{M_\beta}\right)}}{P\, \sigma^2\, \Omega_{11}}$$

Combination laws for Lennard-Jones parameters, ε and σ.

Equation 4.97 and Equation 4.98 - Non-polar pair A and B:

$$\varepsilon_{AB} = \sqrt{\varepsilon_A + \varepsilon_B}$$

$$\sigma_{AB} = \frac{1}{2}(\sigma_A + \sigma_B)$$

Equation 4.99 - Polar H_2O and non-polar CO_2 applying the stockmayer potential:

$$\mu^*_{H_2O} = \frac{\mu_{H_2O}}{\sqrt{(\varepsilon_{H_2O}\ \sigma_{H_2O})^3}}$$

Equation 4.100 - Reduced polarisability of the non-polar molecule, $\alpha^*_{CO_2}$:

$$\alpha^*_{CO_2} = \frac{\alpha_{CO_2}}{\sigma^3_{CO_2}}$$

Equation 4.101 - Correction factor for the polarisation of the H_2O molecules:

$$\xi = 1 + \alpha^*_{CO_2} \frac{{\mu^*_{H_2O}}^2}{\sqrt{8}} \sqrt{\frac{\varepsilon_{H_2O}}{2\varepsilon_{CO_2}}}$$

Equation 4.102 - Combined Lennard jones potential for the well depth potential (bonding strength of the molecules):

$$\varepsilon_{H_2O\ CO_2} = \xi^2 \sqrt{\varepsilon_{CO_2}\ \varepsilon_{H_2O}}$$

Equation 4.103 - Combined Lennard jones potential representing a finite distance where the inter-molecule potential is zero:

$$\sigma_{H_2O\ CO_2} = \frac{1}{2}(\sigma_{CO_2} + \ \sigma_{H_2O})\ \xi^{-\frac{1}{6}}$$

Equation 4.104 - Knudsen diffusivity, $\mathcal{D}_k$:

$$\mathcal{D}_k = \frac{194\ \varepsilon}{S_A} \sqrt{\frac{T}{M_{CO_2}}}$$

Equation 4.105 - Sherwood number, *Sh*:

$$Sh = 2 + 0.552 Re^{\frac{1}{7}} Sc^{\frac{1}{3}}$$

Equation 4.106 - Schmidt number, *Sc*:

$$Sc = \frac{\mu_{gas}}{\rho_{gas} \mathcal{D}_b}$$

4.5. Model validation

To solve the set of equations constituting this model, the following parameters were required as inputs:

- Diameter of particle, $2r$
- Gas composition within the particle and of the bulk gas, x_{CO_2}, x_{H_2O} and x_{N_2}
- Initial temperature of the particle, T_0
- Bulk gas temperature, T_b
- Limestone type – which defines the ε_{eff}, $\rho_{Particle}$, S_A

The particle model was set up using *ODE15s* with an absolute tolerance of 10^{-10} and a relative tolerance of 10^{-9} and specified non- negativity for all parameters solved for (T, C_{CO_2}, C_{H_2O}, C_{N_2} and X).

To confirm the model responded correctly various scenarios were utilised to simplify the model and check its fundamental behaviour. Table 4.8 describes the scenario to be tested, the method of implementing this scenario into the model and the results compared with what is expected of this scenario. Unless otherwise stated the fluidising gases applied within Table 4.8 consist of 20 vol.% steam and 80 vol.% CO_2 at a bulk gas temperature of 950 °C and the particles are longcliffe limestone of diameter 600 μm.

Table 4.8 – Validation of the model by the implementation of various scenarios and their respective results.

Scenario	Implementation	Expected result	Modelled result
Particle starts at bulk gas temperature and bulk gas concentrations No calcination reaction occurs	$T_0 = T_b$ $P_{CO_20} = P_{CO_2b}$ $P_{N_20} = P_{N_2b}$ $P_{H_2O0} = P_{H_2Ob}$ X_0 = 100 %	No change in temperature or gas concentrations	Stable temperature and gas concentrations No over- or under-transfer of heat predicted by the model No over- or under-diffusion of gas predicted by the model
Particle starts at room temperature and bulk gas concentrations No reaction	T_0 = 20 °C $P_{CO_20} = P_{CO_2b}$ $P_{N_20} = P_{N_2b}$ $P_{H_2O0} = P_{H_2Ob}$ X_0 = 100 %	Particle heats up to bulk gas temperature No change in gas concentration	The temperature of the particle rises quickly to reach equilibrium with the bulk gas temperature No over- or under-transfer of heat predicted by the model
Particle starts at bulk gas temperature and atmospheric gas concentrations No reaction	$T_0 = T_b$ P_{CO_20} = 40 Pa (400 ppm) P_{N_20} = 79,000 Pa P_{H_2O0} = 0 X_0 = 100 %	No change in temperature Gases diffuse into the particle and equilibrates with the bulk gas concentrations	Gases diffuse into the particle and reaches equilibrium with the bulk gas concentration No over- or under-diffusion of gas predicted by

Particle starts at bulk gas temperature and bulk gas concentrations Calcination reaction occurs	$T_0 = T_b$ $P_{CO_20} = P_{CO_2b}$ $P_{N_20} = P_{N_2b}$ $P_{H_2O0} = P_{H_2Ob}$ $X_0 = 0$ %	Changes to the temperature and gas concentrations are only caused by the reaction The calcination reaction should release CO_2 and lower the temperature because it is endothermic	Temperature spreads throughout the particle The reaction produces a large CO_2 spike throughout the particle initially which then consumes a lot of energy thus making the reaction dependent upon the external heat transfer for the rest of the reaction
Particle starts at room temperature and atmospheric gas concentrations Calcination reaction occurs This was considered to be the base case for further validation	$T_0 = 20$ °C $P_{CO_20} = 40$ Pa (400 ppm) $P_{N_20} = 79{,}000$ Pa $P_{H_2O0} = 0$ $X_0 = 0$ %	Particle heats up to bulk gas temperature CO_2 diffuses into the particle and equilibrates with the bulk gas concentration Reaction should release CO_2	Reaction occurs when particle reaches the equilibrium temperature for the CO_2 concentration within the particle Reaction completes after about 35 s Internal mass transfer was the main resistance that was observed
Very small particle, 1 μm diameter, which starts at room temperature and atmospheric gas concentrations	$r = 0.5$ μm $T_0 = 20$ °C $P_{CO_20} = 40$ Pa (400 ppm) $P_{N_20} = 79{,}000$ Pa $P_{H_2O0} = 0$ $X_0 = 0$ %	Particle heat up time should be similar to that of the lumped heat capacity model ($\sim 2.4 \times 10^{-5}$ s)	Near instantaneous reaction No resistance can be observed from any possible controlling parameter The reaction was completed within ~1 s Temperature heat up time (even including the fact that the reaction occurred and would have extended the length of time to reach thermal equilibrium) was $\sim 4.5 \times 10^{-5}$ s

Very large particle, 1 cm diameter, which starts at room temperature and atmospheric gas concentrations	r = 5 mm T_0 = 20 °C $P_{CO_2 0}$ = 40 Pa (400 ppm) $P_{N_2 0}$ = 79,000 Pa $P_{H_2O 0}$ = 0 X_0 = 0 %	Reaction should be severely limited by internal mass transfer and heat transfer	The particle takes over 100 s to reach the required temperature for the reaction to start to occur The reaction is limited by both heat and mass transfer
Particle starts at room temperature and atmospheric gas concentrations External heat transfer is limited Calcination reaction occurs	Divide h by 10 T_0 = 20 °C $P_{CO_2 0}$ = 40 Pa (400 ppm) $P_{N_2 0}$ = 79,000 Pa $P_{H_2O 0}$ = 0 X_0 = 0 %	Reaction should be dependent on the heat transfer to the particle from the gas	The reaction begins significantly later (at around 20 s) due to the particle receiving less heat from the gas
Particle starts at room temperature and atmospheric gas concentrations Internal heat transfer is limited Calcination reaction occurs	Divide λ_{eff} by 100 T_0 = 20 °C $P_{CO_2 0}$ = 40 Pa (400 ppm) $P_{N_2 0}$ = 79,000 Pa $P_{H_2O 0}$ = 0 X_0 = 0 %	Reaction should be dependent on the transfer of heat through the particle	The rate of reaction was significantly limited by the internal heat transfer, which was observed by pronounced thermal gradients throughout the particle Conversion of each consecutive region was delayed due to the endothermic reaction utilising the available energy and therefore dropping the particle temperature and thus lowering the rate of reaction

Particle starts at room temperature and atmospheric gas concentrations External mass transfer is limited Calcination reaction occurs	Divide k_g by 100 T_0 = 20 °C P_{CO_20} = 40 Pa (400 ppm) P_{N_20} = 79,000 Pa P_{H_2O0} = 0 X_0 = 0 %	Reaction should be dependent on the transfer of CO_2 out of the particle	In the base case, the particles' surface retained a CO_2 concentration similar to that of the bulk gas, however in this case the surface CO_2 concentration was nearly equal to the CO_2 concentration throughout the particle which was the equilibrium CO_2 concentration at that temperature
Particle starts at room temperature and atmospheric gas concentrations Internal mass transfer is limited Calcination reaction occurs	Divide D_{eff} by 100 T_0 = 20 °C P_{CO_20} = 40 Pa (400 ppm) P_{N_20} = 79,000 Pa P_{H_2O0} = 0 X_0 = 0 %	Reaction should be dependent on the transfer of CO_2 through the particles interior	Internal mass transfer gradient was exacerbated such that CO_2 struggled to diffuse through the particle, CO_2 effectively gets trapped within the particle and reaches the equilibrium CO_2 concentration very quickly thereby limiting the rate of reaction for the inner regions of the particle

During this validation the model responded as expected within the range of scenarios tested, implying that it should be capable of accurately describing the movement of heat and mass throughout the particle as the reaction occurs. This validation also demonstrated the importance of selecting appropriate equations to describe the different parameters that constitute this model.

4.5.1. Model inputs for a test case

As a test case to demonstrate the model's capabilities and limitations, the following inputs were submitted to the model. The particle was divided into 50 shells which allowed for faster solving with an adequate amount of detail in the results.

- Particle diameter = 600 μm
- Gas composition of $x_{CO_2} = 0.8$, $x_{H_2O} = 0.2$, $x_{N_2} = 0$
- Initial particle temperature = 20 °C
- Bulk gas temperature = 950 °C
- Limestone type = Longcliffe
- The rate of calcination was calculated with Equation 4.72

4.5.2. Model outputs for the test case

Figure 4.23 to Figure 4.31 graphically display the outputs from the model of this test case. The general outline of the reaction shows the progression of the calcination reaction starting from the surface moving into to the centre gradually, as evidenced by Figure 4.27. It can also be observed in Figure 4.24 and Figure 4.25, the reason for the progressive calcination throughout the particle, only continuing into the next inner shell when the adjacent outer shell had nearly completed its calcination, was because of the high CO_2 partial pressure within the particle, which effectively slowed the reaction. Once the partial pressure of CO_2 was above the equilibrium partial pressure of CO_2, which at 950 °C is 2.4×10^5 Pa as calculated via Equation 4.76, the calcination stopped. The recarbonation of calcined CaO was not accounted for within this model. Figure 4.24 shows a 2D view of the partial pressure of CO_2 within the particle where each contour represents a shell radii within the particle. Only the profiles of every 5^{th} shell within the particle is shown for clarity.

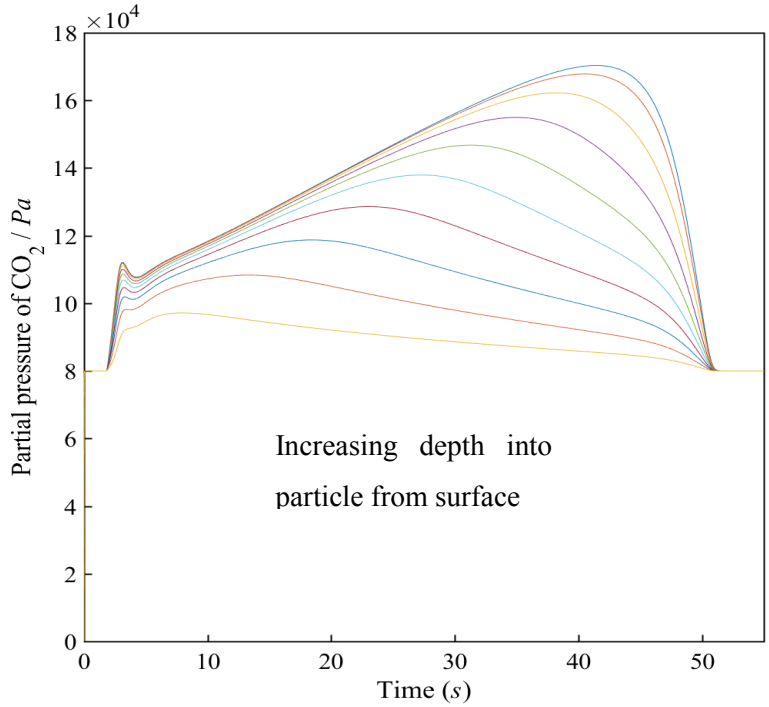

Figure 4.23 – 2D view of the modelled partial pressure of CO_2 within the particle as the calcination reaction occurs.

The partial pressure of CO_2 can be seen to tend towards the equilibrium partial pressure but as it does so the rate of reaction slows and as such less CO_2 is released. Within the first few seconds of the reaction occurring, a near instantaneous release of CO_2 leads to a sharp rise in CO_2 partial pressure throughout the particle, which combined with the low porosity (close to pure $CaCO_3$ at this stage, $\varepsilon_{eff} \approx 15\ \%$) meant that the subsequent rate of calcination slowed whilst CO_2 diffused out of the outer shells of the particle. The partial pressure of CO_2 within the particle did progress to a higher value than this initial spike because the particle temperature increased as time progressed and $P_{CO_2 eq}$ increased too as it is proportionally related to temperature.

This initial spike in CO_2 can be observed again in Figure 4.24 where the modelled calcination rate profile of every 5th shell of the particle is shown for clarity. It can be observed that the centre most shells/region of the particle begins the majority of its calcination from ~35 s which shows that the calcination of the inner shells was limited by the CO_2 partial pressure within the particle produced by the outer shells. Figure 4.24 shows more CO_2 being released form the outer shells because they represent a larger percentage of the overall volume.

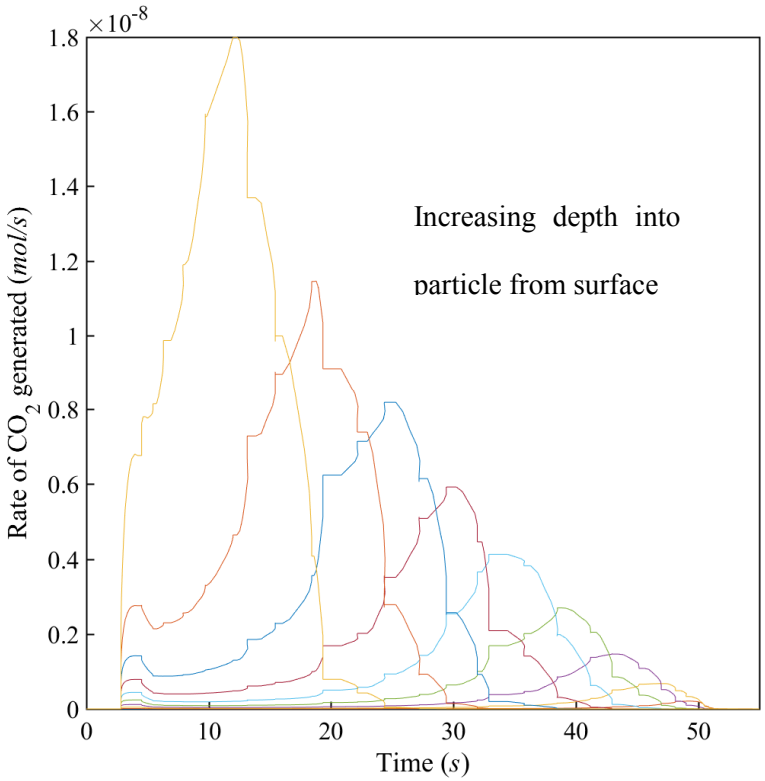

Figure 4.24 – 2D view of the predicted rate of CO_2 generation within every 10th shell of the particle as the calcination reaction occurs.

Figure 4.24 also shows that the initial spike in CO_2 partial pressure was caused by the calcination of all shells in the particle. This was also observed in the rate of energy use by the calcination reaction as presented in Figure 4.25, showing a matching trend but inversed (because the reaction was endothermic) pattern to the rate of CO_2 release. Because the reaction was observed to start evenly throughout the particle but then progress sequentially through the particle a limiting factor must be present. By observing Figure 4.30 it was again confirmed to be the partial pressure of CO_2 limiting the reaction as the temperature profile of the particle at all shells throughout the particle was near isothermal, implying that internal heat transfer was not a limiting factor.

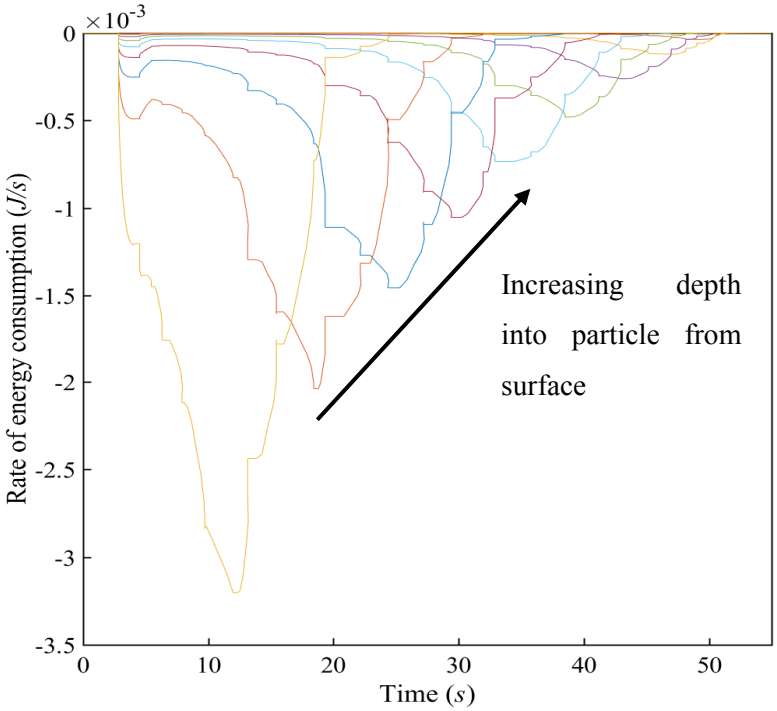

Figure 4.25 – 2D view of the modelled rate of heat consumption within the particle as the calcination reaction occurred.

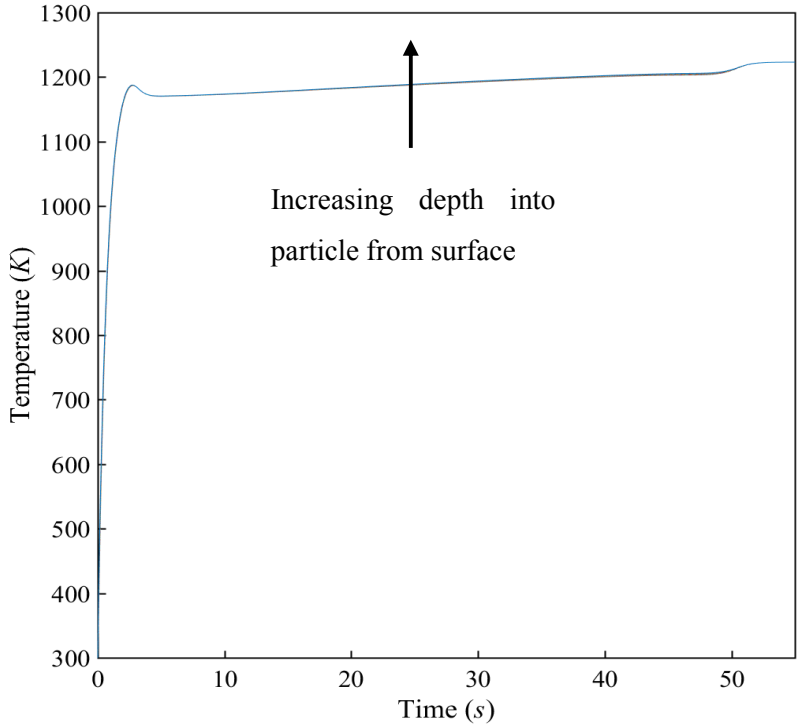

Figure 4.26 – 2D view of the modelled temperature within the particle as the calcination reaction occurred.

Figure 4.26 demonstrates that the modelled temperature throughout the particle drops significantly as the reaction begins and only fully recovering to the input bulk gas temperature when the particle is fully calcined. Furthermore it can be observed that the reaction begins to occur before the particle has equilibrated with the bulk gas temperature.

This isothermality of this test system particle was predicted by the low Biot number, ~0.2. The Biot number is a correlation based on the transfer of heat to a particles surface compared to the conductivity of heat through a particle; a higher number indicates that the particle was not isothermal due to poor conduction of heat within the particles structure, whereas a low Biot number (arbitrarily << 1) indicates isothermality of the particle due to good heat conduction. The Biot number can be calculated via Equation 4.107 as shown below.

Equation 4.107:

$$Bi = \frac{hL_c}{k_b}$$

Where L_c is the characteristic length, usually defined as the volume of the body divided by the surface area, for a perfect sphere $L_c = r/3$.

Figure 4.27 shows that for the shells which had not fully converted the reaction was possible to occur because the $P_{CO_2} < P_{CO_2 eq}$ throughout the majority of the reaction time period. However because the previous figures have provided evidenced that the rate of calcination during the main reaction period for the inner shells was negligible it must be concluded that although these inner particle shells were capable of reacting but the rate was incredibly slow.

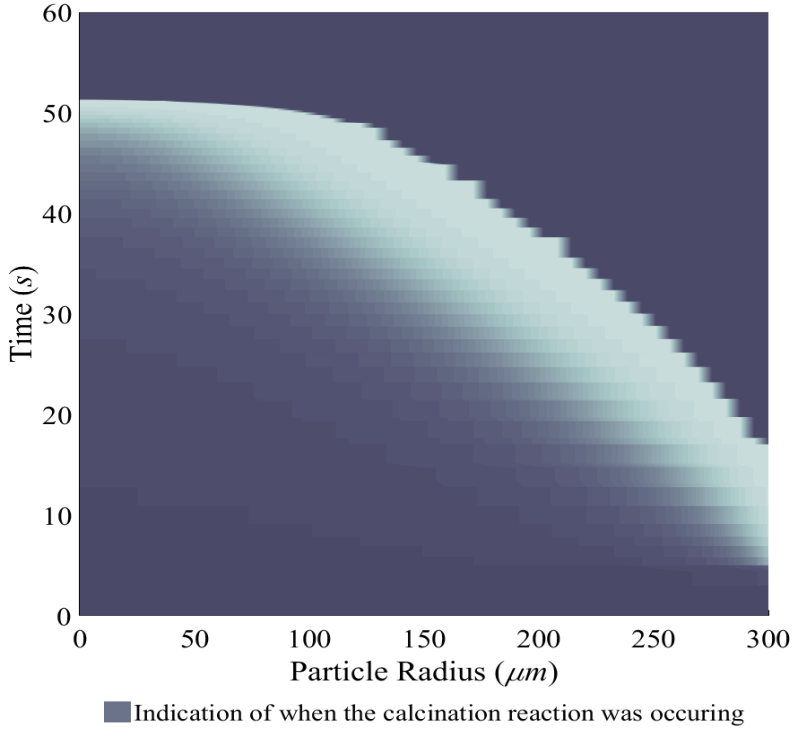

Figure 4.27 – Prediction of when the calcination reaction could have occurred due to ($P_{CO_2} < P_{CO_2eq}$) and conversion at within each shell being less than 1.

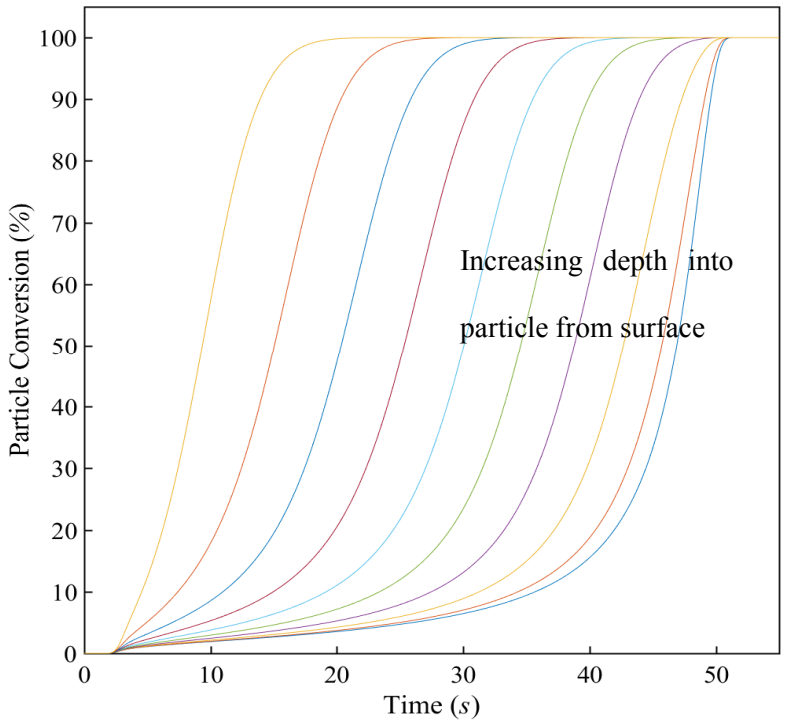

Figure 4.28 – 2D view of the modelled conversion of $CaCO_3$ to CaO within the particle at every 5th shell.

2D and 3D views of the conversion as a function of time and particle radius are observable in Figure 4.28 and Figure 4.29. It can be seen that main calcination reaction of each shell is quite fast, completing within ~7 s of starting, however the rate of conversion of the inner shells is initially slow, because of the high CO_2 partial pressure within the inner shell. Because the conversion of each shell is fast once began it can be assumed that rate of CO_2 diffusing out of the shell was approximately equal to the rate at which it was generated. Figure 4.29 shows that at any one time period only up to 50 µm of particle radii length had actually begun the main part of its calcination.

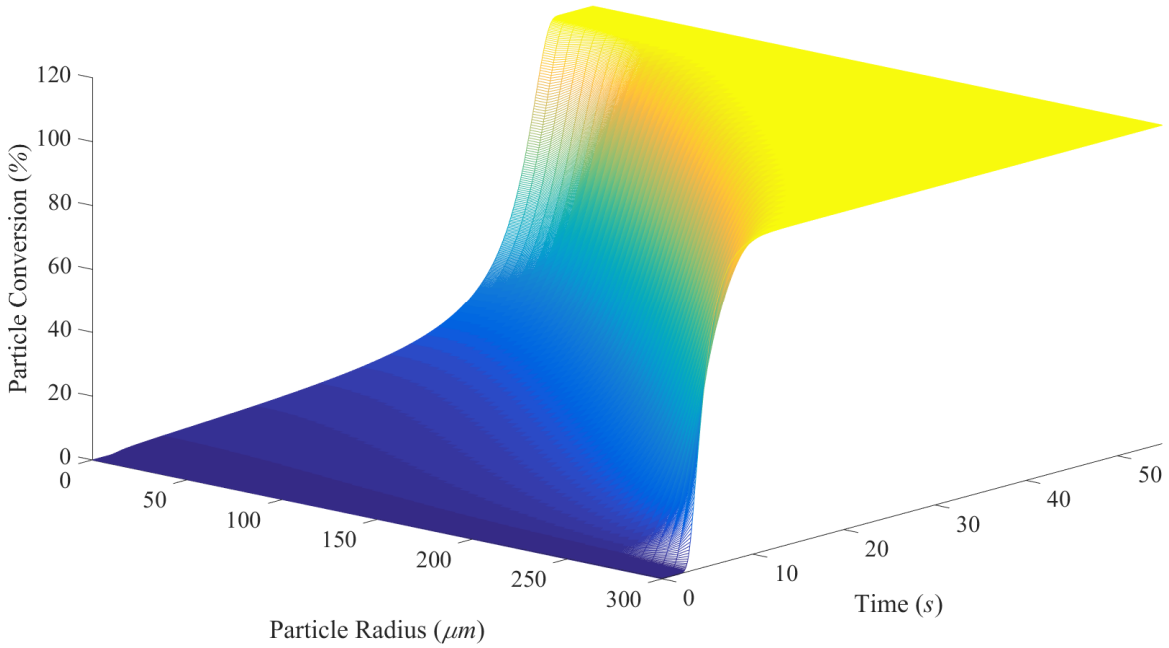

Figure 4.29 – 3D view of the modelled particle conversion as the calcination reaction occurs.

Figure 4.30 shows the concentration profile of CO_2 throughout the particle as the calcination reaction occurred. The initial reaction spike seems excessively large in this figure compared to the partial pressure spike observed in Figure 4.23, this is because the concentration value was dependent upon the gas temperature at that point in time. The temperature was lower during the initial spike compared to later on in the reaction and because temperature and volume are directly proportional through Charles's law the gas volume was also lower meaning the concentration was higher.

Then CO_2 was observed (in Figure 4.30) leaving the particle quickly after the calcination had finished this was due to increase an in particle temperature which therefore increased the Knudsen diffusivity and hence increased the effective diffusivity.

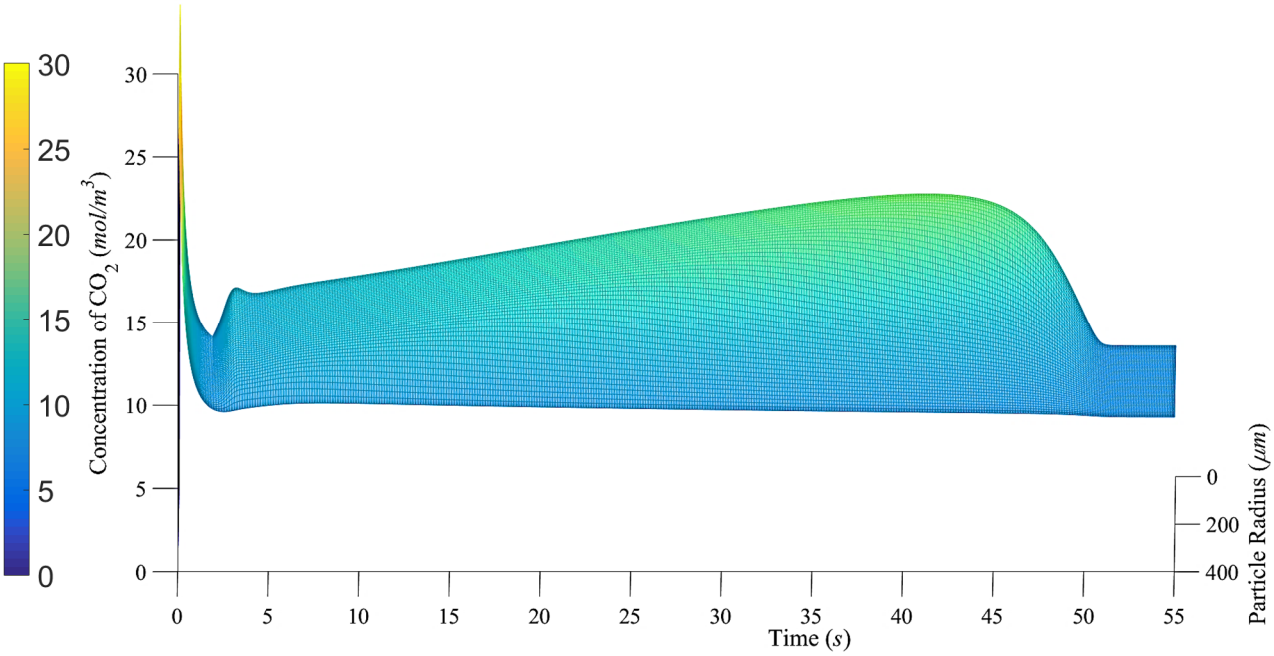

Figure 4.30 – 3D view of the modelled concentration of CO_2 within the particle as the calcination reaction occurs.

The overall modelled rate of CO_2 evolution from calcination and averaged particle temperature can be observed in Figure 4.31. A peak rate of ~5.1 mol/g.s can be observed at a particle temperature of ~1170 K at a bulk gas temperature of 1223 K.

This initial testing of the model has shown that the rate of calcination is severely limited by the diffusion of CO_2 throughout the particle and by the external transfer of heat to the particle. Based on this evidence it can be stated that for this test case, calcination of any internal region will only go to completion once the adjacent exterior region is almost complete.

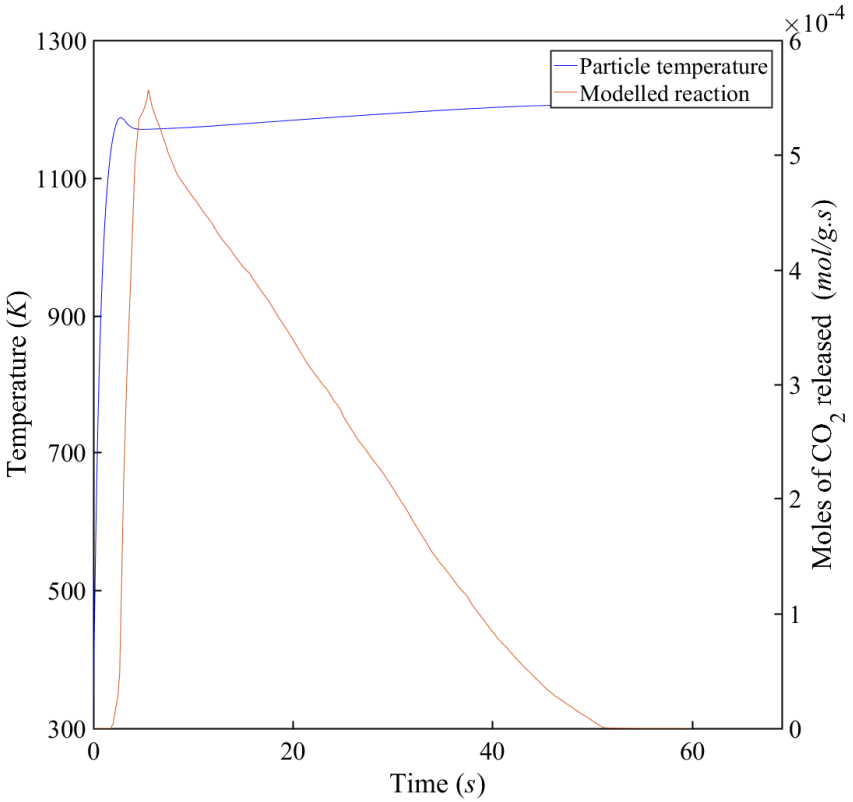

Figure 4.31 – Modelled overall release of CO_2 and the surface particle temperature throughout the calcination reaction.

4.6. Rate constant fitting

Figure 4.32a and b were produced by the application of the observed kinetic parameters presented within Table II.2 (within Appendix II) and applying the conditions stated below (which represent the base case experimental data). Figure 4.32a displays the comparison between the modelled data and the experimental data for a system with steam and CO_2 and Figure 4.32b displays the comparison between the modelled data and the experimental data for a system with N_2 and CO_2. The modelled particle was now divided into 100 shells.

H_2O and CO_2 system conditions:

- Geometric mean particle radius = 300 μm (≈ particle size fraction 500 - 710 μm)
- Gas composition of $x_{CO_2} = 0.79$, $x_{H_2O} = 0.21$, $x_{N_2} = 0$
- Initial particle temperature = 20 °C
- Bulk gas temperature = 955 °C
- Limestone type = Longcliffe
- The rate of calcination was calculated with Equation 4.72

N_2 and CO_2 system conditions:

- Geometric mean particle radius = 300 μm (≈ particle size fraction 500 - 710 μm)
- Gas composition of $x_{CO_2} = 0.8$, $x_{H_2O} = 0$, $x_{N_2} = 0.2$
- Initial particle temperature = 20 °C
- Bulk gas temperature = 950 °C
- Limestone type = Longcliffe
- The rate of calcination was calculated with Equation 4.73

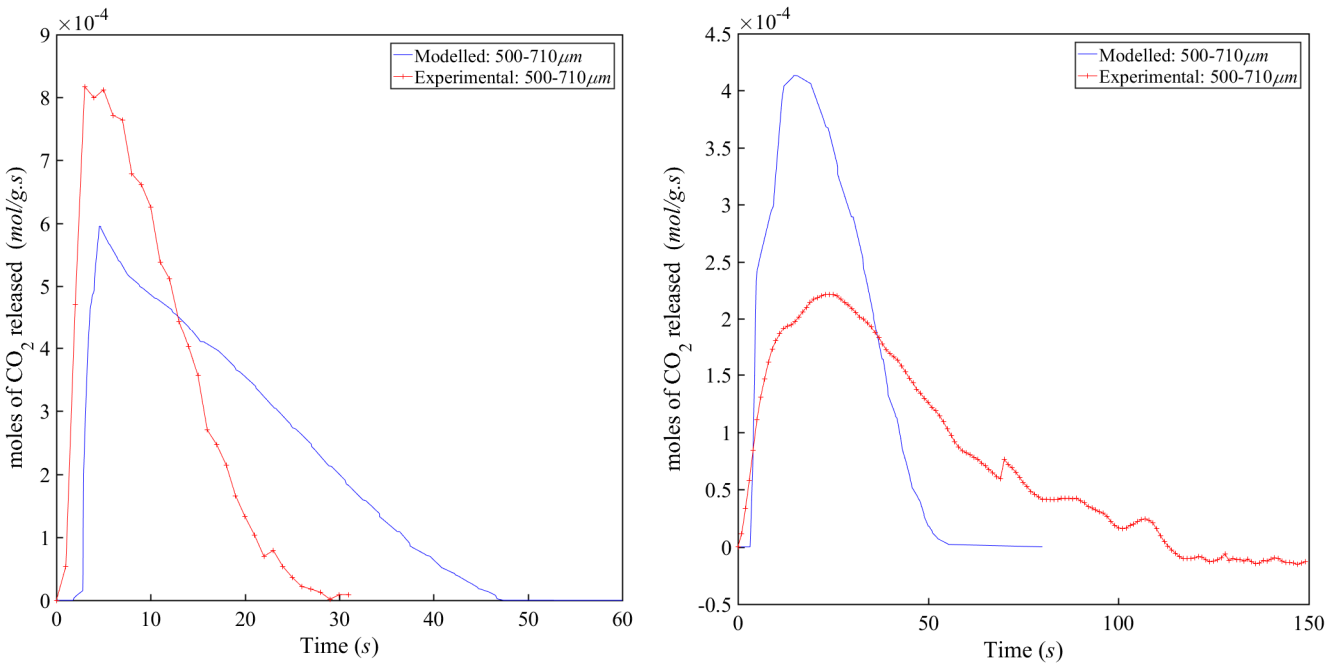

Figure 4.32a and b – The modelled CO_2 response when utilising the observed kinetics with the input parameters set within section 4.5.1 compared to the experimental data for an equivalent system. (a) Calcination with steam and CO_2 and (b) calcination with N_2 and CO_2.

A degree of discrepancy can be observed when comparing the experimental and modelled CO_2 responses under the conditions tested. The modelled calcination with steam shows a slightly slower rate of CO_2 release whereas the modelled calcination with N_2 displays a faster rate of CO_2 release. The reason for this discrepancy between the modelled and experimental data was because the observed kinetic parameters were utilised which were not representative of the intrinsic kinetics at the particle scale.

To combat the apparent disagreement in the kinetic values used within the Arrhenius equation of the model, the Arrhenius parameters were recalculated using a least-squares regression between the experimental and modelled initial rates (from the point reaction starts to the peak rate). The least-squares regression fitting was conducted by increasing the value of the rate constant, *k*, by 10 across a range of values estimated to lie within an acceptable range, after which the range was decreased and through trial and error the values of *k* altered to find the value with the best fit to the data. A calculated value of

the sum of the square errors was utilised as an indicator of the goodness of the fit and was saved and recorded against the input value of *k*. Figure 4.33 and Figure 4.34 show the results of fitting a *k* value of 10 s^{-1} to the system of a particles of radius 300 µm calcining at 963 °C in 80 vol.% CO_2 and 20 vol.% N_2. The modified Arrhenius plots and parameters can be observed in Figure 4.35 and Table 4.9 respectively.

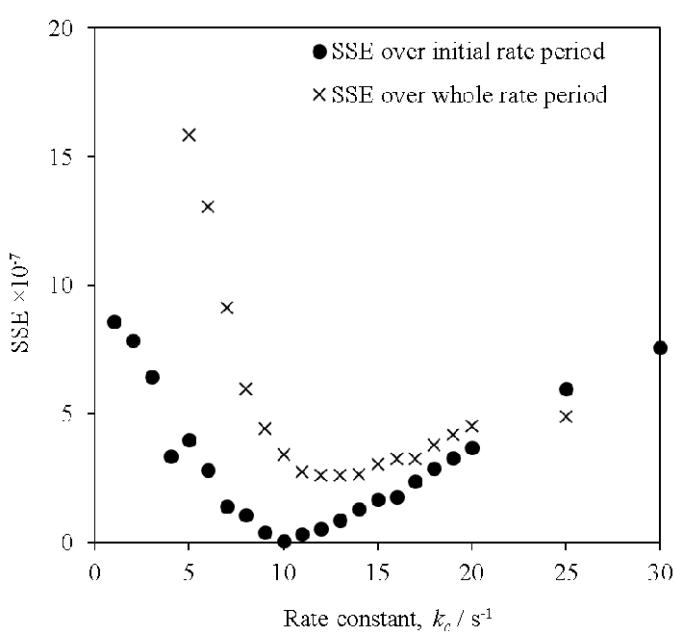

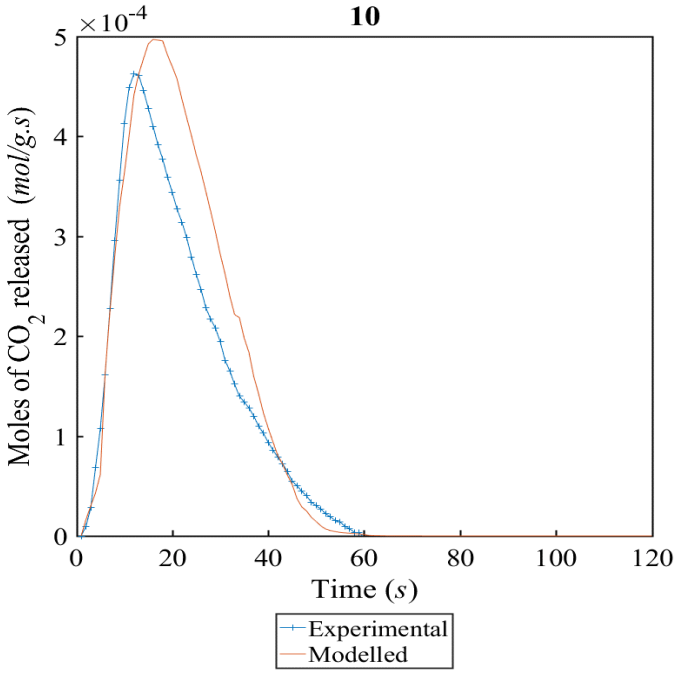

Figure 4.33 (left) – The sum of the square error (SSE) against a fixed initial rate constant.

Figure 4.34 (right) – the subsequent rate profile utilising the optimally found fixed initial value of 10 s^{-1} compared against the experimental data for the system of a particle of radius 300 µm calcining at 963 °C in 80 vol.% CO_2 and 20 vol.% N_2.

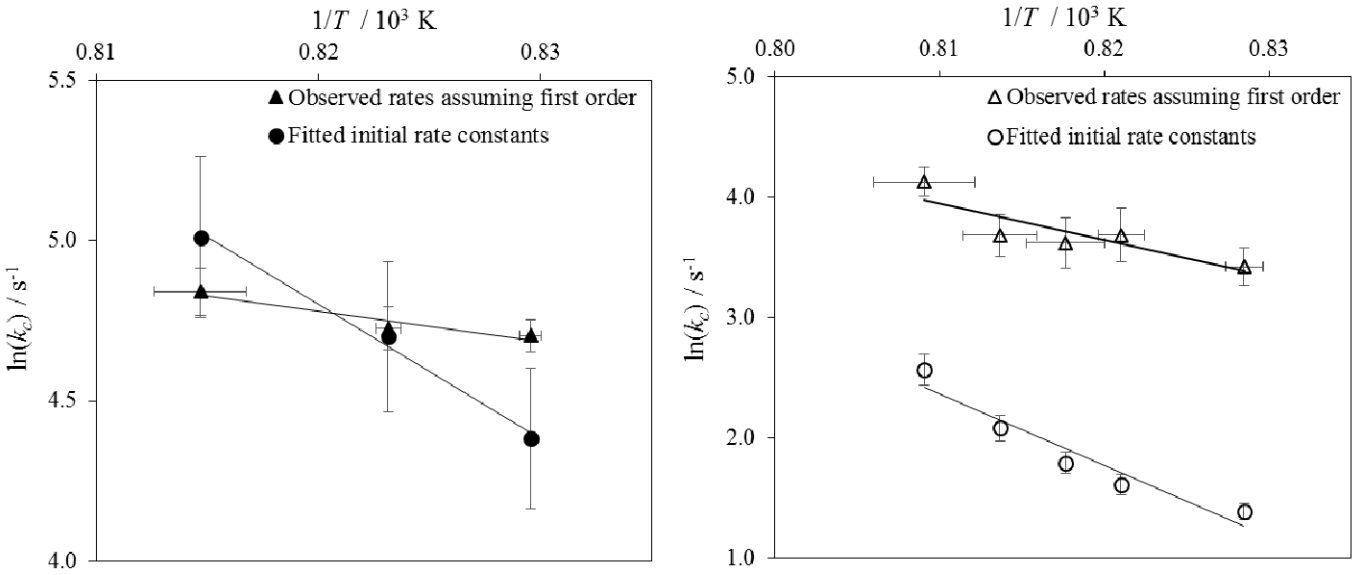

Figure 4.35 – Arrhenius plot for the experiments with steam (left) and N_2 (right): [▲, Δ] - Experimental observed kinetic rates assuming a first order relationship with respect to the partial pressure of CO_2, and [●, ○] – Fitted initial intrinsic rate constants to the model by a least-squares fit.

Table 4.9 – Arrhenius parameters for the Arrhenius plots in Figure 4.35.

	Steam system		**N_2 system**	
	***k₀* / s^{-1}**	***Ea* / kJ/mol**	***k₀* / s^{-1}**	***Ea* / kJ/mol**
Observed rates assuming first order relationship with respect to P_{CO_2}	1.93×10^{16}	326.3 ± 20.1	2.75×10^{23}	504.1 ± 76.9
Least squares regression of initial intrinsic rate constants	5.99×10^{8}	149.7 ± 26.9	1.86×10^{32}	739.3 ± 81.4

Errors displayed within Table 4.9 are the confidence intervals calculated following the laws of uncertainty propagation. A 5% error was assumed for all values of *k* which were found via a least squares regression.

An issue of utilising these fitted 'intrinsic' kinetic parameters within the Arrhenius equation was that because the fitting range was quite small, therefore when applying these rate parameters outside of the fitting range potentially erroneous values could be produced. This error can be observed within Figure 4.36, which shows a logarithmic plot of the calculated rate constant against temperature for the steam calcination system. Although a close fit can be seen in the fitting range (1205 – 1230 K) between the observed and fitted values, outside of this range, particularly at lower temperatures a significant over estimation of the rate constant can be observed.

Figure 4.26, Figure 4.31 and Figure 4.37 show the temperature throughout the modelled particle as the particle calcines. Figure 4.37 shows that when applying the fixed rate constant value which was found to produce the optimal fit to the experimental data by the sum of the square error, it can be seen that the particles' temperature at this peak rate was 1156 K. This was about 72 K below the bulk gas temperature which could have produced to significant errors in the calculation of the Arrhenius parameters. The peak rate temperatures were determined for each of the particle systems when applying the fixed rate constant values derived earlier. By taking an average of the peak rate temperature and the bulk gas temperature and applying this averaged temperature to the Arrhenius equation new rate pre-exponential factors and activation energies were produced. Applying these new Arrhenius parameters and plotting the derived rate constant over the extended temperature range, the grey circles on Figure 4.36were produced. The error was subsequently minimised such that a faster rate was produced at all temperatures but still followed the approximately the same trend line as the observed rate constants. The new Arrhenius parameters are shown in Table 4.10.

Table 4.10 – Arrhenius parameters for the least squares regression of initial intrinsic rate constants at an average temperature (between the bulk and peak rate particle temperatures).

Steam system		**N_2 system**	
k_0 / s^{-1}	***Ea*** / **kJ/mol**	k_0 / s^{-1}	***Ea*** / **kJ/mol**
9.84×10^{12}	241.5	3.67×10^{51}	1157.9

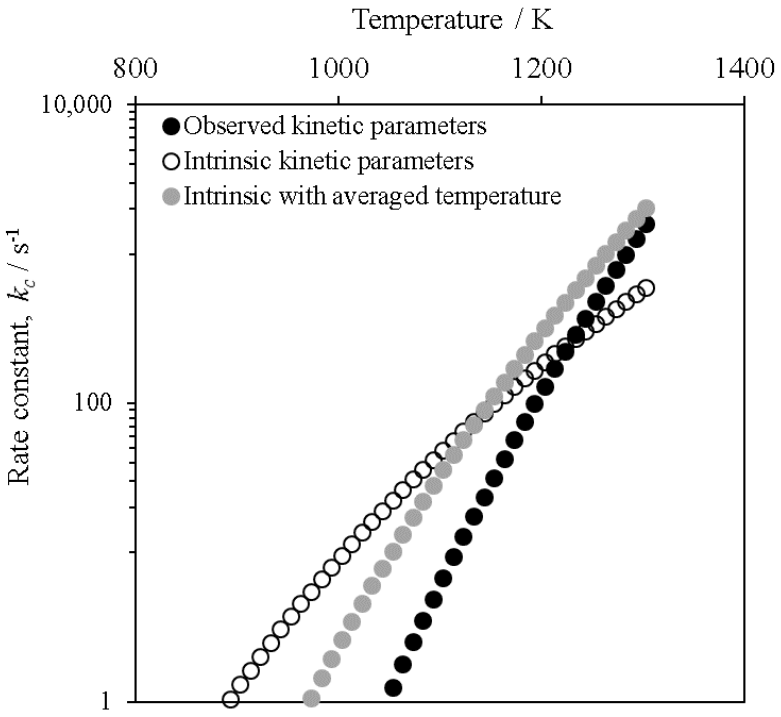

Figure 4.36 – Application of the observed and intrinsic kinetic parameters within the Arrhenius equations for steam and CO_2 calcination across an extended range of temperatures.

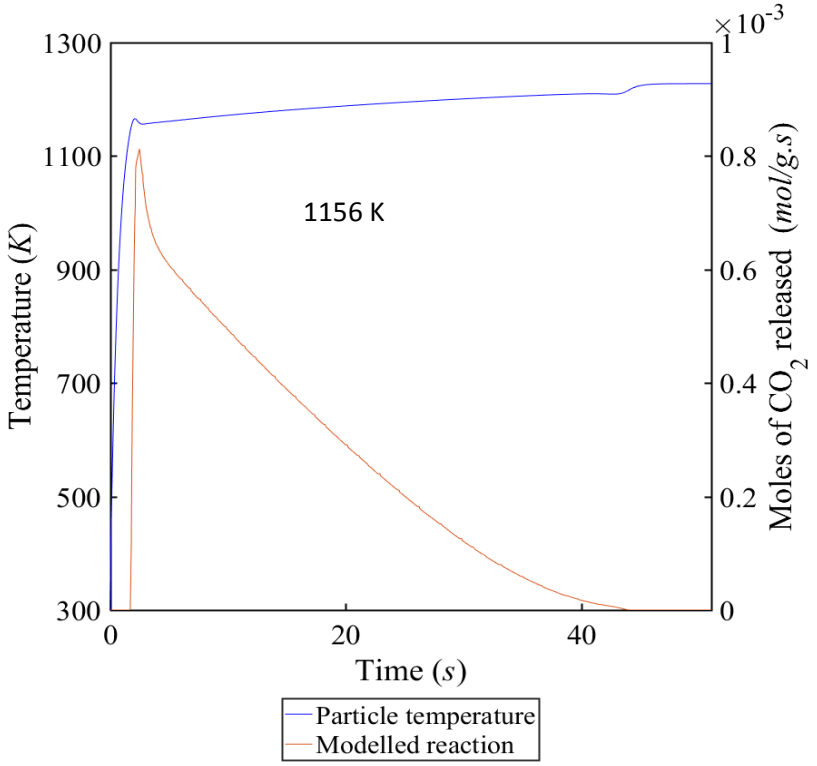

Figure 4.37 – Modelled plot of the CO_2 response and temperature within a particle (300 µm radius) of limestone calcining at 955 °C (1228 K) in 21 vol.% steam and 79 vol.% CO_2 using a fixed rate constant value of 250 s^{-1}.

Figure 4.38 shows the equivalent plot as Figure 4.36 but for the N_2 system calcinations. As can be seen within the range of temperatures that calcination will take place, upon utilising the average temperature of the bulk gas and peak rate particle temperature for the derivation of the Arrhenius parameters a faster rate constant is observed at the lower temperatures but not higher than the observed rate constant. The application of these new Arrhenius parameters within the model will now be demonstrated.

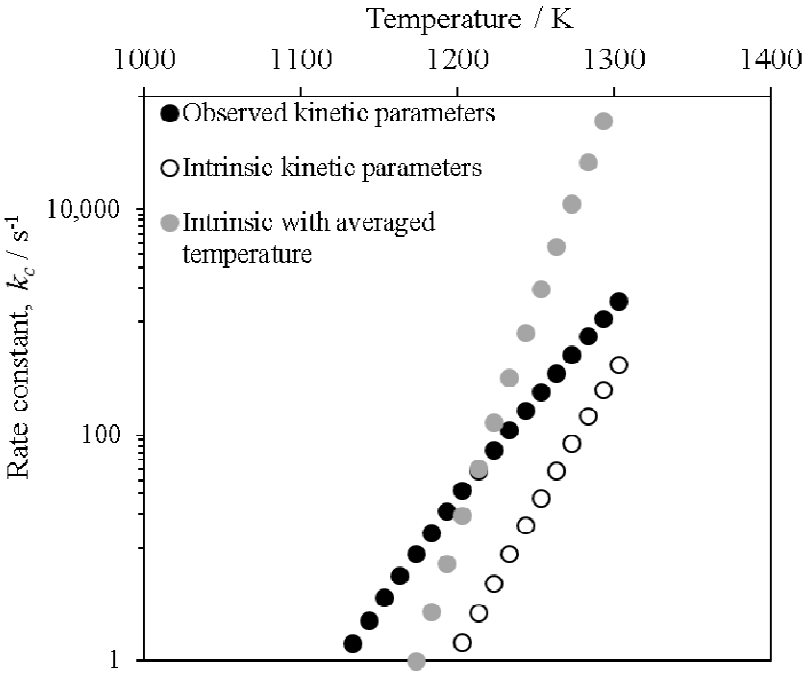

Figure 4.38 – Application of the observed and intrinsic kinetic parameters within the Arrhenius equations for N_2 and CO_2 calcination across an extended range of temperatures.

4.7. Modelled data compared to experimental data

By applying the model under the experimentally tested conditions, the accuracy and physical representation of the model and the fitted kinetic parameters can be verified. Figure 4.39 to Figure 4.48 display the experimental and modelled CO_2 response where the models input conditions were set to be equivalent to the experimental conditions.

The closeness of fit between the modelled data and experimental results was visually quite good especially for the differential form of the data (left hand side figures). The conversion graphs (right hand side figures) present a lower visual similarity compared to the experimental conversions, this was mostly because the tail off of the CO_2 response was longer than measured during the experiments.

The general fit of the modelled CO_2 response compared to the experimental data of calcinations in N_2 and CO_2 data was worse than the fit for the steam calcinations. This was thought to be caused by the poorer mass balance with the N_2 calcination data, which itself was caused by the low signal to noise ratio. A closer fit for the N_2 system was seen where the total conversion in the experimental data was closer to 100 %.

Interesting the model was unable to predict the significant difference in the rate of calcination when the mole fraction of CO_2 was decreased and replaced with N_2. It can also be observed from Figure 4.45 and Figure 4.46 that the model does not account for the effects caused by varying the sample mass, which causes an inter-particle mass transfer diffusional resistance. This additional resistance caused an effect in the experimental data whereby the CO_2 released from the calcination of one particle altered the boundary CO_2 concentration of another particle, this had the overall effect of reducing the driving force when a large sample mass is used.

Considering the experimental error in some of this data, caused by inaccurate readings and measurements, the model was generally quite good at predicting the overall CO_2 response of limestone calcination. The shape of the modelled CO_2 response will always predict an idealised scenario that doesn't take into account gas mixing and gas dispersion with time, which is why the experimental data presented was deconvoluted as explained in section 4.2.3.

4.7.1. Effect of varying bed temperature

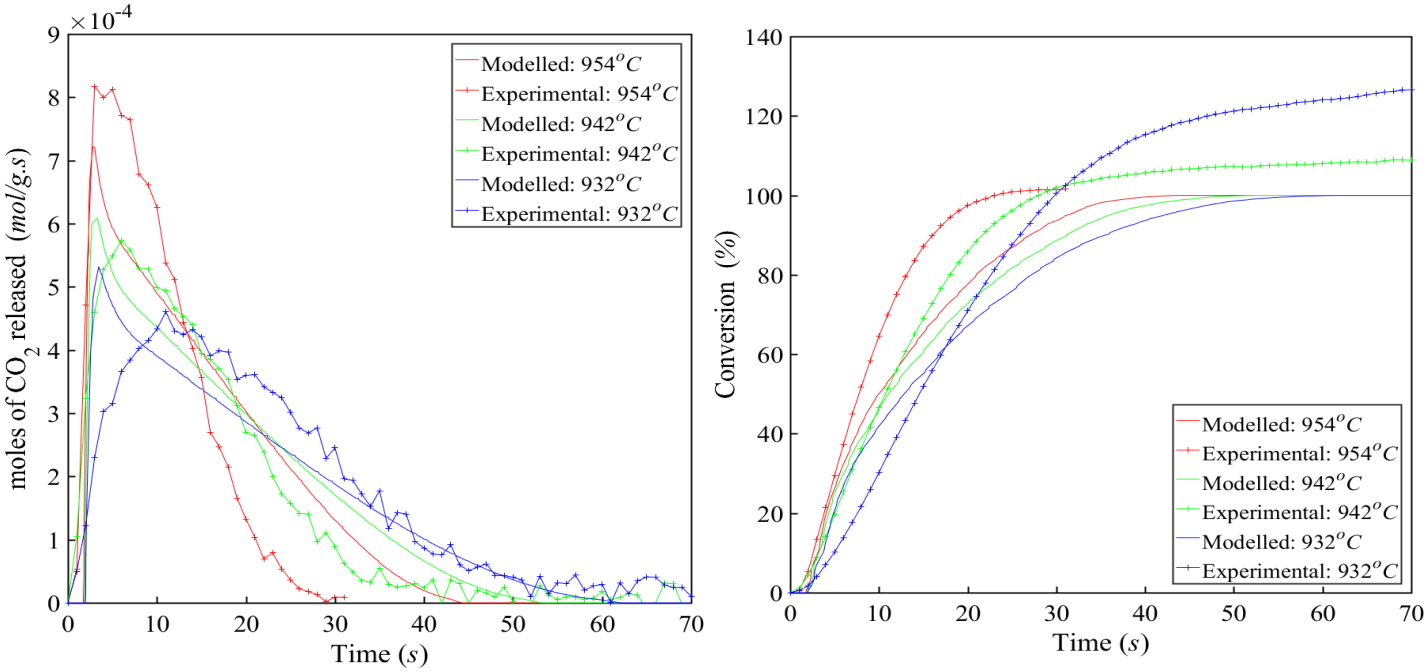

Figure 4.39a and b - Modelled and experimental, reaction and conversion profiles for limestone calcination in 20% steam and 80% CO_2.

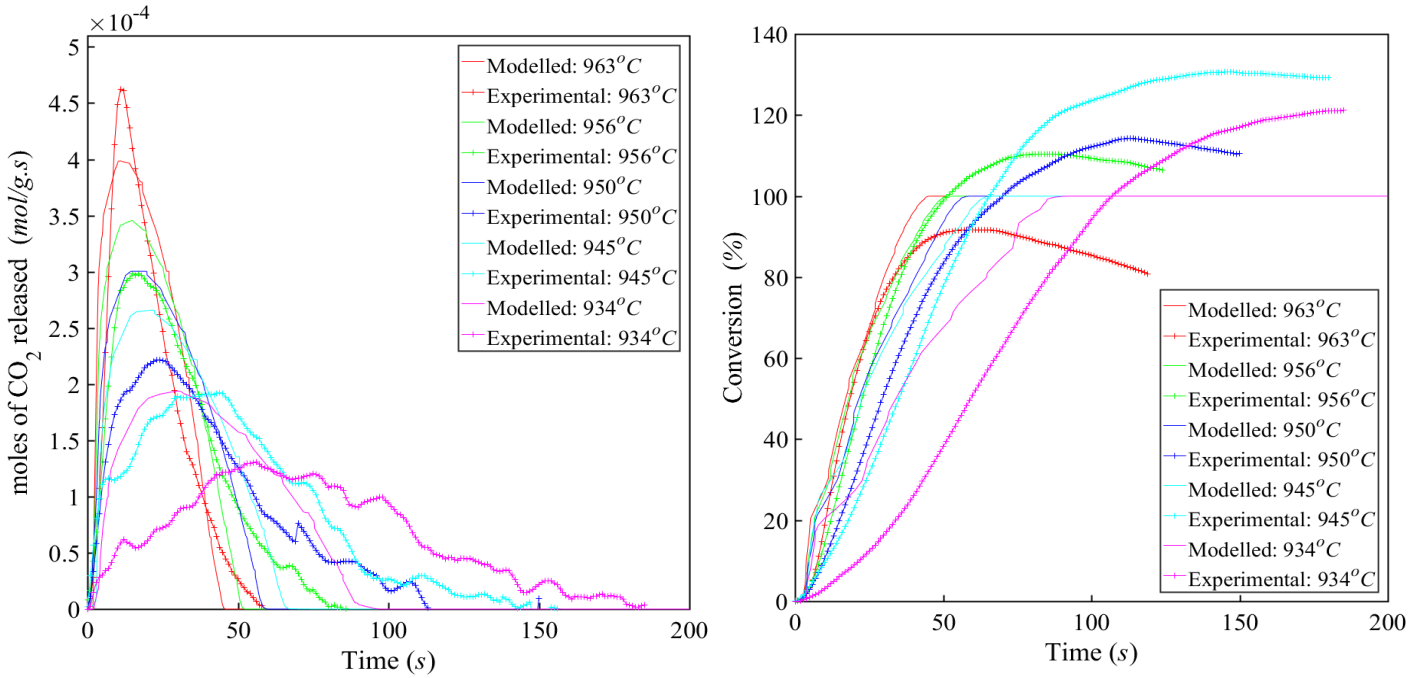

Figure 4.40a and b - Modelled and experimental, reaction and conversion profiles for limestone calcination in 20% N_2 and 80% CO_2.

4.7.2. Effect of varying CO_2 partial pressure

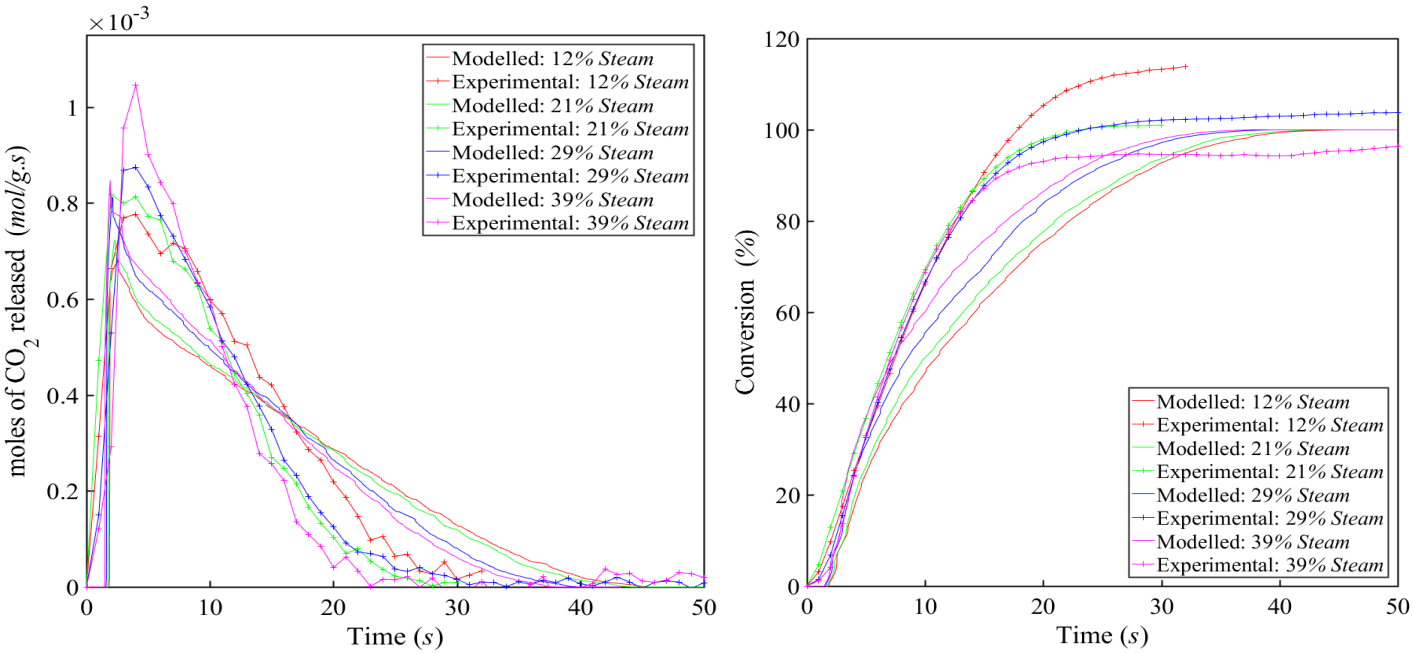

Figure 4.41a and b - Modelled and experimental, reaction and conversion profiles for limestone calcination in at 950 °C with varying steam and CO_2 concentrations.

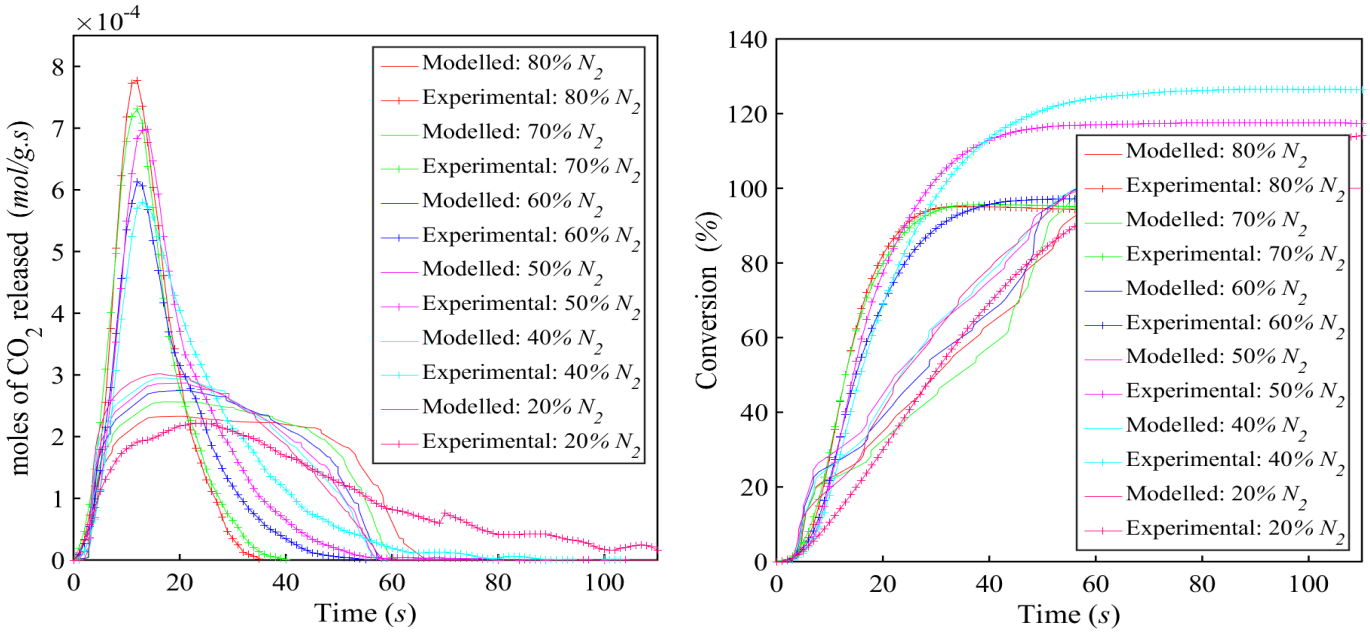

Figure 4.42a and b - Modelled and experimental, reaction and conversion profiles for limestone calcination in at 950 °C with varying N_2 and CO_2 concentrations.

4.7.3. Effect of varying particle size

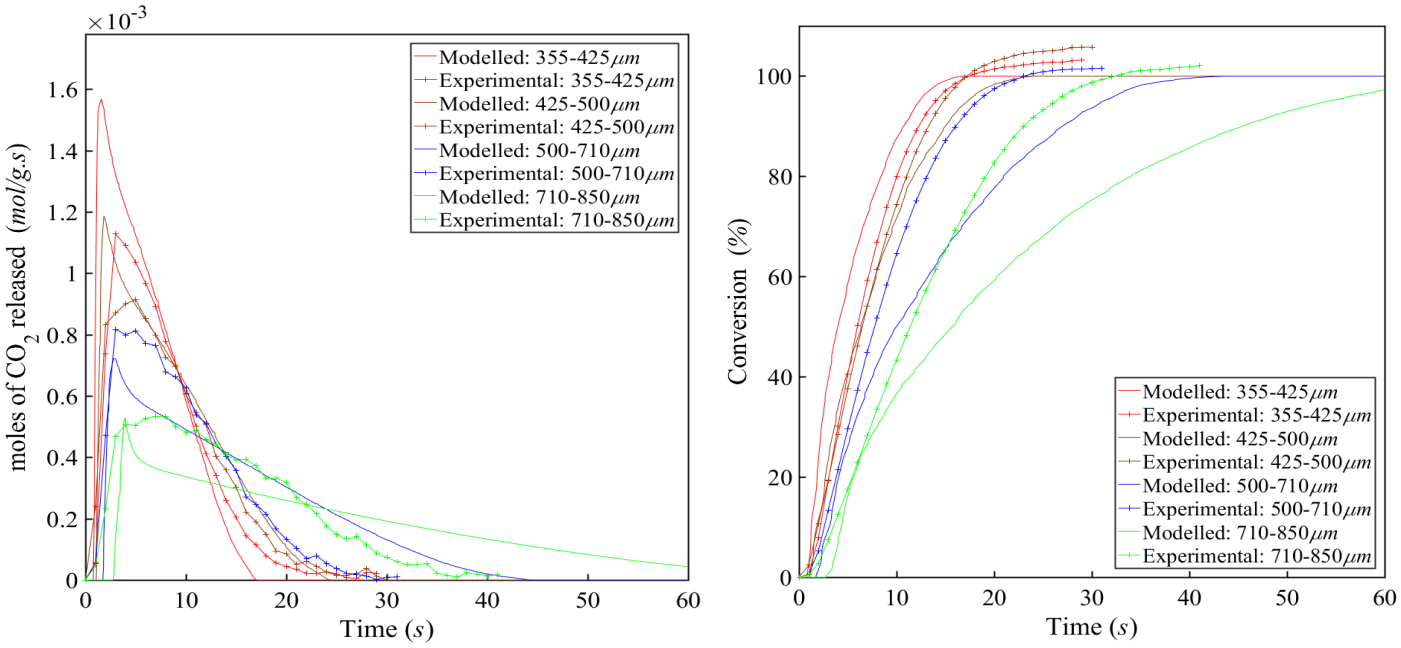

Figure 4.43a and b - Modelled and experimental, calcination reaction and conversion profiles of different limestone particle size fractions at 950 °C in 20 % steam 80% CO_2.

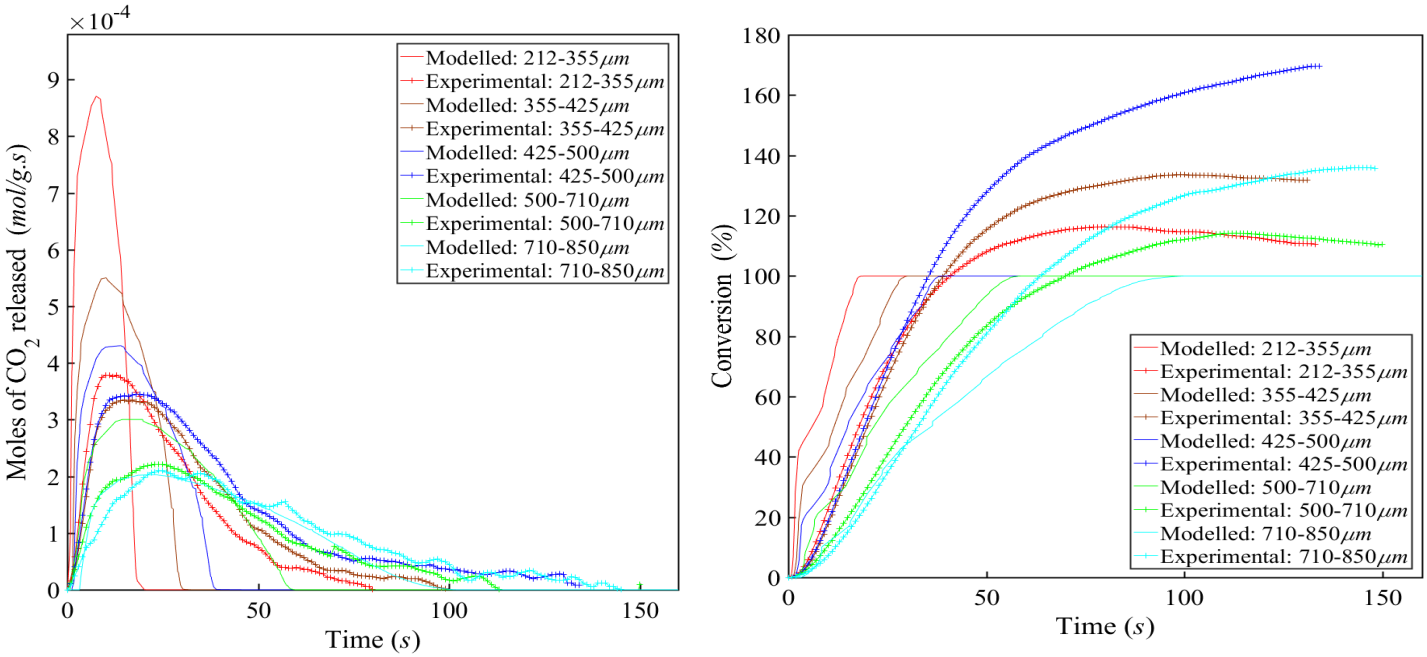

Figure 4.44a and b - Modelled and experimental, calcination reaction and conversion profiles of different limestone particle size fractions at 950 °C in 20 % N_2 80% CO_2.

4.7.4. Effect of varying sample mass

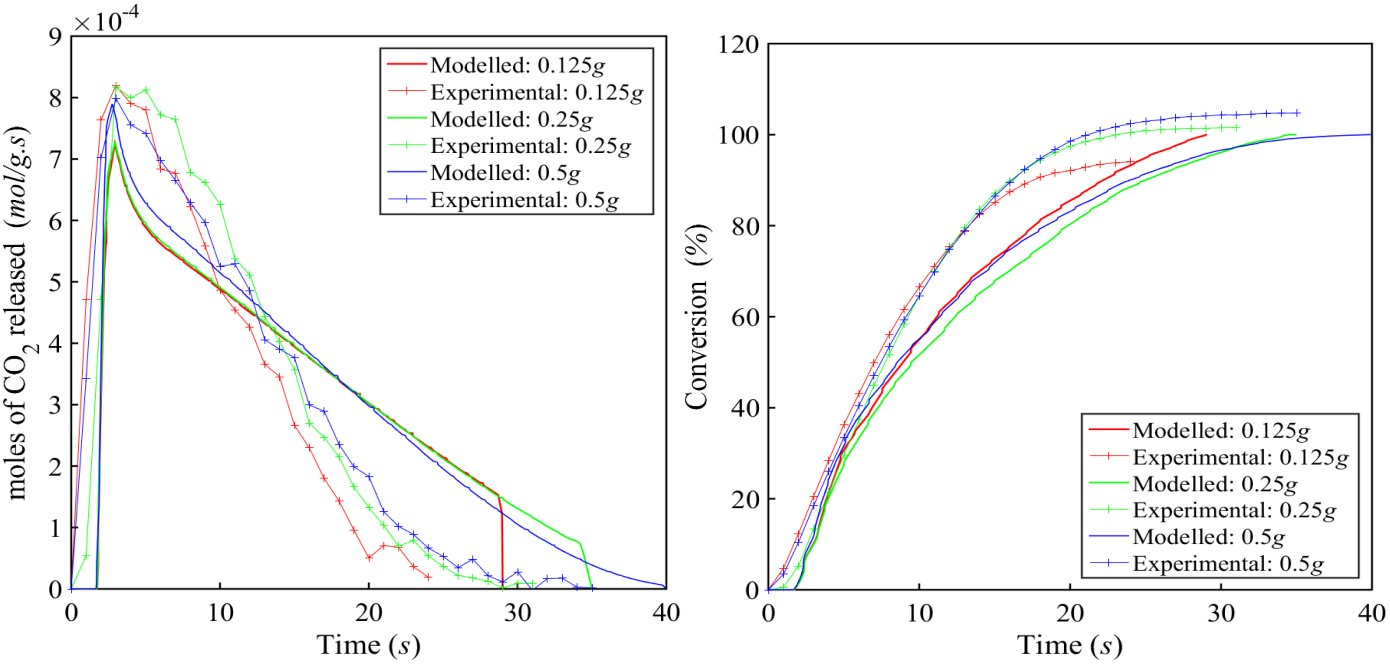

Figure 4.45a and b - Modelled and experimental, reaction and conversion profiles for the calcination of different sample masses of limestone at 950 °C in 20 % steam and 80 % CO_2.

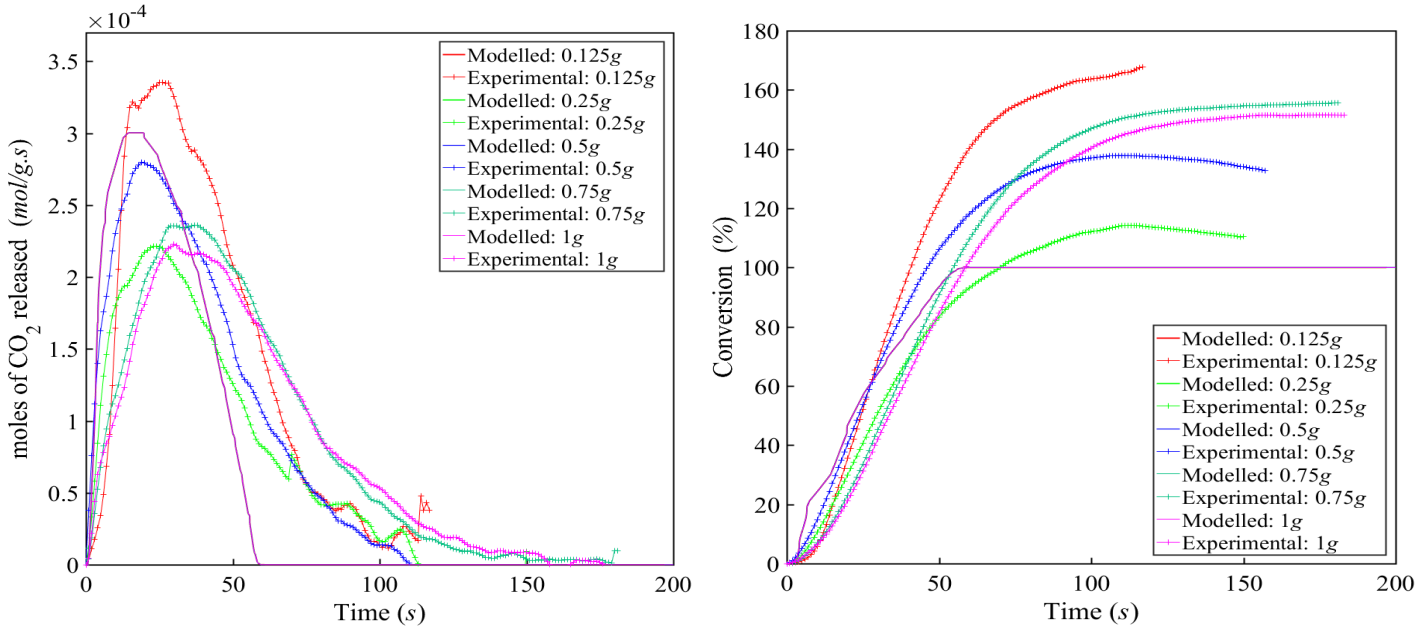

Figure 4.46a and b - Modelled and experimental, Reaction and conversion profiles for the calcination of different sample masses of limestone at 950 °C in 20 % N_2 and 80 % CO_2.

4.7.5. Effect of varying limestone type

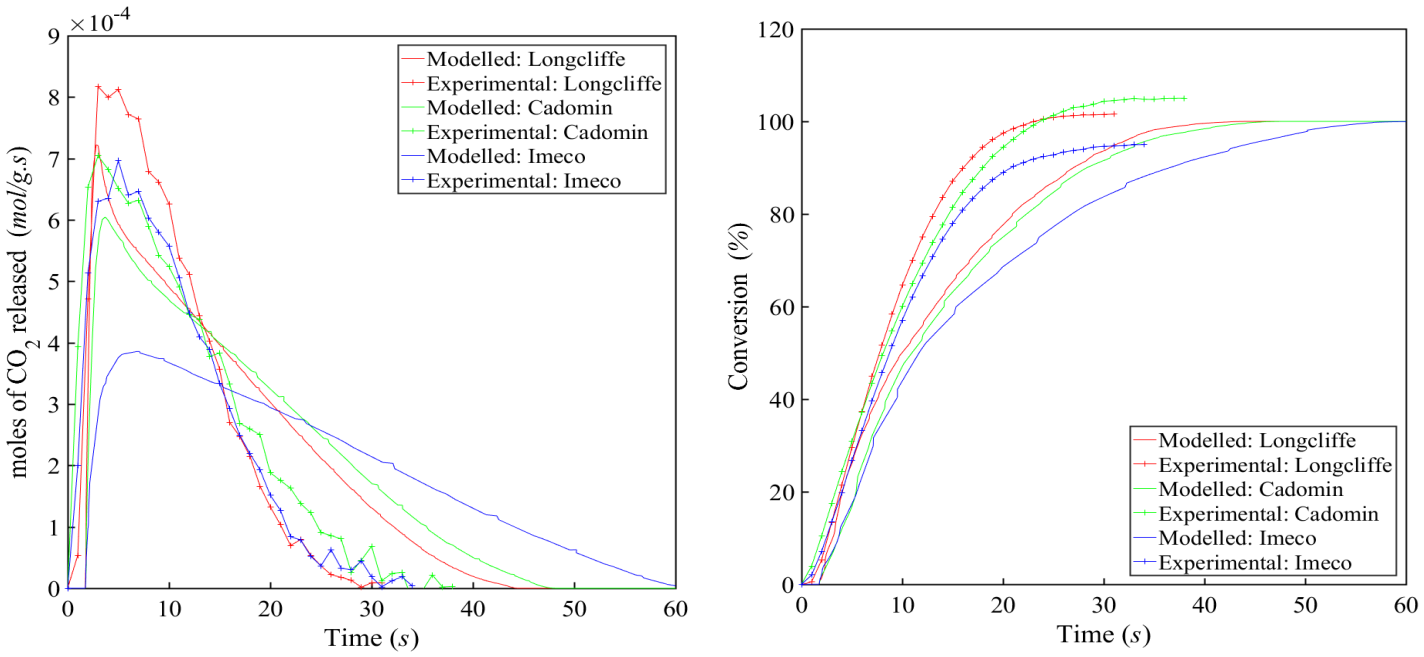

Figure 4.47a and b - Modelled and experimental, reaction and conversion profiles for the calcination of different limestones at 950 °C in 20 % steam and 80 % CO_2.

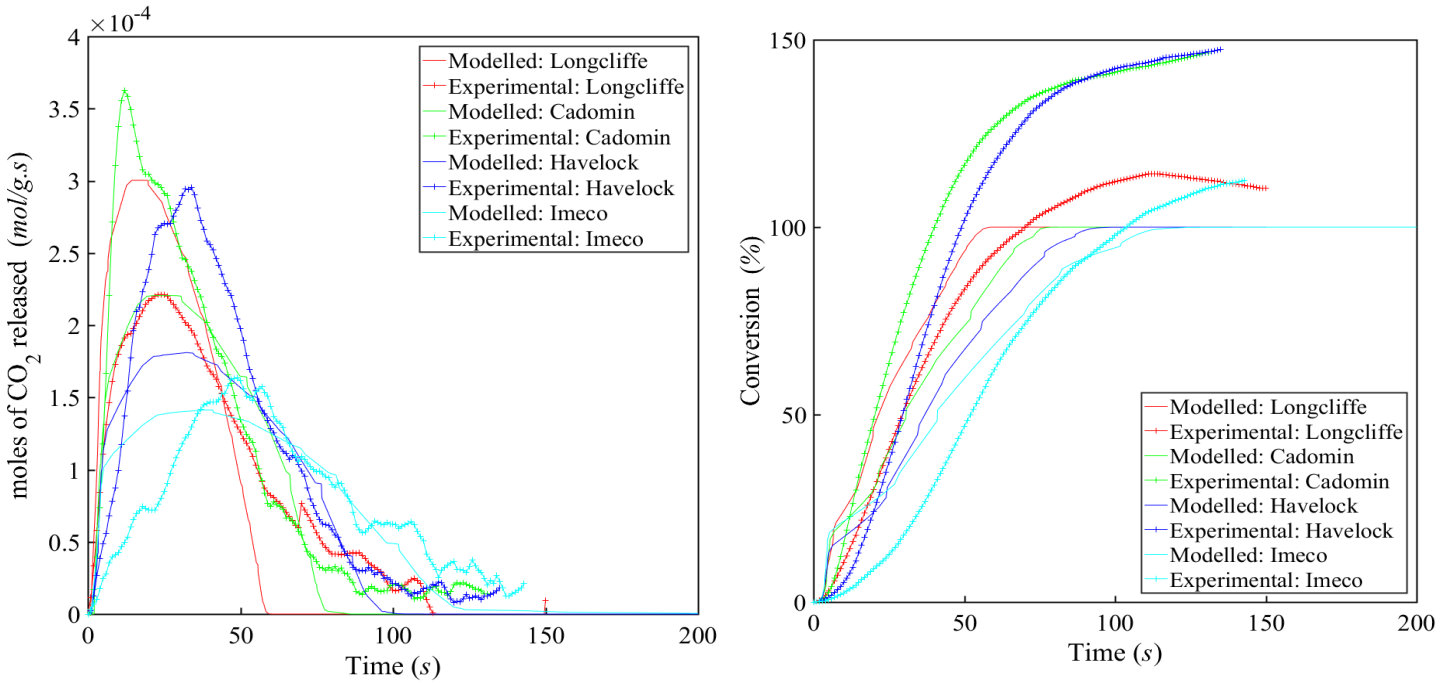

Figure 4.48a and b - Modelled and experimental, reaction and conversion profiles for the calcination of different limestones at 950 °C in 20 % N_2 and 80 % CO_2.

4.8. Modelled prediction of the physical difference due to steam or N_2 addition

It has long been known that the addition of steam to both the carbonation and calcination phases of a CaL system produces faster kinetics compared to a N_2 only system (Donat et al., 2011). This effect caused by the addition of steam has been demonstrated to be applicable to the CO_2 based system as well. The difference in rate, caused by steam addition, has been quantified throughout the experimental and modelling work presented within this chapter, however no explanation of why the addition of steam leads to an increased rate of calcination has yet been given. The literature on this matter is less than clear, some sources have suggested that the addition of steam affects the rate in a catalytic way, where the steam molecules bond to the active surface sites of $CaCO_3$ and lower the binding energy between the CO_2 and the CaO, as per Equation 4.108 (Yin et al., 2014) (Wang and Thomson, 1995).

Equation 4.108:

$$CaCO_3^* \cdot H_2O \rightarrow CaO + H_2O + CO_2$$

Where * represents an active site at the surface of the $CaCO_3$. This was the same idea that was utilised to derive the Langmuir-Hinshelwood equation for the calcination in the presence of steam in Appendix II. To further clarify potential reasons why calcination in presence of steam produces a faster rate of calcination compared to the addition of N_2, the model was applied with the arbitrary parameters shown in Table 4.11, whereby only the parameter that differs is the addition of steam or N_2. The rate equations for both systems was set to be the Equation 4.73 (i.e. the simple rate equation whereby the rate was dependent upon the partial pressure of CO_2 only and the temperature dependant rate constant was calculated (in both the steam and N_2 case) using the values listed in Table 4.11. By doing this, any catalytic or other effects were neglected and instead the only difference in the modelled rate was caused by the physical differences in the gases alone, i.e. the thermal and diffusional properties.

Table 4.11 – Table of arbitrary parameters for comparing steam and N_2 systems.

Parameter	Value	Unit
Bulk fluid temperature	950	°C
Particle radius	300	µm
Limestone type	Longcliffe	-
CO_2 concentration	80	vol.%
N_2 or H_2O concentration	20	vol.%
Arrhenius – pre-exponential factor	1×10^{12}	s^{-1}
Arrhenius – Activation energy	250	kJ/mol

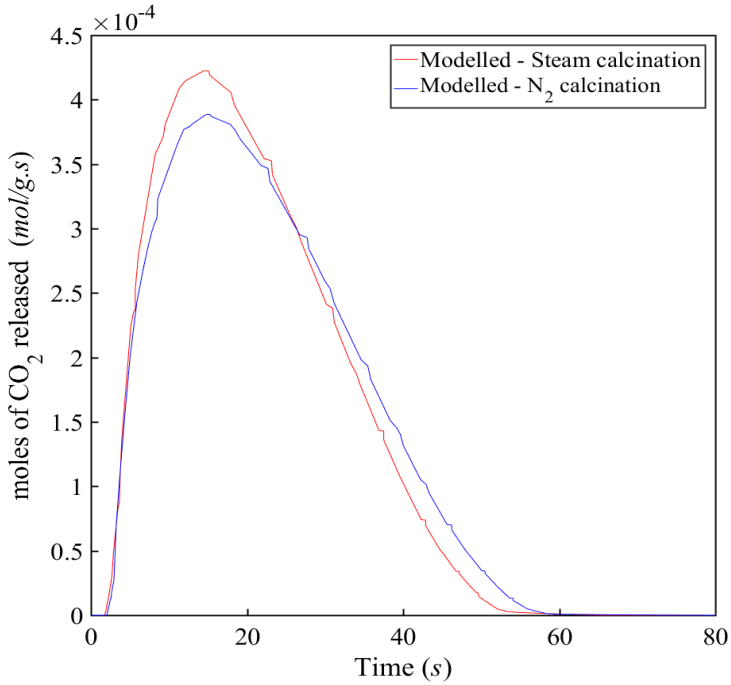

Figure 4.49 – Simulation result of the calcination particle model in the presence of steam and CO_2 or N_2 and CO_2 where kinetic and thermodynamic defining input parameters were equal.

Figure 4.49 was produced utilising the same arbitrary input parameters listed in Table 4.11 for modelling calcination in the presence of steam and calcination in the presence of N_2. The CO_2 response

of the model was compared for the two systems and the observable differences in this figure were caused only by the variances derived from the different combining laws for polar & non-polar gases (H_2O and CO_2) and non-polar & non-polar gases (N_2 and CO_2) as explained in section 4.4.5.

From the experimental data displayed in Figure 4.4 the peak rate of reaction for calcination with steam present was ~4 times greater than without steam. However, by observing Figure 4.49 it is clear that the difference in peak rate between the two modelled systems was negligible, thus it can be concluded that the rate of calcination is only minimally affected by the physical differences of the gas composition alone, this was also suggested by (Yin et al., 2014). An explanation for the increased rate of calcination in the presence of steam could be, as has been previously reasoned by (Yin et al., 2014) and (Dennis and Hayhurst, 1987), that the steam is acting as a catalyst for the reaction. This effect was incorporated into the model by application of the Langmuir-Hinshelwood derived rate equation for calcination in the presence of CO_2 and steam, and as can be observed within the figures presented within Appendix II this did suitably match the experimental data, therefore indicating that steam did play a catalytic role within these reactions.

The physical properties of steam and CO_2 gas mixture enhanced the bulk diffusivity, mass transfer coefficient and effective diffusivity (as shown in Table 4.12), these properties increased the rate of CO_2 removal from the modelled particle system compared to the N_2 calcination particle system.

Table 4.12 – Bulk diffusivity, mass transfer coefficient and effective diffusivity of gas composed of 20 vol.% steam and 80 vol.% CO_2, and 20 vol.% N_2 and 80 vol.% CO_2 at 950 °C.

	Steam system	**N_2 system**
Mass transfer coefficient, k_g	0.86	0.77
Bulk diffusivity, D_b	2.03×10^{-4}	1.80×10^{-4}
Effective diffusivity of CO_2, $D_{k\,CO_2}$	3.07×10^{-6}	2.77×10^{-6}

Another question that was initial set to be answered with this modelling was: "*Could the gas composition be influencing the heating rate of the particle?"*. Figure 4.49 does not indicate that there was a significant difference in heat up time of the particles and certainly doesn't account for the differences observed in Figure 4.4. It is possible that the differences observed in Figure 4.4 were due to experimental error in calculating the time for CO_2 to enter the analyser relative to when the sample was added.

4.9. Model limitations

The limitations of this model were mainly founded upon the choice of equations which inevitably simplified the system down but potentially excluded phenomena that occurred in the experimental data. Inadequacies in models are often accounted for in the form of 'fudge factors' or 'fitting factors', such as n in Equation 4.72 and Equation 4.73, A in Equation 4.74 and the porosity values derived from the line of best fit described in Equation 4.32.

When comparing this model to experimental data it should be noted that the model required a radius value as an input, however it is misleading to say that experiments were conducted utilising only particles of x radius, rather a range of particle diameters existed experimentally. This would have led to some degree of discrepancy between the experimental and modelled results, notably so at 500 – 710 μm which was the largest size fraction range utilised in the experimental study.

This model also lacks the ability to adequately describe the inter-particle mass transfer diffusion effect caused by the volume of the bed mass on the rate of reaction. To do this a CSTR fluidised bed model or another similar model would have been required to be applied which was outside the scope and aim of this work.

4.10. Conclusions

This study experimentally determined the rate of limestone calcination within a high CO_2 partial pressure environment diluted with either steam or N_2 within an atmospheric pressure fluidised bed reactor. The aim of this work was to determine the calcination reaction rate under realistic post combustion conditions, where a high CO_2 concentrations will exist due to the combustion of a fuel and the release of CO_2 from the carbonate material. The observed peak rate of reaction for the calcinations in the presence of steam were approximately 3-4 greater than compared to the analogous N_2 system, where N_2 was used in replacement of steam.

The effect of bed temperature, CO_2 partial pressure, particle size, sample mass and limestone type were investigated by varying each parameter individually to determine their influence. Kinetics were measured by secondary means for the steam and CO_2 experiments and N_2 dilution for the N_2 and CO_2 experiments as the CO_2 concentrations were above the measureable range by most analytical techniques.

The method utilised for determining the kinetics with steam and CO_2 present – inferred from the use of a humidity probe, proved to be more accurate and reliable than the method utilised for determining the rate of calcination in the presence of N_2 and CO_2 – dilution of the gas with additional N_2 which was then measured with an ND-IR gas analyser. The kinetic data for the N_2 and CO_2 system did result in conversions greater than 100 %, sometimes by a significant margin. Conversions over 100 % but by no more than 10 % can usually be said to be within experimental error, which was the case for the steam and CO_2 data. It was thought that the main cause for this error in measurement was the effect on the gas sampling rate caused by the N_2 dilution flow rate. Furthermore because of the relatively slow reaction rate small deviations in either gas stream could have led to significant errors at the point of analysis due to the relatively small change in concentration that was measured.

It was found that rate of calcination with respect to steam concentration was approximately zeroth order and first order with respect to N_2 concentration. The order of reaction with respect to the equilibrium driving force ($P^*_{CO_2}$ - P_{CO_2}) for the reversible calcination reaction was found to be ~4 for the N_2

experiments. Application of these orders lead to impossible and physically un-representative activation energies, therefore the orders of reaction were determined with respect to the partial pressure of CO_2 alone. This method produced much more realistic Arrhenius parameters but for the N_2 data there still lacked an acceptable fit to the experimental data. Because it was thought some other effect was influencing the rate that was not simply explained the partial pressure of CO_2 alone, especially for the set of calcinations in the presence of N_2 a Langmuir-Hinshelwood derivation was undertaken for both the calcination in N_2 and CO_2, and steam and CO_2. A suitable fit between the experimental data and the fitted parameters was achieved for the steam Langmuir-Hinshelwood equation but not for the N_2 system.

Inaccuracies in measuring fundamental particle properties such as density, porosity and surface area were discussed. The limestones tested were found to be very non-porous and lacked any overall pore structure, this convoluted the resulting porosity data significantly and as such an average was taken of the measured geopyc porosity and the calculated porosity (from mercury intrusion porosimetry and helium adsorption) in order to gain a more accurate estimate of particle porosity, thereby minimising the errors of both methods.

The effect of steam addition to the calcination gas stream was highly effective at minimising the differences in rate of calcination caused by varying the sample mass and the limestone type. Further analytical studies are required to determine the exact mechanism by which steam enhances the rate of limestone calcination. With the intention of presenting a fair comparison between the steam and N_2 experiments, all the experiments were conducted with comparable gas concentrations, temperatures and sample masses.

Following this experimental work a model was developed in Matlab to potentially answer why the experiments conducted with steam were significantly faster than with N_2 as the dilution gas. This model was developed from the fundamental heat and mass balances through a spherical particle. The model was shown to represent the experimental data quite well in most scenarios tested. Improvements were made to the Arrhenius parameters by a least squares fitting of the model and the experimental data up to the peak rate of calcination. This lead to the formulation of the following Arrhenius equations, which proved to be very successful in modelling the calcination reactions under most conditions.

Equation 4.109 - 20 vol.% Steam and 80 vol.% CO_2:

$$k_T\ (\mathrm{s}^{-1}) = 9.84 \times 10^{12}\ e^{\frac{-241{,}500}{R_i T}}$$

Equation 4.110 - 20% vol.% N_2 and 80 vol.% CO_2:

$$k_T\ (\mathrm{s}^{-1}) = 3.67 \times 10^{51}\ e^{\frac{-1157{,}900}{R_i T}}$$

Although due to the fitting method that was utilised to obtain the Arrhenius parameters (which are shown in the equations above), the actual values themselves have lost their physical meaning and cannot be said to represent the real process. The model did appear to over emphasise the internal diffusion limitation for CO_2 to leave the particle, leading to a slightly longer tail off period compared to the experimental data. The most likely cause of this was probably errors in the calculation of the porosity and tortuosity and hence the effective diffusivity. Furthermore, the calcining particles could be forming a pore structure that was not described by the model, i.e. via particle explosion due to the internal pressure increase. The model has also demonstrated that the calcination of limestone was controlled by a combination of external heat transfer and internal CO_2 diffusion.

The reaction modelling has concluded that increase in calcination rate was caused predominately by catalytic means only and the physical differences between polar and non-polar gases makes little difference to the overall rate of reaction. Further work is required to determine the mechanism of steam enhancement.

Chapter 5 – A Novel Polymorphic Sorbent for CO_2 Capture

5.1. Introduction

Sorbents for CO_2 capture within high-temperature calcium looping generally come under two main categories, firstly 'natural sorbents' which simply comprise of carbonate rocks (mostly limestones and dolomites) and secondly 'synthetic sorbents' which are materials derived from chemical reagents. Table 5.1 presents an overview of the advantages and drawbacks of each type of sorbent (Erans et al., 2016) (Blamey et al., 2010) (Broda et al., 2015) (Fennell, 2015b).

Natural sorbents like limestone, being so cheap and readily available were originally an ideal candidate for calcium looping. However it was quickly discovered that natural sorbents' initially high CO_2 carrying capacity (1 mol CO_2/mol CaO) dropped off sharply after cycling/reusing the sorbent just a few a times (Barker, 1973a). Some of the most significant improvements to the long term carrying capacity of natural sorbents has been founded on the addition of HBr as a pore stabilising dopant and by the addition of steam during cycling. The combination of these methods resulted in a 13^{th} cycle carrying capacity of 0.37 mol CO_2/mol CaO) ~3 times higher than without HBr doping or steam addition (González et al., 2016). At present, this result is currently the greatest improvement to a natural sorbents CO_2 carrying capacity that has been made.

The alternative to natural CO_2 sorbents is to use of synthetically manufactured CO_2 sorbents that have demonstrated (under certain conditions) very minimal decay in carrying capacity over multiple cycles (Erans et al., 2016). The production of synthetic sorbents is typically through some method of combing an array of chemicals, which after processing forms a precipitated mixture of sorbent and a support in a unified structure. A detailed explanation of the manufacturing techniques utilised to develop synthetic sorbents is given in Chapter 6. The use of the support is a critical element in these synthetic sorbents as they are responsible for facilitating the diffusion of CO_2 into the inner particle structure, limiting the closure of pores caused by the carbonate product layer and preventing the solid-state ion diffusion caused by sintering (Broda et al., 2015).

Table 5.1 – Advantages and disadvantages of natural and synthetic sorbents (Erans et al., 2016) (Blamey et al., 2010) (Broda et al., 2015) (Fennell, 2015b).

	Natural Sorbents	Synthetic Sorbents
Advantages	• High potential CO_2 carrying capacity (Calcite – 0.78 $gCO_2/gCaO$ = 1 mol CO_2/mol CaO) • Relatively cheap (~$\$_{2011}$ 26 ± 10 per tonne of CO_2 avoided) • Readily available • Spent material has potential to be a feedstock material for cement manufacture • Requires minimal processing	• Under certain conditions the rate of carrying capacity decay can be reduced • Stabilised and optimised pore structure • May require lower sorbent purge and replacement rates • The manufacturing process means precise quantities of each component in the final material can be controlled
Disadvantages	• Some minor impurities (commonly silica, alumina, soil/earth) • Requires crushing to suitable particle size • Particles suffer from attrition and fragmentation • Sintering leads to significant decay in carrying capacity • Requires greater sorbent purge and replenishment rates	• Often requires a lengthy preparation time • Can be dependent upon expensive chemicals • Further processing via palletisation is normally required to make the material suitable for application • Potential difficulties in particle production scalability

In the wider context of this body of work, it is understood that the combination of a CO_2 capturing material and a catalytic reforming material in a single particle is beneficial in terms to the mass transfer and overall efficiency of Sorbent Enhanced Steam Reforming (SESR) (Rout and Jakobsen, 2013). It is also understood that whilst a support structure has been investigated before (Radfarnia and Iliuta, 2014) (Zhao et al., 2016), they often focussed on stabilising the catalyst and preventing nickel grain growth rather than optimising the CO_2 sorption potential. Currently the most optimised support for a synthetic

CO_2 sorbent relies on the addition of nano-dispersed silica within the CaO matrix which produces a Ca_2SiO_4 support (Zhao et al., 2014). The work in this chapter focusses on the application of this support material and its associated benefits and drawbacks.

The work presented within this chapter has been published as a full length article within the journal Fuel (DOI: http://dx.doi.org/10.1016/j.fuel.2016.08.098) (Clough et al., 2016).

5.2. Background

In a post-combustion capture setting, the carbonator will typically operate around 650 °C with a CO_2 concentration of ~15 vol.%, whereas the calciner requires a much higher temperature, of around 900-950 °C, in order to regenerate the sorbent and overcome the endothermic reaction. Furthermore, the calciner is likely to have a high CO_2 concentration, >80 vol.%, owing to the release of CO_2 from the sorbent and from the combustion of fuel for heating the reactor.

Equation 2.1 - Carbonation reaction:

$$CaO + CO_2 \rightarrow CaCO_3 \qquad \Delta H = \text{-178 kJ/mol}$$

Equation 2.1 - Calcination reaction:

$$CaCO_3 \rightarrow CaO + CO_2 \qquad \Delta H = \text{+178 kJ/mol}$$

Compared to other solid sorbents, such as hydrotalcites and zirconates, CaO has a significant advantage as its typical initial absorption capacity is ~0.79 gCO_2/g sorbent (or carrying capacity (Blamey et al., 2010)). CaO can be readily obtained in its carbonated form as limestone, a cheap, abundant and non-toxic material, which is the basic feedstock for the calcium looping process. However, the carrying capacity of natural limestone derived sorbents degrades over multiple reaction cycles, eventually leading to a carrying capacity in the region of 0.15 $gCO_2/gCaO$ (this value can be reached in as few as 20 cycles) (Blamey et al., 2015b). The cause of this loss of carrying capacity is primarily due to sintering, which has been shown to occur by reactive and thermal sintering, thermal softening and the coalescence of smaller grains into larger grains, this results in the loss of a fine pore structure and a shift

from smaller micro- and meso-pores to larger macro-pores which are less useful for the capture of CO_2 (Alvarez and Abanades, 2005) (H. Borgwardt, 1989). Calcium looping also offers the further benefit in that when the sorbent particles have lost the majority of their reactivity, the spent material can be used as a de-carbonised feedstock in the cement industry (Dean et al., 2011a).

A range of different approaches have been investigated with the aim of overcoming the issue of sintering of CaO-based sorbents and related decay in the carrying capacity with repeated cycling. These approaches include: the use of dopants (Salvador et al., 2003) (Al-Jeboori et al., 2013) (Sun et al., 2008b); hydration and steam reactivation (Coppola et al., 2014b) (Coppola et al., 2015) (Manovic and Anthony, 2007); thermal pre-sintering (Manovic and Anthony, 2008b) (Chen et al., 2009); spacer molecule incorporation (Liu et al., 2010) and sintering resistant internal supports (Kierzkowska et al., 2013) (Broda and Müller, 2012). Recently, Zhao et al. (Zhao et al., 2014) has reported a CaO-based sorbent incorporating a supporting structure composed of Dicalcium Silicate (Ca_2SiO_4, from here on referred to as C_2S) which enabled the sorbent to retain a very high proportion of its carrying capacity throughout many cycles. The authors attributed this to phase transitions that the C_2S underwent during the normal temperature swings of a calcium looping process.

The phase transition exploited within the study by Zhao et al. (Zhao et al., 2014) was the α' ↔ β C_2S transition, which represents ca. 2 % volumetric expansion. The formation of the α' C_2S phase begins to occur at temperatures greater than 690 °C whereas the β C_2S phase begins to form when the material is already in the α' C_2S phase and the temperature reduces below 680 °C (Remy et al., 1995). Upon the first calcination of this material the α' C_2S phase will develop, thereby forming microporous channels, which the authors proposed provided an accessible pathway for CO_2 to diffuse into the sample, where it could react with free CaO. This reversible phase change leads to predictable and repeatable volumetric changes within the sorbent particles, enabling the microporous channels formed during calcination to be reopened, thereby resisting the effects of sintering. Additionally, a C_2S support is comprised of elements already found in cement and at similar concentrations, which enables the spent sorbent to retain significant value to the cement industry (Dean et al., 2011b) (Dean et al., 2011a) unlike the addition of other typical supports such as Al_2O_3 or ZrO_2.

Previous work (Zhao et al., 2014) on this type of C_2S supported sorbent attempted to evaluate its performance using a TGA operating at conditions that were not a suitable representation of expected industrial operating conditions. Calcination was carried out at a temperature of 850 °C under an atmosphere of 100% N_2 for an extended time period of 30 minutes. These conditions were not representative of a commercial scale CO_2 capture operation where the goal is to produce a concentrated stream of CO_2 ready for transportation and storage.

The use of unrealistic conditions, particularly with new sorbent materials is common (Zhang et al., 2013) (Wang et al., 2014a) (Chen et al., 2012a) (Luo et al., 2013) (Broda et al., 2012b) (Sun et al.) (This is only a small selection of articles where unrealistic conditions were utilised for cycling experiments in a TGA) and the effect of doing so can lead to exaggerated findings. More representative operating conditions were first comparatively investigated in this context by Manovic et al (Manovic et al., 2009) where limestone samples were calcined in 100% CO_2 at 950 °C; showing that harsh conditions during the calcination stage leads to significantly lower carrying capacities. Some synthetic sorbents and natural limestone derived sorbents, have been comparatively tested under realistic operating conditions, the synthetic sorbents showed a greater ability to resist sintering degradation but decayed similarly to the natural sorbents when calcination occurred under the harshest of conditions (Grasa et al., 2007). Limestone-derived sorbents have also been calcined under realistic conditions in the presence of SO_2 whilst at high partial pressures of CO_2 (Lu et al., 2009). It was found that the SO_2 irreversibly reacted to form $CaSO_4$, which in addition to the enhanced sintering caused by high-temperature and high partial pressures of CO_2 led to the characteristic decay in carrying capacity.

Here we attempt to address some of the limitations identified in the previous work (Zhao et al., 2014) involving the C_2S supported CaO by testing the resilience of the polymorphic, pore-reforming nature of this support and its ability to preserve the reactivity of the sorbent over repeated cycling at conditions more similar to those of a commercial post-combustion capture calcium looping system. Principally, the calcination conditions have been modified, as the influence of high-temperature CO_2 on the rate and extent of sintering has been shown to be the most significant parameter on the sorbents longevity (Manovic et al., 2009). The carbonation time was also shortened to 5 minutes since it is not realistic to

have such long carbonation times in an industrial setting, although the authors accept that even 5 minutes could be considered a long time period for carbonation. We also introduce a novel gas switching method that was developed to minimise, as much as possible, any additional carbonation as the temperature was ramped between carbonation and calcination conditions. This gas switching concept involved ramping the CO_2 concentration from 15 % to 100 % CO_2 as the temperature was ramped from the carbonation to the calcination phase in line with the thermodynamic equilibrium position of the system.

5.3. Material and Methods:

A detailed description of the sorbent preparation method used in this work was provided by Zhao et al (Zhao et al., 2014); only a brief outline of the procedure is provided here. A solution consisting of tetraethyl orthosilicate (TEOS, *Sigma Aldrich*) and nitric acid (*VWR*) was prepared and stirred for 1 hour. The nitric acid performed the role of a protonating agent to allow the hydrolysis reaction to go to completion (Equation 5). This solution was then added to a second solution prepared by dissolving calcium acetate (*Sigma Aldrich*) in deionised water. The resulting mixture was stirred thoroughly before the water was removed by freeze drying or heat drying. The freeze dried sample was frozen before it was freeze dried (*VirTis, SP Scientific BenchTop Pro* freeze dryer) at approximately -44 °C and ~50 μBar (this sample will be referred to as FD-C_2S-CaO). The heat dried sample was dried on a hot plate at 75 °C with a magnetic stirring bar until a thick paste was formed (this sample will be known as HD-C_2S-CaO). At this stage, the mixture consisted of a well-mixed fine powder of calcium acetate and hydrolysed orthosilicate; the precursor powder was heated in a Lenton horizontal tube furnace to 950 °C (ramp 20 °C/min) and held for 1 hour under air which acted as an oxidising gas. This ensured that the remaining carbonaceous compounds were completely combusted and removed from the sample, and most importantly, the crystalline C_2S compound was formed (Equation 5.2). The C_2S was formed by a solid-solid reaction that is more commonly associated with the manufacture of cement clinker.

Equation 5.1 - Hydrolysis reaction:

$$Si(OC_2H_5)_4 + 4H_2O \xrightarrow{H^+} H_4SiO_4 + 4C_2H_5OH$$

Equation 5.2 - Calcination reaction:

$$H_4SiO_4 + 2Ca(CH_3CO_2)_2 + 8O_2 \rightarrow Ca_2SiO_4 + 8CO_2 + 8H_2O$$

The molar ratio of Ca to Si was maintained at 9:1 throughout all experiments so that the results were directly comparable with the sorbents reported previously (Zhao et al., 2014). In addition this molar ratio was understandably shown to have the highest carrying capacity of the ratios tested, yet maintained the polymorphic ability of the sorbent.

Analysis with an X-ray Diffractometer (XRD) utilising Cu$K\alpha$ radiation (PANalytical, Almelo) was carried out to assess whether the phase formations had occurred in the correct proportions during the sorbent preparation stages. To quantify the intensity of the XRD peaks and thus derive the proportions of each phase, a quantitative phase analysis via Rietveld refinement was performed on the XRD data using the open source GSAS-II program (Toby and Von Dreele, 2013).

Initially, the temperature of the tube furnace was set to 850 °C for 1 hour to match the conditions of the original paper by Zhao et al. (Zhao et al., 2014), however the XRD results showed an amorphous mix with no distinguishable peaks for any C_2S phases. The temperature setpoint was subsequently altered to produce samples thermally treated at 900 °C and 950 °C (each held for 1 hour), however, it was not until 950 °C that the peaks became apparent in the predicted quantities. The difference here is likely to be because in the paper by Zhao et al. (Zhao et al., 2014), the samples' thermal transition step was undertaken in a box furnace where the temperature control was not as accurately calibrated as the tube furnace that was used in this work.

5.3.1. TGA Setup and Gas Control

The multi-cycle performances of the sorbents for CO_2 capture was investigated using a TGA (TA Q5000IR). The operating conditions for the TGA cycling experiments are presented in Table 5.2.

Table 5.2 – Operating conditions for the TGA during multiple calcium looping cycles.

Parameter	Value
Carbonation temperature / °C	650
Carbonation time / min	5 & 30
Carbonation, CO_2 gas percent / %	15
Calcination temperature / °C	850 & 950
Calcination time / min	1
Calcination, CO_2 gas percent / %	0 & 100
Total gas flow rate / cm^3/min at 20 °C	110
Number of cycles	15

The mass of sample loaded into the TGA was maintained at a constant value of 4 ± 1 mg. Mass transfer effects were investigated by varying the sample size, however no significant effect on the kinetics or extent of reaction was determined for sample masses below 10mg. Samples were pre-calcined in the TGA (not shown in Figure 5.1) under 100% N_2 at 950 °C for consistency and to ensure the samples were completely calcined before beginning the cycling experiments.

Nitrogen (99.9% purity, BOC) was utilised as the balance gas for all concentrations of CO_2 (99.9% purity, BOC) specified. The gas flow rates were controlled using an external mass flow controller (Brooks) set-up which was controlled via a separate program (the code was written in-house) using Agilent VEE. The TGA and MFC control programs were synchronised using the TGAs' output signal function and a USB data acquisition (DAQ) module (Measurement Computing USB-1208FS). A CO_2

concentration of 15 % was used during the carbonation phase of the cycling experiments to simulate the flue gas from a typical coal combustion power plant (Samanta et al., 2012).

To switch between the carbonation conditions and calcination conditions specified, the CO_2 gas concentration had to be carefully adjusted. If a direct switch between 15% and 100% CO_2 (profile A in Figure 5.1) was used after the 5 minutes of carbonation then the temperature would still be well in the carbonation regime and thus the sample would over carbonate leading to erroneous results. This additional over-carbonation is similar to that described by Arias et al (Arias et al., 2012). Nor could the gas be switched to 100% N_2 at the end of the 5 minutes as the sample would begin calcination before the set point temperature was reached and it would defeat the purpose of operating at realistic conditions (profile B in Figure 5.1).

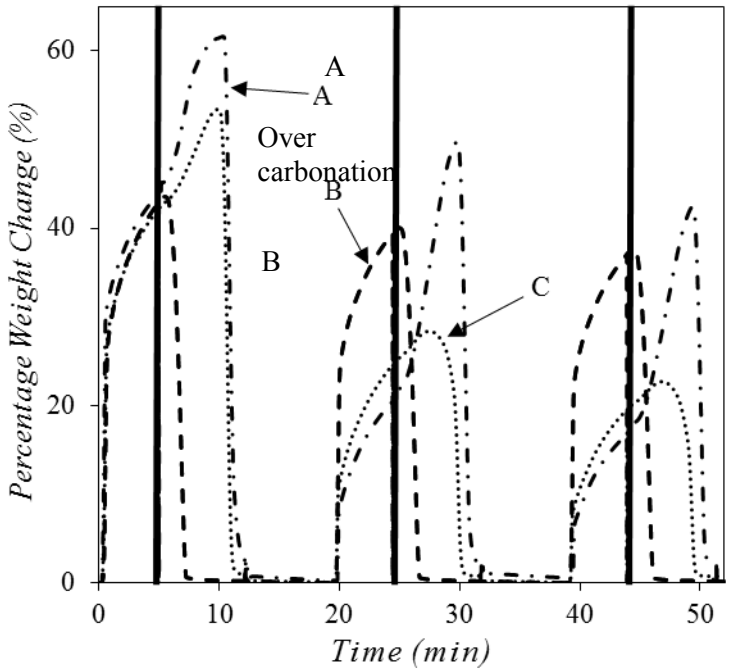

Figure 5.1 – Percentage weight change during the initial 3 carbonation/calcination cycles of the freeze dried CaO-C_2S-CaO sorbent when subjected to different gas switching methods. The thick vertical lines represent the points of gas switching, i.e. end of carbonation, start of calcination. For calcination: profile A switched directly to 100% CO_2 after carbonation, profile B switched to 0% CO_2 after carbonation, profile C uses the temperature programmed ramping of CO_2 after carbonation. Calcination set conditions were: 950 °C for 1 minute. Carbonation set conditions were: 15% CO_2, 650 °C for 5 minutes. Constant total flow rate of 110 cm^3/min (at 20 °C).

Consequently, to overcome this problem, the CO_2 gas concentration was increased at a rate set by the TGA's heating rate (profile C in Figure 5.1); later on, this is referred to as 'temperature programmed CO_2 partial pressure ramping'. Here, the equilibrium thermodynamics of the $CaCO_3$/CaO system were taken into account to produce a best fit third order polynomial for the rate of heating with the rate of CO_2 partial pressure increase. During the temperature programmed CO_2 ramping, the CO_2 partial pressure was kept above the equilibrium partial pressure by an average of 2.4 ± 0.2 kPa, this ensured the sample stayed in the carbonation phase and did not begin calcining before the desired CO_2 concentration was reached. Figure 5.2 displays a plot of CO_2 partial pressure (from the valve output) and time during this ramping period. By keeping the sample in the carbonation phase, there was some unavoidable over carbonation, but this was significantly lower than the case where the CO_2 partial pressure was directly switched, as can be seen in Figure 5.1. The flow of N_2 was adaptively modified to maintain a constant total flow rate throughout.

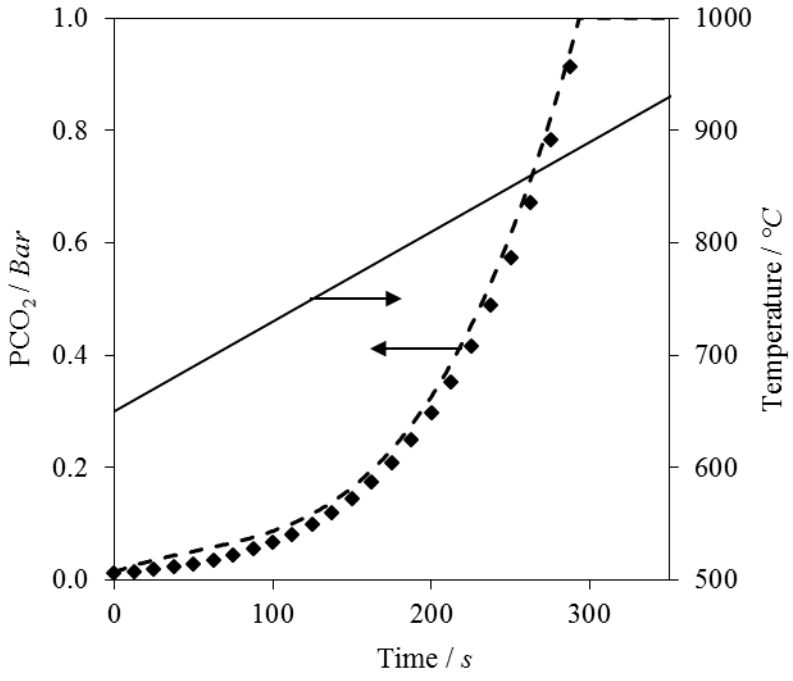

Figure 5.2 – Partial pressure of CO_2 and temperature plotted against time during the temperature ramping period after carbonation but before calcination. (♦) denotes the equilibrium results from ThermoVader (McBride et al., 2004), the dashed line (- - -) denotes the actual mass flow controlled CO_2 partial pressure and the solid line (—) denotes the temperature of the system.

5.4. Results and Discussion:

For comparison, Figure 5.1 displays the effect of changing the gas concentration via the different approaches discussed above is presented for the first 3 cycles. All trials displayed in Figure 5.1 utilised the FD-C_2S-CaO sorbent and were carbonated at 650 °C for 5 minutes, under 15% CO_2 with N_2 as the balance gas. The zeroth calcinations (i.e. the calcination of the original sample) of all samples were conducted under 100% N_2 at 950 °C for consistency. All subsequent calcinations were programmed to take place at 950 °C for 1 minute under 0% CO_2 (profile B) or 100% CO_2 (profiles A & C).

An important detail to notice in Figure 5.1 is the increase in mass at the end of carbonation and start of calcination period (marked by the thick vertical lines). Profile A of Figure 5.1 shows a significant over-carbonation as the gas was switched to 100 % CO_2, as a result of this there was a greater carbonation driving force ($P_{CO_2} - P_{eq}$) that led to the rapid reaction with CO_2 in the period of time leading up to the temperature at which the equilibrium position of the system transitioned from carbonation to calcination. Profile B of Figure 5.1 illustrates the immediate onset of calcination, occurring directly after the carbonation period, as the gas was switched to 100% N_2. The lower temperature calcination will have limited the extent and rate of both thermal and reactive sintering of the sorbent material resulting in the less severe decay observed in carrying capacity (measured after 5 minutes at the end of the carbonation period) compared with the samples calcined under 100% CO_2. Profile C of Figure 5.1 shows the benefit of the temperature programmed CO_2 partial pressure ramping system, where there was less over carbonation. The first cycle in profile C does show considerable over-carbonation compared to the following cycles. This was mostly likely because of highly reactive nascent CaO in the raw material that carbonated even with only a mild driving force. This was much less evident in the subsequent cycles and is thought to be due to the sintering of the sample which also explains why the rate of carbonation was lower during the temperature ramping stage.

The temperature set point for the calcination was evaluated based on the equilibrium line between CaO and CO_2, and the expected CO_2 partial pressure within a commercial calciner. This equilibrium line was calculated using Equation 5.3 (García-Labiano et al., 2002) and was supported with thermodynamic

modelling using the ThermoVader excel add-in (McBride et al., 2004). From application of Equation 5.3 and the thermodynamic data, it was calculated that the temperature required for calcination under 100% CO_2 at atmospheric pressure is at least 898 ± 4 °C. This means that despite setting the calcination temperature to 950 °C, the calcination actually started before this temperature was reached and the rate of calcination increased as the temperature rose further from this value.

Equation 5.3:

$$K_{eq} = 4.137 \times 10^{12} exp\left(\frac{-20474}{T}\right)$$

Here, K_{eq} is the equilibrium constant for the reaction described by Equation 2.1 and T is the temperature (K).

The TGA cycling data was analysed in a Matlab routine that amongst other processes applied Equation 5.4 to calculate the carrying capacities of the novel sorbent (as presented in Figure 5.3).

Equation 5.4:

$$C = n_{CO_2} \frac{RMM_{CaCO_3}}{M_{CaCO_3} P_{CaCO_3}} \times 100\%$$

Here C is the carrying capacity, also referred to as CaO conversion, mol CO_2 / mol $CaCO_3$, n_{CO2} is the total number of moles of CO_2 released during the calcination reaction, calculated from the mass change and the relative molecular mass (RMM), RMM_{CaCO3} is the relative molecular mass of $CaCO_3$, M_{CaCO3} is the mass of $CaCO_3$ equivalent in the original material and P_{CaCO3} is the purity of $CaCO_3$ equivalent in the original material, *%*.

Three repeats of all experiments were carried out and the standard deviation at each cycle was calculated to provide an estimation of error, this error can be seen as error bars in Figure 5.3. The sorbents calcined in atmospheres containing no CO_2 (▲ & ∆) displayed a significantly higher carrying capacity than those that were calcined under more realistic conditions i.e. 100% CO_2 (● & ○). Calcining the sorbents at higher temperatures and high partial pressures of CO_2 is well known to enhance sorbent sintering mechanisms (Lu et al., 2009) (García-Labiano et al., 2002) (Fennell et al., 2007) (Manovic and

Anthony, 2010b) (Borgwardt, 1989) (Agnew et al., 2000). The mechanism for the CO_2 sintering is thought to be grain boundary diffusion and a surface diffusion influenced by CO_2 via catalytic means, this results in an enlargement of the grain size and a reduction in the reactive surface area. It is thought that because this process occurs above the dissociation temperature of $CaCO_3$ the process is therefore catalytic, more information can be found in the literature (Borgwardt, 1989). The sintering leads to a loss of surface area and reduction of the porosity, leading to a transition from fast, surface-controlled reaction to slow solid state diffusion-controlled process within the lattice of the material (Abanades and Alvarez, 2003). The decay in carrying capacity, of the samples calcined in 100% CO_2 (shown in figure 3) display a decline that is consistent with that of all CaO based sorbents, including natural limestone.

On further examination it can be seen that the temperature of calcination had a significant effect on the long term carrying capacity (Figure 5.3), which is consistent with the work of Manovic et al, (Manovic et al., 2009). This can be observed in Figure 5.3 by comparing the sorbents that were each calcined in 0% CO_2 at both the higher temperature of 950 °C (▲ & ∆) and at the lower temperature of 850 °C (◇ & ♦). The samples (◇ & ♦) calcined at 850 °C were aimed to replicate the conditions utilised by Zhao et al, (Zhao et al., 2014), i.e. carbonation under 15% CO_2 balanced with N_2 for 30 minutes at 650 °C and Calcination under 100% N_2 at 850 °C no dwell time. The carrying capacity results for the replicated samples shows a more substantial decline with increasing cycle number than was observed in the original work. All of the experiments were checked and repeated; the results indicate that there was potentially a difference caused by the different production methodology of the C_2S (though it should be noted that the decay in reactivity was still very low).

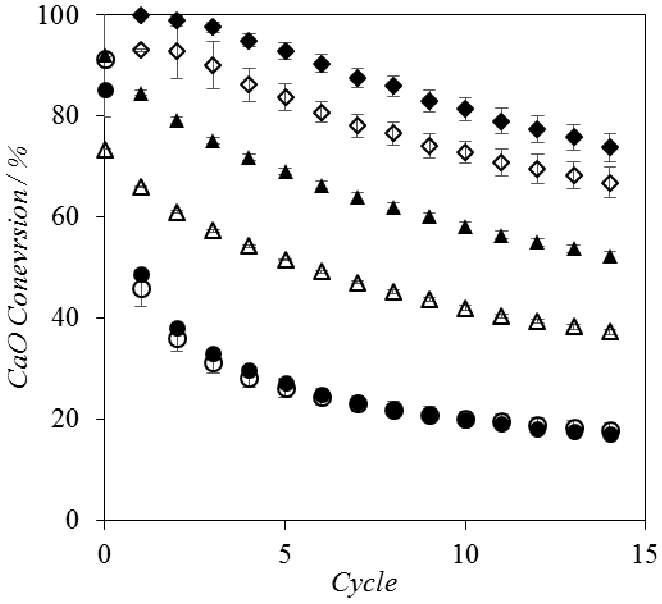

Figure 5.3 – Carrying capacities of the novel sorbent produced by different methods and subjected to either 0% or 100% CO_2 during the calcination step; all other conditions are listed in Table 5.2. For comparison, two replicate samples were created and examined under the same conditions specified in the paper by Zhao et al (Zhao et al., 2014). FD = Freeze dried, HD = Heat dried. (▲) FD-C_2S-CaO 0% CO_2 calcination, (△) HD-C_2S-CaO 0% CO_2 calcination, (●) FD-C_2S-CaO 100% CO_2 calcination, (○) HD-C_2S-CaO 100% CO_2 calcination, (♦) FD-C_2S-CaO Matches the conditions by Zhao et al (Zhao et al., 2014), (◇) HD-C_2S-CaO Matches the conditions by Zhao et al (Zhao et al., 2014). Conditions of Zhao et al's work utilised a 30 minute carbonation at 15 vol.% CO_2 and a calcination in 0% CO_2 for 1 minute.

Figure 5.3 displays evidence that the method of production did influence the trend in carrying capacity decay. The two production methods utilised for the production of the novel sorbent were heat drying and freeze drying; the freeze dried precursor material took longer to produce because the rate of water loss was lower. It has been previously suggested (Zhao et al., 2014) that by freezing the samples, large dendritic ice crystals were formed which left enlarged pores when the water sublimated away. As such, an increased pore volume and an interlinked pore structure was produced which may have improved the diffusion of CO_2 during carbonation. The freeze dried sorbents tended to present a higher initial carrying capacity than the heat dried sorbents under all scenarios investigated, but the relative loss of

each sample's carrying capacity over 15 cycles was irrespective of the production method used. The final carrying capacities, after 15 cycles, for the freeze dried samples calcined in 0% and 100% CO_2 were 0.23 and 0.08 $gCO_2/gCaO$, respectively. For the equivalent heat dried samples, the final carrying capacities, were 0.16 and 0.07 $gCO_2/gCaO$, respectively. The sorbent investigated under identical conditions to those used by Zhao et al (Zhao et al., 2014) presented a much higher 15^{th} cycle carrying capacity; 0.39 $gCO_2/gCaO$ (or a conversion of 74 %) was achieved for the freeze dried sorbent and 0.34 $gCO_2/gCaO$ for a heat dried sorbent. It can thus be shown that using harsh but reasonably realistic calcination conditions led to ~80% drop in 15^{th} cycle carrying capacity.

5.4.1. C_2S sorbent vs limestone sorbent

The reason that this type of sorbent was capable of minimising the extent of deactivation, under certain conditions, was as a result of the C_2S phase changes that took place when the temperature was cycled. During the heating up period to the calcination temperature, the C_2S formed the α' phase and the density increased to 3.38 g/cm^3, then as the samples cooled to the carbonation temperature, the C_2S formed the β phase and its density decreased to 3.31g/cm^3 (Remy et al., 1995). As such, these phase changes produced a small force inside the particle which aided the reformation and reopening of the pore channels. This suggests that more of the CaO was available for carbonation in the following cycle; this was the main advantage for this type of novel sorbent compared to natural limestone. Of course, the phase change, by producing micro-cracks, could change the mechanical stability of the particle, though the powdered nature of the sorbent means that these experiments cannot be used to determine whether or not this is an issue.

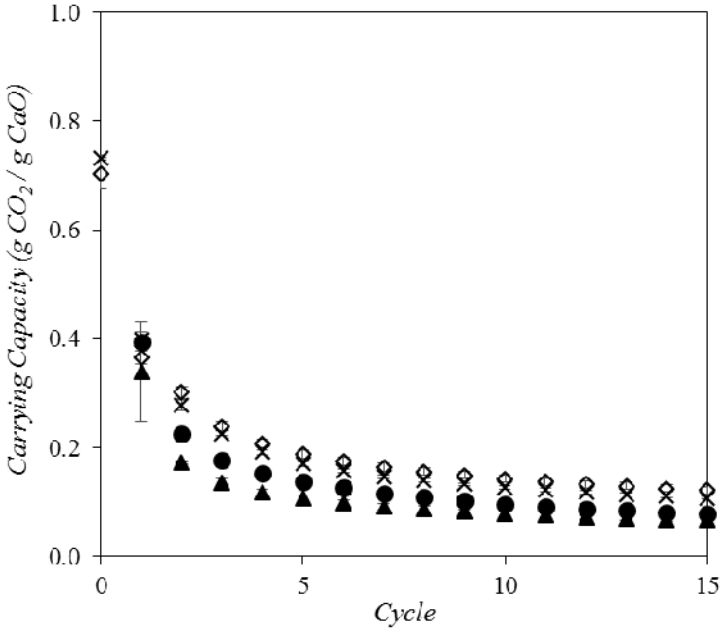

Figure 5.4 – Carrying capacity comparison of the novel sorbent against two natural limestones. Both the limestones and the novel sorbent were calcined under 100% CO_2 at 950 °C for 1 minute using the temperature programmed ramping that was described earlier. Carbonation was performed at 650 °C for 5 minutes under 15% CO_2. FD = Freeze dried, HD = Heat dried. (x) Longcliffe limestone, (◇) Imeco limestone, (●) FD-C_2S-CaO 100% CO_2 calcination, (▲) HD-C_2S-CaO 100% CO_2 calcination.

The effect of realistic cycling conditions can be observed when comparing both the HD and FD novel sorbents against the two commercially available limestones in Figure 6.2. It can be seen that when using harsh conditions, the final carrying capacity was not enhanced by the novel polymorphic spacers, despite the sorbent being very promising when calcined with no CO_2 present. All of the samples, including the two natural limestones (Longcliffe and Imeco) were examined on the same TGA under the same conditions to ensure that the results were directly comparable; the standard deviation of the three repeats is displayed as the error bars in Figure 6.2. The novel sorbent demonstrates a similarly high CO_2 uptake, due to the high CaO to C_2S ratio, before rapidly sintering and eventually leaving only around 20% of the initial CaO accessible for conversion to $CaCO_3$. For the novel sorbent, the 15th (g CO_2 /g CaO) cycle carrying capacities were slightly lower than that of the natural limestone, this was thought to be caused impurities or structural differences in the limestone preventing full sintering of the CaO.

5.5. Conclusions

This TGA study has investigated a novel type of CO_2 sorbent based on the polymorphic ability of dicalcium silicate (C_2S) to change its volume and consequently generate pores during the temperature swings of the calcium looping process. The sorbent has previously displayed an excellent ability to retain a very high carrying capacity over multiple cycles, this study has investigated the sorbent's reactivity decay under more realistic conditions.

The operating conditions for calcination were set to be similar to those of an industrial calciner within a calcium looping process, namely a high CO_2 partial pressure and a correspondingly high-temperature. The phenomenon of high-temperature CO_2 sintering during the calcination dramatically affected the sorbent's ability to absorb and release CO_2. The same effect was observed with natural limestone too.

This paper further underlines the importance of conducting measurements of carrying capacity decay under realistic conditions when working with novel CO_2 sorbents so as to make a fair judgement as to the sorbent's actual potential. The authors have presented an advanced TGA method for assessing a sorbents' CO_2 carrying capacity under realistic conditions by minimising the amount of over carbonation between cycles.

Chapter 6 – Sorbent Enhanced Steam Reforming (SESR) – Combined Particle Production and Testing within a Spout-fluidised Bed Reactor

6.1. Combined Particles for SESR

6.1.1. Introduction

This chapter will investigate the manufacture of combined sorbent and catalyst particles and their application within a spout-fluidised bed reactor (details of the design and construction were presented within Chapter 3) for biomass SESR.

Based on the evidence presented within the literature review (Chapter 2) it was noted that a significant issue regarding the production of H_2 via SESR was the operation position relative to the equilibrium position of the SESR reactions. This operating position, which is defined by the operating temperature, pressure, flow rates and steam to carbon ratio will consequently affect the produced H_2 purity and total gas yield. Furthermore it has been documented that the production of H_2 via the SESR process is limited the mass transfer diffusional resistances that occur between the catalytic active sites and the CO_2 sorbent active sites (Bhat and Sadhukhan, 2009). A method that has been developed to overcome this diffusional resistance is to combine the sorbent and catalyst into a single particle, thereby creating a multifunctional combined particle which significantly reduces the distance that the CO_2/produced gases are required to travel between the different active sites (Dietrich et al., 2005) (Rout and Jakobsen, 2013). Figure 6.1 pictographically displays the diffusion resistances within a SESR system and the benefit of combining the sorbent and catalyst within a single particle compared to an un-combined particle system. As can be observed in Figure 6.1a, the dual particle system requires the produced gases to re-enter the gas phase after they have been catalytically reformed/cracked therefore requiring the gas to undergo two stages of gas-to-solid diffusion. With Figure 6.1b only one stage of gas-to-solid diffusion is required thereby simplifying the diffusion distance and moves the process towards a pseudo one step process. These are of course simplified systems and in reality both the catalytic and sorption reactions are occurring

simultaneously in both the single and dual particle systems (albeit at different rates). It should also be noted that the H_2 production efficiency in both systems is dependent upon the contact (and hence diffusion rate) of steam to the produced gas (which is within the particles structure for the single particle system) as the key H_2 producing reactions such as steam reforming and water-gas shift require steam to be present (Florin and Harris, 2008a).

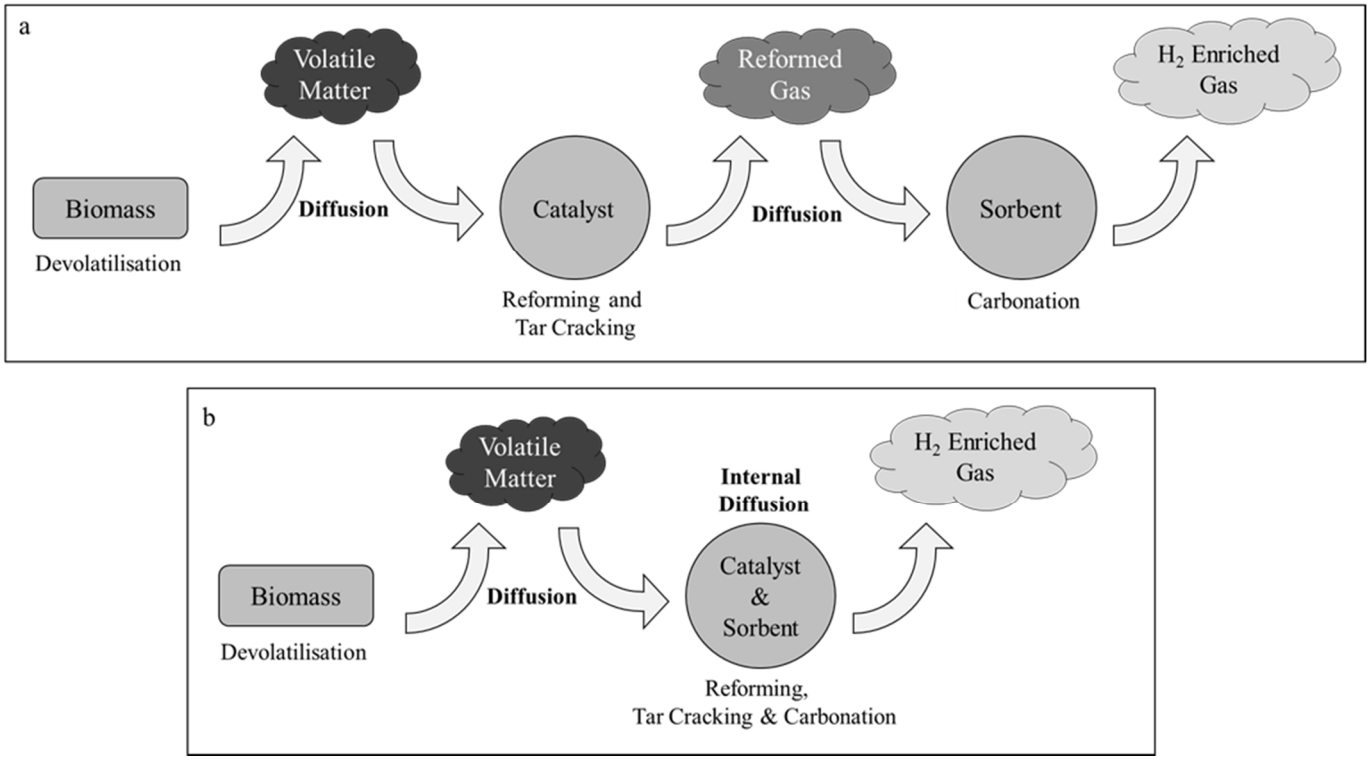

Figure 6.1a and b – Representation of the diffusional resistances present in dual (a - top) and single (b - bottom) particle SESR systems.

Grünewald et Agar (Grünewald and Agar, 2004) and Lugo et Wilhite (Lugo and Wilhite, 2016) presented performance analyses of single combined particles for SESR applications which were structured in multiple variations from a sorbent core and catalyst shell to a catalyst core and sorbent shell, each variant was compared to a single homogenously mixed particle. Modelling of the water-gas shift reaction suggested the greatest conversion enhancement of multifunction combined particles can be found with homogenously mixed particles where the mass transfer Stanton number is low and the Thiele modulus is low. Furthermore their modelling of the Sorption Enhanced – Steam Methane Reforming (SE-SMR) reaction showed a greater adsorbent utilisation when the multifunctional particles were homogeneously mixed as opposed to when a core and shell type particle was applied.

Whilst many models have been developed to describe the utilisation of combined particles for SE-SMR (Aloisi et al., 2016) (Rout and Jakobsen, 2013) (Rout et al., 2011) (Solsvik and Jakobsen, 2011) (Li and Cai, 2007) (Lugo and Wilhite, 2016) (Jakobsen and Halmøy, 2009), biomass SESR (including model compounds of biomass) (Mahishi et al., 2007) and water-gas shift reactions (Grünewald and Agar, 2004) the experimental application of combined particles has been predominantly TGA focussed (García-Lario et al., 2015b). Rout et al. (Rout et al., 2014) investigated the kinetics of SE-SMR within a TGA and fixed bed reactor and concluded that due to gas-solid mass transfer limitations within a TGA, a fixed bed reactor was a better tool for studying the relatively fast kinetics of SE-SMR. Experimental research into the use of combined core and shell and homogenously mixed particles for SE-SMR has been conducted on many occasions within fixed bed reactors (Ding and Alpay, 2000) (Satrio et al., 2005) (Satrio et al., 2007) (Martavaltzi and Lemonidou, 2010) (Chanburanasiri et al., 2011) (Xie et al., 2012a) (Broda et al., 2012a) (Broda et al., 2013) showing, under a range of conditions (usually optimised by a high S/C ratio) and multiple different sorbent/catalyst/particle production techniques, that the produced gas can achieve very high H_2 concentrations (>80 mol.%). As of yet, combined particles for biomass SESR has had little research focus, one example of this system was found in the literature by Li et al. (Li et al.), they employed a two stage fixed bed and Ni-impregnated particles (<124 μm) and looked at the product gas upgrading of pyrolysed and gasified corn-stalk biomass. Their optimal result of 85.1 vol.% H_2 was achieved with a 15 wt.% NiO loading applied to a γ-Al_2O_3 supported, calcined dolomite.

The use of fixed bed reactors, whilst useful for a quick analysis of potential materials for their cyclic ability to undergo SESR, are not representative of the likely operating environment of an SESR reactor for biomass processing, instead circulating fluidised beds are considered to be the most suitable technology for these types of gas-solid reactions (Harrison, 2008) (Johnsen et al., 2006b). Fixed bed reactors are currently the most common method of assessing SESR reactions as they are easier to operate and are comparable to conventional SMR operation which is also a fixed bed process. A fixed bed system also allows simple scale up by adding more beds and provides a lower CAPEX and OPEX compared to fluidised beds. However, fluidised beds offer the potential for efficient mixing of the gas

and solids leading to excellent heat distribution and a minimised external mass transfer resistance and an easier operation that does not require high-temperature gas switching valves as a multiunit fixed system would (Johnsen et al., 2006b) (Fennell et al., 2007) (Harrison, 2008). Fluidised beds are however limited by the attrition of bed material which could be a significant issue if a nickel catalyst is present as the flue gases will need to be thoroughly cleaned in order to minimise the emissions of Nickel into the environment. Nickel is known to be a highly toxic carcinogen and therefore attrition resistance of materials containing nickel operating within a fluidised bed needs to be accurately assessed to enhance the safety of the process. A circulating fluidised bed reactor has been utilised for SE-SMR previously and was able to produce H_2 at 97-98 vol.% purity, continuously (8 hours) when utilising a Ni catalyst that represented approximately 50 % of the bed material (Arstad et al., 2012). A fast fluidised bed setup, much like an entrained flow reactor, has been utilised for SMR previously and was able to demonstrate that with the addition of a H_2 permeable membrane a thermodynamic equilibrium shift can be achieved similar to that achieved by the addition of a CO_2 adsorbent (Chen et al., 2003).

Most of the previous studies that have experimentally investigated the use of combined particles have employed a supporting material within their combined particles. Typically this support is alumina (MgO and ZrO_2 are also common supports), which reacts with calcium oxide at the calcination temperatures to form a calcium-aluminate cementitious structure; the fundamental aim of this and all other supports is to minimise the solid state grain/ion diffusion caused by sintering. A suitable support should have a Tammann temperature high enough to resist thermal sintering during the normal temperature operation of a calcium looping system (approximately the same temperatures are utilised for SESR) (Lu and Dai, 2014). Tammann temperature is defined as half the melting point of the material and is considered the temperature above which atoms have sufficient energy for bulk movement within the lattice structure (Baerns, 2013).

Several different methods of producing these combined catalyst and sorbent materials have been previously investigated. The most utilised material preparation methods for combined particles are summarised in Table 6.1 where a scaled definition has been made between low- and highly-engineered methods. Low-engineered preparation methods involve minimal/simple processing and are often cheaper but can lead to inferior characteristics and performance compared to highly-engineered materials. Highly-engineered materials require more/difficult processing techniques, often start with chemical reagent precursors, require more time and expertise to produce and because of these reasons they can be more expensive but they can also produce very effective materials. The production of particles from these materials is predominantly performed by extruding a paste through a suitable mesh or by forming a bulk solid which is then crushed and sieved.

Table 6.1 – Combined particle material production methods, low- to highly-engineered methods (Merkus and Meesters, 2015) (Brinker and Scherer, 1990) (Li et al., 2005).

	Materials preparation method	Approximate methodology
Low-engineered	*Wet granulation (sometimes referred to as mechanical mixing)*	Solid materials are ground to a powder then dry mixed for homogeneity, a solvent is added to bring the material into a workable paste which can then be formed into particles.
	Hydrolysis	Raw $CaCO_3$ is calcined into CaO, to which DI water and other solvents/binders/supports/catalysts are added to form a highly disperse $Ca(OH)_2$ based mixture. The binders are evaporated and finally the material calcined to convert the $Ca(OH)_2$ to CaO and decompose any remaining binder/support/catalyst precursors.
	Wet impregnation	A support structured particle is produced by another method. These particles are then immersed in a metal salt solution for a period of time. The solution is allowed to dry out leaving the original particles impregnated with the metal salts distributed across their surface area. The dried material is then calcined to decompose the metal salt.
	Spray drying / freeze drying	*Spray drying:* A solution/slurry of the raw materials is prepared then pumped through a spray nozzle. Hot gas is passed around the outside of the spray nozzle which flash evaporates the droplets leaving a porous particles which can be calcined to produce# the final particles. *Freeze drying:* A solution/slurry of the raw materials is prepared then pre-frozen before being placed into a vacuum chamber. The low-pressure sublimates the solvent from the frozen bulk mixture leaving a porous material which can formed into a particles and then calcined.
	Co-precipitation	A solution of metal salts is prepared (typically nitrates), mixed and precipitated out with the addition of a base (typically ammonium hydroxide). The precipitate is then filtered, washed, dried and calcined.
Highly-engineered	*Sol-gel*	A solution of metal salts is prepared, a gelation additive is required to turn the solution into a gel. The solvent can then be removed by filtration, washing and drying, after which the material is calcined.

The co-precipitation method has been used extensively to produce hydrotalcite-like (HTlc) combined particles for SESR which has the advantages of producing a highly dispersed, nanosized structure with a high specific surface area and stability against sintering (Broda et al., 2012a) (Wu et al., 2012) (Dewoolkar and Vaidya, 2016b) (Dewoolkar and Vaidya, 2016a). Hydrotalcites require different operating conditions to effectively adsorb CO_2 compared to CaO-based sorbents, namely lower temperatures (400-500 °C) and higher pressures (up to 40 bar) furthermore the low capture capacity is likely to limit the full scale potential application of HTlc's (Reijers et al., 2006) (Barelli et al., 2008).

Chanburanasiri et al., produced a combined Ni and CaO based particle utilising a wet impregnation method and found an optimal Ni loading of 12.5 wt.% (Chanburanasiri et al., 2011). Phromprasit et al. synthesised a combined catalyst and sorbent material via a similar method by first hydrating CaO then wet mixed in a 20 wt.% Al_2O_3 in NiO mixed powder before drying and calcining. It was found that the addition of the Al_2O_3 support was advantageous in terms of aiding a high H_2 purity during the pre-breakthrough period compared to without the support structure present which was reasoned to be due to an external $CaCO_3$ product layer blocking pores, thereby limiting the access to internal Ni and CaO sites (Phromprasit et al., 2016). Later Phromprasit et al. incorporated Zr, La and Ce into the matrix, which was found to make minimal difference to the CO_2 carrying capacity of the materials, but due to a lack of comparison to an undoped base case it was not possible to infer if the doping improved the H_2 yield or purity (Phromprasit et al., 2017).

A similar method again utilised wet mixing followed by wet impregnation for the production of combined particles from which it was found that excess CaO actually limited the CH_4 conversion during the pre-breakthrough period, which was likely to be caused by pore blocking by $CaCO_3$ product layer (Di Giuliano et al.). Synthetic calcium based CO_2 sorbents were also produced and tested within a fluidised bed by Pacciani et al., who found that sorbents produced via the hydrolysis method were more mechanically stable within a fluidised bed compared to co-precipitated sorbents because of the particles internal structure being denser and more resistant to attrition (Pacciani et al., 2008).

Kalantzopoulos et al., utilised a dry mixing with the subsequent addition of 5 wt.% polyethylene glycol (PEG 4000) as a binder – which was later burned off leaving a porous CaO matrix. A $Ni(NO_3)_2$ solution was then applied via wet impregnation, after drying the nitrates were combusted to leave a combined sorbent and catalyst material (Kalantzopoulos et al., 2015). The use of organic-removable spacers is rare in the literature but in combination with other supporting methods a porous macrostructure can be formed leading to a materials which may expose more external surface area that is not as susceptible to pore blocking by the product layer $CaCO_3$ formation (Broda and Müller, 2012) (Sun et al., 2016).

Each of these particle production methods are techniques of incorporating the materials together such that the distance between individual grains is minimised whilst incorporating porosity yet maintaining physical particle strength. There are advantages and disadvantages to each production method but whichever method is selected the end goal is to achieve a balance between maximising: (Solsvik and Jakobsen, 2011) (Broda et al., 2015)

- Particle porosity
- Catalytic activity
- Reaction kinetics
- Sorbent carrying capacity
- Particle and individual component lifetime
- Particle strength
- Resistance to attrition
- Ability to use/recycle spent material

And minimising:

- Material sintering
- Pore blocking/product layer resistances
- Unintended inter-component interaction
- Expense, difficulty and time to manufacture
- The quantity of unreactive material

6.1.2. Method development

Utilising the information gained from the literature presented here and in chapter 2 it was decided to investigate combined particles produced via a low-engineered manufacturing technique. A low engineered method was selected due to the ability to produce particles which were relatively inexpensive, sourced from readily available natural materials and they involved few processing steps such that they could be scaled up and commercialised with minimal difficulty.

The method that was developed was based on the methods applied by (Phromprasit et al., 2017) (Phromprasit et al., 2016) (García-Lario et al., 2015b) (Pacciani et al., 2008) (Li et al., 2005) and can be thought of as a combination of hydrolysis and wet-mechanical-mixing. The aim of this particle production method is to form homogenous mixture of CaO and NiO where the CaO forms the structure of the particles and the nickel is evenly dispersed throughout the matrix. A flow chart is presented below illustrating the common method applied to the production of all combined particles within this chapter.

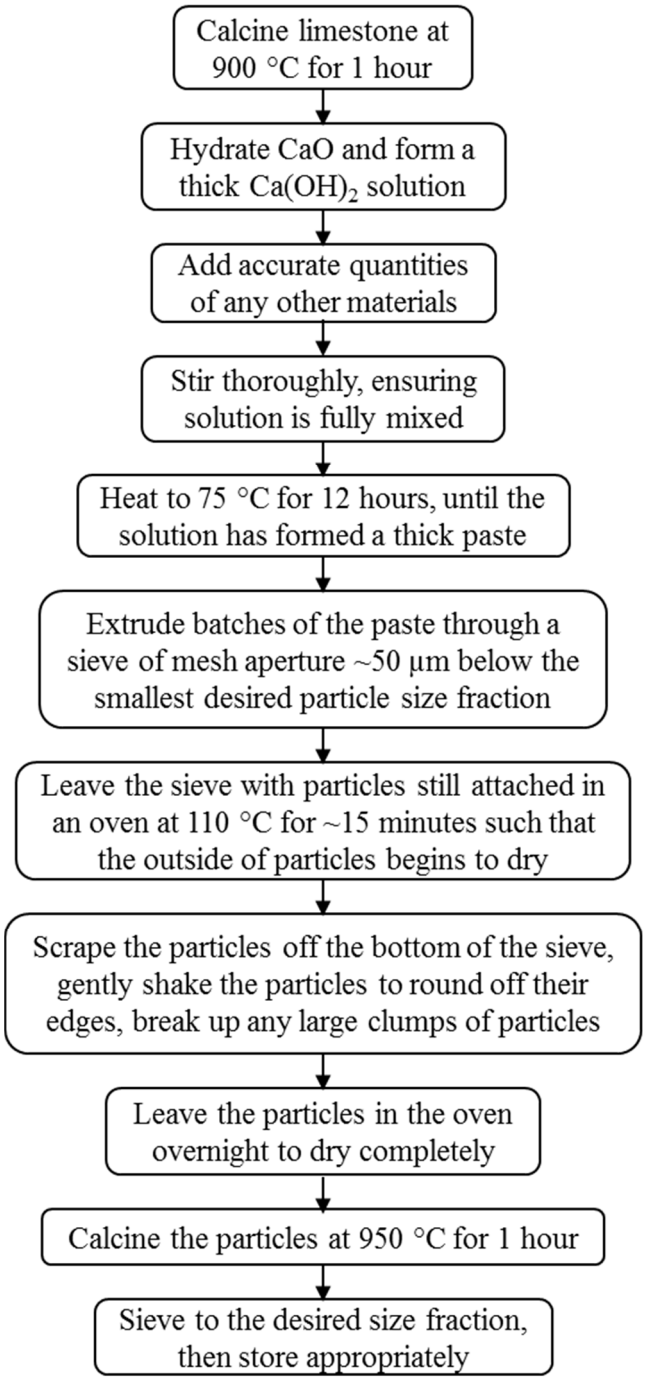

Figure 6.2 – Combined material and particle production methodology applied to all particles within this chapter.

The majority of the porosity within these particles was formed from the conversion of $Ca(OH)_2$ to CaO, thereby a theoretical minimum porosity of 49.9 % could be achieved, as demonstrated by use of Equation 6.1 which calculates the molar expansion/contraction factor (*Z*) that occurs during the decomposition from $Ca(OH)_2$ to CaO. A lesser amount of the particles porosity will be formed from the evaporation of water from the particles as they dry out.

Equation 6.1:

$$Z = \frac{V_{CaO}}{V_{Ca(OH)_2}} = \frac{M_{CaO}}{M_{Ca(OH)_2}} \frac{\rho_{Ca(OH)_2}}{\rho_{CaO}}$$

$$0.501 = \frac{56.077}{74.093} \cdot \frac{2.21}{3.34}$$

Where: (Lide, 2005)

V_{CaO} Molar volume of CaO, m^3/mol

$V_{Ca(OH)_2}$ Molar volume of $Ca(OH)_2$, m^3/mol

M_{CaO} Molecular weight of CaO, 56.077 g/mol

$M_{Ca(OH)_2}$ Molecular weight of $Ca(OH)_2$, 74.093 g/mol

ρ_{CaO} Density of CaO, 3.34 g/cm^3

$\rho_{Ca(OH)_2}$ Density of $Ca(OH)_2$, 2.21 g/cm^3

For particles produced of CaO only (particle size fraction 300 - 500 µm) a porosity of 64.1 % was calculated through the use of Equation 6.2 and Equation 6.3, the skeletal density (determined by Accupyc, Micromeritics - AccuPyc II 1340 Series Pycnometer) and the pore volume (determined by Mercury Intrusion Porosimetry, MIP, Micromeritrics – AutoPore IV). The pore volume was calculated by summing the pore volume of pore diameters <100 µm. The value calculated via this method is higher than the theoretical minimum porosity due to the evaporation of water from the particles, particle formation defects and experimental measurement error.

Equation 6.2 - Porosity of the particle, ε:

$$\varepsilon = \frac{V_p}{V_p + V_s}$$

Equation 6.3 - Volume of the solid fraction of the particle, V_s:

$$V_s = \frac{1}{\rho_s}$$

Where:

ε Porosity of the particle

ρ_s Skeletal density, g/cm^3

V_s Solid volume, cm^3/g

V_p Pore volume, cm^3/g

6.1.3. Unsupported particle production

These combined particles require a source of Ni (the catalyst for these reactions) to be incorporated into the matrix of the CaO particles, which was achieved by adding known quantities of nickel(II) oxide, NiO, powder (Sigma Aldrich, <50 nm (TEM), purity 99.8 %) to the $Ca(OH)_2$ solution followed by continuous and vigorous stirring. The CaO source was calcined limestone (Longcliffe, <90 μm, all other details of this limestone were supplied in Chapter 4). The impact of NiO addition to the matrix of these CaO particles was investigating by introducing 14, 26, 36 and 47 wt.% NiO to the mixture – thereby representing in the reduced form 11, 21, 28 and 37 wt.% Ni. These weight percentages were evaluated using X-ray Florescence (XRF, PANanalytical – Epsilon 3^x). The active form of nickel for the reforming reactions during SESR is zero valence nickel(0) which means that due to the reduction of NiO to Ni some additional porosity would be introduced. Using Equation 6.1 the Ni grains will theoretically be ~59.3 % smaller than the grains of NiO. Figure 6.3indicates that there will be no Ni-Ca interactions formed at all temperatures during the production and operation process. The samples were analysed utilising XRD to confirm the phases that were present – CaO and NiO only, as expected.

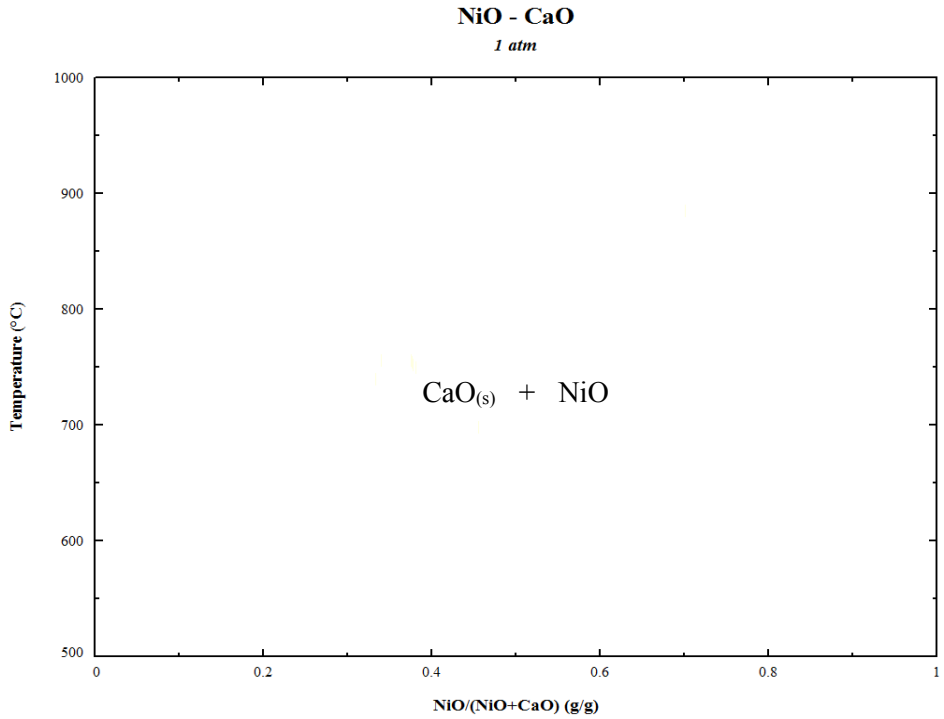

Figure 6.3 – Phase diagram of temperature vs NiO to CaO ratio excluding solid state interactions, produced in FactSage. It is normal to observe no detail on this figure, it indicates that there is no reaction between CaO and NiO.

Table 6.2 presents the characterisation of the combined NiO and CaO particles, from which it is clearly observable that the addition of Ni leads to an increase in particle density (skeletal and envelope) and a decrease in BET surface area and pore volume per g of material. The increase in particle density can be attributed to the higher density of NiO (6.72 g/cm^3) compared to CaO (3.34 g/cm^3). The skeletal density values presented in Table 6.2 for CaO and NiO only particles were close to their literature values (Lide, 2005), slight discrepancies will be present due to measurement error, potential hydration of CaO and imperfect oxidation of the NiO lattice. The decrease in BET surface area and pore volume with increasing NiO content is likely due to pore blocking by the larger NiO grains due to the starting NiO material being <50 nm compared to a dissolved solution of $Ca(OH)_2$. The pore volume utilised in Equation 6.2 was calculated by applying an arbitrary cut off at 100 µm to the MIP volumetric intrusion data (after a blank correction was applied), this is because the reported volumetric intrusion above this value is likely to be interstitial particle space not pore volume, as discussed in Chapter 4. Figure 6.4

shows each material is highly macro-porous (pore diameters mostly > 50 nm) and it can be observed from Table 6.2 that the addition of the NiO decreases the pore volume within the 10 - 100 nm pore diameter range (analysed by BJH – N_2 adsorption), which has previously been demonstrated to be optimal for the absorption of CO_2 (Fennell et al., 2007) (Broda and Müller, 2014). The available reactive pore area and pore volume within the 10 - 100 nm pore diameter range, displayed in Table 6.2 was calculated in Matlab by interpolating *dV/dD* and *dA/dD* data using the '*interp*1 - *pchip*' method to form a pseudo-continuous data set from the discrete values reported in the original BJH adsorption data set, and then integrating across the 10 - 100 nm pore range with the trapezium rule.

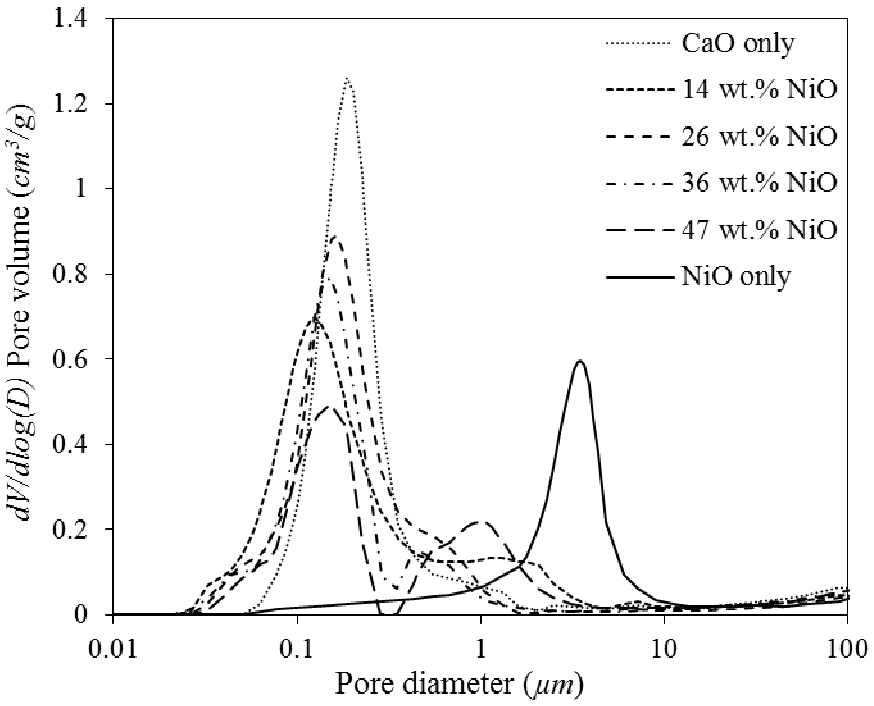

Figure 6.4 – Mercury Intrusion Porosimetry (MIP) *dV/dlog(D)* for combined particles with varying NiO contents.

It can also be observed from Figure 6.4 that an increased nickel content lead to the development of a bi-modal pore structure indicating that nickel grains were coalescing, thus forming a separated pore structure of relatively larger pores compared to the smaller CaO pores. It should however be noted that MIP is known to be less accurate at pore diameters below ~ 10 nm as the error caused by compression of the mercury, the sample and the penetrometer itself is more prominent at these smaller pores; thus to

analyse the pores smaller than this diameter BJH (Barrett-Joyner-Halenda) analysis is recommended (Fennell et al., 2007) (Kissa, 1999). The overall porosity of the particles was changed negligibly by the addition of NiO indicating that the NiO is producing its own sub-structure throughout the CaO matrix as the envelope and skeletal densities were increasing at a similar rate. This point was further evidenced by the 'NiO only' particles having a clearly defined pore structure and high porosity, ~ 62 %, despite presenting a low BET surface area. The evidence suggests that providing the NiO content within the particles is minimised the impact on the available reactive pore surface area and volume will be limited.

Table 6.2 – Combined particles (300 – 500 and 710 – 1000 µm) characteristics from BET, BJH and MIP analysis density and porosity calculated for 300 – 500 µm combined particles only.

Sample	BET Surface area (m^2/g)		Pore volume in 10 – 100 nm range (BJH, cm^3/g)		Pore surface area in 10 – 100 nm range (BJH, m^2/g)		Skeletal density (g/cm^3)	Envelope density (g/cm^3)	Porosity (%)
	300 – 500 µm	710 – 1000 µm	300 – 500 µm	710 – 1000 µm	300 – 500 µm	710 – 1000 µm			
CaO only	16.07	14.52	0.064	0.058	5.87	5.15	3.31	1.19	64.1
14 wt.% NiO	11.32	10.65	0.050	0.048	4.79	4.41	3.23	1.19	63.2
26 wt.% NiO	9.47	8.05	0.032	0.027	3.22	2.59	3.63	1.29	64.6
36 wt.% NiO	9.16	8.97	0.034	0.033	3.42	3.25	3.72	1.44	61.2
47 wt.% NiO	7.10	6.62	0.030	0.028	2.73	2.46	3.93	1.62	58.8
NiO only	0.95	0.93	0.005	0.005	0.45	0.42	5.93	2.25	62.1

To assess the impact on the CO_2 carrying capacity of combining NiO into the CaO structure 15 carbonation/calcination cycles were undertaken on a TGA (Q5000IR, TA Instruments), the results of which are presented as Figure 6.5. The operating conditions utilised were defined as follows:

- Carbonation – 650 °C, 15 vol.% CO_2 with balance N_2, 5 minutes
- Calcination – 950 °C, 100 vol.% CO_2, 1 minute

The CO_2 concentration was ramped between the carbonation and calcination stages following the protocol detailed in Chapter 5. The temperature was ramped and reduced at 50 °C/min.

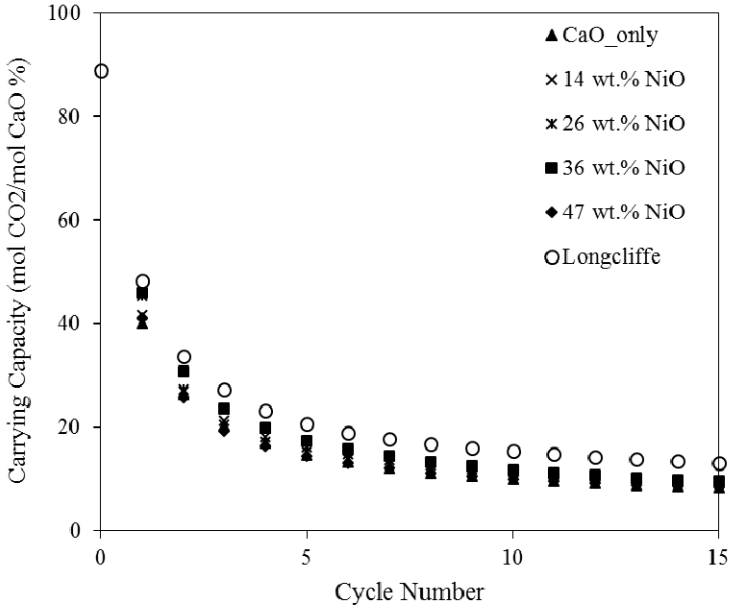

Figure 6.5 – Combined particle (CaO and NiO, 300 - 500 μm) CO_2 carrying capacity in moles of CO_2 absorbed per mole of CaO as a percentage.

The TGA cycling data indicates that the combined particles have a slightly lower long-term carrying capacity than the reference limestone, Longcliffe. Crucially though there seems to be negligible difference between the samples with varying NiO content indicating that the increased presence of NiO did not impact on the sorbents ability to absorb CO_2 – or if it did the effect is greatly outweighed by the degradation caused by high-temperature CO_2 sintering and the particle manufacturing process. The zeroth cycles of the synthetic sorbents was not presented as the samples were in their calcined form therefore the weight changes during the zeroth calcinations were minimal.

6.1.4. Supported particle production

As discussed within the introduction of this chapter, calcium-aluminate based supported particles have been investigated previously, however the use of silica based supports is sparser. One study by Zhao et al., found positive results with the use of a dicalcium silicate support derived from the addition of tetraethyl orthosilicate for calcium looping (Zhao et al., 2012). These authors found that the interactions of the calcium and silicon oxides led to a well-ordered pore structure which could adapt with temperature cycling to produce a stable CO_2 capture performance. It was therefore chosen to investigate if the addition of a silica based support, in the form of dicalcium silicate (C_2S) as investigated within the novel polymorphic sorbent discussed in Chapter 5, would benefit the combined particles structure or influence production of H_2 via SESR.

The calcium source for the novel sorbent was previously calcium acetate, which has the key downside of being an expensive chemical reagent (bulk calcium acetate ~$1.50/kg (Alibaba.com)) compared to crushed limestone (bulk limestone ~$0.07/kg (Alibaba.com)). For this reason the production of the novel sorbent utilising calcined limestone as the calcium source was investigated. However it was important to ensure that the formation of the dicalcium silicate (C_2S, Ca_2SiO_4) was not impeded by the use of an alternative calcium source.

A secondary silica source, high surface area fumed silica (<38 μm, 99 %, Sibelco Ltd), was also investigated as it is moderately cheaper than the silica source used previously, tetraethyl orthosilicate (TEOS, >99 %, Sigma Aldrich). An example calculation for the material cost per kg of Si ions can be found in Appendix III.

Table 6.3 displays the supported combined particles that were produced and their respective component weight percentages and molar ratios. A molar ratio of Ca:Si of 9:1 was aimed for as this was demonstrated by Zhao et al. to be the optimal composition for CO_2 absorption, due to the high availability of free CaO and minimal amount of C_2S support (Zhao et al., 2014).

The samples have been named based on what they were composed of, i.e. the sample with calcium oxide, a C_2S support derived from TEOS and nickel oxide was denoted as CaO – TEOS – NiO. The SiO_2 weight percentages for the TEOS samples were initially calculated based on the mass of SiO_2 that will be produced after the hydrolysis reaction.

Table 6.3 – Supported combined particles and their respective weight percentages and molar ratios. Weight percentages were confirmed and updated by XRF. The terms -SiO_2- and -TEOS- represent the silica source for each sample. The *Actual* C_2S weight percent formation were calculated by quantitative phase analysis by Rietveld refinement using GSASII (Toby and Von Dreele, 2013).

Sample ID	**Weight percentages (wt.%)**				**Theoretical / *Actual* C_2S formation (wt.%)**	**Molar ratios**	
	CaO	**NiO**	**SiO_2**	**Impurity**		**Ca:Si**	**Ca:Ni**
CaO - SiO_2	87.1	0	11.1	1.8	32.4 / *13.8*	9:1	-
CaO - TEOS	87.4	0	10.8	1.8	31.5 / *27.2*	9:1	-
CaO - SiO_2 - NiO	63.0	25.9	9.8	1.3	28.5 / *20.5*	8.7:1.3	7.1:2.9
CaO - TEOS - NiO	63.1	25.9	9.8	1.2	28.4 / *22.6*	8.7:1.3	7.1:2.9

To check the production of the C_2S support structure within these combined particles the samples were analysed by XRD (utilising CuKα radiation, PANalytical, Almelo), these results were then subsequently analysed using quantitative phase analysis via rietveld refinement of the expected species in GSASII (Toby and Von Dreele, 2013). Using the data presented in Table 6.3, combined with the XRD patterns presented in Figure 6.6 it was possible to conclude that a significant proportion of the fumed silica added to the samples denoted by '- SiO_2 -' did not react with the CaO and remained as crystalline SiO_2. This is understandable as the grain size of the original silica material was quite large (<38 μm) and it was therefore expected that the dispersion of SiO_2 was low and the contact area between the Ca and Si molecules was also low.

The measured extent of C_2S formation was less than expected in all samples which was likely caused by a lack of crystallinity within the samples, as the XRD analysis was only able to measure crystalline materials. The sample preparation method could have been altered by increasing the sintering temperature or the length of the sintering phase, both of which would have led to a more crystalline material being produced however to keep the samples comparable with the previously produced unsupported materials this was not performed. A difficulty that occurred when conducting the phase identification, in particular for the C_2S phases, was that the three main peaks of all C_2S phases overlapped with main peaks of CaO. This meant that phase identification and quantification was performed using some secondary peaks, which introduced an unknown error in the results.

The formation of $Ca(OH)_2$ was observed within the XRD patterns and was likely due to the samples exposure to the atmospheric moisture. To prevent $Ca(OH)_2$ formation, the length of time the samples were exposed to the atmosphere was minimised and they were stored in containers which were sealed, Parafilmed and had their atmospheres diluted with N_2, the sample containers were then stored in sealed containers with hygroscopic silica gel crystals. Nevertheless it was inevitable that some $Ca(OH)_2$ did form during the production and analysis processes.

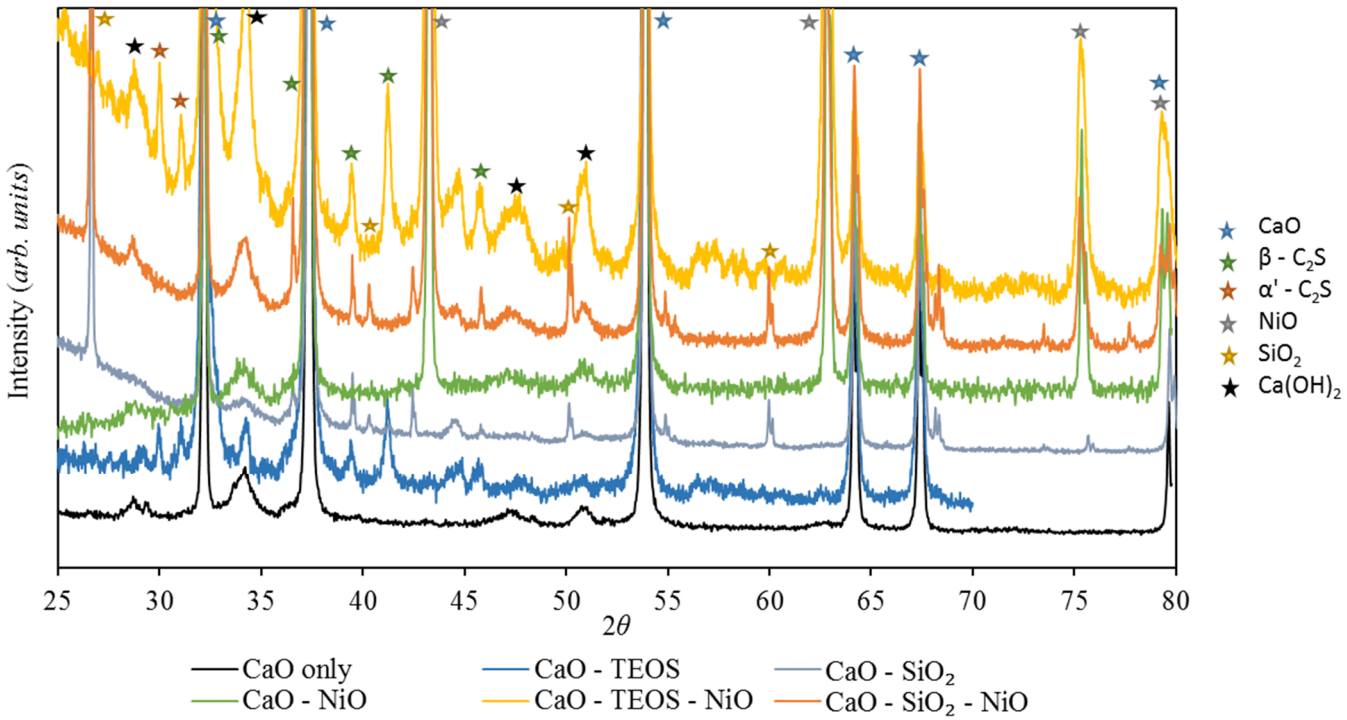

Figure 6.6 – XRD patterns of C_2S supported combined particles produced utilising alternative calcium and silica sources.

The incorporation of NiO into this supported sorbent structure was also investigated as Ni will be required as a catalyst, however before doing so any potential interactions were investigated using FactSage. The system was modelled at 950 °C (the temperature of the tube furnace in which the material is sintered/calcined) assuming the only species initially present were CaO, SiO_2 and NiO. The red circle displayed on Figure 6.6 indicates the phase compositions likely to be present at equilibrium at this temperature, when the following weight percentages were utilised ~64 wt.% CaO, ~10 wt.% SiO_2, ~26 wt.% NiO. It can be observed, CaO preferentially reacted with the SiO_2 to form Ca_2SiO_4 due to the high calcium oxide content of this mixture and due to the lower change in Gibbs free energy (ΔG) of Equation 6.4 compared to Equation 6.5.

Equation 6.4 - Calcium silicate formation:

$$2CaO + SiO_2 \rightarrow Ca_2SiO_4 \qquad \Delta G = -2{,}454 \text{ kJ/mol}$$

Equation 6.5 - Nickel silicate formation:

$$2NiO + SiO_2 \rightarrow Ni_2SiO_4 \qquad \Delta G = -1{,}551 \text{ kJ/mol}$$

Where: $\Delta G = \Delta H^0 - T\Delta S^0$ (kJ/mol).

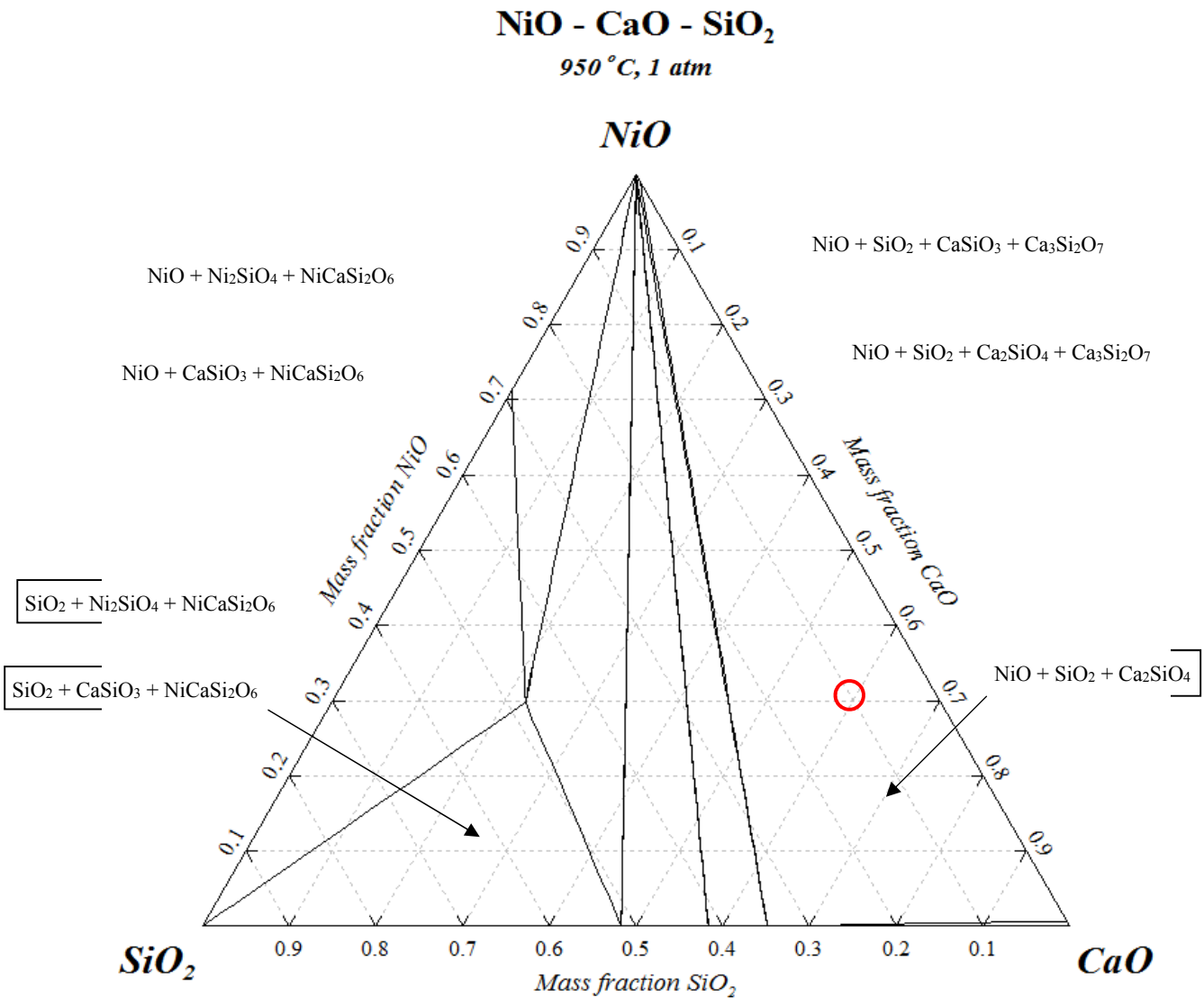

Figure 6.7 – Phase diagram indicating the thermodynamically stable species that could be formed when CaO, SiO_2 and NiO are present at 950 °C, produced in FactSage. The red circle indicates the composition of a material representing ~64 wt.% CaO, ~10 wt.% SiO_2, ~26 wt.% NiO.

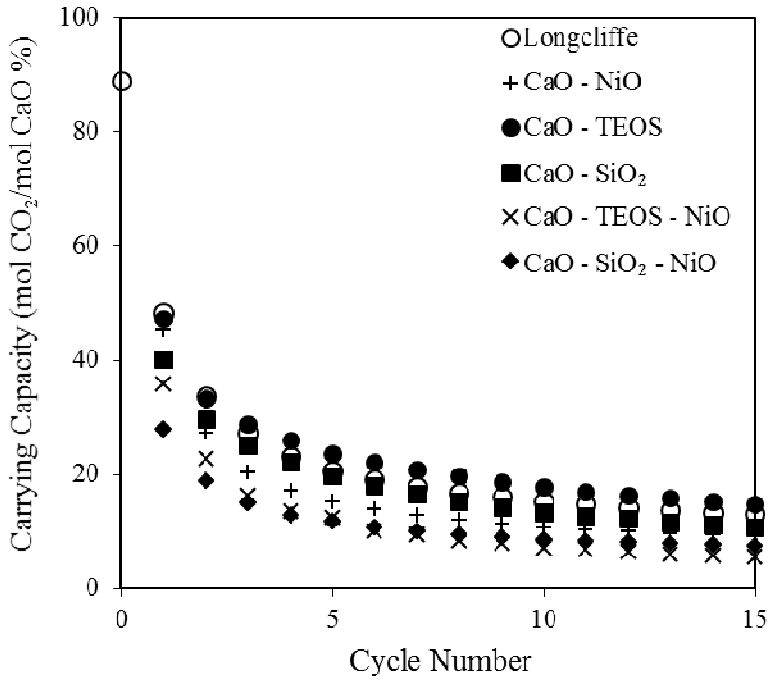

Figure 6.8 – Combined particles (300 - 500 μm) CO_2 carrying capacity in moles of CO_2 absorbed per mole of CaO as a percentage. TEOS and SiO_2 indicate the C_2S support silica source material. A sample without a support structure but equivalent NiO content is also displayed for comparison.

The supported combined particles were cycled in the TGA under the calcium looping conditions previously stated in section 6.1.3 and compared against a longcliffe limestone sample and an unsupported combined particle of equal NiO loading, CaO - NiO. Figure 6.8 displays the results of these TGA cycles, the results of which indicate that the addition of the C_2S support negatively impacted the carrying capacity of the sorbents, which is in line with the results found in Chapter 5. A comparison of the supported and the unsupported combined particles of equal NiO content highlights that the initial the CO_2 sorption capacity was lower for the supported particles and after repeated cycling the supported material presented a 15^{th} cycle carrying capacity which was ~ 42 % lower relative to the unsupported sample. A potential reason for this lower carrying capacity could be due to pore blockage or because the support caused instabilities in the lattice thereby leading to the collapse of larger pores. To investigate these potential causes, the supported and unsupported combined particles were analysed via

BET, BJH and MIP, the analysis of which is displayed in Figure 6.9 and Table 6.4. The MIP and BJH data was analysed utilising the same method as described in section 6.1.2.

Table 6.4 shows that the supported sample produced using the fumed silica, CaO – SiO_2 – NiO, displayed a lower BET surface area and a lower available reactive surface area and volume indicating that the unreacted SiO_2 likely did block some of the pores or alter the pore structure. The same explanation does not seem appropriate for the supported sample derived from the TEOS silica source, CaO – TEOS – NiO, as the surface area and BJH characteristics were not significantly different from the unsupported CaO – NiO sample. The porosity of the samples with TEOS present were shown to be significantly greater than the sample without a support and the samples with a fumed silica support – which was confirmed with the use of a student's t-test, although the error in MIP and helium gas displacement pycnometry measurements and minimal repeats may prove this difference to be negligible.

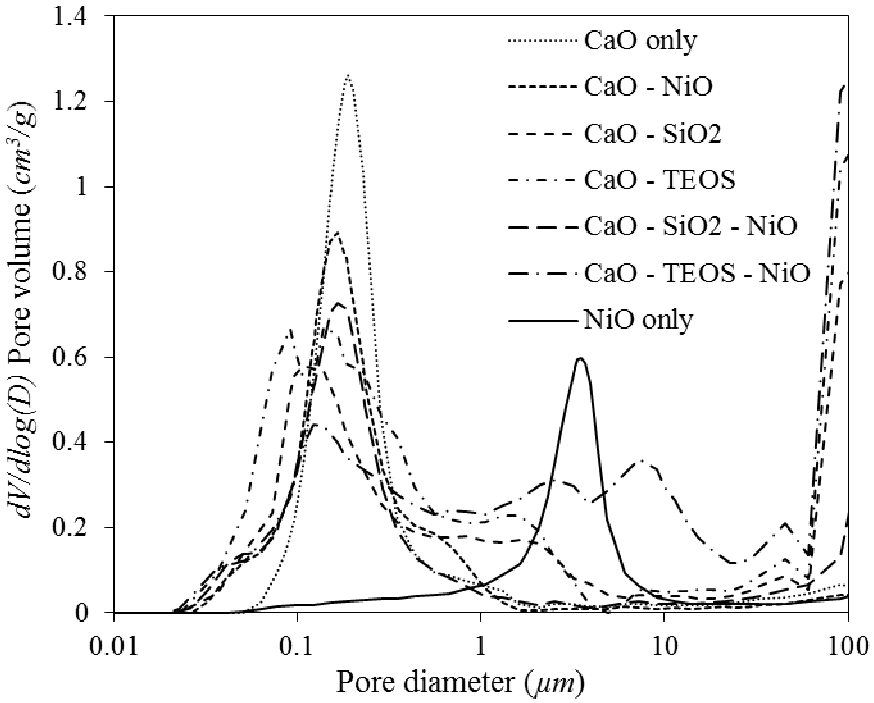

Figure 6.9 – Mercury Intrusion Porosimetry (MIP) *dV/dlog(D)* for combined particles (300 - 500 μm) with C_2S supports compared to an unsupported sample. '– TEOS –' and '– SiO_2 –' indicate the silica support source material for the C_2S. Each material was composed of ~26 wt.% NiO.

Table 6.4 – C_2S supported combined particle (300 - 500 μm) characteristics from BET, BJH and MIP analysis.

Sample	BET Surface area (m^2/g)	Pore volume in 10 – 100 nm range (BJH, cm^3/g)	Pore surface area in 10 – 100 nm range (BJH, m^2/g)	Skeletal density (g/cm^3)	Envelope density (g/cm^3)	Porosity (%)
CaO only	16.07	0.064	5.87	3.31	1.19	64.1
CaO - SiO_2	9.78	0.053	5.25	3.12	1.11	64.5
CaO - TEOS	14.89	0.072	7.57	3.18	0.89	71.9
CaO - NiO	9.47	0.032	3.22	3.63	1.29	64.6
CaO - SiO_2 - NiO	8.17	0.038	3.81	3.50	1.34	61.8
CaO - TEOS - NiO	9.11	0.038	4.42	3.54	0.86	75.8

6.2. Operation within a Spout-Fluidised Bed Reactor

Utilising the spout-fluidised bed reactor described in Chapter 3 the combined particles were assessed for their potential use in biomass SESR. This section will cover the application of these particles, difficulties which occurred during operation and the impact of coke on these particles.

6.2.1. Reaction conditions

An operating operation procedure similar that described with in the SOP shown in Appendix I was utilised with some minor changes to improve the understanding of the complex set of reactions. These experiments were all conducted at 660 ± 5 °C, 1 atm, ~20 ± 2 mol.% steam and a total flow rate of ~80 cm^3/s (@ 293 K – $u/u_{mf} \approx 3.6$ for sand 425 – 500 µm, total flow rate split as follows: main feed N_2 = 59 cm^3/s, bio-knocker N_2 = 5 cm^3/s, steam = 16 cm^3/s). The biomass utilised in each of these experiments was the same oak as identified in section 3.5.

These experiments were all conducted with a 0.9 g/min biomass feeding rate which produced a molar steam to carbon (S:C) ratio of 1.2:1. It is understood that this was a relatively low S:C ratio however the value that could be achieved was limited by the high gas flow rate required to transport the biomass into the reactor which impacted on the stability of the steam concentration that could be generated by the bubbler system. An attempt was made to improve the S:C ratio by reducing the gas flow rate going through the bubbler system and increase the bubblers temperature after which combining the increased steam concentration flow with the remaining N_2 flow before collecting the biomass and entering the reactor. The increased steam concentration that was generated by this alternate set up was negated by the addition of the remaining gas effectively diluting the steam concentration to similar levels as previously achieved; because of this the steam generation and gas mixing set up was maintained as described in section 3.6 and a lower S:C ratio was utilised.

For the utilisation of biomass, a low S:C ratio is not as influential as it would be for SMR, this can explained using Equation 6.6 and Equation 6.7. These equations show that the stoichiometric ratio of $C:H_2O$ is 1:2 for SMR and 1:1.2 for SESR implying that a lower steam demand is required when utilising biomass as the biomass itself contains some oxygen. In Equation 6.7 the oak biomass is

represented by the mole fractions of C, H and O (determined by CHN analysis, Analytical Services at the Sheffield University), these values were then substituted into the reactant side of the equation and finally the equation was balanced to achieve round numbers on the product side.

Equation 6.6:

$$CH_4 + 2H_2O \rightarrow CO_2 + 4H_2$$

Equation 6.7:

$$CH_{1.6}O_{0.8} + 1.2H_2O \rightarrow CO_2 + 2H_2$$

During a commercial operation of both of these processes a greater S:C ratio would be applied to ensure complete conversion of the biomass and to minimise coking, as is the case with SMR where S:C ratios of 3 are typically applied, i.e. 50 % excess (Gupta, 2008). The utilisation of very high S:C ratios is uneconomical for commercial operation of both SMR and SESR due the large operating costs associated with evaporating water and raising its enthalpy. S:C ratios are therefore kept to a minimum such that the energy efficiency and operating cost of the system is not impacted too greatly (Xu et al., 2008) (Großmann et al., 2016).

6.2.2. Bed material

Initially, the fluidised bed consisted of an amount of the combined particles such that the molar CaO to C ratio was ~ 44, which ensured a large excess of CaO (compared to the amount of CO_2 that could be generated). This meant that it was possible to determine the effect of altering the Ni content independent to the concentration of CaO. Sand was also added to the bed to raise the bed mass to 40 g which acted as a thermal ballast within the bed. An excess CaO:C ratio on this extent at commercial scale would greatly impact on the energy and cost penalty of the system as more material would need calcining, a greater bed material would need to be circulated and the OPEX costs of supply and disposal of the material would need to be accounted for.

The combined particles initially contain NiO which is not the catalytically active form for the reforming reactions, therefore before the SESR reaction could take place the NiO had to be reduced to Ni. The H_2

reduction was performed at 650 °C with 5 vol.% H_2 for 30 minutes, whilst observing the steam and H_2 concentration at the outlet of the reactor, which was utilised for visual confirmation that the H_2 reduction was complete. In all cases the reduction was observed to reach completion after approximately 10 minutes.

6.2.3. Unsupported combined particles: Effect of particle size and Ni content

The unsupported combined particles described in section 6.1.3 were studied within the spout-fluidised bed reactor to investigate their ability to favourably produce H_2 through SESR with biomass. A typical experimental reactor response (detailed by thermocouples and gas analysers) to an SESR with biomass reaction followed by calcination and finally coke burn-off, is shown in Figure 6.10.

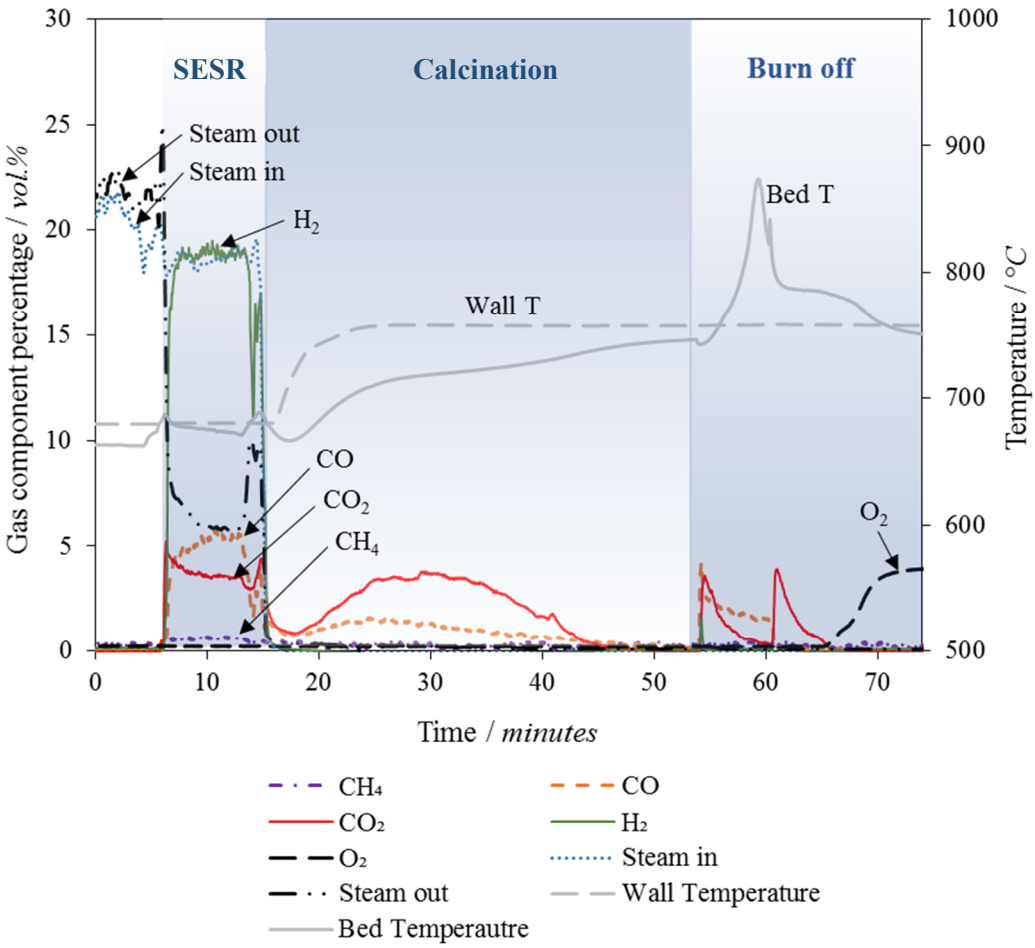

Figure 6.10 – A typical response to a long (~8 minutes) biomass feed during SESR, followed by calcination and then coke burn-off.

Similarly to Figure 6.10, once the bed temperature and steam generation were both stable the biomass feeding system was activated and biomass was continuously fed for 3 minutes at a rate of ~0.9 g/min. A feeding time of 3 minutes was utilised as it was demonstrated from the results obtained from longer feeding runs that steady state H_2 production is reached after ~30 seconds, and after ~8 minutes the impact of sorbent carbonation and particle/inlet tube coking (discussed further in section 6.3) begins to take effect which minimises the effectiveness of the SESR process.

After the SESR process was complete (Time point ≈15 minutes) the steam flow was turned off, leaving just N_2 flow and the wall temperature set point was increased to 750 °C to induce the calcination of the sorbent. This temperature is known to be much lower than the temperature that a realistic calciner would operate at and that conducting these calcinations in N_2 is also not representative. These conditions were chosen however due to the lack of ability to get heat into the reactor fast enough to reach >900 °C and to ensure an accurate mass balance could be achieved by minimising the number of gas changes.

During the period of time spent heating up the bed material to the calcination temperature and during the calcination period itself, CO and CO_2 were both detected by the analysers. This indicates that the CO_2 released form the calcination was reacting with the surface carbon deposits of the particles via the Boudouard reaction (Equation 6.8); this reaction has been thermodynamically modelled using ThermoVader and is shown in Figure 6.11 (McBride et al., 2004). The grey shaded area indicates the heating up zone between the SESR temperature (left dashed line) and the calcination temperature (right dashed line). The grey shaded area demonstrates the Boudouard reaction likely had a significant effect on the CO_2 concentration detected by the analysers during the calcination and thus the moles of CO had to be accounted for when calculating the mole balance and determining the extent of carbonation of the sorbent. When calculating the extent of carbonation, the moles of CO detected were divided by 2 as per the stoichiometry of the Boudouard reaction and added to the total moles of CO_2 detected.

Equation 6.8 – Reverse Boudouard:

$$C + CO_2 \rightleftharpoons 2CO \qquad \Delta H_r^0 = 172 \text{ kJ/mol}$$

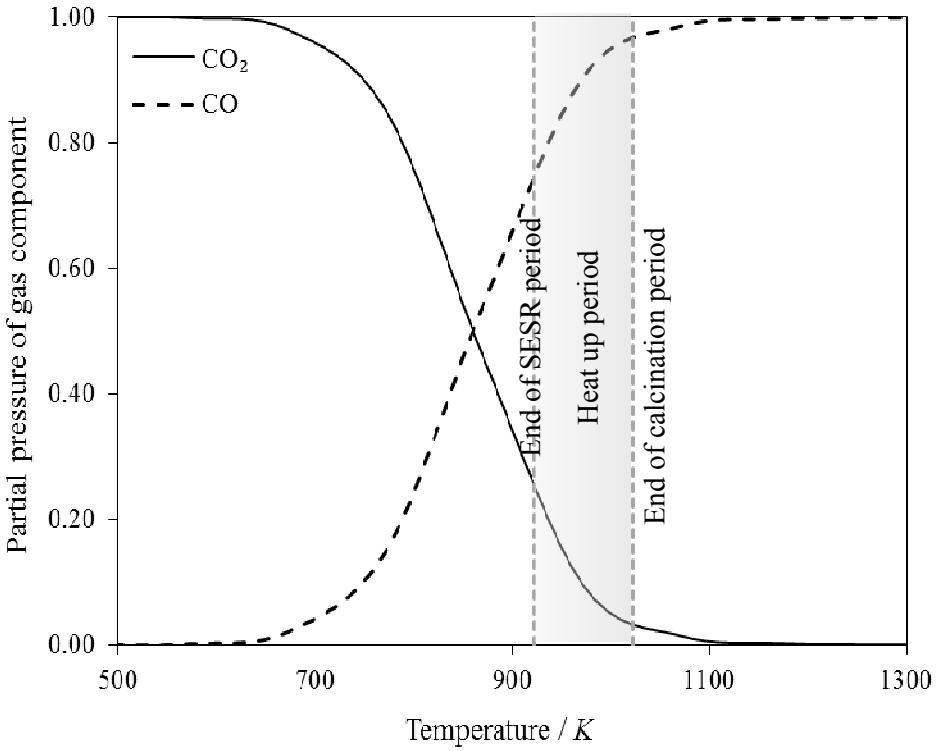

Figure 6.11 – Thermodynamic modelling of the Boudouard reaction using ThermoVader at 1 atm (McBride et al., 2004). The grey shaded area represents the heating up zone between SESR conditions and calcination conditions during which the Boudouard reaction proceeds.

Post calcination (Time point ≈55 minutes), 10 cm^3/s (@ 293 K) of air was added to the fluidising gas stream which began the coke burn-off combustion process within the reactor. Initially the combustion was incomplete leading to the production of both CO and CO_2 after which there was a sharp transition to CO_2 production. This sharp transition is likely caused by the oxygen being used up by the combustion of coke on the interior wall of the feeding tube and it was not until this carbon was removed that oxygen was able to fully mix within the bed and achieve complete combustion. The build-up of coke during biomass feeding will be discussed in section 6.3.

For the analysis of this data a Matlab code was written which, along with many other items, calculates the mass balance across each elemental and compound species. The experimental results obtained from the application of two separate particle sizes (300 – 500 μm and 710 – 1000 μm) of the combined particles described in section 6.1.4 for biomass SESR are presented in Figure 6.12 and Figure 6.13.

Figure 6.12 displays the volumetric gas percentages (dry and N_2 free basis) of the product gas during the steady state period of the SESR phase and Figure 6.13 displays the total moles of each individual gas species produced per gram of biomass during the SESR phase.

Figure 6.12 shows that the as the Ni content within the particles increased, the H_2 purity increased by increasing the volumetric percentage of H_2 and decreasing the CO, CH_4 and CO_2. It can be observed that in most cases the H_2 vol.% was greater for the smallest size fraction of particles, but this difference becomes less apparent when the particles were composed of a greater percentage of Ni. Due to the observed convergence of the gas purities at the highest Ni contents for both particle sizes it can be inferred that any increased diffusion limitation caused by utilising larger particles was offset by the shear amount of Ni lining the exterior of the pore walls. This indicates that the biomass SESR experiments conducted were likely limited by the distribution of Ni at the surface of the pore walls within the particles, which is why some smaller particles with lower Ni contents could outperform some larger particles with higher Ni contents. The effectiveness factor is a key parameter is determining the diffusion limitation observed by the particles and was calculated for these particles in section 6.4.

The common trend of an increased H_2 yield ($mmol_{gas}/g_{biomass}$) with a greater Ni content can be observed in Figure 6.13 for both particle sizes. It can also be observed that CO, CH_4 and CO_2 yields tended to increase to a maximum at around 26 wt.% NiO content and then decrease as the Ni content of the particles increased further; this was thought to be due to the greater amount of Ni at the exterior of the pore walls which enabled the overall reforming reactions to proceed further towards the equilibrium limit.

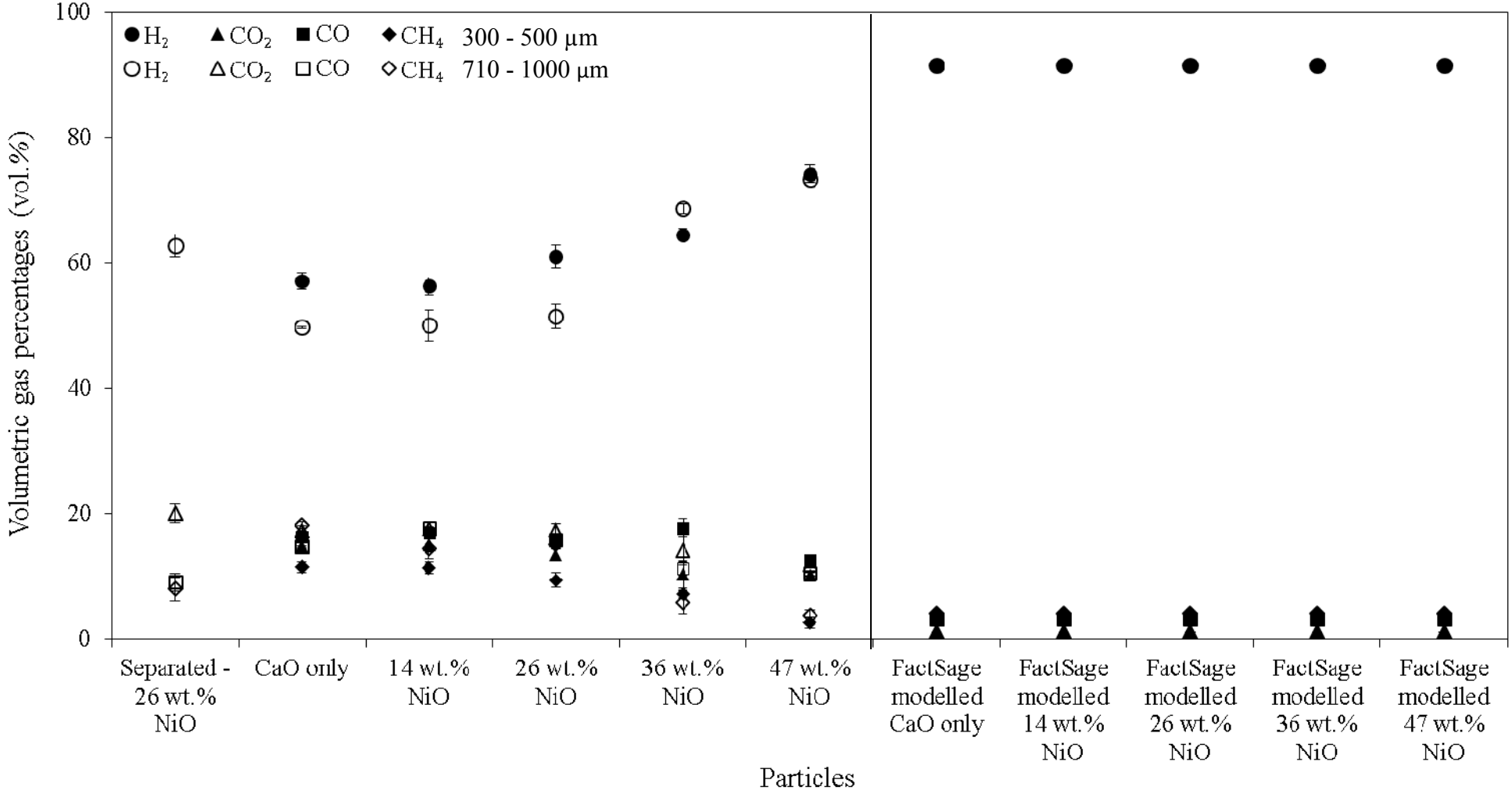

Figure 6.12 – Volumetric gas percentages of the product gas from biomass SESR in a fluidised bed reactor with varying combined particles compositions of CaO and NiO.

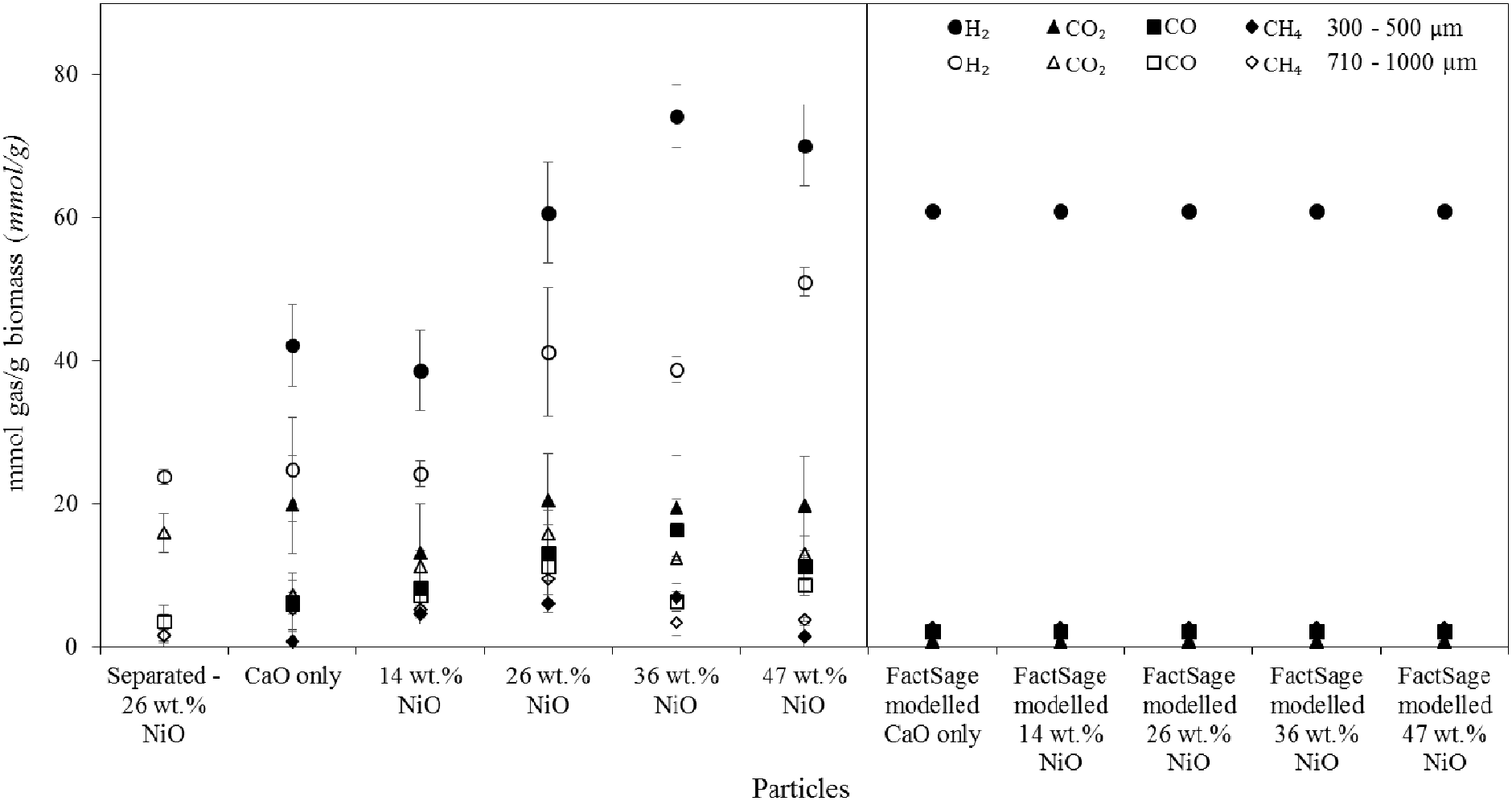

Figure 6.13 – Moles of individual gas species per gram of biomass added during SESR in a fluidised bed reactor with varying combined particles composition of CaO and NiO.

The error bars shown on both Figure 6.12 and Figure 6.13 were calculated by the standard deviation of multiple runs (at least two repeats for each particle size and NiO content). As was stated earlier the vol.% of each gas during SESR was calculated during the steady state period only meaning that the deviation was minimised. However, the yield was calculated across the entire reaction period meaning that if during a run there was a slight variation in the steam concentration or biomass flow rate this impacted greatly on the material balance, thus the error bars were larger for the yields displayed in Figure 6.13.

Also displayed on Figure 6.12 and Figure 6.13 are the results from thermodynamic modelling (dry and N_2 free basis) of the systems within FactSage. Understandably because FactSage can only model the thermodynamics of the system it is unable to account for kinetic or diffusional limitations observed when conducting experimental research, which means FactSage could not predict the impact of Ni addition on the system as its affects were catalytic only. The H_2 yield and vol.% did approach the thermodynamic equilibrium when utilising the combined particles with the highest Ni contents. In all experimental systems the CO, CH_4 and CO_2 differed significantly from the modelled predictions likely due to inefficient steam gasification and mixing between the product gases and the combined particles. The residence time of the gases within the reaction zone (defined as bed volume when expanded due to fluidisation) was calculated to be about 2 seconds meaning some gas likely bypassed the particles unreacted. Furthermore the modelled data overlooks the gradual production of coke on the surface of the particles and the steady rate of pore blocking by the $CaCO_3$ product layer.

A comparison between combined and un-combined (separated) particles was also made and is also displayed on Figure 6.12 and Figure 6.13. The bed material utilised when investigating the separated particle system was composed of masses of CaO only and NiO only particles which equalled the masses of NiO and CaO in the equivalent combined particle system. The separated particles were both of 710 – 1000 μm size fraction and likely separated out during fluidisation because of their differing densities, which meant the biomass likely came into contact with NiO only particles first and then the CaO only particles as the gas progressed up the fluidised bed. It can be observed in Figure 6.12 that the volumetric gas percentages of all gases were quite comparable between the combined and separated 26 wt.% NiO

bed material; however the same cannot be said of the total gas production shown on Figure 6.13. The quantity of gas produced from the separated particle system was significantly lower than that of the combined particle system. This demonstrates that combined particle system can lead to significant improvements in the yield of gas production, but the product gas purity was not affected considerably.

Based on the data gathered in this set of work, the addition of up to 14 wt.% NiO to the combined particles made no observable difference to the purity or yield of H_2 produced compared to the CaO only system. This is likely due to the CaO matrix shielding the majority of the Ni and therefore making it unavailable to react within this system.

Elemental carbon, hydrogen and oxygen balances across the overall process (SESR, calcination and burn off) were conducted and the results of which are displayed in Table 6.5 alongside the percentage of CO_2 captured during the SESR phase. The average C, H and O closure was 100.4 ± 15.4 %. The equations for deriving the mass balances are described in section 6.2.6. The observed deviation in the mass balances was thought to be caused by errors in the gas concentration measurement and the variability in the biomass feeding and steam production. Furthermore the reactor was controlled manually (gas rotameters) over the ~75 minute period and therefore there is a certain degree of systematic error (setting the rotameters to a value) within the operation of the reactor which inevitably affected the mass balances. The amount of CO_2 captured during the SESR phase was measured by comparing the amount of CO_2 measured during the SESR phase compared to the measured amount of CO_2 released during the calcination phase. The values reported were quite consistent across each sample, irrelevant of the wt.% NiO present. There is however a noticeable difference between particles of different size fractions, larger combined particles seemed to absorb less CO_2 compared with the smaller particles, this was probably because the smaller particles had a higher pore surface area (per g of particle) in the optimal pore range (10 – 100 nm) for carbonation as shown in Table 6.4.

Table 6.5 – Carbon, hydrogen and oxygen balance closures across the SESR phase and the percentage of CO_2 captured by the sorbent during the SESR phase (measured by the released of CO_2 during the calcination phase).

Sample	Closure of carbon balance for the SESR reaction (%)		Overall closure of hydrogen balance (%)		Overall closure of oxygen balance (%)		Amount of CO_2 captured during SESR (%)	
	300 – 500 µm	710 – 1000 µm	300 – 500 µm	710 – 1000 µm	300 – 500 µm	710 – 1000 µm	300 – 500 µm	710 – 1000 µm
CaO only	91.4	81.0	90.1	119.2	78.8	120.8	36.7	18.7
14 wt.% NiO	83.7	85.4	111.8	90.6	106.1	84.6	21.4	16.1
26 wt.% NiO	123.6	112.8	94.7	86.7	121.4	117.6	38.7	21.6
36 wt.% NiO	131.8	81.5	70.4	107.4	110.2	107.9	33.7	16.2
47 wt.% NiO	103.1	99.5	108.1	100.8	101.3	89.9	33.6	18.2

6.2.4. Supported combined particles for SESR: Effect of support addition

The supported combined particles described within section 6.1.4 were also assessed for their ability to produce high produce high purity H_2 and the impact on the overall H_2 yield through biomass SESR in the spout-fluidised bed reactor. Based on the results obtained in section 6.2.3, a decision was made to utilise combined particles with a size fraction of 300 – 500 μm and composed of 26 wt.% NiO. The combined particles were named according to Table 6.3.

Figure 6.14 displays the volumetric gas percentages of the product gas during the steady state SESR phase. It can be observed that the addition of the C_2S support reduces the CH_4 content of the gas stream considerably and therefore lead to an increase in the vol.% of H_2 and CO detected. Comparing the moles of steam utilised during the SESR reactions with C_2S supported particles, it was calculated that for every 1 mmol of additional CH_4 reacted approximately 2 mmols of steam was also consumed. This indicates that the increased consumption of methane observed during SESR with C_2S supported particles likely followed the reaction pathway identified by Equation 6.9.

Equation 6.9:

$$CH_4 + 2H_2O \rightarrow CO_2 + 4H_2$$

It is interesting that this has been observed because chemically the addition of SiO_2 into the reactor bed should be no different than adding sand (which is already present as a thermal balance). It may be that the SiO_2/C_2S acts as active sites allowing a lower bonding energy with the surface of the particles, thus providing an intermediary pathway for the reforming reactions. Currently no literature on this observed effect can be found in the available resources and as such this area requires further work to determine if this is a true phenomenon or not.

It can also be observed from Figure 6.15 that the molar quantity of gas produced with the CaO – SiO_2 – NiO sample was lower than each of the other samples which is probably caused by the unreacted SiO_2 grains, blocking the Ni or CaO sites. Repeats were not conducted with the supported particles due to a lack of time, so the error bars which are displayed are those of the unsupported CaO-NiO particles and are present to simply to provide a visual representation of the approximate error associated with the data of similar type.

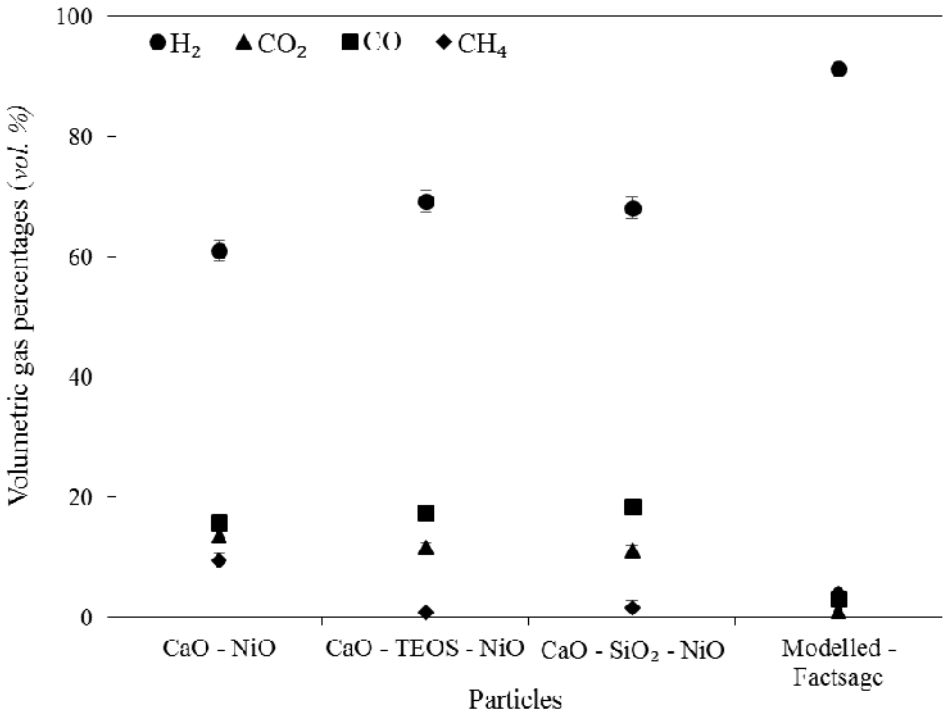

Figure 6.14 – Volumetric gas percentages of the product gas from biomass SESR in a fluidised bed reactor with combined particles composed of CaO and NiO and a C_2S support derived from TEOS or fumed Silica (- SiO_2 -).

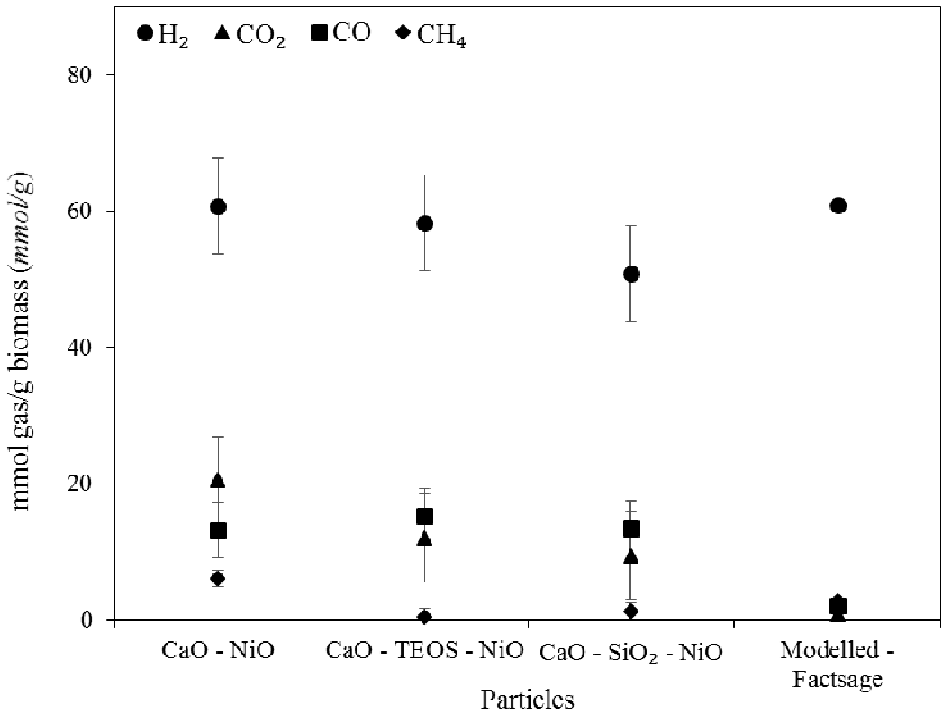

Figure 6.15 – Moles of individual gas species per gram of biomass added during SESR in a fluidised bed reactor with combined particles composed of CaO and NiO and a C_2S support derived from TEOS or fumed Silica (- SiO_2 -).

Table 6.6 – Overall closure of the carbon balances across the entire experiment and the extent of sorbent carbonation.

Sample	Overall closure of carbon balance (%)	Overall closure of hydrogen balance (%)	Overall closure of oxygen balance (%)	Amount of CO_2 captured during SESR (%)
CaO - NiO	123.6	94.7	121.4	38.7
CaO - SiO_2 - NiO	124.6	126.3	123.9	52.1
CaO - TEOS - NiO	112.4	100.7	113.2	59.3

Elemental carbon, hydrogen and oxygen balances across the overall process (SESR, calcination and burn off) were conducted and the results of which are displayed in Table 6.6 alongside the percentage of CO_2 captured during the SESR phase. The equations for deriving the mass balances are described in section 6.2.6. The observed deviation in the mass balances is thought to be caused by errors in the measurement of the different gases and variability in the biomass feeding and steam production. Furthermore the reactor was controlled manually (gas rotameters) over the ~75 minute period and therefore there is a certain degree of systematic error within the operation of the reactor which inevitably affected the mass balances. A further source of error which was not accounted for in the mass balances was the oxidation of Ni by steam and by the oxygen during the burn off stage.

6.2.5. Comparison with literature

The work here focussed on the novel use of solid biomass as its fuel source for SESR and therefore increases the difficulty of the work conducted. Comparisons with other literature data on similar processes will now be made.

The combined particles produced within this work show a similar BET surface area and CO_2 carrying capacity compared to some co-precipitated particles of CaO and NiO only (Wang et al., 2015). Li et al. (Li et al.) also detailed a set of experiments whereby analytically pure $CaCO_3$ was wet impregnated with varying amounts of $Ni(NO_3)_2$ to form a NiO loading of 2.5, 5 and 10 wt.%. These samples were placed within a fixed bed reactor at 650 °C where the vapours from biomass gasification/pyrolysis were passed over them to undergo the SESR process. The outlet gas composition from these reactions was broadly similar to the values found within this work however the addition of the NiO enhanced the reactions so much that the CaO sorbent was not able to absorb the additional CO_2 produced and as such the concentration at the exit was greater.

The use Ca and Ni based combined particles within a packed bed reactor undergoing multiple SE-SMR cycles was investigated by Broda et al. (Broda et al., 2012a) who showed that a CaO-NiO-hydrotalcite structure can reproducibly produce very high purity H_2 (~99 vol.%) effectively from the CH_4 feed. This

combined material was produced via co-precipitation and resulted in a relatively higher BET surface area compared to the values found here. Furthermore, an improved H_2 purity was produced by Broda et al. which is likely down to the much higher S:C ratio of 4 that was utilised (Broda et al., 2012a). An excellent H_2 production of efficiency of 99.1%, dropping to only 96.1% in the 10^{th} cycle of SE-SMR was also reported by Radfarnia et Iliuta. (Radfarnia and Iliuta, 2014) who utilised a fixed bed reactor. Their combined particles were produced by acidification (to open up the pore structure) of limestone followed by the wet impregnation of $Ni(NO_3)_2$. It is likely again that the reason for the much higher H_2 purity produced in their work was because of the much high S:C ratios (3-5) and the higher CaO:C ratio which was controlled by the feeding rate of the methane. Similar work within another fixed bed reactor was carried out by Garcia-Lario et al. who demonstrated that with the use of their combined particles, produced via physical wet mixing, that a H_2 concentration of over 90 vol.% could be produced over multiple cycles when using a methane feed gas (García-Lario et al., 2015b).

A two stage down draft fixed bed reactor (biomass pyrolysis then gasification and reforming) with co-precipitated combined particles of Ni-Mg-Al-CaO has been investigated with the use of biomass and the aim of producing H_2 (Nahil et al., 2013). The researchers found significantly higher CH_4 yields compared to work conducted here which is possibly due to the late introduction of steam into their system. Their work also found a maximum of 20.2 mmol H_2/g biomass (53.9 vol.% purity H_2) when their sample of Ni-Mg-Al-1CaO was utilised, which when compared to the sample most equivalent within this study (CaO – TEOS - NiO) a H_2 production of 58.2 mmol H_2/g biomass (69.3 vol.% purity H_2) was achieved, indicating their system operated further from the equilibrium and may have lacked the mixing that was achieved within the fluidised bed utilised here.

A hydrogen yield of 117 g/kg of pine wood waste biomass (1-2 mm particle size) was produced by Arregi et al. within a two stage reactor set up (spouted bed reactor for pyrolysing biomass followed by a fluidised bed reactor for reforming the produced gases), which is very similar to the value of 121.4 g H_2/ kg of biomass (60.7 mmol H_2/kg biomass) produced within this work (Arregi et al., 2016). This indicates that the process intensification of undertaking the biomass gasification and reforming reactions within one reactor was successfully equivalent in terms of H_2 production compared to a

separated system. CH_4 and CO gas compositions achieved in this work were comparable to the work of Arregi et al. however significantly more CO_2 was produced in their study due to the lack of CO_2 sorbent.

As it can be seen the results obtained within the set of experiments and within the constructed reactor were directly relatable and comparable the work conducted by others. It was also demonstrated the use of simple production methods for the combined particles lead to similar purities and yields of gas being produced. Most other studies do utilise simpler fuels/sources of hydrogen such as methane or sometimes model compounds such as toluene or glycerol which makes direct comparison difficult, especially as biomasses propensity to coke is significantly greater than that of CH_4 due to its far more complex structure.

6.2.6. Mass balance calculations

To calculate the purity (volumetric percentages) and yield (moles per gram of biomass) of each gas component during each phase of the experiment (H_2 reduction, SESR, calcination, burn off) the following generalised equations were implemented.

The outlet gas concentration of gas component, i, was adjusted by removing the baseline/inlet concentration of that gas component by applying a 1 dimensional sloped fit as follows.

Equation 6.10:

$$[i]_{released} = [i]_{out} - [i]_{in}$$

Equation 6.11 – The inlet molar flow rate, Fin, was calculated by:

$$F_{in} = \frac{P\,\dot{V}}{R\,T}$$

During SESR, only N_2 and H_2O were used to fluidise the particles meaning the inlet N_2 mole fraction can be calculated by: (during the calcination, steam was turned off thus $x_{N_2\,in}$ was 1, and during the combustion phase the mole fraction of H_2O was replaced by a constant value equal to the mole fraction of O_2 at steady state after combustion was complete).

Equation 6.12:

$$x_{N_2\ in} = 1 - x_{H_2O\ in}$$

Equation 6.13 – The outlet mole fraction of N_2 can be calculated by subtracting each of the mole fractions of all other gas components:

$$x_{N_2\ out} = 1 - \sum x_{i\ out}$$

Equation 6.14 – The outlet molar flow rate, F_{out}, was calculated by:

$$F_{out} = \frac{F_{in}\ x_{N_2\ in}}{x_{N_2\ out}}$$

Equation 6.15 – The moles of gas component, i, was calculated by:

$$n_{i\ released} = \int_{t=0}^{t=end} F_{out}\ x_{i\ out}$$

Equation 6.16 – The purity (volumetric gas percentages) of gas component i was calculated by:

$$i_{purity\ vol.\ \%} = \frac{n_i}{n_{total}} * 100\%$$

Equation 6.17 – The total closure of across the whole experiment and across each individual reaction phase by:

$$\xi = \left(\frac{n_C\ M_C}{F_{biomass}\ x_{C\ biomass}} + \frac{(n_H + 2n_{unreacted\ steam})M_H}{F_{biomass}\ x_{H\ biomass}} + \frac{(n_O + n_{unreacted\ steam})M_O}{F_{biomass}\ x_{O\ biomass}}\right) \cdot 100\%$$

Where:

ξ Closure of the component sytems, C, H and O as a percentage, %

$[i]$ Concentration of gas component i, vol.%

F_{in} Molar flow rate into the reactor, mol/s

F_{out} Molar flow rate out of the reactor, mol/s

$F_{biomass}$ Mass flow rate of biomas into the reactor (dry, ash free basis), g/s

i Gas component i can represent N_2, H_2O, CO_2, CO, CH_4, O_2 or H_2

i_{Purity} Volumetric gas % of component i, vol.%

$n_{i\ released}$ Moles of component i released during the reaction, moles

$n_{C,H,O}$ Total moles of C, H and O measured during a phase of the experiment, moles

$n_{unreacted\ steam}$ Moles of unreacted steam, moles

n_{total} Total moles of gas components CO_2, CO, CH_4, O_2 and H_2 (depending on experiment phase)

$M_{C,H,O}$ Relative molecular masses of C, H and O, g/moles

P Pressure, assuming 1 atm = 101,325 Pa, Pa

R Universal gas constant, 8.314 J/mol K

t time, s

T Temperature, 298 K

V Volumetric flow rate, m^3/s

$x_{i\ in}$ Mole fraction of component i in

$x_{i\ out}$ Mole fraction of component i out

6.3. Coke production and prevention

6.3.1. Coke formation on the combined particles

During the biomass gasification and SESR reactions, some of the biomass was inevitably converted into coke, which is deposited on the particles (Figure 6.16), the reactor liner, the feeding tube and at the exit of the reactor. The particles of coke that were elutriated from the bed were predominately captured within the glass wool filtration system however some of the finer coke particles were capable of passing through this system entirely. The particles that were captured were weighed at the end of each experiment and were added to the mass of coke combusted during the burn off phase.

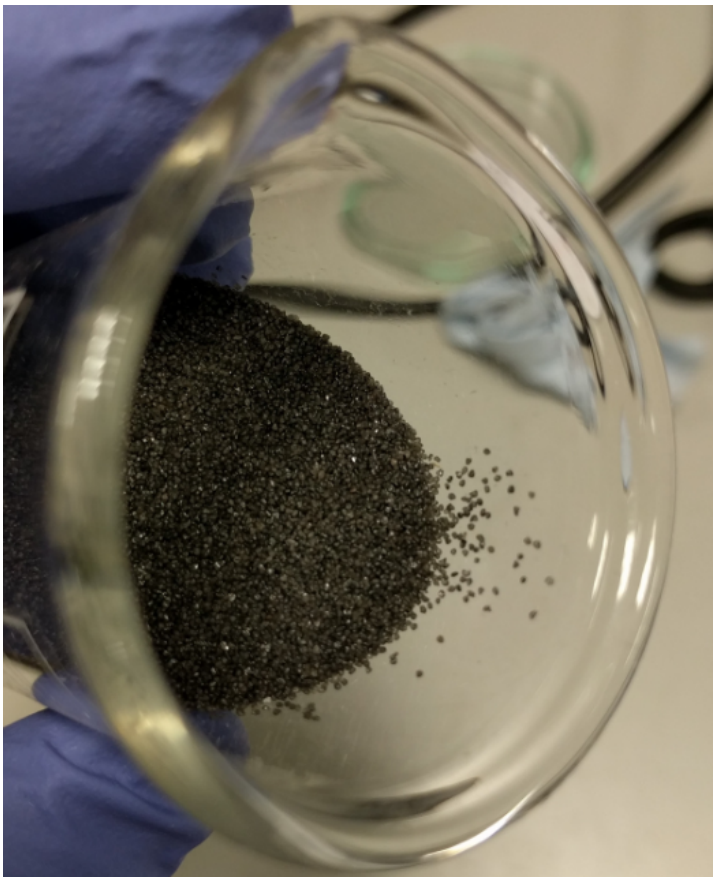

Figure 6.16 – Coked particles post biomass SESR, no calcination or burn off.

The deposition of coke on the combined particles can be detrimental to the activity of the Ni and absorption capabilities of the CaO. Coke is known to take several forms, which have been outlined below (Bartholomew, 2001):

- **Surface carbides** – chemical adsorption as a monolayer (such as Ni-C, nickel carbide), temperature of formation: 200 - 400 °C, slow to form, low steam to fuel ratios required
- **Amorphous films or filaments** – multilayer physical absorption, temperature of formation: 250 - 500 °C, progressive deactivation, low steam to fuel ratios required
- **Graphitic film** – induced crystallinity of amorphous film by increased temperature, temperature of formation: 500 - 550 °C, requires temperatures greater than formation temperature for decomposition to occur

- **Graphitic whiskers/filaments** – induced crystallinity of amorphous film by increased temperature, temperature of formation: 300 - 1000 °C, can potentially lead to the particle break up due to the filaments causing stress within the particles pores, requires temperatures greater than formation temperature for decomposition to occur

It has also been noted recently that the incorporation of iron into the matrix of a Ni-based catalyst led to a significant decrease in the deposition rate of coke on the surface of the catalyst. This effect was linked to the iron oxides increasing the lattice oxygen content (confirmed by XPS) which meant that any carbon that formed on neighbouring Ni sites was readily oxidised. Furthermore a sustained reduction in conversion of amorphous coke into graphitic coke was observed and explained to be due to the ability of the Fe to cycle between oxidation states within the carbonator/reformer where steam and hydrogen were present simultaneously (Hu et al., 2016).

To investigate the deposition of carbon onto the combined particles a ~35 mg sample of CaO-NiO (26 wt.% Ni) post SESR (no calcination or burn off) was analysed on a TGA-MS (Netzsch - TG 209 F1 with QMS 403 D). To obtain this sample, once SESR was complete the steam system was bypassed and the bed material was purged for a few minutes under N_2 to remove any moisture that remained, after which the bed material was dropped into the U-bend by turning off the gas fluidising gas and turning the reactor heating off. This was done in order to try and preserve the state of the combined particles. To assess the degree of coking, the sample placed within the TGA-MS and was first heated to 900 °C under N_2 to calcine the sorbent, then cooled to 100 °C still under N_2 and finally the sample was heated to 900 °C in air at a ramping rate of 10 °C/min to burn off the coke. The calcination step was required to minimise the interface between CO_2 released from the sorbent and CO_2 released from the combustion, however by doing this the coke deposits may have become shifted further into the graphitic carbon range.

The TGA temperature vs weight percentage change profile is displayed in Figure 6.17 showing the loss of hydrates from the sorbent, loss of carbonates in the sorbent and then oxidation of the Ni and burn off of the coke. The weight percentage change is overlaid with the mass spectrometer response for CO_2 (44

g/mol) and molecular oxygen (O, 16 g/mol) which are shown as Figure 6.18. MS data for other gases was also collected (SO_2, CO, O_2, H and Cl) however they are not included here.

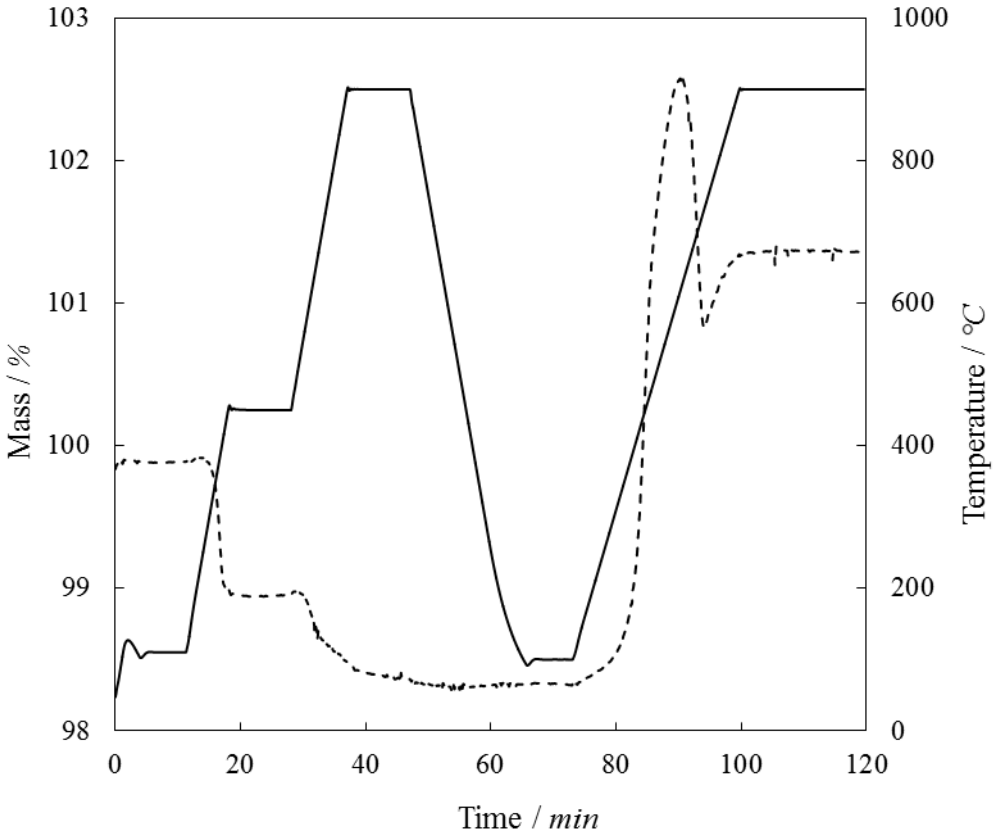

Figure 6.17 – TGA temperature vs weight change as a percentage of the initial mass for a sample of coked combined particles composed of CaO and NiO (26 wt.%).

It can be observed in Figure 6.18 that the oxidation of the coke didn't fully occur until the oxidation of the Ni was almost fully complete, this could be because the Ni has a stronger oxygen affinity and therefore preferentially oxidised. Furthermore the CO_2 MS trace appears to continue long after the pronounced weight change where the formed carbonates decomposed (heating from 450 °C to 900 °C in N_2) indicating that some of the carbon was oxidising even without the presence of air. This effect could be explained by the coke stripping oxygen from residual NiO (formed by steam oxidation during SESR) and thus forming the observed CO_2. The reduction of NiO by carbon has been studied previously and has shown that the formed Ni actually catalysed the process further (Fruehan, 1977). The amount of carbon oxidised by this process is small as can be observed by the change in weight measured, this

is because the solid-solid reaction is slow and the temperature is reducing during this time period and thus the reaction thermodynamics are not favoured.

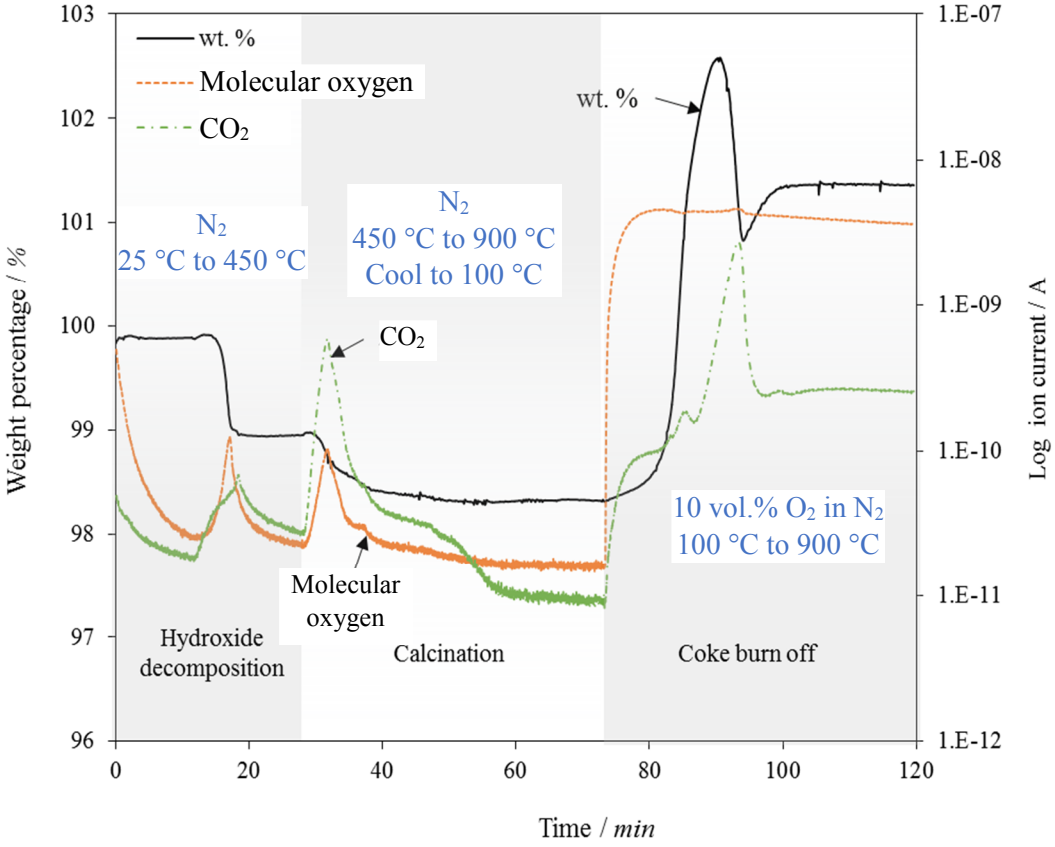

Figure 6.18 – TGA weight change as a percentage of the initial mass and mass spectrometer response for CO_2 and molecular oxygen for a sample of coked combined particles composed of CaO and NiO (26 wt.%).

The temperature programmed oxidation (TPO) of the combined particle sample shown in Figure 6.19 was produced by combining the TGA data with the MS data in Matlab and shows that the majority of the coke was decomposed between 600 – 760 °C indicating that the sample's coke was predominately graphitic in nature. However, as stated earlier the effect of preheating the sample to calcine the sorbent likely had a significant effect on the type of carbon which remained for the TPO. The addition of Fe onto the exterior of the combined particles with the aim of utilising the redox potential of the Fe for coke reduction would certainly be an interesting area to explore in the future (Di Felice et al., 2010).

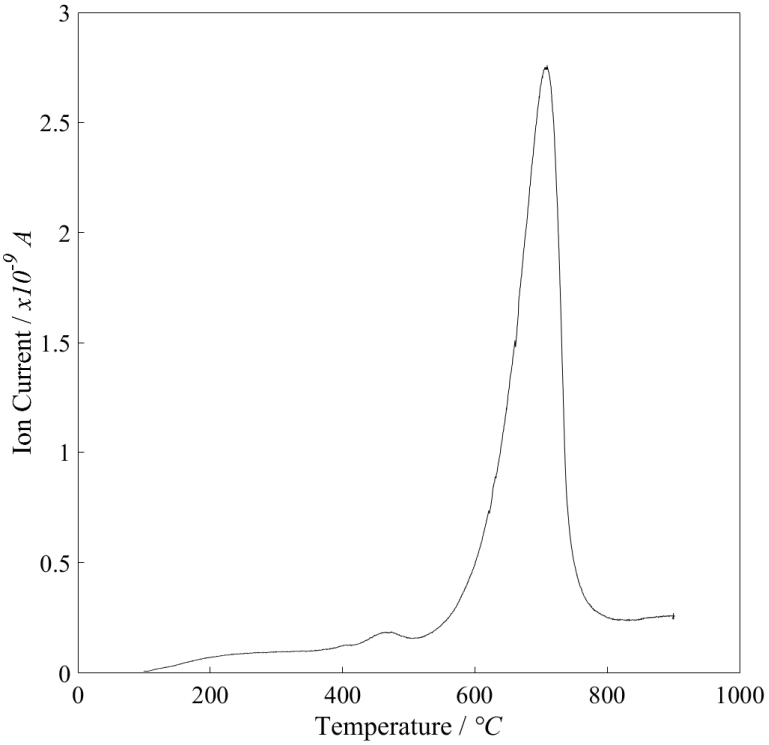

Figure 6.19 – Temperature programmed oxidation showing the CO_2 MS trace against temperature of the TGA for a sample of coked combined particles composed of CaO and NiO (26 wt.%) post SESR (no calcination or burn off).

6.3.2. Coke formation within the reactor

The formation of coke within the reactor itself from the gasification of the biomass led to more operational difficulties than the deactivation of the combined particles through coking. Figure 6.10 has been reproduced and edited to form Figure 6.20 in which a red circle has been added to indicate the point in time during the run at which the at which biomass feeding was halted. Continuous biomass feeding was a very difficult objective to achieve; a problem that was not encountered until the reactor was hot and continuously operating was that as the biomass was fed into the reactor it began to pyrolyse/gasify within the feeding tube (connecting the outlet of the U-bend to the bottom of the quartz liner, which enters only about 1/3rd of the heated length ~ 8 cm). Despite a gas velocity of ~1.4 m/s @ 150 °C (temperature and therefore flow rate increased as the gas and biomass travelled further up the feeding tube into the reactor) the biomass began devolatilising within the feeding tube. This volatile

matter adhered to the side of the feeding tube which due to the lower rate of decomposition/gasification compared to the rate of volatile matter production, an accumulation occurred. The volatile matter subsequently began to carbonise and form coke and gradually, over time, the internal diameter of the feeding tube narrowed and eventually blocked. This blockage would then cause a pressure increase before the reactor and prevent all gas from flowing. The operation of the reactor could not continue for longer than ~8 minutes before this issue became apparent and feeding had to be stopped to prevent the blockage from stopping the gas flow.

The blockage was confirmed to be within the feeding tube and not to be an agglomeration of the bed material as the reactor was taken apart post SESR (no calcination or burn off) and upon inspection it was evident that the blockage had not occurred within the bed but within the feeding tube itself, where the internal diameter of the tube had decreased as coke had formed.

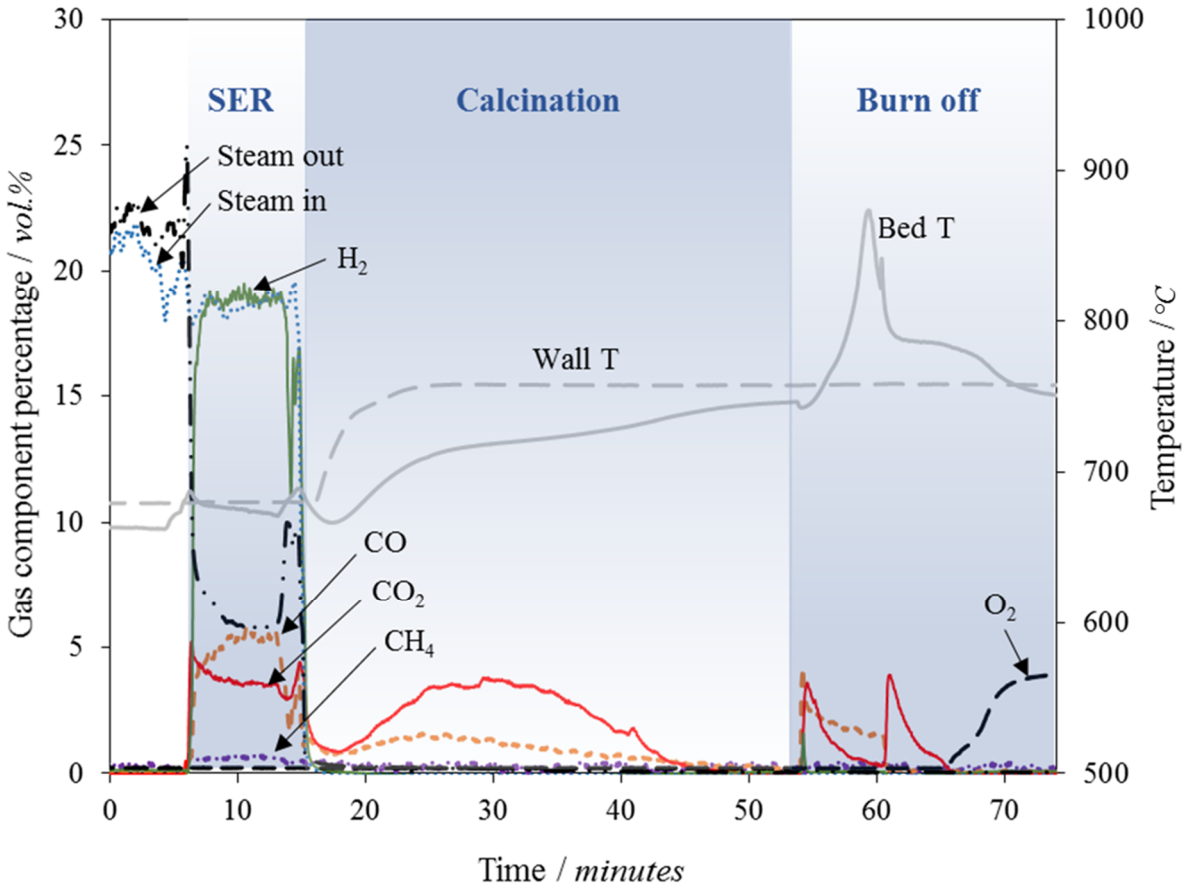

Figure 6.20 – A typical response to a long (~8 minutes) biomass feed during SESR, followed by calcination and then coke burn-off. The area within the red oval shows the position at which the biomass feeding system was interrupted by coking on the inlet feeding tube.

To try and alleviate the issue of coking within the feeding tube, the bio-knocker N_2 gas flow was substituted for air, hoping that the oxygen would combust the coke that was forming within the feeding tube. A large batch of combined particles with 32 wt.% Ni were produced using the same method described earlier for this set of experiments, furthermore all other reaction conditions and operating set points were maintained. Figure 6.21 displays the effect of oxygen addition during SESR on the amount of coke measured during the combustion (and CO production from the Boudouard reaction during the calcination stage) stage. This figure seems to suggest a counter intuitive result, more oxygen in the feed gas equals more coke formation. This data is also convoluted in that it doesn't provide any information as to where the coke was formed/destroyed.

The effect on the product gas composition is also displayed as Figure 6.22, showing that as the O_2 partial pressure was increased the production of CO_2 and CO increased which lowered the overall gas concentration of H_2. The additional CO_2 that was produced was also seemingly not able to be absorbed by the sorbent despite the CaO being well in excess of the CO_2 produced.

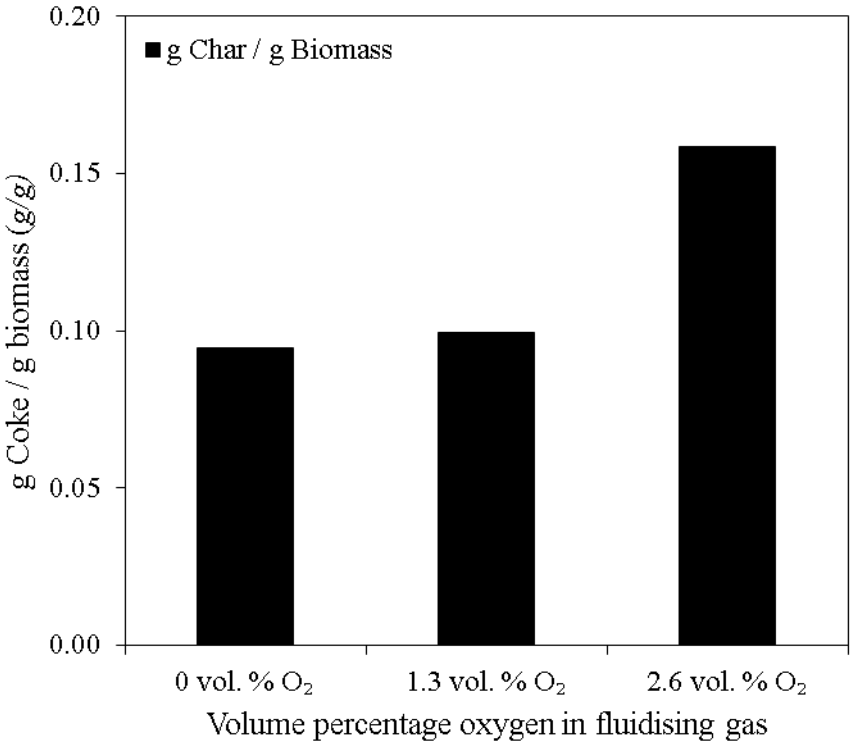

Figure 6.21 – Coke formation per gram of biomass added as a function of oxygen partial pressure in the gas stream during SESR.

It can be stated qualitatively that when adding oxygen the length of time that feeding was successful for increased by approximately 2-3 minutes for every ~1.3 vol.% O_2 increase in the gas stream. Repeats for this data set were not conducted so no approximation of the error can be provided This data is also affected by the fact that for every 1.3 vol.% increase in the O_2 concentration the bed temperature increased by approximately 10 °C, and without the knowledge of how temperature affects the rate and extent of the reaction the data shouldn't be directly compared.

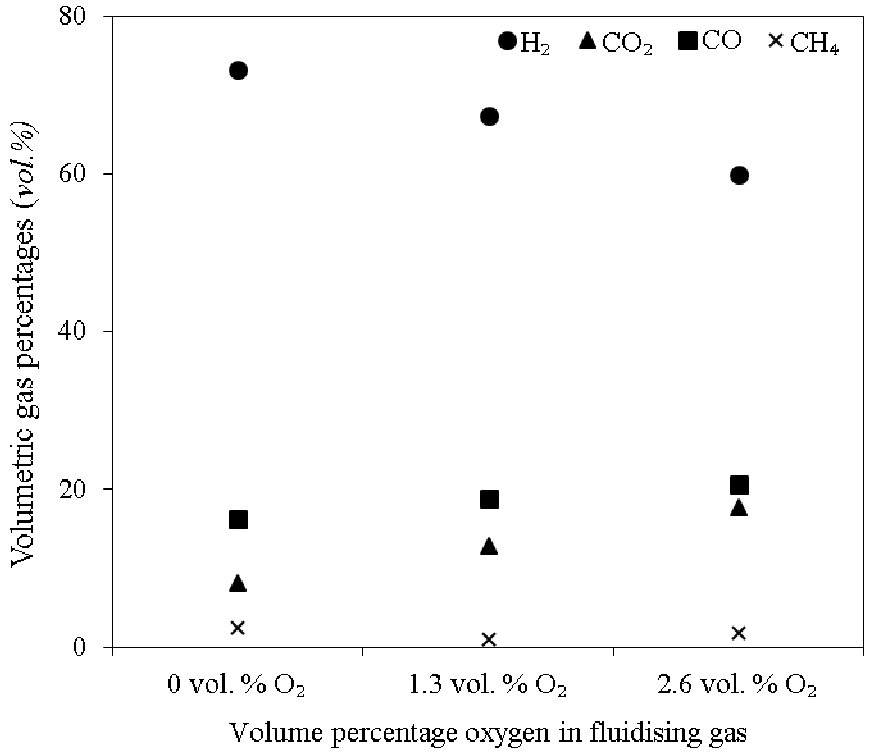

Figure 6.22 – Impact of oxygen addition on the volumetric gas percentages of SESR products.

It may well be demonstrated by future research that the addition of O_2 is necessary for SESR to raise the operating temperature however for the purposes of coke decomposition it is suggested, based on this very short and partial set of data, that O_2 addition is probably not the best method of coke decomposition if H_2 is the end goal. Instead, it is thought that the decomposition of coke would be more effectively executed by destroying the tar before it turns into coke by raising and controlling the steam to carbon ratio and potentially lining the internal wall of the feeding tube with a Ni based coating to act as a catalyst for the decomposition reactions (Sikarwar et al., 2016) (Song et al., 2015) (Trimm, 1997).

6.4. Kinetic Investigation within a High-Pressure Spout-Fluidised Bed Reactor

From observing the data presented in Figure 6.12 and Figure 6.13, it is clear that significant internal diffusional effects were present within the combined particles during the SESR experiments. A good understanding of the kinetics and reaction dependant parameters is important for the accurate design of reaction vessels and commercial operating facilities, which in turn affects the selection of suitable particle size fractions for operation (Fogler, 2006). In heterogeneous reactions such as SESR, the measured kinetics of a reaction are influenced by the reactant gas concentrations and by the following factors (Fogler, 2006):

- External bulk gas diffusion of the gas molecules to and from the exterior surface of the solid particles (ignoring any gas film)
- Internal Knudsen diffusion of the gas molecules through the tortuous path within the pores, to and from the active sites where the actual reaction takes place
- Heat transfer to and from the bulk gas/reactor bed material to the particles surface
- Heat transfer throughout the particles structure

The structure and composition of the particles themselves can also greatly affect the degree to which these factors influence the rate of reaction.

If the observed rate of a reaction is defined as $-r_A$ and the true intrinsic rate of the same reaction is defined as $-r_{AS}$ (where no external diffusion or heat transfer limitations are present, i.e. the particle is said to react at the surface gas concentration), then it is possible to write the following equation.

Equation 6.18:

$$-r_A = \eta(-r_{AS}) = \eta(kC_{AS}^n)$$

Where η is the internal effectiveness factor of the reaction and defines the extent to which surface reaction and diffusion resistances affect the kinetics.

In this section, the carbonation kinetics of the CaO – NiO (26 wt.% NiO) and CaO – TEOS – NiO (26 wt.% NiO) combined particles that were produced and tested within section 6.2 will be investigated. These two sets of combined particles were utilised as they were both shown to be effective at producing high purity H_2 during SESR and would enable a direct comparison between supported and unsupported combined particles.

6.4.1. Literature background

There are many examples of previous work that has investigated the kinetics of CO_2 carbonation of CaO based sorbents. From this prior work the rate of carbonation of a CaO based sorbent is known to follow a dual staged process whereby there is an initial fast reaction kinetics controlled phase followed by a slower diffusion controlled phase (Barker, 1973b). The fast initial carbonation reaction occurs at the external surface of the particles but gradually, as the formation of $CaCO_3$ progresses, the average pore width begins to narrow which increases the diffusion resistance of CO_2 into the particles which means the reaction becomes dependent upon the movement of CO_2 through the $CaCO_3$ product layer (Yu et al., 2012). Steam is known to be an effective reagent at minimising the diffusional resistance through the product layer by maintaining a stable open pore structure and thus increase the rate of reaction and overall conversion of the sorbent (Donat et al., 2012).

An kinetic rate study of limestone and dolomite carbonation was conducted in a TGA by Sun et al., (Sun et al., 2008a), they found a zeroth order dependence on CO_2 partial pressure above 10 kPa and first order dependence below that partial pressure. They also noticed slight variations in their observed activation energies due to structural/compositional differences between the materials tested. Kinetic carbonation parameters for synthetically derived Ca-based sorbents were also derived by Zhou et al., who fitted their experimental data produced from the use of a TGA to the random pore model (RPM) and the overlapping grain model (OGM) with good success (Zhou et al., 2013). A thermodynamic model of CO_2 capture within Aspen modelling software was created and kinetic parameters derived from this study were in good agreement of data collected within a TGA (Mostafavi et al., 2013). However, kinetic data gathered within a TGA is known to suffer from significant deficiencies caused by gas bypass and external mass transfer limitations (Borgwardt, 1985) (Liu et al., 2012).

Measuring the kinetics of SESR or SE-SMR is less frequent in the available literature, which is likely because of the complex set of reactions which take place within these processes. As such it can be difficult to isolate the influencing parameters and intrinsic rates of each near simultaneous reaction each governed by their own set of equilibrium thermodynamics even when efforts are made to separate and isolate the reaction in question (Abbas et al., 2017).

It has been reported previously that the SMR process is greatly limited by internal diffusion and because of this the SMR reactions occur very close to the surface only (Xu and Froment, 1989b) (Xu and Froment, 1989a). Based off the work by Xu and Froment, Obradovic et al. (Obradović et al., 2013), conducted a series of intrinsic kinetic SMR experiments within a small fixed bed reactor with minimal external mass transfer resistance from which they validated the original reaction kinetic parameters determined by Xu and Froment (Xu and Froment, 1989a). The true kinetics of a Ni/Al_2O_3 catalyst material for SMR were measured by Oliveira et al. in a small fixed bed reactor, who found the effectiveness factors of the materials to be ≈ 0.33 with a tortuosity factor of 1.56 (Oliveira et al., 2009).

A small packed bed micro-reactor has been utilised to investigate the kinetics of a sorption enhanced water gas reaction where the researchers were able to effectively minimise the external and internal mass transfer resistances by using a relatively high gas flow rate and small particle size. The produced gas was sampled and analysed utilising a GC every 3 minutes which may sound slow but actually compared to the overall reaction period was roughly acceptable to derive kinetic parameters. The data from which was then compared to a 1-D model of the reactor and was found to be in close agreement to the experimental data gathered (Živković et al., 2016). No attempt was made in this work to check that the kinetics gathered were actually the intrinsic rates and not just the observed rates.

The effectiveness factors for carbonation of un-combined sorbent and catalyst particles compared to combined particles has been modelled as part of an overall SE-SMR model and demonstrated a higher effectiveness factor of the combined particle system (0.9 for combined compared to 0.1 for the un-combined) due to the diffusion distance minimisation (Rout and Jakobsen, 2013). The effectiveness factors of carbonation of synthetically produced CaO sorbents with and without a calcium aluminate support were derived from experimentation within a TGA and a fixed bed reactor, they found an

effectiveness factor of ~0.05 during the fast kinetic controlled carbonation stage which gradually tailed off towards 0 as the product layer diffusion controlled stage began to take dominance (Rout et al., 2014).

Currently there are few kinetic studies into SE-SMR or SESR within fluidised beds, although some modelling work has been conducted (Solsvik and Jakobsen, 2011) (Johnsen et al., 2006a). Some work has been conducted into the kinetics of combined multifunction particles and was highlighted here, although this is often based on modelled predictions. There is also a lack of analysis into the kinetic values derived from experimental work as to whether they are the intrinsic kinetics or simply the observed kinetics, it seems most work present the observed kinetics. Because of the lack of experimental kinetic data for combined CaO and NiO particles for SESR in the literature currently a set of experiments were derived to investigate the details of this process further. Because of the multitude of reactions and there interdependence upon each other it was decided that only the carbonation reaction would be studied and from these kinetic experiments the effectiveness factors and activation energies would be derived. A fluidised bed reactor was chosen to minimise the external mass transfer limitations whilst conducting this study.

6.4.2. Experimental procedure

This set of work was conducted within a 'high' pressure spout-fluidised bed reactor similar to the one designed and constructed as described within Chapter 3. However this reactor has an internal diameter of 30 mm and a quartz liner reactor vessel height of 270 mm and is electrically resistance heated. Further details of this reactor can be found in the work by Zhang et al. (Zhang et al., 2016). The reasons for utilising this reactor as opposed to the one designed and constructed in this body of work were that it had a faster response time (~6 s – therefore the measured gas concentrations were closer to the true gas concentrations and the reactor can be assumed to operate as a CSTR) and this reactor had a much more accurate control over the bed temperature, gas flow rates and operating pressure due to the application of specialised instrumentation (Bronkhorst UK Mass flow controllers and a Bronkhorst UK pressure control valve). The CO_2 concentration during the reactions was deconvoluted in Matlab by applying a CSTR model to the data, as described in previous chapters and utilising Equation 6.19.

Equation 6.19 – Deconvolution of the reaction rate assuming a CSTR (Fennell et al., 2009):

$$C_{CO_2 t} = C_{CO_2 m} + \tau_{bed} \frac{dC_{CO_2}}{dt}$$

Where τ_{bed} is ($\tau_m - \tau_0$) the difference between the measured response time, τ_m, and the measured response time, τ_0, when the gas bypasses the entire bed and enters the gas analyser directly. $C_{CO_2 m}$ refers to the concentration of CO_2 as the reaction progresses and $C_{CO_2 t}$ refers to the concentration of CO_2 after deconvolution. A step impulse of CO_2 was injected into the reactor and the response to 90 % of the final value was used for the response time measurements. The value of τ_m was calculated by taking the inverse of the slope of $ln(1 - C_{CO_2 m} / C_{CO_2 i})$ against t (s) where $C_{CO_2 i}$ is the final concentration of the total step response.

This research was conducted at 1.5 bar(a) as there was a 0.2 bar(g) pressure drop across the system therefore instead of trying to reach 1 atm it was considered more appropriate to control to a set value of 0.5 bar(g). The flow rate utilised for these experiments was aimed to be a similar to that of the unpressurised work, which consisted of a total flow rate of 75 cm^3/s (@ 293 K, 1.5 bar(a) – $u/u_{mf} \approx 3.5$ for sand 425 – 500 μm, this total flow rate was split for the experiments without steam as follows: main feed N_2 = 64 cm^3/s and CO_2 = 11.4 cm^3/s; and for the experiments with steam: main feed N_2 = 20 cm^3/s, steam carrier gas N_2 = 29 cm^3/s, CO_2 = 11.4 cm^3/s and steam = 14.7 cm^3/s). When steam was present a value of 19 vol.% was aimed for and adjusted by altering the water flow rate entering the steam generation system.

The samples utilised in this study were the unsupported CaO and NiO combined particles, denoted as CaO – NiO, with 26 wt.% NiO and a C_2S supported sample derived from TEOS, denoted as CaO – TEOS – NiO, again with 26 wt.% NiO. Each of the samples were produced via the methods described in section 6.1. Before the kinetic experiments could be commenced the samples (the nickel within the particles) had to be reduced into their metallic state, as this is the active state for the reforming reactions and it is important to assess the kinetics under realistic particle conditions. Samples were taken in ~30 g batches and placed within a quartz liner which had a disc of stainless steel mesh at the bottom to support the particles. This loaded quartz liner was then placed within the reactor described in Chapter

3, the reactor was sealed and then heated to 650 °C under a small flow rate (30 cm^3/s) of N_2 to minimise any fluidisation and encourage fixed/packed bed flow regime. Once the temperature had stabilised within the bed, 15 cm^3/s 10 vol.% H_2 (balanced with N_2) was substituted for the 15 cm^3/s of the N_2 flow. H_2 reduction was conducted for 1 hour and was confirmed to be complete by observing the steam concentration in the exit gas flow rate and by observing the H_2 concentration. Post reduction, the samples were cooled under N_2 flow, then removed from the reactor, sieved into separated size fractions and stored in sealed vessels in a sealed container together with CO_2 and moisture sorbents.

These carbonation experiments were conducted by pressure feeding weighed small aliquots of combined particles into the reactors bed material (composed of sand of size fraction 425-500 μm), where the particles were fluidised by N_2 and CO_2 and when required, steam. The pressurised feeding system was unchanged from system described in by Zhang et al. (Zhang et al., 2016). The gas exiting the reactor was then passed over a relative humidity probe (HMT334, Vaisala) and then subsequently onto the steam condensation system and finally the gas concentrations were measured using an ADC multigas analyser (MGA 3000), although only CO_2 was of interest in this piece of work.

The data was analysed in a Matlab code where the average was taken of multiple runs (>3) which was then processed to remove the averaged analyser response to multiple empty feeds, i.e. blank runs. This data was then organised and outputted for collating in excel.

6.4.3. Initial kinetic carbonation experiments with CaO

To determine the optimal sample mass to use, such that the external mass transfer diffusion did not limit the rate of reaction within the bed, CaO only particles (300 – 500 μm) produced within section 6.1.3were utilised initially to determine the optimal sample mass. The results of these experiments are displayed in Figure 6.23.

Figure 6.23 demonstrates that the reactions conducted with a sample mass of 0.125 g presented a significantly higher reaction rate compared to the next sample mass up, 0.25 g. Ideally a sample mass less than 0.125 g should be tested to determine if 0.125 g is itself limited by external mass transfer

diffusion, however to go any lower than this would not have been possible, as the change in CO_2 concentration from the baseline would have been too similar to the blank runs.

It was also noted from the experimental results that the carbonation reactions conducted with steam reached a higher observable conversion after 100 seconds (50 – 60 %) than the carbonation reactions without steam (25 – 33 %). This is in line with the work conducted by Manovic and Anthony (Manovic and Anthony, 2010a). This overall increase in carbonation rate and conversion due to the addition of steam has been explained previously to be due to the enhancement of the solid state diffusion in the product layer (Manovic and Anthony, 2010a) (Donat et al., 2012).

It was decided based on these experiments that a sample mass of 0.125 g would be used for all future experiments as it provided the highest peak reaction rate and had minimal external mass transfer limitations.

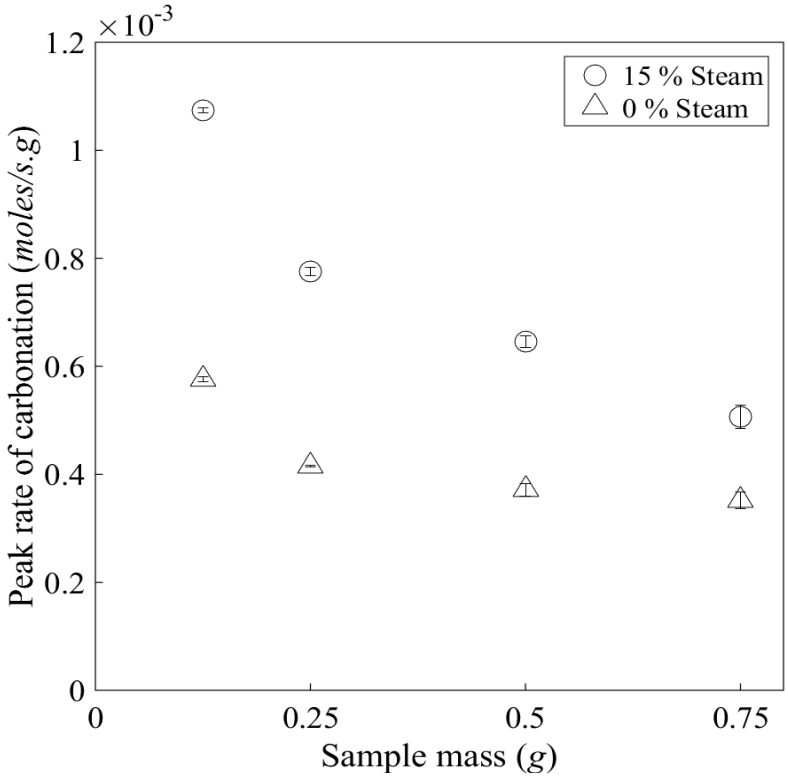

Figure 6.23 – Observed peak rates of carbonation, CaO only particles 300 – 500 μm. Reactions conducted at 650 °C, 1.5 bar(a), 15 vol.% steam (if used) and 15 vol.% CO_2.

6.4.4. Activation energy (observed) of combined particles

To calculate the observed activation energy of carbonation for these combined particles multiple samples were added at 5 temperatures (550, 600, 625, 650 and 700 °C) and the drop in CO_2 concentration was observed.

The peak rates were determined during the Matlab code analysis, which were then converted into rate constants assuming first order reaction kinetics following the relationship described by Equation 6.20.

Equation 6.20 – Rate of reaction, r in mol m^{-3} s^{-1}:

$$r = k\left(C_{CO_2} - C_{CO_2 eq}\right)^n = k\left(\frac{P_{CO_2}}{R\,T} - \frac{P_{CO_2 eq}}{R\,T}\right)^n$$

Where:

k Rate constant in s^{-1}

C_{CO_2} Molar concentration of CO_2 in mol m^{-3}

$C_{CO_2 eq}$ Equilibrium molar concentration of CO_2 in mol m^{-3}

P_{CO_2} Partial pressure of CO_2 in Pa

$P_{CO_2 eq}$ Equilibrium partial pressure of CO_2 in Pa

R Universal gas constant in J K^{-1} mol^{-1}

T Temperature in K

n is a factor to account for the order of reaction, assumed to be 1 here

The Arrhenius plot for the samples can be observed in Figure 6.24. The reactions were conducted with and without steam and were denoted as such. The laws of error propagation were applied to generate the error bars from the standard deviation of the peak rates of multiple runs of the same sample.

A fairly linear increase in the rate of reaction with temperature was observed for all systems, implying that the reaction systems did not approach the thermodynamic equilibrium point at which calcination would be favoured over carbonation. The thermodynamic equilibrium position of these reactions is

described by Equation 6.21 (García-Labiano et al., 2002) which enables calculation of the driving force of the reaction, defined as the difference between the inlet CO_2 partial pressure and the system equilibrium partial pressure of CO_2, P_{CO_2eq}, shown as $(P_{CO_2} - P_{CO_2eq})$. The inlet CO_2 partial pressure was taken at the peak rate but in reality the concentration of CO_2 that the particles were subjected to is somewhere between the bulk inlet CO_2 concentration and the concentration at peak rate, but it was assumed that this reacted behaved as a well-mixed CSTR in which case it is possible to assume the inlet and peak rate concentration were equal. At the lowest temperature (550 °C) and the highest temperature (700 °C) of carbonation the driving forces were calculated to be 0.15 bar and 0.13 bar respectively.

Equation 6.21 – Equilibrium partial pressure of CO_2 , P_{CO_2eq} in bar and T in K:

$$K_{eq} = 4.137 \times 10^7 exp\left(\frac{-20474}{T}\right)$$

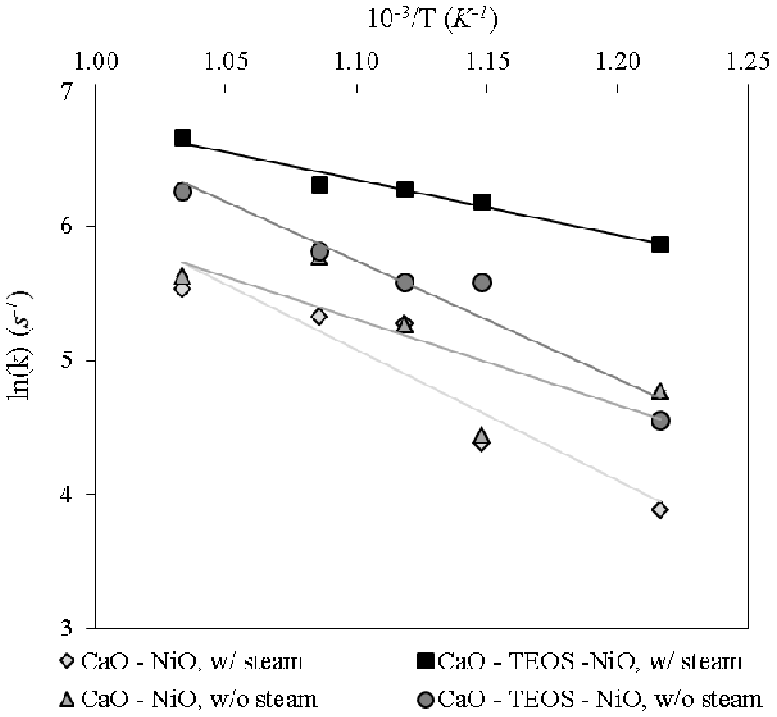

Figure 6.24 – Arrhenius plot of the carbonation observed reactions of combined CaO and Ni particles 300 - 425 μm, with and without a support and with and without 18 vol.% steam present during the reaction. Conducted within a spout-fluidised bed reactor at 550-700 °C, 1.5 bar(a), 15 vol.% CO_2 and 0.125 g sample masses.

Table 6.7 details the fitted apparent Arrhenius equations and their associated pre-exponential factors for the different combined particle samples with and without steam. The CaO – NiO w/ steam sample presented a higher activation energy than that of the same sample without steam; this is more likely due to variability in the experimental data of the CaO – NiO w/o steam sample, evidenced by the R^2 value of the least squares regression fitted Arrhenius equation in Figure 6.24 being ~ 0.6. Previous work into the kinetics of carbonation with steam has demonstrated that the addition of steam benefits the rate of reaction and lowers the activation energy. Activation energies in the literature for CaO carbonation under similar conditions have reported values ranging from ~24 to ~180 kJ/mol (72.2 and 72.7 kJ/mol (Gupta and Fan, 2002), 179.2 kJ/mol (Bhatia and Perlmutter, 1983), 72.0 kJ/mol (Lee, 2004), 20.3 kJ/mol for kinetic control and 163 kJ/mol for CO_2 diffusion control (Grasa et al., 2009), 24 kJ/mol (Yu et al., 2012), 29 kJ/mol (Sun et al., 2008a)). The error ranges provided in Table 6.7 (Equation 6.22 to Equation 6.25) – were calculated by applying a least squares regression from which the uncertainty in the slope of the line was calculated and the laws of error propagation applied. The rates utilised for this analysis were the observed rates as measured by the gas analyser, however it is understood that the true intrinsic activation energies would be higher depending upon the impact of heat and mass transfer control on the reaction (Fogler, 2006).

Table 6.7 – Arrhenius equations detailing the observed activation energies and pre-exponential factors for different combined CaO and Ni particles 300 - 425 μm, with and without a support and with and without 18 vol.% steam present during the reaction. Conducted within a spout-fluidised bed reactor at 650 °C, 1.5 bar(a), 15 vol.% CO_2 and 0.125 g sample masses. R is the ideal gas constant in J/mol.K.

	CaO – NiO w/o steam		CaO – TEOS – NiO w/o steam
Equation 6.22	$k_T = 2.14 \times 10^5 e^{\frac{-52.7 \pm 13.9\ \text{kJ}}{RT}}$	Equation 6.23	$k_T = 4.90 \times 10^6 e^{\frac{-73.0 \pm 11.2\ \text{kJ}}{RT}}$
	CaO – NiO w/ steam		CaO – TEOS – NiO w/ steam
Equation 6.24	$k_T = 6.95 \times 10^6 e^{\frac{-80.7 \pm 17.5\ \text{kJ}}{RT}}$	Equation 6.25	$k_T = 5.37 \times 10^4 e^{\frac{-34.4 \pm 3.7\ \text{kJ}}{RT}}$

6.4.5. Effectiveness factors of the combined particles

One of the main purposes of conducting these kinetic experiments was to determine the influence of internal mass transfer resistance on the combined particles to judge if the combined particle structures would negatively affect the rate of SESR. To simplify the multitude of SESR reactions that take place only the carbonation reaction was studied and the internal effectiveness factors were derived from this data. It was calculated that within the fluidised bed reactor the u/u_{mf} was sufficiently high enough (≈ 3.5) that the external mass transfer resistance from the bulk gas to the surface of the particle would be minimal, as the values of k_g were calculated to be ~0.1-0.4 m/s which is broadly in line with the velocity of gas passing through the reactor (~0.3 m/s). These effectiveness factors should still be valid for the reforming reactions assuming that the Ni grains and CaO grains are homogenously distributed throughout the combined particles and that the effectiveness factors are intrinsic properties of the particles themselves and not the carbonation reaction.

Equation 6.26 – The effectiveness factor of a particle is defined as:

$$Effectiveness\ factor = \eta = \frac{Actual\ rate\ of\ reaction}{\begin{array}{c}Reaction\ rate\ if\ entire\ surface\ area \\ were\ exposed\ to\ the\ surface\ concenration\end{array}}$$

To calculate the effectiveness factors of these combined particles the peak rates of reaction were measured and converted into rate constants (s^{-1}). A plot of the rate constants against particle size can be observed in Figure 6.25. Unfortunately after multiple attempts, inconsistencies in sample feeding meant that not all data points were collected for the CaO – TEOS – NiO sample with steam present, it was therefore decided to exclude this incomplete data set.

It can be observed from Figure 6.25 that the CaO – TEOS – NiO samples' peak rate of carbonation was not significantly limited by the particle size, within the range tested. This implies that the C_2S, TEOS derived supported combined particles benefited from an improved particle structure which aided CO_2 diffusion within the particle and can be evidenced by the greater surface area of pores in the optimal carbonation range – see Table 6.4.

Figure 6.25 also shows that the addition of steam greatly reduced the diffusion resistance within the particle and as such the rates of reaction were significantly improved. The general slope of the fitted line was also decreased by the addition of steam showing that the rate of reaction was enhanced most for the largest particle size fraction tested – where the largest internal mass transfer resistance is expected to be present.

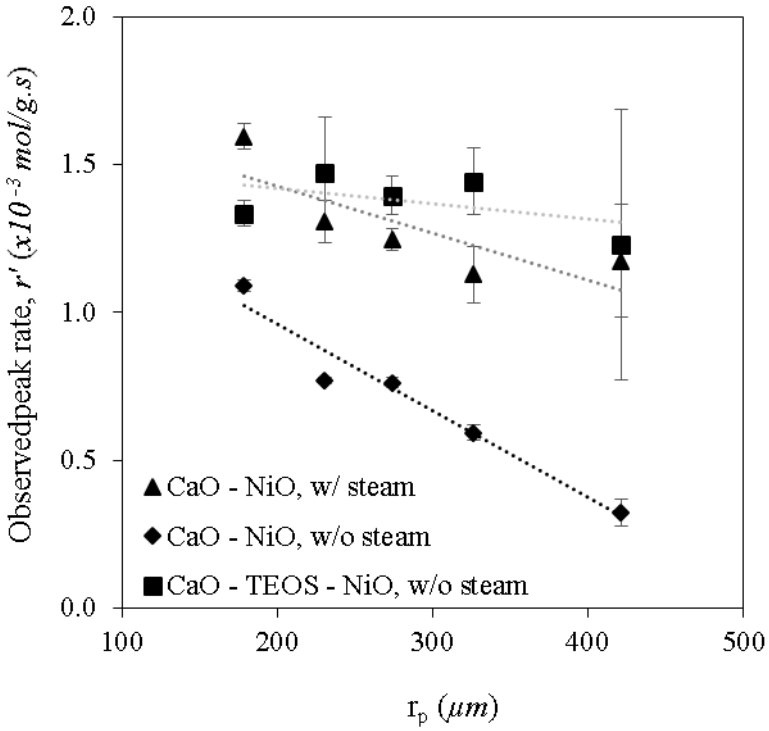

Figure 6.25 – Peak observed carbonation rate constants against the geometric mean radius of the combined particles. Dervied from the peak rates of carbonation of combined CaO and Ni particles, with and without a support and with and without 18 vol.% steam. Experiments were conducted within a spout-fluidised bed reactor at 650 °C, 1.5 bar(a), 15 vol.% CO_2 and 0.125 g sample masses.

The rates plotted in Figure 6.25 are the observed rates measured by the gas analyser. The true intrinsic reaction rates are equivalent to the observed reaction rates multiplied by an effectiveness factor. The effectiveness factors and intrinsic rate constants were iteratively derived where the effectiveness factor represents the percentage decrease in rate due to particle diffusion effects. The iterative fitting process and the equations utilised shall be described next.

Equation 6.27 – As stated earlier the effectiveness factor is defined as the rate observed divided by the rate if no diffusion limitations were present and for a spherical particle it is represented by:

$$\eta = \frac{W_{CO_2\,obs}}{W_{CO_2\,i}} = \frac{4\pi R D_e C_{CO_2}}{\frac{4}{3}\pi R^3 k_i C_{CO_2}} (\phi \coth \phi - 1)$$

Equation 6.28 – Where the Thiele modulus is described by, where *n* is the order of reaction:

$$\phi = R\sqrt{\frac{k_i C_{CO2}^{n-1}}{D_\mathrm{e}}}$$

Equation 6.29 – Simplifying to become:

$$\eta = \frac{3}{\phi^2} (\phi \coth \phi - 1)$$

Equation 6.30 – The mean intrinsic reaction rate in the pores can now be described by:

$$r_i = \eta k_i$$

Equation 6.31 – Combining with the external mass transfer (coefficient in m/s) resistance, an equation relating the observed rate constant (in s^{-1}) and the intrinsic rate constants (in s^{-1}) can be formed:

$$\frac{1}{k_{obs}} = \frac{1}{\eta k_i} + \frac{R}{3k_g}$$

Equation 6.32 – Which upon rearranging forms:

$$k_i = \frac{\eta}{\left(\frac{1}{k_{obs}} - \frac{R}{3k_g}\right)}$$

The iterative solver to calculate the effectiveness factor, Thiele modulus, particle tortuosity and intrinsic rate constants worked by following flow chart shown below, Figure 6.26.

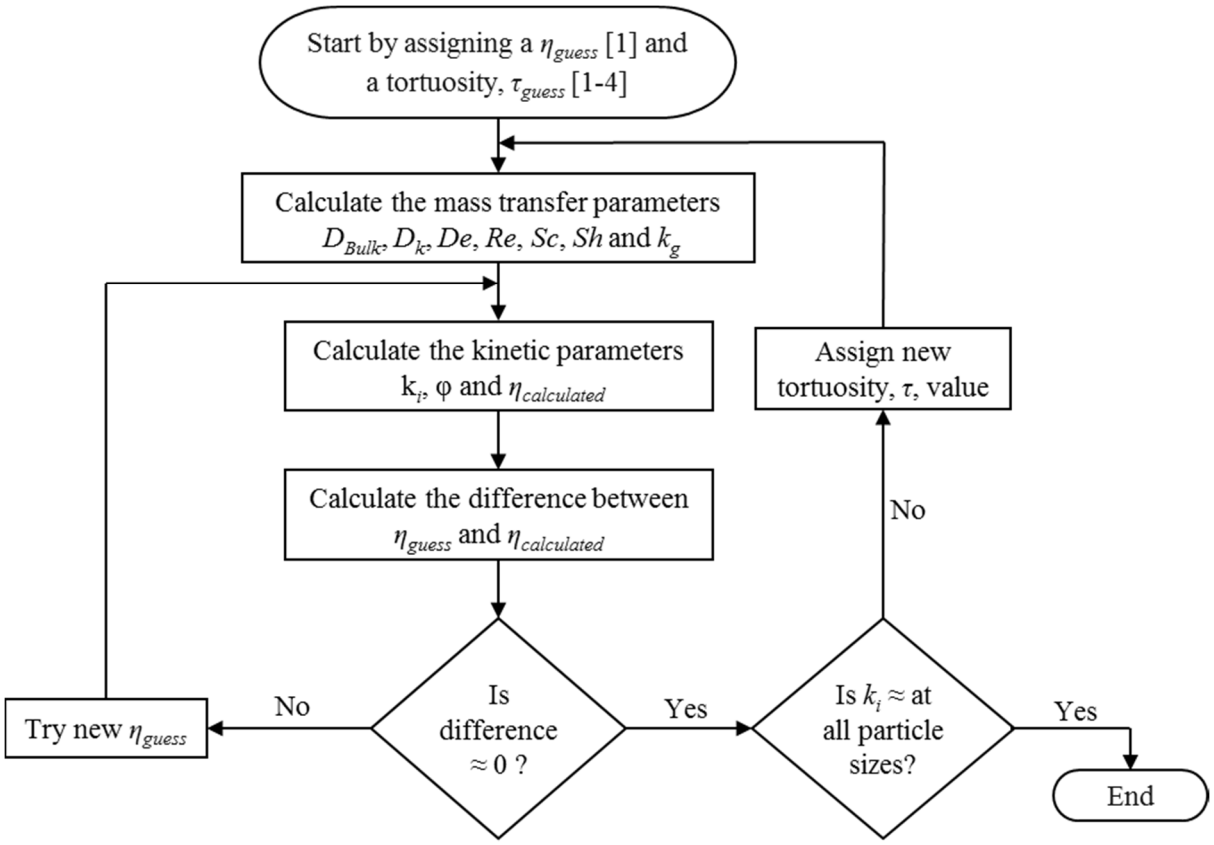

Figure 6.26 – Iterative solver to determine the effectiveness factor, Thiele modulus and intrinsic rate constants.

The equations for calculating the other parameters required for finding the effectiveness factor, Thiele modulus and intrinsic rate constants are described below.

Equation 6.33 – D_{Bulk} is the bulk diffusivity of the gas mixture present within the system, an example of CO_2 in N_2 for the no-steam experiments is shown here (Bird et al., 2007):

$$D_{CO_2\ in\ N_2} = 1.858 \times 10^{-7}\ T^{\frac{3}{2}} \frac{\sqrt{\frac{1}{M_{W\,CO_2}} + \frac{1}{M_{W\,N_2}}}}{P\ \sigma^2_{(CO_2\ N_2)}\ \Omega_{11}}$$

Where T is the bulk gas temperature in K, $M_{W\,CO_2}$ and $M_{W\,N_2}$ are the relative molecular weights of CO_2 and N_2 respectively, P is pressure in atmospheres and $\sigma_{(CO_2\,N_2)}$ is the combined Lennard-Jones parameter that describes the distance at which the intermolecular potential between two particles become zero. ε is the well depth that describes how strongly the particles attract. Combining laws listed below describe

how the $\sigma_{(CO_2\,N_2)}$ parameter is formed. $\Omega_{(1,\,1)}$ is the collision integral for diffusion and can be observed in Table 6.8.

Equation 6.34 and Equation 6.35 – Combining laws for Lennard-Jones parameters, ε and σ (Bird et al., 2007) - Non-polar pair A and B:

$$\varepsilon_{AB} = \sqrt{\varepsilon_A + \varepsilon_B}$$

$$\sigma_{AB} = \frac{1}{2}(\sigma_A + \sigma_B)$$

To calculate the Lennard-Jones parameters for the experiments with steam present the multicomponent mixture of polar H_2O and non-polar N_2 and CO_2 utilised the Stockmayer potential and formed dimensionless variables, where $\mu^*_{H_2O}$ is the reduced dipole moment and provides the ratio between the polar and non-polar gas interactions. $\alpha^*_{CO_2}$ is the reduced polarisability of the nonpolar molecule. The values of α_{CO_2} and α_{N_2} utilised were 2.65 and 1.76 Å^3 respectively (van Leeuwen, 1994) (Burcat et al., 2012).

Equation 6.36, Equation 6.37, Equation 6.38, Equation 6.39 and Equation 6.40 –

$$\varepsilon_{H_2O\ \&\ non-polar} = \xi^2\sqrt{\varepsilon_{non-polar}\ \varepsilon_{H_2O}}$$

$$\sigma_{H_2O\ \&\ non-polar} = \frac{1}{2}(\sigma_{non-polar} + \sigma_{H_2O})\,\xi^{-\frac{1}{6}}$$

Where:

$$\xi = 1 + \frac{\alpha^*_{non-polar}\ {\mu^*_{H_2O}}^2}{\sqrt{8}}\sqrt{\frac{\varepsilon_{H_2O}}{2\varepsilon_{non-polar}}}$$

$$\mu^*_{H_2O} = \frac{1.85}{\sqrt{\varepsilon_{H_2O}\ {\sigma_{H_2O}}^3}}$$

$$\alpha^*_{CO_2} = \frac{\alpha_{CO_2}}{\sigma^3_{non-polar}}$$

Equation 6.41 – For the experiments with steam present the multicomponent bulk diffusivity was calculated via the following method which involved first calculating the binary bulk diffusivities of the different gas species (i.e. CO_2 and N_2, N_2 and H_2O and CO_2 and H_2O) (Bird et al., 2007).

$$D_{ABC} = \frac{\frac{w_A(w_B + w_C)}{y_A D_{BC}} + \frac{w_B(w_A + w_C)}{y_B D_{AC}} - \frac{w_C^2}{y_C D_{AB}}}{\frac{y_A}{D_{AB}D_{AC}} + \frac{y_B}{D_{AB}D_{BC}} + \frac{y_C}{D_{AC}D_{BC}}}$$

Where w_i is the mass fraction of the gas component i, ρ_i is the density of gas component i, y_i is the mole fraction of gas component i and M_i is the molar mass of gas component i. The subscripts A, B and C represent to the different gaseous species in the system (N_2, CO_2 and H_2O).

The Lennard-Jones parameters and bulk diffusivities for the two systems (with and without steam are given in Table 6.8.

Table 6.8 – Lennard-Jones parameters, collision integrals and diffusivity of the difference gases and gaseous mixtures present during the set of experiments. k_b denotes the Boltzmann constant. Where applicable, the values of these parameters shown were determined at 650 °C, 1.5 bar(a) and at the concentrations utilised, namely 15 vol.% CO_2, 18 vol.% H_2O (Klein and Smith, 1968) (Burcat et al., 2012).

Gas component or mixture	**Lennard-Jones parameters**		**Collision integrals, at k_bT/ε, Ω_{11}**	**Diffusivity, D / cm^2/s**
	ε/k_b / K	**σ / Å**		
CO_2	195.2	3.941	-	-
N_2	91.5	3.798	-	-
H_2O	260.0	2.800	-	-
CO_2 & N_2	133.6	3.870	0.792	0.718
CO_2 & H_2O	225.3	3.371	0.885	0.985
H_2O & N_2	154.2	3.241	0.827	1.245
CO_2, N_2 & H_2O	-	-	-	0.925

The viscosity and density of the gas described within the following equations was based on data from the NIST chemistry webbook (NIST, 2011) and were based on N_2 at the operating temperature and pressure alone, the multicomponent Chapman-Enskog model was not applied.

Equation 6.42 – Mass transfer coefficient, in m/s:

$$k_g = \frac{Sh\, D_b}{2R}$$

Equation 6.43 – Sherwood number:

$$Sh = 2 + 0.552 Re^{\frac{1}{7}} Sc^{\frac{1}{3}}$$

Equation 6.44 – Effective diffusivity, in m^2/s (Satterfield, 1970):

$$\mathcal{D}_{eff} = \frac{\varepsilon}{\tau} \cdot \frac{1}{\frac{1}{\mathcal{D}_b} + \frac{1}{\mathcal{D}_k}}$$

Equation 6.45 – Knudsen diffusivity, in m^2/s (Satterfield, 1970):

$$\mathcal{D}_k = \frac{194\, \varepsilon}{S_A} \sqrt{\frac{T}{M_{CO_2}}}$$

Equation 6.46 – Schmidt number:

$$Sc = \frac{\mu_{gas}}{\rho_{gas}\, \mathcal{D}_b}$$

Equation 6.47 – Reynolds number:

$$Re = \frac{\rho_{gas} U_{gas} l}{\mu_{gas}}$$

The effectiveness factors, Thiele modulus and intrinsic rate constants for the unsupported CaO – NiO reduced combined particles without steam are displayed in Figure 6.27, Figure 6.28 and Figure 6.29. A fitted tortuosity factor of 10 was attained for this data set. Tortuosity is defined as the ratio between the actual distance a molecule travels between two points and the shortest distance between those two points (Fogler, 2006). A tortuosity factor of 10 is high but is not in unreported territory, a more typical value of tortuosity lies between 1 and 6 (Xu and Froment, 1989b) (Epstein, 1989) (Wang and Smith, 1983) (Satterfield, 1970). Tortuosity is a measure of pore structure alone, the effect of gas mixture should not influence the value recorded. This value of tortuosity implies that there were considerable diffusion limitations within the particle which is backed up by the moderately high Thiele modulus as shown in Figure 6.29. It is defined that "when the Thiele modulus is large (>20), internal diffusion usually limits the overall rate of reaction; when the Thiele modulus is small, the surface reaction is usually rate-limiting" (Fogler, 2006). Because of this, it is thought that the combined particles had little internal permeability for the CO_2 and that as the particle size was increased the diffusion limitation increased proportionally with it. The calculated Knudsen and bulk gas diffusivities for both the steam and no-steam carbonations were both of similar values and orders of magnitude, which implies that the neither of the diffusional limitations were dominant and both played an approximately equal role.

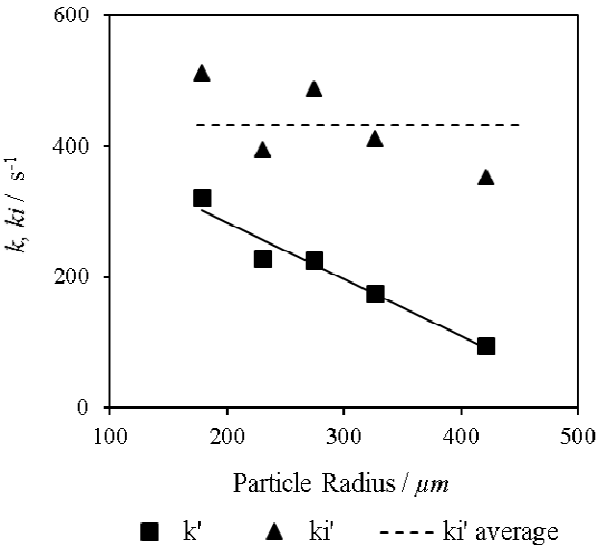

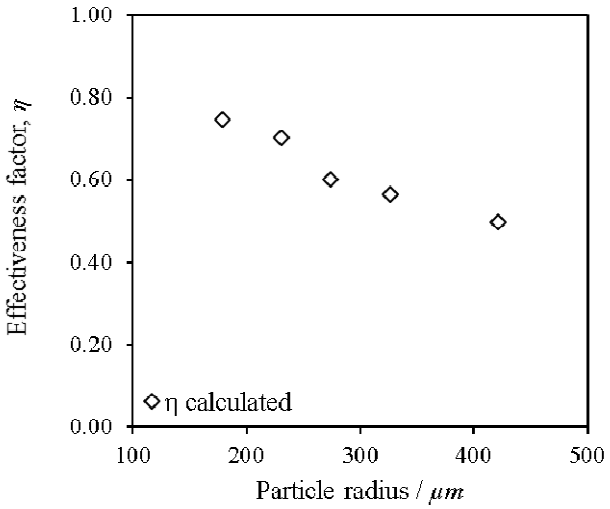

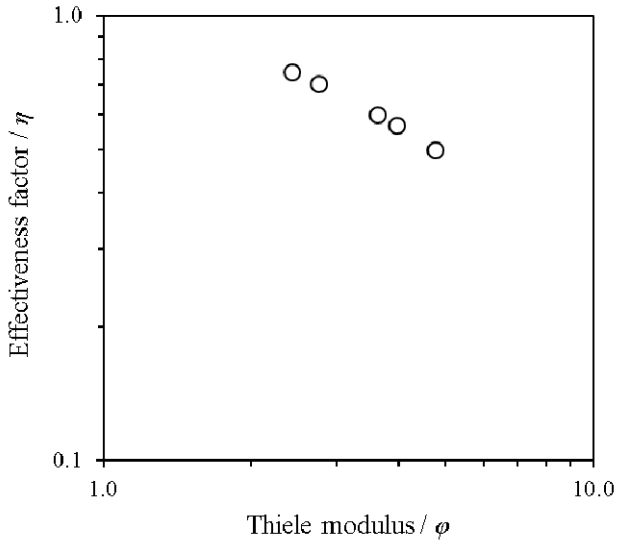

Figure 6.27 (top left) – Observed and intrinsic rate constants against particle size.

Figure 6.28 (top right) – Effectiveness factors against particle size.

Figure 6.29 (bottom centre) –Effectiveness factors against Thiele modulus.

All for the unsupported CaO – NiO combined particles without steam present during the carbonation reactions. A fitted tortuosity of 10 was applied here.

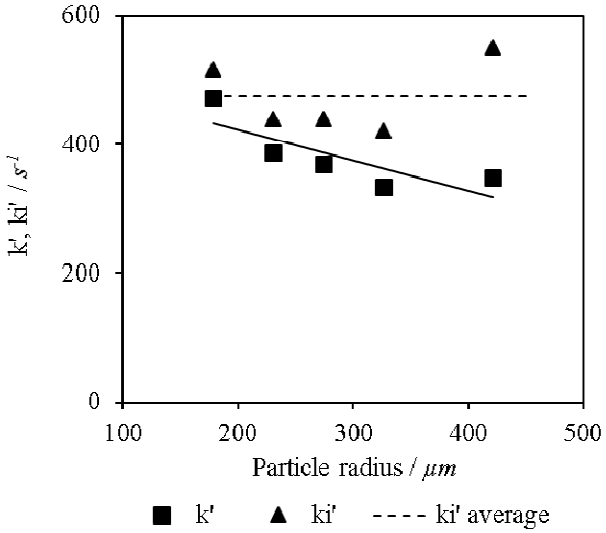

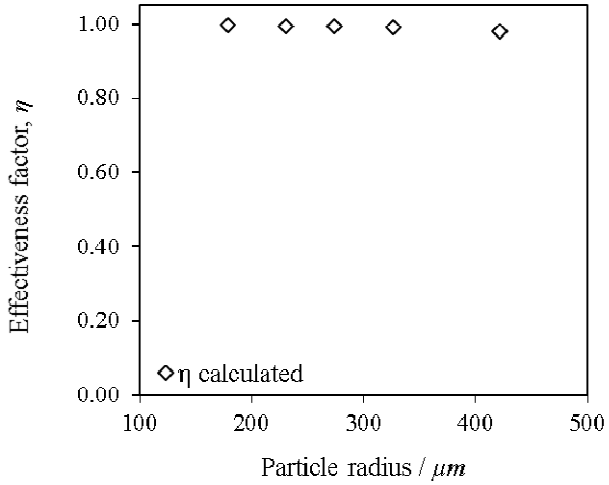

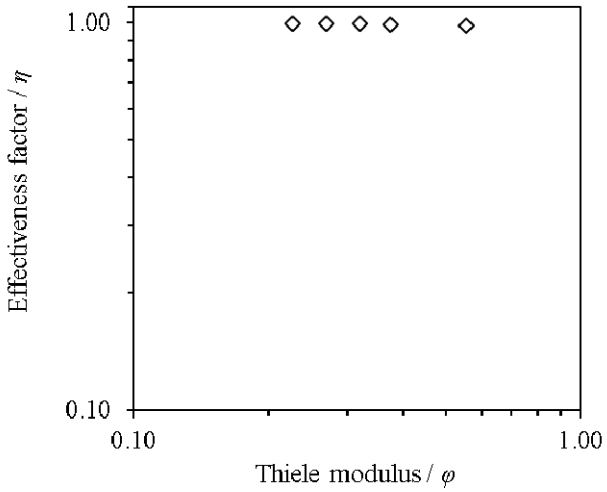

Figure 6.30 (top left) – Intrinsic rate constants against particle size.

Figure 6.31 (top right) – Effectiveness factors against particle size.

Figure 6.32 (bottom centre) – Effectiveness factors against Thiele modulus.

All for the unsupported CaO – NiO combined particles with steam present during the carbonation reactions. A fitted tortuosity of 0.1 was applied here.

The intrinsic kinetic data for the CaO – NiO combined particles with steam during the carbonation is presented in Figure 6.30, Figure 6.31and Figure 6.32. The effectiveness factors were very close to unity for this system and the Thiele moduli at each particle size was also relatively small indicating that the rate was limited by the surface chemical reaction rather than the diffusion of CO_2 into the particle. The partial pressure of CO_2 during these reactions was the same as the CO_2 partial pressure without steam present, therefore the change in observed rate is purely due to the substitution of ~18 vol.% of the N_2 for steam and the effects which this induced. A ~43 % increase was recorded in the observed peak rate of carbonation due to the addition of steam. Due to the effectiveness factors being close to one for all particle sizes it implies that the steam reduced the diffusion resistance of CO_2 into the particle and past the product layer of $CaCO_3$, thus generating an observed rate of reaction was similar to that of the intrinsic rate, as confirmed by Figure 6.30. Based on the calculated diffusivities shown in Table 6.8, the addition of steam to gas mixture increased the bulk gas diffusivity by ~29 %, this would have contributed an increased diffusion of CO_2 to the particles surface. It is well known that the steam enhances the carbonation reaction by reducing the diffusional resistance of CO_2 through the product layer (Donat et al., 2012). It is also thought that the steam aided the transfer of heat from the bulk gas to the particles surface and thus the combined particles in the presence of steam were able to react sooner after entering the reactor.

The effectiveness factors that were determined were very high which meant that there was essentially no diffusion control element in these reactions and calculating an accurate tortuosity value for these particles was not realistically possible. The tortuosity of 0.1 was required in order to bring the effectiveness factors to a suitable value such that the intrinsic rate constants were approximately equal at all particle sizes. However the tortuosity chosen was below the minimum theoretical value of 1, meaning the physical representation of the fitting factor has been lost; this was likely caused by errors in determining the porosity, surface area and envelope density of the particle (Zhang et al., 2016), which influenced the 'mean pore diameter – ε/S_A' in the Knudsen diffusivity calculation shown in Equation 6.45and the porosity value in the effective diffusivity calculation shown in Equation 6.44.

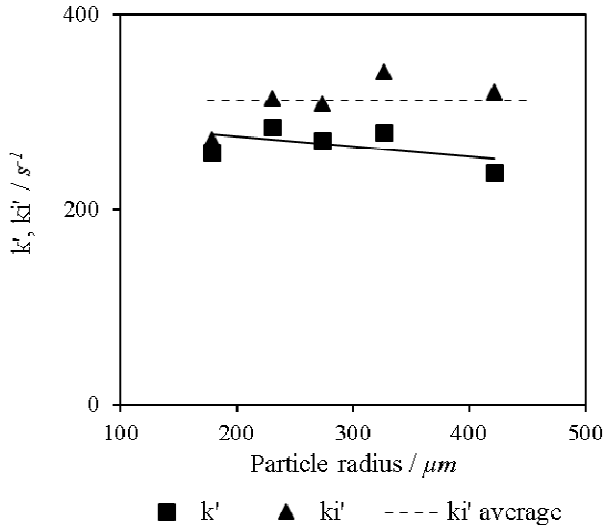

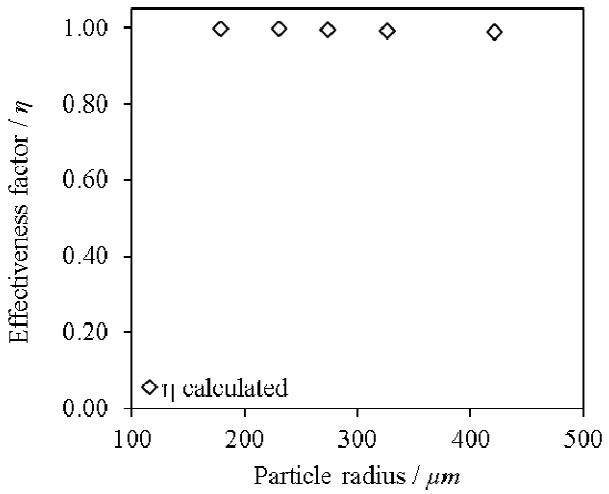

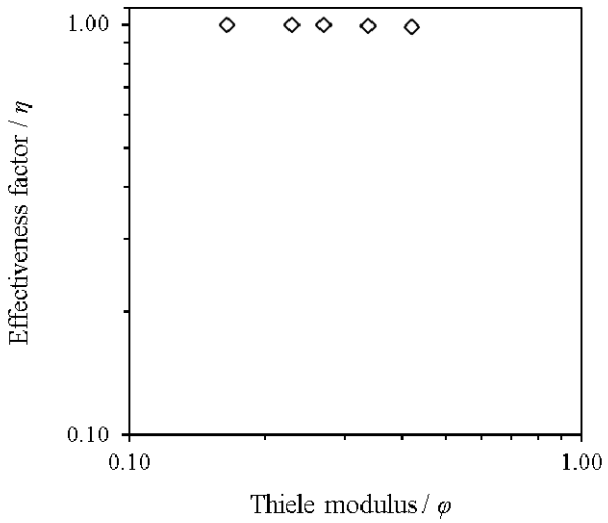

Figure 6.33 (top left) – Intrinsic rate constants against particle size.

Figure 6.34 (top right) – Effectiveness factors against particle size.

Figure 6.35 (bottom centre) – Effectiveness factors against Thiele modulus.

All for the supported CaO – TEOS – NiO combined particles without steam present during the carbonation reactions. A fitted tortuosity of 0.1 was applied here.

The intrinsic rate constants, effectiveness factors and Thiele moduli for the experiments conducted with the supported CaO – TEOS – NiO combined particles are presented in Figure 6.33, Figure 6.34 and Figure 6.35 showing again very high effectiveness factors approaching the theoretical maximum of one. As was observed with the results from the experiments with the unsupported particles with steam the reactions appear to be surface reaction limited rather diffusion limited because of the high effectiveness factors and low Thiele moduli. A fitted tortuosity of 0.1 was again applied here so that the intrinsic rates at all particle sizes were approximately equal, which as before means there was minimal diffusional control over these particles and the tortuosity values are not physically representative.

The peak observed rate constant at the smallest particle size (from the fitted line) was 260 s^{-1} for the CaO – TEOS – NiO sample without steam and 320 s^{-1} for the CaO – NiO sample without steam indicating that both particles systems reacted similarly in scenarios close to the intrinsic rates (small particle size). However due to the slope of the line fitted to the observed rate constants, the particles of the largest size fractions carbonated without steam had vastly different rate constants, namely 95 s^{-1} and 240 s^{-1} for the unsupported CaO – NiO and the supported CaO – TEOS – NiO samples respectively. For these samples to be reacting so differently under the same conditions (650 °C, 1.5 bar(a), 15 % CO_2 without steam) something at the particle scale must be causing this difference. The calculated Knudsen diffusivity of the supported CaO – TEOS – NiO combined particles was ~ 4% greater compared to the unsupported CaO – NiO samples, showing that on a pore scale the larger measured surface area and porosity had little effect on the diffusion of CO_2 through the particle; however this would likely change during the carbonation reaction as the pore size distribution would change and would also be influenced by the presence (or lack off) support structure. As the gas conditions were identical so were the bulk diffusivities and mass transfer coefficients.

It was because of these reasons that the following conclusion was drawn: it was thought that the increased rate of reaction of the larger supported particles compared to the unsupported particles was due to the support material influencing the formation, shape and the overall pore structure, such that the tortuosity within the particle was minimised. This is because the gas composition, reactor bed material and particle densities were mostly equivalent, therefore it is not thought that the rate of heat transfer to

the particles or within the particles would have been significantly different to cause the difference in observed rates. Furthermore the porosities of the supported and unsupported combined particles were approximately the same (although the fitted tortuosity's present evidence that there is error in their determination) which implies that the overall number of pores was broadly similar but it is possible that the supported particles possessed a more interlinked pore structure which meant there were multiple pathways for the CO_2 to access the unreacted CaO. The polymorphic ability of the C_2S in the supported particles could have also influenced the gas pathways within the particles or the surface chemistry/charges. Ideally SEM would be conducted to confirm these changes, unfortunately this hasn't been conducted yet.

Utilising the Weisz-Prater criterion (Fogler, 2006), described by Equation 6.48, a quick estimate of the diffusion limitations can be achieved. If the value of C_{WP} is much less than 1 then it is said that the particles were not subject to internal diffusion limitations, however if C_{WP} is much greater than 1 then the particles were subject to internal diffusion resistances and as such there is a concentration gradient present within the particles. Table 6.9 presents the values of C*WP* for each of the particle systems analysed against particle size.

Equation 6.48:

$$C_{WP} = \eta\phi^2 = \frac{k_{obs}R^2}{D_{eff}}$$

From the data presented in Table 6.9 it is clear that the CaO – NiO w/o steam sample did have internal diffusion resistances present due to its C_{WP} being mostly an order of magnitude above 1. For both the CaO – NiO w/ steam and the CaO – TEOS – NiO w/o steam samples the C_{WP} is much less than 1 meaning that internal diffusion resistances did not play a significant role in the carbonation reaction, which is further evidence that the combined particles with the C_2S support had a different internal pore structure that was beneficial for carbonation. The carbonation in the presence of steam for the CaO – NiO w/ steam sample likely presented a low CWP because the steam was able to enhance the diffusion of CO_2 past the product layer that formed (Donat et al., 2012).

Table 6.9 – Weisz-Prater criterion to determine the influence of internal diffusion of the combined particles.

Combined particle data set	**Geometric mean particle radius / µm**	**Effectiveness factor, η**	**Thiele modulus, φ**	**Weisz-Prater criterion, C_{WP}**
CaO – NiO w/o steam	179	0.75	2.42	4.37
	231	0.70	2.74	5.30
	274	0.60	3.62	7.88
	326	0.57	3.69	8.90
	421	0.50	4.74	11.23
CaO – NiO w/ steam	179	0.99	0.23	0.05
	231	0.99	0.27	0.07
	274	0.99	0.32	0.10
	326	0.99	0.37	0.14
	421	0.98	0.55	0.30
CaO – TEOS – NiO w/o steam	179	0.99	0.16	0.03
	231	0.99	0.23	0.05
	274	0.99	0.27	0.07
	326	0.99	0.34	0.11
	421	0.99	0.42	0.18

6.5. Conclusions of work with combined particles

The production of combined multifunctional particles for Sorbent Enhanced Steam Reforming of biomass derived via a low engineered hydrolysis and wet mixing method has been studied by XRD, TGA CaL cycling, XRF, MIP and BET. These combined particles were composed of a NiO-based catalyst and a CaO-based CO_2 sorbent. A range of NiO contents were tested (14, 26, 36 and 47 wt.% NiO) to note the effects caused by NiO addition to the combined particle matrix. It was noted that the addition of the NiO did lead to a reduction in BET surface area, pore volume and an increase in the density of the particles, but no effect was observed on the sorbents ability to absorb CO_2 over multiple calcium looping cycles under realistic post-combustion conditions.

A set of combined particles with a silica based support structure in the form dicalcium silicate, C_2S, were also produced from two silica sources, TetraEthyl OrthoSilicate (TEOS) and fumed silica. The addition of a C_2S support is known to be beneficial to the long term porosity and CO_2 capture ability of CaO-based CO_2 sorbents due to the polymorphic ability of the C_2S during temperature cycling. XRD analysis demonstrated the difficulties in forming C_2S effectively, especially as the grain size of the fumed silica was significantly larger thus impacting on the contact areas between the Ca and Si ions. Whereas the C_2S, TEOS-derived sample, was able to form C_2S more successfully due to the Ca and Si ions being closer within the matrix.

These supported and unsupported combined particles were tested for their ability to produce H_2 via SESR of oak wood biomass within a spout-fluidised-bed reactor. The SESR reaction conditions were based on the previous literature in this area, principally 650 °C and 1 atm. A relatively low steam to carbon ratio was utilised in this work due to the efforts of balancing a flow rate high enough to overcome the terminal velocity of the biomass particles in the feeding tube and a flow rate high enough to produce effective mixing within the fluidised bed itself. However, low steam to carbon ratios are favourable as they reduce the energy intensity of the process and therefore make it more economically favourable. Despite the low steam to carbon ratios (near stoichiometric values) used the H_2 purity and yield did

approach thermodynamic equilibrium at the highest Ni contents, ~75 vol.% H_2 which represented ~120 g H_2/ kg of biomass (61 mmol H_2/kg biomass).

The addition of both silica supports, despite not fully forming C_2S, were found to be instrumental in the decomposition of CH_4, indicating that the silica may be interacting with the pathways of SESR reactions. This effect has not be observed or studied before and future work must be undertaken to investigate the cause and true potential of silica addition on CH_4/volatiles destruction.

This reactor aimed to overcome the need for a two stage SESR process whereby the gasification of biomass is carried out separately to the reforming reactions. This process intensification required careful design of the reactor however due to the low-temperatures at which biomass will pyrolyse/gasify some of the biomass began to react within the feeding tube. This led to the formation and deposition of tars on the internal surface of the feeding tube, which over time, carbonised and built up layer by layer until the inlet was blocked. The effect of oxygen addition on the product gas composition and length of biomass feeding time before the feeding tube blocked up due to coking was also explored. It was found that the addition of even small amounts of oxygen led to a dramatic decrease in H_2 purity and yield as the oxygen was favourably utilised as the oxidising agent over the steam. The type of coke formation on the particles was studied by the use of a TGA-MS, the results of which seemed convoluted and difficult to draw definitive conclusion from. This was thought to be because some of the nickel was partially oxidised and the amorphous coke on the particles was preferentially reacting with this oxygen thus the only coking observed was high-temperature resistant graphitic carbon. Both of these coke formations could have been managed and reduced by the addition of more steam and thus a higher steam to carbon ratio.

The SESR reactions within this fluidised bed were evidently limited by the rate of CO_2 absorption as it was observed that some of the CO_2 was bypassing the bed unreacted despite a high degree of mixing (U/U_{mf}). Because of this, a set of kinetic experiments were conducted within another spout fluidised bed reactor to determine the kinetic parameters of the rate limiting step. The conditions investigated within these kinetic experiments were 550-700 °C, 300-1000 μm, 1.5 bar(a), 15 vol.% CO_2, with and without 18 vol.% steam, and a 0.125 g sample mass. The operation of this pressurised fluidised bed reactor

aimed to match the conditions utilised within the SESR fluidised bed reactor as closely as possible, although due to the presure drop across the system a controlled pressure of 1.5 bar(a) was utilised. This system was also utilised as the resonse time across the system was faster. External mass transfer was minimised as much as possible by the use of a fast fluidisation vevlocity and moderate $U/U_{mf} \approx 3.5$. External heat tranfer was assumed to be the same across all kinetic experiments and therefore any limitiaion which existed affected the results equally.

It was found that the addition of Ni into the CaO matrix produced observed carbonation activation energies comparable to that of literature values for limestone derived CaO carbonation. It was found that the addition of steam to the reaction gases enabled a faster rate of carbonation, likely because the steam was able to aid overcoming the product layer diffusion resistance, as has been noted by other authors. The rate of carbonation of the TEOS derived C_2S supported sorbents was also studied and found that the change in particle pore structure observed through mercury intrusion porosimetry was about as beneficial as steam addition in enhancing the rate of carbonation and overall conversion of the material.

The intrinsic kinetic parameters were also determined through the use of an iterative method which was described in detail in section 6.4. The intrinsic kinetic parameters rely on fitting the tortuosity of the particle such that the calculated effectiveness factors can account for the variations in internal diffusion caused by the change in the particle size.

These kinetic experiments found very high effectiveness factors (~1) for carbonation of the sorbents with steam or a support present, demonstrating that the internal diffusion limitations of CO_2 were diminished at all particle size fractions. Conversely, it was also noted that the average H_2 yield produced when using the largest size fraction of particles (710 - 1000 μm) during the SESR experiments (where steam was also present) was ~61 % lower than when utilising the smallest size fractions of particles (300-500 μm). This implies that significant internal diffusional resistances were present within the larger particles during SESR. It likely means that the effectiveness factors measured for carbonation were not applicable for SESR as the thermodynamics and rate dependant factors of the system were different. It could be that the low steam to carbon ratios meant that the steam was being consumed by

the SESR reactions which in turn altered the gas properties and wasn't able to aid the CO_2 overcome the product layer diffusion resistance.

In general, it was thought that the use of combined particles for SESR is a good idea for future investigations but efforts must be made to increase the structural rigidity of the particles for effective fluidisation. It has been demonstrated that the use of a cheap and simple combined particle production methodology was effective at producing particles which underwent SESR with similar propensity as those of more complex methods. It should be noted however the incorporation of nickel into a combined matrix requires caution, as the replenishment rates may be higher for the CO_2 sorbents compared to the catalysts, which means a separate process to recycle/reuse the Ni will be required.

Chapter 7 – Summary of Conclusions

The impact of anthropogenic greenhouse gas emissions is well known to be the leading cause of the climatic changes that are currently being observed, and they are predicted to worsen in the coming decades. It is because of these effects that many researchers around the world are working together on different methods to reduce these greenhouse gas emissions, in particular CO_2. Generally speaking, the heavy industries (cement, iron and steel, pulp and paper, chemical, oil and gas, mining and others) and power generation industries are the leading causes of CO_2 emissions. Considering that the end goal is to replace these polluting industries with non-polluting alternatives or to prevent the pollution from being released to the environment, it is understood that this is not always simple or easy to do for all processes/industries. For the power generation industry, a considerable reduction in CO_2 emissions can be achieved by switching from coal to gas, as has been seen in UK recently (Department for Business, 2017). However, to make further reductions to the CO_2 emissions beyond what has already been achieved, a new technology is required. It is possible to replace power generation facilities with renewable power generators, and this is certainly the end goal, though at the moment renewables intermittency is limiting their deployment (Heuberger et al., 2017b). An intermediary alternative is to utilise a technology called carbon capture and storage (CCS), which comes in many different forms. One form is utilising CaO to capture CO_2, thereby converting it into $CaCO_3$, this can then be converted back into CaO thus making the material reusable; this process is called calcium looping (CaL). Although there are limitations in ability for the sorbent to undergo this reversible reaction many times, CaL is thought to be one of the least impacting technologies in terms of the energy penalty and has the benefit of being able to link into the cement industry (Fennell, 2015a).

Further to power generation, the production of H_2 is also a CO_2 intensive process as currently most H_2 is produced from methane via steam methane reforming (SMR) or via the gasification of coal. The market for H_2 is vast, encompassing: fertiliser, ammonia and other chemicals production, hydrocracking of heavy oils, hydrogenation of food stuffs, energy production via combustion or fuel cells, and other niche applications. Nevertheless this is another industry that needs to be decarbonised and one method

of doing this is with the amalgamation of CaL and SMR into a process called Sorbent Enhanced Steam Reforming (SESR). This outlines the broader topic of investigated for this research.

One of the main aims of this research was to design and construct of a spout-fluidised bed reactor suitable for conducting gasification and SESR reactions and a description of how this aim was met was outlined in Chapter 3. Within this chapter a detailed explanation of the design basis and reactor specification was given, which itself was informed from the literature review presented in Chapter 2. Example calculations and the respective formulae for calculating the appropriate reactor dimensions, the minimum fluidisation velocity and the terminal feeding velocity were given. This chapter also described the efforts that were gone to, to ensure that a stable and continuous biomass feeding baseline could be achieved harmoniously with the production of a stable steam concentration.

A set of initial biomass and coal combustion experiments were conducted which showed that a suitable mass balance could be achieved within the reactor. Further to this a series of biomass steam gasification experiments were conducted where the bed material was varied in order to note the differences achieved. These experiments were conducted at 650 °C with ~12 vol.% steam and pulverised oak chip biomass and showed the significant benefit in terms of H_2 production that can be achieved by the addition of both a sorbent and catalyst.

Understanding that the primary drop off in CO_2 carrying capacity of CaO occurs during the calcination process it was decided to perform a series of experiments into the rate of calcination, as this would also aid the design of an SESR calciner; this work was presented in Chapter 4. The experiments conducted consisted of varying the bed temperature, CO_2 partial pressure, particle size, sample mass and limestone type; each parameter was altered individually to determine their influence on the rate. Kinetics were measured by secondary means for the steam and CO_2 experiments and via N_2 dilution for the N_2 and CO_2 experiments as the CO_2 concentrations were above the measureable range by most analytical techniques.

Upon analysing the data from this calcination work it was noted that the order of reaction with respect to the driving force for the reaction was not simple and lead to physically un-representative activation energies, therefore the orders of reaction were determined with respect to the partial pressure of CO_2 alone. Because it was thought some other effect was influencing the rate that was not simply explained the partial pressure of CO_2 alone, especially for the set of calcinations in the presence of N_2 a Langmuir-Hinshelwood derivation was undertaken for both the calcination in N_2 and CO_2, and steam and CO_2. A suitable fit between the experimental data and the fitted parameters was achieved for the steam Langmuir-Hinshelwood equation but not for the N_2 system. The difficulties in obtaining accurate particle properties such as density, porosity and surface area were also discussed within this chapter.

It was noted from the calcination experiments in Chapter 4 that the reactions in the presence of steam were approximately 3-4 times faster than when the steam was replaced with N_2. To understand the differences in the observed rates in greater detail a Matlab model was created, based on the heat and mass balances through an assumed spherical particle of limestone undergoing calcination. The model was shown to represent the experimental data quite well in most scenarios tested. Improvements were made to the Arrhenius parameters by applying a least squares fitting of the model and the experimental data up to the peak rate of calcination. The model demonstrated that the calcination of limestone was controlled by a combination of external heat transfer to the particles and internal diffusion of CO_2. The reaction modelling has concluded that increase in calcination rate when steam was present was caused predominately by catalytic means only and the physical differences between polar and non-polar gases makes little difference to the overall rate of reaction.

Following the commissioning experiments conducted (presented in Chapter 3), work was undertaken into the production of combined particles for SESR, which met another other the initial project aims, namely “the development and testing of a combined sorbent and catalyst particle effective for SESR”. This work looked at the methods utilised within the literature to produce combined particles and resulted in choosing a ‘low engineered’ method of hydrolysis and wet mixing which had the advantage of being simple and relatively inexpensive and could be scaled up if required.

Combined particles of CaO (derived from calcined limestone) and NiO were produced and a range of NiO contents were tested (14, 26, 36 and 47 wt.% NiO) to note the effects caused by NiO addition to the combined particle matrix. It was noted that the addition of the NiO did lead to a reduction in BET surface area, pore volume and an increase in the density of the particles, but no effect was observed on the sorbents ability to absorb CO_2 over multiple calcium looping cycles under realistic post-combustion conditions.

In addition to these combined particles a set of supported combined particles were produced utilising a dicalcium silicate (C_2S) support structure. This structure was developed based upon the work conducted within Chapter 5, where a C_2S support with CaO was tested for its ability to resist sintering under harsh but realistic conditions (high-temperature CO_2). Unfortunately this support was unsuccessful at maintaining the carrying capacity at these conditions.

These particles were investigated for their suitability for biomass SESR within the fluidised bed reactor designed and constructed previously, and presented in Chapter 3. These reactions were conducted at 650 °C, 1 atm and ~20 vol.% steam. A relatively low steam to carbon ratio was utilised in this work due to the efforts of balancing a flow rate high enough to overcome the terminal velocity of the biomass particles in the feeding tube and a flow rate high enough to produce effective mixing within the fluidised bed itself. Despite the low steam to carbon ratios (near stoichiometric) used the H_2 purity and yield did approach thermodynamic equilibrium at ~26 wt.% Ni, ~75 vol.% H_2 which represented ~120 g H_2/ kg of biomass (61 mmol H_2/kg biomass). It was also observed that the addition of the silica support did lead a drop in CH_4 concentration that was not observed in the unsupported particles, although more work is needed to determine the reason for this.

An unfortunate consequence of utilising biomass within this reactor under these conditions was that the reactivity of biomass was so high that it began to gasify within the feeding tube, this eventually lead to formation of coke on the inner walls which in turn led to blockages thereby halting the feeding and hence the reactions. The addition of oxygen for coke removal was investigated however this lead to dramatic drop off in H_2 purity and yield.

An investigation into the kinetics of carbonation of H_2-reduced combined particles was undertaken in another fluidised bed reactor at a range of temperatures and with a selection of different particle sizes. It was found that the addition of Ni into the CaO matrix didn't affect the observed carbonation activation energy of the material and produced comparable values to literature results for the activation energy of limestone derived CaO carbonation. The rate of carbonation of the C_2S supported sorbents was also studied and found that the change in particle pore structure observed through mercury intrusion porosimetry was about as beneficial as steam addition in enhancing the rate of carbonation and overall conversion of the material. A fitted tortuosity was also determined, from which the intrinsic rates and effectiveness factors were determined.

A mismatch between the observed H_2 production during SESR (which showed extensive internal diffusion issues) and the carbonation kinetics derived effectiveness factors (which showed minimal internal diffusion of larger particles). This indicated that the effectiveness factors determined for carbonation were not directly transferable to the SESR reactions. This was thought to be because of steam being utilised during the SESR reactions which impacted on the steams ability to catalyse the carbonation reaction.

Concluding on all the work conducted here it can be said that effective combined particles for SESR were produced via this simple method which were capable of withstanding fluidised bed operation and producing high H_2 purities and yields, however the utilisation of biomass with such low steam to carbon ratios was unsuitable.

Chapter 8 – Future work

Based on the work conducted within this thesis there were several interesting areas that were found to require more work in order to understand the phenomena observed during the research. In particular the following areas were deemed a high priority for the optimisation of SESR and its future commercialisation. In addition, an account will be provided of the limitations and experiences of this investigation such that future researchers can plan the most appropriate experiments/models in order to gain the most from their work.

1. It was noted that near equilibrium purities and yields of H_2 were generated with a near stoichiometric steam to carbon ratio which is positive news for the process in general as less steam means a lower operating cost. However, future researchers should utilise a higher steam to carbon ratio in order to reduce the build of coke and to minimise the production of CH_4 and CO.

   A significant amount of effort was put into obtaining a stable steam and biomass feeding system during this work, it is now thought that the stability of the steam generation system is less important as any spikes can be averaged out over the course of the reaction and with a humidity probe before and after the reactor a good mass balance can be achieved. It was also noted that when conducting SESR the production of tars was negligible and therefore a humidity could be placed at the exit of the reactor, providing care is taken during operation and post-reaction cleaning/maintenance.

   The biomass feeding system designed here did work very effectively but due to limitations of the reactor (needing to preheat the gas and add the biomass into the reactors hot zone), coking issues prevented long term feeding. It was thought that for a larger system an alternative biomass feeding system would be utilised and therefore would avoid these issues. Raising the steam to carbon ratio would have certainly helped though.

2. An interesting observation that requires further work is the effect of decreased CH_4 yields when dicalcium silicate (C_2S) was added to the particle structure. Although the use of C_2S for the stability of CaO carrying capacity was shown to be ineffective under realistic high-temperature CO_2 calcination conditions, it was shown to aid the conversion of CH_4 during SESR. Within this work it was not found if it was the addition of silica that caused this increased CH_4 conversion or if it was the C_2S itself or interactions between the Si, Ca and/or Ni molecules or by some other means, therefore it is recommended that a further short study looks into the use of silica based materials (as a support or otherwise) for SESR methane/tar reduction.

3. Further to this it is recommended that the incorporation of iron oxides in the combined particles for the reduction of surface coke is investigated, as some studies are beginning to show this can be effective due to the reduction and oxidation ability of the iron oxide within the steam/H_2 environment present within the SESR carbonator/reformer.

4. One of the key areas noted with the use of combined particles was their operational performance within the fluidised bed reactor. Whilst attrition rates were not excessive for these particles, it was certainly higher than the attrition rates observed when working with limestone in fluidised beds. It is now thought that an interesting concept to investigate for the SESR process is the use of an entrained flow reactor as this would simplify the process further and negate the requirement to make particles that can be fluidised. It would also remove the concern of attrition and particle/pore sintering. Effective close contact between the catalyst, sorbent and the produced gases could be an issue however with careful reactor design (accounting for the kinetics of each reaction and therefore the residence time of the gases) this could be controlled.

   An entrained flow reactor would also minimise the risk of gas bypass, which was thought to be the predominant cause for the higher CO_2, CO and CH_4 yields noticed during the investigation here.

5. A further area that should be looked into is the reuse and recycling of CaO and Ni materials, whether they are combined in a single particle or separated powders. The recovery of the Ni material is the predominant motivation for this as its value is an order of magnitude over the CaO, so whether it is processed into a reusable form or sold on there is an economic incentive to do so.

6. Finally, a longer term goal would be to observe the mechanism of steam enhancement on the carrying capacity and kinetics of CaO carbonation and calcination. A mechanism has been suggested by other authors and has been found to be in close agreement to the experimental and modelling work conducted here, but it would be quite nice to have some online measurements, at experimental conditions - although impossible via currently available techniques, of steam adsorption onto $CaO/CaCO_3$ with subsequent carbonation/calcination.

References

ABANADES, J. C. & ALVAREZ, D. 2003. Conversion Limits in the Reaction of CO_2 with Lime. *Energy & Fuels,* 17**,** 308-315.

ABANADES, J. C., RUBIN, E. S. & ANTHONY, E. J. 2004. Sorbent Cost and Performance in CO_2 Capture Systems. *Industrial & Engineering Chemistry Research,* 43**,** 3462-3466.

ABBAS, S. Z., DUPONT, V. & MAHMUD, T. 2017. Kinetics study and modelling of steam methane reforming process over a NiO/Al_2O_3 catalyst in an adiabatic packed bed reactor. *International Journal of Hydrogen Energy,* 42**,** 2889-2903.

AGNEW, J., HAMPARTSOUMIAN, E., JONES, J. M. & NIMMO, W. 2000. The simultaneous calcination and sintering of calcium based sorbents under a combustion atmosphere. *Fuel,* 79**,** 1515-1523.

AHRENFELDT, J., THOMSEN, T. P., HENRIKSEN, U. & CLAUSEN, L. R. 2013. Biomass gasification cogeneration – A review of state of the art technology and near future perspectives. *Applied Thermal Engineering,* 50**,** 1407-1417.

AL-JEBOORI, M. J., FENNELL, P. S., NGUYEN, M. & FENG, K. 2012. Effects of Different Dopants and Doping Procedures on the Reactivity of CaO-based Sorbents for CO_2 Capture. *Energy & Fuels,* 26**,** 6584-6594.

AL-JEBOORI, M. J., NGUYEN, M., DEAN, C. & FENNELL, P. S. 2013. Improvement of Limestone-Based CO_2 Sorbents for Ca Looping by HBr and Other Mineral Acids. *Industrial & Engineering Chemistry Research,* 52**,** 1426-1433.

ALAUDDIN, Z. A. B. Z., LAHIJANI, P., MOHAMMADI, M. & MOHAMED, A. R. 2010. Gasification of lignocellulosic biomass in fluidized beds for renewable energy development: A review. *Renewable and Sustainable Energy Reviews,* 14**,** 2852-2862.

ALIBABA.COM. *Calcium acetate powder* [Online]. Available: https://www.alibaba.com/showroom/calcium-acetate-powder.html [Accessed 10/02/2017].

ALIBABA.COM. *Limestone powder* [Online]. Available: https://www.alibaba.com/showroom/limestone-powder.html [Accessed 10/02/2017].

ALOISI, I., JAND, N., STENDARDO, S. & FOSCOLO, P. U. 2016. Hydrogen by sorption enhanced methane reforming: A grain model to study the behavior of bi-functional sorbent-catalyst particles. *Chemical Engineering Science,* 149**,** 22-34.

ALONSO, M., CRIADO, Y. A., ABANADES, J. C. & GRASA, G. 2014. Undesired effects in the determination of CO_2 carrying capacities of CaO during TG testing. *Fuel,* 127**,** 52-61.

ALVAREZ, D. & ABANADES, J. C. 2005. Pore-Size and Shape Effects on the Recarbonation Performance of Calcium Oxide Submitted to Repeated Calcination/Recarbonation Cycles. *Energy & Fuels,* 19**,** 270-278.

AMUTIO, M., LOPEZ, G., ARTETXE, M., ELORDI, G., OLAZAR, M. & BILBAO, J. 2012. Influence of temperature on biomass pyrolysis in a conical spouted bed reactor. *Resources, Conservation and Recycling,* 59**,** 23-31.

ANGELI, S. D., MONTELEONE, G., GIACONIA, A. & LEMONIDOU, A. A. 2014. State-of-the-art catalysts for CH_4 steam reforming at low temperature. *International Journal of Hydrogen Energy,* 39**,** 1979-1997.

ANTZARA, A., HERACLEOUS, E., BUKUR, D. B. & LEMONIDOU, A. A. 2015. Thermodynamic analysis of hydrogen production via chemical looping steam methane reforming coupled with in situ CO_2 capture. *International Journal of Greenhouse Gas Control,* 32**,** 115-128.

ANTZARA, A., HERACLEOUS, E. & LEMONIDOU, A. A. 2016. Energy efficient sorption enhanced-chemical looping methane reforming process for high-purity H_2 production: Experimental proof-of-concept. *Applied Energy,* 180**,** 457-471.

ARIAS, B., DIEGO, M. E., ABANADES, J. C., LORENZO, M., DIAZ, L., MARTÍNEZ, D., ALVAREZ, J. & SÁNCHEZ-BIEZMA, A. 2013. Demonstration of steady state CO_2 capture in a 1.7 MWth calcium looping pilot. *International Journal of Greenhouse Gas Control,* 18**,** 237-245.

ARIAS, B., GRASA, G. S., ALONSO, M. & ABANADES, J. C. 2012. Post-combustion calcium looping process with a highly stable sorbent activity by recarbonation. *Energy & Environmental Science,* 5**,** 7353-7359.
ARREGI, A., LOPEZ, G., AMUTIO, M., BARBARIAS, I., BILBAO, J. & OLAZAR, M. 2016. Hydrogen production from biomass by continuous fast pyrolysis and in-line steam reforming. *RSC Advances,* 6**,** 25975-25985.
ARSTAD, B., PROSTAK, J. & BLOM, R. 2012. Continuous hydrogen production by sorption enhanced steam methane reforming (SE-SMR) in a circulating fluidized bed reactor: Sorbent to catalyst ratio dependencies. *Chemical Engineering Journal,* 189–190**,** 413-421.
AZHAR UDDIN, M., TSUDA, H., WU, S. & SASAOKA, E. 2008. Catalytic decomposition of biomass tars with iron oxide catalysts. *Fuel,* 87**,** 451-459.
BAERNS, M. 2013. *Basic Principles in Applied Catalysis*, Springer Berlin Heidelberg.
BALAT, M. 2008. Potential importance of hydrogen as a future solution to environmental and transportation problems. *International Journal of Hydrogen Energy,* 33**,** 4013-4029.
BALL, M. & WIETSCHEL, M. 2009. *The Hydrogen Economy: Opportunities and Challenges*, Cambridge University Press.
BARELLI, L., BIDINI, G., GALLORINI, F. & SERVILI, S. 2008. Hydrogen production through sorption-enhanced steam methane reforming and membrane technology: A review. *Energy,* 33**,** 554-570.
BARKER, R. 1973a. Reversibility of the reaction $CaCO_3 = CaO + CO_2$. *J. Appl. Chem. Biotechnol.,* 23**,** 733.
BARKER, R. 1973b. REVERSIBILITY OF THE REACTION $CaCO_3$ reversible reaction CaO plus CO_2. *J Appl Chem Biotechnol,* 23**,** 733-742.
BARTHOLOMEW, C. H. 1993. Sintering kinetics of supported metals: new perspectives from a unifying GPLE treatment. *Applied Catalysis A: General,* 107**,** 1-57.
BARTHOLOMEW, C. H. 2001. Mechanisms of catalyst deactivation. *Applied Catalysis A: General,* 212**,** 17-60.
BASU, P. 2006. *Combustion and Gasification in Fluidized Beds*, CRC Press.
BASU, P. 2010. *Biomass Gasification and Pyrolysis: Practical Design,* Oxford, Elsevier Inc.
BASU, P. 2013. *Biomass Gasification, Pyrolysis and Torrefaction: Practical Design and Theory*, Elsevier Science.
BATINI, C., BURRA, K. R. G. & GUPTA, A. K. 2017. Sorption Enhanced Steam Reforming of Methane using Calcium Looping. *55th AIAA Aerospace Sciences Meeting.* American Institute of Aeronautics and Astronautics.
BBC. 2015. *UK government carbon capture £1bn grant dropped* [Online]. Available: http://www.bbc.co.uk/news/uk-scotland-scotland-business-34357804 [Accessed 30/05/2017 2017].
BEIS 2016. Energy Consumption in the UK. Department for Business, Energy & Industrial Strategy.
BHAT, S. A. & SADHUKHAN, J. 2009. Process intensification aspects for steam methane reforming: An overview. *AIChE Journal,* 55**,** 408-422.
BHATIA, S. K. & PERLMUTTER, D. D. 1983. Effect of the product layer on the kinetics of the CO_2-lime reaction. *AIChE Journal,* 29**,** 79-86.
BIOMASS ENERGY CENTRE & FORESTRY COMMISSION. 2011. Wood as Fuel - Technical Supplement. Available: http://www.biomassenergycentre.org.uk/pls/portal/docs/PAGE/RESOURCES/REF_LIB_RES/PUBLICATIONS/WOOD%20AS%20FUEL%20TECHNICAL%20SUPPLEMENT%20201 1-01-25.PDF.
BIRD, R. B., STEWART, W. E. & LIGHTFOOT, E. N. 2007. *Transport Phenomena*, Wiley.
BLAMEY, J., ANTHONY, E. J., WANG, J. & FENNELL, P. S. 2010. The calcium looping cycle for large-scale CO_2 capture. *Progress in Energy and Combustion Science,* 36**,** 260-279.
BLAMEY, J., LU, D. Y., FENNELL, P. S. & ANTHONY, E. J. 2011. Reactivation of CaO-Based Sorbents for CO_2 Capture: Mechanism for the Carbonation of $Ca(OH)_2$. *Industrial & Engineering Chemistry Research,* 50**,** 10329-10334.
BLAMEY, J., MANOVIC, V., ANTHONY, E. J., DUGWELL, D. R. & FENNELL, P. S. 2015a. On steam hydration of CaO-based sorbent cycled for CO_2 capture. *Fuel,* 150**,** 269-277.

BLAMEY, J., YAO, J. G., ARAI, Y. & FENNELL, P. 2015b. 5 - Enhancement of natural limestone sorbents for calcium looping processes. *In:* FENNELL, P. & ANTHONY, B. (eds.) *Calcium and Chemical Looping Technology for Power Generation and Carbon Dioxide (CO_2) Capture.* Woodhead Publishing.

BOCKRIS, J. O. M. 2002. The origin of ideas on a Hydrogen Economy and its solution to the decay of the environment. *International Journal of Hydrogen Energy,* 27**,** 731-740.

BOCKRIS, J. O. M. & APPLEBY, A. J. 1972. The Hydrogen Economy: An Ultimate Economy? *Environment*.

BOOT-HANDFORD, M. E., ABANADES, J. C., ANTHONY, E. J., BLUNT, M. J., BRANDANI, S., MAC DOWELL, N., FERNANDEZ, J. R., FERRARI, M.-C., GROSS, R., HALLETT, J. P., HASZELDINE, R. S., HEPTONSTALL, P., LYNGFELT, A., MAKUCH, Z., MANGANO, E., PORTER, R. T. J., POURKASHANIAN, M., ROCHELLE, G. T., SHAH, N., YAO, J. G. & FENNELL, P. S. 2014. Carbon capture and storage update. *Energy & Environmental Science,* 7**,** 130-189.

BORGWARDT, R. H. 1985. Calcination kinetics and surface area of dispersed limestone particles. *AIChE Journal,* 31**,** 103-111.

BORGWARDT, R. H. 1989. Calcium oxide sintering in atmospheres containing water and carbon dioxide. *Industrial & Engineering Chemistry Research,* 28**,** 493-500.

BRINKER, C. J. & SCHERER, G. W. 1990. CHAPTER 4 - Particulate Sols and Gels. *Sol-Gel Science.* San Diego: Academic Press.

BRODA, M., KIERZKOWSKA, A. M., BAUDOUIN, D., IMTIAZ, Q., COPÉRET, C. & MÜLLER, C. R. 2012a. Sorbent-Enhanced Methane Reforming over a Ni–Ca-Based, Bifunctional Catalyst Sorbent. *ACS Catalysis,* 2**,** 1635-1646.

BRODA, M., KIERZKOWSKA, A. M. & MÜLLER, C. R. 2012b. Application of the Sol–Gel Technique to Develop Synthetic Calcium-Based Sorbents with Excellent Carbon Dioxide Capture Characteristics. *ChemSusChem,* 5**,** 411-418.

BRODA, M., KIERZKOWSKA, A. M. & MÜLLER, C. R. 2015. 4 - Synthetic calcium oxide-based carbon dioxide sorbents for calcium looping processes. *Calcium and Chemical Looping Technology for Power Generation and Carbon Dioxide (CO_2) Capture.* Woodhead Publishing.

BRODA, M., MANOVIC, V., IMTIAZ, Q., KIERZKOWSKA, A. M., ANTHONY, E. J. & MÜLLER, C. R. 2013. High-Purity Hydrogen via the Sorption-Enhanced Steam Methane Reforming Reaction over a Synthetic CaO-Based Sorbent and a Ni Catalyst. *Environmental Science & Technology,* 47**,** 6007-6014.

BRODA, M. & MÜLLER, C. R. 2012. Synthesis of Highly Efficient, Ca-Based, Al_2O_3-Stabilized, Carbon Gel-Templated CO_2 Sorbents. *Advanced Materials,* 24**,** 3059-3064.

BRODA, M. & MÜLLER, C. R. 2014. Sol–gel-derived, CaO-based, ZrO2-stabilized CO2 sorbents. *Fuel,* 127**,** 94-100.

BSI 2012. Specification for unfired fusion welded pressure vessels: PD 5500:2012+A2:2013. BSI.

BURCAT, A., GARDINER, W. C. J., DIXON-LEWIS, G., FRENKLACH, M., HANSON, R. K., SALIMIAN, S., TROE, J., WARNATZ, J. & ZELLNER, R. 2012. *Combustion Chemistry*, Springer New York.

BURHENNE, L., MESSMER, J., AICHER, T. & LABORIE, M.-P. 2013. The effect of the biomass components lignin, cellulose and hemicellulose on TGA and fixed bed pyrolysis. *Journal of Analytical and Applied Pyrolysis,* 101**,** 177-184.

CALVO, E. G., ARRANZ, M. A. & LETÓN, P. 1990. Effects of impurities in the kinetics of calcite decomposition. *Thermochimica Acta,* 170**,** 7-11.

CARBON TRUST. 2012. Biomass Fuel Procurement Guide. Available: http://www.carbontrust.com/media/88607/ctg074-biomass-fuel-procurement-guide.pdf.

CHAMPAGNE, S., LU, D. Y., MACCHI, A., SYMONDS, R. T. & ANTHONY, E. J. 2013. Influence of Steam Injection during Calcination on the Reactivity of CaO-Based Sorbent for Carbon Capture. *Industrial & Engineering Chemistry Research,* 52**,** 2241-2246.

CHANBURANASIRI, N., RIBEIRO, A. M., RODRIGUES, A. E., ARPORNWICHANOP, A., LAOSIRIPOJANA, N., PRASERTHDAM, P. & ASSABUMRUNGRAT, S. 2011. Hydrogen Production via Sorption Enhanced Steam Methane Reforming Process Using Ni/CaO Multifunctional Catalyst. *Industrial & Engineering Chemistry Research,* 50**,** 13662-13671.

CHANG, M.-H., CHEN, W.-C., HUANG, C.-M., LIU, W.-H., CHOU, Y.-C., CHANG, W.-C., CHEN, W., CHENG, J.-Y., HUANG, K.-E. & HSU, H.-W. 2014. Design and Experimental Testing of a 1.9 MWth Calcium Looping Pilot Plant. *Energy Procedia,* 63**,** 2100-2108.

CHAPMAN, S. & COWLING, T. G. 1970. *The Mathematical Theory of Non-uniform Gases: An Account of the Kinetic Theory of Viscosity, Thermal Conduction and Diffusion in Gases*, Cambridge University Press.

CHARITOS, A., RODRÍGUEZ, N., HAWTHORNE, C., ALONSO, M. N., ZIEBA, M., ARIAS, B., KOPANAKIS, G., SCHEFFKNECHT, G. N. & ABANADES, J. C. 2011. Experimental Validation of the Calcium Looping CO_2 Capture Process with Two Circulating Fluidized Bed Carbonator Reactors. *Industrial & Engineering Chemistry Research,* 50**,** 9685-9695.

CHEN, H., ZHAO, C. & REN, Q. 2012a. Feasibility of CO_2/SO_2 uptake enhancement of calcined limestone modified with rice husk ash during pressurized carbonation. *Journal of Environmental Management,* 93**,** 235-244.

CHEN, H., ZHAO, C. & YANG, Y. 2013. Enhancement of attrition resistance and cyclic CO_2 capture of calcium-based sorbent pellets. *Fuel Processing Technology,* 116**,** 116-122.

CHEN, H., ZHAO, C., YANG, Y. & ZHANG, P. 2012b. CO_2 capture and attrition performance of CaO pellets with aluminate cement under pressurized carbonation. *Applied Energy,* 91**,** 334-340.

CHEN, Z., SONG, H. S., PORTILLO, M., LIM, C. J., GRACE, J. R. & ANTHONY, E. J. 2009. Long-Term Calcination/Carbonation Cycling and Thermal Pretreatment for CO_2 Capture by Limestone and Dolomite. *Energy & Fuels,* 23**,** 1437-1444.

CHEN, Z., YAN, Y. & ELNASHAIE, S. S. E. H. 2003. Novel circulating fast fluidized-bed membrane reformer for efficient production of hydrogen from steam reforming of methane. *Chemical Engineering Science,* 58**,** 4335-4349.

CHENG, F. & DUPONT, V. 2017. Steam Reforming of Bio-Compounds with Auto-Reduced Nickel Catalyst. *Catalysts,* 7.

CHEUNG, H., BROMLEY, L. A. & WILKE, C. R. 1962. Thermal conductivity of gas mixtures. *AIChE Journal,* 8**,** 221-228.

CHU, C. Y. & HWANG, S. J. 2002. Attrition and sulfation of calcium sorbent and solids circulation rate in an internally circulating fluidized bed. *Powder Technology,* 127**,** 185-195.

CLOUGH, P. T., BOOT-HANDFORD, M. E., ZHAO, M. & FENNELL, P. S. 2016. Degradation study of a novel polymorphic sorbent under realistic post-combustion conditions. *Fuel,* 186**,** 708-713.

COLLINS-MARTINEZ, V., ESCOBEDO BRETADO, M., MELÉNDEZ ZARAGOZA, M., SALINAS GUTIÉRREZ, J. & ORTIZ, A. L. 2013. Absorption enhanced reforming of light alcohols (methanol and ethanol) for the production of hydrogen: Thermodynamic modeling. *International Journal of Hydrogen Energy,* 38**,** 12539-12553.

COMAS, J., LABORDE, M. & AMADEO, N. 2004. Thermodynamic analysis of hydrogen production from ethanol using CaO as a CO_2 sorbent. *Journal of Power Sources,* 138**,** 61-67.

COPPOLA, A., MONTAGNARO, F., SALATINO, P. & SCALA, F. 2012. Fluidized bed calcium looping: The effect of SO_2 on sorbent attrition and CO_2 capture capacity. *Chemical Engineering Journal,* 207–208**,** 445-449.

COPPOLA, A., PALLADINO, L., MONTAGNARO, F., SCALA, F. & SALATINO, P. 2015. Reactivation by Steam Hydration of Sorbents for Fluidized-Bed Calcium Looping. *Energy & Fuels,* 29**,** 4436-4446.

COPPOLA, A., SALATINO, P., MONTAGNARO, F. & SCALA, F. 2014a. Hydration-induced reactivation of spent sorbents for fluidized bed calcium looping (double looping). *Fuel Processing Technology,* 120**,** 71-78.

COPPOLA, A., SALATINO, P., MONTAGNARO, F. & SCALA, F. 2014b. Reactivation by water hydration of the CO_2 capture capacity of a calcium looping sorbent. *Fuel,* 127**,** 109-115.

CORELLA, J., AZNAR, M.-P., GIL, J. & CABALLERO, M. A. 1999. Biomass Gasification in Fluidized Bed: Where To Locate the Dolomite To Improve Gasification? *Energy & Fuels,* 13**,** 1122-1127.

COUTTENYE, R. A., DE VILA, M. H. & SUIB, S. L. 2005. Decomposition of methane with an autocatalytically reduced nickel catalyst. *Journal of Catalysis,* 233**,** 317-326.

D'ORAZIO, A., DI CARLO, A., DIONISI, N., DELL'ERA, A. & ORECCHINI, F. 2013. Toluene steam reforming properties of CaO based synthetic sorbents for biomass gasification process. *International Journal of Hydrogen Energy,* 38**,** 13282-13292.

DAI, J., CUI, H. & GRACE, J. R. 2012. Biomass feeding for thermochemical reactors. *Progress in Energy and Combustion Science,* 38**,** 716-736.

DAI, J., SOKHANSANJ, S., GRACE, J. R., BI, X., LIM, C. J. & MELIN, S. 2008. Overview and some issues related to co-firing biomass and coal. *The Canadian Journal of Chemical Engineering,* 86**,** 367-386.

DANG, C., YU, H., WANG, H., PENG, F. & YANG, Y. 2016. A bi-functional Co–CaO–$Ca_{12}Al_{14}O_{33}$ catalyst for sorption-enhanced steam reforming of glycerol to high-purity hydrogen. *Chemical Engineering Journal,* 286**,** 329-338.

DEAN, C., HILLS, T., FLORIN, N., DUGWELL, D. & FENNELL, P. S. 2013. Integrating Calcium Looping CO_2 Capture with the Manufacture of Cement. *Energy Procedia,* 37**,** 7078-7090.

DEAN, C. C., BLAMEY, J., FLORIN, N. H., AL-JEBOORI, M. J. & FENNELL, P. S. 2011a. The calcium looping cycle for CO_2 capture from power generation, cement manufacture and hydrogen production. *Chemical Engineering Research and Design,* 89**,** 836-855.

DEAN, C. C., DUGWELL, D. & FENNELL, P. S. 2011b. Investigation into potential synergy between power generation, cement manufacture and CO_2 abatement using the calcium looping cycle. *Energy & Environmental Science,* 4**,** 2050-2053.

DELGADO, J., AZNAR, M. P. & CORELLA, J. 1997. Biomass Gasification with Steam in Fluidized Bed: Effectiveness of CaO, MgO, and CaO−MgO for Hot Raw Gas Cleaning. *Industrial & Engineering Chemistry Research,* 36**,** 1535-1543.

DEMIRBAS, A. 2004. Combustion characteristics of different biomass fuels. *Progress in Energy and Combustion Science,* 30**,** 219-230.

DEMIRBAŞ, A. 2001. Relationships between lignin contents and heating values of biomass. *Energy Conversion and Management,* 42**,** 183-188.

DEMIRBAŞ, A. 2005. Fuel and combustion properties of bio-wastes. *Energy Sources,* 27**,** 451-462.

DENNIS, J. S. & HAYHURST, A. N. 1987. the effect of CO_2 on the kinetics and extent of calcination of limestone and dolomite particles in fluidised beds. *Chemical Engineering Science,* 42**,** 2361-2372.

DEPARTMENT FOR BUSINESS, E. A. I. S. 2017. 2015 UK Greenhouse Gas Emissions, Final Figures. Statistical Release: National Statistics.

DEPARTMENT FOR ENVIRONMENT FOOD AND RURAL AFFAIRS 2008. Waste Wood as a Biomass Fuel. Great Britain.

DEVI, L., PTASINSKI, K. J. & JANSSEN, F. J. J. G. 2003. A review of the primary measures for tar elimination in biomass gasification processes. *Biomass and Bioenergy,* 24**,** 125-140.

DEWOOLKAR, K. D. & VAIDYA, P. D. 2016a. New hybrid materials for improved hydrogen production via sorption-enhanced steam reforming of butanol. *Energy Technology***,** n/a-n/a.

DEWOOLKAR, K. D. & VAIDYA, P. D. 2016b. Tailored hydrotalcite-based hybrid materials for hydrogen production via sorption-enhanced steam reforming of ethanol. *International Journal of Hydrogen Energy,* 41**,** 6094-6106.

DI FELICE, L., COURSON, C., JAND, N., GALLUCCI, K., FOSCOLO, P. U. & KIENNEMANN, A. 2009. Catalytic biomass gasification: Simultaneous hydrocarbons steam reforming and CO_2 capture in a fluidised bed reactor. *Chemical Engineering Journal,* 154**,** 375-383.

DI FELICE, L., COURSON, C., NIZNANSKY, D., FOSCOLO, P. U. & KIENNEMANN, A. 2010. Biomass Gasification with Catalytic Tar Reforming: A Model Study into Activity Enhancement of Calcium- and Magnesium-Oxide-Based Catalytic Materials by Incorporation of Iron. *Energy & Fuels,* 24**,** 4034-4045.

DI GIULIANO, A., GIRR, J., MASSACESI, R., GALLUCCI, K. & COURSON, C. Sorption enhanced steam methane reforming by Ni–CaO materials supported on mayenite. *International Journal of Hydrogen Energy*.

DIEGO, M. E., ARIAS, B., GRASA, G. & ABANADES, J. C. 2014. Design of a Novel Fluidized Bed Reactor To Enhance Sorbent Performance in CO_2 Capture Systems Using CaO. *Industrial & Engineering Chemistry Research,* 53**,** 10059-10071.

DIEGO, M. E., MARTÍNEZ, I., ALONSO, M., ARIAS, B. & ABANADES, J. C. 2015. 6 - Calcium looping reactor design for fluidized-bed systems. *In:* FENNELL, P. & ANTHONY, B. (eds.) *Calcium and Chemical Looping Technology for Power Generation and Carbon Dioxide (CO_2) Capture.* Woodhead Publishing.

DIETER, H., BIDWE, A. R., VARELA-DUELLI, G., CHARITOS, A., HAWTHORNE, C. & SCHEFFKNECHT, G. 2014. Development of the calcium looping CO_2 capture technology from lab to pilot scale at IFK, University of Stuttgart. *Fuel,* 127**,** 23-37.

DIETRICH, W., LAWRENCE, P. S., GRÜNEWALD, M. & AGAR, D. W. 2005. Theoretical studies on multifunctional catalysts with integrated adsorption sites. *Chemical Engineering Journal,* 107**,** 103-111.

DING, Y. & ALPAY, E. 2000. Adsorption-enhanced steam–methane reforming. *Chemical Engineering Science,* 55**,** 3929-3940.

DONAT, F., FLORIN, N. H., ANTHONY, E. J. & FENNELL, P. S. 2011. Influence of High-Temperature Steam on the Reactivity of CaO Sorbent for CO_2 Capture. *Environmental Science & Technology,* 46**,** 1262-1269.

DONAT, F., FLORIN, N. H., ANTHONY, E. J. & FENNELL, P. S. 2012. Influence of High-Temperature Steam on the Reactivity of CaO Sorbent for CO_2 Capture. *Environmental Science & Technology,* 46**,** 1262-1269.

DOU, B., DUPONT, V., RICKETT, G., BLAKEMAN, N., WILLIAMS, P. T., CHEN, H., DING, Y. & GHADIRI, M. 2009. Hydrogen production by sorption-enhanced steam reforming of glycerol. *Bioresource Technology,* 100**,** 3540-3547.

DOU, B., WANG, C., CHEN, H., SONG, Y. & XIE, B. 2013. Continuous sorption-enhanced steam reforming of glycerol to high-purity hydrogen production. *International Journal of Hydrogen Energy,* 38**,** 11902-11909.

DOU, B., WANG, C., SONG, Y., CHEN, H., JIANG, B., YANG, M. & XU, Y. 2016. Solid sorbents for in-situ CO_2 removal during sorption-enhanced steam reforming process: A review. *Renewable and Sustainable Energy Reviews,* 53**,** 536-546.

DUTTA, S. 2014. A review on production, storage of hydrogen and its utilization as an energy resource. *Journal of Industrial and Engineering Chemistry,* 20**,** 1148-1156.

EISSEN, M. 2012. Sustainable production of chemicals - an educational perspective. *Chemistry Education Research and Practice,* 13**,** 103-111.

EON 2009. Carbon Capture and Storage - Building a Bridge to Sustainable Energy Germany.

EPSTEIN, N. 1989. On tortuosity and the tortuosity factor in flow and diffusion through porous media. *Chemical Engineering Science,* 44**,** 777-779.

EPSTEIN, N. & GRACE, J. R. 2011. *Spouted and Spout-Fluid Beds: Fundamentals and Applications*, Cambridge University Press.

ERANS, M., MANOVIC, V. & ANTHONY, E. J. 2016. Calcium looping sorbents for CO_2 capture. *Applied Energy,* 180**,** 722-742.

ESTEBAN-DÍEZ, G., GIL, M. V., PEVIDA, C., CHEN, D. & RUBIERA, F. 2016. Effect of operating conditions on the sorption enhanced steam reforming of blends of acetic acid and acetone as bio-oil model compounds. *Applied Energy,* 177**,** 579-590.

FAUTH, D. J., FROMMELL, E. A., HOFFMAN, J. S., REASBECK, R. P. & PENNLINE, H. W. 2005. Eutectic salt promoted lithium zirconate: Novel high temperature sorbent for CO_2 capture. *Fuel Processing Technology,* 86**,** 1503-1521.

FENNELL, P. 2015a. 1 - Calcium and chemical looping technology: An introduction. *In:* FENNELL, P. & ANTHONY, B. (eds.) *Calcium and Chemical Looping Technology for Power Generation and Carbon Dioxide (CO_2) Capture.* Woodhead Publishing.

FENNELL, P. 2015b. 3 - Economics of chemical and calcium looping. *In:* FENNELL, P. & ANTHONY, B. (eds.) *Calcium and Chemical Looping Technology for Power Generation and Carbon Dioxide (CO_2) Capture.* Woodhead Publishing.

FENNELL, P. S., DENNIS, J. S. & HAYHURST, A. N. 2009. The order with respect to oxygen and the activation energy for the burning of an anthracitic char in O_2 in a fluidised bed, as measured using a rapid analyser for CO and CO_2. *Proceedings of the Combustion Institute,* 32**,** 2051-2058.

FENNELL, P. S., PACCIANI, R., DENNIS, J. S., DAVIDSON, J. F. & HAYHURST, A. N. 2007. The Effects of Repeated Cycles of Calcination and Carbonation on a Variety of Different Limestones, as Measured in a Hot Fluidized Bed of Sand. *Energy & Fuels,* 21**,** 2072-2081.

FERMOSO, J., HE, L. & CHEN, D. 2012. Production of high purity hydrogen by sorption enhanced steam reforming of crude glycerol. *International Journal of Hydrogen Energy,* 37**,** 14047-14054.

FLORIN, N., BOOT-HANDFORD, M. & FENNELL, P. 2015. 7 - Calcium looping technologies for gasification and reforming. *In:* FENNELL, P. & ANTHONY, B. (eds.) *Calcium and Chemical Looping Technology for Power Generation and Carbon Dioxide (CO_2) Capture.* Woodhead Publishing.

FLORIN, N. H. & HARRIS, A. T. 2007. Hydrogen production from biomass coupled with carbon dioxide capture: The implications of thermodynamic equilibrium. *International Journal of Hydrogen Energy,* 32**,** 4119-4134.

FLORIN, N. H. & HARRIS, A. T. 2008a. Enhanced hydrogen production from biomass with in situ carbon dioxide capture using calcium oxide sorbents. *Chemical Engineering Science,* 63**,** 287-316.

FLORIN, N. H. & HARRIS, A. T. 2008b. Mechanistic study of enhanced H2 synthesis in biomass gasifiers with in-situ CO_2 capture using CaO. *AIChE Journal,* 54**,** 1096-1109.

FLORIN, N. H. & HARRIS, A. T. 2008c. Screening CaO-Based Sorbents for CO_2 Capture in Biomass Gasifiers. *Energy & Fuels,* 22**,** 2734-2742.

FOGLER, S. H. 2006. *Elements of Chemical Reaction Engineering,* New Jersey, USA, Pearson Prentice Hall.

FRUEHAN, R. J. 1977. The rate of reduction of iron oxides by carbon. *Metallurgical Transactions B,* 8**,** 279-286.

FU, P., YI, W., LI, Z., LI, Y., WANG, J. & BAI, X. 2013. Comparative analysis on sorption enhanced steam reforming and conventional steam reforming of hydroxyacetone for hydrogen production: Thermodynamic modeling. *International Journal of Hydrogen Energy,* 38**,** 11893-11901.

FUERTES, A. B., MARBAN, G. & RUBIERA, F. 1993. Kinetics of thermal decomposition of limestone particles in a fluidized bed reactor. *Chemical Engineering Research and Design,* 71**,** 421-428.

FUKASE, S. & SUZUKA, T. 1993. Residual oil cracking with generation of hydrogen: deactivation of iron oxide catalyst in the steam-iron reaction. *Applied Catalysis A: General,* 100**,** 1-17.

FURNAS, C. C. 1931. The Rate of Calcination of Limestone. *Industrial & Engineering Chemistry,* 23**,** 534-538.

GARCIA, L. A., FRENCH, R., CZERNIK, S. & CHORNET, E. 2000. Catalytic steam reforming of bio-oils for the production of hydrogen: effects of catalyst composition. *Applied Catalysis A: General,* 201**,** 225-239.

GARCÍA-LABIANO, F., ABAD, A., DE DIEGO, L. F., GAYÁN, P. & ADÁNEZ, J. 2002. Calcination of calcium-based sorbents at pressure in a broad range of CO_2 concentrations. *Chemical Engineering Science,* 57**,** 2381-2393.

GARCÍA-LARIO, A. L., AZNAR, M., MARTINEZ, I., GRASA, G. S. & MURILLO, R. 2015a. Experimental study of the application of a $NiO/NiAl_2O_4$ catalyst and a CaO-based synthetic sorbent on the Sorption Enhanced Reforming process. *International Journal of Hydrogen Energy,* 40**,** 219-232.

GARCÍA-LARIO, A. L., GRASA, G. S. & MURILLO, R. 2015b. Performance of a combined CaO-based sorbent and catalyst on H_2 production, via sorption enhanced methane steam reforming. *Chemical Engineering Journal,* 264**,** 697-705.

GIL, M. V., FERMOSO, J., PEVIDA, C., CHEN, D. & RUBIERA, F. 2016. Production of fuel-cell grade H_2 by sorption enhanced steam reforming of acetic acid as a model compound of biomass-derived bio-oil. *Applied Catalysis B: Environmental,* 184**,** 64-76.

GIL, M. V., FERMOSO, J., RUBIERA, F. & CHEN, D. 2015. H_2 production by sorption enhanced steam reforming of biomass-derived bio-oil in a fluidized bed reactor: An assessment of the effect of operation variables using response surface methodology. *Catalysis Today,* 242, Part A**,** 19-34.

GLOBAL CCS INSTITUTE 2012. CO2 Capture Technologies - Pre-Combustion Capture.
GONZÁLEZ, B., ALONSO, M. & ABANADES, J. C. 2010. Sorbent attrition in a carbonation/calcination pilot plant for capturing CO_2 from flue gases. *Fuel,* 89**,** 2918-2924.
GONZÁLEZ, B., BLAMEY, J., AL-JEBOORI, M. J., FLORIN, N. H., CLOUGH, P. T. & FENNELL, P. S. 2016. Additive effects of steam addition and HBr doping for CaO-based sorbents for CO_2 capture. *Chemical Engineering and Processing: Process Intensification,* 103**,** 21-26.
GONZÁLEZ, B., BLAMEY, J., MCBRIDE-WRIGHT, M., CARTER, N., DUGWELL, D., FENNELL, P. & ABANADES, J. C. 2011. Calcium looping for CO_2 capture: sorbent enhancement through doping. *Energy Procedia,* 4**,** 402-409.
GOTTIPATI, R. & MISHRA, S. 2011. A kinetic study on pyrolysis and combustion characteristics of oil cakes: Effect of cellulose and lignin content. *Journal of Fuel Chemistry and Technology,* 39**,** 265-270.
GRASA, G., GONZÁLEZ, B., ALONSO, M. & ABANADES, J. C. 2007. Comparison of CaO-Based Synthetic CO2 Sorbents under Realistic Calcination Conditions. *Energy & Fuels,* 21**,** 3560-3562.
GRASA, G., MURILLO, R., ALONSO, M. & ABANADES, J. C. 2009. Application of the random pore model to the carbonation cyclic reaction. *AIChE Journal,* 55**,** 1246-1255.
GRASA, G. S. & ABANADES, J. C. 2006. CO_2 Capture Capacity of CaO in Long Series of Carbonation/Calcination Cycles. *Industrial & Engineering Chemistry Research,* 45**,** 8846-8851.
GRASA, G. S., ABANADES, J. C., ALONSO, M. & GONZÁLEZ, B. 2008. Reactivity of highly cycled particles of CaO in a carbonation/calcination loop. *Chemical Engineering Journal,* 137**,** 561-567.
GREEN, D. & PERRY, R. 2007. *Perry's Chemical Engineers' Handbook, Eighth Edition*, McGraw-Hill Education.
GROßMANN, K., TREIBER, P. & KARL, J. 2016. Steam methane reforming at low S/C ratios for power-to-gas applications. *International Journal of Hydrogen Energy,* 41**,** 17784-17792.
GRÜNEWALD, M. & AGAR, D. W. 2004. Enhanced catalyst performance using integrated structured functionalities. *Chemical Engineering Science,* 59**,** 5519-5526.
GUO, Q., CHEN, X. & LIU, H. 2012. Experimental research on shape and size distribution of biomass particle. *Fuel,* 94**,** 551-555.
GUO, S., WANG, H., LIU, D., YANG, L., WEI, X. & WU, S. 2015. Understanding the Impacts of Impurities and Water Vapor on Limestone Calcination in a Laboratory-Scale Fluidized Bed. *Energy & Fuels,* 29**,** 7572-7583.
GUPTA, H. & FAN, L.-S. 2002. Carbonation−Calcination Cycle Using High Reactivity Calcium Oxide for Carbon Dioxide Separation from Flue Gas. *Industrial & Engineering Chemistry Research,* 41**,** 4035-4042.
GUPTA, R. B. 2008. *Hydrogen Fuel: Production, Transport, and Storage*, CRC Press.
H. BORGWARDT, R. 1989. Sintering of nascent calcium oxide. *Chemical Engineering Science,* 44**,** 53-60.
HALABI, M. H., DE CROON, M. H. J. M., VAN DER SCHAAF, J., COBDEN, P. D. & SCHOUTEN, J. C. 2012. Kinetic and structural requirements for a CO_2 adsorbent in sorption enhanced catalytic reforming of methane – Part I: Reaction kinetics and sorbent capacity. *Fuel,* 99**,** 154-164.
HAN, L., WANG, Q., YANG, Y., YU, C., FANG, M. & LUO, Z. 2011. Hydrogen production via CaO sorption enhanced anaerobic gasification of sawdust in a bubbling fluidized bed. *International Journal of Hydrogen Energy,* 36**,** 4820-4829.
HANAOKA, T., YOSHIDA, T., FUJIMOTO, S., KAMEI, K., HARADA, M., SUZUKI, Y., HATANO, H., YOKOYAMA, S.-Y. & MINOWA, T. 2005. Hydrogen production from woody biomass by steam gasification using a sorbent. *Biomass and Bioenergy,* 28**,** 63-68.
HANSEN, P. F. B., DAM-JOHANSEN, K. & ØSTERGAARD, K. 1993. High-temperature reaction between sulphur dioxide and limestone—V. The effect of periodically changing oxidizing and reducing conditions. *Chemical Engineering Science,* 48**,** 1325-1341.
HARRISON, D. P. 2008. Sorption-Enhanced Hydrogen Production: A Review. *Industrial & Engineering Chemistry Research,* 47**,** 6486-6501.

HAWTHORNE, C., DIETER, H., BIDWE, A., SCHUSTER, A., SCHEFFKNECHT, G., UNTERBERGER, S. & KÄß, M. 2011. CO_2 capture with CaO in a 200 kWth dual fluidized bed pilot plant. *Energy Procedia,* 4**,** 441-448.

HELVEG, S., LÓPEZ-CARTES, C., SEHESTED, J., HANSEN, P. L., CLAUSEN, B. S., ROSTRUP-NIELSEN, J. R., ABILD-PEDERSEN, F. & NØRSKOV, J. K. 2004. Atomic-scale imaging of carbon nanofibre growth. *Nature,* 427**,** 426-429.

HEUBERGER, C. F., STAFFELL, I., SHAH, N. & DOWELL, N. M. 2017a. A systems approach to quantifying the value of power generation and energy storage technologies in future electricity networks. *Computers & Chemical Engineering*.

HEUBERGER, C. F., STAFFELL, I., SHAH, N. & DOWELL, N. M. 2017b. A systems approach to quantifying the value of power generation and energy storage technologies in future electricity networks. *Computers & Chemical Engineering*.

HIGMAN, C. & VAN DER BURGT, M. 2008. Gasification (2nd Edition). Elsevier.

HOUSE OF COMMONS COMMITTEE OF PUBLIC ACCOUNTS 2017. Carbon Capture and Storage.

HU, N. & SCARONI, A. W. 1996. Calcination of pulverized limestone particles under furnace injection conditions. *Fuel,* 75**,** 177-186.

HU, S., HE, L., WANG, Y., SU, S., JIANG, L., CHEN, Q., LIU, Q., CHI, H., XIANG, J. & SUN, L. 2016. Effects of oxygen species from Fe addition on promoting steam reforming of toluene over Fe–Ni/Al2O3 catalysts. *International Journal of Hydrogen Energy,* 41**,** 17967-17975.

HUGHES, R. W., LU, D., ANTHONY, E. J. & WU, Y. 2004. Improved Long-Term Conversion of Limestone-Derived Sorbents for In Situ Capture of CO_2 in a Fluidized Bed Combustor. *Industrial & Engineering Chemistry Research,* 43**,** 5529-5539.

IDA, J.-I. & LIN, Y. S. 2003. Mechanism of High-Temperature CO_2 Sorption on Lithium Zirconate. *Environmental Science & Technology,* 37**,** 1999-2004.

IEA 2015. Hydrogen and Fuel Cells: Technology Roadmap. International Energy Agency.

IORDANIDIS, A. A., KECHAGIOPOULOS, P. N., VOUTETAKIS, S. S., LEMONIDOU, A. A. & VASALOS, I. A. 2006. Autothermal sorption-enhanced steam reforming of bio-oil/biogas mixture and energy generation by fuel cells: Concept analysis and process simulation. *International Journal of Hydrogen Energy,* 31**,** 1058-1065.

IPCC 2013. Climate Change 2013: The Physical Science Basis. Contribution of Working Group I to the Firth Assessment Report of the Intergovernmental Panel on Climate Change. *In:* STOKER, T. F., D. QIN, G.-K. PLATTNER, M. TIGNOR, S.K. ALLEN, I. BOSCHUNG, A. NAUELS, Y. XIA, V. BEX AND P.M. MIDGLEY (ed.). Cambridge, UK and New York, NY, USA.

IPCC 2014. *Climate Change 2014: Impacts, Adaptation, and Vulnerability. Part A: Global and Sectoral Aspects. Contribution of Working Group II to the Fifth Assessment Report of the Intergovernmental Panel on Climate Change [Field, C.B., V.R. Barros, D.J. Dokken, K.J. Mach, M.D. Mastrandrea, T.E. Bilir, M. Chatterjee, K.L. Ebi, Y.O. Estrada, R.C. Genova, B. Girma, E.S. Kissel, A.N. Levy, S. MacCracken, P.R. Mastrandrea, and L.L. White (eds.)],* Cambridge, United Kingdom and New York, NY, USA, Cambridge University Press.

IWAN, A., STEPHENSON, H., KETCHIE, W. C. & LAPKIN, A. A. 2009. High temperature sequestration of CO_2 using lithium zirconates. *Chemical Engineering Journal,* 146**,** 249-258.

JAKOBSEN, J. P. & HALMØY, E. 2009. Reactor modeling of sorption enhanced steam methane reforming. *Energy Procedia,* 1**,** 725-732.

JIA, L., HUGHES, R., LU, D., ANTHONY, E. J. & LAU, I. 2007. Attrition of Calcining Limestones in Circulating Fluidized-Bed Systems. *Industrial & Engineering Chemistry Research,* 46**,** 5199-5209.

JOHNSEN, K., GRACE, J. R., ELNASHAIE, S. S. E. H., KOLBEINSEN, L. & ERIKSEN, D. 2006a. Modeling of Sorption-Enhanced Steam Reforming in a Dual Fluidized Bubbling Bed Reactor. *Industrial & Engineering Chemistry Research,* 45**,** 4133-4144.

JOHNSEN, K., RYU, H. J., GRACE, J. R. & LIM, C. J. 2006b. Sorption-enhanced steam reforming of methane in a fluidized bed reactor with dolomite as a CO_2-acceptor. *Chemical Engineering Science,* 61**,** 1195-1202.

KALANTZOPOULOS, G. N., KAZI, S. S., GRASA, G., MASTIN, J., MURILLO, R. & MEYER, J. 2015. Materials and Technologies for Energy Efficiency. *In:* MENDEZ-VILAS, A. (ed.) *The Energy & Materials Research Conference (EMR2015)*. Madrid, Spain: Brown Walker Press.

KALINCI, Y., HEPBASLI, A. & DINCER, I. 2009. Biomass-based hydrogen production: A review and analysis. *International Journal of Hydrogen Energy,* 34**,** 8799-8817.

KHAN, A. A., DE JONG, W., JANSENS, P. J. & SPLIETHOFF, H. 2009. Biomass combustion in fluidized bed boilers: Potential problems and remedies. *Fuel Processing Technology,* 90**,** 21-50.

KIERZKOWSKA, A. M., POULIKAKOS, L. V., BRODA, M. & MÜLLER, C. R. 2013. Synthesis of calcium-based, Al_2O_3-stabilized sorbents for CO_2 capture using a co-precipitation technique. *International Journal of Greenhouse Gas Control,* 15**,** 48-54.

KINOSHITA, C. M. & TURN, S. Q. 2003. Production of hydrogen from bio-oil using CaO as a CO_2 sorbent. *International Journal of Hydrogen Energy,* 28**,** 1065-1071.

KISSA, E. 1999. Dispersions: Characterization, Testing, and Measurement. *Surfactant Science.* Taylor & Francis.

KLEIN, M. & SMITH, F. J. 1968. Tables of collision integrals for the (m,6) potential function for 10 values of m. *The Journal of Research of the National Institute of Standards and Technology,* 72A**,** 359.

KOPPATZ, S., PFEIFER, C., RAUCH, R., HOFBAUER, H., MARQUARD-MOELLENSTEDT, T. & SPECHT, M. 2009. H_2 rich product gas by steam gasification of biomass with in situ CO_2 absorption in a dual fluidized bed system of 8 MW fuel input. *Fuel Processing Technology,* 90**,** 914-921.

KOPPEJAN, J. & VAN LOO, S. 2012. *The Handbook of Biomass Combustion and Co-firing*, Taylor & Francis.

KURAMOTO, K., FUJIMOTO, S., MORITA, A., SHIBANO, S., SUZUKI, Y., HATANO, H., SHI-YING, L., HARADA, M. & TAKARADA, T. 2003. Repetitive Carbonation−Calcination Reactions of Ca-Based Sorbents for Efficient CO_2 Sorption at Elevated Temperatures and Pressures. *Industrial & Engineering Chemistry Research,* 42**,** 975-981.

LEE, D. K. 2004. An apparent kinetic model for the carbonation of calcium oxide by carbon dioxide. *Chemical Engineering Journal,* 100**,** 71-77.

LETCHER, T. M., SCOTT, J. L. & PETER, L. 2012. *Materials for a Sustainable Future*, Royal Society of Chemistry.

LI, B., YANG, H., WEI, L., SHAO, J., WANG, X. & CHEN, H. Absorption-enhanced steam gasification of biomass for hydrogen production: Effects of calcium-based absorbents and NiO-based catalysts on corn stalk pyrolysis-gasification. *International Journal of Hydrogen Energy*.

LI, B., YANG, H., WEI, L., SHAO, J., WANG, X. & CHEN, H. 2017. Absorption-enhanced steam gasification of biomass for hydrogen production: Effects of calcium-based absorbents and NiO-based catalysts on corn stalk pyrolysis-gasification. *International Journal of Hydrogen Energy,* 42**,** 5840-5848.

LI, C. & SUZUKI, K. 2009. Tar property, analysis, reforming mechanism and model for biomass gasification—An overview. *Renewable and Sustainable Energy Reviews,* 13**,** 594-604.

LI, D., NAKAGAWA, Y. & TOMISHIGE, K. 2012. Development of Ni-Based Catalysts for Steam Reforming of Tar Derived from Biomass Pyrolysis. *Chinese Journal of Catalysis,* 33**,** 583-594.

LI, D., SHISHIDO, T., OUMI, Y., SANO, T. & TAKEHIRA, K. 2007. Self-activation and self-regenerative activity of trace Rh-doped Ni/Mg(Al)O catalysts in steam reforming of methane. *Applied Catalysis A: General,* 332**,** 98-109.

LI, X. T., GRACE, J. R., LIM, C. J., WATKINSON, A. P., CHEN, H. P. & KIM, J. R. 2004. Biomass gasification in a circulating fluidized bed. *Biomass and Bioenergy,* 26**,** 171-193.

LI, Z.-H., WANG, Y., XU, K., YANG, J.-Z., NIU, S.-B. & YAO, H. 2016a. Effect of steam on CaO regeneration, carbonation and hydration reactions for CO_2 capture. *Fuel Processing Technology,* 151**,** 101-106.

LI, Z.-S. & CAI, N.-S. 2007. Modeling of Multiple Cycles for Sorption-Enhanced Steam Methane Reforming and Sorbent Regeneration in Fixed Bed Reactor. *Energy & Fuels,* 21**,** 2909-2918.

LI, Z.-S., CAI, N.-S., HUANG, Y.-Y. & HAN, H.-J. 2005. Synthesis, Experimental Studies, and Analysis of a New Calcium-Based Carbon Dioxide Absorbent. *Energy & Fuels,* 19**,** 1447-1452.

LI, Z. S., LIANG, P. T. & CAI, N. S. 2016b. A rate equation theory for the pore size distribution of calcined $CaCO_3$ in calcium looping. *Faraday Discussions,* 192**,** 197-216.
LIDE, D. R. 2005. Section 4 - Properties of the elements and inorganic compounds. *CRC Handbook of Chemistry and Physics, 86th Edition.* Taylor & Francis.
LIU, W., DENNIS, J. S., SULTAN, D. S., REDFERN, S. A. T. & SCOTT, S. A. 2012. An investigation of the kinetics of CO_2 uptake by a synthetic calcium based sorbent. *Chemical Engineering Science,* 69**,** 644-658.
LIU, W., FENG, B., WU, Y., WANG, G., BARRY, J. & DINIZ DA COSTA, J. C. 2010. Synthesis of Sintering-Resistant Sorbents for CO_2 Capture. *Environmental Science & Technology,* 44**,** 3093-3097.
LLORENTE, M. J. F. & GARCÍA, J. E. C. 2005. Comparing methods for predicting the sintering of biomass ash in combustion. *Fuel,* 84**,** 1893-1900.
LOPEZ ORTIZ, A. & HARRISON, D. P. 2001. Hydrogen Production Using Sorption-Enhanced Reaction. *Industrial & Engineering Chemistry Research,* 40**,** 5102-5109.
LU, A. H. & DAI, S. 2014. *Porous Materials for Carbon Dioxide Capture*, Springer Berlin Heidelberg.
LU, D., HUGHES, R., ANTHONY, E. & MANOVIC, V. 2009. Sintering and Reactivity of $CaCO_3$ - Based Sorbents for In Situ CO_2 Capture in Fluidized Beds under Realistic Calcination Conditions. *Journal of Environmental Engineering,* 135**,** 404-410.
LU, D. Y., HUGHES, R. W. & ANTHONY, E. J. 2008. Ca-based sorbent looping combustion for CO_2 capture in pilot-scale dual fluidized beds. *Fuel Processing Technology,* 89**,** 1386-1395.
LUGO, E. L. & WILHITE, B. A. 2016. A theoretical comparison of multifunctional catalyst for sorption-enhanced reforming process. *Chemical Engineering Science,* 150**,** 1-15.
LUNDHOLM, K., NORDIN, A., ÖHMAN, M. & BOSTRÖM, D. 2005. Reduced bed agglomeration by co-combustion biomass with peat fuels in a fluidized bed. *Energy and Fuels,* 19**,** 2273-2278.
LUO, C., ZHENG, Y., GUO, J. & FENG, B. 2014. Effect of sulfation on CO_2 capture of CaO-based sorbents during calcium looping cycle. *Fuel*.
LUO, C., ZHENG, Y., ZHENG, C., YIN, J., QIN, C. & FENG, B. 2013. Manufacture of calcium-based sorbents for high temperature cyclic CO_2 capture via a sol–gel process. *International Journal of Greenhouse Gas Control,* 12**,** 193-199.
LYSIKOV, A. I., SALANOV, A. N. & OKUNEV, A. G. 2007. Change of CO_2 Carrying Capacity of CaO in Isothermal Recarbonation−Decomposition Cycles. *Industrial & Engineering Chemistry Research,* 46**,** 4633-4638.
MAHISHI, M. R. & GOSWAMI, D. Y. 2007. An experimental study of hydrogen production by gasification of biomass in the presence of a sorbent. *International Journal of Hydrogen Energy,* 32**,** 2803-2808.
MAHISHI, M. R., SADRAMELI, M. S., VIJAYARAGHAVAN, S. & GOSWAMI, D. Y. 2007. A Novel Approach to Enhance the Hydrogen Yield of Biomass Gasification Using CO_2 Sorbent. *Journal of Engineering for Gas Turbines and Power,* 130**,** 011501-011501-8.
MALHOTRA, R. 2012. *Fossil Energy: Selected Entries from the Encyclopedia of Sustainability Science and Technology*, Springer New York.
MANOVIC, V., ANTHONY, E. & LONCAREVIC, D. 2010. Sulphation of CaO-Based Sorbent Modified in CO_2 Looping Cycles. *In:* YUE, G., ZHANG, H., ZHAO, C. & LUO, Z. (eds.) *Proceedings of the 20th International Conference on Fluidized Bed Combustion.* Springer Berlin Heidelberg.
MANOVIC, V. & ANTHONY, E. J. 2007. Steam Reactivation of Spent CaO-Based Sorbent for Multiple CO2 Capture Cycles. *Environmental Science & Technology,* 41**,** 1420-1425.
MANOVIC, V. & ANTHONY, E. J. 2008a. Parametric Study on the CO2 Capture Capacity of CaO-Based Sorbents in Looping Cycles. *Energy & Fuels,* 22**,** 1851-1857.
MANOVIC, V. & ANTHONY, E. J. 2008b. Thermal activation of CaO-based sorbent and self-reactivation during CO2 capture looping cycles. *Environ Sci Technol,* 42**,** 4170-4.
MANOVIC, V. & ANTHONY, E. J. 2009a. CaO-Based Pellets Supported by Calcium Aluminate Cements for High-Temperature CO_2 Capture. *Environmental Science & Technology,* 43**,** 7117-7122.

MANOVIC, V. & ANTHONY, E. J. 2009b. Long-Term Behavior of CaO-Based Pellets Supported by Calcium Aluminate Cements in a Long Series of CO_2 Capture Cycles. *Industrial & Engineering Chemistry Research,* 48**,** 8906-8912.
MANOVIC, V. & ANTHONY, E. J. 2010a. Carbonation of CaO-Based Sorbents Enhanced by Steam Addition. *Industrial & Engineering Chemistry Research,* 49**,** 9105-9110.
MANOVIC, V. & ANTHONY, E. J. 2010b. CO_2 Carrying Behavior of Calcium Aluminate Pellets under High-Temperature/High-CO_2 Concentration Calcination Conditions. *Industrial & Engineering Chemistry Research,* 49**,** 6916-6922.
MANOVIC, V. & ANTHONY, E. J. 2010c. Sintering and Formation of a Nonporous Carbonate Shell at the Surface of CaO-Based Sorbent Particles during CO_2-Capture Cycles. *Energy & Fuels,* 24**,** 5790-5796.
MANOVIC, V., ANTHONY, E. J., GRASA, G. & ABANADES, J. C. 2008. CO_2 Looping Cycle Performance of a High-Purity Limestone after Thermal Activation/Doping. *Energy & Fuels,* 22**,** 3258-3264.
MANOVIC, V., CHARLAND, J.-P., BLAMEY, J., FENNELL, P. S., LU, D. Y. & ANTHONY, E. J. 2009. Influence of calcination conditions on carrying capacity of CaO-based sorbent in CO_2 looping cycles. *Fuel,* 88**,** 1893-1900.
MANOVIC, V., FENNELL, P. S., AL-JEBOORI, M. J. & ANTHONY, E. J. 2013. Steam-Enhanced Calcium Looping Cycles with Calcium Aluminate Pellets Doped with Bromides. *Industrial & Engineering Chemistry Research,* 52**,** 7677-7683.
MARTAVALTZI, C. S. & LEMONIDOU, A. A. 2010. Hydrogen production via sorption enhanced reforming of methane: Development of a novel hybrid material—reforming catalyst and CO_2 sorbent. *Chemical Engineering Science,* 65**,** 4134-4140.
MARTÍNEZ, I., GRASA, G., MURILLO, R., ARIAS, B. & ABANADES, J. C. 2012. Kinetics of Calcination of Partially Carbonated Particles in a Ca-Looping System for CO_2 Capture. *Energy & Fuels,* 26**,** 1432-1440.
MARTÍNEZ, I., ROMANO, M. C., CHIESA, P., GRASA, G. & MURILLO, R. 2013a. Hydrogen production through sorption enhanced steam reforming of natural gas: Thermodynamic plant assessment. *International Journal of Hydrogen Energy,* 38**,** 15180-15199.
MARTÍNEZ, I., ROMANO, M. C., CHIESA, P., GRASA, G. & MURILLO, R. 2013b. Hydrogen production through sorption enhanced steam reforming of natural gas: Thermodynamic plant assessment. *International Journal of Hydrogen Energy*.
MATSUOKA, K., SHIMBORI, T., KURAMOTO, K., HATANO, H. & SUZUKI, Y. 2006. Steam Reforming of Woody Biomass in a Fluidized Bed of Iron Oxide-Impregnated Porous Alumina. *Energy & Fuels,* 20**,** 2727-2731.
MCBRIDE, B. J., ZEHE, M. J. & GORDON, S. 2004. NASA report TP-2002-211556, NASA Glenn Coefficients for Calculating Thermodynamic Properties of Individual Species, September 2002. Applied using ThermoVader, Thermodynamic functions for Excel written by Scott, S. and Fennell, P. (2004).
MCKENDRY, P. 2002. Energy production from biomass (part 1): overview of biomass. *Bioresource Technology,* 83**,** 37-46.
MERKUS, H. G. & MEESTERS, G. M. H. 2015. *Production, Handling and Characterization of Particulate Materials*, Springer International Publishing.
MILNE, T. A., EVANS, R. J. & ABATZOGLOU, N. 1998. Biomass Gasifier "Tars": Their Nature, Formation, and Conversion. *In:* NATIONAL RENEWABLE ENERGY LABORATORY, A. N. L. O. T. U. S. D. O. E. (ed.) NREL/TP-570-25357 ed. USA: U.S. Department of Energy.
MIYAZAWA, T., KIMURA, T., NISHIKAWA, J., KADO, S., KUNIMORI, K. & TOMISHIGE, K. 2006. Catalytic performance of supported Ni catalysts in partial oxidation and steam reforming of tar derived from the pyrolysis of wood biomass. *Catalysis Today,* 115**,** 254-262.
MONTAGNARO, F., SALATINO, P. & SCALA, F. 2010. The influence of temperature on limestone sulfation and attrition under fluidized bed combustion conditions. *Experimental Thermal and Fluid Science,* 34**,** 352-358.
MOSTAFAVI, E., SEDGHKERDAR, M. H. & MAHINPEY, N. 2013. Thermodynamic and Kinetic Study of CO_2 Capture with Calcium Based Sorbents: Experiments and Modeling. *Industrial & Engineering Chemistry Research,* 52**,** 4725-4733.

MOULIJN, J. A., VAN DIEPEN, A. E. & KAPTEIJN, F. 2001. Catalyst deactivation: is it predictable?: What to do? *Applied Catalysis A: General,* 212**,** 3-16.
MYRÉN, C., HÖRNELL, C., BJÖRNBOM, E. & SJÖSTRÖM, K. 2002. Catalytic tar decomposition of biomass pyrolysis gas with a combination of dolomite and silica. *Biomass and Bioenergy,* 23**,** 217-227.
NAHIL, M. A., WANG, X., WU, C., YANG, H., CHEN, H. & WILLIAMS, P. T. 2013. Novel bi-functional Ni-Mg-Al-CaO catalyst for catalytic gasification of biomass for hydrogen production with in situ CO_2 adsorption. *RSC Advances,* 3**,** 5583-5590.
NAIR, B. N., YAMAGUCHI, T., KAWAMURA, H., NAKAO, S.-I. & NAKAGAWA, K. 2004. Processing of Lithium Zirconate for Applications in Carbon Dioxide Separation: Structure and Properties of the Powders. *Journal of the American Ceramic Society,* 87**,** 68-74.
NARVÁEZ, I., ORÍO, A., AZNAR, M. P. & CORELLA, J. 1996. Biomass Gasification with Air in an Atmospheric Bubbling Fluidized Bed. Effect of Six Operational Variables on the Quality of the Produced Raw Gas. *Industrial & Engineering Chemistry Research,* 35**,** 2110-2120.
NEAVEL RICHARD, C. 1981. Coal Structure and Coal Science: Overview and Recommendations. *Coal Structure.* AMERICAN CHEMICAL SOCIETY.
NI, M., LEUNG, D. Y. C., LEUNG, M. K. H. & SUMATHY, K. 2006. An overview of hydrogen production from biomass. *Fuel Processing Technology,* 87**,** 461-472.
NIEVA, M. A., VILLAVERDE, M. M., MONZÓN, A., GARETTO, T. F. & MARCHI, A. J. 2014. Steam-methane reforming at low temperature on nickel-based catalysts. *Chemical Engineering Journal,* 235**,** 158-166.
NISHIKAWA, J., MIYAZAWA, T., NAKAMURA, K., ASADULLAH, M., KUNIMORI, K. & TOMISHIGE, K. 2008. Promoting effect of Pt addition to $Ni/CeO_2/Al_2O_3$ catalyst for steam gasification of biomass. *Catalysis Communications,* 9**,** 195-201.
NIST 2011. NIST Chemistry WebBook. U.S. Secretary of Commerce of the United States of America.
NORDGREEN, T., LILIEDAHL, T. & SJÖSTRÖM, K. 2006a. Elemental Iron as a Tar Breakdown Catalyst in Conjunction with Atmospheric Fluidized Bed Gasification of Biomass: A Thermodynamic Study. *Energy & Fuels,* 20**,** 890-895.
NORDGREEN, T., LILIEDAHL, T. & SJÖSTRÖM, K. 2006b. Metallic iron as a tar breakdown catalyst related to atmospheric, fluidised bed gasification of biomass. *Fuel,* 85**,** 689-694.
NUSSBAUMER, T. 2003. Combustion and Co-combustion of Biomass: Fundamentals, Technologies, and Primary Measures for Emission Reduction. *Energy & Fuels,* 17**,** 1510-1521.
NUTALAPATI, D., GUPTA, R., MOGHTADERI, B. & WALL, T. F. 2007. Assessing slagging and fouling during biomass combustion: A thermodynamic approach allowing for alkali/ash reactions. *Fuel Processing Technology,* 88**,** 1044-1052.
OBRADOVIĆ, A., LIKOZAR, B. & LEVEC, J. 2013. Steam Methane Reforming over Ni-based Pellet-type and $Pt/Ni/Al_2O_3$ Structured Plate-type Catalyst: Intrinsic Kinetics Study. *Industrial & Engineering Chemistry Research,* 52**,** 13597-13606.
OLAZAR, M., AGUADO, R., BILBAO, J. & BARONA, A. 2000. Pyrolysis of sawdust in a conical spouted-bed reactor with a HZSM-5 catalyst. *AIChE Journal,* 46**,** 1025-1033.
OLIVEIRA, E. L. G., GRANDE, C. A. & RODRIGUES, A. E. 2009. Steam methane reforming in a Ni/Al_2O_3 catalyst: Kinetics and diffusional limitations in extrudates. *The Canadian Journal of Chemical Engineering,* 87**,** 945-956.
OTSUKA, K., KABURAGI, T., YAMADA, C. & TAKENAKA, S. 2003a. Chemical storage of hydrogen by modified iron oxides. *Journal of Power Sources,* 122**,** 111-121.
OTSUKA, K., YAMADA, C., KABURAGI, T. & TAKENAKA, S. 2003b. Hydrogen storage and production by redox of iron oxide for polymer electrolyte fuel cell vehicles. *International Journal of Hydrogen Energy,* 28**,** 335-342.
OXBURGH, R. 2016. Lowest Cost Decarbonisation for the UK: The Critical Role of CCS, Report to the Secretary of State for Business, Energy and Industrial Strategy from the Parliamentary Advisory Group on Carbon Capture and storage (CCS). Parliamentary Advisory Group on Carbon Capture and Storage.
PACCIANI, R., MÜLLER, C. R., DAVIDSON, J. F., DENNIS, J. S. & HAYHURST, A. N. 2008. Synthetic Ca-based solid sorbents suitable for capturing CO_2 in a fluidized bed. *The Canadian Journal of Chemical Engineering,* 86**,** 356-366.

PAISLEY, M. A. 2000. Biomass Energy. *Kirk-Othmer Encyclopedia of Chemical Technology.* John Wiley & Sons, Inc.

PETERSON, S. B., KONYA, G., CLAYTON, C. K., LEWIS, R. J., WILDE, B. R., EYRING, E. M. & WHITTY, K. J. 2013. Characteristics and CLOU Performance of a Novel SiO_2-Supported Oxygen Carrier Prepared from CuO and β-SiC. *Energy & Fuels,* 27**,** 6040-6047.

PHROMPRASIT, J., POWELL, J., ARPORNWICHANOP, A., RODRIGUES, A. & ASSABUMRUNGRAT, S. 2013. Hydrogen Production from Sorption Enhanced Biogas Steam Reforming Using Nickel-Based Catalysts. *Engineering Journal; Vol 17, No 4 (2013): Regular Issue*.

PHROMPRASIT, J., POWELL, J., WONGSAKULPHASATCH, S., KIATKITTIPONG, W., BUMROONGSAKULSAWAT, P. & ASSABUMRUNGRAT, S. 2016. Activity and stability performance of multifunctional catalyst (Ni/CaO and Ni/$Ca_{12}Al_{14}O_{33}$CaO) for bio-hydrogen production from sorption enhanced biogas steam reforming. *International Journal of Hydrogen Energy,* 41**,** 7318-7331.

PHROMPRASIT, J., POWELL, J., WONGSAKULPHASATCH, S., KIATKITTIPONG, W., BUMROONGSAKULSAWAT, P. & ASSABUMRUNGRAT, S. 2017. H_2 production from sorption enhanced steam reforming of biogas using multifunctional catalysts of Ni over Zr-, Ce- and La-modified CaO sorbents. *Chemical Engineering Journal,* 313**,** 1415-1425.

PIMENIDOU, P., RICKETT, G., DUPONT, V. & TWIGG, M. V. 2010. High purity H_2 by sorption-enhanced chemical looping reforming of waste cooking oil in a packed bed reactor. *Bioresource Technology,* 101**,** 9279-9286.

POLYCHRONOPOULOU, K., BAKANDRITSOS, A., TZITZIOS, V., FIERRO, J. L. G. & EFSTATHIOU, A. M. 2006. Absorption-enhanced reforming of phenol by steam over supported Fe catalysts. *Journal of Catalysis,* 241**,** 132-148.

PORTER, R. T. J., FAIRWEATHER, M., KOLSTER, C., MAC DOWELL, N., SHAH, N. & WOOLLEY, R. M. 2017. Cost and performance of some carbon capture technology options for producing different quality CO_2 product streams. *International Journal of Greenhouse Gas Control,* 57**,** 185-195.

RADFARNIA, H. R. & ILIUTA, M. C. 2014. Development of Al-stabilized CaO–nickel hybrid sorbent–catalyst for sorption-enhanced steam methane reforming. *Chemical Engineering Science,* 109**,** 212-219.

RAO, T. R. 1996. Kinetics of calcium carbonate decomposition. *Chemical Engineering & Technology,* 19**,** 373-377.

RAPAGNÀ, S., JAND, N., KIENNEMANN, A. & FOSCOLO, P. U. 2000. Steam-gasification of biomass in a fluidised-bed of olivine particles. *Biomass and Bioenergy,* 19**,** 187-197.

REDDY, E. P. & SMIRNIOTIS, P. G. 2004. High-Temperature Sorbents for CO_2 Made of Alkali Metals Doped on CaO Supports. *The Journal of Physical Chemistry B,* 108**,** 7794-7800.

REIJERS, H. T. J., VALSTER-SCHIERMEIER, S. E. A., COBDEN, P. D. & VAN DEN BRINK, R. W. 2006. Hydrotalcite as CO_2 Sorbent for Sorption-Enhanced Steam Reforming of Methane. *Industrial & Engineering Chemistry Research,* 45**,** 2522-2530.

REITZ, M., JUNK, M., STRÖHLE, J. & EPPLE, B. 2016. Design and operation of a 300 kWth indirectly heated carbonate looping pilot plant. *International Journal of Greenhouse Gas Control,* 54**,** 272-281.

REMY, C., ANDRAULT, D. & MADON, M. 1997. High-Temperature, High-Pressure X-ray Investigation of Dicalcium Silicate. *Journal of the American Ceramic Society,* 80**,** 851-860.

REMY, C., GUYOT, F. & MADON, M. 1995. High pressure polymorphism of dicalcium silicate Ca_2SiO_4. A transmission electron microscopy study. *Physics and Chemistry of Minerals,* 22**,** 419-427.

RICHARDSON, J. T. & CRUMP, J. G. 1979. Crystallite size distributions of sintered nickel catalysts. *Journal of Catalysis,* 57**,** 417-425.

RICHARDSON, J. T. & PROPP, J. L. 1986. Pore size effects on sintering of $NiAl_2O_3$ catalysts. *Journal of Catalysis,* 98**,** 457-467.

RICHARDSON, Y., BLIN, J. & JULBE, A. 2012. A short overview on purification and conditioning of syngas produced by biomass gasification: Catalytic strategies, process intensification and new concepts. *Progress in Energy and Combustion Science,* 38**,** 765-781.

ROCHELLE, G. T. 2009. Amine Scrubbing for CO_2 Capture. *Science - American Association for the Advancement of Science,* 325**,** 1652-1653.
ROGERS, G. F. C. & MAYHEW, Y. R. 1995. *Thermodynamic and Transport Properties of Fluids*, Wiley.
ROUT, K. R., FERMOSO, J., CHEN, D. & JAKOBSEN, H. A. 2014. Kinetic rate of uptake of a synthetic Ca-based sorbent: Experimental data and numerical simulations. *Fuel,* 120**,** 53-65.
ROUT, K. R. & JAKOBSEN, H. A. 2012. Reactor performance optimization by the use of a novel combined pellet reflecting both catalyst and adsorbent properties. *Fuel Processing Technology,* 99**,** 13-34.
ROUT, K. R. & JAKOBSEN, H. A. 2013. A numerical study of pellets having both catalytic- and capture properties for SE-SMR process: Kinetic- and product layer diffusion controlled regimes. *Fuel Processing Technology,* 106**,** 231-246.
ROUT, K. R., SOLSVIK, J., NAYAK, A. K. & JAKOBSEN, H. A. 2011. A numerical study of multicomponent mass diffusion and convection in porous pellets for the sorption-enhanced steam methane reforming and desorption processes. *Chemical Engineering Science,* 66**,** 4111-4126.
RUCKENSTEIN, E. & PULVERMACHER, B. 1975. Effect of the pore size on the aging of supported metals. *Journal of Catalysis,* 37**,** 416-423.
S G ADIYA, Z. I., DUPONT, V. & MAHMUD, T. 2017. Chemical equilibrium analysis of hydrogen production from shale gas using sorption enhanced chemical looping steam reforming. *Fuel Processing Technology,* 159**,** 128-144.
SADLER, D. 2016. Leeds city gate, h21. Leeds, UK.
SALVADOR, C., LU, D., ANTHONY, E. J. & ABANADES, J. C. 2003. Enhancement of CaO for CO_2 capture in an FBC environment. *Chemical Engineering Journal,* 96**,** 187-195.
SAMANTA, A., ZHAO, A., SHIMIZU, G. K. H., SARKAR, P. & GUPTA, R. 2012. Post-Combustion CO_2 Capture Using Solid Sorbents: A Review. *Industrial & Engineering Chemistry Research,* 51**,** 1438-1463.
SATRIO, J. A., SHANKS, B. H. & WHEELOCK, T. D. 2005. Development of a Novel Combined Catalyst and Sorbent for Hydrocarbon Reforming. *Industrial & Engineering Chemistry Research,* 44**,** 3901-3911.
SATRIO, J. A., SHANKS, B. H. & WHEELOCK, T. D. 2007. A Combined Catalyst and Sorbent for Enhancing Hydrogen Production from Coal or Biomass. *Energy & Fuels,* 21**,** 322-326.
SATTERFIELD, C. N. 1970. *Mass transfer in heterogeneous catalysis*, M.I.T. Press.
SCEATS, M. 2017. Process and Apparatus for Manufacture of Portland Cement. Google Patents.
SCEATS, M. G. & HORLEY, C. J. 2014. System and method for the calcination of minerals. Google Patents.
SEHESTED, J. 2006. Four challenges for nickel steam-reforming catalysts. *Catalysis Today,* 111**,** 103-110.
SEHESTED, J., CARLSSON, A., JANSSENS, T. V. W., HANSEN, P. L. & DATYE, A. K. 2001. Sintering of Nickel Steam-Reforming Catalysts on $MgAl_2O_4$ Spinel Supports. *Journal of Catalysis,* 197**,** 200-209.
SEHESTED, J., GELTEN, J. A. P., REMEDIAKIS, I. N., BENGAARD, H. & NØRSKOV, J. K. 2004. Sintering of nickel steam-reforming catalysts: effects of temperature and steam and hydrogen pressures. *Journal of Catalysis,* 223**,** 432-443.
SHENG, C. & AZEVEDO, J. L. T. 2005. Estimating the higher heating value of biomass fuels from basic analysis data. *Biomass and Bioenergy,* 28**,** 499-507.
SHIMIZU, T., HIRAMA, T., HOSODA, H., KITANO, K., INAGAKI, M. & TEJIMA, K. 1999. A Twin Fluid-Bed Reactor for Removal of CO2 from Combustion Processes. *Chemical Engineering Research and Design,* 77**,** 62-68.
SIKARWAR, V. S., ZHAO, M., CLOUGH, P., YAO, J., ZHONG, X., MEMON, M. Z., SHAH, N., ANTHONY, E. J. & FENNELL, P. S. 2016. An overview of advances in biomass gasification. *Energy & Environmental Science,* 9**,** 2939-2977.
SILCOX, G. D., KRAMLICH, J. C. & PERSHING, D. W. 1989. A mathematical model for the flash calcination of dispersed calcium carbonate and calcium hydroxide particles. *Industrial & Engineering Chemistry Research,* 28**,** 155-160.

SINNOTT, R. K. 2005. Coulson and Richardson's Chemical Engineering Volume 6 - Chemical Engineering Design (4th Edition). Elsevier.
SISINNI, M., DI CARLO, A., BOCCI, E., MICANGELI, A. & NASO, V. 2013. Hydrogen-Rich Gas Production by Sorption Enhanced Steam Reforming of Woodgas Containing TAR over a Commercial Ni Catalyst and Calcined Dolomite as CO_2 Sorbent. *Energies,* 6.
SOLSVIK, J. & JAKOBSEN, H. A. 2011. A numerical study of a two property catalyst/sorbent pellet design for the sorption-enhanced steam–methane reforming process: Modeling complexity and parameter sensitivity study. *Chemical Engineering Journal,* 178**,** 407-422.
SONG, H., SHAH, K., DOROODCHI, E., WALL, T. & MOGHTADERI, B. 2014. Reactivity of Al_2O_3- or SiO_2-Supported Cu-, Mn-, and Co-Based Oxygen Carriers for Chemical Looping Air Separation. *Energy & Fuels,* 28**,** 1284-1294.
SONG, Y., WANG, Y., HU, X., XIANG, J., HU, S., MOURANT, D., LI, T., WU, L. & LI, C.-Z. 2015. Effects of volatile–char interactions on in-situ destruction of nascent tar during the pyrolysis and gasification of biomass. Part II. Roles of steam. *Fuel,* 143**,** 555-562.
SPECIALMETALSCORPORATION 2004. Typical rupture strength of INCOLOY alloys 800H and 800HT. *In:* 800HT®, I. A. H. A. (ed.) SMC - 047 ed.
SPEIGHT, J. G. 2005. *Handbook of Coal Analysis*, Wiley.
STANMORE, B. R. & GILOT, P. 2005. Review—calcination and carbonation of limestone during thermal cycling for CO_2 sequestration. *Fuel Processing Technology,* 86**,** 1707-1743.
STENDARDO, S., ANDERSEN, L. K. & HERCE, C. 2013. Self-activation and effect of regeneration conditions in CO_2–carbonate looping with CaO–$Ca_{12}Al_{14}O_{33}$ sorbent. *Chemical Engineering Journal,* 220**,** 383-394.
STRÖHLE, J., JUNK, M., KREMER, J., GALLOY, A. & EPPLE, B. 2014. Carbonate looping experiments in a 1 MWth pilot plant and model validation. *Fuel,* 127**,** 13-22.
SUN, J., LIU, W., WANG, W., HU, Y., YANG, X., CHEN, H., PENG, Y. & XU, M. 2016. CO_2 Sorption Enhancement of Extruded-Spheronized CaO-Based Pellets by Sacrificial Biomass Templating Technique. *Energy & Fuels,* 30**,** 9605-9612.
SUN, P., GRACE, J. R., LIM, C. J. & ANTHONY, E. J. 2008a. Determination of intrinsic rate constants of the CaO–CO_2 reaction. *Chemical Engineering Science,* 63**,** 47-56.
SUN, P., GRACE, J. R., LIM, C. J. & ANTHONY, E. J. 2008b. Investigation of Attempts to Improve Cyclic CO_2 Capture by Sorbent Hydration and Modification. *Industrial & Engineering Chemistry Research,* 47**,** 2024-2032.
SUN, P., LIM, C. J. & GRACE, J. R. 2008c. Cyclic CO_2 capture by limestone-derived sorbent during prolonged calcination/carbonation cycling. *AIChE Journal,* 54**,** 1668-1677.
SUN, Z., XU, C., CHEN, S. & XIANG, W. Improvements of CaO-based sorbents for cyclic CO_2 capture using a wet mixing process. *Chemical Engineering Journal*.
SWAAN, H. M., KROLL, V. C. H., MARTIN, G. A. & MIRODATOS, C. 1994. Deactivation of supported nickel catalysts during the reforming of methane by carbon dioxide. *Catalysis Today,* 21**,** 571-578.
TAMHANKAR, S. S., TSUCHIYA, K. & RIGGS, J. B. 1985. Catalytic cracking of benzene on iron oxide-silica: catalyst activity and reaction mechanism. *Applied Catalysis,* 16**,** 103-121.
TANKSALE, A., BELTRAMINI, J. N. & LU, G. M. 2010. A review of catalytic hydrogen production processes from biomass. *Renewable and Sustainable Energy Reviews,* 14**,** 166-182.
TAYLOR, H. F. W. 1997. *Cement Chemistry*, Thomas Telford.
TEIXEIRA, P., LOPES, H., GULYURTLU, I., LAPA, N. & ABELHA, P. 2012. Evaluation of slagging and fouling tendency during biomass co-firing with coal in a fluidized bed. *Biomass and Bioenergy,* 39**,** 192-203.
THANGALAZHY-GOPAKUMAR, S., ADHIKARI, S., GUPTA, R. B., TU, M. & TAYLOR, S. 2011. Production of hydrocarbon fuels from biomass using catalytic pyrolysis under helium and hydrogen environments. *Bioresource Technology,* 102**,** 6742-6749.
TILLMAN, D. A. 2000. Biomass cofiring: the technology, the experience, the combustion consequences. *Biomass and Bioenergy,* 19**,** 365-384.
TINGYU, Z., SHOUYU, Z., JIEJIE, H. & YANG, W. 2000. Effect of calcium oxide on pyrolysis of coal in a fluidized bed. *Fuel Processing Technology,* 64**,** 271-284.

TOBY, B. H. & VON DREELE, R. B. 2013. GSAS-II: the genesis of a modern open-source all purpose crystallography software package. *Journal of Applied Crystallography,* 46**,** 544-549.
TOMISHIGE, K., CHEN, Y.-G. & FUJIMOTO, K. 1999. Studies on Carbon Deposition in CO_2 Reforming of CH_4 over Nickel–Magnesia Solid Solution Catalysts. *Journal of Catalysis,* 181**,** 91-103.
TRIMM, D. L. 1997. Coke formation and minimisation during steam reforming reactions. *Catalysis Today,* 37**,** 233-238.
UDOMSIRICHAKORN, J., BASU, P., SALAM, P. A. & ACHARYA, B. 2013. Effect of CaO on tar reforming to hydrogen-enriched gas with in-process CO_2 capture in a bubbling fluidized bed biomass steam gasifier. *International Journal of Hydrogen Energy,* 38**,** 14495-14504.
UDOMSIRICHAKORN, J. & SALAM, P. A. 2014. Review of hydrogen-enriched gas production from steam gasification of biomass: The prospect of CaO-based chemical looping gasification. *Renewable and Sustainable Energy Reviews,* 30**,** 565-579.
URASAKI, K., TANIMOTO, N., HAYASHI, T., SEKINE, Y., KIKUCHI, E. & MATSUKATA, M. 2005. Hydrogen production via steam–iron reaction using iron oxide modified with very small amounts of palladium and zirconia. *Applied Catalysis A: General,* 288**,** 143-148.
VAN LEEUWEN, M. E. 1994. Derivation of Stockmayer potential parameters for polar fluids. *Fluid Phase Equilibria,* 99**,** 1-18.
VAN LOO, S. & KOPPEJAN, J. 2008. *The Handbook of Biomass Combustion and Co-firing*, Earthscan.
VINCENT, A., RENNIE, D., SCEATS, M., GILL, M. & THOMSEN, S. 2016. PUBLIC LEILAC PRE-FEED SUMMARY REPORT, Project Leilac, Low Emission Intensity Lime and Cement project.
VORRIAS, I., ATSONIOS, K., NIKOLOPOULOS, A., NIKOLOPOULOS, N., GRAMMELIS, P. & KAKARAS, E. 2013. Calcium looping for CO_2 capture from a lignite fired power plant. *Fuel,* 113**,** 826-836.
WANG, C., DOU, B., JIANG, B., SONG, Y., DU, B., ZHANG, C., WANG, K., CHEN, H. & XU, Y. 2015. Sorption-enhanced steam reforming of glycerol on Ni-based multifunctional catalysts. *International Journal of Hydrogen Energy,* 40**,** 7037-7044.
WANG, C.-T. & SMITH, J. M. 1983. Tortuosity factors for diffusion in catalyst pellets. *AIChE Journal,* 29**,** 132-136.
WANG, J., ANTHONY, E. J. & ABANADES, J. C. 2004. Clean and efficient use of petroleum coke for combustion and power generation. *Fuel,* 83**,** 1341-1348.
WANG, K., ZHAO, P., GUO, X., HAN, D. & CHAO, Y. 2014a. High-temperature CO_2 capture cycles of hydrated limestone prepared with aluminum (hydr)oxides derived from kaolin. *Energy Conversion and Management,* 86**,** 1147-1153.
WANG, N., PERRET, N. & FOSTER, A. 2011. Sustainable hydrogen production for fuel cells by steam reforming of ethylene glycol: A consideration of reaction thermodynamics. *International Journal of Hydrogen Energy,* 36**,** 5932-5940.
WANG, Q., RONG, N., FAN, H., MENG, Y., FANG, M., CHENG, L. & CEN, K. 2014b. Enhanced hydrogen-rich gas production from steam gasification of coal in a pressurized fluidized bed with CaO as a CO_2 sorbent. *International Journal of Hydrogen Energy,* 39**,** 5781-5792.
WANG, Y., LIN, S. & SUZUKI, Y. 2007. Study of Limestone Calcination with CO_2 Capture: Decomposition Behavior in a CO_2 Atmosphere. *Energy & Fuels,* 21**,** 3317-3321.
WANG, Y., LIN, S. & SUZUKI, Y. 2008. Limestone Calcination with CO_2 Capture (II): Decomposition in CO_2/Steam and CO_2/N_2 Atmospheres. *Energy & Fuels,* 22**,** 2326-2331.
WANG, Y. & THOMSON, W. J. 1995. The effects of steam and carbon dioxide on calcite decomposition using dynamic X-ray diffraction. *Chemical Engineering Science,* 50**,** 1373-1382.
WEI, L., XU, S., LIU, J., LIU, C. & LIU, S. 2008. Hydrogen Production in Steam Gasification of Biomass with CaO as a CO_2 Absorbent. *Energy & Fuels,* 22**,** 1997-2004.
WEN, C. & YU, Y. H. Mechanics of fluidization. Chem. Eng. Prog., Symp. Ser., 1966. 100-111.
WIDYAWATI, M., CHURCH, T. L., FLORIN, N. H. & HARRIS, A. T. 2011. Hydrogen synthesis from biomass pyrolysis with in situ carbon dioxide capture using calcium oxide. *International Journal of Hydrogen Energy,* 36**,** 4800-4813.

WILKE, C. R. 1950. A Viscosity Equation for Gas Mixtures. *The Journal of Chemical Physics,* 18**,** 517-519.
WOJCIECHOWSKI, B. & RICE, N. 2003. *Experimental Methods in Kinetic Studies*, Elsevier Science.
WU, G., ZHANG, C., LI, S., HUANG, Z., YAN, S., WANG, S., MA, X. & GONG, J. 2012. Sorption enhanced steam reforming of ethanol on Ni-CaO-Al_2O_3 multifunctional catalysts derived from hydrotalcite-like compounds. *Energy & Environmental Science,* 5**,** 8942-8949.
WU, Y., BLAMEY, J., ANTHONY, E. J. & FENNELL, P. S. 2010. Morphological Changes of Limestone Sorbent Particles during Carbonation/Calcination Looping Cycles in a Thermogravimetric Analyzer (TGA) and Reactivation with Steam. *Energy & Fuels,* 24**,** 2768-2776.
WU, Y. J., LI, P., YU, J. G., CUNHA, A. F. & RODRIGUES, A. E. 2013. Sorption-enhanced steam reforming of ethanol on NiMgAl multifunctional materials: Experimental and numerical investigation. *Chemical Engineering Journal,* 231**,** 36-48.
XIAO, Q., TANG, X., LIU, Y., ZHONG, Y. & ZHU, W. 2011. Citrate route to prepare K-doped Li_2ZrO_3 sorbents with excellent CO2 capture properties. *Chemical Engineering Journal,* 174**,** 231-235.
XIAO, Y., XU, S., SONG, Y., SHAN, Y., WANG, C. & WANG, G. 2017. Biomass steam gasification for hydrogen-rich gas production in a decoupled dual loop gasification system. *Fuel Processing Technology,* 165**,** 54-61.
XIE, M., ZHOU, Z., QI, Y., CHENG, Z. & YUAN, W. 2012a. Sorption-enhanced steam methane reforming by in situ CO_2 capture on a CaO–$Ca_9Al_6O_{18}$ sorbent. *Chemical Engineering Journal,* 207–208**,** 142-150.
XIE, M., ZHOU, Z., QI, Y., CHENG, Z. & YUAN, W. 2012b. Sorption-enhanced steam methane reforming by in situ CO_2 capture on a CaO–$Ca_9Al_6O_{18}$ sorbent. *Chemical Engineering Journal,* 207–208**,** 142-150.
XIE, Y. R., SHEN, L. H., XIAO, J., XIE, D. X. & ZHU, J. 2009. Influences of Additives on Steam Gasification of Biomass. 1. Pyrolysis Procedure. *Energy & Fuels,* 23**,** 5199-5205.
XU, J. & FROMENT, G. F. 1989a. Methane steam reforming, methanation and water-gas shift: I. Intrinsic kinetics. *AIChE Journal,* 35**,** 88-96.
XU, J. & FROMENT, G. F. 1989b. Methane steam reforming: II. Diffusional limitations and reactor simulation. *AIChE Journal,* 35**,** 97-103.
XU, J., YEUNG, C. M. Y., NI, J., MEUNIER, F., ACERBI, N., FOWLES, M. & TSANG, S. C. 2008. Methane steam reforming for hydrogen production using low water-ratios without carbon formation over ceria coated Ni catalysts. *Applied Catalysis A: General,* 345**,** 119-127.
YAN, F., LUO, S.-Y., HU, Z.-Q., XIAO, B. & CHENG, G. 2010. Hydrogen-rich gas production by steam gasification of char from biomass fast pyrolysis in a fixed-bed reactor: Influence of temperature and steam on hydrogen yield and syngas composition. *Bioresource Technology,* 101**,** 5633-5637.
YANG, G., YU, H., PENG, F., WANG, H., YANG, J. & XIE, D. 2011. Thermodynamic analysis of hydrogen generation via oxidative steam reforming of glycerol. *Renewable Energy,* 36**,** 2120-2127.
YANG, H., YAN, R., CHEN, H., LEE, D. H. & ZHENG, C. 2007. Characteristics of hemicellulose, cellulose and lignin pyrolysis. *Fuel,* 86**,** 1781-1788.
YIN, J., KANG, X., QIN, C., FENG, B., VEERARAGAVAN, A. & SAULOV, D. 2014. Modeling of CaCO3 decomposition under CO_2/H_2O atmosphere in calcium looping processes. *Fuel Processing Technology,* 125**,** 125-138.
YONGBIN, J., JIEJIE, H. & YANG, W. 2004. Effects of Calcium Oxide on the Cracking of Coal Tar in the Freeboard of a Fluidized Bed. *Energy & Fuels,* 18**,** 1625-1632.
YU, Q. Z., BRAGE, C., NORDGREEN, T. & SJÖSTRÖM, K. 2009. Effects of Chinese dolomites on tar cracking in gasification of birch. *Fuel,* 88**,** 1922-1926.
YU, Y. S., LIU, W. Q., AN, H., YANG, F. S., WANG, G. X., FENG, B., ZHANG, Z. X. & RUDOLPH, V. 2012. Modeling of the carbonation behavior of a calcium based sorbent for CO_2 capture. *International Journal of Greenhouse Gas Control,* 10**,** 510-519.

ZAMBONI, I., COURSON, C., NIZNANSKY, D. & KIENNEMANN, A. 2014. Simultaneous catalytic H2 production and CO_2 capture in steam reforming of toluene as tar model compound from biomass gasification. *Applied Catalysis B: Environmental,* 145**,** 63-72.

ZHANG, J., SCHNEIDER, A. & INDEN, G. 2003. Characterisation of the coke formed during metal dusting of iron in CO–H_2–H_2O gas mixtures. *Corrosion Science,* 45**,** 1329-1341.

ZHANG, M., PENG, Y., SUN, Y., LI, P. & YU, J. 2013. Preparation of CaO–Al_2O_3 sorbent and CO_2 capture performance at high temperature. *Fuel,* 111**,** 636-642.

ZHANG, Z., HILLS, T. P., SCOTT, S. A. & FENNELL, P. S. 2016. Spouted bed reactor for kinetic measurements of reduction of Fe_2O_3 in a CO_2/CO atmosphere Part I: Atmospheric pressure measurements and equipment commissioning. *Chemical Engineering Research and Design,* 114**,** 307-320.

ZHAO, C., ZHOU, Z., CHENG, Z. & FANG, X. 2016. Sol-gel-derived, $CaZrO_3$-stabilized Ni/CaO-$CaZrO_3$ bifunctional catalyst for sorption-enhanced steam methane reforming. *Applied Catalysis B: Environmental,* 196**,** 16-26.

ZHAO, M., SHI, J., ZHONG, X., TIAN, S., BLAMEY, J., JIANG, J. & FENNELL, P. S. 2014. A novel calcium looping absorbent incorporated with polymorphic spacers for hydrogen production and CO2 capture. *Energy & Environmental Science,* 7**,** 3291-3295.

ZHAO, M., YANG, X., CHURCH, T. L. & HARRIS, A. T. 2012. Novel CaO–SiO_2 Sorbent and Bifunctional Ni/Co–CaO/SiO_2 Complex for Selective H2 Synthesis from Cellulose. *Environmental Science & Technology,* 46**,** 2976-2983.

ZHOU, Z., XU, P., XIE, M., CHENG, Z. & YUAN, W. 2013. Modeling of the carbonation kinetics of a synthetic CaO-based sorbent. *Chemical Engineering Science,* 95**,** 283-290.

ÖHMAN, M., NORDIN, A., SKRIFVARS, B. J., BACKMAN, R. & HUPA, M. 2000. Bed agglomeration characteristics during fluidized bed combustion of biomass fuels. *Energy and Fuels,* 14**,** 169-178.

ŽIVKOVIĆ, L. A., POHAR, A., LIKOZAR, B. & NIKAČEVIĆ, N. M. 2016. Kinetics and reactor modeling for CaO sorption-enhanced high-temperature water–gas shift (SE–WGS) reaction for hydrogen production. *Applied Energy,* 178**,** 844-855.

Appendix I – Standard Operating Procedure

A typical experiment consisted of the following standard operating procedure:

- Turn on gas cylinders and set to the point of use regulators (supplied by FTI Ltd) to the desired pressure, assume 1 bar(g) N_2
- Set the flow rate on the rotameters to the desired value
- Turn the three way valve to bypass the steam generation system
- Load the Agilent VEE program and start the program running by creating a save file
- Turn the furnace on and set to the desired set point, assume 650 °C
- After ~10 minutes of N_2 flow zero the analysers
- Turn the heating control boxes on, except the steam generator control box
- Weigh out the required bed materials, assume 25 g sand + 10 g CaO + 5 g NiO particles. Sand is added for thermal stability of the bed
- When the bed temperature has reached ~600 °C undo the bed temperature thermocouple fitting and remove the thermocouple
- Insert the bed material feeding tube and slowly add the bed material to the reactor
- Once fully added, replace the thermocouple and tighten fitting back up
- Turn on the propane gas to the Bunsen burner flare stack and ignite with a safety lighter, ensure a blue flame is present then close the flare stack window to the marked position
- Add plenty of ice and enough water to fully cover the pump to the pump bucket, then turn the pump on and wait 5 minutes for the tar and water trap to cool down
- When the bed temperature has recovered and stabilised at 650 °C reduce the N_2 flow rate and turn on the 10% H_2 in N_2 to produce a 5% H_2 mixture
- Start the timer and monitor the hydrogen concentration for 30 minutes
- After 30 minutes, turn off the 10% H_2 gas cylinder and wait for all the pressure and flow rate to fall. As the flow rate falls, increase the N_2 flow rate back up to the desired value
- Turn on the steam generation heating control box and set to the desired value to generate the correct amount of steam

- Turn the HPLC pump to the desired value and turn the three way valve to the steam generation system
- If the RH% is lower than expected then the water level in the bubbler may be low so temporarily increase the flow rate from the HPLC. Watch the RH% response on the control program as the RH% will increase as the water level rises. The calibrated predicted value is also displayed on the steam plot, decrease the flow rate from the HPLC pump when they first become equal
- Whilst waiting for steam concentration stability check the amount of biomass in the hopper and monitor the reactor
- Periodically top up the cooling ice and empty water from the water trap
- Once all parameters are stable and at their correct values, turn on MFC bio-knocker flow (assuming it's connected to an air supply) and the biomass feeder and start the timer
- Ensure the hopper is bashed and knocked from many different angles continuously whilst feeding
- Once the allotted time has occurred stop the timer, turn off the motor, shut off the flow from the bio-knocker MFC and turn the three way valve to divert gas away from the steam generator
- Ramp the temperature up to 750 °C to calcine the produce $CaCO_3$ in the bed
- Turn off steam generation heating control boxes
- Once it has become clear from the gas analyser readings that the calcination has completed, turn on an air supply of known quantity and wait for the combustion to complete. Again this is observable on the control program
- Once combustion is complete turn off air supply and leave N_2 purging the system
- Turn off the control program, all heating sources, the water cooling pump and flare stack
- Wait for reactor to cool then take apart all elements after the reactor, clean, replace glass wool if necessary and then put the reactor back together
- Empty the bed material from the bottom of the reactor by removing the U-bend. Blow out any remaining bed materials with a compressed air supply
- Replace U-bend

Appendix II – Derivation of the Langmuir Hinshelwood Rate Equations and the Influence of CO_2 Partial Pressure on the Rate of Limestone Calcination

The influence of CO_2 partial pressure on the rate of reaction was determined by the application of Equation II.1. Previous literature has consistently utilised the equilibrium driving force ($P^*_{CO_2}$ - P_{CO_2}) for determining the influence of CO_2 on the rate of calcination, as shown in the literature review by Stanmore and Gilot (Stanmore and Gilot, 2005). Therefore initially following the approach of previous literature, the order of reactions with respect to the equilibrium driving force ($P^*_{CO_2}$ - P_{CO_2}) for the reversible calcination reactions were determined and the results of which are shown in Figure II.1 for both the steam and N_2 systems.

Equation II.1:

$$r_c = k\left(P^*_{CO_2} - P_{CO_2}\right)^n$$

The orders shown in Figure II.1 indicate a near second order of reaction for the experiments conducted with steam, within the narrow range of concentrations (12 - 39 vol.% steam) assessed in this work. The order of reaction for the N_2 system, also displayed in Figure II.1, displayed a much higher order of approximately 4, although it must be stated the R^2 value was only 0.86 for this data set. The steam experimental data was collected over a narrower range due to the limitations of a bubbler steam generating system.

The observed peak rates and general rate profiles in shown in Figure 4.11a (N_2 system) drop off rapidly at higher CO_2 concentrations and this can also be seen in Figure II.1. This suggests that at low concentrations of N_2 and hence high concentrations of CO_2 the reactions were limited by something other than the equilibrium position of the system, this resulted in the observed differences in rates and thus the orders of reaction.

Due to the significantly different orders of reaction obtained between the two systems, it is possible to state that for the observed calcination reactions, the presence of gases other than CO_2 can significantly affect the rate of reaction. Furthermore the addition of steam to the calcination gas flow utilised a different reaction mechanism compared to the N_2 system. Utilising these newly determined reaction orders the values of the pre-exponential factors and activation energies were recalculated are displayed in Table II.1.

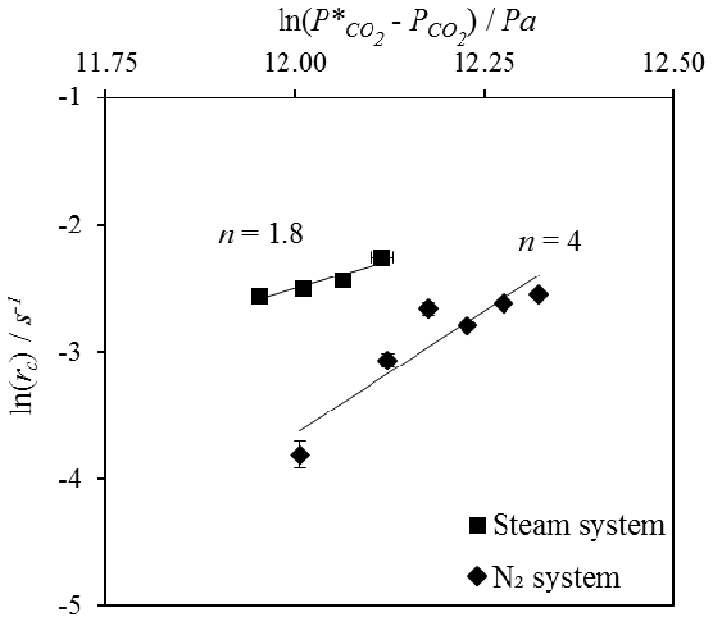

Figure II.1 – Influence of equilibrium driving force ($P^*_{CO_2} - P_{CO_2}$) on the rate of calcination. *n* represents the apparent order of reaction. Kinetic experiments conducted at 950 °C, 1 bar(a).

Table II.1 – Recalculated Arrhenius parameters for the observed kinetics of limestone calcination in 80 vol.% CO_2 and either 20 vol.% steam or N_2 utilising the orders of reaction determined in Figure II.1 with respect to the equilibrium driving force ($P^*_{CO_2} - P_{CO_2}$).

	Steam system wrt. ($C^*_{CO_2} - C_{CO_2}$)^2		**N_2 system wrt. ($C^*_{CO_2} - C_{CO_2}$)^4**	
	$k_{0\,obs}$ (m^3/mol.s)	E_a (kJ/mol)	$k_{0\,obs}$ (mol^{-11}/m^9.s)	E_a (kJ/mol)
Arrhenius parameters using observed orders	7.3×10^{-7}	-162.24	1.0×10^{-22}	-467.01

The Arrhenius parameters determined when utilising this order of reaction were obviously nonsensical and not physically representative. A negative activation energy was determined for both the steam and N_2 systems evidently showing the that although the kinetic data may have presented an order greater than 1 when altering the partial pressure of CO_2, the physical reality of the systems cannot be represented by such a simple rate law fitting. The reason that these recalculated Arrhenius parameters were found to be strange was because the driving force ($P^*_{CO_2}$ - P_{CO_2}) changed by a larger degree than the rate of reaction did, therefore applying an order greater than 1 exacerbated this effect.

By removing the influence of the equilibrium partial pressure of CO_2 on the rate of reaction and instead determining the order of reaction with respect to the bulk/surface partial pressure of CO_2 Figure II.2and the following respective orders were produced. It can be observed that the influence of P_{CO_2} on the rate of calcination with steam present was approximately 1st order, whereas a split order was found again for the N_2 system. This split order showed an approximately zeroth order at low partial pressures of CO_2 but increased rapidly to an observed near 2.5 order relationship at the highest partial pressures of CO_2. A straight line fit through the N_2 data is also given and shows a near first order relationship but the fit had an R^2 value of ~0.65.

When applying a first order relationship with respect to the bulk partial pressure of CO_2 (P_{CO_2}) to both the steam and N_2 data sets and recalculating the Arrhenius parameters, which are shown in Table II.2, the activation energies generated were much higher than that previously found in the literature but were at least physically possible.

These results highlight that the experimental kinetic data for the N_2 system in particular was difficult to represent via simple rate law fitting; a difficulty which was only exaggerated over the broad range of CO_2 partial pressures utilised. It has been concluded that there were other phenomena at play that were not accounted for within this rate equation. To further investigate the mechanism of the calcination reaction in the presence of the steam and N_2 a rate equation derived by the Langmuir-Hinshelwood method was developed for both the steam and N_2 systems applying the Arrhenius parameters derived utilising an assumed first order of reaction with respect to the bulk partial pressure of CO_2 (P_{CO_2}).

Table II.2 – Recalculated Arrhenius parameters for the observed kinetics of limestone calcination in 80 vol.% CO_2 and either 20 vol.% steam or N_2 utilising a first order of reaction with respect to the bulk partial pressure of CO_2 (P_{CO_2}).

	Steam system wrt. (C_{CO_2})[1]		**N_2 system wrt. (C_{CO_2})[1]**	
	$k_{0\,obs}$ (s^{-1})	E_a (kJ/mol)	$k_{0\,obs}$ (s^{-1})	E_a (kJ/mol)
Observed order Arrhenius parameters	2.15×10^{16}	326.29	2.8×10^{23}	504.11

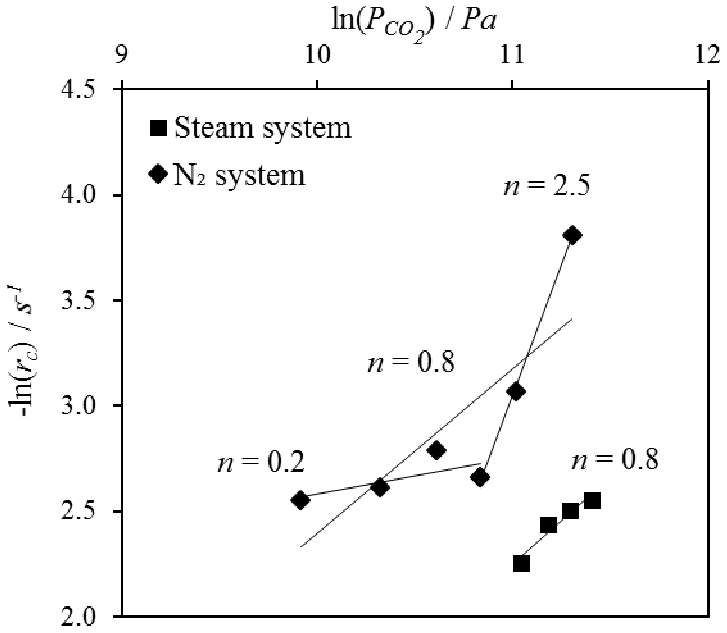

Figure II.2 – Influence of CO_2 partial pressure on the rate of calcination for the steam and N_2 systems. Kinetic calcination experiments conducted at 950 °C, 1 bar(a).

The Langmuir-Hinshelwood approach is based on the work of Hinshelwood applying the principles described by Langmuir. For the CO_2 and N_2 system the following set of equations were considered.

Equation II.2:

$$CaCO_3 \rightleftharpoons CaO + CO_2$$

Equation II.3:

$$CaCO_3 + N_2 \rightleftharpoons CaO + CO_2 + N_2$$

Assuming that all $CaCO_3$ sites are "active sites" – i.e. there is no rate limiting step of their formation – where $CaCO_3$ active sites are in the form of $CaO{\cdot}CO_2$ and that N_2 does not adsorb onto the surface of CaO or $CaCO_3$. Also making the assumption that each species adsorbed onto the surface of the CaO is a reactive intermediate and therefore the net rate of formation of species *i* adsorbed onto the surface will be zero, i.e. applying the pseudo-steady-state hypothesis defined by Equation II.4.

Equation II.4:

$$r_{i\cdot s}^{*} = 0$$

Define the rate limiting step to be: (For the purposes for typing limitations in MS word, $\rightleftharpoons$ will be written as $\rightarrow\leftarrow$)

$$CaCO_3 \underset{k_{1r}}{\overset{k_{1f}}{\rightarrow\leftarrow}} CaO + CO_2$$

Where the equilibrium constant for the reaction is defined as Equation II.5 - $K_1 = \frac{k_{1r}}{k_{1f}}$

Where *f* and *r* represent the forwards and reverse reactions respectively.

Equation II.6 - The overall rate law for the calcination reaction was defined as:

$$-r_{calc} = k_{1f} C_{CaCO_3}$$

Equation II.7 - The net rate of $CaCO_3$ sites generated was defined as:

$$r_{CaCO_3}^{*} = 0 = k_{1r} C_{CaO} P_{CO_2} - k_{1f} C_{CaCO_3}$$

Equation II.8 - Rearranging for the concentrations of sites occupied by $CaCO_3$:

$$C_{CaCO_3} = K_1 C_{CaO} P_{CO_2}$$

Equation II.9 - From the site balance we obtain, where CaO sites are completely vacant:

$$C_t = C_{CaCO_3} + C_{CaO}$$

Equation II.10 - Substitute Equation II.8 into Equation II.9:

$$C_t = K_1 C_{CaO} P_{CO_2} + C_{CaO}$$

$$C_t = C_{CaO}\left(1 + K_1 P_{CO_2}\right)$$

$$C_{CaO} = \frac{C_t}{\left(1 + K_1 P_{CO_2}\right)}$$

Equation II.11 - Substitute Equation II.8 into Equation II.6:

$$-r_{calc} = k_{1f} K_1 C_{CaO} P_{CO_2} = k_{1r} C_{CaO} P_{CO_2}$$

Equation II.12 - Substitute Equation II.10 into Equation II.11:

$$-r_{calc} = k_{1r} C_t P_{CO_2} \cdot \frac{1}{\left(1 + K_1 P_{CO_2}\right)}$$

Equation II.13 - To finally form:

$$-r_{calc} = k_c \cdot \frac{P_{CO_2}}{\left(1 + K_1 P_{CO_2}\right)}$$

$$-r_{calc} = \frac{k_c S_A}{R_i T} \cdot \frac{P_{CO_2}}{\left(1 + K_1 P_{CO_2}\right)}$$

Where k_c is in units m/s, K_1 is in units Pa^{-1}, P_{CO2} is in units Pa, S_A is in units m^2/m^3, R_i is in units J/mol·K, T is in K and the r_{calc} is in units of $mol/m^3 \cdot s$.

The value of k_c was calculated using the values stated in Table II.2, assuming a first order relationship between the rate and partial pressure of CO_2, as shown in Figure II.2. A fitting of r_{calc} (in $mol/m^3.s$)

against $((k_c S_A)/(R_i T))(P_{CO_2}/(1+K_1 P_{CO_2}))$ was produced utilising '*fminsearch*' – Matlabs unconstrained multivariable function – to fit this model to the experimental data by minimising the sum of square errors, the result of which is shown as Figure II.3. To implement fitting the maximum number of function evaluations and iterations was set to 10^7 and the tolerances were set to 10^{-9} and an initial guess value of 1 was selected (although others were tried as well) for K_1. Solving for the value of K_1 a final estimate of 0.88 Pa^{-1} was arrived at. The fit of the line was less than satisfactory at all initial guess values implying that the selected mechanism for the Langmuir-Hinshelwood derivation was not appropriate. Another mechanist route was not investigated because it was not thought that N_2 could adsorb onto the surface of the CaO or $CaCO_3$ nor would multiple sites be involved for the calcination.

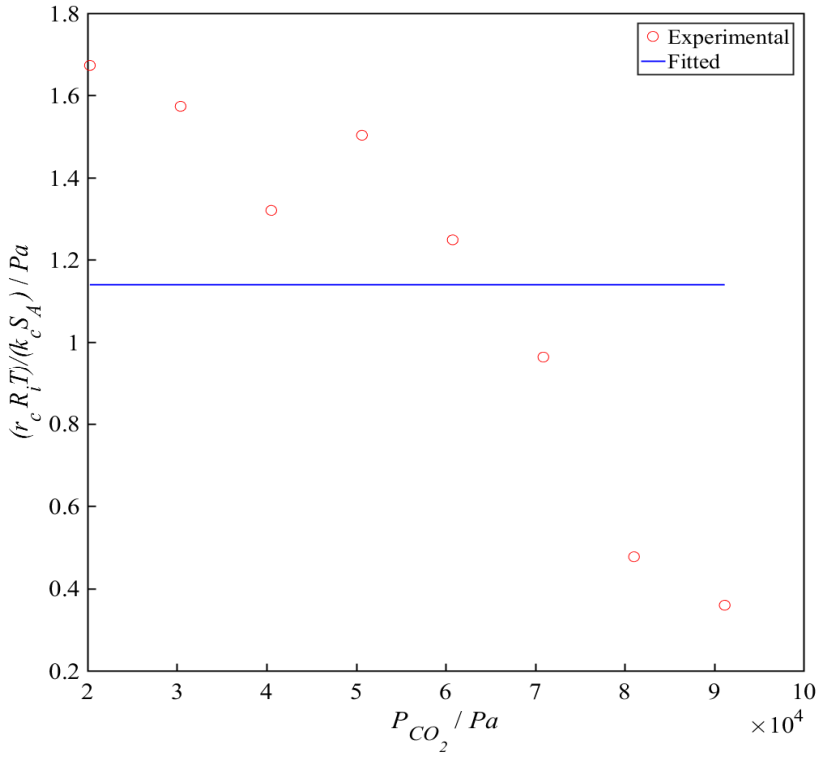

Figure II.3 – Fitting of Equation II.13 derived via the Langmuir-Hinshelwood approach for the experimental calcination data gathered by varying the CO_2 partial pressure in the presence of N_2.

A similar Langmuir-Hinshelwood approach was taken for the steam system calcinations as well, it was derived by the following methodology and considered these two main reactions:

$$CaCO_3 \rightleftharpoons CaO + CO_2$$

$$CacO_3 + H_2O \rightleftharpoons CaO + H_2O + CO_2$$

Assuming that all $CaCO_3$ sites are "active sites" – i.e. there is no rate limiting step of their formation – where $CaCO_3$ active sites are actually in the form of $CaO \cdot CO_2$ and that H_2O does adsorb onto the surface of the CaO active sites, but not the $CaCO_3$. Also making the assumption that each species adsorbed onto the surface of the CaO is a reactive intermediate and therefore the net rate of formation of species *i* adsorbed onto the surface will be zero, i.e. applying the pseudo-steady-state hypothesis defined by:

Equation II.14:

$$r_{i\cdot s}^{*} = 0$$

Define the rate limiting step to be the calcination reaction without steam present, (For the purposes for typing limitations in MS word, $\rightleftharpoons$ will be written as →←) Surface calcination reaction:

$$CaCO_3 \underset{k_{1r}}{\overset{k_{1f}}{\rightarrow\leftarrow}} CaO + CO_2$$

Where the equilibrium constant for the reaction is defined as Equation II.15: $K_1 = \frac{k_{1r}}{k_{1f}}$

Adsorption of H_2O onto the active sites:

$$CaCO_3 + H_2O \underset{k_{2r}}{\overset{k_{2f}}{\rightarrow\leftarrow}} CaCO_3 \cdot H_2O$$

Where the equilibrium constant for the reaction is defined as Equation II.16: $K_2 = \frac{k_{2f}}{k_{2r}}$

Desorption of CO_2 and H_2O from the active sites:

$$CaCO_3 \cdot H_2O \underset{k_{3r}}{\overset{k_{3f}}{\rightarrow\leftarrow}} CaO + H_2O + CO_2$$

Where the equilibrium constant for the reaction is defined as Equation II.17: $K_3 = \frac{k_{3r}}{k_{3f}}$

Where *f* and *r* represent the forwards and reverse reactions respectively.

Equation II.18 - The overall rate equation for the calcination was defined as:

$$-r_{calc} = -r_{CaCO_3} = k_{1f}C_{CaCO_3} - k_{1r}C_{CaO}P_{CO_2} + k_{3f}C_{CaCO_3\cdot H_2O} - k_{3r}C_{CaO}P_{CO_2}P_{H_2O}$$

$$-r_{calc} = -r_{CaCO_3} = k_{1f}\left(C_{CaCO_3} - K_1C_{CaO}P_{CO_2}\right) + k_{3f}\left(C_{CaCO_3\cdot H_2O} - K_3C_{CaO}P_{CO_2}P_{H_2O}\right)$$

Equation II.19 - The net rate of generation of $CaCO_3$ sites was defined as:

$$r^*_{CaCO_3} = 0 = k_{1r}C_{CaO}P_{CO_2} - k_{1f}C_{CaCO_3} + k_{2r}C_{CaCO_3\cdot H_2O} - k_{2f}C_{CaCO_3}P_{H_2O}$$

Equation II.20 - The net rate of generation of $CaCO_3$ and $CaCO_3{\cdot}H_2O$ sites was defined as:

$$r^*_{CaCO_3\cdot H_2O} = 0 = k_{2f}C_{CaCO_3}P_{H_2O} - k_{2r}C_{CaCO_3\cdot H_2O} + k_{3r}C_{CaO}P_{CO_2}P_{H_2O} - k_{3f}C_{CaCO_3\cdot H_2O}$$

Equation II.21 - Rearranging for the concentrations of sites occupied by $CaCO_3$:

$$C_{CaCO_3} = \frac{k_{1r}C_{CaO}P_{CO_2} + k_{2r}C_{CaCO_3\cdot H_2O}}{k_{1f} + k_{2f}P_{H_2O}}$$

Equation II.22 - Rearranging for the concentrations of sites occupied by $CaCO_3{\cdot}H_2O$:

$$C_{CaCO_3\cdot H_2O} = \frac{k_{2f}C_{CaCO_3}P_{H_2O} + k_{3r}C_{CaO}P_{CO_2}P_{H_2O}}{k_{2r} + k_{3f}}$$

Equation II.23 - From the site balance we obtain, where CaO sites are completely vacant:

$$C_t = C_{CaCO_3} + C_{CaO} + C_{CaCO_3\cdot H_2O}$$

Equation II.24 - Substitute Equation II.20 into Equation II.19:

$$C_{CaCO_3} = \frac{k_{1r}C_{CaO}P_{CO_2} + k_{2r}\left[\frac{k_{2f}C_{CaCO_3}P_{H_2O} + k_{3r}C_{CaO}P_{CO_2}P_{H_2O}}{k_{2r} + k_{3f}}\right]}{k_{1f} + k_{2f}P_{H_2O}}$$

$$k_{1f}C_{CaCO_3} + k_{2f}C_{CaCO_3}P_{H_2O} = k_{1r}C_{CaO}P_{CO_2} + k_{2r}\left[\frac{k_{2f}C_{CaCO_3}P_{H_2O} + k_{3r}C_{CaO}P_{CO_2}P_{H_2O}}{k_{2r} + k_{3f}}\right]$$

$$k_{1f}C_{CaCO_3} + k_{2f}C_{CaCO_3}P_{H_2O} = k_{1r}C_{CaO}P_{CO_2} + \frac{k_{2r}k_{2f}C_{CaCO_3}P_{H_2O} + k_{2r}k_{3r}C_{CaO}P_{CO_2}P_{H_2O}}{k_{2r} + k_{3f}}$$

$$k_{1f}k_{2r}C_{CaCO_3} + k_{2f}k_{2r}C_{CaCO_3}P_{H_2O} + k_{1f}k_{3f}C_{CaCO_3} + k_{2f}k_{3f}C_{CaCO_3}P_{H_2O} = k_{1r}k_{3f}C_{CaO}P_{CO_2} + k_{1r}k_{2r}C_{CaO}P_{CO_2} + k_{2r}k_{2f}C_{CaCO_3}P_{H_2O} + k_{2r}k_{3r}C_{CaO}P_{CO_2}P_{H_2O}$$

$$k_{1f}k_{2r}C_{CaCO_3} + \cancel{k_{2f}k_{2r}C_{CaCO_3}P_{H_2O}} + k_{1f}k_{3f}C_{CaCO_3} + k_{2f}k_{3f}C_{CaCO_3}P_{H_2O} = k_{1r}k_{3f}C_{CaO}P_{CO_2} + k_{1r}k_{2r}C_{CaO}P_{CO_2} + \cancel{k_{2r}k_{2f}C_{CaCO_3}P_{H_2O}} + k_{2r}k_{3r}C_{CaO}P_{CO_2}P_{H_2O}$$

Equation II.25 - Which can be rearranged to form:

$$C_{CaCO_3} = \frac{C_{CaO}P_{CO_2}\left(k_{1r}k_{3f} + k_{1r}k_{2r} + k_{2r}k_{3r}P_{H_2O}\right)}{\left(k_{1f}k_{2r} + k_{1f}k_{3f} + k_{2f}k_{3f}P_{H_2O}\right)}$$

Equation II.26 – Substitute Equation II.21 into Equation II.18:

$$-r_{calc} = k_{1f}\left(\frac{C_{CaO}P_{CO_2}\left(k_{1r}k_{3f} + k_{1r}k_{2r} + k_{2r}k_{3r}P_{H_2O}\right)}{\left(k_{1f}k_{2r} + k_{1f}k_{3f} + k_{2f}k_{3f}P_{H_2O}\right)} - K_1C_{CaO}P_{CO_2}\right) + k_{3f}\left(C_{CaCO_3\cdot H_2O} - K_3C_{CaO}P_{CO_2}P_{H_2O}\right)$$

Equation II.27 – Substitute Equation II.21 into Equation II.20:

$$C_{CaCO_3\cdot H_2O} = \frac{k_{2f}\dfrac{C_{CaO}P_{CO_2}\left(k_{1r}k_{3f} + k_{1r}k_{2r} + k_{2r}k_{3r}P_{H_2O}\right)}{\left(k_{1f}k_{2r} + k_{1f}k_{3f} + k_{2f}k_{3f}P_{H_2O}\right)}P_{H_2O} + k_{3r}C_{CaO}P_{CO_2}P_{H_2O}}{k_{2r} + k_{3f}}$$

$$C_{CaCO_3\cdot H_2O} = \left[\frac{k_{2f}}{\left(k_{2r} + k_{3f}\right)}\cdot\frac{\left(k_{1r}k_{3f} + k_{1r}k_{2r} + k_{2r}k_{3r}P_{H_2O}\right)}{\left(k_{1f}k_{2r} + k_{1f}k_{3f} + k_{2f}k_{3f}P_{H_2O}\right)} + \frac{k_{3r}}{\left(k_{2r} + k_{3f}\right)}\right]C_{CaO}P_{H_2O}P_{CO_2}$$

Equation II.28 - Substitute Equation II.24 into Equation II.23:

$$-r_{calc} = k_{1f}\left(\frac{C_{CaO}P_{CO_2}\left(k_{1r}k_{3f} + k_{1r}k_{2r} + k_{2r}k_{3r}P_{H_2O}\right)}{\left(k_{1f}k_{2r} + k_{1f}k_{3f} + k_{2f}k_{3f}P_{H_2O}\right)} - K_1 C_{CaO}P_{CO_2}\right) + k_{3f}\left(\left[\frac{k_{2f}}{\left(k_{2r}+k_{3f}\right)}\cdot\frac{\left(k_{1r}k_{3f} + k_{1r}k_{2r} + k_{2r}k_{3r}P_{H_2O}\right)}{\left(k_{1f}k_{2r} + k_{1f}k_{3f} + k_{2f}k_{3f}P_{H_2O}\right)} + \frac{k_{3r}}{\left(k_{2r}+k_{3f}\right)}\right]C_{CaO}P_{H_2O}P_{CO_2} - K_3 C_{CaO}P_{H_2O}P_{CO_2}\right)$$

$$-r_{calc} = k_{1f}C_{CaO}P_{CO_2}\left(\frac{\left(k_{1r}k_{3f} + k_{1r}k_{2r} + k_{2r}k_{3r}P_{H_2O}\right)}{\left(k_{1f}k_{2r} + k_{1f}k_{3f} + k_{2f}k_{3f}P_{H_2O}\right)} - K_1\right) + k_{3f}C_{CaO}P_{H_2O}P_{CO_2}\left(\frac{k_{2f}}{\left(k_{2r}+k_{3f}\right)}\cdot\frac{\left(k_{1r}k_{3f} + k_{1r}k_{2r} + k_{2r}k_{3r}P_{H_2O}\right)}{\left(k_{1f}k_{2r} + k_{1f}k_{3f} + k_{2f}k_{3f}P_{H_2O}\right)} + \frac{k_{3r}}{\left(k_{2r}+k_{3f}\right)} - K_3\right)$$

$$-r_{calc} = C_{CaO}P_{CO_2}\left[k_{1f}\left(\frac{\left(k_{1r}k_{3f} + k_{1r}k_{2r} + k_{2r}k_{3r}P_{H_2O}\right)}{\left(k_{1f}k_{2r} + k_{1f}k_{3f} + k_{2f}k_{3f}P_{H_2O}\right)} - K_1\right) + k_{3f}P_{H_2O}\left(\frac{k_{2f}}{\left(k_{2r}+k_{3f}\right)}\cdot\frac{\left(k_{1r}k_{3f} + k_{1r}k_{2r} + k_{2r}k_{3r}P_{H_2O}\right)}{\left(k_{1f}k_{2r} + k_{1f}k_{3f} + k_{2f}k_{3f}P_{H_2O}\right)} + \frac{k_{3r}}{\left(k_{2r}+k_{3f}\right)} - K_3\right)\right]$$

Equation II.29 - From the site balance, substitute Equation II.24 and Equation II.22 into Equation II.21:

$$C_t = \frac{C_{CaO}P_{CO_2}\left(k_{1r}k_{3f} + k_{1r}k_{2r} + k_{2r}k_{3r}P_{H_2O}\right)}{\left(k_{1f}k_{2r} + k_{1f}k_{3f} + k_{2f}k_{3f}P_{H_2O}\right)} + C_{CaO} + \left[\frac{k_{2f}}{\left(k_{2r}+k_{3f}\right)}\cdot\frac{\left(k_{1r}k_{3f} + k_{1r}k_{2r} + k_{2r}k_{3r}P_{H_2O}\right)}{\left(k_{1f}k_{2r} + k_{1f}k_{3f} + k_{2f}k_{3f}P_{H_2O}\right)} + \frac{k_{3r}}{\left(k_{2r}+k_{3f}\right)}\right]C_{CaO}P_{H_2O}P_{CO_2}$$

$$C_t = C_{CaO}\left[\frac{P_{CO_2}\left(k_{1r}k_{3f} + k_{1r}k_{2r} + k_{2r}k_{3r}P_{H_2O}\right)}{\left(k_{1f}k_{2r} + k_{1f}k_{3f} + k_{2f}k_{3f}P_{H_2O}\right)} + 1 + \left[\frac{k_{2f}}{\left(k_{2r}+k_{3f}\right)}\cdot\frac{\left(k_{1r}k_{3f} + k_{1r}k_{2r} + k_{2r}k_{3r}P_{H_2O}\right)}{\left(k_{1f}k_{2r} + k_{1f}k_{3f} + k_{2f}k_{3f}P_{H_2O}\right)} + \frac{k_{3r}}{\left(k_{2r}+k_{3f}\right)}\right]P_{H_2O}P_{CO_2}\right]$$

$$C_{CaO} = \frac{C_t}{\frac{P_{CO_2}\left(k_{1r}k_{3f} + k_{1r}k_{2r} + k_{2r}k_{3r}P_{H_2O}\right)}{\left(k_{1f}k_{2r} + k_{1f}k_{3f} + k_{2f}k_{3f}P_{H_2O}\right)} + 1 + \left[\frac{k_{2f}}{\left(k_{2r}+k_{3f}\right)}\cdot\frac{\left(k_{1r}k_{3f} + k_{1r}k_{2r} + k_{2r}k_{3r}P_{H_2O}\right)}{\left(k_{1f}k_{2r} + k_{1f}k_{3f} + k_{2f}k_{3f}P_{H_2O}\right)} + \frac{k_{3r}}{\left(k_{2r}+k_{3f}\right)}\right]P_{H_2O}P_{CO_2}}$$

Equation II.30 - Substitute Equation II.29 into Equation II.28:

$$-r_{calc} = \frac{C_t P_{CO_2}\left[k_{1f}\left(\frac{\left(k_{1r}k_{3f}+k_{1r}k_{2r}+k_{2r}k_{3r}P_{H_2O}\right)}{\left(k_{1f}k_{2r}+k_{1f}k_{3f}+k_{2f}k_{3f}P_{H_2O}\right)}-K_1\right)+k_{3f}P_{H_2O}\left(\frac{k_{2f}}{\left(k_{2r}+k_{3f}\right)}\cdot\frac{\left(k_{1r}k_{3f}+k_{1r}k_{2r}+k_{2r}k_{3r}P_{H_2O}\right)}{\left(k_{1f}k_{2r}+k_{1f}k_{3f}+k_{2f}k_{3f}P_{H_2O}\right)}+\frac{k_{3r}}{\left(k_{2r}+k_{3f}\right)}-K_3\right)\right]}{\frac{P_{CO_2}\left(k_{1r}k_{3f}+k_{1r}k_{2r}+k_{2r}k_{3r}P_{H_2O}\right)}{\left(k_{1f}k_{2r}+k_{1f}k_{3f}+k_{2f}k_{3f}P_{H_2O}\right)}+1+\left[\frac{k_{2f}}{\left(k_{2r}+k_{3f}\right)}\cdot\frac{\left(k_{1r}k_{3f}+k_{1r}k_{2r}+k_{2r}k_{3r}P_{H_2O}\right)}{\left(k_{1f}k_{2r}+k_{1f}k_{3f}+k_{2f}k_{3f}P_{H_2O}\right)}+\frac{k_{3r}}{\left(k_{2r}+k_{3f}\right)}\right]P_{H_2O}P_{CO_2}}$$

$$-r_{calc} = \frac{C_t P_{CO_2}\left[k_{1f}\left(\frac{\left(k_{1r}k_{3f}+k_{1r}k_{2r}+k_{2r}k_{3r}P_{H_2O}\right)}{\left(k_{1f}k_{2r}+k_{1f}k_{3f}+k_{2f}k_{3f}P_{H_2O}\right)}-K_1\right)+k_{3f}P_{H_2O}\left(\frac{k_{2f}}{\left(k_{2r}+k_{3f}\right)}\cdot\frac{\left(k_{1r}k_{3f}+k_{1r}k_{2r}+k_{2r}k_{3r}P_{H_2O}\right)}{\left(k_{1f}k_{2r}+k_{1f}k_{3f}+k_{2f}k_{3f}P_{H_2O}\right)}+\frac{k_{3r}}{\left(k_{2r}+k_{3f}\right)}-K_3\right)\right]}{1+\frac{P_{CO_2}\left(k_{1r}k_{3f}+k_{1r}k_{2r}+k_{2r}k_{3r}P_{H_2O}\right)}{\left(k_{1f}k_{2r}+k_{1f}k_{3f}+k_{2f}k_{3f}P_{H_2O}\right)}+\left[\frac{k_{2f}}{\left(k_{2r}+k_{3f}\right)}\cdot\frac{\left(k_{1r}k_{3f}+k_{1r}k_{2r}+k_{2r}k_{3r}P_{H_2O}\right)}{\left(k_{1f}k_{2r}+k_{1f}k_{3f}+k_{2f}k_{3f}P_{H_2O}\right)}+\frac{k_{3r}}{\left(k_{2r}+k_{3f}\right)}\right]P_{H_2O}P_{CO_2}}$$

Equation II.31 - Simplifying:

$$-r_{calc} = \frac{numerator}{denominator}$$

$$denominator = 1+\frac{P_{CO_2}\left(k_{1r}k_{3f}+k_{1r}k_{2r}+k_{2r}k_{3r}P_{H_2O}\right)}{\left(k_{1f}k_{2r}+k_{1f}k_{3f}+k_{2f}k_{3f}P_{H_2O}\right)}+\left[\frac{k_{2f}}{\left(k_{2r}+k_{3f}\right)}\cdot\frac{\left(k_{1r}k_{3f}+k_{1r}k_{2r}+k_{2r}k_{3r}P_{H_2O}\right)}{\left(k_{1f}k_{2r}+k_{1f}k_{3f}+k_{2f}k_{3f}P_{H_2O}\right)}+\frac{k_{3r}}{\left(k_{2r}+k_{3f}\right)}\right]P_{H_2O}P_{CO_2}$$

$$\begin{aligned} denominator = {} & \frac{1}{\left(k_{1f}k_{2r}+k_{1f}k_{3f}+k_{2f}k_{3f}P_{H_2O}\right)\left(k_{2r}+k_{3f}\right)} \\ & \cdot\left[\left(k_{1f}k_{2r}+k_{1f}k_{3f}+k_{2f}k_{3f}P_{H_2O}\right)\left(k_{2r}+k_{3f}\right)+P_{CO_2}\left(k_{1r}k_{3f}+k_{1r}k_{2r}+k_{2r}k_{3r}P_{H_2O}\right)\left(k_{2r}+k_{3f}\right)\right. \\ & \left.+k_{2f}\left(k_{1r}k_{3f}+k_{1r}k_{2r}+k_{2r}k_{3r}P_{H_2O}\right)P_{H_2O}P_{CO_2}+\left(k_{1f}k_{2r}+k_{1f}k_{3f}+k_{2f}k_{3f}P_{H_2O}\right)k_{3r}P_{H_2O}P_{CO_2}\right] \end{aligned}$$

$$denominator = \frac{1}{\left(k_{1f}k_{2r} + k_{1f}k_{3f} + k_{2f}k_{3f}P_{H_2O}\right)\left(k_{2r} + k_{3f}\right)} \cdot \left[k_{1f}k_{2r}^2 + k_{1f}k_{2r}k_{3f} + k_{2f}k_{2r}k_{3f}P_{H_2O} + k_{1f}k_{2r}k_{3f} + k_{1f}k_{3f}^2 + k_{2f}k_{3f}^2P_{H_2O} + k_{1r}k_{2r}k_{3f}P_{CO_2} + k_{1r}k_{2r}^2P_{CO_2} + k_{2r}^2k_{3r}P_{H_2O}P_{CO_2} + k_{1r}k_{3f}^2P_{CO_2} + k_{1r}k_{2r}k_{3f}P_{CO_2} + k_{2r}k_{3r}k_{3f}P_{H_2O}P_{CO_2} + k_{1r}k_{2f}k_{3f}P_{H_2O}P_{CO_2} + k_{1r}k_{2f}k_{2r}P_{H_2O}P_{CO_2} + k_{2r}k_{2f}k_{3r}P_{H_2O}^2P_{CO_2} + k_{1f}k_{2r}k_{3r}P_{H_2O}P_{CO_2} + k_{1f}k_{3f}k_{3r}P_{H_2O}P_{CO_2} + k_{2f}k_{3f}k_{3r}P_{H_2O}^2P_{CO_2}\right]$$

$$numerator = C_tP_{CO_2}\left[k_{1f}\left(\frac{\left(k_{1r}k_{3f} + k_{1r}k_{2r} + k_{2r}k_{3r}P_{H_2O}\right)}{\left(k_{1f}k_{2r} + k_{1f}k_{3f} + k_{2f}k_{3f}P_{H_2O}\right)} - K_1\right) + k_{3f}P_{H_2O}\left(\frac{k_{2f}}{\left(k_{2r} + k_{3f}\right)} \cdot \frac{\left(k_{1r}k_{3f} + k_{1r}k_{2r} + k_{2r}k_{3r}P_{H_2O}\right)}{\left(k_{1f}k_{2r} + k_{1f}k_{3f} + k_{2f}k_{3f}P_{H_2O}\right)} + \frac{k_{3r}}{\left(k_{2r} + k_{3f}\right)} - K_3\right)\right]$$

$$numerator = C_tP_{CO_2}\left[\frac{\left(k_{1r}k_{1f}k_{3f} + k_{1r}k_{1f}k_{2r} + k_{1f}k_{2r}k_{3r}P_{H_2O}\right)}{\left(k_{1f}k_{2r} + k_{1f}k_{3f} + k_{2f}k_{3f}P_{H_2O}\right)} - k_{1r} + \frac{k_{2f}k_{3f}P_{H_2O}}{\left(k_{2r} + k_{3f}\right)} \cdot \frac{\left(k_{1r}k_{3f} + k_{1r}k_{2r} + k_{2r}k_{3r}P_{H_2O}\right)}{\left(k_{1f}k_{2r} + k_{1f}k_{3f} + k_{2f}k_{3f}P_{H_2O}\right)} + \frac{k_{3r}k_{3f}P_{H_2O}}{\left(k_{2r} + k_{3f}\right)} - k_{3r}P_{H_2O}\right]$$

$$numerator = C_tP_{CO_2} \cdot \frac{1}{\left(k_{1f}k_{2r} + k_{1f}k_{3f} + k_{2f}k_{3f}P_{H_2O}\right)\left(k_{2r} + k_{3f}\right)} \cdot \left[\left(k_{2r} + k_{3f}\right)\left(k_{1r}k_{1f}k_{3f} + k_{1r}k_{1f}k_{2r} + k_{1f}k_{2r}k_{3r}P_{H_2O}\right) - k_{1r}\left(k_{2r} + k_{3f}\right)\left(k_{1f}k_{2r} + k_{1f}k_{3f} + k_{2f}k_{3f}P_{H_2O}\right) + k_{2f}k_{3f}P_{H_2O}\left(k_{1r}k_{3f} + k_{1r}k_{2r} + k_{2r}k_{3r}P_{H_2O}\right) + k_{3r}k_{3f}\left(k_{1f}k_{2r} + k_{1f}k_{3f} + k_{2f}k_{3f}P_{H_2O}\right)P_{H_2O} - k_{3r}\left(k_{2r} + k_{3f}\right)\left(k_{1f}k_{2r} + k_{1f}k_{3f} + k_{2f}k_{3f}P_{H_2O}\right)P_{H_2O}\right]$$

$$numerator = C_t P_{CO_2} \cdot \frac{1}{\left(k_{1f}k_{2r} + k_{1f}k_{3f} + k_{2f}k_{3f}P_{H_2O}\right)\left(k_{2r} + k_{3f}\right)}$$
$$\cdot \left[k_{1r}k_{1f}k_{2r}k_{3f} + k_{1r}k_{1f}k_{2r}^2 + k_{1f}k_{2r}^2k_{3r}P_{H_2O} + k_{1r}k_{1f}k_{3f}^2 + k_{1r}k_{1f}k_{2r}k_{3f} + k_{1f}k_{2r}k_{3r}k_{3f}P_{H_2O} - k_{1f}k_{1r}k_{2r}^2\right.$$
$$- k_{1f}k_{1r}k_{2r}k_{3f} - k_{1r}k_{2f}k_{2r}k_{3f}P_{H_2O} - k_{1f}k_{1r}k_{2r}k_{3f} - k_{1f}k_{1r}k_{3f}^2 - k_{1r}k_{2f}k_{3f}^2P_{H_2O} + k_{1r}k_{2f}k_{3f}^2P_{H_2O} + k_{1r}k_{2r}k_{2f}k_{3f}P_{H_2O}$$
$$+ k_{2r}k_{3r}k_{2f}k_{3f}P_{H_2O}^2 + k_{1f}k_{2r}k_{3r}k_{3f}P_{H_2O} + k_{1f}k_{3r}k_{3f}^2P_{H_2O} + k_{2f}k_{3r}k_{3f}^2P_{H_2O}^2 - k_{1f}k_{2r}^2k_{3r}P_{H_2O} - k_{1f}k_{2r}k_{3f}k_{3r}P_{H_2O}$$
$$\left. - k_{2f}k_{2r}k_{3f}k_{3r}P_{H_2O}^2 - k_{1f}k_{2r}k_{3r}k_{3f}P_{H_2O} - k_{1f}k_{3f}^2k_{3r}P_{H_2O} - k_{2f}k_{3f}^2k_{3r}P_{H_2O}^2\right]$$

$$numerator = C_t P_{CO_2} \cdot \frac{1}{\left(k_{1f}k_{2r} + k_{1f}k_{3f} + k_{2f}k_{3f}P_{H_2O}\right)\left(k_{2r} + k_{3f}\right)}$$
$$\cdot \left[\cancel{k_{1r}k_{1f}k_{2r}k_{3f}} + \cancel{k_{1r}k_{1f}k_{2r}^2} + \cancel{k_{1f}k_{2r}^2k_{3r}P_{H_2O}} + \cancel{k_{1r}k_{1f}k_{3f}^2} + \cancel{k_{1r}k_{1f}k_{2r}k_{3f}} + \cancel{k_{1f}k_{2r}k_{3r}k_{3f}P_{H_2O}} - \cancel{k_{1f}k_{1r}k_{2r}^2}\right.$$
$$- \cancel{k_{1f}k_{1r}k_{2r}k_{3f}} - \cancel{k_{1r}k_{2f}k_{2r}k_{3f}P_{H_2O}} - \cancel{k_{1f}k_{1r}k_{2r}k_{3f}} - \cancel{k_{1f}k_{1r}k_{3f}^2} - \cancel{k_{1r}k_{2f}k_{3f}^2P_{H_2O}} + \cancel{k_{1r}k_{2f}k_{3f}^2P_{H_2O}} + \cancel{k_{1r}k_{2r}k_{2f}k_{3f}P_{H_2O}}$$
$$+ \cancel{k_{2r}k_{3r}k_{2f}k_{3f}P_{H_2O}^2} + \cancel{k_{1f}k_{2r}k_{3r}k_{3f}P_{H_2O}} + \cancel{k_{1f}k_{3r}k_{3f}^2P_{H_2O}} + \cancel{k_{2f}k_{3r}k_{3f}^2P_{H_2O}^2} - \cancel{k_{1f}k_{2r}^2k_{3r}P_{H_2O}} - \cancel{k_{1f}k_{2r}k_{3f}k_{3r}P_{H_2O}}$$
$$\left. - \cancel{k_{2f}k_{2r}k_{3f}k_{3r}P_{H_2O}^2} - \cancel{k_{1f}k_{2r}k_{3r}k_{3f}P_{H_2O}} - \cancel{k_{1f}k_{3f}^2k_{3r}P_{H_2O}} - \cancel{k_{2f}k_{3f}^2k_{3r}P_{H_2O}^2}\right]$$

$$numerator = C_t P_{CO_2} \cdot \frac{1}{\left(k_{1f}k_{2r} + k_{1f}k_{3f} + k_{2f}k_{3f}P_{H_2O}\right)\left(k_{2r} + k_{3f}\right)}$$

Substitute back into numerator and denominator and cancelling common terms:

$$-r_{calc} = \frac{numerator}{denominator}$$

$$-r_{calc} = C_t P_{CO_2}$$
$$\cdot \left(k_{1f}k_{2r}^2 + k_{1f}k_{2r}k_{3f} + k_{2f}k_{2r}k_{3f}P_{H_2O} + k_{1f}k_{2r}k_{3f} + k_{1f}k_{3f}^2 + k_{2f}k_{3f}^2P_{H_2O} + k_{1r}k_{2r}k_{3f}P_{CO_2} + k_{1r}k_{2r}^2P_{CO_2}\right.$$
$$+ k_{2r}^2k_{3r}P_{H_2O}P_{CO_2} + k_{1r}k_{3f}^2P_{CO_2} + k_{1r}k_{2r}k_{3f}P_{CO_2} + k_{2r}k_{3r}k_{3f}P_{H_2O}P_{CO_2} + k_{1r}k_{2f}k_{3f}P_{H_2O}P_{CO_2} + k_{1r}k_{2f}k_{2r}P_{H_2O}P_{CO_2}$$
$$\left. + k_{2r}k_{2f}k_{3r}P_{H_2O}^2P_{CO_2} + k_{1f}k_{2r}k_{3r}P_{H_2O}P_{CO_2} + k_{1f}k_{3f}k_{3r}P_{H_2O}P_{CO_2} + k_{2f}k_{3f}k_{3r}P_{H_2O}^2P_{CO_2}\right)^{-1}$$

$$-r_{calc} = C_t P_{CO_2} \cdot \left(\left[k_{1f}k_{2r}^2 + 2\left(k_{1f}k_{2r}k_{3f}\right) + k_{1f}k_{3f}^2\right] + \left[k_{2f}k_{2r}k_{3f} + k_{2f}k_{3f}^2\right]P_{H_2O} + \left[k_{1r}k_{2r}^2 + k_{1r}k_{3f}^2 + 2\left(k_{1r}k_{2r}k_{3f}\right)\right]P_{CO_2} + \left[k_{2r}^2k_{3r} + k_{2r}k_{3r}k_{3f} + k_{1r}k_{2f}k_{3f} + k_{1r}k_{2f}k_{2r} + k_{1f}k_{2r}k_{3r} + k_{1f}k_{3f}k_{3r}\right]P_{H_2O}P_{CO_2} + \left[k_{2r}k_{2f}k_{3r} + k_{2f}k_{3f}k_{3r}\right]P_{H_2O}^2P_{CO_2}\right)^{-1}$$

$$-r_{calc} = \frac{k_{calc}P_{CO_2}}{K_A + K_BP_{H_2O} + K_CP_{CO_2} + K_DP_{H_2O}P_{CO_2} + K_EP_{H_2O}^2P_{CO_2}}$$

Equation II.32:

$$-r_{calc} = \frac{S_A}{R_iT} \cdot \frac{k_{calc}P_{CO_2}}{K_A + K_BP_{H_2O} + K_CP_{CO_2} + K_DP_{H_2O}P_{CO_2} + K_EP_{H_2O}^2P_{CO_2}}$$

Where k_c is in units m/s, K_A is unitless, the terms K_B and K_C are in units Pa^{-1}, K_D is in units of Pa^{-2}, K_E is in units Pa^{-3}, P_{CO2} and P_{H2O} are in units Pa, S_A is in units m^2/m^3, R_i is in units J/mol·K, T is in K and the r_{calc} is in units of $mol/m^3 \cdot s$.

Equation II.33 – It should be noted that when the partial pressure of H_2O is zero, the Equation II.32 reduces to Equation II.13:

$$-r_{calc} = \frac{k_{calc}P_{CO_2}}{K_A + K_BP_{H_2O} + K_CP_{CO_2} + K_DP_{H_2O}P_{CO_2} + K_EP_{H_2O}^2P_{CO_2}} = \frac{k_{calc}P_{CO_2}}{K_A + P_{CO_2}K_C}$$

Utilising Equation II.32 Figure II.4 was produced utilising '*fminsearch'* to fit this modelled data to the experimental data by minimising the sum of square errors. The implementation of this function was the performed the same as the N_2 system i.e. the maximum number of function evaluations and iterations was set to 10^7 and the tolerances were set to 10^{-9} and the initial guess values were all set to 0 apart from K_A which was set to 1. Solving for the values of the five constants the final estimated parameters and sum of the square errors (SSE) can be observed in Table II.4. In reality the value of these constants would change with temperature, however the experiments have not been conducted to estimate how these values may change with temperature. A relatively good fit can be observed between the experimental data and the fitted line from the Langmuir-Hinshelwood derivation. The initial guess values were altered to determine their effect, the fit of the line was highly dependent upon the initial guess values of K_B, K_C, K_D and K_E however K_A was more flexible towards its initial value. The estimated values of K_B, K_C, K_D and K_E worked to effectively minimise the value of the overall term when multiplied with their respective P_{H_2O} and P_{CO_2} terms. This means that upon calculation of the overall fitting term, shown as Equation II.34, at the experimental conditions a pseudo scaling factor is produced. The values of this scaling factor term, for the experimental conditions utilised are presented in Table II.3.

Equation II.34:

$$Scaling\ factor = \frac{1}{K_A + K_B P_{H_2O} + K_C P_{CO_2} + K_D P_{H_2O} P_{CO_2} + K_E P_{H_2O}^2 P_{CO_2}}$$

Table II.3 – Scaling factor term at experimental conditions.

Experimental conditions		**Scaling factor term**
P_{CO_2}, **Pa**	P_{H_2O}, **Pa**	
9.0×10^4	1.2×10^4	0.96
8.0×10^4	2.1×10^4	1.13
7.2×10^4	3.0×10^4	1.36
6.2×10^4	3.9×10^4	1.87

Figure II.4 presents the fitted line after it had been extended beyond the fitting range to show the effect of utilising this equation outside of the fitted range. Namely, at very high partial pressures of CO_2 the predicted rate will decrease and at low partial pressures of CO_2 the predicted rate will increase exponentially – caution must therefore be used when applying this equation outside of this range. Because the fit of this Langmuir-Hinshelwood derived rate equation was relatively good it can be stated that the mechanism selected was appropriate and fitted the experimental data but further analytical experiments are required to confirm that the calcination with steam at high partial pressures of CO_2 does follow this proposed reaction mechanism.

Table II.4 – Estimated values of the constants for Equation II.32 for the steam system calcinations.

Constants	**Values where variable P_{CO2} in Equation II.32 was P_{CO2}**
K_A	-5.54
K_B	-1.37×10^{-7}
K_C	6.76×10^{-5}
K_D	3.86×10^{-10}
K_E	9.86×10^{-15}
SSE	4.59×10^{-17}

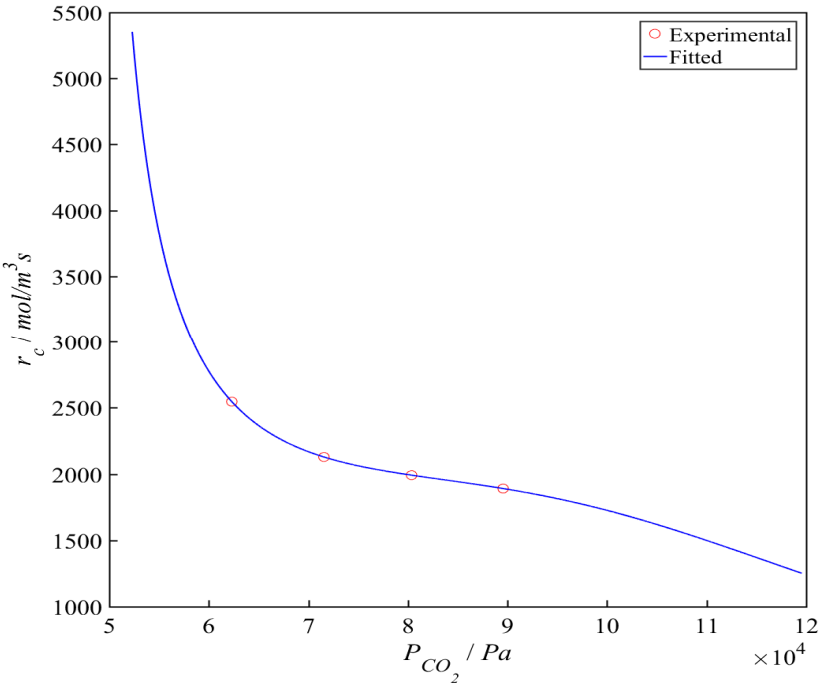

Figure II.4 – Fitting of the experimental data for the steam system calcinations via the Langmuir-Hinshelwood approach for P_{CO2}.

A similar reaction mechanism was suggested by Guo et al., (Guo et al., 2015) through the use of XRD and SEM-EDS measurements of limestones subjected to high-temperature steam. They suggested a mechanism whereby CO_2 required two bonding active sites compared to one for a molecule of steam. Wang and Thomson also examined the mechanism of steam on the release of CO_2 from $CaCO_3$. Their work followed a similar Langmuir-Hinshelwood derivation to that shown above and demonstrated that steam adsorbs to the active CaO sites stronger than the CO_2 molecules do, thus increasing the rate of calcination (Wang and Thomson, 1995).

Appendix III – Costs of Chemical Reagents for Sorbent Synthesis

Example calculation for the cost of Si based chemical reagents

Fumed silica: O_2Si – 60.08 g/mol - £137.60/kg – (Sigma Aldrich, 10/02/2017)

Si – 28.085 g/mol, therefore Si represents ~46.7 wt.% of the material.

Therefore cost per kg of Si ≈ £295 = $368 (on 10/02/2017).

Tetraethyl Orthosilicate (TEOS): $C_8H_{20}O_4Si$ – 208.33g/mol – 0.933 g/cm^3 @ 20 °C – £42.20/L = £45.23/kg – (Sigma Aldrich, 10/02/2017)

Si – 28.085 g/mol, therefore Si represents ~13.5 wt.% of the material.

Therefore cost per kg of Si ≈ £336 = $419 (on 10/02/2017).

Of course bulk purchasing of materials from alternative suppliers would inevitably be cheaper, this analysis just provides a relativistic understanding of the pricing of the two silica sources utilised.

Appendix IV – Calcination Particle Model – Matlab Code

File name: *Parameters_Testing.m*

```
%% System of parameters to run for Heat and mass transfer model
tic1 = tic;

%% Import Data
[Data,~,~] = xlsread('Combined Data Sheet N2.xlsx', 1, 'A8:AS240');
% [Data_noheatup,~,~] = xlsread('Combined Data Sheet without heat up
N2.xlsx', 1, 'A8:AS240');
[~,~,Header_Data] = xlsread('Combined Data Sheet N2.xlsx', 1,
'A1:AS7');

% Header_Data_table - RowNames
% Limestone_type
% Mass
% Particle_size_small
% Particle_size_large
% Temperature
% Mole_Percent
% Gas

% Number of experiments
Num_of_experiments = size(Header_Data,2);

% Convert numbers to strings
for j = 1:Num_of_experiments
    for i = 2:6
        Header_Data{i,j} = num2str(Header_Data{i,j});
    end
end

%% Steam data has all been ×10^3 so need to undo this
% was a mistake from before
for j = 1:Num_of_experiments
    if strcmpi(char(Header_Data(7,j)),'H2O')
        Data(:,j) = Data(:,j)/1000;
    end
end

%% Experimental run information - conversion and preparing data for
comparisions in the testingSteam and testingN2 scripts
% Cumulative totals for each run
Cumulative_cols = cumsum(Data);
Cumulative_cols_total = zeros(1,size(Cumulative_cols,2));
Cumulative_cols_total(1,1:Num_of_experiments) =
max(Cumulative_cols(:,1:Num_of_experiments));
```

```
% Conversions
ExperimentalConversions = zeros(size(Cumulative_cols));
for j = 1:Num_of_experiments
    ExperimentalConversions(:,j) =
(Cumulative_cols(:,j)./(Cumulative_cols_total(1,j))*100);
end

% Add line of NaN at the end of the data as it is needed for the
next section
dimension = size(Data,1);
for j = 1:Num_of_experiments
    Data(dimension+1,j) = NaN;
    ExperimentalConversions(dimension+1,j) = NaN;
end

% Time for plotting
experimental_Time = zeros(1,Num_of_experiments);
Time = zeros(size(Data));
for j = 1:Num_of_experiments
    for i = 2:(find(isnan(Data(:,j)),1,'first')-1)
        Time(i,j) = Time(i-1,j)+1;
    end
    experimental_Time(1,j) = max(Time(:,j));
end

%% Parameters
% Initial Temp
Initial_T_particle = 20; % °C

% Bulk Temp
Tb = zeros(1,Num_of_experiments);
for j = 1:Num_of_experiments
    Tb(1,j) = str2double(cell2mat(Header_Data(5,j)));
end
Bulk_Temps = unique(Tb); % °C

% Particle size testing
R = zeros(1,Num_of_experiments);
for j = 1:Num_of_experiments
    R(1,j) =
(((str2double(cell2mat(Header_Data(3,j))))*(str2double(cell2mat(Head
er_Data(4,j))))).^0.5)/(1000000*2);
end
Particle_sizes = unique(R); % m

% mole fractions
mole_fraction_CO2 = zeros(1,Num_of_experiments);
mole_fraction_H2O = zeros(1,Num_of_experiments);
mole_fraction_N2 = zeros(1,Num_of_experiments);
for j = 1:Num_of_experiments
    mole_fraction_CO2(1,j) = (100-
str2double(cell2mat(Header_Data(6,j))))/100;
    if strcmp(char(Header_Data(7,j)),'H2O') == 1
           mole_fraction_H2O(1,j) =
      str2double(cell2mat(Header_Data(6,j)))/100;
    elseif strcmp(char(Header_Data(7,j)),'N2') == 1
```

```
        mole_fraction_N2(1,j) =
str2double(cell2mat(Header_Data(6,j)))/100;
    end
end
CO2_mf = unique(mole_fraction_CO2);
H2O_mf = unique(mole_fraction_H2O);
N2_mf = unique(mole_fraction_N2);

%% Model
Output_Time = cell(1,Num_of_experiments);
Output_Temperature = cell(1,Num_of_experiments);
Output_PCO2 = cell(1,Num_of_experiments);
Output_PH2O = cell(1,Num_of_experiments);
Output_PN2 = cell(1,Num_of_experiments);
Output_X = cell(1,Num_of_experiments);
Output_CO2_rate = cell(1,Num_of_experiments);
Output_heat_rate = cell(1,Num_of_experiments);
Output_Conversion = cell(1,Num_of_experiments);
Output_reaction_occurring = cell(1,Num_of_experiments);
Output_CO2_mol_per_gs = cell(1,Num_of_experiments);
heatuptime = cell(1,Num_of_experiments);
diffusiontime = cell(1,Num_of_experiments);
Ratetime = cell(1,Num_of_experiments);
N = zeros(1,Num_of_experiments);
% out_MTC = cell(1,Num_of_experiments);
out_RateCalcOut = cell(1,Num_of_experiments);

for j = 1:Num_of_experiments
    fprintf('\nExperiment Number = %i\n', j)

    % Parameters from experimental data
    Tb_Param = Tb(1,j);
    Radius = R(1,j);
    if j == 14 || j == 38
        Limestone_type = 'Cadomin';
    elseif j == 15 || j == 40
        Limestone_type = 'Imeco';
    elseif j == 39
        Limestone_type = 'Havelock';
    else
        Limestone_type = 'Longcliffe';
    end
    CO2 = mole_fraction_CO2(1,j);
    if strcmpi(cell2mat(Header_Data(7,j)),'N2')
        N2 = mole_fraction_N2(1,j);
        H2O = 0;
    elseif strcmpi(cell2mat(Header_Data(7,j)),'H2O')
        H2O = mole_fraction_H2O(1,j);
        N2 = 0;
    end
    experiment_Time = experimental_Time(1,j);
```

```
%      % ARBITARY VALUES
%      Tb_Param = 950;
%      Radius = 45/(1000000);
%      Limestone_type = 'Longcliffe';
%      CO2 = 0.8;
%      H2O = 0.2;
%      N2 = 0;
%      experiment_Time = 5;

    % Iteration points - number of points along a radii
    N_test = 100;


      [Output_Time{1,j},Output_Temperature{1,j},Output_PCO2{1,j},Out
      put_PH2O{1,j},Output_PN2{1,j},Output_CO2_rate{1,j},Output_heat
      _rate{1,j},Output_Conversion{1,j},Output_reaction_occurring{1,
      j},Output_CO2_mol_per_gs{1,j},heatuptime{1,j},diffusiontime{1,
      j},N(1,j),Ratetime{1,j},out_RateCalcOut{1,j},Output_X{1,j}]...
         =
      H_and_M_model_reaction_fastcode(Tb_Param,Initial_T_particle,Ra
      dius,H2O,N2,CO2,experiment_Time,Limestone_type,N_test);
end

%%
toc1 = toc();
disp('Completed');
if toc1 >= 60
    toc1 = toc1/60;
    disp(['Total solving time: ' num2str(toc1) 'mins']);
elseif toc1 >= 3600
    toc1 = toc1/3600;
    disp(['Total solving time: ' num2str(toc1) 'hours']);
else
    disp(['Total solving time: ' num2str(toc1) 's']);
end

%% END OF FILE
```

File name: *H_and_M_model_reaction_fastcode.m*

```
function
[Output_Time,Output_Temperature,Output_PCO2,Output_PH2O,Output_PN2,O
utput_CO2_rate,Output_heat_rate,Output_Conversion,Output_reaction_oc
curing,Output_CO2_mol_per_gs,heatuptime,diffusiontime,N,Ratetime,out
_RateCalcOut,Output_X]...
    =
H_and_M_model_reaction_fastcode(Bulk_T,Initial_T_particle,Radius,H2O
_mf,N2_mf,CO2_mf,experimental_Time,Limestone_type,N)

beep off
tic();
%% Global Variables
global timetaken
global RateTerm_Diffusion_main
```

```
global RateTerm_Heat_main
global iteration
global Conversion_overall
global iter
global Calcination_reaction_occuring_out
global CO2_mol_per_gs_out
global RateCalcOut

%% Put variables into correct format
% Convert to Kelvin
To = Initial_T_particle + 273.15;
T_bulk = Bulk_T + 273.15;

% convert bar to Pa
PCO2_bulk = CO2_mf*100000; % Pa

% H2O bulk
PH2O_bulk = H2O_mf*100000; % Pa

% N2 bulk
PN2_bulk = N2_mf*100000; % Pa

% Co-ordinates of all inside points - Each line is a line from 0 to
the edge of particle
rho_inside = linspace(0,Radius,N);
dr = rho_inside(N)-rho_inside(N-1); % delta R

%% ODE solver - Initial variables
InitialTemp = To*ones(1,N)';
InitialCCO2 = ((0.04/100)*101325)*ones(1,N)';
% InitialCO2 = PCO2_bulk*ones(1,N)';
InitialH2O = zeros(N,1);
InitialN2 = ((0.79)*101325)*ones(1,N)';
InitialX = zeros(1,N)';

% Initialise variable names and allocate memory
RateTerm_Heat_main = zeros(500000,N);
RateTerm_Diffusion_main = zeros(500000,N);
timetaken = zeros(500000,1);
Conversion_overall = zeros(500000,N);
Calcination_reaction_occuring_out = zeros(500000,N);
CO2_mol_per_gs_out = zeros(500000,1);
iter = ones(1,N);
RateCalcOut = zeros(500000,N);
iteration = 1;

% ODE solver time, seconds.
time = 0:0.05:max(experimental_Time+20); % 40
time = time';
```

```
%% The main solver

% Set tolerance for ODE solver
% 1e-6 is equivalent to 0.0001% accuracy
options = odeset('AbsTol',1e-10,'RelTol',1e-
9,'NonNegative',(1:5*N));
[Calculated_Time,DT_DPCO2_DPH2O_DPN2_DX_completed] =
ode15s(@(t,T_PCO2_PH2O_PN2_X)...

dTdt_dPCO2dt_dPH2Odt_dPN2dt_dXdt(t,T_PCO2_PH2O_PN2_X,N,T_bulk,PCO2_b
ulk,PH2O_bulk,PN2_bulk,To,Radius,dr,Limestone_type,CO2_mf,H2O_mf,N2_
mf),time,[InitialTemp;InitialCCO2;InitialH2O;InitialN2;InitialX],opt
ions);

fprintf('\nIterations: %i \n', iteration);

time_zero_point = find(timetaken ~= 0, 1, 'first');
timetaken(all(timetaken(2:end)==0,2),:) = [];
timetaken(end) = Calculated_Time(end);

% Trim off starting and trailing zeros
CO2_mol_per_gs_out(1:time_zero_point-1,:) = [];
CO2_mol_per_gs_out(size(timetaken,1)+1:end,:) = [];
RateTerm_Heat_main(1:time_zero_point-1,:) = [];
RateTerm_Heat_main(size(timetaken,1)+1:end,:) = [];
RateTerm_Diffusion_main(1:time_zero_point-1,:) = [];
RateTerm_Diffusion_main(size(timetaken,1)+1:end,:)=[];
Calcination_reaction_occuring_out(1:time_zero_point-1,:) = [];
Calcination_reaction_occuring_out(size(timetaken,1)+1:end,:) = [];
Conversion_overall(1:time_zero_point-1,:) = [];
Conversion_overall(size(timetaken,1)+1:end,:) = [];
RateCalcOut(1:time_zero_point-1,:) = [];
RateCalcOut(size(timetaken,1)+1:end,:) = [];


% for the output function
Output_Time = Calculated_Time;
Output_Temperature = DT_DPCO2_DPH2O_DPN2_DX_completed(:,1:N);
Output_PCO2 = DT_DPCO2_DPH2O_DPN2_DX_completed(:,N+1:2*N);
Output_PH2O = DT_DPCO2_DPH2O_DPN2_DX_completed(:,2*N+1:3*N);
Output_PN2 = DT_DPCO2_DPH2O_DPN2_DX_completed(:,3*N+1:4*N);
Output_X = DT_DPCO2_DPH2O_DPN2_DX_completed(:,4*N+1:5*N);

Output_CO2_rate = RateTerm_Diffusion_main;
Output_heat_rate = RateTerm_Heat_main;
Ratetime = timetaken;
Output_Conversion = Conversion_overall;
Output_reaction_occuring = Calcination_reaction_occuring_out;
Output_CO2_mol_per_gs = CO2_mol_per_gs_out;
% out_MTC = MTCout;
out_RateCalcOut = RateCalcOut;

%%
% Time to full heat up
for i = 5:size(Output_Temperature,1)-5
```

```
    stability = abs(mean(Output_Temperature(i-4:i,1))-
mean(Output_Temperature(i:i+4,end))); % less than 0.1°C (0.1%)
difference in temp between inside and out.
    if stability <= 0.1
        if abs(Output_Temperature(i) - T_bulk) <= 0.1
            break
        end
    end
end
heatuptime = Output_Time(i);
fprintf('It took %.4f seconds to heat up\n',heatuptime);

% Time to full CO2 diffusion
for i = 5:size(Output_PCO2,1)-5
    stabilityCO2 = abs(mean(Output_PCO2(i-4:i,1))-
mean(Output_PCO2(i:i+4,end))); % less than 1000Pa (0.1%) difference
in partial pressure between inside and out.
    if stabilityCO2 <= 0.1
        if abs(Output_PCO2(i) - PCO2_bulk) <= 0.1
            break
        end
    end
end
diffusiontime = Output_Time(i);
fprintf('It took %.7f seconds for full diffusion\n',diffusiontime);


toc1 = toc();
disp('Completed');
if toc1 >= 60
    toc1 = toc1/60;
    disp(['Solving time: ' num2str(toc1) 'mins']);
elseif toc1 >= 3600
    toc1 = toc1/3600;
    disp(['Solving time: ' num2str(toc1) 'hours']);
else
    disp(['Solving time: ' num2str(toc1) 's']);
end

return

%% END OF FILE
```

File name: *dTdt_dPCO2dt_dPH2Odt_dPN2dt_dXdt.m*

```
function [DT_DPCO2_DPH2O_DPN2_DX] =
dTdt_dPCO2dt_dPH2Odt_dPN2dt_dXdt(t,T_CO2_H2O_N2_X,N,T_bulk,PCO2_bulk
,PH2O_bulk,PN2_bulk,To,Radius,dr,Limestone_type,CO2_mf,H2O_mf,N2_mf)
%% Calculation of dT/dt etc
% Global and persistent variables
global timetaken
global RateTerm_Diffusion_main
global RateTerm_Heat_main
global iteration
```

```
global Conversion_overall
global Calcination_reaction_occuring_out
global CO2_mol_per_gs_out
global RateCalcOut
persistent k
persistent molar_rho_CaCO3_initial
persistent rho_inside
persistent shell_vol
persistent MCaCO3

if iteration == 1
    k = 2;
    rho_inside = linspace(0,Radius,N);
    shell_vol = zeros(N,1);
    for i = 2:N
        shell_vol(i) = (4/3)*pi*(rho_inside(i)^3 - (rho_inside(i-
1))^3);
    end

    MCaCO3 = 100.0869; % g/mol = kg/kmol

    if strcmpi(Limestone_type,'Longcliffe')
        Skeletal_p_LC = 2.82; %g/cm3 Longcliffe
        CaCO3_density = Skeletal_p_LC*1000; % *1,000 to convert
g/cm3 to kg/m3
    elseif strcmpi(Limestone_type,'Havelock')
        Skeletal_p_HL = 2.92; %g/cm3 Havelock
        CaCO3_density = Skeletal_p_HL*1000; % *1,000 to convert
g/cm3 to kg/m3
    elseif strcmpi(Limestone_type,'Cadomin')
        Skeletal_p_CM = 2.94; %g/cm3 Cadomin
        CaCO3_density = Skeletal_p_CM*1000; % *1,000 to convert
g/cm3 to kg/m3
    elseif strcmpi(Limestone_type,'Imeco')
        Skeletal_p_IM = 2.90; %g/cm3 Imeco
        CaCO3_density = Skeletal_p_IM*1000; % *1,000 to convert
g/cm3 to kg/m3
    end
    molar_rho_CaCO3_initial = (CaCO3_density*1000)/(MCaCO3); %
mol/m3 = kg/m3 / kg/kmol * 1000mol/kmol

end

Tempi = T_CO2_H2O_N2_X(1:N);
PCO2i = T_CO2_H2O_N2_X(N+1:2*N);
PH2Oi = T_CO2_H2O_N2_X(2*N+1:3*N);
PN2i = T_CO2_H2O_N2_X(3*N+1:4*N);
Particle_conversion = T_CO2_H2O_N2_X(4*N+1:5*N);

%% Calculate equilibrium CO2 conc and check if the reaction could
occur
PCO2eq = PCO2eq_calc_fast(Tempi);
Calcination_reaction_occurring = zeros(size(Tempi));
for i = 1:N
    if PCO2i(i) >= PCO2eq(i)
        Calcination_reaction_occurring(i) = 0;
```

```
    elseif PCO2i(i) < PCO2eq(i)
            Calcination_reaction_occurring(i) = 1;
    else
        Calcination_reaction_occurring(i) = 0;
    end
end
% Calcination_reaction_occuring = ones(size(Tempi));

%% Variable calculations
[rho_Cp,HTC,eff_thermal_conductivity,MTC,eff_Diff_CO2,eff_Diff_H2O,e
ff_Diff_N2,initial_SA,SA,~,~] =
NEW_conversion_calc_fast(T_bulk,Tempi,To,Radius,Limestone_type,H2O_m
f,N2_mf,CO2_mf,Particle_conversion);
alpha_TD = eff_thermal_conductivity./rho_Cp;

% UNITS
% MTC - Mass transfer coefficent, m/s
% HTC - Heat transfer coefficent, W/m2.K
% eff_thermal_conductivity - W/m.K
% rho_Cp - J/m3.K = J/kg.K * kg/m3
% alpha_TD - m2/s
% eff_diffusivity - m2/s
% Bulk_Diff - m2/s
% Knud_Diff - m2/s

%% Set up the matrices
% Heat
e = ones(N,1);
A_heat = spdiags([e,-2*e,e],[-1,0,1],N,N);
A_heat(1,1) = -1;
B_heat = spdiags([-1*e,e],[0,1],N,N);
boundary_heat = zeros(N,1);
boundary_heat(N) = 1;
Conv_heat = zeros(N,1);

A_heat = bsxfun(@times,A_heat,alpha_TD)./(dr^2);
B_heat = (bsxfun(@times,B_heat,alpha_TD)*2)./(dr*Radius);
boundary_heat =
(boundary_heat.*alpha_TD).*(Tempi(end)*((1/(dr^2))+(2/(dr*Radius))))
;
Conv_heat(N) = ((T_bulk-
Tempi(end))*(HTC/rho_Cp(end)))*dr*((1/(dr^2))+(2/(dr*Radius)));

% Mass - CO2
A_Diffusion_PCO2 = spdiags([e,-2*e,e],[-1,0,1],N,N);
A_Diffusion_PCO2(1,1) = -1;
B_Diffusion_PCO2 = spdiags([-1*e,e],[0,1],N,N);
boundary_Diffusion_PCO2 = zeros(N,1);
boundary_Diffusion_PCO2(N) = 1;
Conv_diff_PCO2 = zeros(N,1);


A_Diffusion_PCO2 =
bsxfun(@times,A_Diffusion_PCO2,eff_Diff_CO2)./(dr^2);
B_Diffusion_PCO2 =
(bsxfun(@times,B_Diffusion_PCO2,eff_Diff_CO2)*2)./(dr*Radius);
```

```
boundary_Diffusion_PCO2 =
(boundary_Diffusion_PCO2.*eff_Diff_CO2).*(PCO2i(end)*((1/(dr^2))+(2/
(dr*Radius))));
Conv_diff_PCO2(N) = ((PCO2_bulk-
PCO2i(end))*MTC)*dr*((1/(dr^2))+(2/(dr*Radius)));

% Mass - H2O
A_Diffusion_PH2O = spdiags([e,-2*e,e],[-1,0,1],N,N);
A_Diffusion_PH2O(1,1) = -1;
B_Diffusion_PH2O = spdiags([-1*e,e],[0,1],N,N);
boundary_Diffusion_PH2O = zeros(N,1);
boundary_Diffusion_PH2O(N) = 1;
Conv_diff_PH2O = zeros(N,1);

A_Diffusion_PH2O =
bsxfun(@times,A_Diffusion_PH2O,eff_Diff_H2O)./(dr^2);
B_Diffusion_PH2O =
(bsxfun(@times,B_Diffusion_PH2O,eff_Diff_H2O)*2)./(dr*Radius);
boundary_Diffusion_PH2O =
(boundary_Diffusion_PH2O.*eff_Diff_H2O).*(PH2Oi(end)*((1/(dr^2))+(2/
(dr*Radius))));
Conv_diff_PH2O(N) = ((PH2O_bulk-
PH2Oi(end))*MTC)*dr*((1/(dr^2))+(2/(dr*Radius)));

% Mass - N2
A_Diffusion_PN2 = spdiags([e,-2*e,e],[-1,0,1],N,N);
A_Diffusion_PN2(1,1) = -1;
B_Diffusion_PN2 = spdiags([-1*e,e],[0,1],N,N);
boundary_Diffusion_PN2 = zeros(N,1);
boundary_Diffusion_PN2(N) = 1;
Conv_diff_PN2 = zeros(N,1);

A_Diffusion_PN2 =
bsxfun(@times,A_Diffusion_PN2,eff_Diff_N2)./(dr^2);
B_Diffusion_PN2 =
(bsxfun(@times,B_Diffusion_PN2,eff_Diff_N2)*2)./(dr*Radius);
boundary_Diffusion_PN2 =
(boundary_Diffusion_PN2.*eff_Diff_N2).*(PN2i(end)*((1/(dr^2))+(2/(dr
*Radius))));
Conv_diff_PN2(N) = ((PN2_bulk-
PN2i(end))*MTC)*dr*((1/(dr^2))+(2/(dr*Radius)));

%% Rate section
RateTerm_heat = zeros(N,1);
RateTerm_Diffusion_PCO2 = zeros(N,1);
DX = zeros(N,1);
k_mpers = zeros(N,1);
rate_calcination = zeros(N,1);
converted_shell_moles = zeros(N,1);
initial_shell_moles = zeros(N,1);
CO2rate_output = zeros(N,1);
k_pers = zeros(N,1);
CCO2i = zeros(N,1);

for i = 2:N
    if Calcination_reaction_occurring(i) == 1
```

```
        if Particle_conversion(i) < 1
            % Rate constant calcs
            % [k_mpers(i),~] =
rateconst_fast(Tempi(i),N2_mf,H2O_mf,initial_SA);
            % T in K
            % from excel - See Rate const (with macro) spreadsheet
            if N2_mf ~= 0
                % experimental - first order wrt PCO2
%                 Ea_N2 = 505.0756; % kJ/mol
%                 k_pers(i) = 2.75270295*10^23*exp((-
1*Ea_N2*1000)/(8.3144598*Tempi(i))); % s-1
                % experimental - first order OLD
%                 Ea_N2 = 418.1631605; % kJ/mol
%                 k_pers(i) = 74262685948866400000*exp((-
1*Ea_N2*1000)/(8.3144598*Tempi(i))); % s-1
                % modelled - Intrinsic
%                 Ea_N2 = 739.3858; % kJ/mol
%                 k_pers(i) = (1.85749*10^32)*exp((-
1*Ea_N2*1000)/(8.3144598*Tempi(i))); % s-1

                % modelled - Intrinsic, averaged temperatures
                Ea_N2 = 1157.9; % kJ/mol
                k_pers(i) = (3.67166*10^51)*exp((-
1*Ea_N2*1000)/(8.3144598*Tempi(i))); % s-1


                % Arbitary values
%                 Ea_N2 = 250; % kJ/mol
%                 k_pers(i) = (1*10^12)*exp((-
1*Ea_N2*1000)/(8.3144598*Tempi(i))); % s-1


                k_mpers(i) = k_pers(i)/initial_SA; % convert units
to m/s by dividing by inital specific surface area (m2/m3)

                CCO2i(i) = (PCO2i(i)/(8.3144598*Tempi(i))); % mol/m3
                rate_calcination(i) = k_mpers(i)*CCO2i(i)*SA(i)*(1-
(PCO2i(i)/PCO2eq(i))); % mol/m3.s = m/s * mol/m3 * m2/m3 * Pa/Pa

            elseif H2O_mf ~= 0
                if PCO2i(i) > 5.5*10^4
%                 % experimental - first order wrt PCO2
%                     Ea_H2O = 326.2929; % kJ/mol
%                     k_pers(i) = 1.9217157*10^16*exp((-
1*Ea_H2O*1000)/(8.3144598*Tempi(i))); % s-1
%                 experimental - first order OLD
%                 Ea_H2O = 243.4034835; % kJ/mol
%                 k_pers(i) = 7352064045254*exp((-
1*Ea_H2O*1000)/(8.3144598*Tempi(i))); % s-1
%
%                 % modelled - intrinsic
%                     Ea_H2O = 803.58211; % kJ/mol
%                     k_pers(i) = (6.21895882*10^36)*exp((-
1*Ea_H2O*1000)/(8.3144598*Tempi(i))); % s-1 50000597174.76

%                 % Arbitary values
```

```
%                 Ea_H2O = 250; % kJ/mol
%                 k_pers(i) = (1*10^12)*exp((-
1*Ea_H2O*1000)/(8.3144598*Tempi(i))); % s-1

%                  % modelled - intrinsic, averaged temperature
                    Ea_H2O = 241.51453; % kJ/mol
                    k_pers(i) = 9.8403856*10^12*exp((-
1*Ea_H2O*1000)/(8.3144598*Tempi(i))); % s-1


                    k_mpers(i) = k_pers(i)/initial_SA; % convert
units to m/s by dividing by inital specific surface area (m2/m3)

                % restrict zone of langmuir-hinshelwood use based
on PCO2 range
                % Langmuir-Hinshelwood
                % -rc = (SA/RT)*kc * ( PCO2/( K_A + (K_B*PH2O) +
(K_C*PCO2) + (K_D*PH2O*PCO2) + (K_E*PH2O^2*PCO2) ))
                % b(1)=K_A; b(2)=K_B; b(3)=K_C; b(4)=K_D;
b(5)=K_E;
                    bs = [-5.542729;-1.372258e-07;6.7593158e-
05;3.8550888e-10;9.862937e-15];
                    rate_calcination(i) =
(SA(i)/(8.3144598*Tempi(i)))*k_mpers(i)*(PCO2i(i)/( bs(1) +
(bs(2)*PH2Oi(i)) + (bs(3)*PCO2i(i)) + (bs(4)*PH2Oi(i)*PCO2i(i)) +
(bs(5)*(PH2Oi(i)^2)*PCO2i(i)) ))*(1-(PCO2i(i)/PCO2eq(i)));



%                     CCO2i(i) = (PCO2i(i)/(8.3144598*Tempi(i))); %
mol/m3
%                    rate_calcination(i) =
k_mpers(i)*CCO2i(i)*SA(i)*(1-(PCO2i(i)/PCO2eq(i))); % mol/m3.s = m/s
* mol/m3 * m2/m3 * Pa/Pa


            else
                rate_calcination(i) = 0;
            end
        end



%             RateTerm_heatPLOT(i) = rate_calcination(i)*(-
178*1000)*(1-Particle_conversion(i))*shell_vol(i); % J/s

            RateTerm_heat(i) = rate_calcination(i)*((-
178*1000)/rho_Cp(i))*(1-Particle_conversion(i)); % K/s  = (mol/m3.s
* J/mol) / J/m3.K
            RateTerm_Diffusion_PCO2(i) =
rate_calcination(i)*8.3144598*Tempi(i)*(1-Particle_conversion(i)); %
Pa/s  = (mol/m3.s * J/mol.K * K)
            CO2rate_output(i) = rate_calcination(i)*shell_vol(i)*(1-
Particle_conversion(i)); % mol/s = mol/m3.s * m3

            % shell volumes cancel out
```

```
            % converted_shell_moles(i) = rate_calcination(i)*(1-
Particle_conversion(i))*shell_vol(i);
            % initial_shell_moles(i) =
molar_rho_CaCO3_initial*shell_vol(i);
            converted_shell_moles(i) = rate_calcination(i)*(1-
Particle_conversion(i));
            initial_shell_moles(i) = molar_rho_CaCO3_initial;
            DX(i) = converted_shell_moles(i) /
initial_shell_moles(i);
        else
            RateTerm_heat(i) = 0;
            RateTerm_Diffusion_PCO2(i) = 0;
            DX(i) = 0;
        end
    else
        RateTerm_heat(i) = 0;
        RateTerm_Diffusion_PCO2(i) = 0;
        DX(i) = 0;
    end
end

RateTerm_heat(1) = RateTerm_heat(2);
RateTerm_Diffusion_PCO2(1) = RateTerm_Diffusion_PCO2(2);
Particle_conversion(1) = Particle_conversion(2);
DX(1) = DX(2);


%% Finalise differential
DT = (A_heat*Tempi) + (B_heat*Tempi) + boundary_heat + RateTerm_heat
+ Conv_heat;
DPCO2 = (A_Diffusion_PCO2*PCO2i) + (B_Diffusion_PCO2*PCO2i) +
boundary_Diffusion_PCO2 + RateTerm_Diffusion_PCO2 + Conv_diff_PCO2;
DPH2O = (A_Diffusion_PH2O*PH2Oi) + (B_Diffusion_PH2O*PH2Oi) +
boundary_Diffusion_PH2O + Conv_diff_PH2O;
DPN2 = (A_Diffusion_PN2*PN2i) + (B_Diffusion_PN2*PN2i) +
boundary_Diffusion_PN2 + Conv_diff_PN2;

DT_DPCO2_DPH2O_DPN2_DX = [DT; DPCO2; DPH2O; DPN2; DX];

%% Save results
if ~mod(iteration,100)

%     disp(fCCO2(:));
%     disp(t);

    % 2437032 is the envelope density of longcliffe in g/m3
    CO2_mol_per_gs_out(k,1) =
sum(CO2rate_output)/(2437032*(4/3)*pi*(Radius^3)); % mol/g.s
%     for i = 1:N
%         if Calcination_reaction_occurring(i) == 0
%             RateCalcOut(k-1,i) = 0;
%         else
%             RateCalcOut(k-1,i) = rate_calcination(i);
%         end
%     end
    RateCalcOut(k-1,:) = rate_calcination;
```

```
%     RateCalcOut(k-1,:) = CO2rate_output;

    Calcination_reaction_occuring_out(k,:) = (CO2rate_output ~= 0)';
    Conversion_overall(k-1,:) = Particle_conversion';
    RateTerm_Heat_main(k-1,:) = (RateTerm_heat.*rho_Cp.*shell_vol)';
%J/s
%     RateTerm_Diffusion_main(k-1,:) = RateTerm_Diffusion_PCO2';
    RateTerm_Diffusion_main(k-1,:) = CO2rate_output'; %mol/s
    timetaken(k,1) = t;
    k = k + 1;
end

iteration = iteration + 1;

if ~mod(iteration,5000)
    disp(t);
end

return

%% END OF FILE
```

File name: NEW_conversion_calc_fast.*m*

```
function
[rho_Cp,h,eff_thermal_conductivity,masstransfercoefficent,eff_Diff_C
O2,eff_Diff_H2O,eff_Diff_N2,initial_SA,Surface_area,SA_CaCO3_specifi
c,Particle_porosity] = ...
NEW_conversion_calc_fast(T_bulk,T,To,Radius,Limestone_type,H2O_mf,N2
_mf,CO2_mf,Particle_conversion)
%% Calculate temperature, partial pressure and conversion dependant
parameters
%% Variables
N2_RMM = 28.0134; % g/mol
CO2_RMM = 44.01; % g/mol
H2O_RMM = 18.02; % g/mol

E_kB_CO2 = 195.2; % K
E_kB_N2 = 71.4; % K
E_kB_H2O = 809.1; % K
sigma_CO2 = 3.941; % Angstroms
sigma_H2O = 2.641; % Angstroms
sigma_N2 = 3.798; % Angstroms

MCaO = 56.0774; % g/mol = kg/kmol
MCaCO3 = 100.0869; % g/mol = kg/kmol

% Specific surface areas
if strcmp(Limestone_type,'Longcliffe')
    SA_LC = 0.057; % m2/g
    SA_CaCO3 = SA_LC*1000; % m2/kg
elseif strcmp(Limestone_type,'Havelock')
    SA_HL = 0.46; % m2/g
```

```
    SA_CaCO3 = SA_HL*1000; % m2/kg
elseif strcmp(Limestone_type,'Cadomin')
    SA_CM = 0.21; % m2/g
    SA_CaCO3 = SA_CM*1000; % m2/kg
elseif strcmp(Limestone_type,'Imeco')
    SA_IM = 1.05; % m2/g
    SA_CaCO3 = SA_IM*1000; % m2/kg
end
SA_CaO = 16.17*1000; % m2/kg

if strcmpi(Limestone_type,'Longcliffe')
    Porosity_CaCO3_LC = (-349.567*Radius + 0.2398)*100; % % from a
fit in density data spread sheet
    Skeletal_p_LC = 2.82; %g/cm3 Longcliffe
    CaCO3_porosity = Porosity_CaCO3_LC/100; % 100 convert from
percentage
    CaCO3_density = Skeletal_p_LC*1000; % *1,000 to convert g/cm3 to
kg/m3
elseif strcmpi(Limestone_type,'Havelock')
%     Porosity_CaCO3_HL = 3.42; % %
    Porosity_CaCO3_HL = 13.89;
    Skeletal_p_HL = 2.92; %g/cm3 Havelock
    CaCO3_porosity = Porosity_CaCO3_HL/100; % 100 convert from
percentage
    CaCO3_density = Skeletal_p_HL*1000; % *1,000 to convert g/cm3 to
kg/m3
elseif strcmpi(Limestone_type,'Cadomin')
%     Porosity_CaCO3_CM = 3.10; % %
    Porosity_CaCO3_CM = 15.13;
    Skeletal_p_CM = 2.94; %g/cm3 Cadomin
    CaCO3_porosity = Porosity_CaCO3_CM/100; % 100 convert from
percentage
    CaCO3_density = Skeletal_p_CM*1000; % *1,000 to convert g/cm3 to
kg/m3
elseif strcmpi(Limestone_type,'Imeco')
%     Porosity_CaCO3_IM = 3.31; % %
    Porosity_CaCO3_IM = 15.36;
    Skeletal_p_IM = 2.90; %g/cm3 Imeco
    CaCO3_porosity = Porosity_CaCO3_IM/100; % 100 convert from
percentage
    CaCO3_density = Skeletal_p_IM*1000; % *1,000 to convert g/cm3 to
kg/m3
end

Skeletal_p_CaO = 3.45; % g/cm3
CaO_density = Skeletal_p_CaO*1000; % kg/m3
initial_SA = SA_CaCO3*CaCO3_density*(1-CaCO3_porosity);

FlowRate_at_20 = 50; % cm3/s
FlowRate_at_T = FlowRate_at_20*T_bulk/(20+273);
FlowRate_at_T = FlowRate_at_T/1000000; % m3/s
% Bed_diameter = 25.5; % mm
% WallThickness = 2; % mm
% Bed_area = (((Bed_diameter-(2*WallThickness))/2000)^2)*3.14; % m2
Bed_area = 0.00036286625; % m2
Superficial_gas_v = FlowRate_at_T/Bed_area; % m/s
```

```
if N2_mf ~= 0
    E_kB_combined = (E_kB_CO2*E_kB_N2)^0.5;
    sigma_combined = 0.5*(sigma_CO2 + sigma_N2);
    RMM_gas2 = N2_RMM;
elseif H2O_mf ~= 0
    mewp_star = 1.85/(sqrt(E_kB_H2O*(sigma_H2O)^3));
    tp_star = (mewp_star^2)/sqrt(8);
    alphan = 2.65; % Angstroms cubed for CO2
    alphan_star = alphan/((sigma_H2O)^3);
    zeta = 1 + alphan_star*tp_star*((E_kB_H2O/(2*E_kB_CO2))^0.5);
    E_kB_combined = ((E_kB_CO2*E_kB_H2O)^0.5)*(zeta^2);
    sigma_combined = (0.5*(sigma_CO2 + sigma_H2O))*(zeta^(-1/6));
    RMM_gas2 = H2O_RMM;
end

Pressure = 1; % atm,
% Don't panic! Yes, it says atmospheres. This is correct, doesn't
need to be in Pa like the rest of the script is. Look at page 526 TP
- bird, stuart and lightfoot

% Collision Integral
TkB_E_combined = T_bulk/E_kB_combined;
% from fit of collision integral Omega11 and kBT/e
omega11_combined = 1.135*TkB_E_combined^(-0.525) + 0.3809;

% Bulk Gas Diffusivity, m2/s
Bulk_Diff = (0.0018583*1e-
4)*(((T_bulk^3)*((1/CO2_RMM)+(1/RMM_gas2)))^0.5)/(Pressure*(sigma_co
mbined^2)*omega11_combined);

%% Determine which variables used and what values they take
% Fitting
if H2O_mf ~= 0
    if T_bulk < 380
        H2O_Dynamic_viscosity_at_T = 1.25E-05; % Dynamic Viscosity
(Pa.s)
        H2O_Cp_at_T = 2.0799*1000; % Specific heat capacity, Cp,
(J/kg.K)
        H2O_Density_at_T = 0.58601; % Density (kg/m3)
        H2O_Thermal_conductivity_at_T = 0.025561; % Thermal
conductivity (W/m.K)
    else
        % Dynamic Viscosity (Pa.s)
        H2O_Dynamic_viscosity_at_T = -3.423e-12*T_bulk^2 + 4.548e-
08*T_bulk + -4.54e-06;

        % Specific heat capacity, Cp, (J/kg.K)
        H2O_Cp_at_T = 2.875e+05*exp(-0.01978*T_bulk) +
1688*exp(0.0003045*T_bulk);

        % Density (kg/m3)
        H2O_Density_at_T = 177*T_bulk^-0.9711;

        % Thermal conductivity (W/m.K)
        H2O_Thermal_conductivity_at_T = (5.06e-6)*T_bulk^1.427;
```

```
    end
elseif N2_mf ~= 0
    % Dynamic Viscosity (Pa.s)
    N2_Dynamic_viscosity_at_T = 3.346e-05*exp(0.000356*T_bulk) + -
3.138e-05*exp(-0.001625*T_bulk);

    % Specific heat capacity, Cp, (J/kg.K)
    N2_Cp_at_T = 1253*exp(-((T_bulk-1795)/2993)^2) + 131.7*exp(-
((T_bulk-12.03)/344.1)^2);

    % Density (kg/m3)
    N2_Density_at_T = 342.3*T_bulk^-1;

    % Thermal conductivity (W/m.K)
    N2_Thermal_conductivity_at_T = 0.0002866*T_bulk^0.7873;

end
% Dynamic Viscosity (Pa.s)
CO2_Dynamic_viscosity_at_T = -1.35e-11*T_bulk^2 + 5.495e-08*T_bulk +
-1.603e-07;

% Specific heat capacity, Cp, (J/kg.K)
CO2_Cp_at_T = 1307*exp(3.139e-05*T_bulk) + -852*exp(-
0.002004*T_bulk);

% Density (kg/m3)
CO2_Density_at_T = 553.3*T_bulk^(-1.005);

% Thermal conductivity (W/m.K)
CO2_Thermal_conductivity_at_T = 0.0004854*T_bulk^0.7568 -0.01986;

%% Chapman Enskog coefficent, pg27 of Bird, Stuart and Lightfoot,
eqn(1.4-16)
if H2O_mf ~= 0
    Phi_CO2 =
((1+((CO2_Dynamic_viscosity_at_T/CO2_Dynamic_viscosity_at_T)^0.5)*(C
O2_RMM/CO2_RMM)^0.25)^2)/(sqrt(8)*(1+CO2_RMM/CO2_RMM)^0.5);
    Phi_CO2_H2O =
((1+((CO2_Dynamic_viscosity_at_T/H2O_Dynamic_viscosity_at_T)^0.5)*(C
O2_RMM/H2O_RMM)^0.25)^2)/(sqrt(8)*(1+CO2_RMM/H2O_RMM)^0.5);
    Phi_H2O_CO2 =
((1+((H2O_Dynamic_viscosity_at_T/CO2_Dynamic_viscosity_at_T)^0.5)*(H
2O_RMM/CO2_RMM)^0.25)^2)/(sqrt(8)*(1+H2O_RMM/CO2_RMM)^0.5);
    Phi_H2O =
((1+((H2O_Dynamic_viscosity_at_T/H2O_Dynamic_viscosity_at_T)^0.5)*(H
2O_RMM/H2O_RMM)^0.25)^2)/(sqrt(8)*(1+H2O_RMM/H2O_RMM)^0.5);

    Sigma_x_Phi_CO2_H2O = CO2_mf*Phi_CO2 + H2O_mf*Phi_CO2_H2O;
    Sigma_x_Phi_H2O_CO2 = CO2_mf*Phi_H2O_CO2 + H2O_mf*Phi_H2O;
elseif N2_mf ~= 0
    Phi_CO2 =
((1+((CO2_Dynamic_viscosity_at_T/CO2_Dynamic_viscosity_at_T)^0.5)*(C
O2_RMM/CO2_RMM)^0.25)^2)/(sqrt(8)*(1+CO2_RMM/CO2_RMM)^0.5);
    Phi_CO2_N2 =
((1+((CO2_Dynamic_viscosity_at_T/N2_Dynamic_viscosity_at_T)^0.5)*(CO
2_RMM/N2_RMM)^0.25)^2)/(sqrt(8)*(1+CO2_RMM/N2_RMM)^0.5);
```

```
    Phi_N2_CO2 =
((1+((N2_Dynamic_viscosity_at_T/CO2_Dynamic_viscosity_at_T)^0.5)*(N2
_RMM/CO2_RMM)^0.25)^2)/(sqrt(8)*(1+N2_RMM/CO2_RMM)^0.5);
    Phi_N2 =
((1+((N2_Dynamic_viscosity_at_T/N2_Dynamic_viscosity_at_T)^0.5)*(N2_
RMM/N2_RMM)^0.25)^2)/(sqrt(8)*(1+N2_RMM/N2_RMM)^0.5);

    Sigma_x_Phi_CO2_N2 = CO2_mf*Phi_CO2 + N2_mf*Phi_CO2_N2;
    Sigma_x_Phi_N2_CO2 = CO2_mf*Phi_N2_CO2 + N2_mf*Phi_N2;
end

%% Calculate the mixed gas properties
if H2O_mf ~= 0
    Thermal_conductivity_gas =
(CO2_mf*(CO2_Thermal_conductivity_at_T/Sigma_x_Phi_CO2_H2O)) +
(H2O_mf*(H2O_Thermal_conductivity_at_T/Sigma_x_Phi_H2O_CO2));
    Cp_gas = (CO2_mf*(CO2_Cp_at_T/Sigma_x_Phi_CO2_H2O)) +
(H2O_mf*(H2O_Cp_at_T/Sigma_x_Phi_H2O_CO2));
    Dynamic_viscosity_gas =
(CO2_mf*(CO2_Dynamic_viscosity_at_T/Sigma_x_Phi_CO2_H2O)) +
(H2O_mf*(H2O_Dynamic_viscosity_at_T/Sigma_x_Phi_H2O_CO2));
    Density_gas = (CO2_mf*(CO2_Density_at_T/Sigma_x_Phi_CO2_H2O)) +
(H2O_mf*(H2O_Density_at_T/Sigma_x_Phi_H2O_CO2));
elseif N2_mf ~= 0
    Thermal_conductivity_gas =
(CO2_mf*(CO2_Thermal_conductivity_at_T/Sigma_x_Phi_CO2_N2)) +
(N2_mf*(N2_Thermal_conductivity_at_T/Sigma_x_Phi_N2_CO2));
    Cp_gas = (CO2_mf*(CO2_Cp_at_T/Sigma_x_Phi_CO2_N2)) +
(N2_mf*(N2_Cp_at_T/Sigma_x_Phi_N2_CO2));
    Dynamic_viscosity_gas =
(CO2_mf*(CO2_Dynamic_viscosity_at_T/Sigma_x_Phi_CO2_N2)) +
(N2_mf*(N2_Dynamic_viscosity_at_T/Sigma_x_Phi_N2_CO2));
    Density_gas = (CO2_mf*(CO2_Density_at_T/Sigma_x_Phi_CO2_N2)) +
(N2_mf*(N2_Density_at_T/Sigma_x_Phi_N2_CO2));
end

%% Particle Reynolds number calculation
Re_p =
(Density_gas.*(Superficial_gas_v*(Radius*2)))/Dynamic_viscosity_gas;



%% Prandtl number calculation
% compares heat conduction to convection, if <<1 then conduction
dominant
Pr = (Cp_gas.*Dynamic_viscosity_gas)/Thermal_conductivity_gas;

%% Nusselt number calculation
Nu = 2 + 0.6*((Re_p.^0.5)*(Pr.^(1/3)));

%% Heat transfer coefficent
% The characteristic length here should be diameter, in Biot number
it should be vol/area.
h = Nu*Thermal_conductivity_gas/(2*Radius); % W/m2.K

%% Mass transfer coefficent, m/s
```

```
Schmidt_num = Dynamic_viscosity_gas/(Density_gas*Bulk_Diff);
% At Reynolds numbers ranging from 2 to 12000 and Schmidt number
ranging from
% 0.6 to 2.7, Froessling (1939) and Evnochides and Thodos (1959)
developed the
% mass transfer coefficient for a single sphere and represented as
follows:
% Sh = 2 + 0.552Re^(1/7)Sc^(1/3)
Sherwood_num = 2 + (0.552*Re_p^(1/7))*(Schmidt_num^(1/3));

masstransfercoefficent = (Sherwood_num.*Bulk_Diff)./(2*Radius);

%% Conversion
% expansion factor = Z
expansion_factor = (MCaO/MCaCO3)*(CaCO3_density/CaO_density);

% Porosity
Particle_porosity = CaCO3_porosity-((expansion_factor-1).*(1-
CaCO3_porosity).*Particle_conversion);

% Cp
Cp_CaCO3_20C = (785+815)/2; % J/kg.K % A Review and Evaluation of
Specific
% Heat Capacities of Rocks, Minerals, and Subsurface Fluids. Part 1:
% Minerals and Nonporous Rocks Douglas W. Waples and Jacob S. Waples
Cp_CaCO3_normalised_20 = (8.95e-10)*To^3 - (2.13e-6)*To^2 +
0.00172*To + 0.716;
Cp_CaCO3_normalised_Temp = (8.95e-10).*T.^3 - (2.13e-6).*T.^2 +
0.00172.*T + 0.716;
Cp_CaCO3 =
Cp_CaCO3_20C.*(Cp_CaCO3_normalised_Temp./Cp_CaCO3_normalised_20); %
J/kg.K

Cp_CaO_20C = 750; % J/kg.K % A Review and Evaluation of Specific
% Heat Capacities of Rocks, Minerals, and Subsurface Fluids. Part 1:
% Minerals and Nonporous Rocks Douglas W. Waples and Jacob S. Waples
Cp_CaO_normalised_20 = (8.95e-10)*To^3 - (2.13e-6)*To^2 + 0.00172*To
+ 0.716;
Cp_CaO_normalised_Temp = (8.95e-10).*T.^3 - (2.13e-6).*T.^2 +
0.00172.*T + 0.716;
Cp_CaO = Cp_CaO_20C.*(Cp_CaO_normalised_Temp./Cp_CaO_normalised_20);
% J/kg.K

rho_Cp = Particle_porosity.*(CaO_density.*Cp_CaO)+(1-
Particle_porosity).*(CaCO3_density.*Cp_CaCO3); % J/m3.K

Thermal_conductivity_CaCO3 = 2.37; %W/m.K @25-100C     2.181041654;
%W/m.K @30C
Thermal_conductivity_CaO = (741.6.*T.^-0.9441 + 6.409);
Thermal_conductivity_solid =
(1./((Particle_conversion./Thermal_conductivity_CaO) + (1-
Particle_conversion)./Thermal_conductivity_CaCO3)); % W/m.K

Surface_area = ((SA_CaO.*Particle_conversion) + (SA_CaCO3.*(1-
Particle_conversion))).*...
```

```
    (((Particle_conversion./CaO_density) + (1-
Particle_conversion)./CaCO3_density).^(-1)).*(1-Particle_porosity);
% m2/m3

SA_CaCO3_specific = SA_CaCO3.*(1-
Particle_conversion).*CaCO3_density.*(1-Particle_porosity); % m2/g

%% Knudsen Diffusion, m2/s
Knud_Diff_CO2 =
((194.*Particle_porosity)./Surface_area).*((T./CO2_RMM).^0.5);
Knud_Diff_H2O =
((194.*Particle_porosity)./Surface_area).*((T./H2O_RMM).^0.5);
Knud_Diff_N2 =
((194.*Particle_porosity)./Surface_area).*((T./N2_RMM).^0.5);

%% Effective Diffusivity, m2/s
eff_Diff_CO2 =
(Particle_porosity.^2).*(((1./Bulk_Diff)+(1./Knud_Diff_CO2)).^-1);
eff_Diff_H2O =
(Particle_porosity.^2).*(((1./Bulk_Diff)+(1./Knud_Diff_H2O)).^-1);
eff_Diff_N2 =
(Particle_porosity.^2).*(((1./Bulk_Diff)+(1./Knud_Diff_N2)).^-1);

%% Use extended maxwell model for effective heat transfer coefficent
% W/m.K
eff_thermal_conductivity =
Thermal_conductivity_solid.*(((((2*Thermal_conductivity_solid)./Ther
mal_conductivity_gas)+1)-
(2*Particle_porosity.*((Thermal_conductivity_solid./Thermal_conducti
vity_gas)-1))))...
./((((2*Thermal_conductivity_solid)./Thermal_conductivity_gas)+1)+(P
article_porosity.*((Thermal_conductivity_solid./Thermal_conductivity
_gas)-1)))); % W/m.K


return



%% END OF FILE
```

File name: PCO2eq_calc_fast.*m*

```
function [PCO2eq] = PCO2eq_calc_fast(T)
%% Equilibrium partial pressure of CO2
% from thermovader modelling of CaCO3 decomposition
% T must come in as a column vector

% This function works in °C not °K
T = T - 273.15; % Convert °K to °C.

eqm_conc = zeros(size(T));
for i = 1:size(T,1)
    if T(i) < 600
        eqm_conc(i) = 0; % 0.003;
    else
```

```
        eqm_conc(i) = 8.1805653997E-13*(T(i)^5)...  in bar
            - 2.8344129739E-09*(T(i)^4)...
            + 3.9788844687E-06*(T(i)^3)...
            - 2.8198493271E-03*(T(i)^2)...
            + 1.0062419480*(T(i))...
            - 1.4431450541E+02;
    end
end

eqm_conc((eqm_conc < 0)) = 0;
PCO2eq = eqm_conc.*100000; % Convert Bar to Pa

return


%% END OF FILE
```

Appendix V – Copyright Permissions

Literature review – figure 1

This Agreement between Mr. Peter Clough ("You") and Elsevier ("Elsevier") consists of your license details and the terms and conditions provided by Elsevier and Copyright Clearance Center.

License Number	4130161401761
License date	Jun 15, 2017
Licensed Content Publisher	Elsevier
Licensed Content Publication	Progress in Energy and Combustion Science
Licensed Content Title	The calcium looping cycle for large-scale CO2 capture
Licensed Content Author	J. Blamey,E.J. Anthony,J. Wang,P.S. Fennell
Licensed Content Date	Apr 1, 2010
Licensed Content Volume	36
Licensed Content Issue	2
Licensed Content Pages	20
Start Page	260
End Page	279
Type of Use	reuse in a thesis/dissertation
Portion	figures/tables/illustrations
Number of figures/tables/illustrations	1
Format	both print and electronic
Are you the author of this Elsevier article?	No
Will you be translating?	No
Order reference number	
Original figure numbers	1
Title of your thesis/dissertation	An Investigation into H2 Production by Sorbent Enhanced Steam Reforming of Biomass

Literature review - Figure 4

This Agreement between Mr. Peter Clough ("You") and Elsevier ("Elsevier") consists of your license details and the terms and conditions provided by Elsevier and Copyright Clearance Center.

License Number	4130170398644

License date	Jun 15, 2017
Licensed Content Publisher	Elsevier
Licensed Content Publication	Energy
Licensed Content Title	Hydrogen production through sorption-enhanced steam methane reforming and membrane technology: A review
Licensed Content Author	L. Barelli,G. Bidini,F. Gallorini,S. Servili
Licensed Content Date	Apr 1, 2008
Licensed Content Volume	33
Licensed Content Issue	4
Licensed Content Pages	17
Start Page	554
End Page	570
Type of Use	reuse in a thesis/dissertation
Intended publisher of new work	other
Portion	figures/tables/illustrations
Number of figures/tables/illustrations	7
Format	both print and electronic
Are you the author of this Elsevier article?	No
Will you be translating?	No
Order reference number	
Original figure numbers	7
Title of your thesis/dissertation	An Investigation into H2 Production by Sorbent Enhanced Steam Reforming of Biomass

Literature review - Figures 6 and 7

This Agreement between Mr. Peter Clough ("You") and Elsevier ("Elsevier") consists of your license details and the terms and conditions provided by Elsevier and Copyright Clearance Center.

License Number	4130170669162
License date	Jun 15, 2017
Licensed Content Publisher	Elsevier
Licensed Content Publication	Chemical Engineering Research and Design
Licensed Content Title	The calcium looping cycle for CO2 capture from power generation, cement manufacture and hydrogen production

Licensed Content Author	C.C. Dean,J. Blamey,N.H. Florin,M.J. Al-Jeboori,P.S. Fennell
Licensed Content Date	Jun 1, 2011
Licensed Content Volume	89
Licensed Content Issue	6
Licensed Content Pages	20
Start Page	836
End Page	855
Type of Use	reuse in a thesis/dissertation
Intended publisher of new work	other
Portion	figures/tables/illustrations
Number of figures/tables/illustrations	2
Format	both print and electronic
Are you the author of this Elsevier article?	No
Will you be translating?	No
Order reference number	
Original figure numbers	10, 11
Title of your thesis/dissertation	An Investigation into H2 Production by Sorbent Enhanced Steam Reforming of Biomass

Literature review – Figure 8

This Agreement between Mr. Peter Clough ("You") and Elsevier ("Elsevier") consists of your license details and the terms and conditions provided by Elsevier and Copyright Clearance Center.

License Number	4130170805118
License date	Jun 15, 2017
Licensed Content Publisher	Elsevier
Licensed Content Publication	Chemical Engineering Research and Design
Licensed Content Title	The calcium looping cycle for CO2 capture from power generation, cement manufacture and hydrogen production
Licensed Content Author	C.C. Dean,J. Blamey,N.H. Florin,M.J. Al-Jeboori,P.S. Fennell
Licensed Content Date	Jun 1, 2011
Licensed Content Volume	89
Licensed Content Issue	6
Licensed Content Pages	20
Start Page	836

End Page	855
Type of Use	reuse in a thesis/dissertation
Intended publisher of new work	other
Portion	figures/tables/illustrations
Number of figures/tables/illustrations	1
Format	both print and electronic
Are you the author of this Elsevier article?	No
Will you be translating?	No
Order reference number	
Original figure numbers	1
Title of your thesis/dissertation	An Investigation into H2 Production by Sorbent Enhanced Steam Reforming of Biomass

Literature review – Figure 9

This Agreement between Mr. Peter Clough ("You") and Elsevier ("Elsevier") consists of your license details and the terms and conditions provided by Elsevier and Copyright Clearance Center.

License Number	4130170927121
License date	Jun 15, 2017
Licensed Content Publisher	Elsevier
Licensed Content Publication	International Journal of Greenhouse Gas Control
Licensed Content Title	Thermodynamic analysis of hydrogen production via chemical looping steam methane reforming coupled with in situ CO2 capture
Licensed Content Author	A. Antzara,E. Heracleous,D.B. Bukur,A.A. Lemonidou
Licensed Content Date	Jan 1, 2015
Licensed Content Volume	32
Licensed Content Issue	n/a
Licensed Content Pages	14
Start Page	115
End Page	128
Type of Use	reuse in a thesis/dissertation
Intended publisher of new work	other
Portion	figures/tables/illustrations
Number of figures/tables/illustrations	1

Format	both print and electronic
Are you the author of this Elsevier article?	No
Will you be translating?	No
Order reference number	
Original figure numbers	4
Title of your thesis/dissertation	An Investigation into H2 Production by Sorbent Enhanced Steam Reforming of Biomass

Literature review – Figure 10

This Agreement between Mr. Peter Clough ("You") and Elsevier ("Elsevier") consists of your license details and the terms and conditions provided by Elsevier and Copyright Clearance Center.

License Number	4130171038285
License date	Jun 15, 2017
Licensed Content Publisher	Elsevier
Licensed Content Publication	International Journal of Hydrogen Energy
Licensed Content Title	Enhanced hydrogen-rich gas production from steam gasification of coal in a pressurized fluidized bed with CaO as a CO2 sorbent
Licensed Content Author	Qinhui Wang,Nai Rong,Hongtao Fan,Yongjie Meng,Mengxiang Fang,Leming Cheng,Kefa Cen
Licensed Content Date	Apr 4, 2014
Licensed Content Volume	39
Licensed Content Issue	11
Licensed Content Pages	12
Start Page	5781
End Page	5792
Type of Use	reuse in a thesis/dissertation
Intended publisher of new work	other
Portion	figures/tables/illustrations
Number of figures/tables/illustrations	1
Format	both print and electronic
Are you the author of this Elsevier article?	No
Will you be translating?	No
Order reference number	

Original figure numbers	7
Title of your thesis/dissertation	An Investigation into H2 Production by Sorbent Enhanced Steam Reforming of Biomass

Literature review – Figure 11

This Agreement between Mr. Peter Clough ("You") and Elsevier ("Elsevier") consists of your license details and the terms and conditions provided by Elsevier and Copyright Clearance Center.

License Number	4130171242184
License date	Jun 15, 2017
Licensed Content Publisher	Elsevier
Licensed Content Publication	Energy
Licensed Content Title	Hydrogen production through sorption-enhanced steam methane reforming and membrane technology: A review
Licensed Content Author	L. Barelli,G. Bidini,F. Gallorini,S. Servili
Licensed Content Date	Apr 1, 2008
Licensed Content Volume	33
Licensed Content Issue	4
Licensed Content Pages	17
Start Page	554
End Page	570
Type of Use	reuse in a thesis/dissertation
Intended publisher of new work	other
Portion	figures/tables/illustrations
Number of figures/tables/illustrations	1
Format	both print and electronic
Are you the author of this Elsevier article?	No
Will you be translating?	No
Order reference number	
Original figure numbers	10
Title of your thesis/dissertation	An Investigation into H2 Production by Sorbent Enhanced Steam Reforming of Biomass

Literature review – Figure 12

Title:	Change of CO2 Carrying Capacity of CaO in Isothermal Recarbonation−Decomposition Cycles
Author:	Anton I. Lysikov, Aleksey N. Salanov, Aleksey G. Okunev
Publication:	Industrial & Engineering Chemistry Research
Publisher:	American Chemical Society
Date:	Jun 1, 2007

PERMISSION/LICENSE IS GRANTED FOR YOUR ORDER AT NO CHARGE

This type of permission/license, instead of the standard Terms & Conditions, is sent to you because no fee is being charged for your order. Please note the following:

- Permission is granted for your request in both print and electronic formats, and translations.
- If figures and/or tables were requested, they may be adapted or used in part.
- Please print this page for your records and send a copy of it to your publisher/graduate school.
- Appropriate credit for the requested material should be given as follows: "Reprinted (adapted) with permission from (COMPLETE REFERENCE CITATION). Copyright (YEAR) American Chemical Society." Insert appropriate information in place of the capitalized words.
- One-time permission is granted only for the use specified in your request. No additional uses are granted (such as derivative works or other editions). For any other uses, please submit a new request.

Literature review – Figure 13

This Agreement between Mr. Peter Clough ("You") and Elsevier ("Elsevier") consists of your license details and the terms and conditions provided by Elsevier and Copyright Clearance Center.

License Number	4130171440765
License date	Jun 15, 2017
Licensed Content Publisher	Elsevier

Licensed Content Publication	Chemical Engineering Research and Design
Licensed Content Title	The calcium looping cycle for CO2 capture from power generation, cement manufacture and hydrogen production
Licensed Content Author	C.C. Dean,J. Blamey,N.H. Florin,M.J. Al-Jeboori,P.S. Fennell
Licensed Content Date	Jun 1, 2011
Licensed Content Volume	89
Licensed Content Issue	6
Licensed Content Pages	20
Start Page	836
End Page	855
Type of Use	reuse in a thesis/dissertation
Intended publisher of new work	other
Portion	figures/tables/illustrations
Number of figures/tables/illustrations	1
Format	both print and electronic
Are you the author of this Elsevier article?	No
Will you be translating?	No
Order reference number	
Original figure numbers	3
Title of your thesis/dissertation	An Investigation into H2 Production by Sorbent Enhanced Steam Reforming of Biomass

Literature review – Figure 14

This Agreement between Mr. Peter Clough ("You") and Elsevier ("Elsevier") consists of your license details and the terms and conditions provided by Elsevier and Copyright Clearance Center.

License Number	4130180143265
License date	Jun 15, 2017
Licensed Content Publisher	Elsevier
Licensed Content Publication	Fuel
Licensed Content Title	On steam hydration of CaO-based sorbent cycled for CO2 capture
Licensed Content Author	John Blamey,Vasilije Manovic,Edward J. Anthony,Denis R. Dugwell,Paul S. Fennell
Licensed Content Date	Jun 15, 2015

Licensed Content Volume	150
Licensed Content Issue	n/a
Licensed Content Pages	9
Start Page	269
End Page	277
Type of Use	reuse in a thesis/dissertation
Intended publisher of new work	other
Portion	figures/tables/illustrations
Number of figures/tables/illustrations	1
Format	both print and electronic
Are you the author of this Elsevier article?	No
Will you be translating?	No
Order reference number	
Original figure numbers	3
Title of your thesis/dissertation	An Investigation into H2 Production by Sorbent Enhanced Steam Reforming of Biomass

Chapter 5 – full article

This Agreement between Mr. Peter Clough ("You") and Elsevier ("Elsevier") consists of your license details and the terms and conditions provided by Elsevier and Copyright Clearance Center.

License Number	4130180257220
License date	Jun 15, 2017
Licensed Content Publisher	Elsevier
Licensed Content Publication	Fuel
Licensed Content Title	Degradation study of a novel polymorphic sorbent under realistic post-combustion conditions
Licensed Content Author	Peter T. Clough,Matthew E. Boot-Handford,Ming Zhao,Paul S. Fennell
Licensed Content Date	Dec 15, 2016
Licensed Content Volume	186
Licensed Content Issue	n/a
Licensed Content Pages	6
Start Page	708

End Page	713
Type of Use	reuse in a thesis/dissertation
Intended publisher of new work	other
Portion	full article
Format	both print and electronic
Are you the author of this Elsevier article?	Yes
Will you be translating?	No
Order reference number	
Title of your thesis/dissertation	An Investigation into H2 Production by Sorbent Enhanced Steam Reforming of Biomass

Appendix VI – Materials Characterisation Methods

VI.1. BET (Brunauer–Emmett–Teller, analysed with BJH Barrett-Joyner-Halenda)

This non-destructive technique utilised the adsorption of N_2 molecules at 77K (boiling temperature of liquid N_2) to determine the specific BET surface area. By measuring the relative amount of pressure required to achieve a certain adsorption point the material can be assessed for its specific pore volume and pore area. Theory of this technique is widely available in the literature and is only suitable for pores >2 nm.

To conduct BET/BJH analysis, a clean BET penetrometer is first weighed to determine its empty weight. An amount of sample is then added to this penetrometer and its weight is recorded, typically 0.3-0.5 g for the work conducted here. After this, the penetrometer is sealed, insulated with a jacket and connected to the apparatus and a vacuum is applied. The instrument will gradually and precisely add N_2 into the penetrometer and determine the amount of N_2 adsorbed. After multiple steps the an adsorption isotherm is produced, a desorption isotherm is produced by gradually lowering the pressuring inside the penetrometer.

VI.2. MIP (Mercury Intrusion Porosimetry)

This destructive technique examines the pore structure of the material by injecting pressurised mercury into the sample. A similar technique is utilised as in the BET tests, a clean BET penetrometer is first weighed to determine its empty weight. An amount of sample is then added to this penetrometer and its weight is recorded, typically 0.5 g for the work conducted here. After this, the penetrometer is sealed, and a low pressure (<15 psi) test is conducted where the penetrometer and sample is effectively fully saturated with mercury. The filled penetrometer is then removed from the instrument and weighed to determine its filled weight. This is used for determining the sample mass specific data. The penetrometer is then inserted into the high pressure side of the instrument where more mercury is injected into the

penetrometer, measuring the pressure applied and amount of amount of additional mercury utilised. This gives a detailed description of the meso- and micro-pore structure of the sample.

VI.3. AccuPyc

AccuPyc is a non-destructive gas-displacement pycnometry which determines the skeletal density of the material. A large quantity of the sample (>1 g) is added into a vessel and weighed. The sample vessel is then inserted into the instrument and the instrument is sealed. Helium is used to fill the void space of the material and by difference the amount skeletal volume is determined.

VI.4. GeoPyc

Geopyc is a non-destructive solids displacement technology for determining the envelope density. A known quantity of sample is added into a sample vessel and mixed with a fine powder which fills the spaces around the sample. The instrument gently compresses and agitates the mixture to determine the space around the sample by comparing it to a test completed without the sample (maintaining the quantity of fine powder though).

VI.5. TGA-MS (Thermogravimetric analyser with mass spectrometer)

A TGA is effectively a very finely tuned balance that can operate at high temperatures and measure how the sample mass changes with time. The tests consist of weighing a blank sample pan then adding ~0.1-0.3 mg of sample onto the pan and then running a temperature and gas control program.

The mass spectrometer (if used) takes the exit gas stream and breaks the gas molecules down to the ionised molecules and then passes this ionised gas mixture through a strong magnetic field which splits/diverts the ions depending on how big and ionised they are. An output of ‘counts’ at each molecular weight is achieved which can be measured over time to determine how the gases evolved and changed as a reaction occurred within the TGA.

VI.6. XRF (X-ray Florescence)

This non-destructive technique involves packing a large quantity of sample (>5 g) into a sample container with a thin poly-propylene base. The sample container with sample is then inserted into an x-ray chamber where it is irradiated with x-rays. Some of these x-rays interact with the atoms of the sample and the atoms affected fluoresce with a signature pattern ("a fingerprint"), which is detected and interpreted by the instrument. A semi-quantitative (mass/mole percentages) result is outputted noting the amount of each element in the sample.

VI.7. XRD (X-ray Diffraction)

This non-destructive technique again utilises x-rays but by applying a range of incident angles the crystal structure of the material can be determined. The sample is typically ground to a fine powder and compacted into a shallow container where the machine rotates above it. The output from this technique are peaks of intensity at each 'theta' (angle of incidence or reflection) which via the Bragg equation is directly relatable to the crystal structure and crystallite size. The peaks are again a fingerprint of the material and can be correlated in tables to determine the materials present. Revelt refinement can be applied to produce a semi- quantitative analysis of the material. Only crystalline materials can be analysed by this technique.